Springer Series on
ATOMIC, OPTICAL, AND PLASMA PHYSICS 50

Springer Series on

ATOMIC, OPTICAL, AND PLASMA PHYSICS

The Springer Series on Atomic, Optical, and Plasma Physics covers in a comprehensive manner theory and experiment in the entire .eld of atoms and molecules and their interaction with electromagnetic radiation. Books in the series provide a rich source of new ideas and techniques with wide applications in .elds such as chemistry, materials science, astrophysics, surface science, plasma technology, advanced optics, aeronomy, and engineering. Laser physics is a particular connecting theme that has provided much of the continuing impetus for new developments in the f ield. The purpose of the series is to cover the gap between standard undergraduate textbooks and the research literature with emphasis on the fundamental ideas, methods, techniques, and results in the field.

47 Semiclassical Dynamics and Relaxation
By: D.S.F. Crothers

48 Theoretical Femtosecond Physics
Atoms andMolecules in Strong Laser Fields
By F. Großmann

49 Relativistic Collisions of Structured Atomic Particles
By A. Voitkiv and J. Ullrich

50 Cathodic Arcs
From Fractal Spots to Energetic Condensation
By A. Anders

51 Reference Data on Atomic Physics and Atomic Process
By B.M. Smirnov

Vols. 20–46 of the former Springer Series on Atoms and Plasmas are listed at the end of the book

André Anders

Cathodic Arcs

From Fractal Spots to Energetic Condensation

With 262 Figures and 25 Tables

Springer

André Anders
Plasma Applications Group
Lawrence Berkeley National Laboratory
Berkeley, CA
USA
aanders@lbl.gov

ISSN: 1615-5653
ISBN: 978-0-387-79107-4 e-ISBN: 978-0-387-79108-1
DOI: 10.1007/978-0-387-79108-1

Library of Congress Control Number: 2008929568

Printed on acid-free paper

springer.com

In memoriam Ingmar Kleberg (1971–2003).

Ingmar wrote an excellent PhD thesis on cathode spot processes, a significant contribution to the physics of arc spot operation and retrograde motion. He was a good friend whose time ended abruptly in a tragic accident. He is fondly remembered by his many friends.

Preface

Not too long ago, after watching Disney's *Hercules* movie, my then-6-year-old daughter tested me by asking, "Dad, did you know that there are four elements: Earth, Water, Air, and Lightning?" Because she did not use the common terms *Earth, Water, Air, and Fire*, it struck me that the Greeks may have had an appreciation for phases: just replace "element" by "phase," and you will see the parallel to the modern terminology: solid, liquid, gas, and *plasma*!

Although the *plasma* phase is by far the most prevalent in the universe (well, set aside the mysterious dark matter), we have little experience with it in our daily life. Most plasmas we encounter are man-made, be it the plasma in fluorescent discharge lamps, plasma displays, or in a welder's arc. In this book, a very special case of discharge plasma is explored, the plasma formed at electrodes.

Cathodic arc plasma deposition is one of the oldest and at the same time one of the modern, emerging deposition technologies. This is an apparently contradictory statement. I will span a view from more than a couple of centuries ago to recent research in the hope to transpire excitement, provide background knowledge, and review important progress.

Although cathodic arc plasma deposition belongs to the family of physical *vapor* deposition (PVD) techniques, I deliberately call it *plasma* deposition to emphasize an important feature: energetic condensation of plasma ions, as opposed to condensation of atoms from the neutral vapor phase. The synthesis of films from ions, each carrying substantial kinetic and potential energy, can lead to film properties that are unique.

As the name suggests, cathodic arcs are determined by cathode processes. Indeed, cathode processes are quite different than processes in other, less "violent" forms of discharges. The current densities and associated power densities at cathode spots are extremely high, and this is true despite the characteristic low cathode fall voltage of typically only 20 V. The electron emission processes involve non-stationary stages and phase transitions, ultimately leading to the destruction of the electron emission center. The phase transition from the solid

cathode material to plasma is precisely what enables operation of the arc discharge and what makes cathodic arc plasmas and the films deposited so special.

This book is written in the hope to be useful to the experts, practitioners, students, and newcomers alike. It is assumed that the reader is familiar with basic concepts of plasma physics and thin films. There are many excellent text books and review articles in the field, and therefore the basics are developed here only as they directly apply to cathodic arcs and the films produced. Each chapter contains an extensive list of references for further reading, and a very brief introduction to plasmas and sheaths is given in Appendix A.

Writing this book had its challenges. For one, our understanding is still far from complete, despite the impressive progress seen in experimental techniques and theoretical modeling. Yet, it turned out to be difficult to determine what is really secured knowledge based on accepted, self-consistent data and what are just hypotheses, even if plausible. The reasons for this difficulty are twofold. First, arc data scatter appreciably due to the nature of the cathode spot phenomena, and second, some theories contradict each other, even when each is self-consistent and in "good agreement with experimental observations," as usually claimed. The underlying problem in modeling is the choice of the simplifying assumptions, which are necessary to make due to the complex character of the arc phenomena. Therefore, in some instances, I failed in my desire to produce a text book that would be acceptable to all experts in the field. Sometimes I needed to divert to reviewing what has been done and leave it up to the reader and further research to select the most appropriate description of the nature of cathodic arcs and the films produced. Although I believe that the review portions are relatively extensive and inclusive, there is certainly work that has been overlooked or is not sufficiently appreciated. I will not claim to have produced a "balanced view."

There was the temptation to be as comprehensive and accurate as possible, which may have led to a huge book nobody could read and that may have never been finished. Perhaps all authors realize at some point that it is impossible to do a perfect job. Periods of productive work flow were interrupted by times of distraction and procrastination. Why writing another arc book? There has been a number of great books, and why could or should I add to this line of work? Having a special interest in history, I look with admiration at a series of books by Joseph Priestley (1767), Vasilii Petrov (1803), Hertha Ayrton (1902), Clement Child (1913), Igor Kesaev (1964, 1968), Vadim Rakhovskii (1970), James Lafferty (1980), Gennady Mesyats and Dmitry Proskurovsky (1989), and, last but not least, the edited Handbook by Raymond Boxman, David Sanders, and Phil Martin (1995). Each of them represented the state of knowledge and added substantially to the work of their predecessors. Not to count the numerous important publications that did not result in a book but became much cited classics in the field. Since the field is vital and much knowledge has been added in recent years, there appeared to be a lack of systematic presentation, and so I hope to provide a modern view on the field of cathode arcs and the coatings made with cathodic arc plasma.

A book like this one would not be possible without the input by many colleagues and friends. Here is the perfect opportunity to express my sincere gratitude for their generous help in finding the necessary supply of information, diagrams, illustrations, photographic material, raw data, etc. The list of the many dear colleagues is long, and if I listed them here, some may still be forgotten. So, I will only mention a few representative names of those who deserve special recognition. I will start with Ingmar Kleberg, a young friend of mine whose very untimely death in a mountaineering accident shocked us all. Some results of his thesis can be found in Chapter 3. I dedicate this book to him. Next, I should stress that this work was greatly influenced by the thinking of my former mentors, Burkhard Jüttner and Erhard Hantzsche, with whom I spent a very productive time in the 1980s in East Berlin before the Berlin Wall fell. From them I learned about explosive plasma formation and the special role of cathode surface conditions that lead to various arc modes and spot types. Special thanks go to Ian Brown, Berkeley, who introduced me to the world of charge state analysis and application of arc plasmas to thin films and multilayers. Ian is also one of the pioneers of combining arc plasmas and pulsed bias, enabling the synthesis of very special surfaces. His work planted a seed for the technique of stress control via atomic scale annealing with high-energy ions. Othon Monteiro, former staff scientist of the Plasma Applications Group, contributed greatly, especially on the issues of energetic condensation and metallization of semiconductor structures. Much of the data I was able to collect came through the help of the technical staff of the Plasma Applications Group (thanks to you, Bob MacGill, Michael Dickinson, Joe Wallig, Tom McVeigh) and the visitors of the Plasma Applications Group at Berkeley Lab; many of them have become distinguished researchers in the field. Just to name a few: Efim Oks (Russia), Gera Yushkov (Russia), Marcela Bilek (Australia), Jochen Schneider (Germany), Jochen Schein (Germany), Michael Keidar (USA), Johanna Rosén (Sweden), Sunnie Lim (Australia), Eungsun Byon (Korea), and Joakim Andersson (Sweden).

The list of helpful colleagues could go on and on, but here I will conclude by thanking my family for understanding that I was busy so many days and evenings. . .Love you, Christine, Mark, Mika, and George!

Berkeley, California *André Anders*

Contents

1

Introduction

Trying to understand the way nature works involves a most terrible test of human reasoning ability. It involves subtle trickery, beautiful tightropes of logic on which one has to walk in order not to make a mistake in predicting what will happen.

Richard P. Feynman, in: *The Meaning of It All*, 1963

Abstract The introduction contains the essence of the book in simplified language – the main ideas are outlined and summarized and some reasoning is provided for the structure of book. In essence, one follows the path of the cathode material from the solid through the plasma phase all the way to the condensed phase on the substrate, i.e., when a film has formed by energetic condensation.

The reader may have come across the terms "vacuum arcs" and "cathodic arcs" and wondered what the difference was, if there was any. To clarify this, let us first consider the term "vacuum arc." Obviously, it suggests that there was vacuum between the electrodes before the arc discharge was ignited, and therefore carriers of the electric current were initially absent. Once the discharge has started, one can observe tiny, mobile spots on the cathode surface, which are a characteristic of the kind of arc that is the subject of this book. These small bright spots are generically called "cathode spots," although we will see that there is a variety of spots and associated phenomena.

Cathode spots are centers of electron emission *and* plasma production. Electron emission alone is not sufficient for arc operation. Ions of the cathode material are produced, and it will be shown that they are crucial for the arc's cathode mechanism as well as for establishing the plasma, which by definition is quasi-neutral (i.e.,the amount of positive and negative charge is equal in a given volume of consideration). The plasma can be envisioned as a kind of fluid conductor between the electrodes.

A. Anders, *Cathodic Arcs*, DOI: 10.1007/978-0-387-79108-1_1,

Cathode spots are highly unusual physical objects and notoriously difficult to measure. The plasma pressure in cathode spots exceeds atmospheric pressure by orders of magnitude (so much for the accuracy of the term "vacuum arc"!). It is therefore not surprising that cathode processes observed at vacuum arcs can also be observed for arc discharges in the presence of some gas between electrodes. The gas, though, may have important secondary effects, especially on the surface conditions of the cathode. While the term "vacuum arc" is used to emphasize the absence of any significant gas pressure *before* the discharge, the term "cathodic arc" is more generally used because it includes vacuum arcs as well as arcs in gases. Arc discharges are always of the cathodic arc type as long as the overall cathode temperature is low. Cathodic arcs are always characterized by small, non-stationary cathode spots: a deeper reasoning will be given in Chapter 3 when we look at electron emission mechanisms.

The description above contains the qualifier "low temperature," indicating that the situation is somewhat more complicated. For example, there exists the possibility that the cathode can operate in a thermionic arc mode. Additionally, there are situations when the anode is not just a passive electron collector. If the anode is allowed to reach high temperatures, it may emit vapor of the anode material ("anodic arc") or material of the cathode that has previously condensed on the anode ("hot refractory anode arc"). These modes will be briefly mentioned in Chapter 3, but the main body of this book is limited to *cathodic* arcs with globally cold cathodes, where the plasma is produced at non-stationary cathode spots.

The plasma produced at cathode spots has many features that are rather unusual and often quite unique (though to some degree comparable to laser ablation plasmas). This makes working with cathodic arcs interesting, and sometimes challenging. Here is a list of some remarkable features of spots and spot-produced plasmas:

(i) The cathode spots are prolific producers of plasma of the cathode material. This feature makes cathodic arcs interesting to manufacturers of coatings – time is money!
(ii) The plasma emitted from spots is fully ionized.
(iii) In almost all cases, the plasma contains multiply charged ions, which especially for the refractory metals reach 3, 4, and even higher.
(iv) Even as the plasma contains multiply charged ions, there may be disproportionately large amounts of neutrals present: they are not produced at the active cathode spot but have other sources such as the cooling craters and evaporating macroparticles.
(v) Ions have a high velocity, typically about 10^4 m/s, and the ion flux is directed *away* from the cathode, hence they move in the "wrong" direction if judged by the concepts of usual discharge physics.
(vi) Because of (v), the electron current from the cathode must compensate the electric current associated with the ion flow, and therefore the electron current is larger than the total arc current (even some experts overlook this strange feature!).

(vii) All plasma parameters fluctuate due to the non-stationary nature of electron emission and plasma production at cathode spots.
(viii) The plasma is non-uniform because of its generation at tiny cathode spots. The plasma density near the spot is very high and drops sharply as the plasma expands.
(ix) Investigations of the cathode spot with increasingly sophisticated diagnostic techniques revealed ever smaller structures and shorter events, pointing to self-similar (fractal) properties in time and space.

The main body of the book starts with a relatively long and detailed consideration of the history of arc research and the development of coatings technology based on cathodic arcs. The observation of (initially unintentional) arcs was practically inevitable as soon as sufficient electrical energy could be stored. This puts the beginning of arc research to the mid 1700s. It is quite fascinating so see the struggle of "electricians" to grasp what is happening, and how the development of electrodynamics in the 1800s and plasma physics in the 1900s brought light to the mysteries. We will also see how economic needs and even politics affected arc technology in the second half of the twentieth century. I had great pleasure in digging deeper into both classic and rather unknown or forgotten literature, and hopefully the reader will feel the sense of (re-)discovery too.

The development of vacuum switches, or "vacuum interrupters," is not the subject of this book but needs to be mentioned in the context of vacuum arc physics and history because many discoveries and results came from that development. Some results from switching research are cited and utilized. In fact, much research related to cathode spots, spot modes, spot motion in magnetic fields, current chopping, etc., was motivated by the design and manufacture of switches for high currents and high voltage. Electrode phenomena were recognized as critical, and they are often the limiting components of these devices.

A center part of this book is the physics of cathode spots. I will not claim that all can be explained, even with the availability of modern, high-resolution characterization tools and advanced computation. Rather, it is a presentation of well-known processes and models at the interface of a solid (the cathode) and plasma on the one hand, and the conceptual emphasis on the time and space variations that govern electron emission and plasma generation processes on the other hand. Regarding the latter point, the book is different from previous texts and may be questioned by some. Based on the observation that the "characteristic size" and the "characteristic time," and derived physical parameters such as the "characteristic current density," become smaller and shorter in the history of research, i.e., with increasing resolution capability of measurement, we can state that the "noisy" properties of spots and plasma are *fractal*. The main feature of a fractal is self-similarity, that is, when properties and pattern appear similar regardless of the resolution.

To illustrate this point, let us pick the arc burning voltage, for example. We could measure it by connecting a voltmeter between the anode and cathode. Since the bandwidth of such a device is very limited, we would see some slow

variations but essentially measure an average voltage. This could be the RMS (root-mean-square) average, but it may be the specifics of the circuit response that somewhat determine (skew) the displayed value. Naturally, since we know that the actual value is fluctuating, we would opt to use a higher resolution device, such as an oscilloscope. We would see fluctuations on the scope's screen. The fractal property becomes obvious when changing the sweep speed (time resolution): the fluctuations look about independent of the sweep speed until we reach a fairly high setting. Aha! one might be tempted to say, on those time scales the voltage becomes smooth, and we are able to see "elementary" processes because there are now clearly visible, fairly periodic ups and downs of the voltage trace. However, the theory of circuits tells us that the bandwidth of the measuring circuit and oscilloscope determine the limits of resolution, and indeed faster circuits and oscilloscopes push these apparent "elementary" processes to shorter and shorter times. Self-similarity is evident by *not* knowing which sweep speed was set when looking at the measured trace. If there were true elementary times one could use them to approximately estimate the sweep speed.

The same arguments could be brought forward to practically all arc parameters. In space, for example, one could image the light emission from a spot with increasing magnification. Soon we realize that spatial and temporal resolutions are intertwined because long exposure times would smear out the image of a fast changing object.

Fractal objects in the real world have cutoffs, where the self-similarity by "zooming in" or "zooming out" breaks down. So far, no convincing cutoffs have been found for fractal spots.

One consequence of the fractal approach is that the quest for the "true" current density of cathode spots needs to be reconsidered: no such thing exists. This also puts in question all models that are based on fixed assumptions, such as a certain current density or emission area of a cathode spot.

In the chapter on cathode processes, another essential concept is that of emission stages related to the "life cycle" of an emission center. In a nutshell, one has to realize that there is a short, explosive stage that is responsible for the formation of fully ionized plasma containing multiple charge states. The explosive stage is followed by a much longer decay and cooldown period where the crater, formed in the explosion stage, is emitting vapor. The vapor forms a background into which the successive, explosively formed plasma expands. When we switch on a cathodic arc, the neutral vapor does not yet exist, and so we can see, for a very short time, the kind of plasma generated at cathode spots. It is characterized by higher charge states than usually known.

In the literature on coatings using arcs, the term "arc evaporation" is sometimes used in analogy to thermal or electron beam evaporation. "Arc evaporation" is somewhat misleading since it disregards the presence of ions, and the energetic condensation processes enabled by the high degree of ionization. It is correct, though, that evaporation of the cathode material occurs, too.

This leads us to the whole complex of interaction of the expanding plasma with gas and surfaces. Chapter 4 describes the expanding plasma, with a lot of

information on the evolution of charge states and ion energy distribution functions. Much of the information is based on averaging over extended periods of time (DC arcs) or many pulses (pulsed arcs). In doing so, correlations between the solid-state cathode properties and the plasma properties can be established, which allows us to formulate empirical rules. The most physical is the Cohesive Energy Rule because it is essentially based on energy conservation. According to this rule, cathode materials with higher cohesive energy require higher burning voltage, and higher charge states and ion energies follow.

After having set the basis of cathodic arc physics on the cathode (Chapter 3) and in the expanding plasma (Chapter 4), some practical hardware is considered, i.e., arc sources and the specifics of their implementation including trigger systems.

The next chapter deals with the infamous macroparticle problem. The cathode spot is not only a source of electrons and plasma of the cathode material but also a source of microscopic droplets. They are commonly called "macroparticles" because they are very massive compared to ions and electrons. These debris particles are detrimental to coating quality. The macroparticle problem is the main reason why cathodic arc plasma deposition is not broadly used in high-tech applications. The formation and transport of macroparticles are considered, having in mind that we want to reduce and possibly eliminate them.

Many efforts were focused on the removal (filtering) of macroparticles from the plasma. Chapter 7 outlines the principles of guiding the arc plasma in plasma optics systems; a solenoid is the simplest example of such plasma optics systems. The chapter contains a rather comprehensive review of filter geometries. Many examples are illustrated in figures. The different approaches are grouped, and one way of classification is to consider filters using a duct with the magnetic filter coils surrounding it, and filters of "open architecture," characterized by openings through which the macroparticles can escape from the filter volume. In the open architecture, we utilize the fact that macroparticles tend to "bounce" from surfaces. In the simplest realization, an open filter is a freestanding coil made from stiff copper wire carrying the current that generates the magnetic field necessary for plasma guiding.

All the efforts were made to produce a flux of plasma suited to fabricate coatings of unique properties through a process called *energetic condensation*. In Chapter 8, we will explore how ions interact with the surface when they arrive with a kinetic energy exceeding the displacement energy. Shallow ion implantation, or "subplantation," occurs, leading to dense and hard coatings that are generally under high compressive stress. Hardness and compressive stress are related. Excessive compressive stress is detrimental because it leads to catastrophic failure of the coating by delamination. Stress control becomes paramount for high-performing coatings, e.g., for the tool industry. Here, hardness, or better toughness, is achieved via advanced approaches that involve graded layers, multilayers, and nanostructures. Though, in any case, the high compressive stress in energetic condensation can be controlled by utilizing the high degree of ionization: biasing the substrate is very efficient in giving ions a controlled high energy capable of generating small collision cascades in the subsurface layer of the solid. Such cascades are tiny volumes of transient liquids; they exist for about a picosecond before being quenched. Stress

can be relieved through atom rearrangement facilitated by the short period of high mobility. This is best controlled by sophisticated biasing techniques, such as pulsed biasing with optimized pulse duration and duty cycle. One can maximize stress relief while maintaining a high level of hardness and elastic modulus.

This technique, also known as Metal Plasma Immersion Ion implantation and Deposition (MePIIID), has been shown to work well, and thick (μm) films have been made, some of them even freestanding. As a special example we will consider, at several places, the hydrogen-free form of diamond-like carbon (DLC), also known as tetrahedral amorphous carbon (ta-C) or amorphous diamond. This material shows generally higher density, hardness, and elastic modulus than other forms of DLC, especially when compared to the hydrogenated (a-C:H) and nitrogenated (a-C:N) materials. MePIIID has also other special features and applications, such as conformal coatings on lithographically structured substrates, e.g., wafers for integrated circuits and microelectromechanical systems (MEMS).

Many of the industrial applications are based on reactive deposition, which simply means that the cathodic arc is operated in a gas mixture containing a reactive gas for compound synthesis. For example, one would use nitrogen, oxygen, or a hydrocarbon gas like acetylene to produce a nitride, oxide, or carbide, respectively. In recent years, multi-element compounds have become popular; they contain more than one metal, like TiAlN, or more than one reactive gas, like TiO_xN_y. Some ternary and quarternary compound films show superior performance, often caused by the resulting nanostructure. Those and other structure–property relationships will be considered in Chapter 10, although it is clear, and emphasized several times, that no comprehensive treatment can be given – the subject would require a book or more on its own.

The book is concluded by compiling some additional information that might be useful reference material to the reader. In Appendix A, a brief summary is given on plasmas and sheaths, the latter being the boundary of a plasma to any wall. The concepts and properties of plasmas and sheaths are important to the understanding of arcs and they are also of value to other fields; hence, it made sense to provide a summary for general reference. Second, in Appendix B, data on cathode materials as well as on arc plasmas are provided. Those data would appear just as numbers and values, without much physical reasoning, if sorted by alphabet of the material or by the atomic number. Therefore, these data are presented in the physically more meaningful format of Periodic Tables, which give a clear indication of the grouping of properties, both for the (usually solid) cathode materials and for the plasma. The latter is just yet another representation for the Cohesive Energy Rule mentioned before.

This introduction outlined the main points of the book, following the logical path of the cathode material: starting from the solid in Chapter 3, going to the expanded plasma in Chapter 4, a brief rendezvous with hardware in Chapter 5, macroparticles in Chapter 6, filters in Chapter 7, and finally arriving at the surface of the substrate in Chapter 8, and Chapter 9 in case a reactive gas is present, to be concluded by looking at a number of quite diverse applications, up to where arc plasma meets blood plasma. Enjoy!

2

A Brief History of Cathodic Arc Coating

Examining the spots with a microscope, both the shining dots that formed the central spot, and those which formed the external circle, appeared evidently to consist of cavities, resembling those on the moon, as they appear through a telescope, the edges projecting shadows into them, when they were held in the sun.

Joseph Priestley, 1775 ([1], pp. 261, 262)

Abstract This chapter is unusually detailed and describes arc-related research over two and half centuries. Not only do the over 200 references of this chapter cover the well-known milestones of arc physics but we connect the dots to many contributions of researchers that are forgotten. It is clearly shown that many advances have been made several times and they have only become part of permanent knowledge and technology when the community was ready to accept those new ideas. The chapter is subdivided into chronological sections covering each century, starting with Priestley's experiments on the initially unintentional arc coatings on glass in the 1760s. Since arc discharges require a reasonably high current to exist, the role of the supply of electrical energy plays an important factor for the initial research, and the quality of available vacuum is another important consideration. The development is followed all the way to modern high-resolution plasma diagnostics and the formation of coatings containing nanostructures and nanolaminates.

2.1 Introduction

Cathodic arc discharges and arc coatings are one of the oldest – but still "emerging" – plasma technologies. Their roots can be traced back to the eighteenth century when researchers struggled to develop the basic concepts of electricity. The general history of electricity has been the subject of numerous studies [2, 3, 4, 5, 6, 7, 8, 9] and therefore will not be reproduced here; instead, only a few

A. Anders, *Cathodic Arcs*, DOI: 10.1007/978-0-387-79108-1_2,

glimpses are mentioned as far as they are relevant to tell the story of cathodic arcs and arc deposition.

Cathodic arcs represent one mode of arc discharges, and here it will be assumed that the reader has a basic understanding of cathodic arcs. Readers not familiar with the subject may want to browse through the introductory chapter first.

The early development of arc plasma[1] physics is intimately related to the development of suitable sources of electrical energy [11, 12]. Each major advancement of generation and storage of electrical energy enabled the discovery of new phenomena. However, there was usually a large gap between initial observation and understanding. Arcs can be produced in a pulsed or continuous mode. Because there have been two distinct developments of electrical energy sources, namely the capacitor and the electrochemical battery, the distinction between early pulsed and oscillating (eighteenth century) and early continuous arc discharges (beginning of the nineteenth century) appears quite natural. The nineteenth century brought the development of classical electrodynamics, culminating in electromagnetic induction, Maxwell's equations, the discovery of electromagnetic waves, and finally the electron. At the end of the nineteenth century, first attempts were made for commercialization of cathodic arcs. The actual technical exploration and application for coatings started only in the second half of the twentieth century, mainly pioneered by physicists and engineers of the former Soviet Union. These developments lead to today's broad application of cathodic arcs for hard and decorative coatings. At the beginning of the twenty-first century, substrate bias techniques and cathodic arc filtering are perfected, allowing the technology to enter the arena of high-tech applications of ultrathin films, nanostructures, functional multilayers, and biocompatibly engineered surfaces.

The highlights of this development will be traced in the following sections. Of course, this chapter cannot be a comprehensive presentation with sufficient depth satisfactory to the historian. Still, the topics will be presented as a number of steps of interwoven progress, and in this way each "breakthrough" appears as a rather logical evolution of knowledge, understanding, and ultimately utilization.

2.2 Cathodic Arcs in the Eighteenth Century

2.2.1 The Capacitor: Energy Storage for Pulsed Discharges

A seminal event in the early history of discharges was the invention of the capacitor. The invention was made independently, and practically simultaneously, by Ewald Jürgen von Kleist (1715–1759), dean of the cathedral at

[1] Although the term "plasma" was introduced by Irving Langmuir (1881–1957) only in 1927 [10], we will apply it also to the earlier science of this field.

Cammin in Pomerania (Germany), and by Andreas Cunaeus (1712–1788), a frequent visitor to Professor Pieter van Musschenbroek (1692–1761) at the University of Leiden (spelled Leyden in the eighteenth century) in the Netherlands. Von Kleist reported his observation in a letter, dated November 4, 1745, to Johannes Nathaniel Lieberkühn (1711–1756), member of the Academy of Sciences in Berlin. About at the same time, Musschenbroek tried to draw "electrical fire" from glass vessels filled with water, an idea proposed by Georg Matthias Bose (1710–1761), professor at the University of Wittenberg, Germany. Electrification of water was previously described by Andreas Gordon (1712–1751), a Scottish-born professor in Erfurt, Germany [13]. Cunaeous, a lawyer who occasionally assisted Musschenbroek, tried to arrange Bose's experiment by himself, holding the bottle in one hand and drawing the spark with the other, giving himself a terrible shock. He reported this to Musschenbroek and his colleague Jean Nicolas Sébastien Allamand (1713–1787). Musschenbroek repeated the experiment and described it as follows in a letter to René Antoine Ferchault de Réaumur (1757–1783), correspondent at the Paris Academy:

> . . . I would like to tell you about a new terrible experiment, which I advise you never to try yourself, nor would I, who have experienced it and survived by the grace of God, do it again for all the kingdom of France. I was engaged in displaying the powers of electricity. An iron tube AB was suspended from blue-silk lines; a globe, rapidly spun and rubbed, was located near A, and communicated its electrical power to AB. From a point near the other end B a brass wire hung, in my right hand I held the globe D, partly filled with water, into which the wire dipped, with my left hand E I tried to draw the snapping sparks that jump from the iron tube to the finger, thereupon my right hand F was struck with such force that my hole body quivered just like someone hit by lightning. . . . [14]

The news of the greatly enhanced power of electricity spread quickly and the conditions for the correct operation were determined, allowing others to build and improve Leyden jars, as they were named. Most noticeably, Sir William Watson (1715–1787) and Dr. John Bevis (1693–1771) improved the jar by coating the inside and outside with tin foil. The Leyden jar became the standard device for storing electric energy in the second half of the eighteenth century.

Quickly after the discovery of the charge storage capabilities of the Leyden jar, it was recognized that capacity increases with larger area and thinner glass wall. For example, Benjamin Wilson (1721–1788), a leading English "electrician" (as they called themselves), writes on October 6, 1746, in a letter to John Smeaton (1724–1792) that "the electrical matter in the Leyden bottle. . . was always in proportion to the thinness of the glass, [and] the surface [15] of the glass. . . " ([2] p. 119). Ignoring these findings, eighteenth-century publications usually give the surface area but are silent about the glass thickness. Measurements on historic Leyden jars show that the glass thickness of most Leyden jars was 1–3 mm depending on the size of the jar. The wall thickness was thicker on the bottom and around the neck because these areas must withstand stress. Some of the less advanced Leyden jars were made from wine bottles and have thus greater wall thickness with less capacity [16].

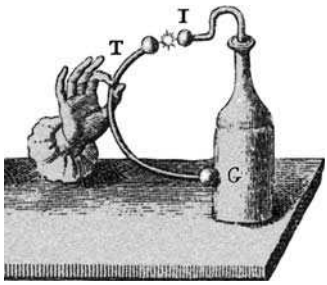

Fig. 2.1. The young Volta discharging a battery of Leyden jars, producing a spark arc in air

In 1746, Watson short circuited a jar with a wire: "the charged phial will explode with equal violence, if the hoop of the wire be bent, so as to come near the coating of the phial. . . " ([2] p. 117). Figure 2.1 shows a similar experiment as described by the still young Alessandro Volta (1745–1827). With today's knowledge we can estimate that the discharge current must have been high, the peak limited by the inductance of the circuit, and decaying exponentially or, more likely, oscillating in the LC circuit. One can estimate $C \sim 1$ nF and $E_C \sim 1$ J for early Leyden jars [11]. The stored energy is still clearly below the hazardous level, and some of the early reports on "terrible" experiences appear exaggerated but understandable because the physiological effects were not anticipated.

In his *History* (see below), Joseph Priestley also mentioned an interesting experiment by Watson, namely that

> He [17] made this vacuum part of a circuit necessary to make the discharge of a phial; and, at the instant of the explosion, there was seen a mass of very bright embodied fire, jumping from one of the brass plates in the tube to the other. ([2] vol. I p. 349)

Most likely, no significant resistance was in the circuit, and thus the discharge appears to have transitioned into a high-current discharge with explosive emission at the cathode, such as one would find in a short-pulsed arc discharge. The *very bright embodied fire, jumping from one of the brass plates*, may refer to incandescently glowing macroparticles. Other researchers, depending on their circuit and setup, appear to have observed variations of glow discharges rather than arcs and sparks. In 1759, however, when Wilson repeated experiments "first contrived by Lord Charles Cavendish," he observed a "singular appearance of light upon one of the surfaces of the quicksilver" ([2] vol. I, p. 355). The quicksilver (mercury) was part of the evacuation scheme, and it is not clear, but possible, that Wilson was referring to a cathode spot on mercury.

2.2.2 Priestley's Cathodic Arc Experiments

Joseph Priestley (1733–1804), an English theologian and chemist, is best known for the identification of ammonia, nitrous oxide, and oxygen [18]. Priestley's life

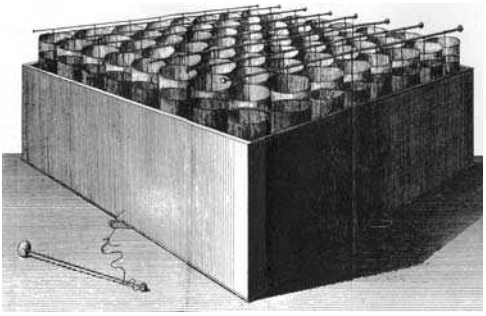

Fig. 2.2. A battery of Leyden jars. (From Priestley's History [2])

and work is well documented [19, 20]. The young Priestley became interested in electricity in the early 1760s and he collected all information on electricity accessible to him, and even repeated all of the important electrical experiments he was going to describe. Priestley wrote *The History and Present State of Electricity* [2], which became the most comprehensive textbook on electricity of the time. It was standard for at least a generation of scientists and remained influential for the rest of the eighteenth century [21]. The first edition appeared in 1767 in London; translations into French [22] and German [23] became available soon thereafter. The third edition of 1775 [2] was reprinted in 1966 with a detailed introduction by Schofield [21].

Having completed his historical "chore," Priestley went on performing his own experiments on electrical phenomena, which also include observations on cathodic arcs. As an energy source he used a battery of Leyden jars as shown in Figure 2.2. Priestley reported about his "original experiments" in the Philosophical Transactions and in later editions of his *History*.

Priestley discovered erosion craters left by cathode spots:

> June the 13th, 1766. After discharging a battery, of about forty square feet, with a smooth brass knob, I accidentally observed upon it a pretty large circular spot, the center of which seemed to be superficially melted... after an interruption of melted places, there was an intrie and exact circle of shining dots, consisting of places superficially melted, like those at the center, Plate 1, Fig. 5, No. 1 (here Figure 2.3).

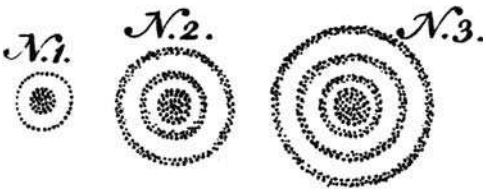

Fig. 2.3. Drawings of spots found on metal plates after a discharge. (From Priestley's History [2])

> June the 14th. I took the spot upon smooth pieces of lead and silver. It was, in both cases, like that on the brass knob, only the silver consisted of dots disposed with the utmost exactness, like radii from the center of the circle, each or which terminated a little short of the external circle. Examining the spots with a microscope, both the shining dots that formed the central spot, and those which formed the external circle, appeared evidently to consist of cavities, resembling those on the moon, as they appear through a telescope, the edges projecting shadows into them, when they were held in the sun. ([1] pp. 261–262)

The formation of circles of craters may be associated with damped oscillations of the electrical circuit. Priestley even found that the size of erosion craters depends on the electrode material:

> I took the circular spot upon polished pieces of several metals, with the charge of the same battery, and observed that the cavities in them were some of them deeper than others, as I thought, in the following order, beginning with the deepest, tin, lead, brass, gold, steel, iron, copper, silver... The semi-metals bismuth and zink received the same impression as the proper metals; being melted about as much as iron. ([1] pp. 263–264)

Today we know that a higher discharge current causes the number of arc spots operating simultaneously to increase rather than a change in the character of individual spots. The number of spots, or the current per spot, also depends on the material and its surface conditions. Priestley observes

> When the battery was charged very high, the central spot was the most irregular, many of the dots which composed it spreading into the outer circle, and some dots appearing beyond the outer circle... I imagined that...two or more concentric circles might be produced, if a greater quantity of coated glass was used, or perhaps if the explosion was received upon metals that were more easily fused than brass... upon tin, I first observed a second outer circle... it consisted of very fine points hardly visible, except when held in an advantageous light... (Plate I, fig. 5, No. 2). ([1], cf. Figure 2.3)

Formation of arc craters is associated with formation of macroparticles. Referring to his experiment with a brass electrode, Priestley continues [1]

> "Beyond this central spot was a circle of black dust, which was easily wiped off." Using gold, "there were... hollow bubbles of the metal, which must have been raised when it was in a state of fusion. These looked very beautiful when examined with a microscope in the sun, and were easily distinguished from the cavities... The whole progress seems to have been first a fusion, then an attraction of the liquid metal, which help to form the bubbles; and lastly the bursting of the bubbles, which left the cavities."

He investigated the nature of the black dust from brass in another contribution [24]. He discharged a bank of parallel capacitors, a "battery of thirty-two square feet," through a brass chain.

> I had before observed that the electric sparks betwixt each link to be most intensely bright, so as, sometimes, to make the whole chain appear like one flame in the dark; but the appearance of the chain in the instant of the shock, as it hung freely in the air, was exceedingly beautiful; the sparks being largest and brightest at the bottom, and smaller by degrees, towards the top, where they were scarcely visible; the weight of the lower links having brought them so much nearer together. ([24] pp. 281–282)

The electrical contacts between the links for the brass chain were insufficient to carry the high short-circuit current, and thus short arcs in air formed – today a well-known phenomenon on electrical contacts of switches. That weight pulling on the chain would improve the electrical contacts between the chain's links was not new; in fact, in his *History* (but not in the *Original Experiments*), Priestley refers to a letter of 1746, written by Wilson to Benjamin Hoadley (1706–1756):

> When he [Wilson] made the discharge with one wire only, he found the resistance to be less than when a chain was used. . . . He caused the chain to be stretched with a weight, that the links might be brought nearer in contact, and the event was the same as when a single wire had been used. ([2] p. 120)

Furthermore, also Watson, in 1747, made

> ". . . use of wires, in preference to chains" because "the electricity conducted by chains was not so strong as that conducted by wires. This was occasioned by the junctures of the links not being sufficiently close, as appeared by the snapping and slashing at every juncture. . . ." ([2] p. 132)

Using white paper on and under the brass chain, Priestley tried to determine the origin, composition, and amount of material eroded from each link by the passage of the electric fluid:

> To ascertain whether this appearance depended upon the discontinuity of the metallic circuit, on the 13th of the same month [June 1766], I stretched the chain with a considerable weight and found the paper, on which it lay as the shock passed through it, hardly marked at all. Finding that it depend upon the discontinuity, I laid the chain upon white paper, making each extremity fast with pins struck through the links. . . September the 18th [1766]. Observing that a pretty considerable quantity of black matter was left upon the paper, on every discharge with the same chain; I imagined it must have lost weight by the operation. . . I found it had lost exactly half a grain of its weight. ([24] pp. 278–279)

Since the discharge occurred in air, metal ions upon condensation on a surface, as well as the hot macroparticles, must have reacted readily with the oxygen and formed an oxide. Cathodic arc deposition can be used to deposit oxides such as black copper oxide (see Chapter 9), and it is safe to assume that the "black dust" from brass contained this oxide. Priestley's description agrees with this supposition:

> [The black dust] was so extremely light as to rise like a cloud in the air, so as sometimes to be visible near the top of the room; I concluded that it could not be the metal itself, but probably the calx [oxide], or the calx and phlogiston, in another kind of union than that which constitutes the metal; and that the electric explosion reduced metals to their constituent principles as effectually as any operation by fire do it, and in much less time. I was confirmed in this opinion by finding. . . that this black dust collected from a brass chain would not conduct electricity. ([24] p. 289)

One might speculate that the black dust contained clusters and nanoparticles, which, as we know today, can be obtained by expanding plasma in a background atmosphere of sufficiently high density.

One of the "*original experiments*" finally contains a direct record on what we call today cathodic arc coating:

> I next laid the chain upon a piece of glass;... the glass was marked in the most beautiful manner, wherever the chain had touched it; every spot the width and colour of the link. The metal might be scraped off the glass at the outside of the marks; but in the middle part it was forced within the pores of the glass; at least nothing I could do would force it off. On the outside of the metallic tinge was the black dust, which was easily wiped off. ([24] p. 285)

Remarkably, one of the advantages of cathodic arc coatings is their superior adhesion due to the energetic condensation of the metal plasma on the substrate, and this feature has been noticed even at this early stage. Priestley did not only use brass on glass:

> I have since given the same tinge to glass with a silver chain, and small pieces of other metals. ([24] p. 285)

He continued the deposition and observed that the coatings show interference colors. Since his experiments were done in air, a freshly deposited metal film tends to oxidize and form a more or less transparent compound. He correctly associates his observations with Sir Isaac Newton's discovery

> "that the color of bodies depends upon the thickness of the fine plates which compose their surfaces" ([25] p. 329) and continues,
> "Having occation to take a great number of explosions,... I observed that a piece of brass, through which they were transmitted, was not only melted, and marked with a circle by a fusion round the central spot, but likewise tinged beyond the circular with a greenish colour, which I could not easily wipe out with my finger. ... I continued the explosions till, examining with a microscope, I plainly perceived all the prismatic colours, in the order of the rainbow." ([25] pp. 330–331)

Today, a straightforward approach to improve uniformity of coatings is to increase the distance between the arc plasma source and the substrate. Greater distance allows the plasma to expand, increasing the coated area, improving film uniformity but reducing deposition rate. The idea is not new, as one can see from the following:

> 1. When a pointed body is fixed opposite to a plain surface, the nearer it is placed, the sooner the colours appear, the closer do they succeed one another, and the less space they occupy. It seems, however, that when the point is at such distance that the electric matter has room to expand, and form as large a circular spot as the battery will admit, this coloured space is as large as it is capable of being made; but still the colours appear later, in proportion to the distance beyond that. ... 2. The more accutely pointed is the wire, from which the electric fire issues, or at which it enters, the greater is the number of [interference] rings. A blunt point makes the rings larger but fewer... 5. All the colours make their first appearance about the edge of the circular spot. More explosions make them expand towards the extremity of the space first marked out; while others succeed in their places; till, after thirty of forty explosions, three distinct rings appear, each consisting of all colours. ([25] pp. 331–333)

The limitation of energy storage in batteries of Leyden jars allowed only pulsed and oscillating discharges to exist – no continuous discharge was yet possible. Therefore, cathodes could not heat up to operate in the thermionic mode, and early discharges utilized electrode emission mechanisms characteristic for globally

cold cathodes. As a consequence, these discharges show characteristics today associated with cathodic arc discharges: explosive emission processes, formation of erosion craters, macroparticles, and well-adhering coatings on surfaces placed in the plasma stream.

Because Priestley's "*original experiments*" were included in his widely distributed *History*, electricians of the eighteenth century were well aware of them; however, no practical application could be derived at that time. His observations remained a laboratory curiosity, and they were largely forgotten.

2.2.3 Experiments Leading to the Electrochemical Battery

Near the end of the eighteenth century, a completely new branch of electrical science appeared: "animal electricity." It was known that some kind of creatures, like the "electric eel" or the "electric torpedo" had electrical properties. The emerging field went on center stage when the professor of anatomy, Luigi Galvani (1737–1798), performed numerous experiments in Bologna, Italy, on "animal electricity." In a 1791 publication [26], he reported about the motion of frog legs when the frog is placed on an iron plate and its spinal cord is touched with a copper hook. The story of this discovery is very interesting on its own [5] but not of central importance here. While Galvani and his nephew, Giovanni Aldini (1762–1834), defended the theory of animal electricity, Volta, by that time already a well-respected scientist, developed a different theory of Galvani's animal experiments. Volta developed the contact theory, which says that electricity is generated when two dissimilar metals are brought in contact with a "conductor of the second art," such as salt water. The exchange of arguments, with Galvani and Aldini on one side and Volta on the other, is well documented and discussed, e.g., by Dibner [5].

To really make his point, Volta recognized that he needed to replace Galvani's frog legs by other, non-animal detectors, such as an electrometer. Electrometers had been developed, for example, by William Henley (unknown-1779) [27], Timothy Lane (1733/34–1809)[28], Abraham Bennet (1750–1799), and Volta himself. The problem was that all electrometers were only suited to measure electricity of higher "tension." Apparently, the *forza motrice* (electromotive force, a term Volta had introduced in 1796 [29] p. 135) of a single contact pair of dissimilar metals was too small to show a consistently measurable deflection in an electrometer. The need for amplification lead to Volta's breakthrough invention at the end of 1799, which opened a new chapter in chemistry, electricity, and discharge physics.

By the end of 1799, Volta accomplished a seminal improvement of the Galvanic effect by adding many pairs of unlike metals separated by wet cardboard (Figure 2.4). Volta reported the invention of the "electric pile" in his famous letter, dated March 20, 1800, to Sir Joseph Banks (1743–1820), president of the Royal Society in London [30, 31]. Using up to 60 pairs of zinc and silver plates, Volta finds

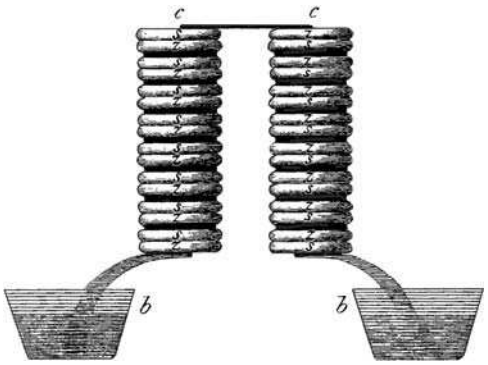

Fig. 2.4. Volta's pile, a battery of electrochemical cells, consisting of unlike metals (zinc, copper) and wet cardboard. (After [30, 31])

> To obtain such slight shocks from this apparatus which I have described, and which is still too small for great effects, it is necessary that the fingers, with which the two extremities are to be touched at the same time, should be dipped in water, so that the skin, which otherwise is not a good conductor, may be well moistened. . . . I can obtain a small pricking or slight shock . . . by touching. . . the fourth or even third pair of metallic pieces. By touching then the fifth, the sixth, and the rest in succession till I come to the last, which forms the head of the column, it is curious to observe how the shocks gradually increase in force. ([31] pp. 292, 293)

One should note that Volta mentioned here that his battery "is still too small for great effects," suggesting that larger, more powerful batteries should be built. A few years later, in 1805, Volta explicitly calls for a pile of 1800–2000 pairs to obtain 35° deflection of his straw electrometer ([32] p. 94). Back in 1800, Volta continues

> The effects sensible to our organs produced by an apparatus formed of 40 or 50 pairs of plates. . . are reduced merely to shocks: the current and variety of different conductors, silver, zinc, and water, disposed alternately in the manner above described, excites not only contractions and spasms in the muscle, convulsions more or less violent in the limbs through which it passes in its course; but it irritates also the organs of taste, sight, hearing, and feeling. ([31] p. 302)

Frighteningly from today's perspective, he then elaborates on the different levels of pain felt by various senses as a function of the number of metal pairs.

The English chemist William Nicholson (1753–1815) and the surgeon Sir Anthony Carlisle (1768–1840) learned about Volta's letter to Sir Banks before it was published. In June of 1800 they constructed a voltaic pile and succeeded in decomposing water, which they published in Nicholson's own journal [33]. Their publication triggered tremendous interest in Volta's invention and, importantly for the discovery of the arc discharge, further development of the battery itself.

Among the excited researchers was the chemist William Cruickshank (1745–1800). In 1800, just months before his death, Cruickshank designed a

Fig. 2.5. Cruickshank's design of a horizontally arranged Voltaic pile, the prototype for larger electrochemical batteries that enabled research on discharges, consisting of rectangular zinc and copper plates in a resin-insulated wooden trough. (After [34])

horizontal voltaic pile (Figure 2.5) consisting of rectangular zinc and copper plates in a resin-insulated wooden trough [34]. Using his version of the pile, Cruickshank decomposed magnesium, sodium, and ammonium chlorides and precipitated silver and copper from solutions, an observation leading to electroplating. He also found that the liquid around the anode became acidic, and that around the cathode alkaline. Cruickshank's style of the electrochemical battery became a widely used standard until the introduction of Daniell cells in 1836.

2.3 Cathodic Arcs in the Nineteenth Century

2.3.1 Improvements to the Voltaic Pile

Following the publication of Volta's sensational results, many researchers built their own copy of Volta's pile (increasingly using Cruickshank's version) and started experiments, mainly focusing on the physiological and chemical effects of electricity. For example, Ritter examined the decomposition of water and the electrical effects on various senses. He moved on, asking "Can we increase the action of a battery to infinity?" [35]. He struggled, like others, with electrical quantities other than the number of metal pairs. He showed that increasing the area of the electrode plates does not increase the voltage but it increases "the strength of a spark." A similar effect can be obtained by choosing an electrolyte of better conductivity (e.g., ammonia (solution) versus salt water and pure water). We have to recall that it was only in 1825 when Georg Friedrich Ohm (1787–1854) formulated the fundamental law that couples voltage, current, and resistance [36]. The concept of internal resistance was not clear in the early 1800s, although it was empirically recognized that batteries of large electrode area and well-conducting electrolytes are more powerful.

Improvements to the voltaic pile were made not only by Cruickshank but also by William Hyde Wollaston (1766–1828), best known for his contributions to

optics, the French Antoine-Francois Fourcroy (1755–1809), and Robert Hare (1781–1858) of Philadelphia. Large voltaic piles were also constructed by Andrew Crosse (1784–1855), who is often portrayed as the archetypical "mad scientist" on whom "Frankenstein" by Mary Shelley (1797–1851) was modeled.

The observation of the "first" continuous arc discharge is intimately related to the development of more powerful electrochemical batteries. Having the discovery of new electrochemical and physiological effects in mind, researchers at several institutions and universities lobbied for much larger voltaic batteries. Among them were Humphrey Davy (1778–1829) in England and Vasilii V. Petrov (1761–1834) in Russia.

2.3.2 Davy's Observation of Pulsed Discharges

Davy, still in Bristol, i.e., before his move to London in 1801, acquainted himself with Volta's pile and performed electrochemical experiments in which he already noticed discharges, and in particular with graphite electrodes:

> The earlier experimenters (*) on animal electricity noticed the power of well-burned charcoal to conduct the common galvanic influence. I have found that this substance possesses the same properties as metallic bodies in producing the shock and spark (**), when made a medium of communication between the ends of the galvanic pile of Signore Volta...
> (*) The inventor of the galvanic pile discovered the conducting power of charcoal. His experiments were confirmed by Creve and Schmuck. See Paff on Animal Electricity, p. 48.
> (**) The spark is most vivid when the charcoal is hot. [37]

In one detail, Davy was respectfully corrected in the only letter sent to Davy by Joseph Priestley:

> Sir – I have read with admiration your excellent publications,... I thank you for the favourable mention you so frequently make of my experiments, and have only to remark, that in Dr. Nicholson's Journal you say that the conducting power of charcoal was first observed by those who made experiments on the pile of Volta, whereas it was one of the earliest I made and gave account of in my history of electricity and in the Philosophical Transactions.... [38]

He was referring to his work done in 1766 [2]. Davy's reference to charcoal is interesting because the development of the first truly continuous arc discharges made use of graphite electrodes. Cathodic arc discharges on relatively cold graphite electrodes are today used for the deposition of diamond-like carbon films. From his early publications, we can infer that Davy had produced, observed, and reported on "spark" discharges with carbon electrodes, which in modern interpretation were, most likely, low-current arcs of short duration. The early voltaic piles could not sustain continuous arcs due to their high internal resistance.

In the following year, 1801, Davy began his extraordinarily successful electrochemical research. Using increasingly powerful voltaic piles of Cruickshank's construction, he noticed discharges producing plasma:

> The apparatus employed in these experiments was composed of 150 series of plates of copper and zinc of 4 inches square, and 50 of silver and zinc of the same size. The metals were carefully cemented into four boxes of wood in regular order, after the manner adopted by Mr. Cruickshank, and the fluid made use of was water combined with about 1/100 part of its weight on nitric acid.
>
> The shock taken from the batteries in combination by the moistened hands, was not so powerful but that it could be received without any permanently disagreeable effects... When the circuit in the batteries was completed by means of small knobs of brass, the spark perceived was of a dazzling brightness, and in apparent diameter at least 1/8 of an inch. It was perceived only at the moment of the contact of the metals, and it was accompanied by a noise or snap.
>
> When instead of the metals, pieces of well-burned charcoal were employed, the spark was still larger and of a vivid whiteness, an evident combustion was produced, the charcoal remained red hot for some time after the contact and threw off bright corruscations.
>
> Four inches of steel wire 1/170 of an inch in diameter, on being placed in the circuit became intensely white hot at the points of connection, and burnt with great vividness being at the same time red throughout the whole of their extent.
>
> Tin, lead, and zinc, in thin shavings were fused and burnt at their points of contact in the circuit, with a vivid light and with a loud hissing noise. Zinc gave a blue flame, tin a purplish, and lead a yellow flame violet at the circumference.
>
> When copper leaf was employed it instantly inflamed at the edges with a green light and vivid sparks,... silver leaf gave a vivid light, white in the centre and green towards the outline, with red sparks of corruscations. Platina in thin slips, when made to complete the circuit, became white hot, and entered into fusion....
>
> A few only of these experiments have any claim to originality. On the phenomena of the combustion of bodies by galvanism we have been already furnished with many striking experiments, by our own countrymen, and by the German and French philosophers.... [39]

One may speculate that Davy, when reporting that charcoal "threw off bright corruscations," was referring to the cathodic arc mode of an arc, and the *corruscations* were "macroparticles" in modern terminology. At this time, however, he did not yet observe a *continuous* arc discharge.

2.3.3 Petrov's Observation of Continuous Arc Discharges

The news about Volta's invention of the pile made it also quickly to St. Petersburg, capital of Russia since 1710. Although still a new city, St. Petersburg had already a history and reputation in science when Vasilii Petrov became a professor in 1795 at the Military-Medical (formerly Medical-Surgical) Academy. Petrov had already investigated electrical phenomena at that time. He strongly advocated the expansion of the Physical Cabinet by acquisition of equipment. The academy agreed to spend 300 rubles, that is, 200 rubles to order 200 zinc and copper plates, 25 cm diameter each, and the remaining 100 rubles were assigned for a glass and copper container on a pedestal to accommodate stacks of metal and cardboard disks in wooden boxes. This battery was comparable in size with devices being built at European institutions at that time.

Petrov realized that a larger battery would not only result in amplified effects but could lead to principally new effects. He successfully raised funds for an "enormous" battery, 20 times larger than the first. Count Dmitrii Petrovich

Buturlin donated 28,000 rubles to the St. Petersburg and Moscow Medical-Surgical Academy ([40] p. 2). The "enormous" battery consisted of 4200 copper and zinc disks. Stacks of plates were mounted in four boxes of red wood and sealed by wax. Each box was 12 in. (about 30 cm) wide and 10 ft (about 3 m) long and consisted of two segments connected with movable copper bars. The bars could be used to connect or disconnect parts of the battery ([40] pp. 19–22). The four boxes were placed parallel to each other but alternately ended with zinc and copper so when connected represented a serial circuit of all 4200 electrochemical cells ([40] pp. 22–25, Figure 2.6). Petrov defined and used the term "enormous battery" in the sense when all stacks were connect this way; however, other configurations were possible too ([40] p. 25).

ИЗВѢСТІЕ

О

ГАЛЬВАНИ - ВОЛЬТОВСКИХЪ

ОПЫТАХЪ,

которые производилъ

Профессоръ Физики Василій Петровъ,

посредствомъ огромной наипаче баттереи, состоявшей *иногда* изъ 4200 мѣдныхъ и цинковыхъ кружковъ, и находящейся при Санкт - Петербургской Медико - Хирургической Академіи.

ВЪ САНКТ-ПЕТЕРБУРГѢ.

Въ Типографіи Государственной Медицинской Коллегіи, 1803 года.

Fig. 2.6. Cover page of Petrov's report "Announcements on Galvano-Voltaic experiments, conducted by the Professor of Physics Vasilii Petrov, based on an enormous battery, consisting of 4200 copper and zinc disks, located at St. Petersburg's Medical and Surgical Academy (in Russian)," published in 1803

Once the large battery was completed, experiments could begin. Petrov noticed sparks at metal pieces when he interrupted the electric circuit. Using graphite electrodes, he observed

> If two or three charcoal pieces are placed on a glass plate or on a bench with glass legs, and if the charcoal is connected to both ends of an enormous battery using metallic but isolated conductors, and if the two pieces are brought in close distance of one to three lines [2.5–7.5 mm], then a very bright cloud of light or flame shines, burning the charcoal more or less fast, and one may illuminate a dark room as bright as one wants to. ([40] pp. 163–164)

Petrov had made, observed, and described the first continuous arc discharge. Moreover, he suggested that the bright light or "flame" (plasma) could be used for lighting purposes – the first possible real application of electricity apart from the entertainment of aristocrats. It is reasonable to assume that at the beginning of the discharge, when the electrodes are still cold, the arc burned in the cathodic (i.e., explosive) mode, while it may have quickly transitioned into the thermionic mode in which the arc burns more or less stable.

When Petrov replaced one of the electrodes with metal, he observed melting, burning, and erosion of the metal.

> If an iron spiral... holding a drop of mercury as one electrode, was ... brought to the charcoal, which is connected to the other pole of the battery, then also between them a more or less bright flame appears, from which the mercury burns, but the end of the wire, almost in an instant, becomes red glowing, melts, and starts burning with a flame and throwing a very large number of sparks in different directions. ([40] pp. 165–166)

While the carbon arc may have quickly switched into thermionic mode, the iron wire "throwing sparks in different directions" was certainly in the cathodic arc mode, emitting the characteristic incandescent macroparticles.

Petrov also investigated the phenomena in "vacuum" (rarefied background gas by today's understanding).

> The light, accompanying the flow of the Galvano-Voltaic liquid in the airless space, was bright, of white color, and not rarely from the glowing ends of the needles [electrodes], or from the sparks coming off like little stars. ([40] p. 176)

Here, there is little doubt that Petrov refers to a cathodic arc with macroparticle emission. He found the light emission in low gas pressure was enhanced compared to atmospheric air, and he emphasizes

> The electric light in most perfect evacuated air represents an unequaled greatest phenomenon, as I could not have wished to obtain from the Galvano-Voltaic liquid. ([40] p. 190)

The question may arise as to why his work disappeared in obscurity for about a hundred years. First, Petrov published his work only in Russian, a language that was generally ignored in the rest of the world. Second, the scientific community of Russia was isolated. Regular communication around 1800 largely depended on time-consuming travel. Finally, there was a "German Sway" in St. Petersburg that was at odds with Petrov [41]. A group of foreign scientists in

St. Petersburg, most notably the academicians Kraft, Fuchs, and Georg Friedrich Parrot (1767–1852), delayed Petrov's election as member of the academy and prevented the distribution of his work [41].

2.3.4 Davy's Work on Continuous Arc Discharges

About 3 years after Petrov's publication, and unaware of it, Davy in London made a breakthrough in electrochemical experiments using a large voltaic battery of several hundred metal pairs. He succeeded in the electrolytic decomposition of potash and soda, obtaining the metals potassium and sodium, which he announced at his famous Bakerian Lecture of 1807 [42, 43]. He continued, isolating the elements barium, strontium, calcium, and magnesium in 1808. Because he used fairly large batteries, discharge phenomena accompanied the chemical research. Davy writes

> ... I acted upon aqueous solutions of potash and soda, saturated at common temperatures, by the highest electrical power I could command and which was produced by a combination of Voltaic batteries belonging to the Royal Institution, containing 24 plates of copper and zinc of 12 inches square, 100 plates of 6 inches, and 150 of 4 inches square, charged with solutions of alumn and nitrous acid....
>
> The flame of a spirit lamp, which was thrown on a platina spoon containing potash, this alkali was kept for some minutes in a strong red heat, and in the state of perfect fluidity. The spoon was preserved in communication with the positive side of the battery of the power of 100 of 6 inches, highly charged; and the connection from the negative side was made by a platina wire.
>
> By the arrangement some brilliant phenomena were produced. The potash appeared to be a conductor in a high degree, and as long as the communication was preserved, a most intense light was exhibited at the negative wire, and a column of flame, which seemed to be owing to the development of combustible matter, arose from the point of contact.
>
> When the order was changed, so that the platina spoon was made negative, a vivid and constant light appeared at the opposite point: there was no effect of inflammation round it: a aerifom globules, which inflamed in the atmosphere, rose through the potash.
>
> The platina, as might have been expected, was considerably acted upon: and in the cases when it had been negative, in the highest degree. ([43] pp. 58–60)

Not surprisingly, by 1808 his large battery at the Royal Institution was exhausted (the zinc consumed by oxidation, [7] p. 9). In July of 1808, Davy laid a request before the managers of the Royal Institution for a public subscription for the purchase of a very large voltaic battery. Davy, who was later knighted (1812) and became president of the Royal Society (1820), was already a leading figure of English science at that time, and his request was taken seriously. To continue his experiments he was provided with a battery of 2000 pairs of plates, whose total active electrode area was $80\,m^2$ ([44] p. 21). This battery (Figure 2.7) was so powerful that it allowed him to obtain continuous arcs, which he demonstrated several times, starting in 1809, to a very impressed audience in the theatre of the Royal Institution [45]. Davy's presentations of the carbon arc light (Figure 2.8) made this type of discharge well known; it

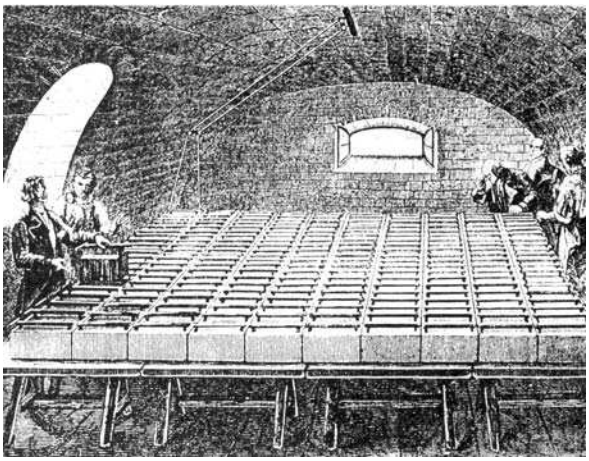

Fig. 2.7. An electrochemical battery used for experiments involving high voltages and currents, most likely the one in the basement of the Royal Institution, London, about 1808

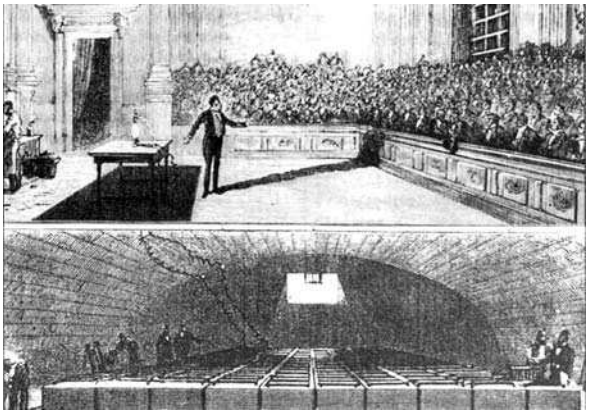

Fig. 2.8. Presentation of arc light by Davy, in or after 1809

became part of established science. However, the cost of a large voltaic battery was prohibitively high, and its capability for delivering power over longer times was limited. Further development of arc technology was dependent on an energy source that went beyond capacitor banks and electrochemical batteries. Such source came along with the discovery of electromagnetic induction and the invention of the electrical power generator.

2.3.5 Electromagnetic Induction

The history of electromagnetic induction is well researched and much has been written about it [6, 7, 8, 44, 46, 47, 48]. Therefore, only a few sentences should suffice here, even with the extraordinary importance of the discovery both for scientific and for technological progress.

In the late eighteenth and early nineteenth centuries, there was a strong belief in the unity of all natural forces, and such belief was sometimes used as a guide to design experiments. The Danish chemist Hans Christian Ørsted (also spelled Oersted) (1777–1851) was not surprised when he observed in 1820 that a compass needle moved when electric current was sent through a wire nearby. A large number of scientists investigated Oersted's findings, and many contributed to the growing field of electromagnetism. At the Ecole Polytechnique in Paris, André-Marie Ampère (1775–1836), professor of mechanics, developed a mathematical theory, and Francois Arago (1786–1853), professor of analytical geometry, discovered magnetization of iron by a coil and the magnetic effect of a rotating copper disc. In Germany, Georg Simon Ohm (1789–1854) made careful measurements leading to the law named after him [36], and Thomas Johann Seebeck (1770–1831) discovered a connection between electricity and heat (Seebeck effect, 1821). In Albany, New York, Joseph Henry (1797–1878) increased the power of electromagnets and devised the first electromagnetic telegraph, leading to the discovery of electromagnetic induction (1831). Due to his failure to publish his discovery, Henry did not receive the same recognition as Faraday.

Among all, Michael Faraday (1791–1867) stands out; he is generally considered as the greatest experimentalist of the nineteenth century (see, for example, his biography by Thomas [48]). Faraday was trained as electrochemist by Davy and also worked at the Royal Institution in London. In 1821 he constructed a "rotator," which essentially was the first electric motor, but it was only in 1831 when he returned to electromagnetic research. He discovered electromagnetic induction using rather simple pieces of equipment, such as a ring of soft iron, wrapped with copper wire, with a trough battery supplying current and a compass needle as a meter. Electromagnetic induction became later the basis for large-scale power generation, a precondition for the next chapters in arc history.

2.3.6 Rühmkorff Coil and Pulsed Discharges

Before electromagnetic induction made it from Faraday's and Henry's laboratories to industrial scale use, researchers still relied for many years on electrochemical cells and batteries as their power source. The voltage of cells and batteries is continuous and needed to be interrupted to produce an induction effect. Electromagnetic induction started to play an important role for making high-voltage devices (though pulsed, of course), enabling smaller, affordable experiments with gas discharges.

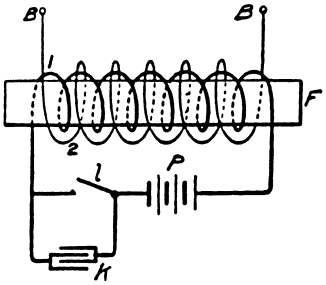

Fig. 2.9. Principal circuit of an induction coil (mid-nineteenth century)

Induction coils [49] were developed, based on interrupting current in a primary coil circuit, thereby generating a large dI/dt and a proportional voltage, which is stepped up in a secondary coil according to the transformer's turns ratio. Figure 2.9 shows the principal circuit. The switch was the weak point in the primary circuit. To generate frequent voltage pulses, the switch must be operated more frequently. One approach was to use a mechanism [50] as shown in Figure 2.10. Ultimately, the electromagnetic force of the coil itself was used to move the switch, a concept invented by Heinrich Daniel Rühmkorff (1803–1877). Rühmkorff was a German-born instrument maker who went to Paris in 1819 where he spent the rest of his life ([51] p. 591). He conducted a long series of experiments on electromagnetic induction and developed the induction coil that made him famous throughout Europe. From 1851 he sold induction coils which became an important tool for discharge physics for decades to come. These devices played an important role in the discovery of cathode rays and X-rays [8]. A Rühmkorff coil (Figure 2.11) consists of a central cylinder of soft iron on which were wound two insulated coaxial coils. The inner coil was

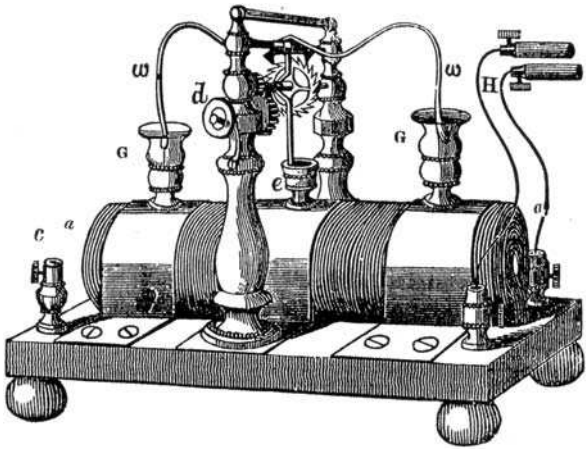

Fig. 2.10. Improved induction coil using a mechanized switching mechanism. (After [50])

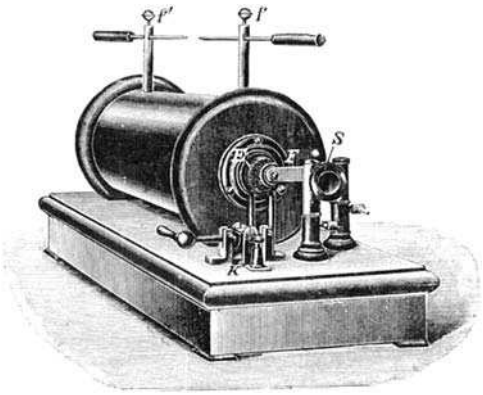

Fig. 2.11. Rühmkorff coil: an improved induction coil with integrated electromagnetic interrupter (second half of the nineteenth century): this device enabled numerous plasma and deposition studies with Geissler tubes

the primary, consisting of a few turns of relatively thick copper wire, and the outer coil was the secondary with a very large number of much thinner wire. An interrupter automatically makes and brakes the current in the primary, thereby inducing in the secondary an intermittent (pulsed) high voltage. Rühmkorff's coil enabled numerous early plasma experiments, including the synthesis of coatings by pulsed sputtering.

2.3.7 Discharge Experiments in Gases and "In Vacuo"

Using the best vacuum technology of the time, Faraday investigated in 1835 the ability of a given gas in a glass tube to pass the discharge current in terms of the pressure of the gas (cf. [46] pp. 113–116, and [48] p. 56). By observing the emitted light he found that the nature of the discharge between metal electrodes in evacuated vessels changed as the pressure changed. In particular, he noted a dark space near the cathode, which was later named after him.

Vacuum technology has developed since Otto Guericke (1602–1686) demonstrated his Magdeburg hemisphere experiment (1654), though until the early 1850s, *vacuum* referred to about 1/50th of a millimeter mercury (~1 Pa), at best. Figure 2.12 shows "Bianchi's air pump," illustrating the large manual effort it took to get even to this degree of evacuation.

One of the great problems was leakage at the pump's pistons. Great progress was made in 1855 when the German glass blower Johann Geissler (1814–1879) developed a vacuum pump based on moving a column of liquid mercury instead of mechanical pistons (Figure 2.13, right), which allowed him to eventually reach about 10^{-5} of atmospheric pressure. Further improvements were made in the 1860s by Herrmann Johann Philipp Sprengel (1834–1906) by introducing re-circulating mercury (Figure 2.13, left), which was perfected by L. von Babo in

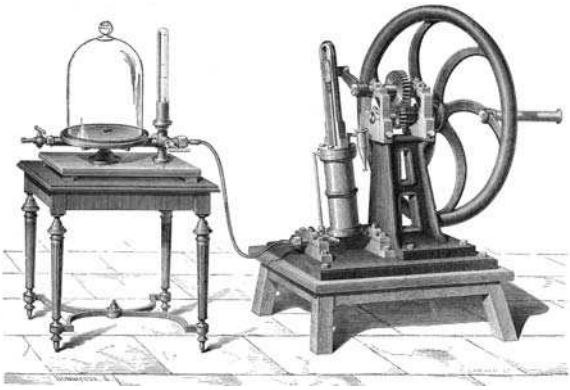

Fig. 2.12. Bianchi's air pump illustrating the difficulty to obtain vacuum (mid-nineteenth century)

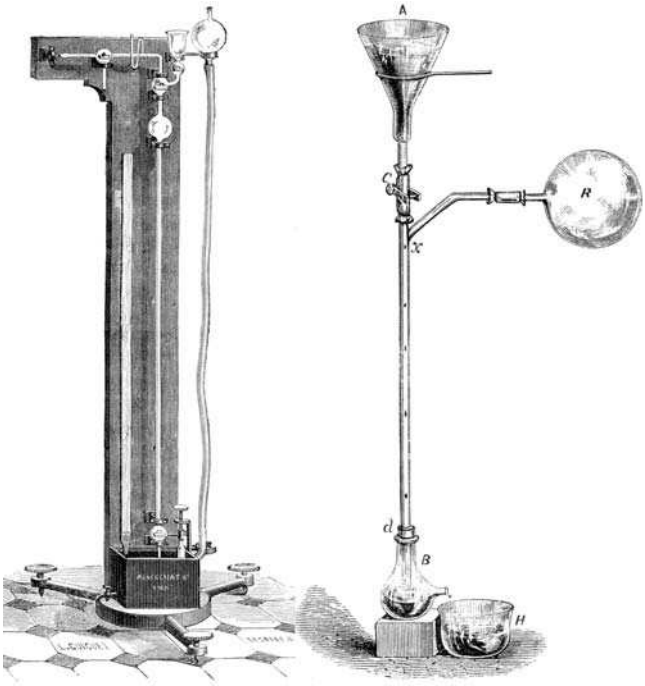

Fig. 2.13. Geissler vacuum pump (*right*) based on moving a column of liquid mercury instead of mechanical pistons; Sprengel vacuum pump (*left*): an improved Geissler pump with re-circulating mercury

1876 as the self-recycling, mercury-drop pump. The ultimate pressure was now reduced to the vapor pressure of mercury. These pumps were used by Edison in Menlo Park (see later this chapter).

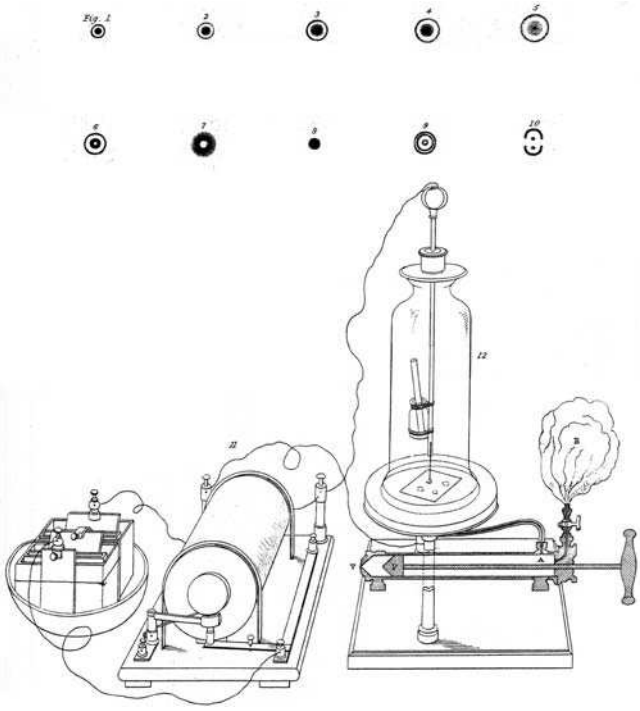

Fig. 2.14. Plate from Grove's original work [53] describing coating by cathode disintegration (sputtering)

Geissler's tubes enabled the first true vacuum-based plasma experiments, including film deposition by "cathodic disintegration" [52, 53, 54]. Based on the gas pressures and the electrical circuits used (Figure 2.14), we know that "cathode disintegration" is due to sputtering of the cathode by pulsed glow discharges. Less certain is the case of experiments by Julius Plücker who observed in 1858 that when the cathode was made from platinum,

> small particles of platinum were torn off... and deposited upon the internal surface of the glass bulb enclosing the electrode... this glass bulb becomes gradually blacked, and after the long-continued action, the bulb... becomes coated internally with a beautiful metallic mirror. [55]

Did Plücker observe what we call now macroparticles? Or was he referring to indiscernible particles (atoms) that were sputtered when talking about *small particles*?

2.3.8 Faraday's Deflagrator

In his Bakerian Lecture of 1857, Faraday described optical properties of thin metal films in great detail [56]. The films were made by various methods,

including mechanical, chemical, and electrical discharge techniques. Faraday's experimental skills were exceptional, as one can realize from the following short quote:

> Beaten gold-leaf is known in films estimated at the 1/282000th of an inch [90 nm] in thickness; they are translucent, transmitting green light, reflecting yellow, and absorbing a portion... so a leaf of beaten gold occupies an average thickness no more than from 1/5th to 1/8th part of a single wave of light. ([56] pp. 146–147)

The electrical coating techniques described by Faraday are based on discharges of a battery of Leyden jars (high voltage) or battery of voltaic cells (low voltage). The Bakerian Lectures were usually accompanied by experimental demonstrations, but unfortunately the written description of the experiments does not include a lot of detail. One may argue whether the setup was a wire explosion or a discharge with clearly defined anode and cathode.

> Gold wire deflagrated by explosions of a Leyden battery produces a divided condition, very different to that presented by gold leaves. Here the metal is separated into particles... When the deflagration has been made near surfaces of glass, rock-crystal, topaz, flour-spar, card-board, &c., the particles as they are caught are kept separate from each other and in place, and generally those which remain in the line of the discharge have been heated by the passage of electricity. The deposits consist of particles of various sizes, those at the outer parts of the result being too small to be recognized by the highest powers of the microscope. Besides making these deflagrations over different substances, I made them in different atmospheres, namely, in oxygen and hydrogen, to compare with air. ([56] p. 152)

The source of electrical energy can also be the voltaic battery, and so Faraday continues

> When gold is deflagrated by the voltaic battery near glass..., a deposit of metallic gold in fine particles is produced....The deposited gold was easily removed by wiping, except actually at the spot where the discharge had passed. ([56] p. 154)

One may easily see striking similarities to Priestley's experiments of 1766, when the links of a brass chain were arc-eroded and the erosion products deposited on a glass plate. While most of Faraday's experiments were with gold, he also used other metals:

> I prepared an apparatus by which many of the common metals could be deflagrated in hydrogen by the Leyden battery, and being caught upon glass plates could be examined as to reflexion, transmission, colour, &c. whilst in the hydrogen and in the metallic, yet devided state. ([56] p. 154)

Optical properties of thin films of Cu, Sn, Fe, Pb, Zn, Pd, Pt, Al, Ag, Rh, and Ir were included in his work. Faraday called the explosive process "deflagration," defined in Webster's as "burning with a sudden and sparkling combustion" ([57] p. 441). Interestingly, Webster's also knows about a "deflagrator," an "instrument for producing rapid and powerful combustion, as of metals, by electricity." Did Faraday present a "deflagrator," a predecessor of a cathodic arc plasma source that can be used for film deposition?

2.3.9 Optical Emission Spectroscopy

Faraday's friend Charles Wheatstone (1802–1875) used a prism to study the light emitted by electrical discharges (cf. [46] pp. 113–116). He found that the spectrum is not continuous but consists of many spectral lines of distinct color, which at least in part depend on the kind of metal used for the electrodes.

George Gabriel Stokes (1819–1903) was one of the first, or the first, to study the spectrum emitted from metal plasma of a cathodic discharge. Stokes is mainly known for his research in fluid mechanics but he also contributed, among others, to optics and spectroscopy (e.g., he coined the term *fluorescence*). In 1862 he published observations on light emitted by discharges:

> "... the spectrum of a powerful discharge from a Leyden jar extends no less than six or eight times the length of the visible spectrum." Especially in the ultraviolet, "the lines seen vary from metal to metal, and therefore are to be referred to the metal and not to the air. They are further distinguished from the air lines by being formed only at the almost insensible distance from the tips of the electrodes, whereas air lines would extend right across.... The metal spectra of which I have observed are platinum, palladium, gold, silver, mercury, antimony, bismuth, copper, lead, tin, nickel, cobalt, iron, cadmium, zinc, aluminium, magnesium. Several of those show invisible lines of extraordinary strength, which is especially the case with zinc, magnesium, aluminium, and lead, which last, in a spectrum not generally remarkable, contains one line surpassing perhaps all the other metals...." [58]

2.3.10 Maxwell

Although the Scottish physicist James Clerk Maxwell (1831–1879) did not directly work on arcs and coatings, his influence on science is so significant that his work deserves special mentioning. Most noteworthy, Maxwell extended earlier work on electricity and magnetism by Faraday, Ampere, and others. In 1864, he presented to the Royal Society a set of linked differential equations describing electric and magnetic fields and their interaction with matter [59]. The original 20 equations in 20 variables were later reformulated in vector and quarternion notation and became known as Maxwell's equations. Maxwell made also major contributions to other fields relevant to arc physics, such as the kinetic theory of gases. The equilibrium distribution function is named after him.

2.3.11 Wright's Experiments: Coatings by Pulsed Glow or Pulsed Arc?

While most of the early work in "vacuum" discharges noted coatings on the glass container, research was usually focused on other phenomena. In 1877, Arthur W. Wright, a professor at Yale University, New Haven, CT, was one of the first to systematically describe the color and reflectance of coatings obtained when using different cathode materials [54]. Unfortunately, Wright did not show any figure in his paper and was very sparse in describing the electrical circuit

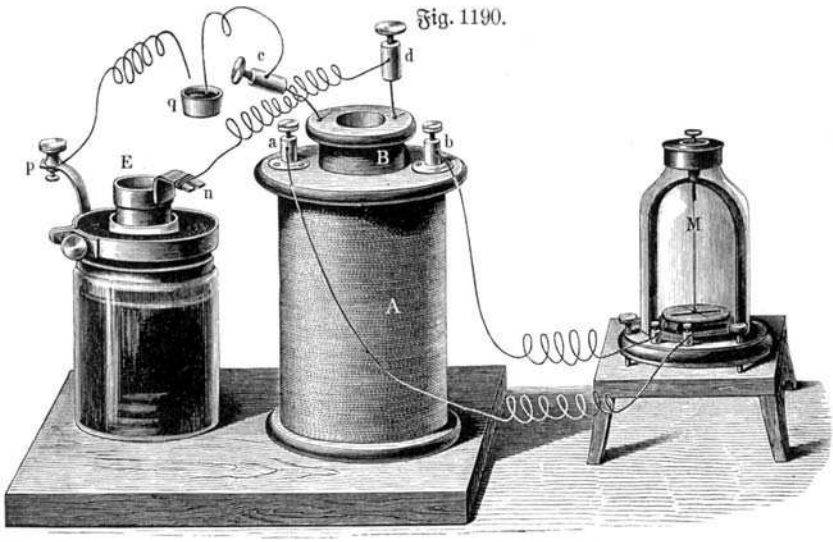

Fig. 2.15. Coating experiment on the inner side of the glass vessel (*right*) by a pulsed discharge using a Rühmkorff coil – it is likely that such setup was used by Wright [54] (drawing from a German text book, about 1900)

parameters. From his verbal description and other sources of contemporary work, one may conclude that his setup must have been similar to what is shown is Figure 2.15. Because Wright used an induction coil, the voltage was stepped up and the current was stepped down proportionally, which suggests that his discharge was a pulsed glow, not an arc. Sputtering experiments were popular after the discovery by William Robert Grove in 1852 [52, 53]. In any case, Wright deserves recognition as one of the first who systematically studied plasma-assisted coatings. His work gained attention because it was (mis)interpreted as cathodic arc coating by the patent examiner who rejected Edison's patent claims (see next sections) based on Wright's prior art [60, 61].

2.3.12 Lecher's Arc Experiments: Discontinuous Current Transfer

Stimulated by several experiments by Edlund, Gustav Wiedemann, and Heinrich Hertz, the Austrian physicist Ernst Lecher (1856–1926) did numerous experiments to disprove Edlund's hypothesis of an electromotoric force in spark and arc discharges. Lecher, who was at the time assistant at the "Physikalisches Cabinet" at the University of Vienna, derived a number of interesting conclusions using a setup shown here as Figure 2.16. The arc was burning between horizontally positioned electrodes e and e' in air, with the right side grounded. The electrode materials were Cu, Fe, Ag, Pt, and graphite. In order to investigate the continuous or rapidly pulsing nature of current transport, he

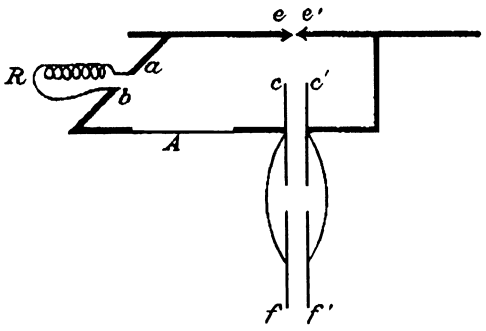

Fig. 2.16. Experimental setup of Lecher showing that the current transfer is discontinuous, i.e., occurring in small portions – a predecessor experiment to the modern explosive electron emission. (After [62])

connected a circuit branch parallel to the arc. That branch consisted of a capacitor cc' (1 μF), apparatus "A" which was mainly a thin brass wire of 50 μm diameter and 50 cm length, and the primary coil of a Rühmkorff induction coil. The Rühmkorff induction coil could be bypassed by a switch $a\,b$, and the capacity of cc' could be increased by a parallel capacitor ff'.

The thin brass wire was part of a sensitive current-measuring instrument (apparatus "A" in the figure) originally introduced by Heinrich Hertz, the discoverer of electromagnetic waves. When current flowed through the wire, its temperature increased and the wire expanded. One end of the wire was pulled by a spring, and before the wire was connected to the spring, it was wrapped around a vertical steel needle. Therefore, expansion of the brass wire caused a slight rotation of the steel needle. A small mirror was mounted on top of the needle projecting a beam of light onto a scale mounted 5 m distant from the mirror.

The idea was that if the current in the arc was flowing continuously and the potential difference between the electrodes was constant, the capacitor should charge to the constant arc burning voltage and the charging current should quickly cease. Lecher observed this case for the carbon arc in its quiet mode ("non-hissing" or thermionic arc mode). In other cases, he found significant fluctuation and pulsing of the arc voltage, leading to charging and discharging currents of the capacitor but only when the Rühmkorff coil was bypassed. When Lecher had the Rühmkorff coil in the circuit, no current was flowing in the capacitor circuit. After varying electrode material and polarity, Lecher concluded

> The transition of electricity in the Galvanic arc is discontinuous. When using copper and silver electrodes, the individual pulses appear to be so rapid that in fact it is impossible to prove it. The number of pulses with iron and platinum is much smaller, and one can already state the existence of the phenomenon with the experimental techniques applied here. . . . The main direction of convection appears to be from the negative to the

positive electrode. The light phenomenon flows so violently from the negative electrode that for example metal vapor and smoke coming from below are pushed away into this direction. ([62] pp. 630, 636–637)

With these observations, Lecher is one of the pioneers of the cathodic arc mode; he anticipated what we now call explosive electron emission.

2.3.13 Goldstein's Canal Rays

Among the many interesting experimental approaches in the second half of the nineteenth century to the physics of gas discharges and related phenomena belongs the discovery of canal rays, or ion beams as would we say today. Eugene Goldstein reported to the Academy in Berlin, Germany, that one can observe fine beams emanating from small holes drilled in the cathode of a glow discharge tube [63]. One would need a special vessel that has the discharge on one side and a gas volume on the other side (Figure 2.17). Ions accelerated in the cathode fall of the discharge side continue to travel through the cathode to reappear at the other side where collisions with gas atoms create a luminous phenomenon. This early observation of ion beams is mentioned here because it marks the beginning of controlled ion acceleration and interaction with matter. These processes belong to the foundation of modern plasma-assisted processing.

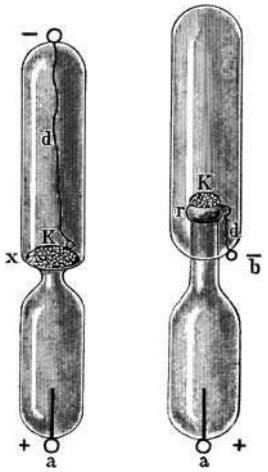

Fig. 2.17. Discharge tube of Goldstein who observed cathode rays coming from holes drilled in the cathode: Some ions accelerated in the cathode fall can cause gas excitation on the other side of the cathode. (From [63])

2.3.14 Edison's Coating Patents

In the 1880s, Thomas Alva Edison in Menlo Park experimented with a number of ideas. Among the challenges was to find a duplication process of phonographs,


(Specimens.) 2 Sheets—Sheet 1.

T. A. EDISON.

ART OF PLATING ONE MATERIAL WITH ANOTHER.

No. 526,147. Patented Sept. 18, 1894.

Fig 1.

Fig. 2.18. Figure 1 of Edison's plating patent US 526147, granted in 1894

the new, revolutionary way to record and store sound. It appears that he was the first who explored cathodic arc coating as described in his patent application "Art of plating one material with another," filed on January 28, 1884 [64] (Figure 2.18). The application was initially declined due to apparent prior art by Wright. Edison filed another application in 1888, "Process of duplicating phonograms," where he narrowed his claims [65]. The latter patent was granted first, on October 18, 1892, and so it constitutes the first granted patent that describes cathodic arc coating. The earlier application was finally granted in 1894, after Edison limited its claims to a continuous discharge in order to distinguish his claims from Wright's pulsed work (which most likely was sputtering). Ironically, a continuous arc has the "danger of injuring the very delicate phonographic-record surface, particularly from the heat of the arc," as he admitted in his 1902 patent "Process of Coating Phonograph-Records," [66] and therefore Edison decided to use sputtering for the production of phonogram copies. Some details of Edison's work and patent disputes can be found in publications by Boxman [60] and Waits [67].

As is well known, Edison was a prolific inventor, and his interest encompassed a range of phenomena. In 1883 he discovered thermionic emission of electrons (see Chapter 3), at a time when the electron was still a hypothetical particle. In 1899, J.J. Thompson showed that the "Edison effect" is indeed emission of electrons [68, 69].

2.3.15 Cathodic Arc Ion Velocity Measurements

At the end of the nineteenth century, measuring techniques (of what we call today plasma diagnostics) became more sophisticated. For example, a remarkable measurement was the determination of ion velocity with optical and spectroscopic means. The researcher A. Schuster [70] used a mechanical streak

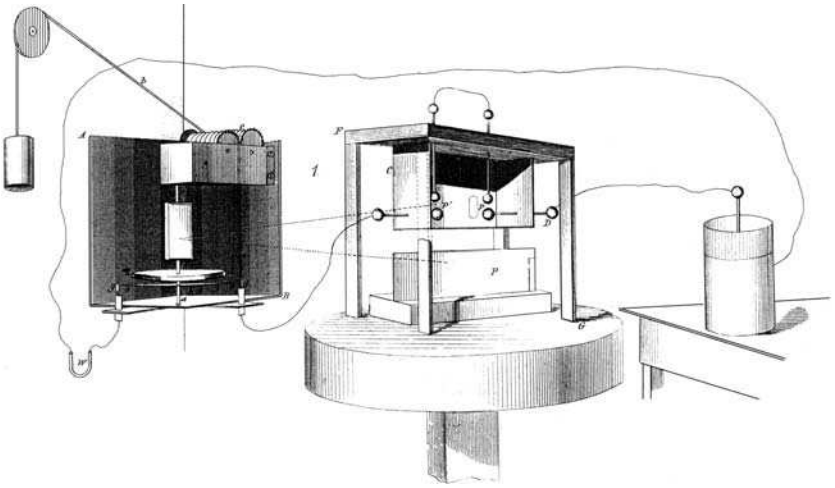

Fig. 2.19. Rotating mirror streak camera developed to investigate the development of discharges in air; remarkably, this device was used as early as 1861 and made use of photography as a detector. (From [71])

camera originally developed by Feddersen [71] (Figure 2.19) to determine the velocity of zinc ions in air. Due to the interaction of zinc with the gas molecules, he found that the velocity is reduced from an initial 2000 m/s at 1 mm distance from the cathode to 400 m/s at 4 mm distance, i.e., values that are quite reasonable based on much-later measurements.

2.3.16 Early Probe Experiments in Arc Plasmas

Electrical probes have been used to study plasmas long before a correct probe theory was developed. Among the early pioneers was Ernst Lecher, who was previously introduced as a physicist finding evidence of discontinuous current transfer at the cathode. In Lecher's 1888 paper one can read:

> As far as I know, there are no experiments on the potential distribution within the arc... I directly placed a thin carbon rod, 1.2 mm thick, inside the middle of the arc... the rod was connected to an electrometer. One side of the electrometer was grounded, so the electrometer must directly assume the local potential of the carbon rod.... First, I confirmed that the introduction of the rod did not significantly change the potential difference between the arc electrodes (iron, platinum, and graphite).... One could move the rod along the length of the arc without finding much change of the potential of about 36 Volts. Therefore, the potential in the carbon arc has two drops [at anode and cathode], and the resistance of the arc appears very small... The results are the same when a small platinum rod is immersed in the arc, except, unfortunately, the platinum melts quickly. ([62] pp. 628–629)

Near the end of the nineteenth century, several researchers investigated arcs with the goal to develop arc lamps for general illumination. The carbon arc was

already well established for special purposes, such as light sources in lighthouses. However, there was the need for adjusting mechanisms compensating for graphite electrode erosion, and thus a better lamp was still to be developed. Discharges with mercury electrodes seemed to be a promising alternative.

At the Physical Institute of the University of Berlin, in Berlin, Germany, Leo Arons experimented with specially formed glass tubes that could be evacuated and partially filled with mercury or amalgams (mercury alloys with metals such as K, Ag, Sn, and Cd). In his publication of 1896 [72], Arons reported about the potential distribution in an arc. Using platinum probes and the method of adjustable electrode distance he found that the mercury arc of 6.5 A current has a cathode fall of only 5.4 V and a drop in the arc column of only 0.67 V/cm. With today's knowledge we have to realize that he did not account for the sheath of his probe, which accounts for an error of several volts in the determination of the cathode fall. The discharge lamps or tubes are also characterized by a substantial anode drop, which enhances anode heating and evaporation, affecting Hg pressure and thus all plasma parameters.

2.4 Cathodic Arcs in the Twentieth Century

2.4.1 Around the Year 1905: Einstein, Weintraub, Stark, and Child

The year 1905 was extraordinarily fruitful for physics. Albert Einstein (1879–1955) made three seminal contributions, one on Brownian Motion [73], one on the Special Theory of Relativity [74, 75], and one on light quanta (photo-electric effect) [76]. For the last he was awarded the Nobel Prize in 1922 for the year 1921. Einstein's work, although not directly related to discharge physics, had a profound effect on all physical sciences, including those related to plasma, thin film, and solid-state physics.

The period around 1905 saw also a surge in interest for a deeper understanding of discharges, and especially arcs. Stark and co-workers [77] mentioned 23 papers on arc physics for the years 1904 and 1905 alone. The surge was perhaps triggered by the discovery of the electron, interpretation of the Edison effect as electron emission, and understanding of gas ionization by accelerated electrons. In the years 1903–1905, E. Weintraub, Johannes Stark (1874–1957), and Clement Dexter Child (1898–1933) published notable contributions to cathodic arc physics.

In 1900, General Electric's management decided to establish a new research laboratory in Schenectady, NY [78]. The General Electric Company (GE) was formed in 1892, following a merger between Edison General Electric with the Thomson-Houston Company. The company had its roots in Thomas Edison's invention of the high-resistance incandescent lamp, but GE was not just a manufacturer of light bulbs. Its activities encompassed electromechanical systems including the generation and distribution of electric power. Dr. E. Weintraub worked at GE's research laboratory on the development of mercury arc

lamps and rectifiers, both of tremendous value to the rapidly growing electrical industry.

Stark, a physics professor at the University of Göttingen, Germany, predicted in 1902 the Doppler effect in ion beams ("canal rays"). His major contribution to physics was the discovery of the influence of strong electric fields on spectral lines (Stark effect), for which he won the Nobel Prize in 1919. Later in his career he became an outspoken proponent of "Aryan Physics," supporting nationalist conservative politics [79].

Child was a professor at Colgate University (1898–1933) in Hamilton, NY. Experiments reported in 1905 were mainly made at the Physical Laboratory of Cornell University, where he had taught some years earlier (1893–1897). Child's most important work was still to come, namely his investigations on thermionic electron emission from hot CaO [80]. He solved the Poisson equation and discovered current limitation by space charge (today known as Child's law; for derivation and discussion, see [81]).

The Mercury Arc in Vacuum

Building on numerous investigations of mercury discharges in air and in glass tubes at low pressure, the arc discharge was once more considered for lighting purposes at the beginning of the twentieth century. It was realized that the arc in mercury vapor appeared very different depending on the electrode polarity or direction of current and therefore it could also be used as a rectifier for AC currents.

At GE, Weintraub [82] made detailed investigations on mercury arcs using discharge tubes such as shown in Figure 2.20. He found a number of important

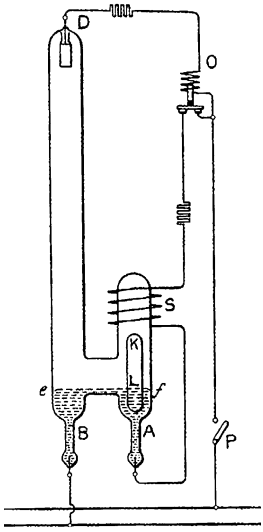

Fig. 2.20. Discharge tube used by Weintraub for cathodic arc experiments. (From [82])

features of cathodic arcs that today are considered well known or obvious. He clearly recognized the role of the cathode:

> In order that an arc should start between two mercury electrodes, placed inside a highly evacuated space, and connected to a source of moderate voltage (magnitude of a few 100 volts), the cathode must first be rendered active, and we will interpret this in light of the ionic theory by assuming that an ionization process must be started at the surface of the cathode in order to allow the passage of an arc through metallic vapours. The anode behaves differently and receives the arc, the ionization process once started at the cathode, without any difficulty. (p. 98 of [82])
> The [arc] discharge is characterized by a relative low voltage across the terminals, by a high current, and by higher temperature of the anode in comparison with the cathode. . . in common with all the arcs, the voltage across the mercury arc varies only little with the current. (p. 105 of [82])
> The arc around the anode is quiet and steady, while on the surface of the cathode there is a small bright spot which is constantly wandering about that surface. The fundamental importance of the cathode in the process of starting that arc leads one naturally to the conclusion that the production of ions takes place at the cathode surface. . .
> . . .The properties of the arc are independent of the nature of the anode, whether this may be made of iron, graphite, silicon, or mercury itself. In the case of iron and graphite, a slight disintegration of the anodes takes place; but this is exceedingly small, so it takes days to notice any black deposit on the glass; and it is obviously a secondary phenomenon, due to volatilization of the material of the anode in vacuum in consequence of the high temperature of the anode. ([82] p. 109)

In the last sentences, although dismissed as ineffective, one may detect the seed for the ideas of two technological approaches using hot anodes: (i) the "anodic arc" [83], in which evaporated anode material is the plasma feedstock material, and (ii) the "hot refractory anode vacuum arc," where cathode material is re-evaporated from a hot anode [84].

Major points of discussion were the issue of the arc attachment area and its temperature (a discussion that goes on until today, see Chapter 3). Stark used spectroscopy and showed that it is possible that the arc spot has a very high temperature while the bulk of the cathode liquid remains relatively cold.

> . . . to the eye, the cathode current basis is a yellow to white glowing spot which moves erratically on the cathode surface. If one brings the entrance slit of a powerful spectrograph close to the surface, the main lines of the Hg spectrum can be recognized; however, if the glowing basis moves in its irregular motion in front of the slit, a continuum spectrum shoots through the line spectrum,. . . . We can conclude that the basis of the arc has the temperature of yellow to white thermal glow. ([85] pp. 750–751)

From Mercury to Cathodic Arcs of Other Materials

In the previously described experiments, Weintraub [82] identified the cathode of a mercury arc as the electrode on whose surface ionization occurs in a small, wandering spot. Weintraub asked himself what would happen if he reversed the polarity of his arrangement, making the solid anode of graphite, iron, etc., the cathode. First, he could not ignite the arc on solid cathodes but soon he figured out

> The simplest way to make a cathode active is that used in all arcs, i.e. separating the two electrodes after having brought them into contact. This is realized in the following experiment. In a vertical carefully-exhausted glass tube there is a mass of mercury at the bottom and a rod of graphite suspended from a platinum wire, and reaching within a short distance from the mass of mercury at the bottom of the tube. The graphite rod is connected to the negative, the mass of mercury to the positive terminal of the source. By shaking the tube it is easy to bring the mercury and the graphite rod into contact and separate them again, whereupon the arc starts with a graphite cathode. ([82] p. 111)

Cathode erosion, the precondition for cathodic deposition, is observed after the arc has started:

> There is a wide hot spot, wandering about the surface of the cathode, just as there was a bright spot on the surface of the mercury cathode. Rapid disintegration of the cathode takes place from the very beginning, and a deposit of carbon forms all over the walls of the tube and the surface of mercury. This disintegration goes on as long as the arc lasts, and takes place whatever the material of the cathode (graphite, iron, etc.). The cathode is, therefore, the electrode which disintegrates in the arc. This mechanical disintegration is probably intimately connected with the ionization which takes place on the surface.... ([82] p. 111)

Child confirmed Weintraub's observation on the role of anode and cathode:

> A series of experiments was also tried using graphite as one of the terminals and for the other one of the following metals – platinum, iron, nickel, copper, silver, aluminum, antimony, zinc, lead, cadmium, bismuth and tin. It was found that in all cases when the graphite was negative the behavior of the arc was much the same as when both terminals were graphite. In other words, with a pressure of less than 1 mm, the character of the anode has little or no effect on the arc. On the other hand at this pressure the character of the cathode had a very great effect on the arc. ([86] p. 370)

Chopping Current

The arc discharge was often characterized, or even defined, as a discharge of relatively high current. What does that mean? How low could one go in current and still speak of an arc discharge? Weintraub observed that the value of the "impressed" (open-circuit) voltage is crucial for arc stability, and that a resistor in series can greatly stabilize the arc. (Often, a large portion of the open-circuit voltage is actually dropping across the stabilizing resistor when the arc is burning, but shifts to the arc load when the arc becomes unstable). Investigating a mercury arc for potential illumination purposes, Weintraub writes in 1903

> First, as in any other arc, there must always be a certain amount of steadying resistance in series with the lamp. Second, again in common with all other arcs, for any given impressed voltage there is a certain lower limit of current below which the arc is not stable. With 100 volts applied to a tube consuming about 80 this low limit is in the neighborhood of 3 amperes. If, however, the 250 volts are impressed, the lamp will run steadily with much lower current.... The explanation is to be looked for in the properties of the cathode. The supply of ions coming from the cathode, one must assume that the ionization process to be stable requires at each voltage a certain current, and dies out when the current is lowered below a certain limit.... When the current in the arc is reduced below that critical value, the lamp suddenly goes out after a certain interval of

> time, no gradual change in the potential drop across the lamp is observed. This phenomenon points to the existence of a cause which ceases to act in a discontinuous way. ([82] p. 108, 109)

With these words Weintraub anticipated the much-later developed model of explosive emission. However, Weintraub was still far from understanding. The "supply of ions" was not just a supply of ions in today's meaning. Weintraub considered also negative "ions" as charge carriers produced at the cathode; he did not yet distinguish between ions and electrons. J.J. Thomson had discovered the electron a few years earlier [68] (Nobel Prize 1906), and it is understandable that the electron concept was not yet widely used in 1903. However, Weintraub noticed that "the amount of matter carrying the current is a very small part of that required by Faraday's law." (p. 112 of [82])

Using a 100-V circuit and limiting the arc current to 10 A, Child checked for the possibility to burn a stable arc with various cathode materials [86]. He found that the more noble metals were not suited to operate a stable arc, while some burn easily. This is further considered in Role of Oxides on Cathodes (later in this Chapter).

The chopping effect has been associated with a minimum amount of plasma that needs to be generated, facilitating ignition of the next emission centers, as further discussed in Chapter 3.

Spot Steering

Evacuated glass discharge tubes with mercury electrodes were convenient objects for arc research, and therefore it is not surprising that also the effect of magnetic fields has been explored using such tubes. In a 1904 publication, Weintraub reports

> The action of the magnetic field on the arc has also been investigated. It is very peculiar and not easily accounted for. . . . The field and arc being both horizontal and perpendicular to each other, the arc is deflected up or downward, according to the common rule of the action of a magnetic field on a current. The deflexion downward is accompanied by a motion of the bright cathode-spot along the surface of the cathode in the direction of the cathode. . . . Changing the direction if the field changes of course the direction in which the arc is deflected, as well as that in which the cathode move. . . . If the arc is vertical and the field is horizontal, the deflexion of the arc and that of the spot are in opposite directions. ([82] p. 114)

As many researchers after him, Weintraub could not give a convincing answer about the reason for this spot behavior. He only remarks that

> It is interesting to note that the action of the field on the cathode-spot can be in most cases formally accounted for by assuming that the positive current elements leave the cathode surface in a direction perpendicular to that surface.

Similar observations were made by Stark in 1903:

> The cathode is not uniformly covered with light, instead, there is an intensely glowing light tuft. . . the electric current transfers at the basis of the light tuft from the liquid to the vaporized metal. The glowing anode layer and positive light column of the mercury

> arc is deflected in a transverse magnetic field, the same way as an ordinary, current-carrying conductor. The upper part of the light tuft on the cathode is also deflected in that direction; its root, however, is displaced in the opposite direction until it reaches the glass wall, where it digs itself into the liquid. . . . ([87] p. 442)

Arc Voltage

In his 1905 work "The Electric Arc in Vacuum," Child [86] investigated a carbon arc at various pressures down to 20 mTorr. For pressures below 1 Torr (at the time commonly labeled as "mm Hg" or short "mm"), he observed "a bright spot on the cathode from which particles were driven off in straight lines so that it appeared as if the current was proceeding from that point" (p. 365 [86]). The "particles driven off" are most likely hot, glowing macroparticles, which can easily be observed for carbon cathodes. Child further observes "at a pressure 0.4 mm, the current was varied from 6 to 25 amperes without producing any apparent effect on the potential difference" (p. 366 [86]). Many years later, this observation was associated with spot splitting: as the current increases, the number of parallel-operating emission centers increases (Chapter 3).

Weintraub [82] and Child [86] made careful measurements of the arc burning voltage, which they found to be about 20 V at low pressure ("vacuum") and about 10–15 V higher when the pressure was increased (up to atmospheric pressure). Child even states that "the drop in potential at the cathode is a function both of the melting point and of the thermal conductivity of the metal" (p. 372 [86]). This could be considered as a precursor of the empirical "Cohesive Energy Rule" (Chapter 3).

Measurements of the voltage were difficult due to fluctuations:

> The arc was then tried between iron terminals in hydrogen, but there was very great irregularity. . . . At lower pressures the total potential difference was somewhat smaller but the ends of the arc were continually moving from one place to another on the electrode, and the reading of the voltmeter continually showed large variations. It was evident that no measurements would be of value until all oxide was removed from the electrodes, and it is necessary to postpone this work for the present. ([86] p. 374)

Probes, Potential Distribution, and Sheaths

The history of plasma probes is far beyond the scope of this chapter, and thus just a few points shall be mentioned. The theory of probes is rightfully associated with the work of Nobel Prize winner Irving Langmuir (1881–1957) and co-workers [88, 89, 90]. However, probes have been used in plasmas long before Langmuir's theories, though without appreciation of the sheath that surrounds a probe making its potential different from the local plasma potential. Still, probes are simple and can provide a direct indication of the potential distribution.

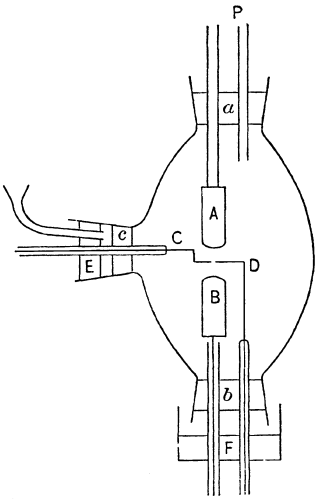

Fig. 2.21. Double probe diagnostic of the arc plasma by Child. (From [91])

Weintraub describes in 1904

> By inserting two platinum wires in the [mercury] arc and measuring the potential drop between each of the electrodes and the platinum wire, as well as that between the platinum one finds that the drop at the cathode amounts to about 5 volts, at the iron or graphite anode about 1½ volts, and at the mercury anode 8 volts. ([82] p. 106)

Child [91] also used the by-then well-established technique of electrical probes. He inserted two platinum wires into the arc and applied "an electromotive force of 4 volts" through a "galvanometer of 75 ohms resistance" (Figure 2.21) In essence, he was already using a double probe, although full and correct interpretation of measured data came only later with the work of Irving Langmuir.

Stark used platinum wires and clever, adjustable electrode arrangements to determine the potential distribution and electrode falls (Figure 2.22). Among his conclusions was that the cathode fall does not depend on the arc current (measured in the range 2–55 A) and that "an increase of the current merely implies an increase of the current basis [15]" (p. 216, [77]).

Plasma Transport Along Magnetic Field Lines

Child observed plasma transport along magnetic field lines, an effect that was used decades later in macroparticle filters. Child reported that

> When a magnetic field was produced about the arc at a pressure of 0.7 mm or less, the gas in all parts became more luminous than before, and a bright stream appeared to run from the arc along the lines of force toward the magnet. . . . ([86] pp. 366–367)

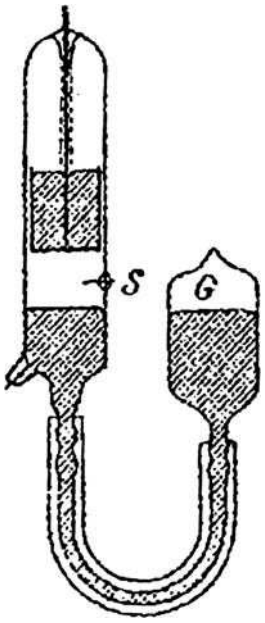

Fig. 2.22. Discharge tube used by Stark, "G" is the grounded electrode, and "S" is the probe ("Sonde" in German). (From [77])

Arc Modes

In the summer 1901, Gustav Granqvist of the Physical Institute in Upsala (now Uppsala, Sweden) investigated the influence of thermal conductivity of electrodes on arc phenomena at the *Politechnikum* in Zürich, Switzerland [92]. He chose two extreme cases, carbon and copper, and found that the arc behaves quite differently in terms of stability, which can be associated with different arc modes, thereby confirming earlier observations by Zuchristan [93]. By calorimetric measurements he found that about 42% of the energy supplied ends up in the anode, 37% in the cathode, and the rest must have been radiated by the gas (i.e., plasma). Such data were later often used when designing cooling systems for arc devices.

Child reported an arc mode transition observed with carbon electrodes. At relatively high pressure, the arc can operate in the thermionic mode, while at lower pressure the arc switches to the cathodic arc mode because the ion bombardment heating becomes insufficient. In contrast to thermionic arcs, cathodic arcs are characterized by rapid fluctuations of arc parameters (for more on arc modes, see Chapter 3). Child writes

> . . . it seemed well to secure lower pressure than those previously used. . . . At 0.1 mm the potential difference about the arc was continually varying, so that is was impossible to make accurate measurements. The voltage would gradually increase from 20 to 30 or

> 35 volts and would then suddenly decrease to less than 20. With this gradual increase in voltage the gas in the tube became more and more luminous, becoming suddenly less luminous when the voltage dropped to the lower value. This tendency to fluctuate became more noticeable as the pressure of the gas was diminished. ([86] p. 368)

Using hydrogen as a filling gas and a circuit with 500 V, Child distinguished three different discharge forms, which in today's nomenclature one would designate as glow discharge, cathodic arc, and thermionic arc.

> The first two forms of the arc were quite unstable and were liable to break down into the third form. Apparently they required comparatively low temperature of the electrodes and of the gas. ([86] p. 373)

Role of Oxides on Cathodes

In many studies, made decades later, the role of surface conditions on electron emission and spot ignition was demonstrated, eventually leading to the introduction of type 1 spots (on oxidized or "poisoned" surfaces) and type 2 spots (on metallically clean surfaces). Iron and copper form oxides on their surface, while carbon does not. Child states that

> It has been pointed out by Stark that oxide on the metal causes an arc to pass with greater ease [94]. This, no doubt, is the cause of some of these phenomena. When the air is first pumped out the arc can be maintained without great difficulty, but after the oxide on the surface of the metal is reduced this can not be done, so that measurements on the arc between metals in a vacuum are of little value, so long as the surface of the metal and the constitution of the surrounding gas are varying. The behavior of the arc with the metals and with graphite are thus seen to be radically different. . . . ([86] p. 369)

Since metals have different affinity to form oxides there are great differences between them, and those differences are amplified by the different vapor pressures that also play a role. Child continues

> . . . When the graphite was positive it was very difficult to secure an arc with some of the metals and very easy with others. Thus on a 100-volt circuit it was impossible to maintain an arc with platinum, iron, silver, and copper or nickel, and very easy with aluminum, antimony, zinc, lead, cadmium, bismuth, and tin. ([86] p. 370)

It should be mentioned that the arc circuit was limited to 10 A, which is relatively low for an arc; hence arc chopping occurs (see Chopping Current).

Cathode Erosion, Gettering Effect, and Coatings

The affinity of some metals to getter gas molecules was much later used in getter pumps, but observations related to the arc getter pump were already made:

> The vacuum improved on producing the arc. Thus at one time the pressure decreased from 0.4 mm to less than 0.01 mm without any air being pumped out. ([86] p. 368)

The eroded cathode material must have been deposited and reacted with the residual gas. Child reports also explicitly on coatings formed. Working with carbon electrodes, he states that

> "The tube became coated after a time with carbon, so that it was impossible to see the gaseous part of the arc" (p. 368). Using iron, he continues, "with iron in a vacuum the phenomena were much the same as with copper. . . . On the cathode were many bright spots instead of one as with graphite. . . . A deposit was quickly formed on the tube with the metals, so that after the arc had been running a few seconds, it was impossible to see what was happening in the gaseous part of the arc." (p. 369)

The erosion of the material from the cathode surface exposed clean bulk metal:

> after removing the metals any oxide on their surface was found to be reduced, the copper having the usual color of clean copper and the iron being white, appearing much like tin.

Cathode spots were identified as the source of the deposited material:

> The platinum was brought to red heat by being made the anode, it could then be used as the cathode and the arc maintained for several seconds. . . there were many bright points on the platinum. The platinum was apparently vaporized and sparks [macroparticles] were driven off from it, so it lost much in weight. ([86] p. 370)

2.4.2 The Decades Until WWII

By the 1920s, cathodic arcs were widely used in mercury vapor lamps and arc rectifiers [95, 96]. Most technical research focused on improving these devices.

After the surge of activity at the beginning of the century, interest remained high but progress was slow due to the all-too-familiar difficulties of arc spot phenomena: unstable appearance, fast fluctuations, and small spot size. Though, physics made great progress in other fields, such as quantum mechanics and instrumentation, which eventually would open the door for the next great steps in arc physics. Among the leading researchers in related fields were Clement Dexter Child and Irving Langmuir (both of whom we met before), Owen Willians Richardson (1879–1959, Nobel Prize 1928), and Saul Dushman (1883–1954).

These names are closely related to the understanding of electron emission, space-charge limitation, and sheath formation [80, 88, 89, 90, 97, 98, 99, 100]. Much has been written about these topics (see Redhead's review [69]), and therefore we can here move on to remarks that are more arc specific.

Walter Schottky (1886–1976), a German physicist who later became well known for the Schottky effect and the pioneering work on p/n junctions, described in 1923 the enhancement of the electric field at cathode surface irregularities [101].

In a few publications of the late 1930s, the role of surface contaminants, and especially oxide films, was clearly established. M.J. Dryvesteyn (1901–1995), who worked for Philip's *Gloeilampenfabrieken* in Eindhoven, The Netherlands, and who was already well known for the electron distribution function named after him, considered the role of oxides on copper cathodes and concluded that an insulating layer must be charged until it breaks down electrically, igniting an

arc spot. He speculated that "it may be that the breakdown of the insulator causes the wandering of the cathode spot of an arc in some cases" [102].

A couple of years later, Suits and Hocker of the General Electric Company, Schenectady, reported that an arc on copper is only stable when an oxide layer is involved [103]. In the same year, James D. Cobine, who published in 1941 his classic textbook on gas plasma physics [104], was working in 1938 at the Harvard Graduate School of Engineering in Cambridge, MA. He investigated low-current arcs and found that "the discharge is influenced markedly by the conditions of the copper cathode" and that arc conditioning of the cathode surface occurs within seconds. Checking with other cathode materials (Cd, Fe, Al, and Zn) he found similar behavior and he concluded that "the random variation is quite probably due to the variation in impurities at the cathode which influences the mechanisms of arc reignition..." [105]. This was actually not new: it was a generation earlier described by Child [86] and Stark [94], as mentioned before. This is an example that many discoveries were made several times and remained only permanently in the community's consciousness when there was a technical application or deeper scientific implication.

With quantum mechanics firmly established in physics, Nottingham revisited the issue of energy balance for thermionic emission and discovered that electron emission does not always lead to cooling but may be a source of additional cathode heating (Nottingham effect) [106].

2.4.3 Secret Work During WWII

Cathodic arc plasmas of uranium were considered for the isotope separation task in the Manhattan Project. Not much is known due to the classified nature of the work. However, from now-declassified reports one can learn that various sources of uranium ions were investigated, including cathodic arcs and thermionic arcs in uranium vapor. In the report "The 'Isotron' method of separating tuballoy isotopes," H.D. Smyth and R.R. Wilson (Robert Rathbun Wilson, 1915–2000) described that "tuballoy" ions can be extracted from plasma using a modulated extraction voltage, which leads to bunching of the beam [107]. Mass separation can be accomplished through phased deflection of bunches. "Tuballoy" was the code word for uranium. In the introduction to the report it is pointed out that "for the purpose of secrecy we have now coined the deliberately meaningless word 'Isotron' as the name of the device." Wilson, who became later director of Fermilab, was the inventor of the ion beam bunching principle, which in many respects is a predecessor to the successful time-of-flight mass spectrometer developed by Ian Brown at Berkeley's vacuum arc ion facility [108, 109]. Theoretical contributions were also delivered by Richard P. Feynman (Nobel Prize 1965). The reports were directed to Ernest O. Lawrence (1901–1958, Nobel Prize 1938), founder of what are now Lawrence Berkeley and Lawrence Livermore National Laboratories.

The cold cathode ion source, however, gave some headaches to the researchers. They report

> The essential principle was to strike an arc in vacuum between two electrodes one of which at least was made of tuballoy and then draw ions out of the plasma of the arc. It was found that simple arcs between two electrodes were very unstable and difficult to keep in place. A great many attempts were made to keep the arc confined within some refractory metal. However, at arc temperature tuballoy vapor attacked every material that was tried. As the problem of material was being met by those working on hot cathode arcs, the work on cold cathode arcs was discontinued. ([107] p. 1)

The hot cathode arc refers to work using a thermionic arc in uranium vapor, which ultimately was also abandoned in 1943.

2.4.4 The Quest for the "Correct" Current Density and Cathode Model

The non-stationary nature of the cathode spot made it difficult to carefully measure the size of the spot, which is assumed to give the cross-section area for current transfer between cathode and plasma. Besides the technical difficulty, there is a conceptual issue. The generally accepted paradigm said that current is transferred through the area occupied by the spot, and that a characteristic current density can be assigned to the spot. As discussed in Chapter 3, the explosive nature and fragment structure negate these assumptions, ultimately leading to a fractal model for the cathode spot. Nevertheless, the search for the average current density value was of great importance to the development of cathodic arc theory.

At the beginning of the twentieth century, values for the current density were generally estimated to be a few 10^6 A/m^2 [85]. In 1922, using a mirror camera, Günterschulze [110] projected an enlarged image of the spot on a photographic plate. Assuming the width of the streak is the characteristic current-carrying spot diameter, he determined that the current density is about 4×10^8 A/m^2. This value was widely accepted for the next three decades. Measurements by Tonks in 1935 [111] using a moving film camera gave slightly higher values but essentially supported Günterschulze's findings.

In the years after WWII, James Dillon Cobine and C.J. Gallagher [112], working for the General Electric Company in Schenectady, NY, utilized the feature that a spot can be driven or steered by a tangential magnetic field (tangential refers to a direction parallel to the cathode surface). In this way, apparent broadening of the spot due to random motion or splitting is suppressed. Additionally, they decided to use a very small current of only 2.6 A to avoid spot splitting and operation of multiple spots. Using microscopic imaging and a photocell, they found much higher current density of up to 2×10^9 A/m^2 for the arc spot operating in atmospheric air and at a pressure of a few Pascal on Hg, Al, W, and Cu cathodes. In 1948, Erwin Schmidt of the Siemens-Schuckertwerke AG in Berlin [113] studied arc cathode spot motion on mercury with a fast framing camera. He concluded that spot motion follows a random walk model in the

absence of a magnetic field, with the individual steps of motion taking 40 μs or less, i.e., shorter than the resolution of his camera.

Almost simultaneously, K.D. Froome [114] of the National Physical Laboratory, Teddington, Middlesex, UK, used high-magnification imaging and a fast Kerr-shutter to obtain "instantaneous" pictures of the spot, with the exposure time between 0.1 and 6 μs. Froome identified that the spot has a structure, like a bundle of smaller spots. Assuming that the luminous plasma is indicative of current transport, he concluded that each emitting site carries about 1 A with a current density of between 2×10^{10} and 10^{11} A/m^2. These values were unexpectedly high and were disputed for many years. In a rebuttal to a publication by Bertele [115], who proposed that the current density is a function of time after spot ignition, Froome emphasized that any measurements with low temporal resolution are "widely in error" and that

> the bright, erratically moving spot is actually a relatively slow-moving envelope containing several minute emitting areas each carrying a current of the order of 1 A. When the arc current exceeds 5–30 A two or more such groups are formed, and so on for increasing current. ([116] p. 91)

With this description, he essentially laid the groundwork for a fractal spot model. Bertele, however, had also a point in stressing the temporal variation of the spot, which indeed will lead us to a fractal spot model in the time domain, and not just in space.

The idea of using higher magnification and faster voltage pulses was pursued by Walter P. Dyke and J.K. Trolan of the Linfield College, McMinnville, OR. They experimented with carefully prepared Mueller projection tubes [117]. The displayed field emission patterns suggested that current densities of 10^{11}–10^{12} A/m^2 necessarily lead to the explosive destruction of the field emission center [118]. Their discovery was the beginning of a new area in the field of electrical vacuum breakdown and explosive electrode processes.

The realization of very high current densities was also recognized by Igor Greogevitch Kesaev who worked in the late 1950s on "cold cathode arcs" at the Gas Discharge Apparatus Laboratory of the Lenin All-Union Electrical Engineering Institute in Moscow, Soviet Union. Kesaev made a number of observations and careful measurements, which he summarized as Report No. 67 of the Institute in 1961. An English translation of this work became available in 1964 [119]. Although he focused on mercury arcs due to their industrial relevance as high-current rectifiers, his research included other cathode materials as well. One of his many contributions was the confirmation of a spot sub-structure, which he called *cells*. He confirmed the notion that the cathodic arc spot is a location where current density is unevenly distributed with peaks in spot cells reaching about 10^{11} A/m^2. He stressed that the increase of measured current density values is directly related to the improvement of experimental technology rather than a physics phenomenon. He suspected that future improvements may uncover even higher peak values in current density, with important implications for the theoretical modeling of spot operation and electron emission mechanism.

His interpretations, later further developed in a Russian-only published book [120], became paradigms for a whole generation of Soviet physicists and engineers dealing with cathodic arcs. This is of importance because cathodic arc deposition technology was originally developed in the Soviet Union in the 1960s and 1970s, sponsored by the Soviet Government, as further discussed below.

Until the middle of the twentieth century, the luminous appearance of the spot was identified with the current-carrying area [121] although much later it was made clear that light emission and current transfer are not identical but correlated at best [122, 123].

As electron microscopes became widely available, arc traces on cathode spots were thoroughly investigated, and a new approach to determining current density was found [124]. Craters were understood to be the relics of spot activity; they are witnesses of explosive events. Each crater could be assumed to be associated with a spot cell, fragment, or emission site. The current density can be determined by assuming that the crater area was the actual current-carrying area, provided one has information on the number of emission sites that were simultaneously active. With this approach, even higher current densities of up to 10^{12} A/m^2 have been determined by Burkhard Jüttner [125] of Berlin, East Germany, and others in the 1970s and 1980s.

With the concept of explosive electron emission in the 1970s and 1980s developed by Gennady A. Mesyats and co-workers including (but not limited to) Sergey P. Bugaev, E.A. Litvinov, and Dmitry I. Proskurovskii [126, 127, 128], the observation of very high current densities was related to the non-stationary nature of electron emission coupled to cathode phase transitions from solid to plasma. Taking ignition statistics into account, the current density shows self-similarity [129] and has fractal properties in the spatial and temporal domains [130].

2.4.5 Ion Velocities: Values and Acceleration Mechanism

The early measurements of metal ion velocity in air, using a precursor of a streak camera [131], indicated that the velocities are very high, exceeding 10^3 m/s in air [70]. This suggests that even higher velocities might exist if the plasma was generated in vacuum because collisions with background gas would not slow down the metal plasma.

It was popular in the 1920s and 1930s to determine the pressure or force upon electrodes caused by the arc plasma [132], which might give some clues on ion velocities. In a 1930 publication, R. Tanberg [133] reported about his 1929 experiments in which he determined that copper ion velocities are greater than 10^4 m/s. He speculated that there could be an excessively high temperature in the cathode spot. Tanberg's work stirred the community and triggered a series of papers on the subject. E. Kobel [134] acknowledged Tanberg's earlier publication and mentioned that he, too, observed similar velocities for mercury in early 1929. Karl T. Compton [135] objected to the excessively high spot temperature

and pointed out that ions might be attracted to the cathode but not accommodated, thereby contributing to the force on the cathode. Joseph Slepian and R.C. Mason [136] came to Tanberg's defense and pointed out that Compton's argument is flawed because one should consider the whole cathode region, not just the surface, and the arguments by Tanberg do apply. Tanberg conceded in a 1931 paper with Berkey [137] that the cathode spot temperature is not as high as originally claimed, but this did not change the fact that ions of very high velocity ($v > 10^4$ m/s) were found. Lewi Tonks [138] pointed out that not just ions but also electrons can contribute to the force acting on the cathode, and Randal M. Robertson [139] essentially confirmed Tanberg's result by investigating the force by the arc operating in air and vacuum. By the late 1930s, the astonishingly high ion velocities were recognized as a property of cathodic arcs in vacuum.

This, of course, immediately raised the question what could possibly cause such high velocities. One approach was to assume a potential hump in front of the cathode: the cathode releases neutrals which are likely to be ionized near the hump of potential. In this way, ions are accelerated away from the cathode or toward the cathode, depending on which side of the hump the initial ionization occurred. A potential hump was never measured, and there were doubts because a purely electrical mechanism would cause the ion energy to be proportional to the charge state and voltage drop between start and end point of ion motion. Charge state-resolved velocity measurements were needed.

The 1960 and 1970s were characterized by a number of important improvements of experimental techniques applied to cathodic vacuum arc research. Milestone papers describing cathodic arc plasmas as energetic with multiple charge states were published by Kesaev [140], Plyutto and co-workers [141], Davis and Miller [142], and Lunev and co-workers [143]. The charge state-resolved data of that time did not give a clear-cut confirmation to the potential hump hypothesis because ions' energies were found higher for higher charge states but the differences were not really proportional to the charge state. That caused theoreticians to look for other mechanisms, and it was realized that highly mobile electrons affect ions. In one extreme, one may neglect any possible potential humps and interpret ion acceleration by the coupling to electrons (electron–ion "friction") [144]. Electrons see strong acceleration via the cathode fall and by the electron pressure gradient. Models have been developed (and are being improved to this day) which include the self-consistent field and related electron–ion coupling (e–i friction), ion–ion collisions, and electron–electron interaction (gradient of electron pressure) [145, 146].

2.4.6 Cathodic Arc Deposition Is Emerging as an Industrial Process

Coatings of Refractory and Transition Metals

Coating by vacuum arcs was observed in the 1950s and 1960s as a byproduct to the vacuum arc metal refining process. At that time, metal coatings were almost exclusively deposited using evaporation. Lucas and co-workers [147, 148]

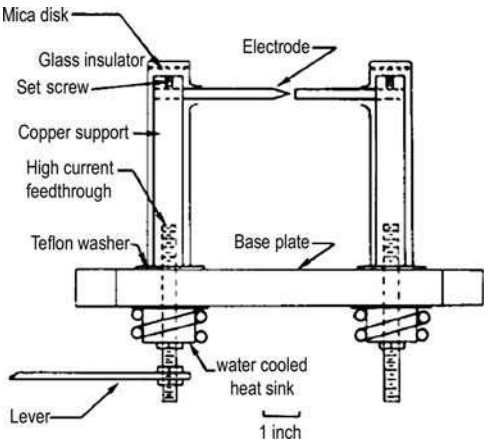

Fig. 2.23. Simple deposition setup for forming films of metals; the lever on the left bottom was used to manually trigger the arc discharge. (After [147])

realized that the coating can be made from refractory metals, which are very difficult to evaporate at high rate. They contemplated that the high deposition rate of the arc process could enable the deposition of superconducting tantalum, vanadium, and niobium films. These three metals are interesting because their transition temperature below which superconductivity is observed is higher than the boiling temperature of liquid helium (4.2 K at one atmosphere). High rates are needed to minimize impurities from the residual gas. They experimented with coatings of Ta, Nb, V, and stainless steel, and demonstrated a rate greater than 5 nm/s for a sample placed 4 cm from the arc cathode [148] using a very simple setup with a stationary and a movable electrode (Figure 2.23). The idea of making superconducting Nb films using the arc process was revived about 50 years later [149, 150].

Coatings of Ferrites

With the broader development of microwave technology in the 1960s there was a need to develop thick coatings of ferrites for use in electromechanical transducers, for example. Using a cathodic arc coating process, Naoe and Yamanaka [151, 152] of the Tokyo Institute of Technology found that the film composition was approximately equal to the composition of the cathode. Through small adjustments of the cathode composition they were able to make very thick (up to 100 μm) stoichiometric mixed ferrite films like $Ni_{0.3}Zn_{0.7}Fe_2O_4$ and $(Ni_{0.85}Cu_{0.15})Fe_{2.06}O_4$ with a deposition rate of about 0.4 μm/h. One should note that the ferrite cathode is a semiconductor that can only be used as a cathode when heated. This issue was solved by bringing the anode rod (molybdenum) in short-circuit contact and letting the current flow through the cathode before the anode

was detached to start the actual discharge. This pre-arc heating technique was later used by others to operate arcs on other semiconductors, such as boron, for example.

From Pump Research to Coatings

The history of broad application of cathodic arc deposition is closely related to work done in the 1960s by of a group of researchers at the National Science Center, Kharkov Institute of Physics and Technology (NSC KIPT) [153]. Kharkov is a sizeable city in Ukraine, which was part of the Soviet Union at that time. Researchers at the Plasma Physics Division studied means of obtaining high vacuum using sorption properties of condensates made by vacuum arcs. In 1964, Leonid P. Sablev and co-workers succeeded in burning a steady-state vacuum arc on titanium, and a Soviet Patent was issued in 1966 for a vacuum arc sorption pump [154].

This pump research was expanded by Anatoliy A. Romanov and Anatoliy A. Andreev to coating applications, including the synthesis of diamond-like carbon using graphite as the arc cathode material. Soviet patents were filed [155, 156], but otherwise the work was kept secret and only published in part years later [157]. Apart from titanium and graphite, molybdenum was used in reactive mode to produce molybdenum nitride coatings with microhardness of 32–36 GPa. Although (or rather because!) these results were pioneering and of great practical importance, the work was not published until years later [158, 159]. Significant improvements of wear performance of diesel engine piston rings and cutting tools were demonstrated, as explained by Aksenov in his account of Soviet-area arc coatings history [153].

Hard and Decorative Coatings in the Soviet Union

Understandably, these results caused great interest in the new technology by tool and machine manufacturers in the Soviet Union. A decision to construct a pilot commercial facility was reached. Based on outline drawings from the NSC KIPT group, technical designers of the Malyshev Plant, Kharkov Branch, detailed the design plans and specifications under supervision by Alexandr A. Ehtingant. Detailed drawings and specifications as well as the manufactured cathodic arc sources were delivered to the KIPT group. In 1973, the KIPT group started collaborating with the Moscow Machine Tool Institute and the All-Union Research Institute for Tools. Additionally, in joint work with the Tomilin Diamond Tool Plant, metallization of natural and synthetic diamond was demonstrated. The KIPT group grew by a number of researchers who should later become well known for their work on filtered cathodic arcs: Vladimir M. Khoroshikh, Vladimir E. Strel'nitskij, Ivan I. Aksenov, and Vitaly A. Belous.

The Soviet Union did not have a market economy but was centrally state-controlled. Therefore, in order to bring the technology to its full potential, high-level government support was needed. In 1974, the USSR State Committee of

Science and Technology issued a decree ordering nationwide commercialization of the technology under the leadership of KIPT, i.e., the Kharkov Institute where the first steps were made and where most expertise was concentrated. This decree covered the development and commercialization of arc technology for the deposition of wear-resistant coatings on tools and machine components, metallization of diamond, and the synthesis of superhard materials. The decree had wide-ranging consequences for the development of arc deposition technology in the Soviet Union, and with the transfer of the technology to the United States in 1979 affected the coatings industry in many countries.

Still in 1974, a couple of pilot arc systems, dubbed "Bulat[2]-2," were set up by KIPT at a Kharkov Plant. They represented the first industrial arc coating machines, typically used for the deposition of titanium nitride. With these machines, knowledge of arc deposition processing went from an R&D lab to industry. In the fall of 1974, KIPT was re-organized; Valentin G. Padalka became the head of the laboratory, and a large material science group under V.V. Kunchenko was established. The greater group, funded by the Soviet Decree, expanded pioneering research in tool coating [160, 161], magnetic spot steering [162, 163, 164, 165], interaction of streaming metal plasma with background gas [158, 166], transport of plasma streams [165], and synthesis of superhard materials including tetrahedral amorphous carbon [157, 167, 168, 169, 170, 171, 172, 173].

While these physical measurements and materials development activities were ongoing, the next generation of cathodic arc sources, Bulat-3, was designed (Figure 2.24). The first 20 units were manufactured by plants in Kharkov in 1977 and 1978. Mass production of these sources started in 1979 not only in Kharkov but also in other plants in Tallinn (Estonian Soviet Republic) and Kiev

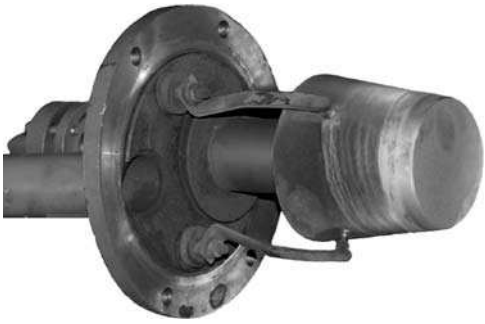

Fig. 2.24. Bulat-3 cathodic arc source, the "workhorse" of large-scale industrial coatings in the Soviet Union; one can see the two trigger electrodes and the conical shape of the cathode, which facilitated spot steering in the axial magnetic field provided by an external coil. (Photo by the author)

[2] The Russian word "Bulat" refers to "damascene steel," relating to the ancient art of making hard materials.

(Ukraine), and later also in Saratov and Novosibirsk. By the late 1980s, a total of about 4000 cathodic arc coating systems (Bulat-3 and its successor models) were produced and in operation in many manufacturing plants throughout the Soviet Union.

From Soviet Union to America

In the United States and elsewhere, the role of vacuum-based coating technology was recognized and gained rapidly in popularity (however, here we mostly refer to evaporation and sputter deposition, rather than arc coating). The Society of Vacuum Coaters (SVC) was founded in 1957, and in 1960 the International Symposia on Discharges and Electrical Insulation (ISDEIV) started, a biannual series of symposia dealing with vacuum arcs and arc-based coatings (among the larger topics of electrical insulation, breakdown, and vacuum-based switching). In 1965, Kikuchi and co-workers of the Tokyo Institute of Technology pointed out that vacuum arc deposition might be especially advantageous for the "refractory and hard superconducting materials" [174]. Their electron diffraction studies of films deposited at room temperature showed that the films were "amorphous or composed of very small crystallites." At the 1978 Technical Conference of the SVC, I. Kuznetsov from the *U.S. Vacuum Technology Delegation* gave an overview on "Electron Beam Evaporation Processes in the Soviet Union" [175]. The development of arc sources outside the Soviet Union was "in the air," as evidenced by the following:

- Arc spot steering by magnetic fields was patented in 1961 by Harold Wroe in England [176, 177], although the spot's retrograde motion was observed much earlier, e.g., by M. Minorsky in 1928 [178], and extensively discussed in the 1950s literature (e.g., by Charles Smith [179] and A. E. Robson and A. von Engel [180]).
- Fundamental research on vacuum arc erosion was done by Clive W. Kimblin at Westinghouse Research Laboratories in Pittsburgh, PA, and by Jaap E. Daalder at the Eindhoven University of Technology in Eindhoven, The Netherlands [181].
- A first book dedicated to vacuum arcs was published outside the Soviet Union by James Lafferty, in 1980 [182].
- Alexander Gilmour and David Lockwood from the State University of New York at Buffalo reported on pulsed arc plasma generators [183].
- First U.S. patents, describing the principal construction of commercial-grade (random motion) cathodic arc sources, were granted in 1971 to the American Alvin Snaper [184].

Attempts were made to bring the latest Soviet technology of magnetically steered arc sources to the West. In December of 1979, despite much Cold War secrecy and restrictions, the Bulat-3 arc technology for the deposition of titanium nitride on tools was licensed to the American company "Noble Field," which a little later was renamed Multi-Arc Vacuum Systems. Through the initial work by Multi-Arc, cathodic arc deposition became well known outside the Soviet Union.

2.4.7 Large-Scale Industrial Use in the 1980s and 1990s

Even with the first commercial arc sources operating in the United States, the eye was of course on the vast experience hidden behind the Iron Curtin. At the 1983 SVC conference, H.R. Smith, Jr., of *Industrial Vacuum Engineering* talked about "Current Vacuum Coating Processes in the Soviet Union" [185]. Clark Bergman of Multi-Arc Systems Inc. presented the company's first contribution in 1985 entitled "Arc Plasma Physical Vapor Deposition" [186], which was a useful summary of arc physics and practical steps for coating, including the use of high negative bias for metal ion etching, as later used and patented in the arc-bond-sputtering (ABS) process.

A handful of companies, such as Multi-Arc, Vac-Tec Systems, and Hauzer, made *arc evaporation*, as it is sometimes called, their core technology for hard and decorative coatings. In the 1980s, not much detail was reported at technical meetings (exception [187]), perhaps to protect the proprietary recipes developed by these companies; however, reviews on arcs physics and coating properties appeared in the scientific literature [188, 189].

Users critically looked at the economical advantages and the performance, and macroparticles clearly diminished the value of arc coatings. For example, Gary Vergason, well familiar with evaporation, sputtering, and (unfiltered) cathodic arc coatings, concluded that "of the three deposition techniques, sputtering offers the widest range of coatings with a high degree of process control and production repeatability" [190]. The presence of macroparticles is one of the greatest drawbacks of the large-scale cathodic arc technology until today. Yet cathodic arc deposition was established for mass production using both batch and in-line coaters, although the former are clearly in the majority in coating plants. It is common that large numbers of parts ($>10^6$ annually) are coated in one plant [191] using rapid cell cycling technology, which includes systems for automated cleaning and pre-heating. The coatings are usually multifunctional (corrosion resistant, decorative, etc.) and the parts are mainly supplied to the automotive and buildings industry (e.g., car headlights, faucets).

Cathodic arc coatings are among the preferred coatings technologies because they are economical and they allow a greater variety of colors, a very important factor for consumers. In the 1990s, further improvements to the products were made by combining traditional, thick electroplated coatings with thinner but denser and harder coatings. It was reported that decorative coating by arc PVD on top of electroplated coatings improves the corrosion resistance and enhances the palette of colors [192]. Interestingly, the reverse order, a plated film on top of a hard arc PVD coating can also be used, in the case of gold-plated TiN for high-end decorative produces such as watch wristbands and frames for eyeglasses [193].

Another interesting use of cathodic arc plasmas is its use for material *removal* by metal ion *etching*, rather than film deposition. In the arc-bond-sputtering (ABS) technology, introduced in the early 1990s, argon sputter cleaning was replaced by sputtering using ions from the cathodic arc plasma. The to-be-sputtered parts

are highly negatively biased (about 1 kV) in the cleaning process before being coated. The metal ion etch improved the adhesion of coating on parts such as cutting tools [194].

2.4.8 Macroparticle Filtering: Enabling Precision Coating for High-Tech Applications

To eliminate, or at least reduce, the defects and roughness caused by macroparticles, magnetic macroparticle filters were considered very early but they were not broadly introduced to any production due to significant plasma losses, leading to lower deposition rates, hence lost economical benefits. Clearly, the application of filters needed to be limited to high-end application where the quality of the coating is of utmost importance.

Magnetic guiding of plasma from the cathode to the substrate had been suggested much earlier than is generally known. For example, in a patent filed in 1937, the Germans Wilhelm Burkhardt and Rudolf Reinecke claimed a method of coating articles where charged particles of vaporized material (i.e., ions of the cathodic arc plasma) are

> concentrated in the form of a beam proceeding from the fused material towards the surface to be coated by a magnetic field produced above the fused material... and extending towards the surface to be coated. [195]

Apart from such early experiments, one may state that the invention of macroparticle filtering was a spin-off from thermonuclear fusion research and not a targeted result of cathodic arc development.

In the 1950s, the Soviet Union and the United States developed sizeable research programs for thermonuclear fusion of the hydrogen isotopes deuterium and tritium [196]. One concept was the Tokamak fusion reactor, a toroidal (doughnut-shaped) plasma machine. By the 1960s, plasma physicists made detailed investigations of transport and stability of hydrogen plasma and its heavy-element contaminants in toroidal magnetic confinement. The motion of pulsed plasma jets, or "plasmoids," was studied theoretically and experimentally. For this purpose, quarter and half-torus devices were built. By injecting plasmoids in curved filters, one attempted to separate the light hydrogen isotopes from the much heavier contaminations. Figure 2.25, from V.S. Voitsenya et al.'s 1967 publication [197], shows a quarter torus used for the investigation of plasmoid transport and filter properties. One can easily recognize the similarity with what became the 90° duct filter used a decade later (Figure 2.26). The work of Ivan Aksenov and co-workers [198, 199] in Ukraine led to the now-classic 90° filtered arc system; this group deserves recognition for the pioneering work done in the field of cathodic arc filtering, including not only the classic 90° filter but also a number of other filter geometries [200].

The filtered arc source became the core technology for the arc coating system "Bulat-4" (Figure 2.27). After publishing their approach in the late 1970s and 1980s [198, 201], it took about a decade before several groups in

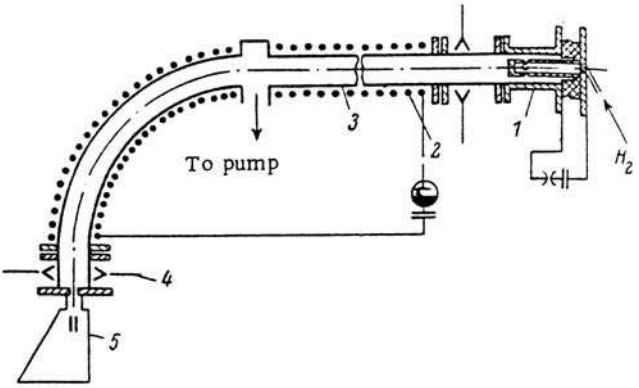

Fig. 2.25. Quarter torus plasma guide for the investigation of plasma transport (after V.S. Voitsenya et al.'s 1967 publication [197]); such setup became the prototype of cathodic arc macroparticle filters

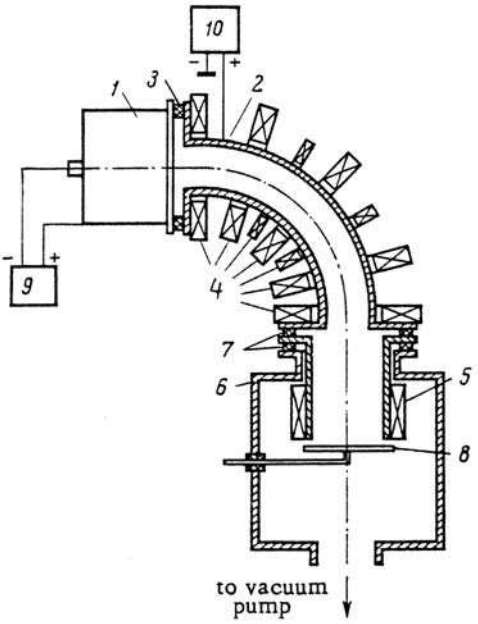

Fig. 2.26. Classic 90° duct filter introduced by Aksenov and co-workers; the labels have the following meaning: 1: cathodic arc source, 2: plasma duct; 3: insulator, 4: coils; 5: solenoid, 6: vacuum chamber, 7: insulators, 8: substrate (after Fig. 1 of [198])

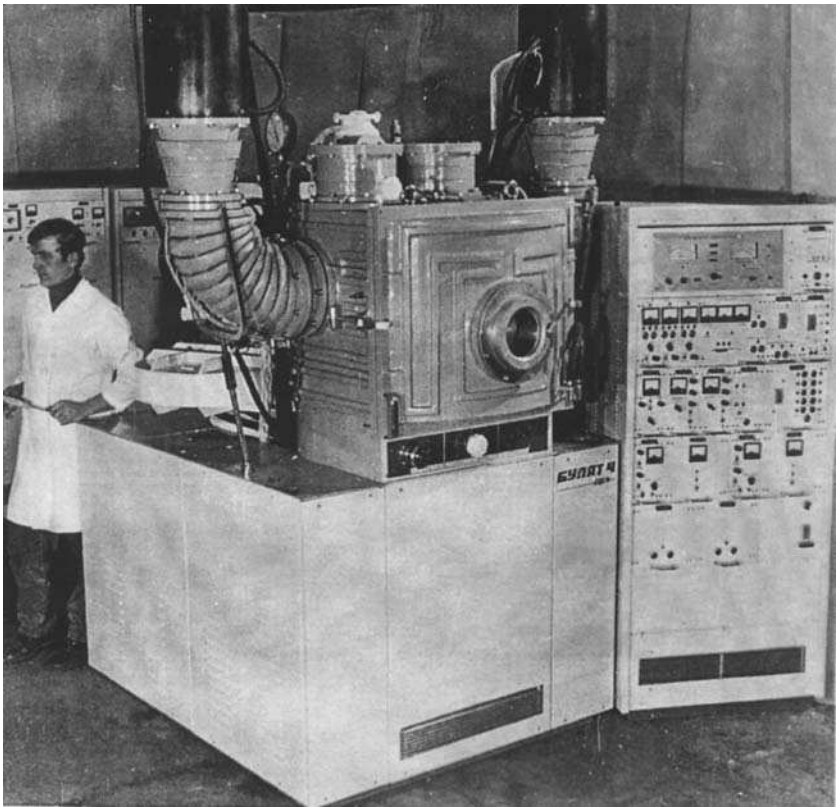

Fig. 2.27. Vacuum chamber with filtered cathodic arc sources (Bulat-4) in the 1970s. (Photo courtesy of Ivan Aksenov)

the world copied and further developed the concept. For example, Schemmel and co-workers at Vac-Tec in Boulder, CO, reported in 1989 that filtered arc is promising for the high rate deposition of high-quality aluminum oxide [202]. Phil Martin and co-workers reported in 1993 on properties of their filtered arc-deposited films [203], which included carbides, nitrides, and oxides of optical quality [204, 205]. In the early 1990s, Commonwealth Scientific Corporation commercialized in the United States an arc system with a 45° *knee-filter* [206].

The occasional presence of macroparticles and uncertainty in film uniformity and thickness are issues not acceptable in high-tech applications such as metallization of semiconductors and deposition of protective layers on magnetic storage media and devices. Therefore, further improvements were sought, leading to novel geometries such as the *off-plane double bend* (OBDB) *filter* by Shi Xu, Beng Kang Tay and co-workers at the Nanyang Technological University, Singapore [207, 208], the *S-filter* [209] and *Twist filter* [210] investigated at Berkeley Lab in

California, Ryabchikov's *Venetian Blind filter* [211, 212] in Siberia, and the *modular filter* developed by Peter Siemroth and co-workers [213] in Germany.

More information on these filter concepts and geometries can be found in reviews [214, 215, 216] and in Chapter 7.

2.5 Cathodic Arcs at the Beginning of the Twenty-First Century

2.5.1 Advances in Diagnostics and Modeling of Arc Plasma Processes

Arc spots presented (and still do) a challenge to investigators due to short duration and very small scale of microexplosions and related plasma gradients. Fast, high-resolution diagnostics has brought greatly improved insight. Until the 1990s, fast oscilloscopes provided evidence for short events [128, 217], and electron microscopy of the erosion traces brought best evidence of small scales [124, 218, 219]. Fast image-converter cameras became available and enabled observation of spot dynamics [220, 221] and spot structures, sometimes called fragments, and elementary processes associated with the apparent spot motion [222, 223]. Another route to high-resolution diagnostics is via short-pulsed illumination, e.g., from sub-nanosecond lasers. By tuning the laser wavelength, the time-dependent density distribution of selected species can be determined, e.g., the density of free electrons, or the densities of ions and atoms in the ground state or in specific exited states, by either laser absorption imaging [224, 225] or interferometry [226].

The conceptual understanding of cathode spot processes is still developing and closely associated with advances in plasma diagnostics and modeling. Based on experimental evidence, Mesyats [227, 228] introduced his "ecton" concept, which essentially postulates that the arc spot processes can be interpreted as a sequence of elementary microexplosions, each having a quantum-like minimum action. This approach allowed Mesyats and co-workers to model basic features of the erosion process and plasma parameters.

Noteworthy is also the concept that spot processes superimpose in random fashion, and the concept of elementary steps need to be supplemented with a statistical component, ultimately leading to self-similarity and a rather wide range of temporal and spatial fluctuations [129], which can be best interpreted by a fractal model of cathode processes [130].

The transport of plasma in the absence and presence of a magnetic field was investigated by deposition probes [229], a technique that has been made much more powerful by using low-cost scanners and imaging software [230]. Plasma transport models include the computationally effective (but not self-consistent) drift model by Shi and co-workers [231] and the hydrodynamic models by Alterkop and co-workers [232, 233] and Beilis [234, 235, 236].

2.5.2 Improvements of Coating Quality and Reproducibility, Enabling High-Tech Applications

In the last years of the twentieth century, a number of modern developments expanded the use of cathodic arc technology toward several high-tech applications, as is evident by the development of macroparticle filters. Additional work focuses on improvement of the arc trigger mechanisms and tighter control of arc spot location. The goal is to utilize the highly ionized arc plasma not just for commodities but for high-end applications by bringing the cathodic arc systems to precision levels long known to other coatings techniques (Figure 2.28). By combining control and reproducibility with the inherent advantages of cathodic arc technology, such as high deposition rates, high degree of ionization, and the presence of ions with hyperthermal velocities (corresponding to energies of many tens of eV), a unique type of coating tools is emerging.

The high compressive stress exhibited by cathodic arc films can be reduced in controlled ways by advanced biasing techniques [237]. Inserting film-forming ions at high energy (1 keV or higher) can locally anneal the material and reduce stress while largely maintaining many other film properties, which is now well established by experiment as well as by molecular dynamics simulation [238].

Of importance are the development of improved filters, the utilization of the filtered, fully ionized arc plasma by substrate bias techniques, and the expansion of the technology from hard and decorative coatings into the fields of ultrathin films, nanostructures, and biomedical coatings. Advances in computerized control equipment with fast feedback loops become enabling for precision coatings.

Of special interest is the deposition of tetrahedral amorphous carbon (ta-C), the most diamond-like material within the family of diamond-like carbon (DLC) materials. Filtered arc enables the deposition of continuous, extremely

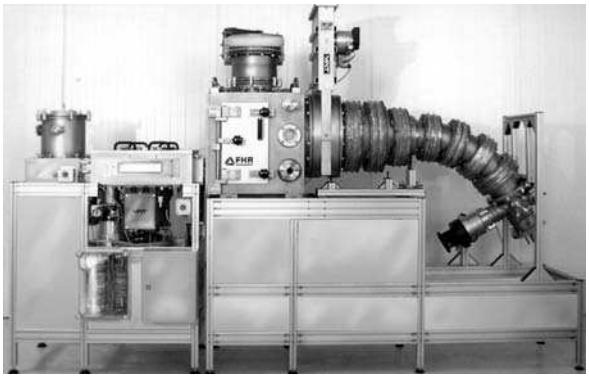

Fig. 2.28. High rate, filtered pulsed arc source developed at the Fraunhofer Institute IWS, Dresden, Germany. (Photo courtesy of P. Siemroth)

thin films, down to the nm range, suitable for the protection of magnetic storage disks and read–write heads [239, 240, 241, 242]. Another example of unusual precision coatings is the filtered arc metallization of semiconductor integrated circuits [213, 243].

2.5.3 Cathodic Arcs for Large-Area Coatings

For almost all deposition processes, the question of scaling to large areas needs to be addressed to reach the economy of scale. The cathodic arc process is challenging to scale because the source of plasma is the cathode *spot*, i.e., inherently a small area, even at higher current and when using large cathodes. Plasma expansion is naturally used to improve uniformity but large-area coatings require the spot location to *move* over large cathode areas. Alternatively, a number of "point" sources can be used.

Several practical solutions have been found, among them is Vergason's concept of switched arcs [244, 245] where the spot travels rapidly in a controlled fashion on cathodes of arbitrarily large size, usually exceeding 1 m in length. Alternatively, spot motion can be magnetically steered on very elongated cathodes, and by managing the magnetic field strength with computer control, large-area coatings are possible [246, 247]. Linear filter concepts have been put forward to accommodate large, essentially linear cathodes [248, 249]. Using an S-filter of elongated, rectangular cross-section (Figure 2.29), films of optical quality on medium-size glass panes have been demonstrated [250].

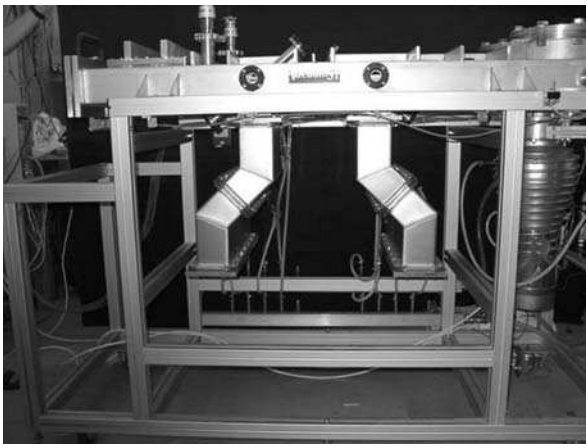

Fig. 2.29. In-line coater for the filtered deposition of SnO_2 on large-area glass substrates using two rectangular S-filter systems in deposition–up position. (Photo courtesy of Ray Boxman and Samuel Goldsmith, Tel Aviv University, Tel Aviv, Israel)

2.5.4 Multilayers and Nanostructures of Multi-component Materials Systems

In recent years, the design of arc coatings has been stimulated by the science and technology of nanostructures. In the sense of multilayers of nm-thick film deposition, this was actually already practiced for some years. However, deeper understanding and high-resolution materials characterization are recent achievements. Examples of multi-component coatings fabricated by arc (and sputtering) techniques are (TiCr)N [251], $Ti_{1-x}Al_xN$ [252, 253], TiC_xN_{1-x} [254], and nanolaminates thereof [255]. These structures have unique properties related to intrinsic stress or/and their nanostructure [256, 257]. Spinodal decomposition was found as an important formation mechanism of nanocrystals [253]. High toughness materials and material systems that are self-lubricating at high temperature have been developed, as needed for high-speed cutting tools [258, 259]. New multi-component materials are being explored, sometimes by combining cathodic arc coatings with sputtering (like the CrN/NbN system [260]) or with plasma-enhanced chemical vapor deposition (e.g., the Zr–Si–N system [261]). Many papers and books were published recently to describe or review these developments, see, for example, [262, 263, 264, 265, 266, 267, 268].

References

1. Priestley, J., "Experiments on the circular spots made on pieces of metal by large electrical explosions," in *The History and Present State of Electricity with Original Experiments, Third Edition, Vol. II*. pp. 260–276, London, (1775).
2. Priestley, J., *The History and Present State of Electricity*, 3rd ed, London, (1775).
3. Hoppe, E., *Geschichte der Elektrizität*. J. A. Barth, Leipzig, (1884).
4. Hoppe, E., "Geschichte der Physik – Dritte Periode von Galvani bis 1820 – 12. Galvanismus," in *Handbuch der Physik I - Geschichte der Physik*, Geiger, H. and Scheel, K., (Eds.). pp. 70–80, (1926).
5. Dibner, B., *Galvani - Volta. A Controversy that led to the Discovery of Useful Electricity*. Burndy Library, Norwalk, Connecticut, (1952).
6. Meyer, H.W., *A History of Electricity and Magnetism*. Burndy Library, Norwalk, Connecticut, (1971).
7. Bowers, B., *A History of Electric Light and Power*. Peter Peregrinus Ltd., London, (1991).
8. Dahl, P., *Flash of the Cathode Ray. A History of J J Thomson's Electron*. Institute of Physics Publishing, Bristol, (1997).
9. Heilbron, J.L., *Electricity in the 17th and 18th Centuries*. Dover Publications, Mineola, New York, (1999).
10. Mott-Smith, H.M., *Nature* **233**, 219, (1971).
11. Anders, A., Tracking down the origin of arc plasma physics. I Early pulsed and oscillating discharges, *IEEE Trans. Plasma Sci.* **31**, 1052–1059, (2003).
12. Anders, A., Tracking down the origin of arc plasma physics. II Early continuous discharges, *IEEE Trans. Plasma Sci.* **31**, 1060–1069, (2003).
13. Gordon, A., *Versuch einer Erklärung der Electricität (2 vol.)*, Erfurt, Germany, (1745, 1746).

14. van Musschenbroek, P., "Letter to Réaumur, dated Jan. 20, 1746, in: Académie des Sciences, Paris, Procès verbaux LXV, 1746; see also p. 313 in J.L. Heilbron, Electricity in the 17th and 18th Century, Dover Publications, Mineola, NY, 1999.
15. Perez, A., Melinon, P., Paillard, V., et al., "Nanocrystalline structures prepared by neutral cluster beam deposition," Second International Conference on Nanostructured Materials, Stuttgart, Germany, 43–52, (1994).
16. Kuhfeld, E., "The Bakken, Library and Museum of Electricity in Life, Minneapolis, MN, personal communication," 2002.
17. Gorokhovsky, V., Heckerman, B., Watson, P., and Bekesch, N., The effect of multilayer filtered arc coatings on mechanical properties, corrosion resistance and performance of periodontal dental instruments, *Surf. Coat. Technol.* **200**, 5614–5630, (2006).
18. Priestley, J., *Experiments and observations on different kinds of air (in three volumes)*. J. Johnson, London, (1775).
19. Schofield, R.E., *The Enlightment of Joseph Priestley. A Study of His Life and Work from 1733 to 1773*. The Pennsylvania State University, University Park, PA, (1997).
20. Priestley, J., *Autobiography of Joseph Priestley (with an Introduction by Jack Lindsay, and Memoirs written by Himself)*. Adams & Dart, Bath, UK, (1970).
21. Schofield, R.E., "Introduction," in *The History and Present State of Electricity by J. Priestley, Reprint of the 3rd edition of 1775*, vol. I. pp.ix–xlix, Johnson Reprint Corporation, New York, (1966).
22. Priestley, J., *Histoire de l'Electricite. Traduite de 'Anglois avec de Notes critiques*, 3rd ed. Herissant, Paris, (1771).
23. Priestley, J., *Geschichte und gegenwärtiger Zustand der Elektricität, nebst eigenthümlichen Versuchen. Nach der zweyten und verbesserten Ausgabe aus dem Englischen übersetzt und mit Anmerkungen begleitet von D. Johann Georg Krünitz*. Gottlib August Lange, Berlin und Stralsund, (1772).
24. Priestley, J., "Experiments on the effect on the electrical explosion discharged through a brass chain, and other metallic substances," in *The History and Present State of Electricity with Original Experiments, Third Edition, Vol. II*. pp. 277–307, London, (1775).
25. Priestley, J., "Experiments in which rings, consisting of all the prismatic colours, where made by electrical explosions on the surface of metals," in *The History and Present State of Electricity, vol. II*. pp. 329–335, London, (1775).
26. Galvani, L., De viribus electricitatis in motu musculari, *Commentarii Bononiesi* **VII**, 363, (1791).
27. Henly, W., An account of a new electrometer, contrived by Mr. Henly, and of several electrical experiments made by him, *Phil. Trans. Roy. Soc. (London)* **62**, 359–364, (1772).
28. Lane, T., Description of an electrometer invented by Mr. Lane; with an account of some experiments made by him with it: Letter to Benjamin Franklin, LLD FRS, of October 15, 1766., *Phil. Trans.* **57**, 451–460, (1767).
29. Kragh, H., "Confusion and Controversy: Nineteenth-Century Theories of the Voltaic Pile," in *Nuova Voltania: Studies on Volta and his Times*, vol. 1, Bevilacqua, F. and Fregonese, L., (Eds.). pp. 133–157, Editore Ulrico Hoepli, Milano, Italy, (2000).
30. Volta, A., On the electricity excited by the mere contact of conducting substances of different kinds, *Phil. Trans.* **II**, 403–431, (1800).
31. Volta, A., On the electricity excited by the mere contact of conducting substances of different kinds, *Phil. Mag.* **VIII**, 289–311, (1800).
32. de Andrade Martins, R., "Romagnosi and Volta's pile: Early difficulties in the interpretation of Voltaic electricity," in *Nuova Voltania: Studies on Volta and his*

Times, vol. 3, Bevilacqua, F. and Fregonese, L., (Eds.). pp. 81–102, Editore Ulrico Hoepli, Milano, Italy, (2000).
33. Nicholson, W., Account of the new electrical or galvanic apparatus of Sig. Alex. Volta, and experiments performed with the same, *J. Nat. Philos. Chem. Arts*. **4**, 179, (1800).
34. Nicholson, W., Carlisle, A., and Cruickshank, W., Experiments on galvanic electricity, *Phil. Mag*. **7**, 337–350, (1800).
35. Ritter, J.W., Neue Versuche und Bemerkungen über den Galvanismus, *Annalen der Physik* **19**, 1–44, (1805).
36. Ohm, G.S., *Die galvanische Kette, mathematisch bearbeitet*. T.H. Riemann, Berlin, (1827).
37. Davy, H., Additional experiments on Galvanic electricity, in a letter to Mr. Nicholson, dated September 22, 1800, *(Nicholson's) J. Nat. Philos. Chem. Arts* **IV**, also in The Collected Works of Sir Humphry Davy, edited by his brother John Davy, vol. II, Early Miscellaneous Papers, London: Smith, Elder, and Cornhill, 1839, pp. 155–163, (1800).
38. Priestley, J., "Letter from Dr. Priestley [to Humphry Davy], dated October 31, 1801," in *Fragmentary Remains, Literary and Scientific, of Sir Humphry Davy*, Davy, H., (Ed.). pp. 51–53, John Churchill, London, (1858).
39. Davy, H., "An account of some experiments on galvanic electricity made in the theatre of the Royal Institution (From Journals of the Royal Institution, vol. i, 1802)," in *The Collected Works of Sir Humphry Davy. Vol. II: Early Miscellaneous Papers*, Davy, J., (Ed.). pp. 211–213, Smith, Elder, and Co. Cornhill, London, (1839).
40. Petrov, V.V., *Announcements on Galvano-Voltaic experiments, conducted by the Professor of Physics Vasilii Petrov, based on an enormous battery, consisting of 4200 copper and zinc disks, located at St. Petersburg's Medical and Surgical Academy (in Russian)*. St. Petersburg's Medical and Surgical Academy, St. Petersburg, Russia, (1803).
41. Kartsev, V., *Learning and discovering in a library (in Russian)*. posted at http://n-t.ru/ri/kr/pu26.htm, (2001).
42. Davy, H., On some chemical agencies of electricity (Bakerian Lecture of 1807), *Phil. Trans. Roy. Soc. (London)* **97**, 1–56, (1807).
43. Davy, H., "Bakerian Lecture read before the Royal Society, Nov. 19, 1807: On some new phenomena of chemical changes produced by electricity, particularly the decomposition of the fixed alkalies, and the exhibition of the new substances which constitute their bases; and on the general nature of alkaline bodies," in *The Collected Works of Sir Humphry Davy. Vol. V: Bakerian Lectures and Miscellaneous Papers from 1806 to 1815*., Davy, J., (Ed.). pp. 57–101, Smith, Elder, and Co. Cornhill, London, (1840).
44. Alglave, E. and Boulard, J., *The Electric Light: Its History, Production, and Application*. D. Appleton and Company, New York, (1884).
45. Knight, D., *Humphry Davy, Science and Power*. Cambridge University Press, Cambridge, UK, (1992).
46. Bowers, B., *Lengthening the Day. A History of Lighting Technology*. Oxford University Press, Oxford, (1998).
47. James, F.A.J.L., "Guides to the Royal Institution of Great Britain: 1. History," Royal Institution of Great Britain, London http://www.rigb.org/heritage/, (2000).
48. Thomas, J.M., *Michael Faraday and the Royal Institution. The Genius of Man and Place*. Institute of Physics Publishing, Bristol and Philadelphia, (1991).

49. Armagnat, H., *The Theory, Design and Construction of Induction Coils*. McGraw Publishing Company, New York, (1908).
50. Davis Jr., D., *Davis's Manual of Magnetism, including Galvanism, Magnetism, Electro-Magnetism, Electro-Dynamics, Magneto-Electricity, and Thermo-Electricity*, 12th ed. Palmer and Hall, Boston, (1857).
51. Porter, R., *The Biographical Dictionary of Scientists*, 2nd ed. Oxford University Press, New York, (1994).
52. Grove, W.R., On the electro-chemical polarity of gases, *Phil. Trans. Roy. Soc. London* **142**, 87–101, (1852).
53. Grove, W.R., On the electro-chemical polarity of gases, *Phil. Mag*., 498–515, (1852).
54. Wright, A.W., On the production of transparent films by the electrical discharge in exhausted tubes, *Am. J. Sci. Arts 3rd Series* **13**, 49–55, (1877).
55. Plücker, J., Observations on the electrical discharge through rarefied gases, *The London, Edinburgh, and Dublin Philosophical Magazine* **16**, 408–418, (1858).
56. Faraday, M., Experimental Relations of Gold (and other metals) to light (The Bakerian Lecture), *Phil. Trans*. **147**, 145–181, (1857).
57. Webster, N., *Webster's Universal Dictionary*. The World Publishing Company, Cleveland, OH, (1940).
58. Stokes, G.G., On the long spectrum of electric light, *Phil. Trans. Roy. Soc. London* **152 part II**, 599–619, (1862).
59. Campbell, L. and Garnett, W., *The Life of James Clerk Maxwell, with a Selection from his Correspondence and Occasional Writings and a Sketch of His Contributions to Science*. MacMillan and Co., London, (1882).
60. Boxman, R.L. and Goldsmith, S., "Vacuum arc deposition in the 19th century," XIV Int. Symp. Discharges and Electrical Insulation in Vacuum, Santa Fe, NM, (1990).
61. Boxman, R.L., Early history of vacuum arc deposition, *IEEE Trans. Plasma Sci*. **29**, 759–761, (2001).
62. Lecher, E., Ueber electromotorische Gegenkräfte in galvanischen Lichterscheinung, *(Wiedemann's) Annalen der Physik und Chemie* **33**, 609–637, (1888).
63. Goldstein, E., Über eine noch nicht untersuchte Strahlungsform an der Kathode inducirter Entladungen, *Sitzungsberichte der Königlichen Akademie der Wissenschaften zu Berlin* **39**, 691–699, (1886).
64. Edison, T.A., "Art of plating one material with another," patent U.S. 526,147 (1894).
65. Edison, T.A., "Process of duplicating phonograms," patent U.S. 484,582 (1892).
66. Edison, T.A., "Process of coating phonograph-records," patent US 713,863 (1902).
67. Waits, R.K., Edison's vacuum coating patents, *J. Vac. Sci. Technol. A* **19**, 1666–1673, (2001).
68. Thomson, J.J., *Phil. Mag*. **48**, 547, (1899).
69. Redhead, P.A., The birth of electronics: Thermionic emission and vacuum, *J. Vac. Sci. Technol. A* **16**, 1394–1401, (1998).
70. Schuster, A., On the constitution of the electric spark, *Nature* **57**, 17, (1897).
71. Feddersen, W., Über die electrische Funkenentladung, *(Poggendorff's) Annalen der Physik und Chemie* **113**, 437–467, (1861).
72. Arons, L., Ueber den Lichtbogen zwischen Quecksilber-electroden, Amalgamen, und Legirungen, *(Wiedemann's) Annalen der Physik und Chemie* **58**, 73–95, (1896).
73. Einstein, A., Über die von der molekularkinetischen Theorie der Wärme geforderte Bewegung von in ruhenden Flüssigkeiten suspendierten Teilchen, *Annalen der Physik* **17**, 549–560, (1905).

74. Einstein, A., Zur Elektrodynamik bewegter Körper, *Annalen der Physik* **17**, 891–921, (1905).
75. Einstein, A., Ist die Trägheit eines Körpers von seinem Energieinhalt abhängig?, *Annalen der Physik* **18**, 639–641, (1905).
76. Einstein, A., Über einen die Erzeugung und die Verwandlung des Lichtes betreffenden heuristischen Gesichtspunkt, *Annalen der Physik* **17**, 132–148, (1905).
77. Stark, J., Retschinsky, T., and Schaposchnikoff, A., Untersuchungen über den Lichtbogen, *Annalen der Physik* **18 (4th Series)**, 213–251, (1905).
78. Boersma, K., Structural ways to embed a research laboratory into the company. A comparison between General Electric and Philips in the inter war period, *Hist. Technol.* **19**, 109–126, (2003).
79. Cornwell, J., *Hitler's Scientists*. Viking-Penguin, New York, (2003).
80. Child, C.D., Discharge from hot CaO, *Phys. Rev.* **32**, 492–511, (1911).
81. Forrester, A.T., *Large Ion Beams*. Wiley, New York, (1988).
82. Weintraub, E., Investigation of the arc in metallic vapours in an exhausted space, *Phil. Mag.* **7 (of Series 6)**, 95–124, (1904).
83. Ehrich, H., Hasse, B., Mausbach, M., and Müller, K.G., The anodic vacuum arc and its application to coatings, *J. Vac. Sci. Technol. A* **8**, 2160–2164, (1990).
84. Beilis, I.I., Boxman, R.L., Goldsmith, S., and Paperny, V.L., Radially expanding plasma parameters in a hot refractory anode vacuum arc, *J. Appl. Phys.* **88**, 6224–6231, (2000).
85. Stark, J., Quecksilber als kathodische Basis des Lichtbogens, *Physikalische Zeitschrift* **5**, 750–751, (1904).
86. Child, C.D., The electric arc in a vacuum, *Phys. Rev. (Series I)* **20**, 364–378, (1905).
87. Stark, J., Induktionserscheinungen am Quecksilberlichtbogen im Magnetfeld, *Z. f. Physik* **4**, 440–443, (1903).
88. Langmuir, I. and Blodgett, K.B., Current limited by space charge between coaxial cylinders, *Phys. Rev.* **22**, 347–356, (1923).
89. Langmuir, I., The effect of space charge and initial velocities on the potential distribution and thermionic current between parallel plane electrodes, *Phys. Rev. (Series II)* **21**, 419–435, (1923).
90. Langmuir, I. and Blodgett, K.B., Current limited by space charge between concentric spheres, *Phys. Rev.* **24**, 49–59, (1924).
91. Child, C.D., The electric arc, *Phys. Rev. (Series I)* **19**, 117–137, (1904).
92. Granqvist, G., Über die Bedeutung des Wärmeleitvermögens der Elektroden bei dem elektrischen Lichtbogen, *Nova Acta Reg. Soc. Sc. Upsala* **20 (series III)**, 1-56 and 2 plates, (1903).
93. Zuchristan, *Wien. Ber.* **102**, 567–576, (1893).
94. Stark, J., Zündung des Lichtbogens an Metalloxyden, *Physikalische Zeitschrift* **5**, 81–83, (1904).
95. Buttolph, L.J., The Cooper Hewitt mercury vapor lamp, *Gen. Elec. Rev.* **23**, 741–751, (1920).
96. Germeshausen, K.J., A new form of band igniter for mercury-pool tubes, *Phys. Rev.* **55**, 228, (1939).
97. Richardson, O.W., On the negative radiation from hot platinum, *Proc. Cambridge Phil. Soc.* **11**, 286–295, (1901).
98. Richardson, O.W., *Emission of Electricity from Hot Bodies*, 2nd ed. Longmans, Green & Co., New York, (1921).
99. Dushman, S., Electron emission from metals as a function of temperature, *Phys. Rev.* **21**, 623–636, (1923).

100. Dushman, S., Thermionic emission, *Rev. Mod. Phys.* **2**, 381–476, (1930).
101. Schottky, W., *Zeitschrift für Physik* **14**, 80, (1923).
102. Dryvesteyn, M.J., Electron emission of the cathode of an arc, *Nature* **137**, 580, (1936).
103. Suits, C.G. and Hocker, J.P., Role of oxidation in arc cathodes, *Phys. Rev.* **53**, 670, (1938).
104. Cobine, J.D., *Gaseous Conductors: Theory and Engineering Applications*. Dover, New York, (1958 (first edition 1941)).
105. Cobine, J.D., Effects of oxides and impurities on metallic arc reignition, *Phys. Rev.* **53**, 911, (1938).
106. Nottingham, W.B., Remarks on the energy loss attending thermionic emission of electrons from metals, *Phys. Rev.* **59**, 906–907, (1941).
107. Smyth, H.D. and Wilson, R.R., "The "Isotron" method of separating tuballoy isotopes. General report covering period from December 1, 1941, to May 15, 1942. Princeton University OSRD project SSRC-5. – SECRET. Classification canceled April 23, 1952.," Princeton University, Princeton (1942).
108. Brown, I.G., Galvin, J.E., MacGill, R.A., and Wright, R.T., Improved time-of-flight charge state diagnostic, *Rev. Sci. Instrum.* **58**, 1589–1592, (1987).
109. Brown, I.G., Feinberg, B., and Galvin, J.E., Multiply stripped ion generation in the metal vapor vacuum arc, *J. Appl. Phys.* **63**, 4889–4898, (1988).
110. Günterschulze, A., *Z. f. Physik* **11**, 71, (1922).
111. Tonks, L., *Physics* **6**, 294, (1935).
112. Cobine, J.D. and Gallagher, C.J., Current density of the arc cathode spot, *Phys. Rev.* **74**, 1524–1530, (1948).
113. Erwin, S., Untersuchungen über die Bewegung des Brennflecks auf der Kathode eines Quecksilberdampf-Niederdruckbogens, *Annalen der Physik (Leipzig)* **439**, 246–270, (1949).
114. Froome, K.D., The rate of growth of current and the behavior of the cathode spot in transient arc discharges, *Proc. Phys. Soc. (London)* **60**, 424, (1948).
115. Bertele, H.V., Current densities of free-moving cathode spots on mercury, *Brit. J. Appl. Phys.* **3**, 358–360, (1952).
116. Froome, K.D., Current densities of free-moving cathode spots on mercury, *Brit. J. Appl. Phys.* **4**, 91, (1953).
117. Mueller, E.W., *Z. f. Physik* **106**, 541, (1937).
118. Dyke, W.P. and Trolan, J.K., Field Emission: large current densities, space charge, and the vacuum arc, *Phys. Rev.* **89**, 799–808, (1953).
119. Kesaev, I.G., *Cathode Processes in the Mercury Arc (authorized translation from the Russian)*. Consultants Bureau, New York, (1964).
120. Kesaev, I.G., *Cathode Processes of an Electric Arc (in Russian)*. Nauka, Moscow, (1968).
121. Rakhovskii, V.I., *Physical Foundations of Switching Electric Current in Vacuum (in Russian)*. Nauka, Moscow, (1970).
122. Anders, S., Anders, A., and Jüttner, B., Brightness distribution and current density of vacuum arc cathode spots, *J. Phys. D: Appl. Phys.* **25**, 1591–1599, (1992).
123. Hantzsche, E., Jüttner, B., and Ziegenhagen, G., Why vacuum arc cathode spots can appear larger than they are, *IEEE Trans. Plasma Sci.* **23**, 55–64, (1995).
124. Achtert, J., Altrichter, B., Jüttner, B., Pech, P., Pursch, H., Reiner, H.-D., Rohrbeck, W., Siemroth, P., and Wolff, H., Influence of surface contaminations on cathode processes of vacuum discharges, *Beitr. Plasmaphys.* **17**, 419–431, (1977).

125. Jüttner, B., Erosion craters and arc cathode spots, *Beitr. Plasmaphys.* **19**, 25–48, (1979).
126. Bugaev, S.P., Litvinov, E.A., Mesyats, G.A., and Proskurovskii, D.I., Explosive emission of electrons, *Sov. Phys. Usp.* **18**, 51–61, (1975).
127. Litvinov, E.A., Mesyats, G.A., and Proskurovskii, D.I., Field emission and explosive emission processes in vacuum discharges, *Sov. Phys. Usp.* **26**, 138, (1983).
128. Mesyats, G.A. and Proskurovsky, D.I., *Pulsed Electrical Discharge in Vacuum*. Springer-Verlag, Berlin, (1989).
129. Schülke, T. and Siemroth, P., Vacuum arcs cathode spots as a self-similarity phenomenon, *IEEE Trans. Plasma Sci.* **24**, 63–64, (1996).
130. Anders, A., The fractal nature of cathode spots, *IEEE Trans. Plasma Sci.* **33**, 1456–1464, (2005).
131. Feddersen, W., Über die electrische Funkenentladung, *(Poggendorff's) Annalen der Physik und Chemie* **116**, 132–171, (1862).
132. Sellerio, A., *Phil. Mag.* **44**, 765–777, (1922).
133. Tanberg, R., On the cathode of an arc drawn in vacuum, *Phys. Rev.* **35**, 1080–1089, (1930).
134. Kobel, E., Pressure and high velocity vapour jets at cathodes of a mercury vacuum arc, *Phys. Rev.* **36**, 1636–1638, (1930).
135. Compton, K.T., An interpretation of pressure and high velocity vapor jets at cathodes of vacuum arcs, *Phys. Rev.* **36**, 706–708, (1930).
136. Slepian, J. and Mason, R.C., High velocity vapor jets at cathodes of vacuum arcs, *Phys. Rev.* **37**, 779–780, (1931).
137. Tanberg, R., On the temperature of cathode in vacuum arc, *Phys. Rev.* **38**, 296–304, (1931).
138. Tonks, L., The pressure of plasma electrons and the force on the cathode of an arc, *Phys. Rev.* **46**, 278–279, (1934).
139. Robertson, R.M., The force on the cathode of a copper arc, *Phys. Rev.* **53**, 578–582, (1938).
140. Kesaev, I.G., Laws governing the cathode drop and the threshold currents in an arc discharge on pure metals, *Sov. Phys. – Techn. Phys.* **9**, 1146–1154, (1965).
141. Plyutto, A.A., Ryzhkov, V.N., and Kapin, A.T., High speed plasma streams in vacuum arcs, *Sov. Phys. JETP* **20**, 328–337, (1965).
142. Davis, W.D. and Miller, H.C., Analysis of the electrode products emitted by dc arcs in a vacuum ambient, *J. Appl. Phys.* **40**, 2212–2221, (1969).
143. Lunev, V.M., Padalka, V.G., and Khoroshikh, V.M., Plasma properties of a metal vacuum arc. II, *Sov. Phys. Tech. Phys.* **22**, 858–861, (1977).
144. Wieckert, C., The expansion of the cathode spot plasma in vacuum arc discharges, *Phys. Fluids* **30**, 1810–1813, (1987).
145. Hantzsche, E., Two-dimensional models of expanding vacuum arc plasmas, *IEEE Trans. Plasma Sci.* **23**, 893–898, (1995).
146. Beilis, I.I., "Theoretical modeling of cathode spot phenomena," in *Handbook of Vacuum Arc Science and Technology*, Boxman, R.L., Martin, P.J., and Sanders, D. M., (Eds.). pp. 208–256, Noyes, Park Ridge, N.J., (1995).
147. Lucas, M.S.P., Owen, J.H.A., Stewart, W.C., and Vail, C.R., Vacuum-arc evaporation of refractory metals, *Rev. Sci. Instrum.* **32**, 203–204, (1961).
148. Lucas, M.S.P., Vail, C.R., Stewart, W.C., and Owen, H.A., "A new deposition technique for refractory metal films," 8th National Vacuum Symposium combined with the Second International Congress on Vacuum Science and Technology, Washington D.C., 988–991, (1961).

149. Catani, L., Cianchi, A., Lorkiewicz, J., et al., Cathodic arc grown niobium films for RF superconducting cavity applications, *Physica C: Superconductivity* **441**, 130–133, (2006).
150. Langner, J., Mirowski, R., Sadowski, M.J., et al., Deposition of superconducting niobium films for RF cavities by means of UHV cathodic Arc, *Vacuum* **80**, 1288–1293, (2006).
151. Naoe, M. and Yamanaka, S., Nickel ferrite thick films deposited by vacuum-arc discharge, *Jap. J. Appl. Phys.* **9**, 293–301, (1970).
152. Naoe, M. and Yamanaka, S., Vacuum-arc evaporations of ferrites and compositions of their deposits, *Jap. J. Appl. Phys.* **10**, 747–753, (1971).
153. Aksenov, I.I. and Andreev, A.A., Vacuum arc coating technologies at NSC KIPT, *Problems Atomic Sci. Technol., Series: Plasma Physics* **3**, 242–246, (1999).
154. Sablev, L.P., Usov, V.V., Romanov, A.A., Dolotov, J.I., Lunev, V.M., Lutsenko, V.N., Atamansky, N.P., and Kushnir, A.S., patent USSR N235523 (1966).
155. Romanov, A.A. and Andreev, A.A., patent USSR N367755 (1970).
156. Romanov, A.A., Andreev, A.A., and Kozlov, V.N., patent USSR N284883 (1969).
157. Lunev, V.M. and Samoilov, V.P., (in Russian), *Sintetis Almazy (Diamond Synthesis)* **no.4**, 28, (1977).
158. Aksenov, I.I., Bren', V.G., Padalka, V.G., and Khoroshikh, V.M., Chemical reactions in the condensation of metal-plasma streams, *Sov. Phys -Tech. Phys.* **23**, 651–653, (1978).
159. Andreev, A.A., Bulatova, L.V., Kartmasov, G.N., Kostritsa, T.V., Lunev, V.M., and Romanov, A.A., *Fizika i Khimiya Obrabotki Materialov* **2**, 169, (1979).
160. Odintsov, L.G., Romanov, A.A., Andreev, A.A., Ehtingant, A.A., Gorelik, V.M., Vereshchaka, A.S., and Pylinin, O.V., patent USSR N607659 (1976).
161. Andreev, A.A., Romanov, A.A., Ehtingant, A.A., and Vereshchaka, A.S., patent USSR N819217 (1976).
162. Sablev, L.P., Dolotov, Y.I., Stupak, R.I., and Osipov, V.A., Electric-arc vaporizer of metals with magnetic confinement of cathode spot, *Instrum. Exp. Tech.* **19**, 1211–1213, (1976).
163. Aksenov, I.I. and Andreev, A.A., Motion of the cathode spot of a vacuum arc in an inhomogeneous magnetic field, *Sov. Tech. Phys. Lett.* **3**, 525–526, (1977).
164. Sablev, L.P., Electric-arc vaporizer of metals with magnetic confinement of cathode spot, *Instrum. Exp. Tech.* **22**, 1174, (1979).
165. Aksenov, I.I., Padalka, V.G., and Khoroshykh, V.M., Investigation of a flow of plasma generated by a stationary erosion electric arc accelerator with magnetic confinement of the cathode spot, *Sov. J. Plasma Phys.* **5**, 341, (1979).
166. Lunev, V.M., Padalka, V.G., and Khoroshikh, V.M., Plasma properties of a metal vacuum arc. I, *Sov. Phys. Tech. Phys.* **22**, 855–858, (1977).
167. Lunev, V.M., Samoilov, V.P., Zubar', V.P., Digtenko, V.G., and Kokoshko, M.D., (in Russian), *Sintetis Almazy (Diamond Synthesis)* **no.4**, 26, (1978).
168. Matyushenko, N.N., Strel'nitskii, V.E., and Romanov, A.A., (in Russian), *Doklady Akad. Nauk UkrSSR, Ser. A* **5**, 459, (1976).
169. Strel'nitskii, V.E., Matyushenko, N.N., Romanov, A.A., and Tolok, V.T., (in Russian), *Doklady Akad. Nauk UkrSSR, Ser. A* **8**, 760, (1977).
170. Strel'nitskii, V.E., Padalka, V.G., and Vakula, S.I., Properties of the diamond-like carbon film produced by the condensation of a plasma stream with an RF potential, *Sov. Phys.-Techn. Phys.* **23**, 222–224, (1978).
171. Vakula, S.I., Padalka, V.G., Strel'nitskii, V.E., and Cheoskin, A.I., *Sverkhtverdye Materialii (Superhard Materials)* **no.1**, 18, (1980).

172. Vakula, S.I., Padalka, V.G., Strel'nitskii, V.E., and Usoskin, A.I., Optical properties of diamond-like carbon films, *Sov. Techn. Phys. Lett.* **5**, 573–574, (1979).
173. Aksenov, I.I., Vakula, S.I., Kunchenko, V.V., Matyushenko, N.N., Ostapenko, I.L., Padalka, V.G., and Strel'nitskii, V.E., *Sverkhtverdye Materialii (Superhard Materials)* **no.3**, 12, (1980).
174. Kikuchi, M., Nagakura, S., Ohmura, H., and Oketani, S., Structures of the metal films produced by vacuum-arc evaporation method, *Jap. J. Appl. Phys.* **4**, 940, (1965).
175. Kuznetsov, I., "Electron beam evaporation processes in the Soviet Union," 21st Annual Technical Conference Proceedings of the Society of Vacuum Coaters, 87, (1978).
176. Wroe, H., The magnetic stabilization of low pressure d.c. arcs, *Brit. J. Appl. Phys.* **9**, 488–491, (1958).
177. Wroe, H., "Stabilisation of low pressure D.C. arc discharges," patent US 2,972,695 (1961).
178. Minorsky, M.N., La rotation de l'arc électrique dans un champ magnétique radial, *Le Journal de Physique et Le Radium* **9**, 127–136, (1928).
179. Smith, C.G., Motion of an arc in a magnetic field, *J. Appl. Phys.* **28**, 1328–1331, (1957).
180. Robson, A.E. and von Engel, A., Origin of retrograde motion of arc cathode spots, *Phys. Rev.* **93**, 1121–1122, (1954).
181. Daalder, J.E., Components of cathode erosion in vacuum arcs, *J. Phys. D: Appl. Phys.* **9**, 2379–2395, (1976).
182. Lafferty, J.M., *Vacuum Arcs – Theory and Applications*. Wiley, New York, (1980).
183. Gilmour, A. and Lockwood, D.L., Pulsed metallic-plasma generator, *Proc. IEEE* **60**, 977–992, (1972).
184. Snaper, A.A., "Arc deposition process and apparatus," patent US 3,836,451 (1974).
185. Smith Jr., H.R., "Current vacuum coating processes in the Soviet Union," 25th Technical Conference Proceedings, Society of Vacuum Coaters, 179–189, (1983).
186. Bergman, C., "Arc plasma physical vapor deposition," 28th Annual SVC Technical Conference, Philadelphia, PA, 175–191, (1985).
187. Johnson, P.C., "Cathodic arc plasma deposition processes and their applications," 30th Annual SVC Technical Conference, 317–324, (1987).
188. Randhawa, H., Cathodic arc plasma deposition technology, *Thin Solid Films* **167**, 175–185, (1988).
189. Sanders, D.M., Boercker, D.B., and Falabella, S., Coatings technology based on the vacuum arc – a review, *IEEE Trans. Plasma Sci.* **18**, 883–894, (1990).
190. Vergason, G. and Papa, A., "Selection of materials and techniques for performance coatings," 42 nd Annual SVC Technical Conference, 53–57, (1999).
191. Vergason, G. and Papa, A., "Rapid cycle coating techniques for cell manufacturing," 40th Annual SVC Technical Conference, New Orleans, LA, 54–57, (1997).
192. Fleischer, W., Trinh, T., van der Kolk, G.J., Hurkmans, T., and Franck, M., "Decorative PVD hardcoatings in a wide colour range on different substrate materials," 41st Annual SVC Technical Conference, 33–37, (1998).
193. Bouix, M.H., "The combination of "gold plating" and high wear resistance of PVD," 42 nd Annual SVC Technical Conference, Boston, MA, 83–84, (1998).
194. Münz, W.-D., Schulze, D., and Hauzer, F.J.M., A new method for hard coatings – ABS (arc bond sputtering), *Surf. Coat. Technol.* **50**, 169–178, (1992).

195. Burkhardt, W. and Reinecke, R., "Method of coating articles by vaporized coating materials," patent US 2,157,478 (1939).
196. Lawson, J.D., (ed.) *Fusion's History*, http://www.iter.org/, (1993).
197. Voitsenya, V.S., Gorbanyuk, A.G., Onishchenko, I.N., Safronov, B.G., Khizhniyak, N.A., and Shkoda, V.V., Motion of a plasmoid in a curvilinear magnetic field, *Sov. Phys. Tech. Phys.* **12**, 185–192, (1967).
198. Aksenov, I.I., Belous, V.A., Padalka, V.G., and Khoroshikh, V.M., Apparatus to rid the plasma of a vacuum arc of macroparticles, *Instrum. Exp. Tech.* **21**, 1416–1418, (1978).
199. Aksenov, I.I., Belous, V.A., Padalka, V.G., and Khoroshikh, V.M., Transport of plasma streams in a curvilinear plasma-optics system, *Sov. J. Plasma Phys.* **4**, 425–428, (1978).
200. Axenov, I.I., Belous, V.A., Padalka, V.G., and Khoroshikh, V.M., "Arc plasma generator and a plasma arc apparatus for treating the surface of work-pieces, incorporating the same arc plasma generator," patent US 4,452,686 (1984).
201. Aksenov, I.I., Belokhvostikov, A.N., Padalka, V.G., Repalov, N.S., and Khoroshikh, V.M., Plasma flux motion in a toroidal plasma guide, *Plasma Phys. Controlled Fusion* **28**, 761–770, (1986).
202. Schemmel, T.D., Cunningham, R.L., and Randhawa, H., Process for high rate deposition of Al_2O_3, *Thin Solid Films* **181**, 597–601, (1989).
203. Martin, P.J., Netterfield, R.P., Bendavid, A., and Kinder, T.J., "Properties of thin films produced by filtered arc deposition," 36th Annual SVC Technical Conference, Dallas, TX, 375–378, (1993).
204. Martin, P.J., Netterfield, R.P., Kinder, T.J., and Descotes, L., Deposition of TiN, TiC, and TiO_2 films by filtered arc evaporation, *Surf. Coat. Technol.* **49**, 239–243, (1991).
205. Martin, P.J., Netterfield, R.P., Bendavid, A., and Kinder, T.J., The deposition of thin films by filtered arc evaporation, *Surf. Coat. Technol.* **54**, 136–142, (1992).
206. Baldwin, D.A. and Fallabella, S., "Deposition processes utilizing a new filtered cathodic arc source," Proc. of the 38th Annual Techn. Conf., Society of Vacuum Coaters, Chicago, 309–316, (1995).
207. Shi, X., Flynn, D.I., Tay, B.K., and Tan, H.S., "Filtered cathodic arc source," patent WO 96/26531 (1996).
208. Shi, X., Fulton, M., Flynn, D.I., Tay, B.K., and Tan, H.S., "Deposition apparatus," patent WO 96/26532 (1996).
209. Anders, S., Anders, A., Dickinson, M.R., MacGill, R.A., and Brown, I.G., S-shaped magnetic macroparticle filter for cathodic arc deposition, *IEEE Trans. Plasma Sci.* **25**, 670–674, (1997).
210. Anders, A. and MacGill, R.A., Twist filter for the removal of macroparticles from cathodic arc plasmas, *Surf. Coat. Technol.* **133–134**, 96–100, (2000).
211. Ryabchikov, A.I. and Stepanov, I.B., Investigations of forming metal-plasma flows filtered from microparticle fraction in a vacuum arc evaporator, *Rev. Sci. Instrum.* **69**, 810–812, (1998).
212. Bilek, M.M.M., Anders, A., and Brown, I.G., Characterization of a linear Venetian-blind macroparticle filter for cathodic vacuum arcs, *IEEE Trans. Plasma Sci.* **27**, 1197–1202, (1999).
213. Siemroth, P. and Schülke, T., Copper metallization in microelectronics using filtered vacuum arc deposition – principles and technological development, *Surf. Coat. Technol.* **133–134**, 106–113, (2000).

214. Anders, A., Approaches to rid cathodic arc plasma of macro- and nanoparticles: a review, *Surf. Coat. Technol.* **120–121**, 319–330, (1999).
215. Martin, P.J. and Bendavid, A., Review of the filtered vacuum arc process and materials deposition, *Thin Solid Films* **394**, 1–15, (2001).
216. Boxman, R.L. and Zhitomirsky, V.N., Vacuum arc deposition devices, *Rev. Sci. Instrum.* **77**, 021101–15, (2006).
217. Jüttner, B., Characterization of the cathode spot, *IEEE Trans. Plasma Sci.* **PS-15**, 474–480, (1987).
218. Secker, P.E. and George, I.A., Preliminary measurements of arc cathode current density, *J. Phys. D: Appl. Phys.* **2**, 918–920, (1969).
219. Guile, A.E. and Jüttner, B., Basic erosion processes of oxidized and clean metal cathodes by electric arcs, *IEEE Trans. Plasma Sci.* **8**, 259–269, (1980).
220. Siemroth, P., Schülke, T., and Witke, T., Microscopic high speed investigations of vacuum arc cathode spot, *IEEE Trans. Plasma Sci.* **23**, 919–925, (1995).
221. Siemroth, P., Schülke, T., and Witke, T., Investigations of cathode spots and plasma formation of vacuum arcs by high speed microscopy and spectrography, *IEEE Trans. Plasma Sci.* **25**, 571–579, (1997).
222. Kleberg, I., "Dynamics of cathode spots in external magnetic field (in German)," Humboldt University: Berlin, Germany, 2001.
223. Jüttner, B. and Kleberg, I., The retrograde motion of arc cathode spots in vacuum, *J Phys. D: Appl. Phys.* **33**, 2025–2036, (2000).
224. Anders, A., Anders, S., Jüttner, B., Bötticher, W., Lück, H., and Schröder, G., Pulsed dye laser diagnostics of vacuum arc cathode spots, *IEEE Trans. Plasma Sci.* **20**, 466–472, (1992).
225. Jüttner, B., The dynamics of arc cathode spots in vacuum, *J. Phys. D: Appl. Phys.* **28**, 516–522, (1995).
226. Vogel, N., The cathode spot plasma in low-current air and vacuum break arcs, *J. Phys. D: Appl. Phys.* **26**, 1655–1661, (1993).
227. Mesyats, G.A., Ecton mechanism of the vacuum arc cathode spot, *IEEE Trans. Plasma Sci.* **23**, 879–883, (1995).
228. Mesyats, G.A., *Explosive Electron Emission*. URO Press, Ekaterinburg, (1998).
229. Anders, A., Anders, S., and Brown, I.G., Transport of vacuum arc plasmas through magnetic macroparticle filters, *Plasma Sources Sci. Technol.* **4**, 1–12, (1995).
230. Bilek, M.M.M. and Brown, I.G., Deposition probe technique for the determination of film thickness profiles, *Rev. Sci. Instrum.* **69**, 3353–3356, (1998).
231. Shi, X., Tu, Y.Q., Tan, H.S., and Tay, B.K., Simulation of plasma flow in toroidal solenoid filters, *IEEE Trans. Plasma Sci.* **24**, 1309–1318, (1996).
232. Alterkop, B., Gidalevich, E., Goldsmith, S., and Boxman, R.L., The numerical calculation of plasma beam propagation in a toroidal duct with magnetized electrons and unmagnetized ions, *J. Phys. D: Appl. Phys.* **29**, 3032–3038, (1996).
233. Alterkop, B., Gidalevich, E., Goldsmith, S., and Boxman, R.L., Propagation of a magnetized plasma beam in a toroidal filter, *J. Phys. D: Appl. Phys.* **31**, 873–879, (1998).
234. Beilis, I., Djakov, B.E., Jüttner, B., and Pursch, H., Structure and dynamics of high-current arc cathode spots in vacuum, *J. Phys. D: Appl. Phys* **30**, 119–130, (1997).
235. Beilis, I.I., Keidar, M., Boxman, R.L., and Goldsmith, S., Theoretical study of plasma expansion in a magnetic field in a disk anode vacuum arc, *J. Appl. Phys.* **83**, 709–717, (1998).
236. Beilis, I.I., The vacuum arc cathode spot and plasma jet: Physical model and mathematical description, *Contrib. Plasma Phys.* **43**, 224–236, (2003).

237. Anders, A., Metal plasma immersion ion implantation and deposition: a review, *Surf. Coat. Technol.* **93**, 157–167, (1997).
238. Bilek, M.M.M. and McKenzie, D.R., A comprehensive model of stress generation and relief processes in thin films deposited with energetic ions, *Surf. Coat. Technol.* **200**, 4345–4354, (2006).
239. Anders, A., Fong, W., Kulkarni, A., Ryan, F.R., and Bhatia, C.S., Ultrathin diamondlike carbon films deposited by filtered carbon vacuum arcs, *IEEE Trans. Plasma Sci.* **29**, 768–775, (2001).
240. Casiraghi, C., Ferrari, A.C., Ohr, R., Chu, D., and Robertson, J., Surface properties of ultra-thin tetrahedral amorphous carbon films for magnetic storage technology, *Diam. Rel. Mat.* **13**, 1416–1421, (2004).
241. Druz, B., Yevtukhov, Y., Novotny, V., Zaritsky, I., Kanarov, V., Polyakov, V., and Rukavishnikov, A., Nitrogenated carbon films deposited using filtered cathodic arc, *Diam. Rel. Mat.* **9**, 668–674, (2000).
242. Druz, B., Yevtukhov, Y., and Zaritskiy, I., Diamond-like carbon overcoat for TFMH using filtered cathodic arc system with Ar-assisted arc discharge, *Diam. Rel. Mat.* **14**, 1508–1516, (2005).
243. Monteiro, O.R., Novel metallization technique for filling 100-nm-wide trenches and vias with very high aspect ratio, *J. Vac. Sci. Technol. B* **17**, 1094–1097, (1999).
244. Vergason, G.E., "Electric arc vapor deposition device," patent US 5,037,522 (1991).
245. Vergason, G.E., Lunger, M., and Gaur, S., "Advances in arc spot travel speed to improve film characteristics," Annual Technical Conference of the Society of Vacuum Coaters, Philadelphia, 136–140, (2001).
246. Siemroth, P., Zimmer, O., Schulke, T., and Vetter, J., Vacuum arc evaporation with programable erosion and deposition profile, *Surf. Coat. Technol.* **94–95**, 592–596, (1997).
247. Zimmer, O., "Magnetische und elektrische Steuerung der Vakuumbogenbeschichtung," Ruhr-Universität Bochum: Bochum, Germany, 2002.
248. Gorokhovsky, V.I., "Apparatus for application of coatings in vacuum," patent US 5,435,900 (1995).
249. Welty, R.P., "Rectangular vacuum-arc plasma source," patent US 5,840,163 (1998).
250. Boxman, R.L., Zhitomirsky, V., Goldsmith, S., David, T., and Dikhtyar, V., "Deposition of SnO_2 coatings using a rectangular filtered vacuum arc source," 46th Annual Technical Meeting of the Society of Vacuum Coaters, San Francisco, CA, 234–239, (2003).
251. Vetter, J., Vacuum arc coatings for tools – potential and application, *Surf. Coat. Technol.* **77**, 719–724, (1995).
252. Hörling, A., Hultman, L., Odén, M., Sjolén, J., and Karlsson, L., Thermal stability of arc evaporated high aluminum-content $Ti_{1-x}Al_xN$ thin films, *J. Vac. Sci. Technol. A* **20**, 1815–1823, (2002).
253. Mayrhofer, P.H., Hörling, A., Karlsson, L., Sjolen, J., Larsson, T., Mitterer, C., and Hultman, L., Self-organized nanostructures in the Ti-Al-N system, *Appl. Phys. Lett.* **83**, 2049–2051, (2003).
254. Karlsson, L., Hultman, L., Johansson, M.P., Sundgren, J.E., and Ljungcrantz, H., Growth, microstructure, and mechanical properties of arc evaporated TiC_xN_{1-x} ($0 <= x <= 1$) films, *Surf. Coat. Technol.* **126**, 1–14, (2000).
255. Kok, Y.N., Hovsepian, P.E., Luo, Q., Lewis, D.B., Wen, J.G., and Petrov, I., Influence of the bias voltage on the structure and the tribological performance

of nanoscale multilayer C/Cr PVD coatings, *Thin Solid Films* **475**, 219–226, (2005).
256. Veprek, S., The search for novel, superhard materials, *J. Vac. Sci. Technol. A* **17**, 2401–2420, (1999).
257. Veprek, S., J. Veprek-Heijman, M.G., and Zhang, R., Chemistry, physics and fracture mechanics in search for superhard materials, and the origin of superhardness in nc-TiN/a-Si_3N_4 and related nanocomposites, *J. Phys. Chem. Solids* **68**, 1161–1168, (2007).
258. Hörling, A., Hultman, L., Odén, M., Sjölén, J., and Karlsson, L., Mechanical properties and machining performance of $Ti_{1-x}Al_xN$-coated cutting tools, *Surf. Coat. Technol.* **191**, 384–392, (2005).
259. Hovsepian, P.E., Lewis, D.B., Luo, Q., Munz, W.-D., Mayrhofer, P.H., Mitterer, C., Zhou, Z., and Rainforth, W.M., TiAlN based nanoscale multilayer coatings designed to adapt their tribological properties at elevated temperatures, *Thin Solid Films* **485**, 160–168, (2005).
260. Lewis, D.B., Reitz, D., Wüstefeld, C., Ohser-Wiedemann, R., Oettel, H., Ehiasarian, A.P., and Hovsepian, P.E., Chromium nitride/niobium nitride nano-scale multilayer coatings deposited at low temperature by the combined cathodic arc/unbalanced magnetron technique, *Thin Solid Films* **503**, 133–142, (2006).
261. Winkelmann, A., Cairney, J.M., Hoffman, M.J., Martin, P.J., and Bendavid, A., Zr-Si-N films fabricated using hybrid cathodic arc and chemical vapour deposition: Structure vs. properties, *Surf. Coat. Technol.* **200**, 4213–4219, (2006).
262. Anders, A., (ed.) *Handbook of Plasma Immersion Ion Implantation and Deposition*, John Wiley & Sons, New York, (2000).
263. Chun, S.-Y. and Chayahara, A., Pulsed vacuum are deposition of multilayers in the nanometer range, *Surf. Coat. Technol.* **132**, 217–221, (2000).
264. Chen, P., Wong, S.P., Chiah, M.F., Wang, H., Cheung, W.Y., Ke, N., and Xiao, Z. S., Magnetic properties of (Pr0.17Co0.83)(69)C-31 nanocomposite films prepared by pulsed filtered vacuum arc deposition, *Appl. Phys. Lett.* **81**, 4799–4801, (2002).
265. Byon, E., Oates, T.H., and Anders, A., Coalescence of nanometer silver islands on oxides grown by filtered cathodic arc deposition, *Appl. Phys. Lett.* **82**, 1634–1636, (2003).
266. Huang, H., Woo, C.H., Wei, H.L., and Zhang, X.X., Kinetics-limited surface structures at the nanoscale, *Appl. Phys. Lett.* **82**, 1272–1274, (2003).
267. Werner, Z., Stanisawski, J., Piekoszewski, J., Levashov, E.A., and Szymczyk, W., New types of multi-component hard coatings deposited by arc PVD on steel pretreated by pulsed plasma beam, *Vacuum* **70**, 263–267, (2003).
268. Mayrhofer, P.H., Mitterer, C., Hultman, L., and Clemens, H., Microstructural design of hard coatings, *Prog. Mater. Sci.* **51**, 1032–1114, (2006).

3

The Physics of Cathode Processes

About thirty years ago – I remember it very well – I wondered about the incompatibility of model ideas and experimental facts. What does really happen in the cathode arc spot? At that time, I imagined the great magma lake of the Halemaumau crater in Hawaii, with its red-hot, glowing, molten surface, steaming, boiling, bubbling, gushing, in restless motion, flowing and whirling, rising and falling, covered by clouds of hot vapours, and often throwing gigantic, bright fountains of liquid magma, coupled with ejection of large showers of glowing droplets and pieces and lumps of magma. – So, similar, as it seemed to me, must be the surface of an arc spot, if we could observe it in action, in quite different time and space scales, of course.

Erhard Hantzsche, in his Dyke Award Address, XX ISDEIV, Tours, France, 2002

The fractal approach is both effective and "natural." Not only should it not be resisted, but one ought to wonder how one could have gone so long without it.

Benoit Mandelbrot, in "The Fractal Geometry of Nature," 1982

Abstract This chapter is at the heart of the book. It is the longest chapter that deals with electron emission processes. The basic mechanisms of electron emission are outlined, including thermionic emission, field emission, their nonlinear combination, as well as explosive emission. This leads to the non-stationary emission centers, which are the sources of electrons and plasma. The statistical nature of emission center ignition, coupled with self-similar features of emission centers in space and time, lead naturally to a description of cathode spots as a fractal phenomenon. If taken seriously, the old discussion of the "true" current density and "true" characteristic time of cathode spots needs to be re-evaluated: those properties are fractal down to the physical cutoffs, which are generally still below the resolution limits of the experimental equipment. As a consequence,

A. Anders, *Cathodic Arcs*, DOI: 10.1007/978-0-387-79108-1_3,

some new features of cathode phenomena are introduced, such as the existence of transient holes in the cathode sheath.

3.1 Introduction

Cathode processes are at the heart of cathodic arc plasma production. Cathodic arc processes have features that are surprising or strange, even for scientists and engineers familiar with discharges and plasmas. The plasma "root" or "attachment" on the cathode is localized in bright, tiny spots that appear to quickly move more or less randomly on the cathode surface. In the presence of an external magnetic field, spot motion appears to be steered in a preferred (close to the "anti-Amperian," $-\mathbf{j}\times\mathbf{B}$) direction. In any case, the cathode material suffers a transition to dense plasma at these spots, and the dense cathode plasma expands rapidly into the vacuum or low-pressure gas ambient. The anode is merely a passive collector of electrons unless its area is very small or it is thermally isolated or the discharge current is very high. In these cases, anode spots may appear and/or the anode may evaporate. Because this book focuses on cathodic arc deposition, these special anode conditions are not much considered.

The structure and dynamics of cathode spots are still the subject of discussions and research. The current density plays a central role in many models because it is critically important for power density distribution and energy balance, which, in turn, govern all processes of electron emission, phase transitions, and plasma production. Most, but not all, experts agree that explosive electron emission and the associated "ecton" model is closest to reality. An emerging model is the concept of a stochastic fractal model for the cathode spot, which includes ecton processes as the determining lower limit of self-similar scaling. The fractal model may be suitable to describe what Erhard Hantzsche expressed in his Dyke Award Address (see the quote at the beginning of this chapter). Throughout this and other chapters, the fractal model approach will be described to the extent known at this time.

The first question that may arise could be formulated as follows: Why is the cathode active but the anode passive? This question touches the general role of cathode and anode in gas discharges. It is clear that electric current in both cathode and anode is associated with electron motion in the conduction band of the metals (solid or liquid) that make up cathode and anode. If plasma happens to be present between cathode and anode, current can flow by motion of free and mobile charged particles. In the plasma, most of the electric current is carried by electrons because electron mobility is much higher than the mobility of ions, a consequence of their very different masses.

The critical places of current continuity are the *interfaces* between plasma and metal. Electrons move to the anode and fall there into the anode's conduction

band, liberating the potential energy known as the work function (about 4 eV per electron for most metals), which leads to heating of the anode. Current continuity (Kirchhoff's law, 1846) is therefore easily accomplished at the anode. A small anode potential drop usually appears to adjust the arrival rate of electrons at the anode surface to the right current as required by current continuity.

In contrast, electrons in the conduction band of the cathode are prevented from escaping by a potential barrier, the work function of the cathode. Electrons need to be given the work function energy to "free" them from the cathode. Here is where the nature of the discharge creates special conditions enabling electrons in the cathode to overcome the potential barrier that keeps them normally inside the cathode. Depending on the character of those "special conditions," we distinguish different electron emission mechanisms, and they ultimately lead to different forms of electrical discharges. Going a step further one can define the type of discharge by the electron emission mechanism.

To understand and appreciate cathodic arc operation, a brief overview of these "special conditions" leading to electron emission needs to be given. As we will see, electrons can be emitted by individual events, such as ion impact or by collective effects affecting all electrons in the cathode, such as high cathode temperature and/or high electric field on the cathode's surface. Following pioneering work of Hantzsche [1, 2], one can use the distinction between individual and collective emission processes to define glow and arc discharges in a very general, physical manner, regardless of phenomenological appearance or absolute values of current and voltage.

The potential distribution between cathode and anode is generically and schematically shown in Figure 3.1. The voltage is not evenly distributed but

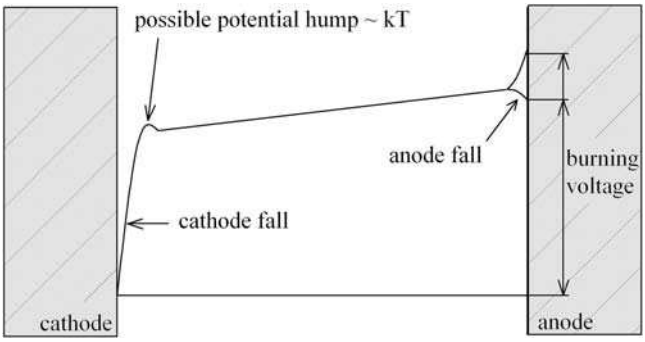

Fig. 3.1. Schematic, generic, one-dimensional presentation of the potential distribution between cathode and anode; the sheaths are actually very thin and shown not to scale. One should note that cathode-spot formation, as explained later, requires modeling of a two or better three-dimensional potential distribution near the cathode surface, not the simplified one shown here

concentrated in the sheaths near the cathode and anode. The potential drop in the cathode sheath is most significant for the mechanism that liberates electrons from the cathode. The anode drop, in contrast, can be positive or negative depending on arc current, anode area, and other factors affecting the electron current arriving at the anode.

The magnitude of the cathode fall is a "fingerprint" of the cathode mechanism. The cathode mechanism adjusts the cathode fall (i.e., the voltage drop in cathode sheath) that is needed to maintain the discharge. In glow discharges, ions coming from the bulk plasma are accelerated toward the cathode when they enter the cathode sheath, and thus they arrive at the cathode surface with approximately the energy (in eV) gained in the cathode fall (expressed in V), if we assume that they are typically singly charged and did not suffer collisions. The yield of secondary electron emission is greatly affected by the potential energy of the impacting ion (potential emission, discussed in greater detail in Chapter 8). The voltage drop in a glow discharge usually exceeds 300 V and is often in the region of 400–500 V in order to give secondary electrons enough energy to heat plasma electrons and to cause ionization in the plasma bulk. The cathode fall is self-adjusting as one can see by the following argument. If electrons do not gain enough energy in the sheath, the plasma generation will be reduced, the plasma density starts to drops, and the plasma impedance (complex resistance) increases. This will cause an increase in the burning voltage, which also means that the voltage drop in the sheath increases, thereby leading to an increase in secondary electron energy, which is followed by an increase in plasma density.

Secondary electrons are vital for the operation of glow discharges. In arcs, in contrast, electrons are not released by individual ion impact but by a *collective* mechanism, which can be thermionic (i.e., the cathode is at very high temperature) or determined by a strong electric field. The hot cathode case leads to thermionic arcs, which can be stationary. In some situations, a hot cathode is also subject to a high electric field. Nonlinear amplification of thermionic and field emission can occur, known as thermo-field emission.

Thermo-field emission can be coupled to a thermal runaway process, namely when emission is related to energy dissipation and net heating of the cathode, which in turn can enhance the temperature and associated electron emission. Locations where this occurs can explosively evaporate, leading to a new form of electron emission that is inherently non-stationary because the emission location is changed by the explosion, subsequent plasma expansion, and the increase of the hot spot area by thermal conduction. This non-stationary form of emission is called explosive electron emission. The explosive phase requires a minimum action to be invested, a "quantum" of the explosive process, the so-called *ecton*. The ecton phase is generally much shorter than the overall cycle or "lifetime" of an emission center. Ignition of a competing emission center is closely related to the existence of the current center. The dense plasma provides the conditions for the ignition while "choking" the already operating emission center by its limited conductivity. These features will be discussed later in the chapter.

Ignition of emission center appears to be a very important element to understanding cathodic arcs. Ignition in this sense is not just the triggering of the arc discharge but the arc's perpetual mechanism to "stay alive." The probabilistic distribution of perpetual ignition of emission centers can be associated with a fractal spot model [3].

In the remainder of this chapter, electron emission theory will be briefly described as it is related to arcs, before explosive emission, crater formation, metal plasma generation, ectons, the fractal features of the cathodic arc spots, spot types, and arc modes are discussed in greater detail.

3.2 Theory of Collective Electron Emission Processes: Steady-State Models

3.2.1 Thermionic Emission

The theory of electron emission has been dealt with in many publications and textbooks. Therefore only the essential results are reproduced here. They are the foundation for the development of a theory of cathodic arc operation.

Electrons in the conduction band of a metal can be described by the model of a free electron gas. At the beginning of the twentieth century, Boltzmann statistics was applied to free electrons (Drude model), and some but not all properties could be explained. Later it was recognized that electrons, spin ½ particles, are subject to Fermi–Dirac quantum statistics. The expression

$$f_F(E,T) = \frac{1}{1+\exp\left(\frac{E-E_F}{kT}\right)} \tag{3.1}$$

is the Fermi distribution function which describes the probability that a state of energy E will be occupied in thermal equilibrium at a temperature T. Figure 3.2

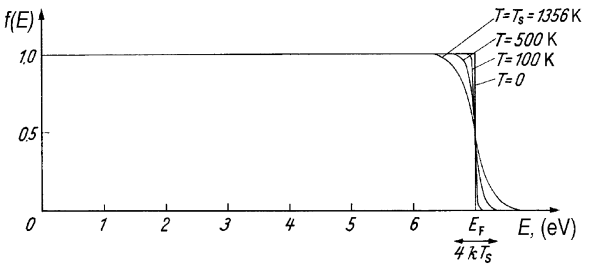

Fig. 3.2. Fermi distribution function of electrons in metal at zero and elevated temperatures. This example illustrates the situation for copper: even at the melting temperature, only a small fraction of electrons is thermally excited and smears out the region around the Fermi energy, E_F (see [4] p. 15)

illustrates this function using the example $E_F \approx 7\text{eV}$, which is approximately applicable to copper. The Fermi energy, E_F, can be defined as the highest energy of occupied states at temperature $T = 0$; it depends only on the density:

$$E_F = \left(\frac{\hbar^2}{2m_e}\right)\left(3\pi^2 n\right)^{2/3}. \tag{3.2}$$

In the above equation, $\hbar = h/2\pi$, h is the Planck constant, k is the Boltzmann constant, and m_e is the electron mass. The Fermi distribution implies that only a small fraction of electrons can acquire energy of order kT above the Fermi energy. From Figure 3.2 one can see that even at the boiling temperature of copper, $T = 1,356\text{K}$, most of the electrons are still part of the rectangular distribution and not influenced by the high temperature. This feature will be important later when discussing the Nottingham effect.

The expression

$$\frac{dN(E,T)}{dE} = \frac{4\pi(2m_e)^{3/2}}{h^3}\frac{E^{1/2}}{1+\exp\left(\frac{E-E_F}{kT}\right)} \tag{3.3}$$

is called the Fermi–Dirac distribution and describes the number of electrons with a kinetic energy in the range $(E, E+\mathrm{d}E)$. The shape of the Fermi–Dirac distribution is shown in Figure 3.3, left. Often, for convenience of energy considerations, the same function is presented with the abscissa and ordinate exchanged (Figure 3.3, right).

The electrons of the "electron gas" are confined to the solid volume by a potential barrier, ϕ, above the Fermi level (Figure 3.4). ϕ is generally known as the work function and expressed in eV (electron-volt[1]). Data on work functions are available from many experiments [5] and from quantum-mechanical modeling [6].

An intuitively clear picture is to heat the electron gas so that some electrons will have enough energy to overcome the barrier. The classic condition for escape would be simply

$$E_z \geq \phi, \tag{3.4}$$

where $E_z = m_e v_z^2/2$ is the kinetic energy of an electron in the z-direction, the direction perpendicular to the surface. The emission current density is

$$j_{thermionic} = en(E)v_z, \tag{3.5}$$

where $n(E)$ is the density of electrons satisfying the condition (3.4). For $T = 0$ obviously no electrons satisfy (3.4). For elevated temperature one can calculate $n(E)$ by integrating the distribution function from $-\infty$ to $+\infty$ in the x- and y-directions and from ϕ to ∞ in the z-direction. Here one can use a convenient simplification. At elevated temperature, the high-energy tail of the Fermi

[1] In some context, the barrier is expressed as a potential, with the unit volts; the factor of proportionality is simply the elementary charge, e.

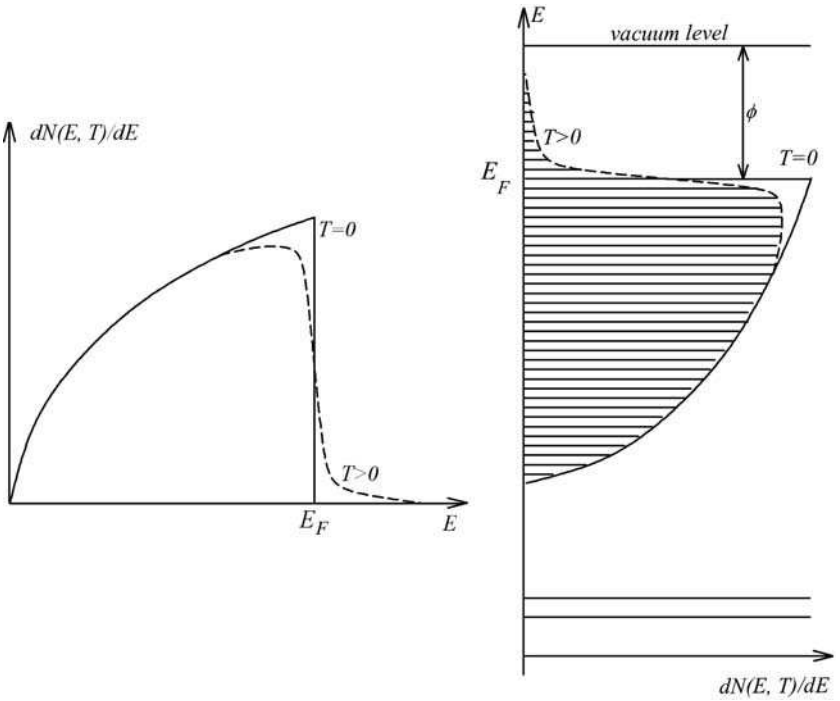

Fig. 3.3. *Left:* The Fermi–Dirac distribution (3.3). At temperature greater than zero, energy states higher than the Fermi energy are occupied, and some states lower than the Fermi energy are not occupied. *Right:* Presentation of the Fermi–Dirac distribution with abscissa and ordinate exchanged, as it is common for energy considerations. The energy levels indicated *below* are electrons not part of the electron gas but bound to a specific lattice site. The energy level of free electrons outside the solid is indicated by *vacuum level* at the very top of the energy scale. The difference ϕ between the Fermi level and the vacuum level is called the work function, as discussed in the text

distribution (3.1) is dominated by the exponential term, where $(E - E_{\mathrm{F}}) > kT$, and the quantum-statistical Fermi distribution can be well approximated by the classic Boltzmann distribution

$$f_B(E, T) = \exp\left(-\frac{E - E_F}{kT}\right). \tag{3.6}$$

The result of the integration, using the Boltzmann distribution, is

$$j_{thermionic} = AT^2 \exp\left(-\frac{\phi}{kT}\right), \tag{3.7}$$

where

$$A = \frac{4\pi e m_e k^2}{h^3} = 1.202 \times 10^6 \ \mathrm{A/m^2\ K^2}. \tag{3.8}$$

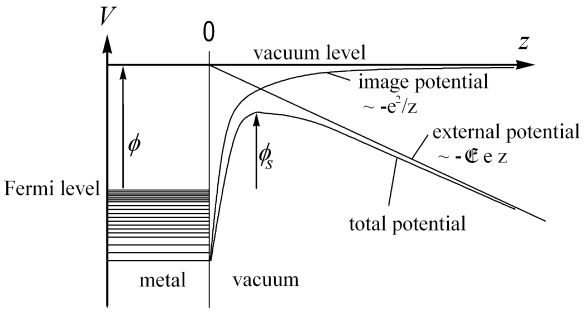

Fig. 3.4. Potential barrier for electrons at the surface of a metal. The barrier is deformed and its height reduced due to the mirror image field and the applied external electric field. The reduced barrier height, ϕ_S, allows more electrons to classically leave the metal at high temperature (Schottky effect)

Equation (3.7) is the well-known Richardson–Dushman equation for thermionic emission,[2] and A is the universal Richardson constant.

In the above derivation it was assumed that the potential barrier is uniform throughout the surface, and hence effects of the atomic modulation, crystallographic structure, and direction were neglected. Additionally, the likely presence of oxide or water layers, adsorbates, and surface defects was not taken into account. Because of the simplifications, it should not surprise that experimental values for the constant A vary widely. The relation (3.7) has been verified many times, but usually the data are fitted by adjusting both the work function ϕ and the Richardson constant A. Representative data for ϕ and A are compiled in Table B2 (Appendix B).

3.2.2 Field-Enhanced Thermionic Emission

In the previous section, any effects of a possible electric field were not considered. In practically all cases, however, an electric field is present, namely the field caused by the emitted electron and external fields. A free electron located at a distance z from the surface outside the solid causes a rearrangement of electrons of the electron gas in the solid in such a way that the resulting charge distribution in the solid looks like a mirror image of the free charge. The free electron and its "image" experience the Coulomb force

[2] Owen Williams Richardson [7], when still a graduate student at Trinity College, made an almost correct derivation, read before the Cambridge Philosophical Society in 1901, i.e., at a time before quantum statistics was known. He later published a book on the subject [8]. Saul Dushman made improvements in the 1920s [9] and wrote a comprehensive review [10].

$$F = \frac{e^2}{4\pi\varepsilon_0 (2z)^2} \tag{3.9}$$

and their interaction potential is

$$W = \frac{e^2}{16\pi\varepsilon_0 z}. \tag{3.10}$$

An external electric field can be written in linear approximation near the surface since it will slowly vary over the distance of interest. The potential distribution perpendicular to the surface can hence be written as

$$V(z) = \phi - \frac{e^2}{16\pi\varepsilon_0\, z} - e\mathfrak{E}z, \tag{3.11}$$

where the symbol $\mathfrak{E}$ is used for the external electric field near the surface.[3] The maximum of the potential barrier can be determined by $\mathrm{d}V/\mathrm{d}z = 0$, which gives the location for the maximum of the potential barrier

$$z_{\max} = \left(\frac{e}{16\pi\varepsilon_0 \mathfrak{E}}\right)^{1/2} \tag{3.12}$$

from the surface. Putting (3.12) in (3.11) results in the maximum height of the potential barrier

$$\phi_S = \phi - \left(\frac{e^3\mathfrak{E}}{4\pi\varepsilon_0}\right)^{1/2}, \tag{3.13}$$

which is illustrated in Figure 3.4. One can interpret this result that the barrier height is reduced compared to the usual work function, which of course leads to a higher emission current (Schottky effect). The current density with Schottky effect can therefore be written as

$$j_{thermionic,Schottky} = AT^2 \exp\left(-\frac{\phi_S}{kT}\right). \tag{3.14}$$

One needs to note that the correction term $\left(e^3\mathfrak{E}/4\pi\varepsilon_0\right)^{1/2}$ needs to be small compared to the work function. If this is not the case, the general expression of thermo-field emission needs to be applied, as discussed in Section 3.2.4.

Up to now, the emission of electrons has been dealt with classically. Only the appearance of the Planck constant, h, in the Richardson constant A, (3.8), indicated that quantum effects may be involved. So far, the quantum nature of the electron gas was mentioned but the emission process was entirely classical since electrons were given energy to overcome the potential barrier. The situation changes when the electric field is very strong, which is described in the next section.

[3] The symbol $\mathfrak{E}$ is here used for the electric field to avoid confusion with E, the symbol for energy.

3.2.3 Field Emission

At very high field strength, the potential barrier changes its shape to become a hill of sufficiently small width through which electrons can tunnel quantum-mechanically (Figure 3.5). Tunneling through the barrier can even occur at temperature $T = 0$. A general approach to calculate the emission current density is to write

$$j_e = e \int_{-eV_{\min}}^{\infty} N(E_z, T) D(E_z, \mathfrak{E})\, dE_z, \tag{3.15}$$

where $N(E_z, T)$ is the electron supply function that essentially contains the Fermi distribution (3.1) with the variable $E_z = m_e v_z^2/2$, the kinetic energy of electrons in the z-direction, which is defined as perpendicular to the surface, and $D(E_z, \mathfrak{E})$ is the tunneling probability through the potential hump. The integration covers all electron energies beginning from the lowest energy of electrons of the electron gas in the metal. To calculate the tunneling probability, one solves Schrödinger's wave equation in the three regions: inside the metal, inside the barrier, and outside the metal and barrier. In the limiting case of low temperature one obtains the Fowler–Nordheim formula [11]

$$j_{FN}(\mathfrak{E}) = \frac{e^3}{8\pi h\, \phi\, t^2(y)} \mathfrak{E}^2 \exp\left[-\frac{8\pi\sqrt{2m_e\phi^3}}{3eh\mathfrak{E}} v(y) \right], \tag{3.16}$$

where

$$y \equiv \sqrt{\frac{e^3\mathfrak{E}}{4\pi\varepsilon_0}}\, \frac{1}{\phi} \tag{3.17}$$

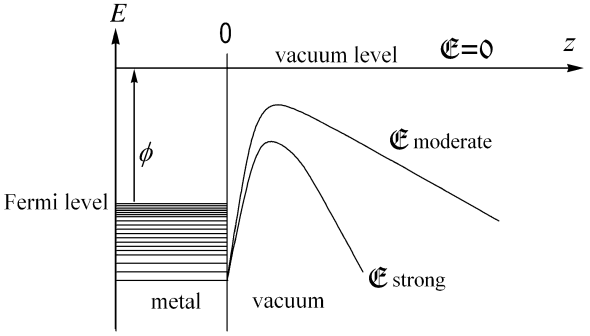

Fig. 3.5. Potential barrier at the surface of a metal: at very high electric field strength, its shape becomes a hill of sufficiently small width through which electrons can tunnel quantum-mechanically

and $t(y)$ and $v(y)$ are elliptical functions whose numerical values [12–14] are given in Table 3.1. A convenient numerical form of (3.16) is

$$j_{FN}(\mathfrak{E}) = 1.541 \times 10^{-6} \frac{\mathfrak{E}^2}{\phi\, t^2(y)} \exp\left[-6.831 \times 10^9 \frac{\phi^{3/2} v(y)}{\mathfrak{E}}\right] \tag{3.18}$$

with

$$y = 3.795 \times 10^{-5} \frac{\sqrt{\mathfrak{E}}}{\phi} \tag{3.19}$$

using $\mathfrak{E}$ in V/m, ϕ in eV, and j_{FN} in A/m^2. One should note that the function $t(y)$ has only a marginal influence whereas $v(y)$ greatly affects the calculated current

Table 3.1. Numerical values of elliptical functions used in Fowler–Nordheim formula

y	$t(y)$	$V(y)$
0.00	1.000	1.000
0.05	1.001	0.995
0.10	1.004	0.982
0.15	1.007	0.962
0.20	1.011	0.937
0.25	1.016	0.907
0.30	1.021	0.872
0.35	1.026	0.832
0.40	1.032	0.789
0.45	1.038	0.741
0.50	1.044	0.690
0.55	1.050	0.635
0.60	1.057	0.577
0.65	1.063	0.515
0.70	1.070	0.450
0.75	1.076	0.383
0.80	1.083	0.312
0.85	1.090	0.238
0.90	1.097	0.161
0.95	1.104	0.082
1.00	1.110	0.000
1.1	1.125	–0.172
1.2	1.139	–0.353
1.3	1.153	–0.545
1.4	1.167	–0.745
1.5	1.180	–0.954
2.0	1.249	–2.122
3.0	1.380	–5.213
4.0	1.501	–8.458
5.0	1.615	–12.438

density. Therefore, $v(y)$ requires careful treatment. Hantzsche [15] provided the convenient analytical approximation

$$v(y) \cong \begin{cases} 1 - y^2[0.375\ln(1/y) + 0.9673] - 0.0327y^4 & \text{for } y \geq 1 \\ -1.3110y^{3/2} + 0.8986y^{1/2} + 0.4936y^{-1/2} - 0.0812y^{-3/2} & \text{for } y \leq 1. \end{cases} \tag{3.20}$$

3.2.4 Thermo-field Emission

Up to now we have emission formulas for two limiting cases. At very high temperature and relatively low electric field one would use the Richardson–Dushman formula with Schottky correction for the work function, see (3.14). The other extreme case is for very high electric fields but low temperature: here one would use the Fowler–Nordheim formula (3.16). In many practical cases, however, especially when considering arc discharges, both temperature and electric field strength are high and therefore the general approach (3.15) has to be solved without the assumption of low temperature. The resulting theory is not simply a superposition of classic thermionic emission and quantum-mechanical field emission but the quantum-mechanical solution of (3.15). Pioneering work was done by Dolan and Dyke [16], and Murphy and Good [17] in the 1950s. The general expression for the current density is somewhat cumbersome:

$$j_{TF}(T, \mathrm{E}, \phi) = \frac{4\pi m_e k T}{h^3} \left\{ \begin{array}{l} \displaystyle\int_{-W_A}^{W_l} \frac{\ln\left[1 + \exp\left(-\frac{E_z+\phi}{kT}\right)\right]}{1 + \exp\left[\frac{8\pi(2m_e)^{1/2} v(y) E_z^{3/2}}{3he}\right]} dE_z. \\ \displaystyle + \int_{W_l}^{\infty} \ln\left[1 + \exp\left(-\frac{E_z + \phi}{kT}\right)\right] dE_z \end{array} \right\}, \tag{3.21}$$

where y was defined in (3.17),

$$v(y) = \begin{cases} -\sqrt{\frac{y}{2}}[-2\mathsf{E}(k_1) + (1+y)\mathsf{K}(k_1)] & \text{for } y \geq 1 \\ \sqrt{1+y}\,[\mathsf{E}(k_2) - y\,\mathsf{K}(k_2)] & \text{for } y \leq 1 \end{cases}, \tag{3.22}$$

$$\mathsf{E}(k) = \int_0^{\pi/2} \left(1 - k^2 \sin^2\theta\right)^{1/2} d\theta, \tag{3.23}$$

$$\mathsf{K}(k) = \int_0^{\pi/2} \left(1 - k^2 \sin^2\theta\right)^{-1/2} d\theta, \tag{3.24}$$

$$k_1 = \left(\frac{y-1}{2y}\right)^{1/2} \text{ and } k_2 = \left(\frac{1-y}{1+y}\right)^{1/2}. \tag{3.25}$$

In the integral boundary, W_A is the height of the potential barrier with respect to the lowest energy of free electrons in the metal (ϕ was the barrier height relative to the Fermi level) and

$$W_l \equiv -\left(\frac{e^3\mathfrak{E}}{8\pi\varepsilon_0}\right)^{1/2}. \tag{3.26}$$

Because these formula are quite involved, simplified formula are often used that are good approximations for certain temperature and field regions. For example, Christov [18] developed a general expression with three relatively simple integrals. Hantzsche [15] developed a number of additive and harmonic combinations of thermionic and field emission formula such as

$$j_{TF}(T,\mathfrak{E}) \approx k\left(AT^2 + B\mathfrak{E}^{9/8}\right)\exp\left[-\left(\frac{T^2}{C}+\frac{\mathfrak{E}^2}{D}\right)^{-1/2}\right], \tag{3.27}$$

where $A = 120$, $B = 406$, $C = 2.727 \times 10^9$, $D = 4.252 \times 10^{17}$; the units for (3.27) are j_{TF} in A/cm^2, T in K, $\mathfrak{E}$ in V/cm, and $\phi \approx 4.5$ eV. The constants A, B, C, and D are fitted such as to minimize deviation from the more accurate formula (3.21). Although the expressions (3.21)–(3.25) can be easily programmed with today's computers and software, the use of fit formula (3.27) may still be valuable if computational speed matters.

Coulombe and Meunier [19] compared emission current densities calculated by the Richardson–Dushman equation (including Schottky correction) with current densities by Murphy and Good. It was shown that the Richardson–Dushman equation always gives lower values than the more accurate treatment by Murphy and Good.

3.3 Refinements to the Electric Properties of Metal Surfaces

3.3.1 Jellium Model and Work Function

A simple model for the electronic properties of a metal surface is called the *jellium model* [20, 21]. In this model, the atoms of the solid metal are described as positive ion cores in a sea of free electrons; the ion cores are seen as smeared out to produce a uniform positive charge.

The electronic charge density at the surface does not drop in a mathematically sharp manner but exponentially. The electrons accumulated on the outer edge leave a positively charged region behind, thus forming a dipole layer (Figure 3.6). The potential related to this dipole is the surface space charge or dipole potential, $V_{\text{dipole}}(z)$.

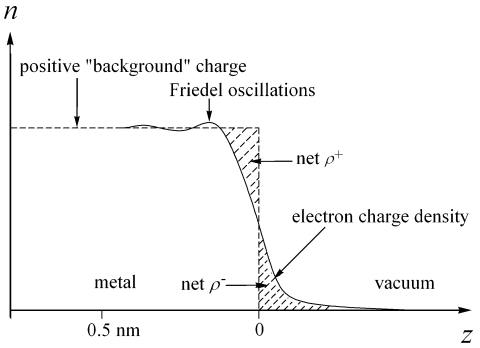

Fig. 3.6. Distribution of the electronic charge density at the surface of a metal

The electron contribution of the electric potential can be divided into three contributions [21]:

$$V(z) = V_{core}(z) + V_{exchange}(z) + V_{dipole}(z). \tag{3.28}$$

The term $V_{\text{core}}(z)$ describes the potential between core electrons and valence electrons; $V_{\text{core}}(z)$ is practically independent on whether the atom is in the bulk or on the surface of the solid because of the localized nature of the core electrons. Therefore, $V_{\text{core}}(z)$ cannot significantly contribute to surface effects such as the formation of the potential barrier (work function). $V_{\text{exchange}}(z)$ is the exchange potential between valence electrons, also known as exchange–correlation potential. Electrons lower their energy by "avoiding" other electrons of like spin (Pauli exclusion principle) and due to Coulomb interaction (correlation interaction). As a result, a deficit of electronic charge is around each electron, which, together with the dipole potential, is responsible for keeping electrons inside the metal.

In one approach, one can solve the one-dimensional Poisson equation

$$\frac{d^2V(z)}{dz^2} = -\frac{1}{\varepsilon\varepsilon_0}\rho(z), \tag{3.29}$$

where $\rho(z)$ is the electric charge density, ε is the dielectric constant in the solid, and ε_0 is the permittivity of free space. One can define the boundary conditions $V(\lambda_{\text{D}}) = 0$ and $V(0) = V_{\text{s}}$, where λ_{D} is the distance from the surface into the solid where the electron concentration attains bulk value and the electrostatic potential becomes zero; the potential height on the surface is designated as V_{s}. The solution shows that [21]

$$\lambda_D = \left(\frac{2\varepsilon\varepsilon_0 V_s}{en_e^{bulk}}\right)^{1/2} \tag{3.30}$$

is the characteristic screening length, usually called the Debye length. Later, when discussing arc plasmas, a similar Debye length is introduced, where the potential energy eV_s is replaced by the thermal kinetic energy kT of charged plasma particles. The solution $V(z)$ is shown in Figure 3.6. It shows damped

oscillations penetrating the solid to some depth. They are sometimes called Friedel oscillations. For typical electron concentrations of a metal, about 10^{28} m^{-3}, the depth defined by (3.30) is extended to only about one atomic layer because free electrons of the metal screen the field. For semiconductors and insulators, the electron concentration is much smaller and therefore the field may penetrate thousands of atomic layers into the bulk.

In another approach of treating the jellium model [20], the wave function of the whole system of electrons can be written as a superposition of one-electron Schrödinger wave functions

$$-\left(\frac{\hbar^2}{2m_e}\right)\nabla^2\psi_i + V\psi_i = E_i\psi_i, \tag{3.31}$$

where E_i is the total allowed electron energy. If one supposes that the solid is infinite in x- and y-directions and has a surface at $z = 0$ and it can be divided into boxes (cubes) of side length L, the solution are the eigenvalues of the wave equation:

$$\psi_{\mathbf{k}} = \left(\frac{2}{L^3}\right)^{1/2} \sin(k_z z)\exp\left[i\left(k_x x + k_y y\right)\right], \tag{3.32}$$

where $\mathbf{k}$ is the electron wave vector, with the allowed values $k_z = N\pi/L$, $N = 1,2,3,....$ The charge density is related to the wave function by the general relation

$$\rho = -e\sum_k |\psi_k|^2 \tag{3.33}$$

from which one also obtains damped oscillations of the charge density from the surface into the solid. In this approach, the Fermi length

$$\lambda_F = \frac{2\pi}{k_F} = \left(\frac{8\pi}{3n_e^{bulk}}\right)^{1/3} \tag{3.34}$$

is an often-used scaling length, which is typically 0.5 nm for metals, and

$$k_F = \left(3\pi^2 n_e^{bulk}\right)^{1/3} \tag{3.35}$$

is the Fermi momentum corresponding to the momentum of electrons at the highest energy at $T = 0$, the Fermi energy (3.2).

At the beginning of this section, the work function was simply introduced as the potential barrier height for the most energetic electrons at $T = 0$, i.e., for electrons at the Fermi energy. Now, with a deeper understanding of the electronic structure of the surface, one can write

$$\phi/e = V_{exchange} + V_{dipole} - V_{Fermi}, \tag{3.36}$$

where $V_{\mathrm{Fermi}} = E_{\mathrm{F}}/e$ is the Fermi potential. If we go beyond the jellium model and consider the crystalline structure of metals, it is not difficult to comprehend that the surface dipole potential, V_{dipole}, depends on the distance and charge of the positive ion cores. Therefore, different crystalline surfaces, even of the same

element, exhibit differences in the work function, as was experimentally confirmed; see, e.g., [22].

3.3.2 The Role of Adsorbates

In all of the previous sections, it was assumed that the surface of the metal is uniform and free of any defects or adsorbed layers. These assumptions were useful and necessary to derive a fundamental understanding of the emission processes. The reality, however, is much more complicated. In fact, the idealized situation almost never applies, except in cases of carefully prepared surfaces in ultrahigh vacuum. Cathode surfaces in typical deposition systems are usually covered with non-metallic atoms and films. As will be discussed, adsorbates and roughness affect the work function and the electric surface field. Since the work function appears in the exponential terms of the emission formula derived earlier, careful consideration is necessary. First it will be shown how quickly cathode surfaces are covered with adsorbates. After the presence of adsorbates has been demonstrated, their effect on the work function will be explained.

Any surface is subject to impingement of the atoms or molecules[4] of the gas the surface is exposed to. From the kinetic theory of gases [20, 23, 24] we have the impingement rate

$$J_g = \frac{p}{\sqrt{2\pi m_g k T_g}}, \tag{3.37}$$

where p, m_g, and T_g are the pressure, mass, and temperature of the gas, respectively. Even at high vacuum with a typical pressure of $\sim 10^{-4}$ Pa, the impingement rate cannot be neglected. For a system operating with background gases, typical for reactive film deposition, the rates are very high (Table 3.2).

Table 3.2. Pressure (in Pascal and Torr), impingement rate, and monolayer formation time for selected vacuum and process conditions

p (Pa)	p (Torr)	J_g (m^{-2} s^{-1})	τ (s)
		Nitrogen	
1	7.5×10^{-3}	2.9×10^{22}	3.5×10^{-4}
10^{-1}	7.5×10^{-4}	2.9×10^{21}	3.5×10^{-3}
10^{-2}	7.5×10^{-5}	2.9×10^{20}	3.5×10^{-2}
		water vapor	
10^{-3}	7.5×10^{-6}	3.6×10^{19}	0.28
10^{-4}	7.5×10^{-7}	3.6×10^{18}	2.8
10^{-5}	7.5×10^{-8}	3.6×10^{17}	28

[4] The terms "atoms" and "molecules" are used synonymously in this chapter.

It is interesting to consider how long it would take to cover an initially clean metal surface with a layer of gas molecules. For the purpose of this exercise one could assume that all arriving gas molecules stick to the surface. With this assumption, the monolayer formation time can be estimated by

$$\tau_{ML} = \sigma / J_g, \tag{3.38}$$

where $\sigma \approx 10^{19}\mathrm{m}^{-2}$ is the areal atom density of the metal surface. Typical results are included in Table 3.2. One can see that if a metal surface was initially chemically clean, i.e., free of adsorbates, this feature can be maintained for minutes or hours only under ultrahigh vacuum (UHV) conditions.

The above assumption that all gas molecules stick to the clean metal surface is of course over-simplified. When a gas molecule approaches the surface it interacts with the atoms of the surface experiencing attractive and repulsive forces. In most cases, the superposition of the attractive and repulsive potentials shows a minimum at a small distance r_0 from the surface, which can lead to trapping (bonding) of the arriving atom (Figure 3.7). The nature of the attractive forces determines the depth of the potential minimum $\Delta V_a < 0$ (to be discussed in greater detail in the chapter on film growth). The trapped atom has a probability of escape that can be expressed in an Arrhenius form [20] as

$$v_{des} = \nu_0 \exp\left(-\frac{\Delta G^*_{des}}{kT_s}\right), \tag{3.39}$$

where $\nu_0 \approx 10^{13}\mathrm{s}^{-1}$ is called the attempt frequency, which is associated with the vibration frequency of surface atoms, $\Delta G^*_{\mathrm{des}}$ is the free energy of activation of the

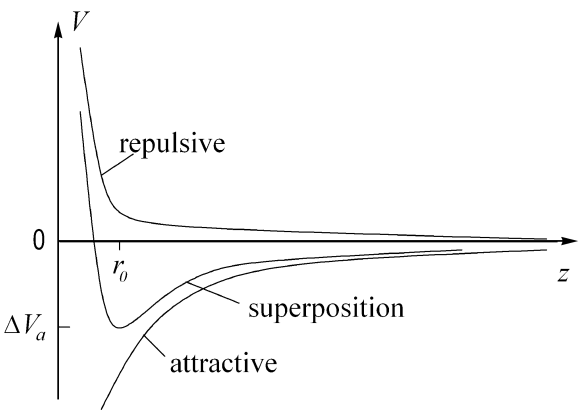

Fig. 3.7. Schematic potential diagram for atom interacting with surface atoms; z is the distance from the surface, r_0 indicates the minimum of potential energy corresponding to the equilibrium distance of the atom becoming trapped. The repulsive term is mainly due to overlap of filled electron orbitals of surface atoms with orbitals of the arriving gas atom. The attractive term depends greatly on the specific nature of the interaction (Coulomb, covalent, polar, van der Waals)

desorption process, and T_s is the temperature of surface atoms. The desorption probability can also be expressed through the enthalpy $\Delta H_{\text{des}} = -e\Delta V_a$ via

$$v_{des} = \nu_0 \frac{f^*}{f} \exp\left(-\frac{\Delta H_{des}}{kT_s}\right), \tag{3.40}$$

where f and f^* are the molecular partition functions of the system in the equilibrium and activated states, respectively [20]. The reciprocal is the mean surface lifetime of the atom in the trapped state,

$$\tau_a = \tau_0 \exp\left(\frac{\Delta H_{des}}{kT_s}\right), \tag{3.41}$$

with

$$\tau_0 = \frac{f}{f^*}\frac{1}{\nu_0}. \tag{3.42}$$

Values of the adsorption energy, or energy necessary to desorb the adsorbed atom, ΔH_{des}, varies greatly, as does the mean surface lifetime, τ_a. Depending on the depth of the potential minimum, and thus the strength of bonding, one customarily distinguishes between weak physical adsorption (or physisorption) and much stronger chemical adsorption (or chemisorption). van der Waals forces are typical for physisorption. Hydrogen bonding, covalent chemical bonding, and metal bonding are typical for chemisorption. The transition is customarily set to about 0.2 eV/atom, as the physicist would say, or 5 kcal/mol or 21 kJ/mol, as the chemist sees it. Table 3.3 shows examples of physisorbed and chemisorbed gases on cathode surfaces. As is clear from the exponential factor in (3.41), the ratio $\Delta H_{\text{des}}/kT_s$ is critical. Obviously, heating the cathode makes physisorption extremely short-lived; however, chemisorbed atoms may be difficult or impossible to remove even when the metal approaches its melting temperature. We can conclude that a real surface is a highly dynamic object on which atoms frequently adsorb

Table 3.3. Examples of the mean surface lifetime, τ_a, of physisorped and chemisorped gases on cathode surfaces [21], assuming $T_s = 300$ K (equivalent to $kT_s = 0.0258$ eV) and $\tau_0 \approx 10^{-13}$s. The point of these examples is not the exact data but to demonstrate the huge effect of ΔH_{des}

Example	Approximate ΔH_{des} (eV/atom)	Approximate τ_a (s)
H_2 physisorped on metal	0.07	1.3×10^{-12}
Ar, CO, N_2, CO_2 physisorped on metal	0.15–0.18	10^{-10}
Carbohydrates physisorped or weakly chemisorped	0.4–0.6	10^{-6}–10^{-2}
H_2 chemisorped on metal	0.9	100
CO on Ni	1.3	4×10^9
O on W	6.5	10^{1100} > age of the universe

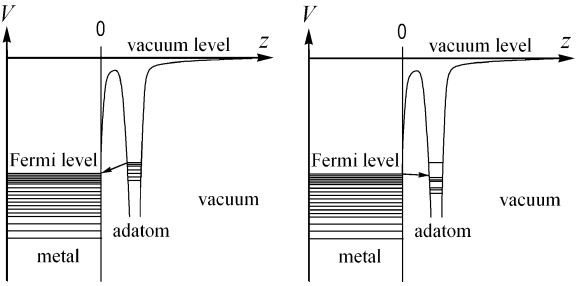

Fig. 3.8. Charge transfer from and to adatoms on a metal surface. *Left*: The adatom has an occupied electronic state above the Fermi level of the metal, and thus full or partial electronic charge transfer from the adatom to the metal will occur, causing a net positive charge of the adatom, reducing the work function. *Right*: The adatom has an unoccupied state slightly below the Fermi level, which causes electron transfer from the metal to the atom and an increase of the work function

and desorb but also a more or less permanent non-metallic layer may have formed. In any case, the presence of adsorbates is the rule, not the exception.

The presence of adsorbates changes the work function. Figure 3.8 shows two situations when an atom approaches the surface and the electronic charge of the solid starts to overlap with the orbitals of the atom, i.e., adsorption occurs, and thus full or partial charge transfer between the adatom and the metal will occur. On the left side, the adatom has a filled electronic state slightly above the Fermi level of the metal. In this case, electron transfer from the atom to the metal will occur, and the adsorbed atom will assume a net positive charge, which will cause a reduction of the work function. This becomes plausible if one considers that the work function was associated with a dipole potential, (3.36), where the *negative* charge was sticking out from the surface. The right side of Figure 3.8 shows the other case: the adsorbed atom has an unfilled state below the Fermi energy, and therefore charge transfer to the adatom will occur, giving it a net negative charge, which will enhance the work function.

If a polar molecule is adsorbed, a similar phenomenon can occur even without full electron transfer to the metal. If the polarized molecule is adsorbed with the positive side of the dipole pointing away from the surface, the work function will be reduced, and in the opposite case the work function will be enhanced.

Inert gas, like argon, is polarizable and will therefore "feel" the dipole field of the surface. Adsorption of noble gases will change the charge distribution of adsorbed noble gases slightly in such a way that the work function is slightly lowered ([21] p. 369). Usually, chemisorption of hydrocarbons on transition metals also *reduces* the work function by 1.2–1.4 eV [21]. On the other hand, adsorption of hydrogen and oxygen atoms usually *increases* the work function of metals.

The formation of an oxide layer (or more general, insulating layer) of several atoms thickness prevents charge transfer to the metal in the case of an *ion* arriving at the surface. If the kinetic energy of the ion is low, it may adsorb to

the oxide layer surface and retain its positive charge, thereby affecting the potential barriers such as to lower the work function. If the insulating layer is thin, not only field emission, but also violent electrical "breakdown" of the insulating layer may occur. "Electrical breakdown" refers to a phenomenon where the previously insulating path becomes suddenly conducting, which is usually associated with violent repositioning of atoms along the insulating path. The energy for this repositioning of atoms is provided by the strong electric field.

In a typical cathode situation, which will be discussed later in greater detail, ions arrive from the plasma after they have transitioned the cathode sheath. They have therefore sufficient kinetic energy to displace a few atoms of the oxide or similar surface layer. The positive charge can cause a strong local rearrangement of the electric charge distribution, the work function can be locally lowered, electrons emitted, and atoms desorbed. In fact, the presence of plasma in a real cathode situation makes the situation much more complicated as described so far because there are a number of processes contributing to the dynamics of adsorption and desorption, including (but not limited to) desorption induced by incident ions, electrons, photons, and energetic neutrals.

Even the strong electric field by itself is able to affect the balance of adsorption and desorption, as illustrated in Figure 3.9. The formation of a potential minimum resulted from attractive and repulsive forces (Figure 3.7). In the presence of a strong external field, the resulting total potential is "bent" down and thus the minimum is much shallower or not present all at, leading to *field-induced desorption* or *field evaporation*.

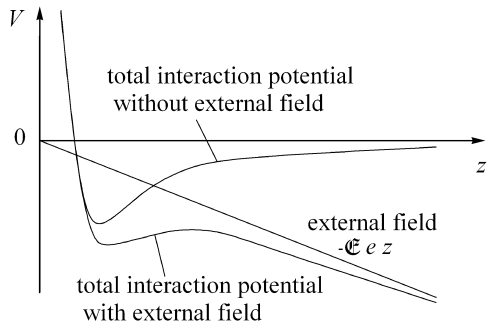

Fig. 3.9. Potential illustrating field-induced desorption or field evaporation. In contrast to Figure 3.7, where the formation of a potential minimum resulted from attractive and repulsive forces, the presence of a strong external field "bends" the total potential and thus the minimum is much shallower or not existent

3.3.3 The Role of Surface Roughness

Previous considerations assumed that the cathode surface was smooth. They did not account for the effects of the periodicity of the lattice, atomic scale steps, and

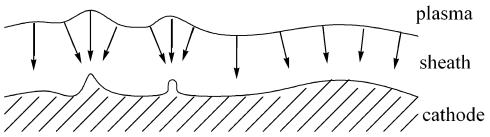

Fig. 3.10. Illustration of non-uniform ion flux to a cathode (or other negatively biased metal) and field enhancement. The non-uniformity is associated with a roughness that is much larger than atomic scale. *Arrows* indicate ion trajectories

larger-scale roughness. A decreasing atomic density reduces the dipole created by electrons "spilling out" beyond the nominal surface [21], hence reducing the work function. Surface steps on the atomic scale also reduce the work function. These effects on the atomic scale reduce ϕ typically by a few tenths of one electron-volt.

Real surfaces generally show much larger than atomic scale roughness. Even in cases where the initial roughness is only on the atomic scale, the action of cathode spots will cause roughening of the surface on the nanometer or even micron scale. This much larger-scale roughening leads to an enhancement of the local surface electric field strength and to non-uniform ion bombardment as illustrated by the cartoon (Figure 3.10). The influence of surface roughness on the emission properties of metals was recognized early by Walter Schottky [25], who later became famous for his work on semiconductors.

The enhancement of the field strength of real surfaces is often captured by the *ad hoc* introduction of a field enhancement factor, β, such that

$$\mathfrak{E}_{real} = \beta \mathfrak{E}_0, \tag{3.43}$$

where $\mathfrak{E}_0$ is the electric field on the surface if the surface is atomically smooth and free of non-metallic contamination. The value of β can be high and may exceed 100 (see the review by Farall [26]). Experimental studies on field emission indicated that β appeared to be greater than 1,000 in some cases, which implied that either the geometry of the electron-emitting centers is extremely pointed, needle-like, or that other factors play an important role. Although extremely acute shapes of emitters have been detected [27], their general presence appeared unlikely, and therefore Latham [28] suggested that experimental data on β usually include not only roughness effects but also the influence of non-metallic layers and dielectric particles or inclusions in the surface layer as investigated earlier by Cox [29].

3.4 Theory of Collective Electron Emission Processes: Non-stationary Models

3.4.1 Ion-Enhanced Thermo-field Emission

Until now, in describing the theory of electron emission due to high cathode temperature, high electric surface field, or both, temperature and field were

assumed as given and stationary. For the case of a cathodic arc, the surface field exists due to a space-charge layer or "sheath," which is not stationary. Considering the nature of changes more closely one may recognize at least two timescales.

One timescale is associated with changes of the sheath, which can be mainly attributed to changes of the plasma density, and one may expect here changes measured in nanoseconds. These are quasi-stationary changes on a timescale of an actual electron emission event (femtoseconds).

A second timescale and a strong modification of the original thermo-field emission picture comes into play when considering the electric field of individual ions. Ecker and Müller [30] proposed to modify the thermo-field mechanism for the case of an arc by not just considering the average field of the sheath but the actual, momentary field caused by an ion coming from the plasma and approaching the surface. They showed that thermo-field emission can be significantly enhanced without having to enhance the cathode temperature or surface field.

The deformation of the potential barrier by the approaching ion is shown in Figure 3.11. The ion can only be effective in a narrow range of about 1 nm of distance from the surface. At large distances (> 5 nm), the deformation of the potential barrier by the ion is negligible, and at small distances (< 0.4 nm), the ion captures one or more electrons (if it was multiply charged) and becomes neutralized (Figure 3.12). The timescale of action is thus $\tau \sim \Delta s / v_i \sim 1\ \text{nm} / 10^4 \text{m/s} = 100$ fs. According to calculations for copper by Vasenin [31], ion enhancement of the thermo-field mechanism can be significant, even exceeding a yield of 10 electrons per incident ion, when the system is already in a highly emissive state, i.e., at temperatures $> 4{,}000$ K and fields $> 10^9$ V/m. Despite the individual nature of the ion-field enhancement effect, ion-enhancement thermo-field emission belongs to the group of collective emission mechanisms, and the discharge is an arc, not a glow discharge, as explained in the Introduction to this chapter.

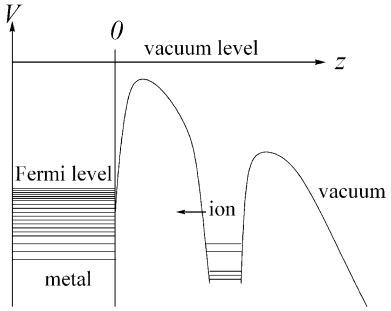

Fig. 3.11. Deformation of the potential barrier by an ion approaching the cathode surface ($z = 0$). Tunneling of electrons that can occur in the presence of a strong electric field is enhanced when the ion is sufficiently close to the surface, narrowing and lowering the barrier. The ion charge is neutralized by capturing electron(s) and the enhancing effect is terminated

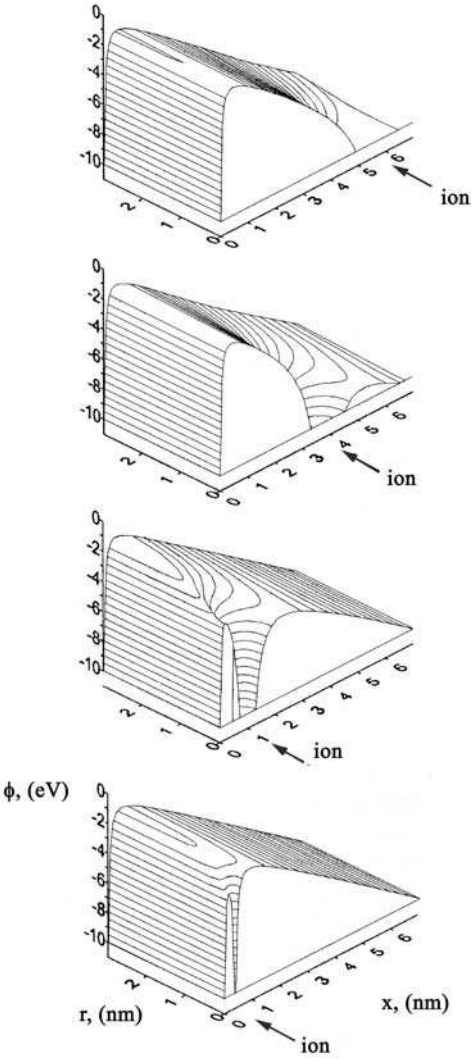

Fig. 3.12. Illustration of the time-dependent potential when an ion approaches a cathode, calculated for a Cu^{2+} ion and an average field of 1.4×10^9 V/m (adapted from Figure 6 of [31]); x is the distance from the surface, r is the radial distance from the projected impact location. At large distances ($x > 5$ nm), the deformation of the potential barrier by the ion is negligible, and at small distances ($x < 0.4$ nm), the ion captured one electron

Coulombe and Meunier expanded such consideration to the case when arcs are operated at relatively high gas pressure, that is, when bombardment of the cathode with gas ions plays an important role. They showed that the Richardson equation for thermionic emission is inadequate [19]: field-enhanced thermionic emission (Richardson equation) underestimates electron emission

by at least 20% compared to thermo-field emission [17] enhanced by slowing moving ions [19].

3.4.2 The Existence of a Critical Current Density

The emission of electrons by high temperature and high field will become intense as the surface temperature and electric field strength $\mathfrak{E}_{real}$ approach typically 2,000 K and 10^9 V/m, respectively. However, none of the emission equations (3.7), (3.14), (3.16), or (3.21) indicate that there might be an upper limit of emission current density.

In the 1950s, field emission projection tubes became a popular tool [32] to study the effects of surface features on the distribution of the field emission current. Walter P. Dyke and his colleagues [33, 34] applied the technique to study the onset of vacuum discharges. They found that the tips of field emission cathodes exploded in less than 1 μs when the current density of electron emission reached a critical value of about 10^{12} A/m^2. They concluded that thermal effects of the emission current itself were responsible for the explosive destruction of the field emission tip and the onset of a vacuum arc.

The experiments of Dyke and co-workers indicated that stationary modes may exist at relatively low current densities while current densities exceeding 10^{11}–10^{12} A/m^2 imply explosive destruction of the emitting material. It was clear that there is a need to consider the time-dependent energy balance of cathodes during emission and ultimately consider the energy situation in a local and time-dependent manner. The development of a non-stationary emission model was of course much more challenging than the development of stationary models because relevant non-stationary models require not only the explicit introduction of time, but also the consideration of at least two, and better three, spatial dimensions, the temperature dependence of material parameters, and phase transitions.

3.4.3 The Tendency to Non-uniform Emission: Cathode Spots

It is interesting to notice that the emission equations for thermionic and field emission assign to the emission area a very different role than to the governing parameters, temperature and electric field, respectively. While an increase in area, at otherwise constant conditions, increases the emission current *linearly*, increase in temperature or field affects the emission current *exponentially*. Surface temperature and field have a vastly greater effect on emission and the system as a whole than an increase of the emitting surface. Since a moderate increase in temperature or field on a very small area requires less energy than even a somewhat smaller increase on a large area, stability considerations based on minimum energy dissipation will clearly favor the formation of small-area, hot spots. Different geometries, thermal conduction conditions, and materials may lead to

solutions of the energy balance that are stationary or non-stationary. These different solutions manifest themselves as arc modes, which are later discussed in Section 3.6.

3.4.4 Energy Balance Consideration for Cathodes

Heat Conduction Equation

It is clear that the highest current densities occur most readily when both high temperature and high electric field strength are present. An attempt to describe the situation could start by writing the general heat conduction equation for the cathode:

$$C\rho\frac{\partial T(\mathbf{r},t)}{\partial t} - \nabla(\kappa\,\nabla T(\mathbf{r},t)) = \mathbf{j}(\mathbf{r},t)\mathfrak{E}(\mathbf{r},t), \tag{3.44}$$

where C is the specific heat capacity (in J/kg K), ρ is the mass density (in kg/m^3), κ is the thermal conductivity (in J/s m K), $T(\mathbf{r},t)$ is the temperature field (in K), $\mathbf{j}(\mathbf{r},t)$ is the current density distribution inside the cathode, and $\mathfrak{E}(\mathbf{r},t)$ is the electric field inside the cathode.

Joule Heat

The expression on the right-hand side of (3.44) is Joule heating. Joule heat is caused by transfer of kinetic energy of free electrons in the metal to phonons (lattice vibrations). Free electrons in the metal are accelerated by the electric field, $\mathfrak{E}$, causing the current density

$$\mathbf{j} = \sigma\mathfrak{E}. \tag{3.45}$$

This expression is Ohm's law, where σ is the electrical conductivity. The heat produced in the volume of the cathode (in J/s m^3) is

$$S_{joule} = \mathbf{j}\mathfrak{E} = \sigma\mathfrak{E}^2 = \frac{j^2}{\sigma}. \tag{3.46}$$

Apart from energy transport (heat conduction) and dissipation (Joule heat) in the cathode *volume*, the local temperature of the cathode *surface* is determined by energy fluxes associated with the ion, atom, and electron fluxes, as well as with radiation:

$$q \equiv \kappa(\nabla T)_n = q_i + q_a + q_e + q_{rad}. \tag{3.47}$$

The subscript "n" refers to the surface normal, which is directed away for the cathode. The energy fluxes through the surface are expressed in J/s m^2. They include heating and cooling terms depending on the sign of flux considered. Relation (3.47) represents a boundary condition for (3.44). The energy flux terms are discussed below.

Ion Bombardment Heating

Ions leaving the surface will remove energy from the surface, and ions arriving will bring energy to it. The dominance of one or the other depends on the stage of development of the cathode spot. Ions arriving have acquired kinetic energy in the space-charge layer, i.e., in the sheath, which is present between cathode surface and quasi-neutral plasma. The voltage drop of the sheath is called the cathode fall, here designated as V_c. The energy density associated with arriving ions can be written as

$$q_i^{heat} \approx \sum_Q \frac{j_Q^{arrive}}{eQ}\left(eQV_c + \hat{E}_Q - Q\phi + \alpha E_{coh}\right), \tag{3.48}$$

where the summation is over all charge states $Q = 1,2,3,...,Q_{\max}$ present in the plasma. The term $j_Q^{\text{arrive}} \Big/ eQ$ is the particle current density of ions of charge state Q. The second and third terms in the parenthesis are the total ionization energy of the ion minus the work function of the electron(s) needed to neutralize the ion when it arrives at the metal surface. The total ionization energy of a Q-charged ion can be calculated as the sum of all energies in stepwise ionization:

$$\hat{E}_Q = \sum_{i=0}^{Q-1} E_i \tag{3.49}$$

where E_0 is the energy needed to produce a singly charged ion from a neutral, E_1 is the energy needed to produce a doubly charged ion from a singly charged, etc. The last term of (3.48) is the cohesive energy, which is defined as the energy needed to remove an individual atom from its bonded position in the solid to an isolated position at infinite distance. The cohesive energy contributes to cathode heating only when the ion condenses on the cathode and actually becomes part of it. Only a fraction $0 \leq \alpha \leq 1$ is actually accommodated; the rest, $\alpha - 1$, returns to the plasma after its charge is neutralized. For that reason, the accommodation (or sticking) coefficient α was introduced to (3.48).

The energetics of ions arriving at a surface is also important for film deposition on a substrate, and therefore the situation is further considered in energetic condensation of thin films (Chapter 8).

Ion Emission Cooling

Depending on the stage of spot development (see Section 3.4.8), ions may mainly leave the cathode rather than arrive. This is especially true for stage (ii), the explosive stage. In fact, the time-averaged net flux of ions is from, not to, the cathode surface, which is sometimes labeled as "anomalous" ion emission [35]. In contrast to most other discharges, cathodic arcs are characterized by the net flux of positive ions moving *away* from the cathode, which is ultimately associated with the explosive nature of the cathode processes. The existence of spot

development stages is considered in the ecton model, and spatial and temporal superposition of spots leads to fractal features of cathode phenomena.

The cooling of the cathode by "anomalous" ion emission can be described by

$$q_i^{cool} \approx -\sum_Q \frac{j_Q^{emit}}{eQ}\left(2kT_c + \hat{E}_Q - Q\phi + E_{coh}\right). \tag{3.50}$$

This expression contains terms similar to (3.48); however, the kinetic energy terms are now associated with the temperature of the cathode, T_c. In writing down this expression it is implied that the ions are formed in the explosive process, hence their ionization energy is taken from the cathode.

This view on spot modeling with ion cooling is, however, not generally accepted since it is possible to consider that most ions are formed at some distance from the cathode surface by ionization of an intense flux of atom vapor [36]. Under such conditions, ion emission cooling would not play a role but the energy removed by evaporation.

Atom Evaporation Cooling

For ions produced by ionizing the flow of evaporated atoms, one could omit the terms $\hat{E}_Q - Q\phi$ in the parenthesis of (3.50), arriving at a corresponding expression describing cooling caused by evaporation of atoms from the surface:

$$q_a^{cool} \approx -J_0^{evap}(2kT_c + E_{coh}), \tag{3.51}$$

where J_0^{evap} is the flux density of evaporating atoms. In evaporation equilibrium, the number of evaporating and condensing atoms are equal and the net flux of atoms is zero:

$$n_a\sqrt{\frac{kT}{2\pi m_a}} = \frac{p_{vapor}}{\sqrt{2\pi m_a kT}}. \tag{3.52}$$

In equilibrium, the temperature of atoms is equal to the temperature of the evaporating surface and T does not need to have an index. Following Langmuir's argument, the flux of evaporated atoms does not depend on whether or not condensation is actually happening. Therefore, the evaporation rate can always be related to the material's equilibrium vapor pressure, and one may write

$$J_0^{evap} = \frac{p_{vapor}}{\sqrt{2\pi m_a kT_c}}. \tag{3.53}$$

The vapor pressure increases approximately exponentially with surface temperature. The material-dependent data curves were tabulated by Honig [37]. One should note that the vapor pressure curves go smoothly through the melting temperature and therefore, from an evaporation point of view, the phase state of the cathode does not matter. However, this state matters a lot when we consider

the pressure of the plasma on the cathode: a liquid surface will yield, and the most apparent result is the generation of macroparticles which in turn become sources of vapor. Macroparticles are further described in Chapter 6.

In the framework of a fractal model, evaporation cooling can be neglected during the explosive spot stage since the emitted material is fully ionized and thus already taken into account in the ion flux term. In other spot stages or, equivalently, outside the spot center, evaporation may occur but its energetic consequences are small compared to other forms of energy flux due to the very strong temperature dependence of the vapor pressure.

Atom Condensation Heating

Analogous to (3.51), the energy brought to the cathode by condensing neutral atoms is

$$q_a^{heat} \approx J_0^{cond}(2kT_a + E_{coh}), \tag{3.54}$$

where T_a is the atom or vapor temperature. In the explosive stage, no atoms can flow against the stream of material due to collisions. Atoms may condense in other spot stages (or equivalently, outside the spot center) but the associated energy flux can be neglected compared to other energy fluxes. For example, returning ions will have gained energy by acceleration in the field of the cathode sheath but (neutral) atoms do not "see" this field.

Electron Emission Cooling

The emission and return of electrons can have an important influence on the energy balance of the cathode. As extensively discussed before (Section 3.3.1), electrons are confined inside the metal by a potential barrier, whose height above the Fermi level is ϕ, the work function, or better ϕ_S, the Schottky-corrected work function, see (3.13). For a hot cathode, electrons can leave the metal classically, going over the barrier and hence carrying away the energy:

$$q_e^{cool} \approx -\frac{j_e^{emit}}{e}(2kT_c + \phi_S). \tag{3.55}$$

If the emitting cathode location is still cold (in terms of thermionic or thermo-field emission), significant emission can only occur via field emission in a strong electric field. As discussed before, electrons tunnel quantum-mechanically through the barrier, which has become narrow by its deformation in the strong field. Now something strange can happen, namely that the emission of electrons can actually lead to heating rather than cooling, which is known as the *Nottingham effect* [13, 38]. This becomes clear if one recalls that electrons in a metal have a Fermi distribution, as was illustrated in Figure 3.2. Electrons below the Fermi level may tunnel and leave the metal; their replacement from the current supply fills the electron "sea" at the Fermi level. The energy

difference between the electron lost and the electron replaced constitutes a small heat gain. As the cathode heats up, this heating becomes less and eventually reverses to the more familiar, classical cooling. The inversion temperature, T^*, at which heating turns into cooling has been determined to [13, 39]

$$T^* = 5.67 \times 10^{-7} \frac{\mathfrak{E}}{\phi^{1/2}} t(y), \tag{3.56}$$

where T^* is in K, $\mathfrak{E}$ is in V/m, ϕ is in eV, and $t(y)$ is the elliptical function introduced before and tabulated in Table 3.1. From this expression one can see that Nottingham heating can only be important in the pre-explosion stage, when the local cathode surface temperature is still low. Therefore, one needs to consider the Nottingham effect only for the onset of thermal runaway and the early development of a local emission center.

Heating by Returning Electrons

While the net electron current is *away* from the cathode and electrons are accelerated in the cathode fall, electron–electron interaction in the dense plasma will quickly lead to a Maxwellian energy distribution. Electrons in the energetic tail of the distribution may have enough energy to return to the cathode, essentially delivering the work function energy

$$q_e^{heat} \approx \frac{j_e^{return}}{e} \phi_S. \tag{3.57}$$

The return current,

$$j_e^{return} \approx e n_e \sqrt{\frac{kT_e}{2\pi m_e}} \exp\left(-\frac{eV_c}{kT_e}\right), \tag{3.58}$$

contains an extremely small exponential factor because $(-eV_c/kT_e) \sim -10$. Therefore, heating by return electrons can be neglected. In models that assume vapor ionization in a more or less pronounced potential hump, the electron return current is even smaller.

Radiation Cooling

The cathode spot is bright and obviously energy is removed from the cathode via radiation. In a rough approximation, one may assume that the spot area is a black body radiator whose power density is given by

$$q_{rad}^{cool} = \varepsilon_c \sigma_{SB} T_c^4, \tag{3.59}$$

where ε_c is the surface emissivity ($\varepsilon_c = 1$ if the surface was a true black body, but realistically $0 < \varepsilon_c < 1$), $\sigma_{SB} = 5.67 \times 10^{-8} \mathrm{W/m^2\,K^4}$ is the Stefan–Boltzmann constant, and T_c is the temperature of the emitting cathode surface. Here and

elsewhere we have a conceptual problem since T_c is not well defined for the case of a microexplosion. For the sake of an estimate, one may assume that T_c exceeds the melting temperature. Even for refractory metals and given the strong T_c^4 dependence, one can easily determine that radiation cooling is small compared to other energy terms.

Radiation Heating from Plasma

The light seen from a cathode spot is mainly emitted from the spot plasma. The statement above in the first paragraph of "radiation cooling" was therefore a bit deceptive! The plasma formed in a microexplosion is very dense and optically thick, hiding (shielding) the radiation emitted from the cathode-spot surface. The term *optically thick* refers to a medium in which the mean free path of photons is small compared to the physical size of the medium. Photons are absorbed and re-emitted again and again, and photon transport resembles diffusion [40]. With its expansion, however, the plasma becomes quickly transparent or *optically thin*.

Radiation coming from the plasma will be in part reflected and in part absorbed; only the latter contributes to heating of the cathode. A quantitative determination of this heating is difficult because it involves the black body radiation of the transient plasma of the explosive stage of the cathode spot and line radiation from the expanding plasma corresponding to later stages. Only the black body radiation with temperature of a few eV (say, $T_c \geq 50,000$K) would be noticeable; however, even this can be neglected in the overall balance.

3.4.5 Stages of an Emission Center

The previous discussion already indicated that electron emission becomes nonstationary and localized. The terms "spot" and "emission center" were used, calling for more refined considerations, which will be given later in the framework of a fractal approach. At this point one may think of a spot or an emission center as a location on the cathode surface where one can describe the evolution of electron and plasma generation. The evolution may be divided into four stages: (i) the pre-explosion stage, (ii) the explosive emission stage, (iii) the immediate post-explosion stage, where cooldown has started but electron emission and evaporation are still large, and (iv) the final cooldown stage. Each of the four stages is highly dynamic. In the following paragraphs, these stages are briefly described, followed by a discussion of plasma and sheath properties.

In the beginning of the pre-explosion stage, the cathode surface has assumed surface conditions determined by its history, such as mechanical and heat treatment, and the exposure to specific intentional or residual gas conditions. Since we consider the *operation* of an arc (and not the specifics of the initial arc triggering), plasma is already generated at some distance, causing cathode locations to be exposed to bombardment by ions, accompanied by a flux of electrons,

atoms, and radiation. Furthermore, the temperature of the solid may be increasing, e.g., due to heat conduction and ion bombardment.

Each location on the surface might be a candidate for the ignition of an emission center but in reality each location has its own history and properties such as the work function. For example, the conditions are different at grain boundaries and in the middle of a grain. Oxides and other dielectrics might be present, and surface roughness will certainly give each location unique properties.

Suppose one could pick a location that is going to experience explosive emission. The conditions will be such that the local energy input will be higher than at neighboring locations due to its specific properties and its relation to the plasma and sheath conditions produced by predecessor emission sites. The conditions are indeed favorable if the local work function is low and the field is enhanced due to the presence of dielectric contamination and/or the presence of micro- or nanoprotrusions. If such favorable conditions are coupled to a very high electric field strength (e.g., thin sheath due to high plasma density) and a high intensity of ion bombardment, the local energy input can lead to electron emission with thermal runaway, bringing the location to stage (ii), characterized by *explosive* electron emission. This stage is at the heart of the "ecton" model developed by Mesyats and co-workers [41, 42]. Thermal runaway and ecton model are discussed later in this chapter. The microexplosion causes destruction (erosion) of a microvolume, which is later evident as a crater on the cathode surface. Theoretical models of cathode-spot development differ in the literature, although most agree that repetitive ignition of microexplosions is real and well supported by experimental evidence. The main discontent is about the duration and relative importance of explosion and post-explosion stages.

In one view, each microexplosion is immediately followed by the next microexplosion, and therefore the cathode operation is based on a rapid sequence of microexplosions, each being on a timescale of the order of 10^{-8} s [41, 42]. In this view, stage (iii) is of relatively little importance.

High-resolution, fast optical diagnostics support this view, at least the notion that the sequence of explosive events is indeed rapid. For example, very fast optical imaging of very low current arcs, 3–12 A, only shows bursts of light every 50–70 ns with the most intense phases having a duration of 10–20 ns [43].

Another view considers the explosive stage (ii) as a short, transient, beginning stage for a much longer, quasi-steady-state, post-explosion stage in which electrons are emitted from the hot, liquid metal layer of the freshly created crater formed under the action of dense plasma. In this view, cathode material is evaporated and becomes ionized very close to the surface due to the intense electron beam formed in the thin cathode sheath. Electrons in this beam have the energy corresponding to the cathode fall (about 20 V) and their current density is determined by field-enhanced thermionic emission. Most ions are formed by electron–atom interaction in an electron beam relaxation zone in close proximity to the cathode surface [36].

Putting these differences aside, for the time being, it is clear that a fourth, final stage must exist in which electron emission and evaporation have ceased because the thermal conduction has led to an increase of spot area, lowered the power density, and hence lowered the surface temperature. The explosively formed plasma has expanded, its density is lowered, therefore the cathode sheath thickness has increased, and the surface field is reduced. Despite lower cathode surface temperature and lower field strength, this stage may be important to the overall cathode erosion since the hot surface may still deliver metal vapor, especially when the cathode material is of high vapor pressure [44].

3.4.6 Plasma Jets, Sheaths, and Their Relevance to Spot Ignition and Stages of Development

Neglecting the small voltage drop inside the cathode, one may state that the cathode is at the cathode potential and the plasma far from the surface is at plasma potential. "Far" can be understood as a distance much larger than the spot size and larger than the greatest cathode sheath thickness. The potential difference

$$\Delta V = V_{cath} - V_{pl} \tag{3.60}$$

is located very close to the cathode surface and is generally known as the cathode fall. The thickness of the sheath, across which the potential falls, depends strongly on the local plasma density. Local emission and explosive processes immediately imply that we deal with a time-dependent and non-uniform distribution of plasma density and sheath thickness. The situation is quite different than often simplifyingly illustrated: the sheath edge or boundary is not at a constant distance from the surface. Quite contrarily, the sheath boundary depends on the local plasma conditions and changes rapidly with the evolution of the emission center.

Let us consider an instantaneous snapshot of the near-cathode zone and preliminarily adopt the concept of the Child sheath (Appendix A):

$$s_{Child} = \frac{\sqrt{2}}{3}\lambda_{De}\left(\frac{2e\,|\Delta V|}{kT_e}\right)^{3/4}. \tag{3.61}$$

The Child sheath thickness scales with the Debye length $\lambda_{\mathrm{De}} = \left(\varepsilon_0 kT_e/n_e e^2\right)^{1/2}$, which varies greatly over the surface. The Child sheath thickness depends on the voltage drop, ΔV, and on the local electron density and, to a lesser degree, electron temperature. One can therefore immediately see that different locations have different sheath thickness: a location of denser plasmas has a thinner sheath than the surrounding locations.

Although these considerations appear intuitively right, they do not stand a rigorous proof because the conditions of validity for (3.61) do not apply for all locations, or equivalently, stages of spot development. One of the assumptions in the derivation of (3.61) was that ions move from the sheath boundary through

the sheath *toward* the cathode surface. However, the net flux of a cathodic arc process points in the opposite direction. The assumption of arriving ions is greatly violated at least in stage (ii), the explosive stage, where the phase transitions solid→liquid→gas→plasma occur rapidly in an expanding volume. The voltage difference ΔV drops mainly in the dense, non-ideal *plasma* because the conductivity of the non-ideal plasma is less than the conductivity of the metal and the conductivity of the expanded, ideal plasma ("valley of low conductivity" [45]; more about non-ideal plasmas are said in the next section).

The plasma conditions change rapidly and therefore the sheath boundary should be understood as a highly dynamic object with transient "holes." A "hole" means that a location may exist without a sheath: the voltage is dropping in non-ideal, quasi-neutral plasma, as opposed to a space-charge layer. The sheath holes are at locations where *dense* plasma of microexplosions can be found, hence they exist only at some locations for a very short time (nanoseconds). Figure 3.13 shows a cartoon snapshot of such situation. This description illustrates the difficulties of modeling cathode processes of cathodic arcs: the different stages of spots and fragments require different model approaches and different scales. Explosive models need to be matched with models describing simultaneously occurring processes far from the explosive center. These different processes are coupled; they operate electrically in parallel and create boundary conditions for each other.

At this point some more remarks should be made about model assumptions. In order to make the difficult situations tractable, simplifying assumptions are made on the structure of layers and geometry of emission sites. Furthermore, sometimes, models are not based on first principle equations but on solutions of fundamental equations that apply to certain conditions.

For example, instead of solving the Poisson equation, a second-order differential equation, special solutions such as the Child–Langmuir law for the current and the Mackeown equation for the electric surface field are often utilized. Mackeown's equation [46, 47] in one dimension is simply

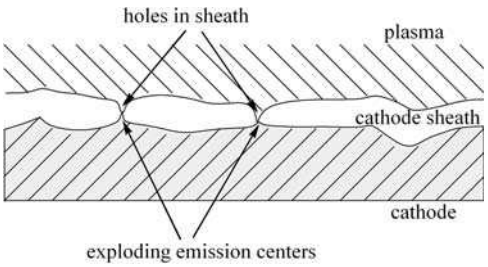

Fig. 3.13. Schematic of "holes" in the cathode sheath: these are locations where *dense* plasma of microexplosions is found; "sheath holes" exist only for a very short time (nanoseconds)

$$\mathrm{E}_{surface} = \left.\frac{\partial V_c}{\partial z}\right|_{\text{surface}} \approx \frac{4}{3}\frac{V_c}{s_{Child}}, \tag{3.62}$$

where $V_c \approx 20\,\mathrm{V}$ is the cathode fall and s_{Child} is the Child sheath thickness, (3.61). However, these special solutions are only valid under certain conditions, such as the net ion flux is going toward the surface, as already mentioned. Such conditions may be satisfied far from the spot or, equivalently, at times other than the explosive stage.

Simplifying assumptions are also made in models focusing on the explosive stage. Most importantly, to model thermal runaway, the field enhancement needs to be known, and therefore assumptions are made about the shape of a "typical" emission site. Very popular is the cone shape because a cone has a very high field enhancement factor at its tip, and furthermore it is argued that cones are naturally formed when a liquid surface is subject to strong electric fields (Taylor cones) and dynamic pressure (nonlinear surface waves) [48].

The sheath thickness is of critical importance to the ignition of an emission center because it determines the surface electric field, which needs to be sufficiently high to cause thermal runaway at this location. Even as the Child solution (3.61) and the Mackeown field (3.62) are not applicable, one can qualitatively say that high plasma density is associated with thinner sheath and higher surface field strength. Therefore, as we look for reasons why a potential emission site actually becomes an emission site, we need to consider the site's surface conditions as well as the evolution of plasma above the surface. This approach will naturally lead to understanding of random versus "steered" motion of cathode spots.

In the previous section on stages of development, it was already mentioned that ignition of a new emission site occurs when a location with favorable surface conditions is exposed to dense plasma. The dense plasma simultaneously produces two important effects: one is the shrinking of the sheath thickness and the associated *increase in electric surface field* and the other is an *increase in ion bombardment heating*. The combination of both gives rise to intensified local energy input, which leads to a microexplosion if the energy input rate exceeds the energy removal rate, as will be discussed in the framework of explosive electron emission (see (3.63)). At this point it should only be mentioned that experiments by Puchkarev and Bochkarev [49] and simulation by Uimanov [50] provided evidence that ion bombardment heating is critical for the formation of the explosive emission stage. Active emission sites emit plasma that is rather non-uniform on the microscopic scale (jets) due to focusing in the strong magnetic field associated with the arc's high current density. These micro-plasma jets provide the ion bombardment and field enhancement conditions for potential emission sites. In the absence of an external magnetic field, the self-field is rather symmetric, and there is no preferred direction for the emission of microjets. Hence the ignition of new emission sites is equally likely in all directions from the active site. If an external magnetic field is applied transverse to the surface normal, the symmetry is broken, and one should expect a preferred direction of plasma jets and spot ignition.

3.4.7 Explosive Electron Emission and Ecton Model

The central stage in the development of emission centers is stage (ii), the explosive stage. The idea of explosive electron emission was developed by Mesyats and co-workers including Bugaev, Litvinov, and Proskurovsky [51–53]. The term "explosive electron emission," sometimes with the acronym "EEE," may refer to the whole development cycle of an explosive center, or specifically to the explosive stage.

Already in his early work in the 1960s, Mesyats recognized the similarity between metal→plasma phase transitions of exploding wires and cathodic arcs. Based on much improved experimental data, Mesyats introduced a rather specific model of explosive electron emission in the 1990s, the "ecton model" [54, 55], which is based on the explosion of a liquid metal cone formed by the action of a strong electric field on the hot cathode surface.

The term "ecton" refers to an "*e*xplosion *c*enter" with the ending "ton" in analogy to other particles or quasi-particles (like photon, proton, exciton, etc.). In doing so, Mesyats wanted to emphasize the *discrete*, "quantum-like" appearance of each explosive event [35, 41, 42, 56]. Interestingly, one can also see the *collective* character of electron emission (recall: Hantzsche defined an arc cathode mechanism to be a collective phenomenon, see the discussion at the beginning of this chapter). According to the ecton model, each ecton liberates about 10^{11} electrons in an explosion with duration of the order of 10 ns. The microexplosion also produces plasma of the cathode material and generates the conditions for the ignition of the next ecton. Mesyats refers in his work generally to emission centers of cathode spots; the physics applies to individual emission centers or cells or spot fragments in Kesaev's [57] and Jüttner's [58] classifications.

The explosive emission concept will now be described in somewhat greater depth because it contains processes that explain a number of features of the cathodic arc plasma. These features (supersonic ion velocities, multiple charge states, etc.) distinguish cathodic arc plasmas from most other plasmas; and they are the reason that cathodic arc plasma deposition is an energetic condensation process leading to films that are denser than most other processes.

A microscopically small volume, such as a microprotrusion or particular volume under an oxide layer, will explode if the rate of specific energy input, $\mathrm{d}w/\mathrm{d}t$, is much greater than the maximum rate of heat removal. The latter can be expressed as the energy of sublimation or cohesive energy, E_c, divided by the characteristic time of energy removal, τ, [54], hence the condition for explosion is

$$\frac{dw}{dt} \gg \frac{E_c}{\tau}. \tag{3.63}$$

The cohesive energy can be expressed as energy per mass (J/kg) or per particle (eV/particle), and the characteristic time of energy removal can be determined by

$$\tau = d/v_s, \tag{3.64}$$

where d is the characteristic (linear) size of the microvolume and v_s is the speed of sound in the cathode. The conditions so far are rather general and not necessarily bound to the conical shape of an emitter. Explosive emission may occur on rather plane surfaces [49] as long as condition (3.63) is meaningful and satisfied. If heat removal is exclusively by heat conduction, the linear dimension of the exploding microvolume is

$$d < \sqrt{a\tau}, \tag{3.65}$$

where a is the thermal diffusivity. For example, with $w_e \sim 10^7$ J/kg, $v_s \sim 10^3$ m/s, $d \sim 10^{-6}$ m, one obtains $dw/dt \gg 10^{16}$ J/kg s.

Explosive phase transitions are known from wire explosions [59]. A segment of wire can be considered equivalent to a current-carrying microprotrusion on the cathode surface. A wire (or microprotrusion) will explode with a delay time, t_d, if a *thermal runaway* instability occurs [60]. Joule heating is proportional to the current density and voltage drop; the latter, in turn, is proportional to the current density and resistance of the wire segment (or microprotrusion). For metals, the resistance increases with temperature and, provided the power source can deliver greater power at increased voltage, the Joule energy dissipation increases with increasing temperature. This, in turn, increases the temperature, which increases the energy dissipation, etc., and thus the runaway feedback loop closes until the wire segment (or microprotrusion) is destroyed by a microexplosion.

From the theory of wire explosions [61], the current density, j, and explosion delay time, t_d, satisfy

$$\int_0^{t_d} j^2 dt = \overline{h}, \tag{3.66}$$

where $\overline{h}$ is called the specific action whose value depends on the cathode material but is approximately independent of current density, wire cross-section, or other discharge quantities (Table 3.4).

Table 3.4. Specific action, $\overline{h}$, for selected materials. (From [41, 62])

Material	$\overline{h}$ (A^2s/m^4)
C	1.8
Al	18
Fe	14
Ni	19
Cu	41
Ag	28
Au	18

According to the ecton model [41, 54, 56], thermal runaway occurs on microprotrusions until they explode with a delay time associated with the material-specific action. Cathodic arc operation includes plasma production and electron emission via a rapid sequence of microexplosions. This concept may appear questionable because it explicitly calls for explosions of microprotrusions. Different materials have certainly different densities of such protrusions, and of course they are destroyed by the explosive processes. Therefore, to be consistent, the ecton model must include not only the explosion but the *formation* of microprotrusions or similar explosion-promoting structures or other conditions that can lead to thermal runaway in a limited volume. The latter may occur on any metal surface if plasma microjets provide intense local ion bombardment and high electric surface field [49].

Not all modeling work is based on explosive emission theory (used widely in this book), where electron current actually exceeds the arc current because it needs to compensate for ions going the "wrong" way (from cathode to anode). In a more traditional one-dimensional model, the current transfer at the cathode surface is composed of electron emission current and ion return current. Using this and other assumptions, Beilis [63] calculated that multiply charged ions may be formed for refractory metals at a relatively small electron-to-ion current ratio of 0.7–0.9. A similar model was developed by Coulombe and Meunier [64] for the operation of a copper arc with current densities in the range from 10^8 A/m^2 (upper limit for non-vaporizing cathode models) to 4×10^{10} A/m^2. Their results showed that current densities greater than 10^{10} A/m^2 can only be accounted for with metal plasma pressures exceeding 35 atm and electron temperatures ranging from 1 to 2 eV. The current transfer to the cathode is mainly assumed by the ions at relatively low current densities ($<10^{10}$ A/m^2) and by the thermo-field electrons for higher current densities. The heat flux to the cathode surface under the spots is mainly due to the flux of returning ions and ranges from about 10^{10} to 10^{11} W/m^2 for current densities ranging from about 10^9 to 10^{10} A/m^2.

3.4.8 Explosive Electron Emission on a Cathode with Metallic Surfaces

For fragments of spot type 2, i.e., emission sites on clean metal cathode surfaces as further discussed below, the formation of microprotrusions is not difficult to recognize when investigating the crater traces left by the microexplosions (right side of Figure 3.14). The microexplosion produces a thin layer of molten cathode material, which yields to the high plasma pressure. The liquid material is ejected from the explosion crater and is rapidly quenched, producing macroparticles (see Chapter 6) and microprotrusions, which can serve as new ignition points. One of them will be most suited to go through thermal runaway, leading to the next microexplosion. According to this picture, the location of the next explosion is displaced by about one crater radius from the location of the predecessor [65]. It is common for this arc spot type that long chains of craters are formed

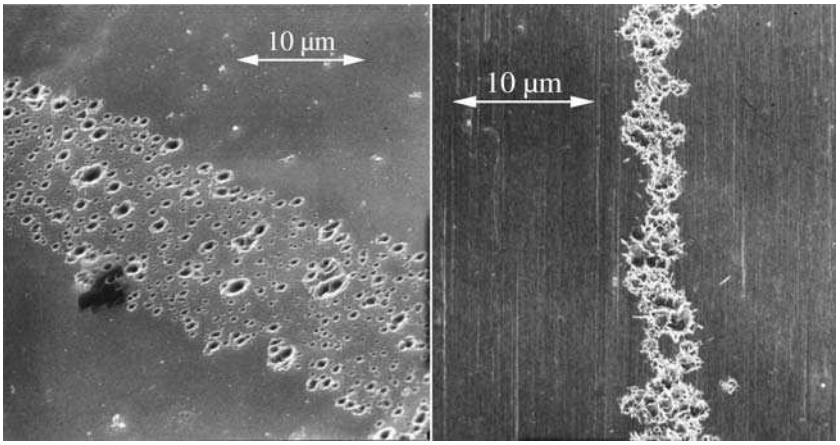

Fig. 3.14. Track of erosion craters left by spots of type 1 (*left*) and type 2 (*right*); a transverse magnetic field was applied to "drive" apparent spot motion leaving a rather straight trace. (Photos courtesy of B. Jüttner)

(Figure 3.14, right). These chains of craters show a preferred (retrograde) direction when an external magnetic field is present.

At first sight, the situation is less obvious for atomically smooth cathodes or liquid cathode surfaces like with mercury or gallium or cathodes with non-metallic layers (type 1 cathode spots). Here, additional processes need to be considered.

Let us consider a liquid metal surface subject to a strong electric field. Already Tonks considered in 1930 that the electrostatic force on a liquid metal surface may overcome the stabilizing forces of surface tension and gravitation [66]. A surface instability can lead to the development of liquid metal cones,[5] which could well serve as the microprotrusions needed to maintain the explosive electron emission process. Figure 3.15 shows microprotrusions formed on a liquid metal surface in a strong electric field [48]. Although this figure was obtained by intense and quenched electron bombardment in a specially constructed electron microscope, similar conditions may occur on the surface in the vicinity of an emission center because ions from the dense plasma bombard the surface, corresponding to stage (i) of the fragment development.

Numerical modeling needs to include the temporal evolution (time is an explicit variable) and, in order to keep the problem manageable, simplifications

[5] Very sharp liquid metal cones (Taylor cones) are used in liquid metal ion sources (LMIS) [67, 68] where field evaporation and ionization occurs for use in focus ion beams (FIBs), for example. However, the polarity of those devices is opposite to our cathodic arc configuration, and the currents are in the range of hundreds of nA per tip, i.e., many orders of magnitude less than arc currents.

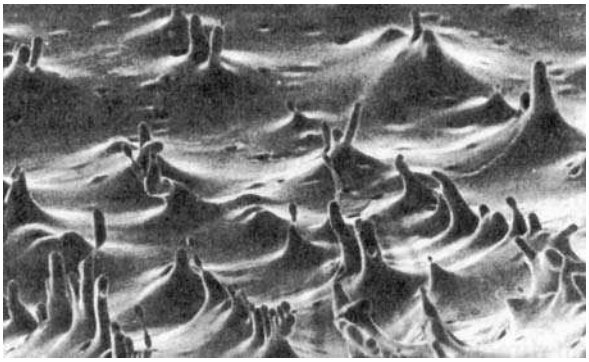

Fig. 3.15. Microprotrusions formed on a liquid metal surface in a strong electric field. This photograph was obtained in a scanning electron microscope where a plane copper surface was placed in a field of 10^7 V/m and exposed to plasma flow, which provided intense heating that led to surface melting. When the flow was terminated, the surface profile quenched, allowing us to observe quenched microprotrusions. (From [48])

are done in terms of geometry, for example by assuming a slender cone with given material properties. The explosive stage was shown to be consistent with a time regime of 1–10 ns, peak current density of up to 10^{13} A/m^2, and surface field at the tip of the cone of up to 10^{10} V/m [69], although there is evidence for even higher, transient current densities in the sub-nanosecond time regime and much lower values when looking at "most probable" quantities [70]; this wandering over several orders of magnitude is re-considered in the fractal model, Section 3.5.

Numerical simulation using a time-dependent, two-dimensional hydrodynamic model indicated that the current distribution at the end of the explosive stage is ring-link, rather than peaked in the center of the emission site [71, 72]. In the absence of a transverse magnetic field, any place on the rim of the newly formed crater could turn into a new, active emission site, whereas the current-carrying ring is not symmetric when the plasma above the emission site is bent by the transverse magnetic field. This asymmetry can contribute to the non-isotropic probability for igniting new sites of type 2 spots.

3.4.9 Explosive Electron Emission on a Cathode with Non-metallic Surfaces

Turning to surfaces with non-metallic (e.g., oxide) layers, one should recall that a microexplosion occurs when the rate of specific energy input, dw/dt, is much greater than the maximum rate of heat removal. This condition does not necessarily imply a conical shape of the emitting surface. More importantly, the *rate of rise* of local temperature must exceed a threshold value. By limiting the explosion time to less than 100 ns (a reasonable though arbitrary value), Abbaoui and co-workers [73] calculated for a range of materials that the power density must exceed about 5×10^{12} W/m^2 otherwise the phase transitions will

not occur. Simulating local power input with a focused, 20-ns pulsed laser beam, Vogel and Höft [74] found that about 2×10^{11} W/m^2 are need to obtain localized melting; however, in order to produce craters that look like arc craters one needs a power density in the range 10^{12}–10^{13} W/m^2.

As discussed in previous sections, the presence of non-metallic layers profoundly changes the electronic structure of the surface. The work functions can be lowered, which is important because electron emission depends on the work function in a highly nonlinear manner. If there is insulating material on the surface, it will charge up under ion bombardment and create strong field within the insulator, which in turn can lead to the enhancement of electron emission and thermal runaway at some locations. (Similar processes can also occur on negatively biased substrates leading to "arcing," and the topic is therefore picked up again at the beginning of Chapter 9.)

The *rate* of surface charging, field enhancement, and emission onset can be very fast, which can be more important than the absolute energy input, as was expressed in (3.63). It is conceivable that several emission centers may switch on nearly simultaneously. Such multiple centers are electrically in parallel, hence share the total arc current and the same total voltage drop. They "compete" for current and energy dissipation. In the average, emission centers in this situation will have less current per center, in agreement with observations. Emission centers that have high impedance will have less current and less heat dissipation and in absolute terms may not maintain the rate of rise required to fully form explosion craters: such centers will stop producing phase transition of cathode material, they will "die" in an early stage. Indeed, electron microscope pictures of arc traces on "contaminated" (i.e., non-metallic) surfaces show craters of type 1 spots dispersed over the cathode surface, with a large number of small and very small craters (diameter $\sim$ 1 μm and less, Figure 3.14 left). In this picture, the "death" of an emission site is associated with the ignition, presence, and competition of other emission sites. This is consistent with the observation that spots of type 1 have faster apparent motion, need less voltage to ignite, erode less cathode material, emit less light, and produce a plasma that contains metal and non-metal species.

3.5 Fractal Spot Model

3.5.1 Introduction to Fractals

Cathodic arcs show many features that suggest to model cathodic spot phenomena using the well-known theory of fractals [75, 76]. For example, random walk of cathode spots was discussed in the 1980s [77, 78], $1/f$-noise of ion current has been found in the late 1980s [79], arc traces by the spot's random walk showed a fractal dimensions of about 2 [80], and self-similarity in the patterns of emitted light was recognized [81, 82]. As has been argued in a recent publication [3], fractal features are not superficial but fundamental to the nature of cathode

spots. After reviewing all evidence, one can agree with Mandelbrot's sentiment quoted at the beginning of this chapter.

With this motivation, let us start with a brief introduction to the world of power laws, random colored noise, and fractals.

Many laws in physics are linear and periodic and show invariance to additive translation. However, not all physical phenomena can be described in this manner; in fact, a great number of phenomena are nonlinear, aperiodic, and chaotic. In the 1980s, a branch of mathematics and physics started to flourish: the science of deterministic chaos and self-similar structures, dubbed "fractals" by Benoit Mandelbrot [75]. Fractals are mathematical or physical objects invariant to scaling, which makes them "self-similar" to *multiplicative* changes of scale. A self-similar object appears (approximately) unchanged after increasing or decreasing the scale of measurement and observation. Self-similarity may be discrete or continuous, deterministic or probabilistic.

Power laws are an abundant source of self-similarity [76]. Consider the homogenous power law

$$f(x) = cx^{\alpha} \tag{3.67}$$

where c and α are constants. It is self-similar because rescaling (i.e., multiplication with a constant) preserves that $f(x)$ is proportional to x^{α} albeit with a different constant of proportionality. A fruitful approach to fractal modeling is to look for *power laws* describing the physical phenomena.

Self-similarity can be mathematically exact and infinite or only approximate and asymptotical. The latter applies to the physical world, and scaling cutoffs exist at the small scale and large scale. Mathematical objects are strictly self-similar with infinite scaling; they are often named after their "inventors" and have sometime colorful names, like Cantor sets, Julia sets, Koch flakes, Sierpinski gaskets, Mandelbrot trees, Farey trees, Arnold tongues, Devil's staircase [75, 76, 83].

Fractals can be characterized by dimensional measures, such as the Hausdorff dimension (named after Felix Hausdorff, 1868–1942). The fractal dimension is often non-integer and smaller than the embedding topological dimension. To illustrate the concept, Mandelbrot [75] used the now-classical question "How long is the coast of Great Britain?" The essence of this consideration is reproduced here, having in mind that the question of current density and other parameters should be considered in the same way. Mandelbrot showed that (i) the answer depends on the scale length of measurement and (ii) different coastlines have different values for the fractal dimensions, depending on their "ruggedness." More detail is revealed by "zooming in," therefore, the finer the scale unit r, the longer the apparent coastline length L. If the coastline is self-similar, a power low can be found connecting the measured length $L(r)$ with the measuring scale unit r:

$$L(r) \propto r^{\varepsilon}, \tag{3.68}$$

where $\varepsilon < 0$ if L increases as r decreases. In contrast, if the coastline was smooth, the measured length should approach an asymptotic value when a smaller scale is used, L is finite as $r \to 0$, hence $\varepsilon = 0$. The Hausdorff dimension

$$D = \lim_{r \to 0} \frac{\log N(r)}{\log(1/r)} \tag{3.69}$$

can be introduced, where $N(r)$ is the minimum number of circular areas of diameter r needed to cover the coastline. In this example, $N(r) = L(r)/r$, leading to

$$D = 1 - \varepsilon. \tag{3.70}$$

Because $\varepsilon < 0$, D will exceed 1, which can be intuitively interpreted as a dimension because a coastline is more than a one-dimensional object (straight line) and less than a two-dimensional object (filled area). Coastlines with only few bays and points have D just little over 1, while rugged coasts such as the coast of Britain or Norway exceed 1 significantly.

Fourier transform of stochastic, fluctuating data often reveals that the Fourier power spectrum follows a power law

$$F(f) \sim 1/f^{\alpha}, \tag{3.71}$$

where f stands for frequency. According to convention, the exponent α determines the color of random colored noise (RCN, [84]). The noise is *white* for $\alpha = 0$ (i.e., it does not depend on frequency); $\alpha = 1$ describes *pink* noise, which is often found in physical systems of self-organized, barely stable structures [85]; $\alpha = 2$ is *brown* (hinting at a relation to Brownian motion); and $\alpha > 2$ refers to *black* noise observed in self-similar systems that tend to have positive feedback, like the stock market.

3.5.2 Spatial Self-Similarity

The connection between discharge phenomena and fractals is well established for branching and treeing of the conducting plasma channels in lightning and Lichtenberg figures (Figure 3.16). Crystal growth by diffusion-limited aggregation (DLA) leads to structures that look very similar to Lichtenberg figures as well as spot traces obtained by high-current pulsed arcs. Therefore, it appears to be instructional to consider well-established modeling of DLA.

In DLA, a single molecule performs a random walk until it bonds to an aggregate; it gets "stuck" and provides an attachment site for the next molecule. A kind of dendritic growth is observed because the molecule has a greater probability to attach near one of the tips of the fractal cluster than in the "fjords" [76, 87]. Different sites have different probabilities for attachment, and the probability for attachment decreases with increasing depth inside a "fjord." Figure 3.17 shows a simulation of a DLA growth cluster (left) and the points of enhanced attachment probability (right) [87]. Lichtenberg figures and

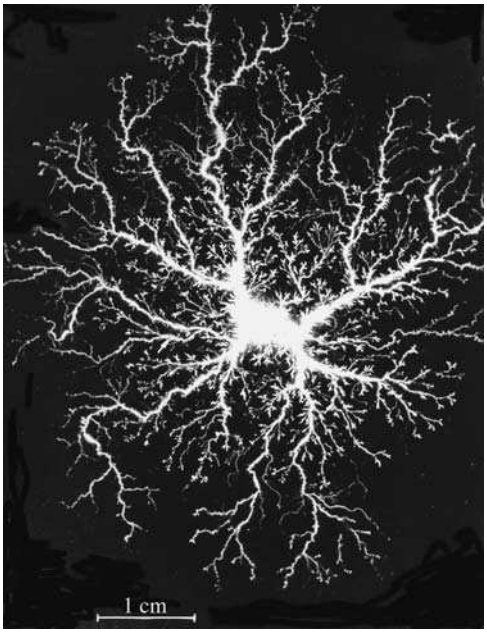

Fig. 3.16. Lichtenberg figure: a pulse discharge on the surface of an insulator [86]

multi-spot arc traces have similar shapes, which is not accidental because all of these phenomena are governed by the Laplace equation for a potential. In DLA, the cluster is an equipotential surface and the gradient of the potential corresponds to the diffusion field. In discharge physics, the tips of a growing Lichtenberg figure and ignition locations of a developing multi-spot arc have the same potential due to the high conductivity of the plasma channels.

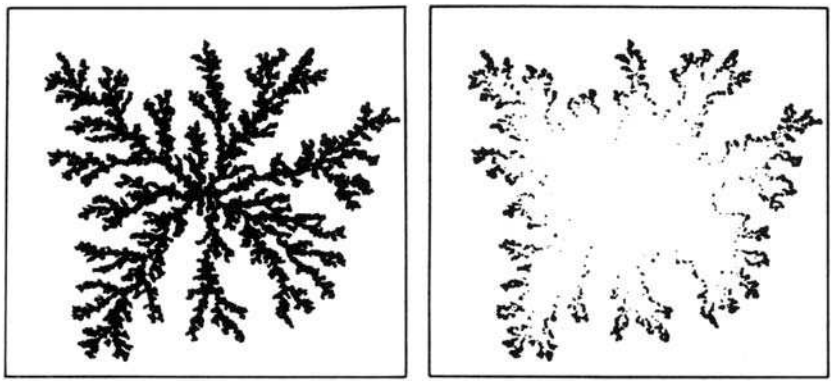

Fig. 3.17. Simulation of a DLA growth cluster (*left*) and the points of enhanced attachment probability (*right*) [87]

It should be noted that a multiplicative random process on a fractal, rather than on an interval, leads to a multifractal spectrum, a concept now widely used in turbulence research. Diffusion-limited aggregation is one example of a *multifractal* [76], and one should expect to discover multifractal properties for arc spots.

One of the early works on spots and fractals is by Siemroth, Schülke, and Witke who recognized self-similarity in at least four levels of spatial resolution [81, 82]. According to their work, one might distinguish group-spot level, macrospot level, microspot level, and crater level and find self-similar features in each of those levels. In this chapter, and throughout the book, it is argued that the fractal cathode-spot model is fundamental both for spatial and temporal phenomena, while elementary processes like explosive events (ectons) represent the lower cutoff for self-similar description in time and space.

Stochastic self-similarity exists not just because we can "zoom" with different resolution and find similar spot appearance; rather, the stochastic but field-dependent (deterministic) nature of spot ignition provides a physical basis for a fractal model of cathodic arc spots. By incorporating the "quantum" of explosive emission (ectons) as the cutoff limit and considering stages of spot development, the ecton model and vapor ionization model can be reconciled with observations on both short and long scales of time and space.

It should be noted that the non-zero, finite lifetime of excited states presents a fundamental limit to "zoom in" with optical emission methods. The location of de-excitation processes, in which observable photons are emitted, is shifted with respect to the location of excitation, and therefore there is a fundamental limit of resolution using emission methods [88–90]. Images of emission centers show a diameter of typically 100 μm or larger, even when the optical resolution is a few micrometers, while the diameter of the underlying erosion crater may be just a few micrometers or less. Of course, this has implication for the limits of current density measurements [88–90]. Going beyond that, the non-zero lifetime of excited states represents a lower observation limit (cutoff) for the fractal cathode spot when observed by optical emission methods.

Self-similarity can also be found in traces left by cathodic arcs. This includes macroparticles left by the arc on surfaces which were in line of sight with the cathode. Macroparticles are discussed in Chapter 6, and here it is only pointed out that size distribution functions are power laws extending over several orders of magnitude, exhibiting a self-similar (fractal) property: An observer looking at electron microscope photographs of macroparticles would not be able to decide which magnification was used in making the images.

3.5.3 Temporal Self-Similarity

Practically all cathode-spot parameters show fluctuations. Whatever we measure, e.g., voltage, light emission, particle fluxes, and ion charge states distributions, we always see "noise." One may argue that there are exceptions, for example the arc current may appear rather constant. This is an artifact of the

circuit that occurs when the circuit impedance is much greater than the impedance of the arc plasma.

By measuring spot data with increasingly higher temporal resolution, one would "zoom in," just like one could look at coastlines with increasingly higher spatial resolution. Analogously, one might find fractal features in the time domain, known from time series analysis. Figure 3.18 shows an example of time-resolved light emission from a copper vacuum arc. Similarly looking curves can be obtained with different time resolutions and from different physical quantities, such as ion current collected by probes or shields.

In the late 1980s, Smeets and Schulpen [79] studied the correlation of light emission and ion current signals for low-current copper arcs. Taking time-of-flight of ions into account they found that high-frequency fluctuations of voltage and ion current were correlated, while the average light intensity was proportional to the arc current. Fast Fourier transform (FFT) of noisy ion current signals did not reveal distinct peaks, indicating that the measurements did not reach the lower cutoff. The FFT spectrum showed a $1/f$-character for the spectrum up to about 15 MHz and approximate "white" noise for faster fluctuations (Figure 3.19).

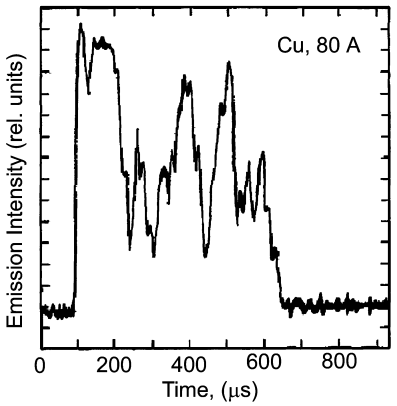

Fig. 3.18. Example of time-resolved light emission from a copper vacuum arc; the *curve* is a representative of time-resolved data with fractal character. Similar curves can be obtained on changing the time resolution [88]

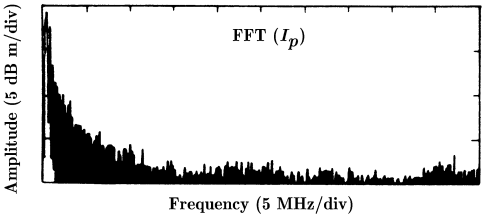

Fig. 3.19. Fast Fourier transform (FFT) of noisy ion current signals [79]; the spectrum does not reveal distinct peaks but has $1/f$ character up to 15 MHz

Unfortunately, their display of data was linear and it is hard to judge how well the noise was indeed represented by a $1/f$ dependence. The slope of a power law, if present, is much easier to find when data are displayed in log–log presentation. Furthermore, they did not explicitly distinguish between Fourier amplitude and Fourier power spectrum but we may assume that they referred to the amplitude spectrum. The corresponding power spectrum would be $\sim 1/f^{\alpha}$ with $\alpha \approx 2$, i.e., *brown* noise.

Using more recent data [91], *random color noise* (RCN, [84]) was found within the physically meaningful frequency interval. Most data curves show three characteristic segments. There was white noise at high frequencies. At intermediate frequencies, a RCN slope of $\alpha > 1$ was found. Many curves had a kink at lower frequencies, giving $0 < \alpha < 1$, which should be disregarded, as discussed below. Figure 3.20 shows such curve for the noise of Cu ions for a pulsed vacuum arc.

White noise at high frequencies is possibly due to ion velocity mixing [91], that is, all information from emission sites is mixed because faster ions overtook slower ions on their way from the cathode to the ion collector. "Scrambled" information would result in white noise. In the case of carbon, Figure 3.21, the segment of white noise is particularly pronounced. Carbon ions are lighter and faster than other metal ions, and the effect of velocity mixing could be more pronounced. However, research is still ongoing; white noise can also be caused by measurement limitations, in particular when the amplitude of the noisy signal approaches the noise of the measuring system itself.

At low frequencies, the curve is quite uncertain due to insufficient data. Mathematically, because we deal with a finite discrete sample of data, the limits

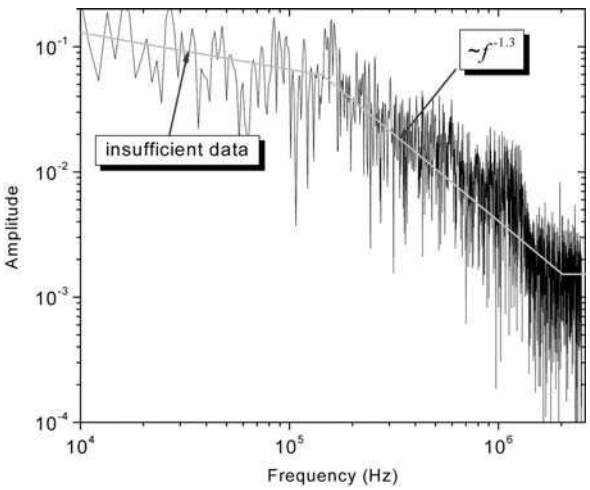

Fig. 3.20. FFT of ion current for a copper vacuum arc pulse. One can see the approximate power law in the physically relevant interval. (From [3])

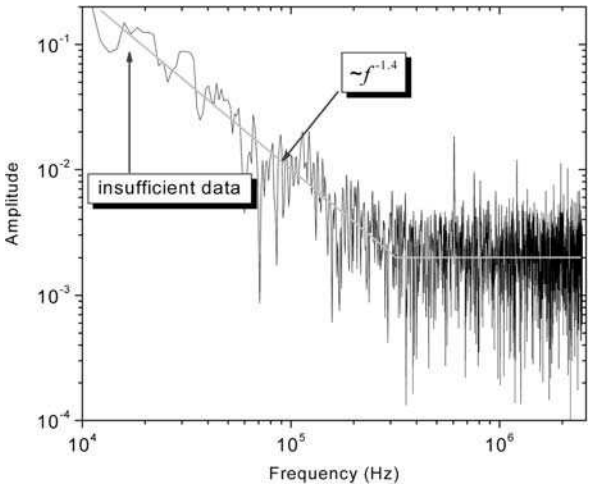

Fig. 3.21. FFT of ion current for a carbon vacuum arc pulse, which is similar to the copper case, Figure 3.2, but white noise extends to lower frequencies. (From [3])

of discrete Fourier transforms (DFT) apply: The inverse of the sampling period represents a lower limit to the resolution of the transformed data, and the upper limit is half of the sampling interval (Nyquist sampling theorem). Only few data points contribute to the lower frequency part of the FFT curve, and therefore it should be disregarded.

More research is needed to really learn what information can be extracted from the RCN segment of such FFT curves. So far, one can see that the relevant segment appears close to brown noise, an indication for the relation to Brownian motion of spot ignition. One should note that the greater the color coefficient α the more one is tempted to search for "characteristic" frequencies or time intervals. For example, emitted light appears to have same smaller peaks and valleys and larger peaks and valleys suggesting periodicity [88, 92]. Beilis and co-workers [92] identified brightness fluctuations for copper arcs with intervals of 17±3 μs. However, Fourier analysis with sufficient data is needed to determine whether the peaks and valleys are periodic or stochastic.

The arc voltage is an especially suitable parameter to research cathode processes because it reflects them in a less distorted way than ion current or most other parameters. This is because phase mixing, as it is prevalent with ion currents [91], or "smearing out" of emitted light due to finite, non-zero lifetime of excited states [88] does not play a role. Using voltage noise, the signal generated by the cathode processes can be recorded with maximum fidelity, only limited by the bandwidth of the recording circuit.

Using a coaxial arc discharge arrangement and broad-band voltage divider and attenuator measurements, the FFT of arc burning voltage was determined

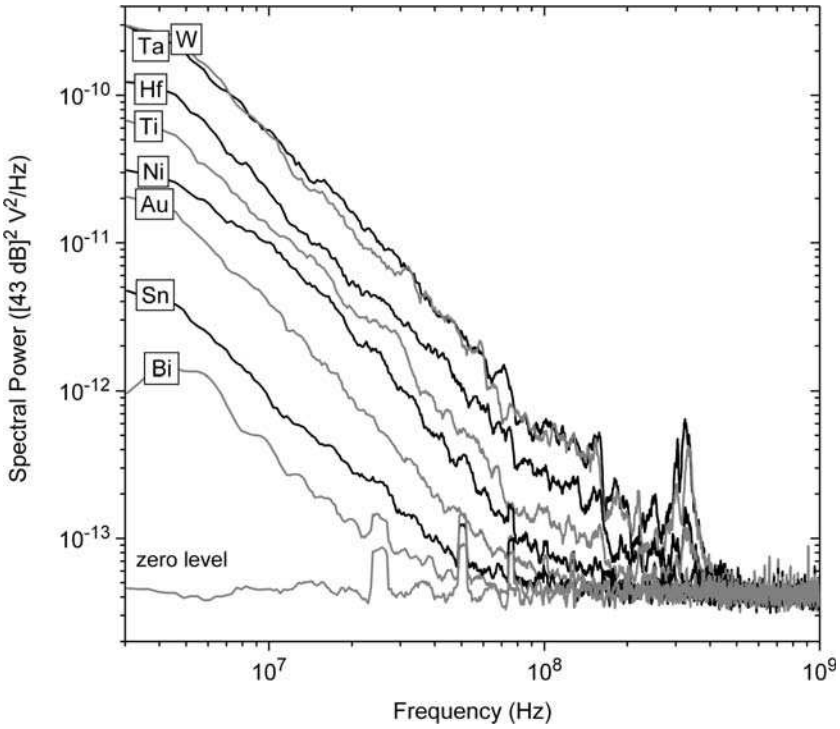

Fig. 3.22. FFT of the burning voltage for eight cathode materials. One can clearly see the power law describing brown noise (spectral power $\sim 1/f^2$) (after [215]). The FFT of the measuring system noise (no arc) is also displayed

with maximum resolution possible [93]. Figure 3.22 shows the result for eight cathode elements. As with ion current, one can recognize the $1/f^2$ character in the power spectrum, i.e., the voltage noise has fractal character which can be associated with Brownian motion of spots (see next section). The differences between materials will be considered in Section 3.7.

3.5.4 Fractal Character and Ignition of Emission Centers

While fractal character results from many stochastic events, research of elementary processes requires reducing (avoiding) the superposition of spot fragments and ignition events, and hence research was done with the smallest current possible. In a careful study with very small arc currents, Puchkarev and Murzakaev [94] found a correlation between voltage fluctuation and appearance of erosion craters. Figure 3.23a shows a track of erosion craters with a gap between one crater and a chain of craters. In this particular event, the gap could be associated with a spike in voltage (Figure 3.23b). The interpretation is

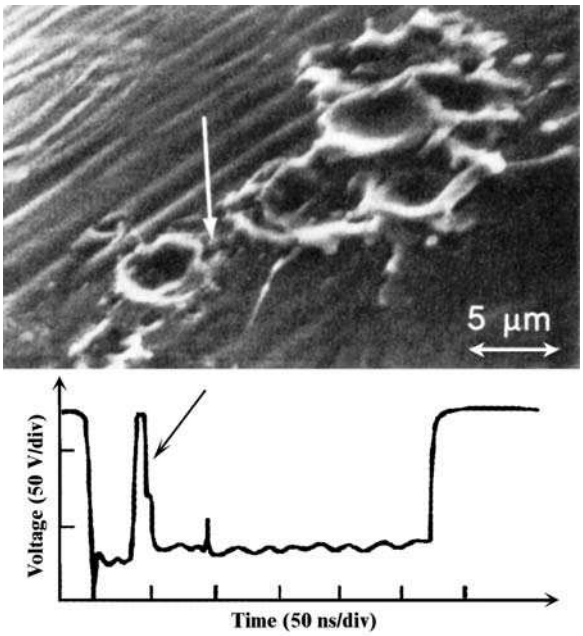

Fig. 3.23. Track of erosion craters with a gap between one crater and a chain of craters (*top*). In this particular event, the gap could be associated with a spike in voltage (*bottom*). (After Puchkarev and Murzakaev [94])

as follows: After an explosive event, which created the crater, the emission center ceased to produce plasma, the impedance of the discharge increased, causing the voltage to rise up to the full applied voltage. One should note how remarkably fast the production of plasma ceased. At this point, the arc might have become extinguished ("chopped"). However, the increase in voltage increased the field strength on the surface, which in turn increased the energy of returning ions through acceleration in the cathode sheath, as well as emission of electrons, as explained at the beginning of this chapter. New emission centers were ignited, and in this example the sequence of further ignition events was rapid and practically uninterrupted.

This study supports what is intuitively clear: Ignition and "death" of emission centers are related to voltage fluctuations, and ignition is affected by electric field strength and ion bombardment heating. The momentary and local field strength results from the combination of momentary voltage, local sheath thickness (plasma density), and local field enhancement factors. Even if we have for a moment a homogenous sheath, the cathode–sheath–plasma system is not stable against changes caused by a local enhancement of electron emission [95]; the electrons have a nonlinear feedback on local plasma density, sheath thickness, and emission current.

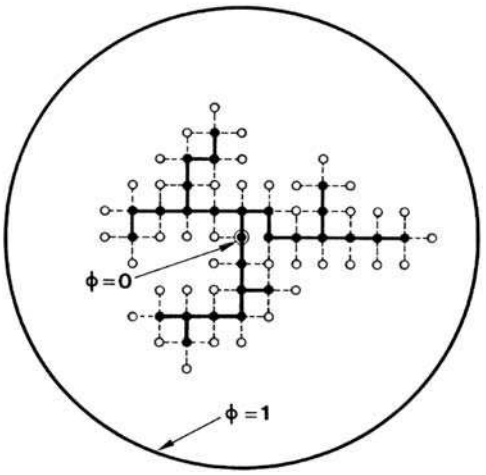

Fig. 3.24. A stochastic DLA model for spot ignition, originally developed by Niemeyer and co-workers [96] to describe the formation of Lichtenberg figures. The *dark spots* at the end of branches indicate active spots, while *empty spots* correspond to the potential ignition sites

Suitable ignition sites may be distributed randomly or evenly over the surface but the distribution of actual ignition events may be modeled using DLA-like approach. In a first approximation, one may apply a simple stochastic DLA model which was originally developed by Niemeyer and co-workers [96] to describe the formation of Lichtenberg figures. As illustrated in Figure 3.24, dark spots correspond to locations with plasma, having potential $\phi = 0$, surrounded by locations of potential $\phi = 1$. The initial location of ignition is in the center. Suppose the current is high enough to require several emission centers to be active. They correspond to the tips of the branches coming from the center. Empty circles indicate the locations where a new emission center could be ignited. The dashed lines between full circles and empty circles symbolize possible bonds in the diffusion-limited aggregation or steps in Lichtenberg figures or arc spot displacement. A probability can be assigned to each of those dashed lines expressed by

$$p(i,k \to i',k') = \frac{\left(\phi_{i',k'}\right)^{\eta}}{\sum \left(\phi_{i',k'}\right)^{\eta}}, \tag{3.72}$$

where the exponent η is introduced to adjust the relation between local field and probability. For $\eta = 1$, the growth probability is directly proportional to the local field, resulting in a fractal with Hausdorff dimension of about 1.75, which is comparable with Lichtenberg figures (Figure 3.16) or arc traces of spots (Figure 3.25).

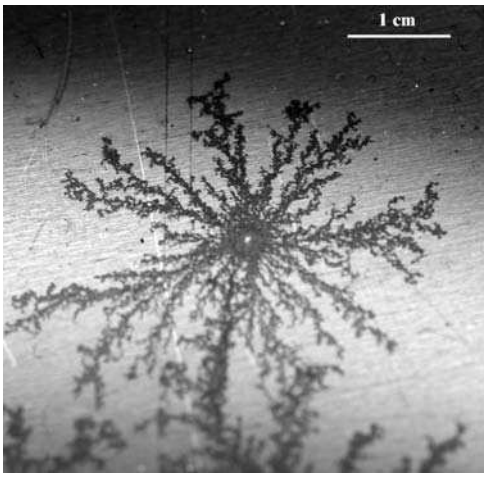

Fig. 3.25. Traces of arc spots observed on an oxide-coated metallic shield. Note the similarity between Lichtenberg figures (like in Figure 3.16) and DLA clusters (like Figure 3.24). The Hausdorff dimension is about 1.7

The model above introduces an important element to a more comprehensive spot model: it conceptually connects the distribution of the ignition probability with the local field distribution, which in turn resulted from previous ignition events. This recursive relation to previous behavior is the basis for a fractal: the result of the next step of development depends on the immediate previous condition, which will be mentioned again as a Markov process in the discussion of apparent spot motion. It will be argued that cathode-spot types, apparent spot velocity, retrograde motion, and other spot effects can be described by a stochastic fractal model for spot ignition.

Picosecond laser interferometry and absorption shadow imaging were used by Batrakov and co-workers [97] to study plasma formation on a liquid metal cathode. Using relatively small currents of less than 50 A, they observed spot fragments and determined the plasma density to be of the order of 10^{26} m^{-3}. The same group investigated a capillary-type cathode of gallium–indium alloy using resonant laser absorption imaging with the spectral lines of neutral vapor, finding that fragments operate in a cyclic manner [98]. Such cyclic processes would constitute the small-scale, fast-process physical cutoff for a fractal spot.

At even lower current, about 10 A, less emission sites are simultaneously active. Therefore, the ignition of fragments and arc instabilities are best investigated at low arc currents. Low current conditions were selected by Tsuruta and co-workers [99] showing that the voltage rises when the current drops, as one would expect from models based on ignition of emission sites. Consistently, an axial magnetic field does not help to stabilize the arc, rather makes it more unstable, especially when the anode becomes magnetically insulated, i.e., when electrons need to cross magnetic field lines on their way from cathode to anode.

Explosive emission events excite a broad range of sound waves that propagate in the solid cathode body and its surface. Techniques of acoustic surface waves analysis are often used to determine Young's modulus of coatings [100], and they can also be used to learn about the processes at cathode spots. Laux and Pursch [101] studied sound waves on graphite, carbon fiber reinforced carbon, and stainless steel cathodes. They detected distinct frequencies in the power spectrum. Most of the sound modes showed strong damping demonstrating that the nonlinear disturbance associated with the initial breakdown excited a wide spectrum. They modified the electrode geometry to identify eigen-oscillations of the cathode plate. So far, it was concluded that different disturbances during the lifetime of the moving arc are reflected in different selections of sound eigenmodes. This approach might deliver interesting information when coupled to other diagnostic techniques.

3.5.5 Spots, Cells, Fragments: What Is a Spot, After All?

It was mentioned that the appearance of spots depends on the resolution of the equipment used for observation. Every time equipment of higher spatial and temporal resolution became available, new smaller and faster structures were detected. This is particularly evident in the still ongoing debate on the current density of cathode spots. In the framework of a fractal spot model, one has to recognize that there is no single value, or even single peak value, of current density. Figure 3.26 illustrates the debate on current density over the decades; the presentation was originally shown with a wink in the 1980s but can now be

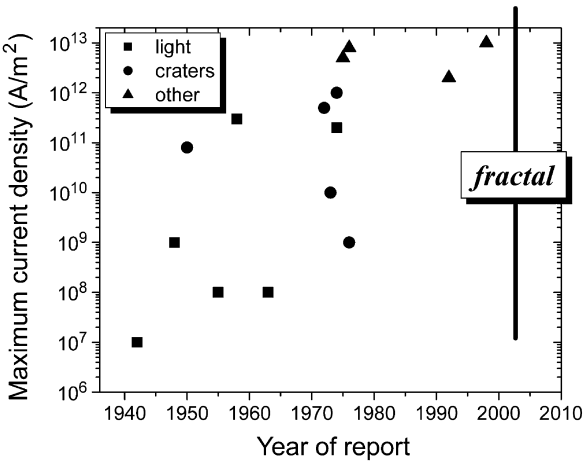

Fig. 3.26. Measurements of current densities of cathode spots: different measuring approaches gave different results, and with the availability of higher resolution equipment, smaller structures (hence higher current densities) were claimed. The debate loses most of its contention when the spot is seen as a fractal object

reinterpreted via the fractal approach. In this sense, the quest for the current density is comparable with the now-famous quest for the "true" length of coastlines.

Cathode spots are often discussed as if they were circular with a uniform or peaked current density. As early as in the 1960, Kesaev [57] postulated the existence of a substructure of "cells" within each cathode spot. Harris [102] considered cells to explain the retrograde motion of cathode spot. Modern, high-resolution imaging techniques such as pulsed laser absorption photography [103, 104], pulsed laser interferometry [105], and high-speed image-converter photography [90, 106–108] confirmed a substructure within each spot. Much research has focused on finding the smallest spatial structures and fastest temporal events below which magnifying or "zooming" would *not* reveal self-similar structures. Many researchers believe that at the scale of crater dimensions and nanosecond explosions, the lower cutoff of self-similar scaling has been reached. That, however, remains to be shown by future research. So far, ever smaller structures have been identified when increasing the resolution [109]. Well-defined plasma jets ejected by plasma instabilities from within a cathode spot [110] indicate that even finer structures may exist at even shorter timescales (see also section on retrograde motion). These smallest units of explosive events would represent ectons, which were introduced before.

These arguments are supported by the highest resolution pictures available to date. Figure 3.27 shows a cathode spot consisting of two fragments imaged for 10 ns by an image-converter camera [108]. The highest resolution photographs indicate that each of the fragments may have a substructure or they are highly

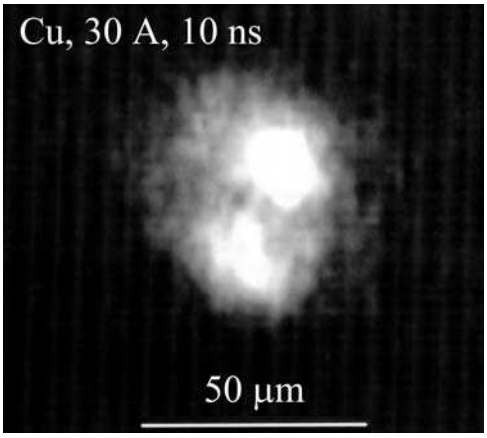

Fig. 3.27. Image-converter photograph of a cathodic arc type 2 spot on copper at a current of 30 A. The spot consists of two fragments. The short exposure time of 10 ns suggests that the two fragments exist simultaneously, rather than subsequently. Their irregular form is indicative for either a further, finer substructure or dynamics occurring within the 10-ns exposure. (From [108], Figure 4.13)

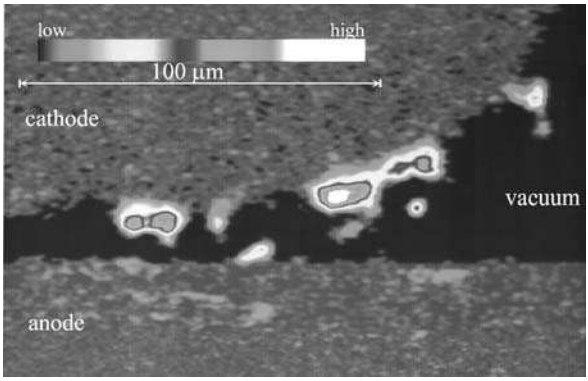

Fig. 3.28. Laser absorption photograph of a cathodic arc type 2 spot on copper at a current of 90 A, clearly showing substructure of what normally appears as a single spot. The laser pulse length (picture exposure time) was 400 ps. The gray scale represents the degree of laser light absorption (originally color coded). The electrode shape was added by image processing. (From [103])

dynamic emission centers, showing local displacement within nanoseconds. This kind of imaging reaches the physical limits that are given by the finite (non-zero) lifetime of excited levels. The emission of photons that are registered with the image-converter camera result from fast moving atoms and ions, and the location of photon emission (de-excitation) is shifted with respect to the location of excitation. To circumvent this limitation, absorption techniques using short laser pulses can be used. Figure 3.28 is an example of a laser absorption photograph of a cathodic arc type 2 spot on copper for a discharge current of 90 A with an exposure time of 400 ps [103]. It shows a diverse distribution of densities in a region that one would characterize as a single spot if judged by light emission. Similar results were obtained using even shorter "exposure time" of 100 ps in laser absorption photography [70].

The simple question "What is a cathode spot?" does not have a simple answer but the definition "A cathode spot is an assembly of emission centers showing fractal properties in spatial and temporal dimensions" captures the essential elements. The terms spot fragment, cell, and emission center are used synonymously. Each ignition event and resulting emission center may be described as an elementary step, corresponding to a sequence of emission stages, which includes the explosive or "ecton" stage in Mesyats' framework. The assembly of fragments exhibits fractal properties, and the individual steps are the small-scale, short-time cutoffs of spatial and temporal self-similarity.

3.5.6 Cathode Spots of Types 1 and 2

Cathode-spot types 1 and 2 have already been introduced in Sections 3.4.8 and 3.4.9. Here we return to this topic because the surface effects are among the most

critical for cathodic arcs, and their role has been re-discovered several times. Apparently, they deserve special attention and need to be brought in perspective for the fractal approach to arc spots.

Systematical studies started in the middle of the twentieth century trying to nail down the links between phenomenological appearance and underlying microscopic processes. Among the first reported observations where those by Dryvesteyn, Suits, Hocker, and Cobine. Dryvesteyn [111] realized that the formation of an insulating film, such as an oxide, allows charge to accumulate on the surface, thereby enhancing the electric field strength. Suits and Hocker [112] and Cobine [113] investigated the glow-to-arc transition. They found a large element of randomness on the one hand but a clear influence by the presence or absence of an oxide layer. Looking at relatively small arc currents in the range 1–10 A on a copper cathode, reduction of the oxide layer with hydrogen plasma forced the random arc to return to a high-current glow mode [112]. The observation that either the arc or glow mode is preferred, depending on the surface conditions, was also confirmed for other cathode materials, such as Cd, Fe, Al, and Zn [113].

The distinction between cathode-spot types 1 and 2 was introduced in the 1970s when the role of surface contamination and surface condition on spot formation and operation was systematically investigated [114]. The availability of electron microscopes for the investigation of arc traces was certainly an important factor. The association with numbers "1" and "2" can easily be remembered by recalling that the erosive action of the cathode spot effectively cleans the cathode surface. Spot operation starts with type "1" on a contaminated surface, which is initially always present (unless the system was treated in ultrahigh vacuum), and it switches to type 2 when surface contaminations are removed by action of spot operation.

There are numerous phenomenological differences between type 1 and 2 spots, as becomes obvious by in situ optical and electrical observations as well as by postmortem examination of the cathode in an electron microscope [65, 80, 115]. Spot type 1 appears dim compared to type 2; the velocity of the plasma front and the apparent spot motion are much greater for type 1. The arc voltage and cathode material erosion is smaller for type 1. The average current per spot is much smaller for type 1 spots; at small current, spot type 2 may not operate at all. This also explains why the discharge went to the glow mode rather than transitioned into type 2 in the 1930s' experiments mentioned before [112, 113]. When the cathode is examined in an electron microscope one clearly recognizes that craters left by type 1 spots are much smaller than craters of spot type 2 [65, 116]. Spot type 1 craters are isolated and spread apart by many crater diameters, whereas spot type 2 craters are larger and next to each other, forming characteristic chains of craters [117]. In the presence of an external magnetic field, arc craters are aligned in a band of well-separated craters for type 1, and in a more or less linear chain of craters for type 2, as illustrated in Figure 3.14. Table 3.5 summarizes some phenomenological differences between type 1 and 2 spots.

Table 3.5. Phenomenological, qualitative differences between type 1 and 2 spots. All statements should be seen as relative for a given cathode material; due to large variations between cathode materials, absolute values are not given here

	Type 1	Type 2
Surface conditions	Contaminated (i.e., oxide)	Clean (metal)
Apparent brightness	Dim	Bright
Typical crater diameter	Small	Large
Crater appearance	Separate from each other	Adjacent to each other
Apparent spot velocity	High	Low
Cathode erosion rate	Low	High
Relative ease of arc triggering and burning	Easy	Difficult
Chopping current	Low	High
Plasma composition	Metal and gas (hydrogen, oxygen, etc.)	Metal only
Average ion charge state	Low	High
Relative amplitude of fluctuations	Low	High

Cathodic arc investigations before the 1960s were usually done with type 1 spots because typical vacuum conditions did not allow for clean, metallic surfaces. However, since the arc spots remove material hence performing *in situ* cleaning, it is possible, or even likely, that transitions to type 2 spots occurred when the arc duration was long and the vacuum conditions were reasonable. Results of early work must therefore be judged with some caution since the type of operation may not be clear. In the newer literature, researchers have become aware of the importance of surface conditions, and often the type is clearly defined [115, 118]. In fact, most cathode-spot research after 1980 focused on spot type 2 observed on clean surfaces, because only here reproducible results could be obtained. In the other case, the nature of the surface contamination or coverage needed to be characterized, which made the task much more difficult. Worse, even if one was successful in characterizing the cathode surface conditions prior to the occurrence of a cathodic arc, the erosive cleaning action will change the surface rapidly in a manner that will depend on numerous factors, some of them difficult to control. Among these factors are the residual gas pressure and gas species, pumping speed, nature of cathode material, and cathode temperature. Great progress has been made in measurement and modeling of cathode spots of type 2 because the existence conditions are well defined.

For spots of type 1, relatively little has been done because the task is daunting due to the large variety of surface conditions possible. For the purpose of cathodic arc coatings, reactive gases (often nitrogen or oxygen) are commonly introduced in the deposition chamber, and the measurements and models for spot type 2 are only of limited value. In practical coating systems, containing

reactive gas, arc spots most likely work primarily via type 1 or a mixture of type 1 and 2 spots. Much research remains to be done to clarify spot processes under the conditions of reactive deposition. Szente and co-workers [119–121] have done pioneering research in this direction. Among other results, they found that the cathodic arc on cleaned copper electrodes operates with spot type 2 when high-purity argon is present; however, the copper erosion rate was drastically reduced by the addition of only 1% of nitrogen and was further reduced as the nitrogen content increased in the gas mixture. The decrease was found to be correlated to an increase in arc velocity [119], clearly indicating a change to type 1 spots.

3.5.7 Cathode Spots on Semiconductors and Semi-metals: Type 3

Cathodic arcs require that the cathode has sufficient conductivity to carry the arc current, which is often 50 A and higher. If the conductivity is too low, high voltage drops and associated high ohmic losses would occur in the cathode. Therefore, as a rule, cathodic arcs are limited to metals. A number of sufficiently conducting semiconductors and semi-metals have successfully been used, including highly doped Si and Ge, graphite, hot boron, and boron carbide. The appearance and mechanisms of cathode spots on these materials are modified compared to operation on true metals.

One important phenomenological difference is in the apparent spot velocity, which is much smaller than on metals; in fact, the arc spot has a tendency to stick to the same location for considerable time. Using a far-distance microscope, Laux and co-workers [122] observed this spot behavior in situ on B_4C, and the observation is supported by cathode erosion profiles. Experiments with a graphite cathode often show deep holes that relatively stationary spots have "dug" into the cathode.

It seems to be clear that the temperature dependence of the electrical conductivity plays an important role since, in contrast to ordinary metals,

$$\frac{d\rho}{dT} < 0, \tag{3.73}$$

i.e., the higher the local temperature the lower the local resistivity. While this may contribute to stabilizing the spot, thermal conductivity will also occur here, increasing the spot area and decreasing the power density until it is insufficient for cathodic arc operation. Because the appearance of spots on semiconductors and semi-metals is quite different compared to type 1 and 2 spots on metals, one may assign the term "type 3" to arc spots on non-metals.

Using his model of cathode layers, Beilis [123] formulated a system of time-dependent equations and applied it specifically to graphite. Spot parameters varied strongly when the spot lifetime was assumed to be shorter than 10 μs. In the case of graphite, Joule heating in the cathode body is significant and may

exceed cathode heating by the ion heat flux, which is contrary to conclusions for metals found by Jüttner [107].

The physical properties of graphite can vary widely depending on the manufacturing procedures. Kandah and Meunier [124] found that the cathode-spot velocity is higher on graphite of large grain size, low electrical resistivity and high density, small pore size and less porosity.

Arc spots on hot boron (heated up to 1,000°C) have been investigated by Richter and co-workers [125] using fast framing photography, mass spectroscopy, and ion energy analysis. They detected an extended molten area on the cathode surface in which cathode spots move. The ions emitted were B^+ and B^{2+} with kinetic energies up to 90 eV, indicating that the fundamental character of the emission sites is cathodic, as opposed to thermionic, although the spot motion is distinctly different (slower) than on metals.

3.5.8 Arc Chopping and Spot Splitting

Many experiments have shown that there exists a minimum arc current needed for stable, self-sustained arc operation. Discharge currents lower than what is called the "chopping current" will lead to spontaneous extinction of the arc. A minimum current is required to ensure sufficient plasma production, which ensures a very high likelihood of ignition of a new cathode emission center when the power density at the active center has dropped. Such "minimum arc maintenance value" was already known in the early twentieth century for the continuous operation of mercury arc lamps [126]. This minimum current depends on the cathode material as well as on the surface state of the cathode. For example, the chopping current for pure titanium is about 50 A [127]. Electrode materials developed for vacuum arc switches, such as CuCr, CuW, and AgWC, show very small chopping currents of order 1 A [128], which is important in order to minimize the induced voltage. High induced voltage could cause re-ignition of an arc and failure of the switching event.

Going in the other direction of higher currents, it was found that the amount of plasma produced is directly proportional to the arc discharge current. Interestingly, other parameters such as burning voltage, average ion velocity, and mean ion charge state show only small changes with increasing arc current.[6] This may be surprising at first sight but it becomes plausible if one considers that higher currents lead to "spot splitting." Spot splitting means that a larger *number* of simultaneously active emission sites exist, proportional to the arc current, where each of the spots maintains approximately the same operational mechanism and carries about the same average current [92]. The literature, in most cases,

[6] This is not true for very high currents, e.g., arcs with currents in the kiloampere region, when anode activity occurs and when the magnetic self-field cannot be neglected.

refers here to current per "spot" and it is likely that each spot is an assembly of fragments or emission sites, as discussed before.

3.5.9 Random Walk

The spot plasma or the spot "itself" does not move on the surface but it is the location of ignition that moves. Therefore, although the term *spot motion* is intuitive and reflects a phenomenon that can be visually observed, it is rather abstract because this motion should always be understood as a sequence of ignition and extinction of active emission sites.

Random walk [129] is generally introduced by assuming that a "particle" (the spot in our case) starts at the origin (the location of first ignition) and takes a step of length s in a random direction specified by the vector $\mathbf{n}$, with $|\mathbf{n}| = 1$. The position after N steps is $\mathbf{R}_N$. In the next step,

$$\mathbf{R}_{N+1} = \mathbf{R}_N + s\mathbf{n}, \tag{3.74}$$

with $\mathbf{R}_0 = 0$. Taking the average over many trajectories,

$$\langle \mathbf{R}_{N+1} \rangle = \langle \mathbf{R}_N \rangle + s\langle \mathbf{n} \rangle = \langle \mathbf{R}_N \rangle \tag{3.75}$$

because $\langle \mathbf{n} \rangle = 0$. This leads to

$$\langle \mathbf{R}_N \rangle = \langle \mathbf{R}_0 \rangle = 0. \tag{3.76}$$

This result was expected because there is no preferred direction, therefore the average over many test walks of our "particle" must be the starting point.

Looking at a trajectory of a walk after $N+1$ steps, the spot has reached a distance squared from the origin

$$|\mathbf{R}_{N+1}|^2 = |\mathbf{R}_N|^2 + s^2 + 2s\mathbf{n}\,\mathbf{R}_N \tag{3.77}$$

and averaged over many trajectories,

$$\left\langle |\mathbf{R}_{N+1}|^2 \right\rangle = \left\langle |\mathbf{R}_N|^2 \right\rangle + s^2 + 2s\langle \mathbf{n}\,\mathbf{R}_N \rangle. \tag{3.78}$$

The directional unit vector $\mathbf{n}$ is not correlated with $\mathbf{R}_N$ and therefore $\langle \mathbf{n}\mathbf{R}_N \rangle = \langle \mathbf{n} \rangle \langle \mathbf{R}_N \rangle$, which together with $\langle \mathbf{n} \rangle = 0$ turns (3.78) into

$$\left\langle |\mathbf{R}_{N+1}|^2 \right\rangle = \left\langle |\mathbf{R}_N|^2 \right\rangle + s^2 \tag{3.79}$$

and with $\mathbf{R}_0 = 0$ one obtains

$$\left\langle |\mathbf{R}_N|^2 \right\rangle = Ns^2. \tag{3.80}$$

Thorough investigations by Schmidt [130], Daalder [78], and Hantzsche and co-workers [77] established that in the absence of an external magnetic field, spot motion may be modeled as random walk. One may assume that each displacement occurs in a small elementary step, s, which takes an average elementary time τ. When considering a *two*-dimensional random walk (i.e., on a surface), the

probability $P(R)$ for a total spot displacement to be in the interval $(R,\ R+\mathrm{d}R)$, with $R = |\mathbf{R}|$, measured from the starting point, is given by [131]

$$P(R)dR = \frac{R}{2Dt}\exp\left(-\frac{R^2}{4Dt}\right)dR \text{ for } t \gg \tau. \tag{3.81}$$

The function $P(R)$ is also known as Raleigh distribution. The diffusion constant, D, contains the parameters of the elementary step:

$$D = \frac{1}{4}\frac{s^2}{\tau}. \tag{3.82}$$

The diffusion constant is material dependent, for example Jüttner found experimentally $D = (2.3 \pm 0.6) \times 10^{-3}\,\mathrm{m^2/s}$ for copper [107] and $D \approx 10^{-3}\,\mathrm{m^2/s}$ for molybdenum [132], and Beilis and co-workers [92] determined $(1 \pm 0.3) \times 10^{-3}\,\mathrm{m^2/s}$ for copper and $(4 \pm 1) \times 10^{-4}\,\mathrm{m^2/s}$ for CuCr contact material.

The mean value for displacement is

$$\langle R\rangle = \int_0^\infty R\ P(R)\ dR = (\pi Dt)^{1/2} = \frac{s}{2}\sqrt{\pi\frac{t}{\tau}}, \tag{3.83}$$

and the observable, apparent spot velocity is

$$v_{spot} = \frac{d\langle R\rangle}{dt} = \frac{1}{2}\sqrt{\frac{\pi D}{t}} = \frac{s}{4}\sqrt{\frac{\pi}{t\tau}}. \tag{3.84}$$

From (3.84) one can see that the spot velocity decreases as the observation time increases, which is a consequence of the random nature of this motion.

At this point it should again be emphasized that this motion is apparent and a *velocity* is only defined in the sense of "smearing out" elementary steps and considering changes of R for long observation times: $t >> \tau$. Strictly speaking, elementary steps are associated with ignition events, and therefore this "motion" does not have a derivative, hence a velocity in the usual sense is not defined.

The assumption of an elementary step s deserves further critical review. Based on analysis of arc traces on clean metal surfaces (spot type 2), Hantzsche and co-workers [77] suggested using the mean crater radius as the elementary step length. The assumption is justified by the appearance of crater chains, though its general validity was disputed by Daalder [133]. He also questioned whether or not there are two distinct cathode mechanisms, one producing craters adjacent to each other, associated with spot type 2, and another producing clearly separated caters, typical for type 1. Using the fractal approach to spot phenomena, this dispute loses its relevance because the issue is reduced to a probabilistic distribution of ignition of emission centers. In this picture, the step length is not a constant, as assumed in a simple random walk model. In particular, the distances between ignition locations (corresponding to grid nodes in a random walk model) can be large or very small.

The displacement dynamics of random walk can be modeled using a probabilistic approach with application of simple ad hoc displacement rules for ignition of new emission centers on a two-dimensional grid. Such a model was developed by Coulombe [134] for high-pressure arcs, though some of the findings are applicable to vacuum arcs as well. The model predicts a power law signature of the frequency power spectrum, (3.71), where the exponent α depends on the large-jump probability. For the condition simulated [134], the exponent varied from $\alpha = 0$ for smooth diffusion conditions (no jumps to distant grid nodes) to $\alpha = 1.6$ for a 0.9 likelihood of ignition far from the active emission site. The appearance of a power law is again a signature of fractal behavior.

Analyzing the 50-A arc traces on an aluminum film, which are qualitatively similar to arc traces on oxidized surfaces (like Figure 3.25) or Lichtenberg figures, Anders and Jüttner [80] found a fractal dimension of 2 within 5%, which is the expected dimension for two-dimensional Brownian motion.

The well-known Brownian motion is the scaling limit of random walk. This means that if random walk occurs with very small steps, $s \to 0$, random walk becomes an approximation to Brownian motion. Often, to make modeling and computation more efficient, Brownian motion is approximated by a random walk. Random walk is a discrete fractal exhibiting stochastic self-similarity on large scales, but self-similarity is cut off as scales approach the elementary step width s. Brownian motion in two dimensions is a true fractal showing self-similarity on all scales. Brownian motion has the fractal (Hausdorff) dimension 2.

By superimposing a narrow Gaussian distribution of light intensity on a plasma emission center making a random walk, it was possible to simulate the light emission patterns observed from cathode spots [88]. A physical interpretation for a Gaussian distribution is based on the finite (non-zero!) lifetime of excited levels of atoms and ions. The location and size of the rapidly expanding plasma of an emission site is observed by photons, many of them originating from bound–bound transition of ions and atoms (e.g., for copper [135]). The longer the lifetime of excited levels, which is especially important for long-living metastable levels, the further the distance between excitation near the spot center and de-excitation in the expanding plasma, and therefore the broader the Gaussian distribution.

3.5.10 Self-Interacting Random Walks

In a random walk, the next position depends only on the current position of the "walker" (the emission site). The random walk has no memory of all other previous positions, i.e., walk history. Such process is called a first-order Markov process [76]. Provided that cathodic arc processes occur on clean metal surfaces, such as well-arced cathodes, all sites next to the active site have approximately the same probability to serve as the next emission site, and the walk may be modeled as a Markov process.

More realistic, however, is that the arc changed the surface conditions and local temperature in such a way that the distribution of the ignition

probability is changed. Experiments (like the breakdown experiments by Kraft and Stuchenkov [136]) show that arcing on contaminated surfaces is relatively easy, while arcing on metallic, clean surfaces is relatively difficult. Therefore, the cleaning action of arc erosion will markedly reduce the ignition probability

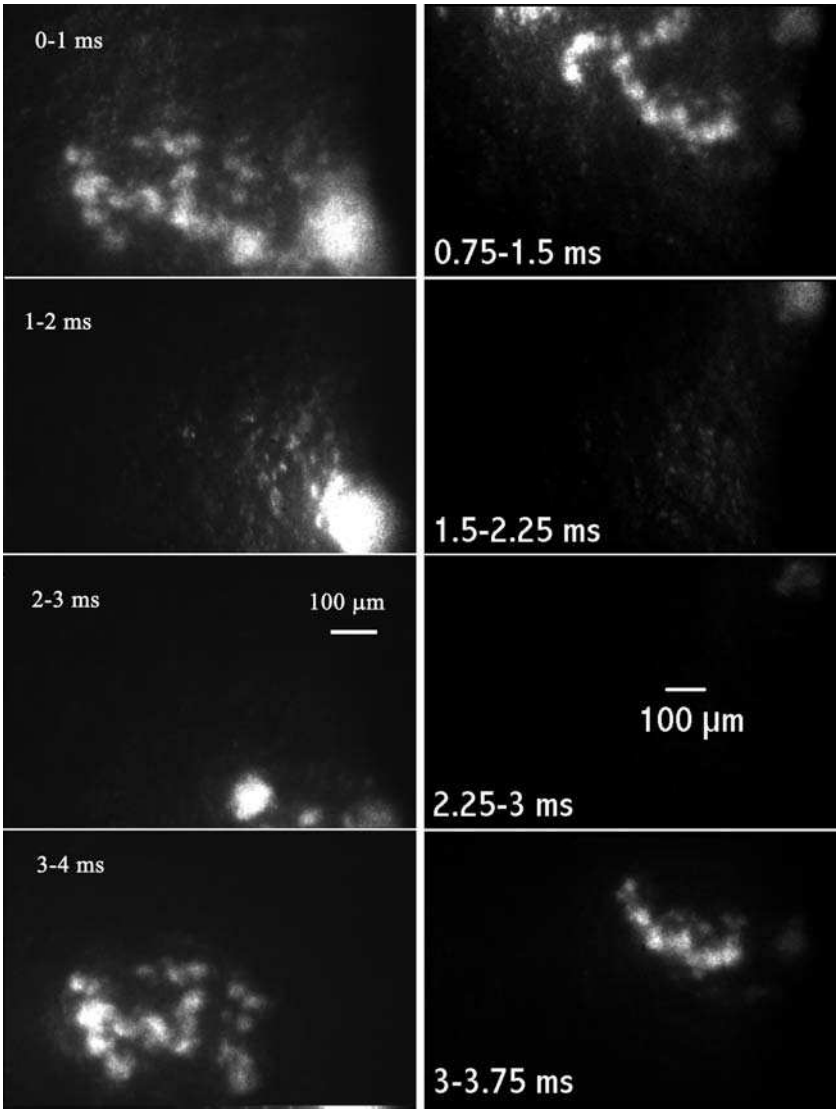

Fig. 3.29. Two examples of observation of the memory effect using high-speed photography on a low-current copper arc. One should compare first and last frames of the *left* and *right* sequence, which shows that the spot returns to emission sites previously used. (Courtesy of B. Jüttner, [140])

of locations where the arc has already burned. Starting with an oxidized or otherwise "contaminated" cathode, the random walk will turn into in a special class of self-interacting walk, the self-avoiding random walk [137, 138]. As a result of arc cleaning, the next emission is much more likely to be ignited at locations that still have the surface-field-enhancing oxide layer rather than on the arc-cleaned surface. As long as there is surface area with oxide layer (or similar contamination) available, emission sites will avoid the cleaned surfaces. This feature has been utilized in arc cleaning of steel surfaces where oxide surfaces were intentionally created to optimize cleaning effects [139].

If arcing occurs in a reactive gas environment or poor vacuum, the surface will quickly "age" by becoming "poisoned," i.e., the metal atoms on the cathode surface will react with oxygen or water from the residual gas. In this way, the surface will "forget" its memory on the local emission event, and the walk can again become Markovian rather than self-avoiding.

If arcing of the surface occurs in ultrahigh vacuum (UHV), or in noble gas free of reactive components, prolonged arcing may eventually completely remove the oxide layer. As a consequence, all surface locations become equivalent, and also in this case the self-avoiding walk will switch back to a random (Markovian) walk.

Therefore, in both extreme cases, arcing with reactive gas and arcing in UHV, there is a tendency to go from random walk through a phase of self-avoiding walk, which eventually may be followed by another phase of random walk.

The picture, however, is even more complicated. Not all self-interacting random walks are self-avoiding walks [138]. For example, investigating clean, well-arced cathodes, it has been observed that after a short cooldown time, a previously active and still-hot emission site may preferably re-ignite [140]. In this case, the walk is not self-avoiding but rather shows a preference to return to a familiar location (Figure 3.29). Jüttner's experiments showed that ignition of arcs on hot cathodes require higher ignition voltages than on cold cathodes, which fits with the picture that emission centers appear on new locations rather than on the already hot sites. Therefore, other factors must play a role for the memory effect. The rough structures on a rim of cathode craters seem to play a role: in a photo series with very high resolution, Jüttner and Kleberg succeeded in observing the "dance" of ignition around the sharp asperities of a large crater (Figures 3.30 and 3.31).

3.5.11 Steered Walk: Retrograde Spot Motion

In the presence of a transverse magnetic field, the "motion" of ignition locations deviates from random. Rather, this apparent or virtual motion becomes increasingly directed with increasing field, i.e., the ignition of emission centers is more likely in a preferred direction. Spot motion is magnetically "steered." The term "steered arc" is often used by the arc coating community. The preferred direction of the virtual motion is opposite to the Amperian direction $\mathbf{j} \times \mathbf{B}$ which one would expect if the Lorentz force was responsible for motion. The plasma column is indeed bent in the $\mathbf{j} \times \mathbf{B}$ direction, as indicated in Figure 3.32, though

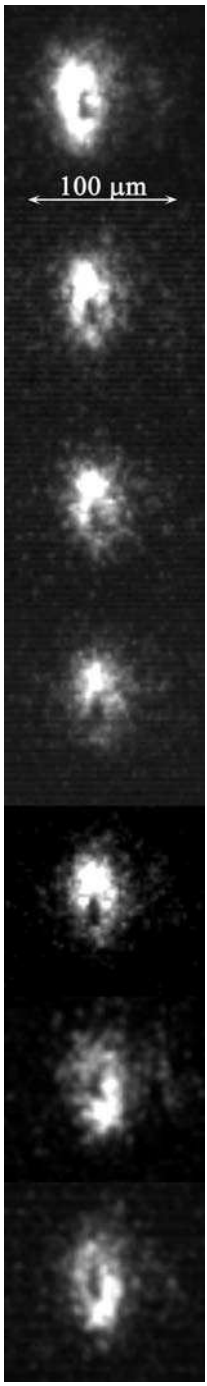

Fig. 3.30. High-resolution imaging of spot fragments igniting preferably on the asperities of a large cater. Copper cathode, arc current 30 A, frame exposure time 10 ns, first frame taken 300.00 µs after arc triggering. (Courtesy of B. Jüttner, [140])

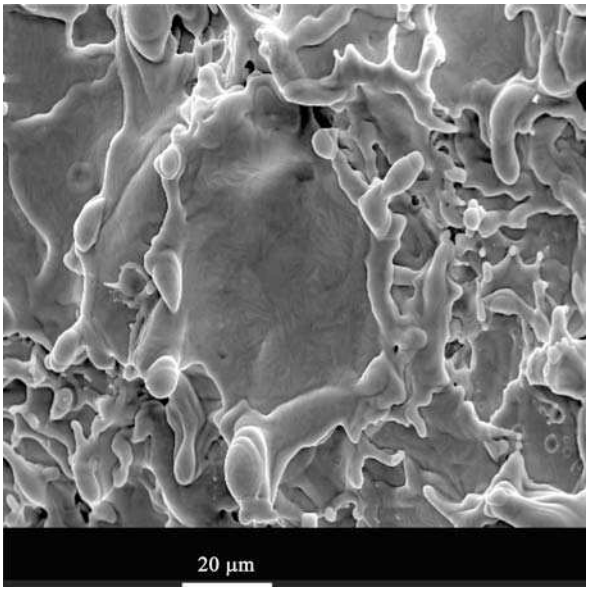

Fig. 3.31. Large crater on a copper cathode, corresponding to fast framing pictures shown in Figure 3.30. (Courtesy of B. Jüttner, [140])

the virtual motion is to the opposite (anti-Amperian or "retrograde") direction. Since its discovery [141, 142], retrograde motion has stimulated much research [102, 121, 143–178], resulting in a number of more or less convincing explanations. One of the most comprehensive descriptions is by Jüttner and Kleberg [108, 110] who base their model on observations using image-intensified cameras of very high spatial and temporal resolution. Much of this section is based on findings by Kleberg [108].

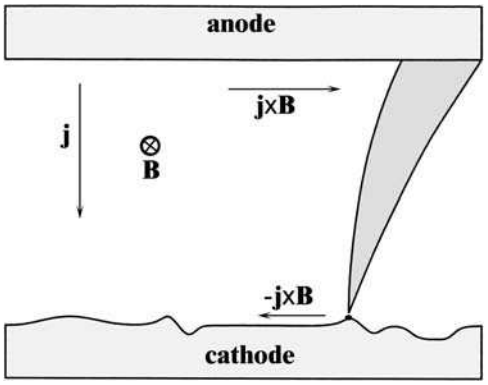

Fig. 3.32. Bending of the plasma column in the $\mathbf{j} \times \mathbf{B}$ direction, with spot motion (i.e., ignition of new emission centers) in anti-Amperian ($-\mathbf{j} \times \mathbf{B}$) direction

As the magnetic field increases, the virtual motion loses its random character and becomes increasingly directed, which allows us to assign a macroscopic velocity rather than diffusion constant [171]. The directed retrograde velocity depends on a few conditions, including magnetic field strength and cathode material. It is typically 10–15 m/s for a steering field strength of about 15 mT [179]. The directed velocity is approximately proportional to the transverse field B_t, i.e., the field component parallel to the cathode surface,

$$\nu_{steered} = c\, B_t, \tag{3.85}$$

where c is a material constant that also depends on the surface conditions. For clean surfaces under vacuum conditions, Zabello and co-workers [178] determined c to be 60 and 200 m/(s T) for copper and CuCr cathodes, respectively. The parameter c is smaller when the cathode is hot ($> 600^{\circ}$C in the case of copper) [169].

The direction reverses into the Amperian when the pressure exceeds a critical value, which is relatively high, namely in the range 1–100 kPa (i.e., from a few percent of to about atmospheric pressure) [157, 164].

Let us further consider the phenomenology of the vacuum and low-pressure case. As the magnetic field vector intersects the cathode not normal but tilted, the direction of the virtual motion is also tilted to the retrograde direction (Figure 3.33).

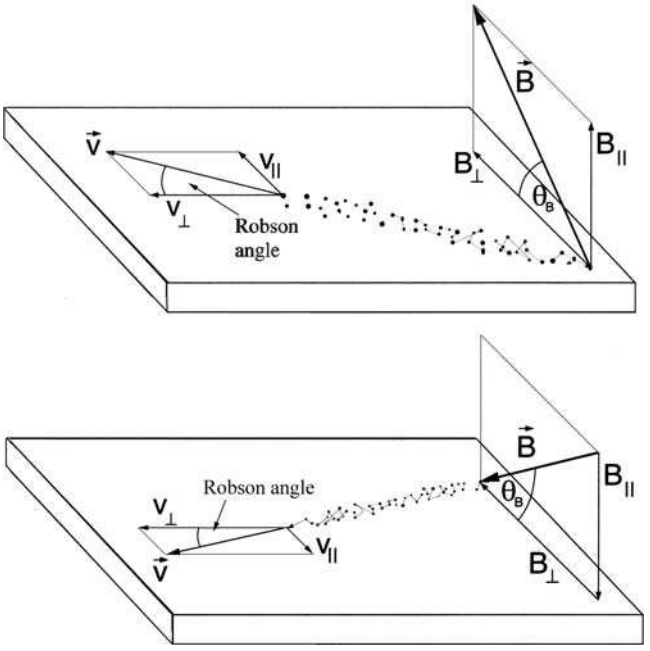

Fig. 3.33. The direction of the apparent motion is tilted to the direction of retrograde motion as the magnetic field vector intersects the cathode at an angle other than normal

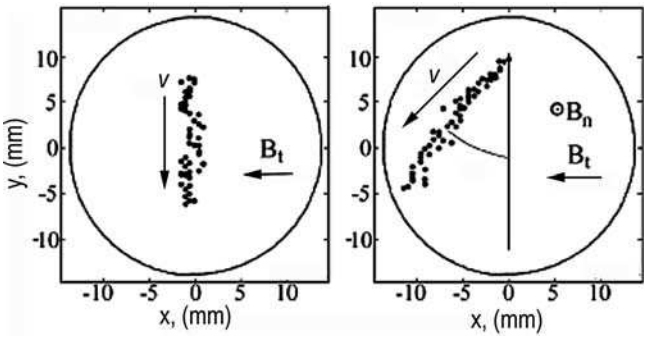

Fig. 3.34. Experimental observation of steered spot motion on copper in (*left*) a pure transverse field and (*right*) a tilted field, i.e., where both normal and transverse magnetic field components exist. The transverse field was 65 mT in both cases, and the normal component was 60 mT for the tilted case (*right*). (Adapted from Figure 6 of [178])

The angle between retrograde direction and actual direction is often called the Robson angle, after A.E. Robson who worked on the issue with A. von Engel in the 1950s [153]. Measurements by Zabello and co-workers confirmed that the Robson angle depends directly on the field inclination [177, 178] (Figure 3.34). As the temperature of the cathode increases, larger craters are observed and the retrograde velocity decreases [168, 169]. In an early work of 1948, Smith [147] observed a reversal of motion direction but that has not been confirmed; most likely his observation was a pressure rather than a temperature effect.

The interpretation and modeling of steered and retrograde motion has been found to be difficult. It is associated with the ignition probability distribution. In the absence of an external field, the magnetic self-field is azimuthal and thus axially symmetric, provided the discharge geometry, like position of the anode, does not break the symmetry. If the magnetic field has a component parallel to the cathode surface (often called the transverse or tangential field), the axial symmetry is broken. Putting the physical reason for preferred spot ignition aside, for the time being, one could use probabilistic models for spot motion, in extension to previously mentioned random walk models. Care [180] constructed a Markov process on a two-dimensional grid where the probabilities for the directions are not equal but depend on the steering magnetic field. If the grid size and time intervals are allowed to go to zero, and appropriate limits are taken, a partial differential equation for the probability density of the arc position is obtained, which is equivalent to a Fokker–Planck equation for the system.

One of the difficulties is associated with the fact that one would expect the ignition probability higher on the side to which the plasma column is bent (Figure 3.32) and where therefore ion bombardment should be higher [169]; however, ignition is more likely in the opposite direction.

Modeling of retrograde motion can be done making more or less specific assumptions. For example, Beilis [176] applied his cathode layer model and

assumed that (i) heat loss in the cathode bulk is small compared to the heat influx, (ii) the plasma flow in the Knudsen layer is impeded, and (iii) the plasma kinetic pressure is comparable to the self-magnetic pressure in the acceleration region of the cathode plasma jet. With these assumptions, a number of features can be reproduced, like the linear increase of apparent spot velocity with increasing magnetic field strength and arc current.

The electric current causes a magnetic self-field, which greatly affects the motion of emitted electrons. Arapov and Volkov [181] developed a model for ignition of emission centers in which electrons form a current vortex whose axis is perpendicular to the surface. The current vortex is shown to be unstable, leading to the formation of a spatial structure. Similar effects are known from the theory of self-organization when energy is pumped into a system. Locations of enhanced power density would promote the ignition of the next emission center.

Taking an experimental approach, Kleberg and Jüttner [108, 110] used spot imaging with the highest temporal and spatial resolution available. They discovered that emission sites in transverse magnetic fields emit microscopic plasma jets whose angular distribution is determined by the transverse field direction. The jets form in a stage of maximum plasma production. It is known that current-carrying plasma in a magnetic field is subject to plasma instabilities [182]. Although the exact nature of the instability is still subject to research, it has been found that the ejection of plasma jets occurs every few microseconds in directions that deviate from the retrograde direction up to 45°. Figure 3.35 shows the ejection of two jets into approximate retrograde direction, which is toward the right in this photo. Using the sophisticated exposure features

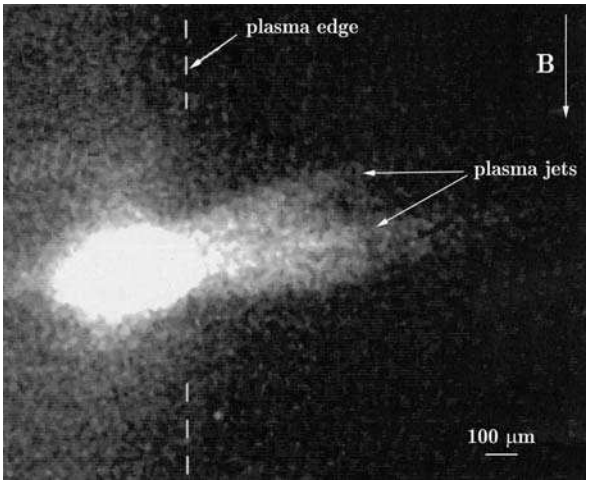

Fig. 3.35. Ejection of two jets into approximate retrograde direction. The intensity of light emission of the plasma jets is weaker than the emission from the spot itself, and therefore the exposure was selected such as to make the jets visible, while the cathode spot is overexposed. (Adapted from [108], Abb.4.17)

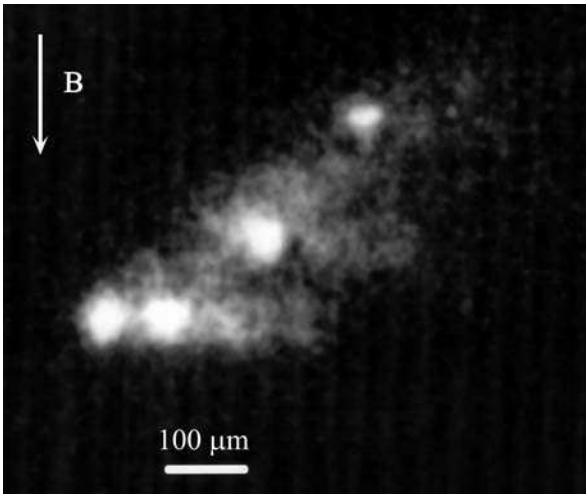

Fig. 3.36. Superposition of four exposures of 200 ns, each, separated by 10 μs. (Adapted from [108], Abb.4.20)

of the image-converter camera, it was possible to superimpose four exposures separated by 10 μs. The result is shown in Figure 3.36, which illustrates the relationship of microjets and ignition of new emission sites. The first spot is at the left, and retrograde motion is to the right. This picture leads to the *Jüttner–Kleberg model* of retrograde motion (Figure 3.37): retrograde motion is actually composed of a microscopic "zigzag" ignition of new emission sites caused by microjets. The microjets enhance the local electric field strength by $\mathbf{E} = \mathbf{v}_{\mathbf{jet}} \times \mathbf{B}$. The local electric field strength was previously identified as a critical parameter for ignition. The additional field component can be estimated by the measured jet velocity ($\sim 5 \times 10^3$ m/s) and applied field (~ 0.2 T). Although it is found to be only of the order 1 kV/m, this field may be crucial for ion motion and

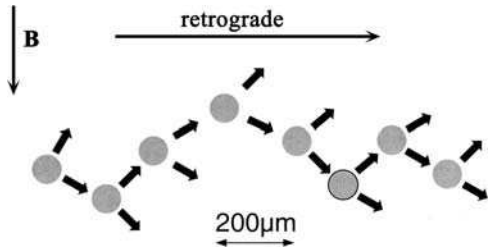

Fig. 3.37. Jüttner–Kleberg model of retrograde motion: retrograde motion is actually composed of a microscopic "zigzag" ignition of new emission sites caused by microjets. For low-current arcs in copper, the typical step length is 200 μm. (Adapted from [108], Abb.4.21)

local ion bombardment of the cathode, helping to provide the conditions of site ignition, (3.63).

At a first glance, one is tempted to identify the bright spots in Figures 3.35 and 3.36 with the emission sites. One needs to recall that these photos were obtained by intentionally overexposing the spot area to make the less luminous jets visible. One should be suspicious because the size of the highly luminous area is much larger than the typical size of craters. If one increases the spatial and temporal resolution, one finds highly dynamic fluctuations associated with fragments, schematically illustrated in Figure 3.38. Imaging using the emitted light is reaching the technical and physical limits. To stress the point again: the non-zero lifetimes of excited states necessarily cause a "smearing out" of the imaged plasma, and therefore the emission sites may be smaller and shorter lived than suggested by the emitted light.

The Jüttner–Kleberg model of retrograde motion reduces the Robson drift to a shift of microjet direction. It was argued that the direction of the microjet ejection is determined by the presence of the magnetic field, and it is therefore not surprising that tilting the magnetic field leads to a shift in microjet directions. It is, however, not clear why the zigzag emission appears to have a "memory" of previous emissions: an analysis of the motion perpendicular to the averaged directed velocity shows that this component is not random. Rather, the motion is zigzag in a more regular way, allowing the spot to deviate only slightly from

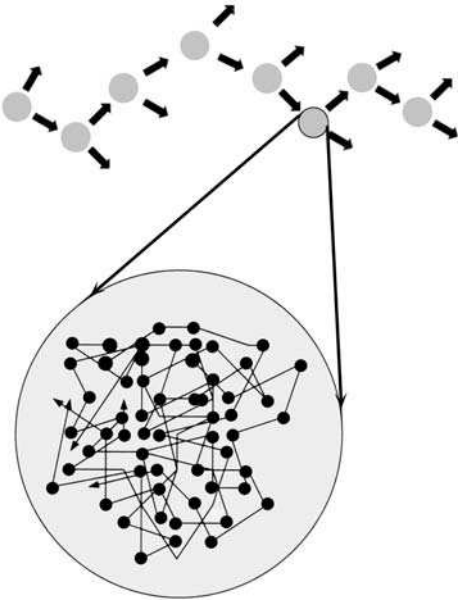

Fig. 3.38. Schematic of fragment dynamics within the Jüttner–Kleberg model, as observed when increasing the spatial and temporal resolution. (Adapted from [108], Abb.6.2)

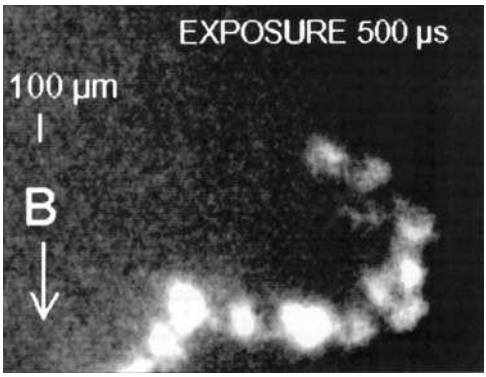

Fig. 3.39. Reversal from retrograde to Amperian direction before current-zero or the end of a discharge. (Adapted from [108], Abb.4.28)

the averaged steered direction. This has been found by Laux and co-workers [183] on tungsten layers on carbon base material placed in very strong magnetic fields (a configuration relevant to walls of large thermonuclear fusion devices such as Tokamaks and Stellarators). It can also be seen on massive cathodes as shown in Figures 3.14a,b.

It should be mentioned that Kleberg found an interesting reversal from retrograde to Amperian direction before current-zero or the end of a discharge [108]. Figure 3.39 shows a characteristic U-shape of spot traces, indicating such reversal of direction.

A more practical approach to steered motion will be given in Chapter 5 when discussing the design of arc sources. There we will not consider the physical reasons based on cathode processes but reduce the apparent motion to two rules: the retrograde motion rule and the acute angle rule.

3.5.12 But Why Is the Cathode Spot Moving in the First Place?

After this exhaustive discussion on modeling, including fractal description, the reader may still ask himself/herself: "But why is the cathode spot moving in the first place?" First, to stress the point, the cathode spot is not moving. It only appears to move. What we see is a sequence of ignition and extinction of electron and plasma emission centers. So, a better question is: Why is there repetitive, stochastic ignition and extinction, rather than a steady operation ("burning") of the cathode spot?

Once an emission center is ignited by a thermal runaway process, as explained before, the conditions for electron emission, plasma generation, and current transfer between cathode bulk and the plasma very quickly deteriorate for three reasons.

First, due to the increase in resistance with temperature for all metals, $d\rho/dT > 0$, the region of the cathode bulk directly under the cathode spot is more resistive than all other areas or parts of the cathode. Hence, if there was an

alternative, less resistive way for the current to flow, the current would switch to the new path.

Second, and this is perhaps the strongest argument, the emission center builds a highly resistive barrier as the result of the emission. That might sound puzzling at first. In the explosive stage, the cathode matter transitions from the solid to the plasma phase, and it may initially bypass the gas phase by circumnavigating the critical point in the phase diagram (see Section 3.9). At this stage, the most resistive zone for the current path is the non-ideal plasma phase. As time passes (and here we consider some tens of nanoseconds), the area of the emission site increases by heat conduction, and the area power density falls accordingly, which leads to a change of the path in the phase diagram: the material has now the time to transition through all conventional phases: solid–liquid–gas–plasma. From those four, the gas phase is by far the most resistive phase: solid and liquid metal and metal plasma are good conductors, but metal gas (vapor) is not. *The metal vapor "chokes" the flow of electricity*. As the growth of the emission area continues, the power density and related local surface temperature is reduced, electron emission decreases rapidly, though there may still be significant evaporation from the hot crater left by the explosion. At this point, the composition of the gas or plasma in front of the site becomes increasingly influenced by neutral vapor, and the current transfer capability suffers greatly.

In this situation, the third factor kicks in: competition! The dense plasma near the emission site has caused the sheath to be very thin, which implies high electric field strength on the surface, and the most preferred site may experience a runaway, starting a microexplosion at a new site. Now, the new site and the older, much larger site are electrically in parallel, and of course the path of lower resistance (lower metal gas density!) takes over the current.

In this sense, the growing but decaying emission site generates the condition for its own "death." The situation for carbon, boron, and other semi-metals or semiconductors is somewhat modified in that $\mathrm{d}\rho/\mathrm{d}T<0$ and therefore at least this reason for the apparent spot motion is removed: quite contrary, the condition $\mathrm{d}\rho/\mathrm{d}T<0$ is stabilizing the spot at one location. Yet, even with those materials, one can see some (yet slower) apparent spot motion. The low-conducting vapor mechanism takes its toll.

3.6 Arc Modes

In the previous sections, cathodic arc spot types 1, 2, and 3 were introduced. In this section, phenomenological spot types are put in relation to arc modes. There are several solutions of the energy balance problem and current transport task between cathode and anode. Depending on the gas type and gas pressure, the role of ion current, ion bombardment heating, thermal properties of the cathode material, cathode surface condition, cathode geometry, and cooling provisions, the solutions may be stationary or quasi-stationary for cathodes with relatively large hot areas, leading to *thermionic arcs*, or non-stationary for globally cold cathodes, leading to

cathodic arcs. Additionally, other components of the discharge circuit may play a decisive role, like the metal vapor coming from a hot, evaporating anode, leading to *anodic arcs* (see below). For a practical means to decide whether a cathodic arc or thermionic arc is occurring, one should look at the arc burning voltage in a time-resolved manner, e.g., by using a fast voltage divider probe and an oscilloscope. If the discharge is burning in the cathodic arc mode one will find the characteristic noise. In comparison, the noise of thermionic arcs is very small.

If one bases arc classification exclusively on the cathode mode of operation, one may distinguish *thermionic arcs* and *cathodic arcs*, with each of them occurring with different sub-modes and spot types (Figure 3.40). Most of this book focuses on the cathodic arc mode with spots of types 1 and 2. Thermionic arcs are only mentioned to clearly define and limit the scope. Thermionic arcs [47] are widely used in arc discharge lamps [184, 185], plasma torches (e.g., for plasma spraying [186]), and plasma ion plating systems [187, 188]. Thermionic modes are governed by the thermionic emission of electrons. There are two main sub-modes: the thermionic spot mode and the thermionic spotless mode.

In the thermionic spot mode, electron emission occurs via the (field-enhanced) thermionic emission mechanism, (3.14), from a relatively large hot spot, which has a diameter of order 1 mm or greater. In the thermionic spot mode, ion bombardment heating and the ion current contribution to the discharge current are crucial. The net ion flow near the cathode is toward the cathode. The thermionic spot mode occurs, for example, in high-pressure gas discharge lamps. The thermionic spot mode can be stationary, as it is desired in commercial discharge lamps [184, 185], otherwise a lamp would be considered defective. Stationary arc spot models can be used to describe this mode [47, 189].

The thermionic spotless mode is similar to the thermionic spot mode but electron emission occurs from a larger, more diffuse, very hot area that occupies the entire available working surface of the cathode. To achieve the spotless mode, the construction of the cathode is usually made in such a way as to minimize thermal conduction and thermal energy loss by radiation. For example, the cathode could be made from a two-segment cathode which has a cylindrical base of small diameter. The cathode attains a high temperature,

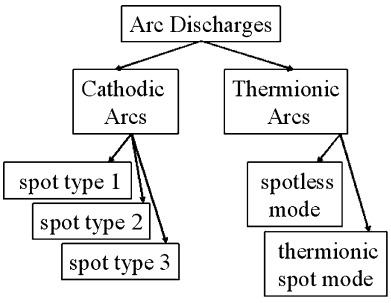

Fig. 3.40. Classification of cathode modes based on electron emission mechanisms

which is sufficiently high for significant thermionic emission. The thermionic spotless mode is achieved when thermionic electron emission current approaches the discharge current. At this point, the ion contribution, which is crucial for current balance in the thermionic spot mode, is not critical to satisfy current continuity because electron emission is large enough. However, ion bombardment heating may still be critical to maintain the necessary high cathode temperature. The transition from the thermionic spot mode to the spotless mode is usually sudden, and associated with a slight reduction of the burning voltage. From the minimum energy principle, the spotless mode is preferred because less energy is needed to operate the discharge in the spotless mode at the discharge current determined by the impedance of the external circuit.

After the thermionic spotless mode has been established, it may be stable or, after a thermal time constant which is often on the order of seconds of minutes, it may switch back into the thermionic spot mode due to the lack of sufficient ion heating. The spotless mode is only stable if the cathode energy balance allows the discharge to maintain the necessary high cathode temperature. The spotless mode is observed, for example, in so-called super-high-pressure discharge lamps filled with xenon, which are commercially used in projection devices for computers. Convective heating can play an important role for the cathode energy balance. Since ion impact heating is reduced when the spotless mode is reached, the cathode temperature may fall, reducing thermionic emission. This may force the cathode to switch back in a mode where only a fraction of the area is hot, i.e., the thermionic spot mode. The increased ion bombardment heating may increase the overall cathode temperature, eventually again satisfying the existence condition of the thermionic spotless mode. Oscillations between thermionic modes have been observed in gas discharge lamps (of course, such lamps are declared faulty and in need of replacement).

Another approach to arc classification is to consider the origin and nature of the plasma between anode and cathode (Figure 3.41). Of special interest are

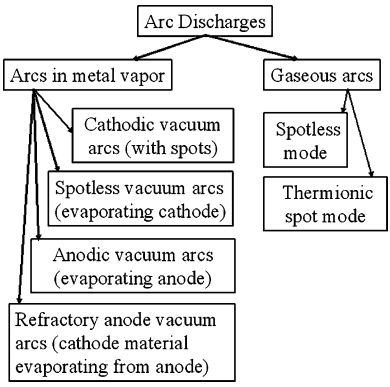

Fig. 3.41. Classification of cathode modes based on discharge medium

cases where the plasma contains a large fraction of metal species or is even exclusively composed of metal, obtained by evaporation of the cathode ("spotless cathodic vacuum arc" [190–192]) or by evaporation of the anode ("anodic arc" [193–197]) or by evaporation of cathode material that was deposited on the anode ("refractory anode vacuum arc" [198]). All of these modes have the advantage that metal plasma production does not rely on microscopic explosive processes that are characteristic for cathodic arcs, and hence macroparticle generation is avoided or does not play an important role. Deposition rates can be high, and uniformity issues can be addressed with technological means that are similar to conventional evaporation techniques. However, the kind of plasma obtained is different than cathodic arc plasmas in terms of the degree of ionization, ion charge state distribution, and ion energy. These plasmas are not further discussed in this book.

Yet other modes of cathodic arcs are obtained at very high arc currents ($I_{arc} >> 1\,kA$), when the anode is no longer a simple electron collector but various "active" anode modes appear. In the world of high-current arcs, typical for vacuum arc switches and vacuum arc circuit interrupters, the pathological "low-current" case of a passive anode is often called *diffuse arc*, which must not be confused with a spotless arc or other modes: *diffuse* refers here to the anode, while the cathode shows typical cathode spots, which are numerous, small, point-like, and non-stationary. High-current modes include the footpoint mode, the anode spot mode, and the intense arc mode, see the reviews by Miller [199, 200].

3.7 The Cohesive Energy Rule

3.7.1 Formulation

Each material has certain characteristics such as "the ease to burn." This "ease" is related to the likelihood that the arc does not spontaneously extinguish; it also describes the level (amplitude) of fluctuations in burning voltage, light emission, ion charge state distribution, ion energies, etc. In this section, these more or less subtle differences between cathode materials are discussed in terms of empirical rules. Among them, the Cohesive Energy Rule [201, 202] appears to be the most physically reasonable because it can be associated with fundamental considerations of energy conservation and power distribution.

The Cohesive Energy Rule can be formulated as follows: "The average arc burning voltage of a vacuum arc at a given current is approximately directly proportional to the cohesive energy of the cathode material."

The cohesive energy is the energy needed to form a free, electrically neutral atom by removing it from its bound position in a solid at 0 K. Table B8 (Appendix B) includes the cohesive energy expressed in eV/atom. It is often given in kJ/mol or kcal/mol or J/g, but it can be expressed in eV/atom, representing the average binding energy of the atom in the solid.

The arc burning voltage determines the energy dissipated for a given arc current, the latter being determined by the electrical discharge circuit. Because the dissipated energy affects practically all plasma parameters, the Cohesive Energy Rule implies a number of secondary rules. This is non-trivial since the cohesive energy is just one of many physical characteristics of a solid, and it is not obvious why it should be suited to predict the parameters of the expanding vacuum arc plasma. Before this issue is addressed, one may consider other empirical rules that have been used.

3.7.2 Other Empirical Rules

For decades, researchers have tried, with some success, to identify simple relationships that could help to understand cathode-spot physics and to predict plasma parameters. For example, Kesaev [203] and Grakov [204] attempted to correlate the burning voltages with arc current and thermophysical properties of the electrode material. Kesaev suggested that there is a correlation between arc voltage and the product of the boiling temperature and the square root of the thermal conductivity. Nemirovskii and Puchkarev [205] derived a relatively complicated relation between burning voltage, the thermal conductivity, and the specific heat of the cathode material. Brown and co-workers [206, 207] found a correlation between the boiling temperature of the cathode material (in Kelvin) and the mean ion charge state of the vacuum arc plasma:

$$\overline{Q} = 1 + 3.8 \times 10^{-4} T_{boil}. \tag{3.86}$$

With the large body of experimental data known today it is clear that plasma parameters such as average ion charge state [206, 208, 209], electron temperature [210, 211], and ion velocity [208, 212] can be correlated to the periodic properties of the solid cathode materials – this led to the idea to arrange solid state and plasma properties in Periodic Tables (Appendix B).

3.7.3 Experimental Basis

Measurements of the burning voltage have been done many times. In one of the more recent systematic studies [202], the vacuum arc ion source "Mevva V" [209] was used. The use of this facility had the advantage that the voltage data can be directly associated with other data measured at the same facility, such as ion charge state distributions [207], electron temperatures [211], and directed ion velocities [212]. Corrections to the measured voltage data were obtained by using the same setup without plasma, i.e., by measuring the voltage for a shorted cathode–anode gap. The latter measurements were done not in vacuum but in air or under inert gas when using reactive cathode materials. The difference between the voltage measured with plasma and without plasma (shorted gap) is approximately equal to the burning voltage. It is not precisely equal since the shorted gap situation includes the small but non-zero contact resistance of the short. The

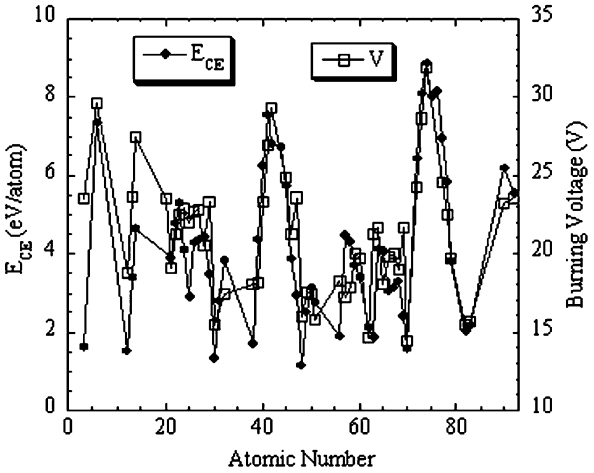

Fig. 3.42. Experimentally found correlation between arc voltage and cohesive energy; cohesive energy E_{CE}, and arc burning voltage V, for cathode materials of atomic number Z. E_{CE} was taken from [213], and the burning voltage was measured at an arc current of 300 A. (From [202])

error in the measurements increases with increasing current. The contact resistance caused the error to be less for noble metals (such as Au, Pt) and higher for very reactive metals (such Li, Ca, Sr, Ba).

The results of systematic measurements are shown in Figure 3.42 and Table B8 of Appendix B. The experimental data reported in Table B8 are somewhat higher than some literature data because they do not represent the cathode fall or the minimum voltage needed but rather the voltage obtained by averaging over the typical noise of the data.

3.7.4 Physical Interpretation

The transition from the cathode's solid phase to the plasma phase requires energy, which is supplied via the power dissipated by the arc,

$$P_{arc} = V\, I_{arc}, \tag{3.87}$$

where V is the voltage of the arc (i.e., measured between anode and cathode, and not to be confused with the voltage provided at the power supply). The energy needed for the phase transitions is only a fraction of the total energy balance. The total balance of the cathode region has been discussed in Section 3.4.3, and here it is summarized as

$$I_{arc} V \tau = E_{phon} + E_{CE} + E_{ionization} + E_{kin,i} + E_{ee} + E_{th,e} + E_{MP} + E_{rad}, \tag{3.88}$$

where τ is a time interval over which observation is averaged, E_{phon} is the phonon energy (heat) transferred to the cathode material, E_{CE} is the cohesive energy

needed to transfer the cathode material from the solid phase to the vapor phase, $E_{\text{ionization}}$ is the energy needed to ionize the vaporized cathode material, $E_{\text{kin,i}}$ is the kinetic energy given to ions due to the pressure gradient and other acceleration mechanisms, E_{ee} is the energy needed to emit electrons from the solid to the plasma (latent work function), $E_{\text{th,e}}$ is the thermal energy (enthalpy) of electrons in the plasma, E_{MP} is the energy invested in melting, heating, and acceleration of macroparticles, and E_{rad} is the energy emitted by radiation. The various terms of (3.88) contribute very differently to the balance, and some of the terms such as energy invested in macroparticles and radiation are small. The input energy is mostly transferred to heat the cathode, to emit and heat electrons, and to produce and accelerate ions. The cohesive energy E_{CE} is relatively small and may be neglected if one wants to calculate the more prominent energy contributions. However, the correlation between burning voltage and cohesive energy suggests to have a closer look at the physical situation.

There are two arguments in the interpretation of the Cohesive Energy Rule, which seems to hold despite the relatively small fraction of energy needed for the phase transition.

The first argument is based on the *spatial distribution of the energy input*. Figure 3.43 schematically shows that most of the dissipated energy is concentrated near the cathode surface and associated with the cathode fall. Interestingly, driven by the extreme pressure gradient, both electrons and ions are accelerated *away* from the cathode surface, carrying away the energy invested in them. Therefore, a very large fraction of input energy is not available to accomplish the phase transition. Materials with large cohesive energy require more energy for the transition from the solid to the vapor phase. The discharge

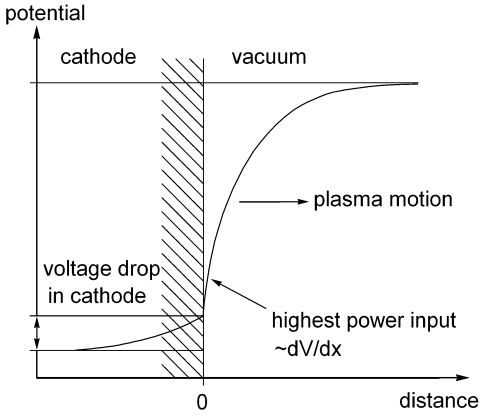

Fig. 3.43. Schematic illustration of the potential drop near the cathode surface. The dissipated power density is proportional to the gradient of the potential. The dense plasma adjacent to the surface receives most of the dissipating power density and is therefore heated rapidly and accelerated away from the cathode, thereby removing most of the input energy

system can provide this greater energy to the solid by increasing the overall burning voltage. Of course, when this happens, the fraction of energy going to other energy forms, as described by (3.88), increases as well. If this is true, solids with greater cohesive energy require higher burning voltage, and more energy is also available for ionization and acceleration of ions, in agreement with measurements.

The second interpretation for the Cohesive Energy Rule and its derived rules is based on the *periodicity of many material properties*. Periodicity refers here to properties that are due to the electronic shell structure and that can be grouped according to the Periodic Table of the Elements. For example, the melting temperature and boiling temperature show the same periodicity as the cohesive energy (Tables B1 and B8, Appendix B), which of course is not coincidental but related to the electronic structure of atoms and the formation and strength of chemical bonds in the solid phase. Periodicity is the physical reason that a relation identified for the cohesive energy can be approximately formulated as a relation to the melting or boiling temperature, for example. The question may rise if a physical relation expressed for the cohesive energy is equivalent to a corresponding relation to the boiling temperature, for example. That is not quite the case because relations based on the cohesive *energy* can be associated with the thermodynamic law of *energy conservation*. Energy is a physical quantity for which one can formulate a balance equation, but temperature is not. Therefore, an empirical rule based on energy should be preferred over a rule related to temperature.

3.7.5 Quantification

In a zero-order approximation one can state that the vacuum arc burning voltage is about 20 V, with somewhat lower values for cathode materials of smaller cohesive energy and higher values for materials of greater cohesive energy. Quantifying the Cohesive Energy Rule in a first-order approximation gives [214]

$$V = V_0 + A\, E_{CE}, \tag{3.89}$$

where, for the specific experiments with 300-A arcs in a vacuum arc ion source [202], the values $V_0 = 14.3$ V and $A = 1.69$ $V/(\text{eV/atom})$ were found. For other arc configurations and considering threshold currents rather than 300-A arcs, the constant will be smaller, perhaps as low as $V_0 \approx 8$ V. Figure 3.44 shows how well the simple approximation (3.89) represents the Cohesive Energy Rule. Further refinements are discussed in [214].

3.7.6 Related Observations: Ion Erosion and Voltage Noise

The main focus in formulating the Cohesive Energy Rule was the material-dependent arc burning voltage and the underlying energy balance. Other

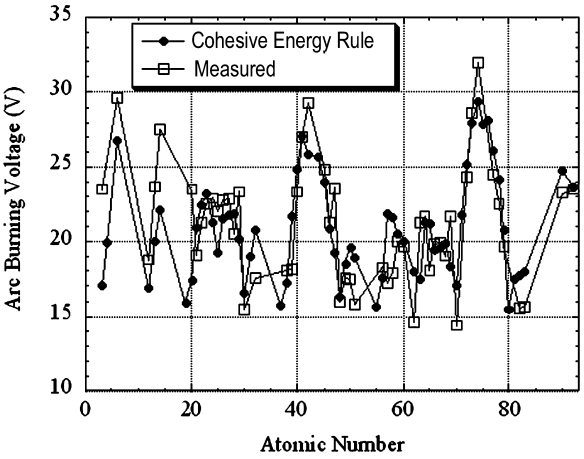

Fig. 3.44. Comparison of experimental data and Cohesive Energy Rule, approximation (3.89). (From [214])

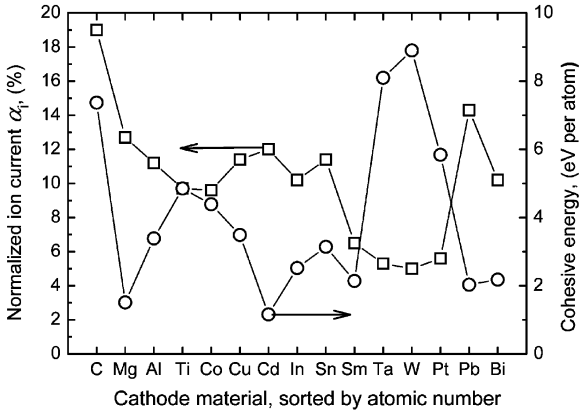

Fig. 3.45. Ion erosion rate, expressed as ion current normalized by arc current, and cohesive energy, for most metals of the Periodic Table. One can see that materials of high cohesive energy have low ion erosion rates and vice versa. (From [91])

observations are related such as the metal-dependent ion erosion rate and the amplitude of voltage fluctuations (noise). It is clear that if more energy is needed to accomplish the phase transitions from cathodic solid to liquid, gas, plasma, less material can go through these transitions for a given energy (see also Section 3.8). This has been experimentally confirmed by carefully studying the ion erosion rate (Figure 3.45): One can clearly see that cohesive energy and ion erosion rate are in opposing phase, i.e., the materials of high cohesive energy show low ion erosion and vice versa.

Another observation that can be related to the Cohesive Energy Rule is the amplitude of voltage noise generated when using different cathode materials. While the Cohesive Energy Rule established an empirical, energy-based rule for the burning voltage, we now consider the *fluctuating component* of the burning voltage. This component can be investigated using fast data acquisition and Fourier transform analysis [93, 215]. The result was already shown in Figure 3.22. The curves of the spectral power are slightly shifted and their order reflects the amplitude of noise: one can see that the higher the cohesive energy the greater the voltage noise. Apparently, the higher cohesive energy is again a suitable measure for the "difficulty" to ignite emission centers.

3.8 Cathode Erosion

The cathode material is the feedstock material for the cathodic arc plasma, and therefore, as the cathodic arc is burning, the cathode loses mass. Cathode erosion is actually comprised of three components: material leaving the cathode surface region as ions, neutral vapor, and macroparticles, i.e.,

$$\Gamma_{total} = \Gamma_i + \Gamma_0 + \Gamma_{MP}. \tag{3.90}$$

The usually desired form of erosion for cathodic arc coatings is ion erosion because ions can be influenced by electric and magnetic fields, and the condensation of ions leads to the desirable film properties.

Cathode erosion is typically expressed as mass loss per charge (with the unit μg/As or μg/C). It is most often determined by the weighing method which implies that the mass of the cathode is carefully measured before and after arc operation, and the charge transferred is determined by measuring arc current and arc duration, i.e.,

$$\Gamma_{total} = \frac{\Delta m_{cathode}}{\int I_{arc} dt}. \tag{3.91}$$

If the arc current is constant, one may simply use

$$\Gamma_{total} = \frac{\Delta m_{cathode}}{I_{arc} t_{arc}}. \tag{3.92}$$

This method does not give any information in which form the loss occurred, i.e., as ion, neutral, or macroparticle loss.

It should be noted that while this definition of erosion is common, it is not the best approach from a physical point of view. The normalization of mass loss to charge transferred works relatively well only because the differences in arc voltage are relatively small when the material or discharge conditions are changed. A better, more fundamental normalization is mass loss per energy, i.e.,

$$\widetilde{\Gamma}_{total} = \frac{\Delta m_{cathode}}{\int I_{arc} V_{arc} dt}. \tag{3.93}$$

The corresponding unit is μg/J.

One may also define specific erosion rates considering the loss of mass in the form of ions, neutrals, or macroparticles. To determine the ion erosion rate one would need to measure the total flux of ions coming from the cathode. This is a non-trivial task because at least a fraction of ions will condense on the anode. Weighing the anode is not helpful because macroparticles will also be deposited. One solution is to measure the ion current to screens, meshes, or shields and to use geometric correction factors [91].

It was already mentioned in Section 3.7.6 that ion erosion rates were found in opposite phase to the cohesive energy of the cathode material, i.e., the higher the cohesive energy the lower the ion erosion rate (see Figure 3.45). Because of this property, the often-quoted "10%-rule" is very approximate.[7] The "10%-rule" states that the maximum ion current that can be obtained from a cathodic arc is about 10% of the arc current. This percentage was identified by erosion studies, e.g., by Kimblin [216] and Daalder [217]. More recent studies of different cathode materials [91] confirmed that ion erosion is proportional to the arc current but they also showed that the percentage scales with the inverse of the cohesive energy. The percentage can be lower or higher than 10% (Figure 3.46 and Table 3.6).

We have the least information on Γ_0, the mass loss by evaporation of neutrals from the cathode surface. Charge state distribution studies and their interpretation (e.g., [211]) showed that the plasma generated at cathode spots is fully ionized, and with very few exceptions (like carbon) one can be sure that the fraction of neutrals in the spot plasma is very small (less than 1%). However, as discussed earlier in this chapter, the spot phenomena are fractals in space and time, and therefore the concept of giving simple percentages for ions and atoms emitted from the spot region is flawed unless we realize that these are average values. Only by integrating over time and space we can arrive at those meaningful *average* data. They include the vapor from previously active emission centers, i.e., locations that are not producing plasma anymore but still hot enough to cause evaporation (stages (iii) and (iv) of the emission site evolution). We can expect that the vapor pressure of the cathode materials will play an important role because this quantity can vary over many orders of magnitude [37].

Macroparticle erosion can be the largest fraction of cathode mass loss [219]. It strongly depends on the material properties, surface conditions, and on the discharge configuration (like presence of spot-steering magnetic fields). Macroparticle formation is separately discussed in Chapter 6.

---

[7] Ion erosion is sometimes expressed as ion current normalized by the arc current, giving the unit "%." Contrary to popular reading, this does not mean that ions contribute x% to the arc current, and electrons (100–x)%. Because the measured ion flux moves *away* from the cathode, electrons need to carry more than 100% of the arc current, compensating for the current of ions going in the "wrong direction."

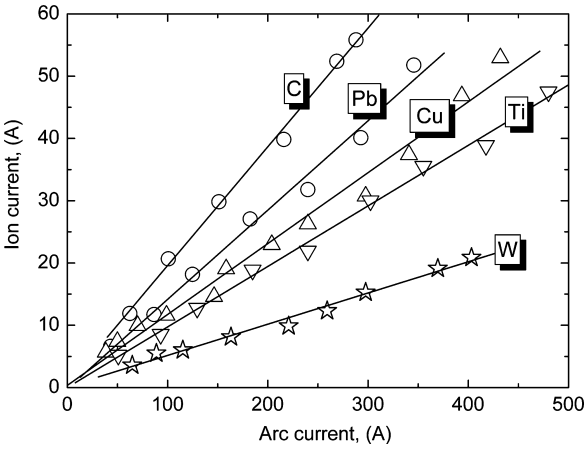

Fig. 3.46. Ion current from a cathodic arc discharge, as a function of arc current, with the material as a parameter. (After [91])

Table 3.6. Ion current normalized by arc current, α_i, and ion erosion rates, Γ_i, for various cathode materials. The last column shows the ion erosion rate normalized by arc energy, $\tilde{\Gamma}_i$, calculated from Γ_i and the arc voltage given in Table B8

Cathode meterial	Reference [216]	Reference [218]	Reference [42]	Reference [91]	Reference [91]	
	α_i (%)	α_i (%)	Γ_i (μg/C)	α_i (%)	Γ_i (μg/C)	$\tilde{\Gamma}_i$ (μg/J)
C	10.0	19	13–17	19	23.8	0.804
Mg	–	12.7	19–25	12.7	18.8	1.00
Al	–	11.2	22–25	11.2	15.9	0.674
Ti	8.0	9.7	–	9.7	22.4	1.05
Co	8.0	9.6	–	9.6	30.4	1.33
Cu	–	11.4	35–39	11.4	33.4	1.42
Zr	–	10.5	–	10.5	36.3	1.55
Cd	8.0	12	128–130	12	94.6	5.90
In	–	10.2	–	10.2	80.5	4.60
Sn	–	11.4	–	11.4	83.1	4.75
Sm	–	6.5	–	6.5	46.1	3.16
Ta	–	5.3	–	5.3	31.2	1.09
W	7.0	5	62–90	5	27.1	0.850
Pt	–	5.6	–	5.6	50.6	2.25
Pb	–	14.3	–	14.3	172.8	11.1
Bi	–	10.2	–	10.2	171.5	11.0

3.9 Plasma Formation

3.9.1 Phase Transitions

Let us have a closer look at the phase transformations that lead to the three kinds of cathode erosion (ions, neutrals, macroparticles). In particular we will consider how the cathodic arc plasma is formed by studying the path of the material in phase diagrams. With few exceptions, such as mercury which is already in the liquid phase at room temperature, it is clear that the cathode processes start with the cathode material in its solid phase. Due to the high energy density of the cathode-spot region, the cathode material goes through all four phases: solid → liquid → vapor → plasma.

One may plot a density–temperature phase diagram containing all phases, phase boundaries, and critical points, should they exist. For the axes of the phase diagram one could select temperature and density of heavy particles or electrons. It is acceptable to speak of one temperature, as opposed to electron temperature or ion temperature, provided collisions are sufficiently frequent. The phase diagram, Figure 3.47, contains regions of solid, liquid, and gas (vapor) as well as coexistence regions for solid–liquid, liquid–gas, and solid–gas. It also shows a critical point "C" which is the point of highest temperature where liquid and gas are still in equilibrium. Beyond C, one cannot distinguish between liquid and vapor. In the example

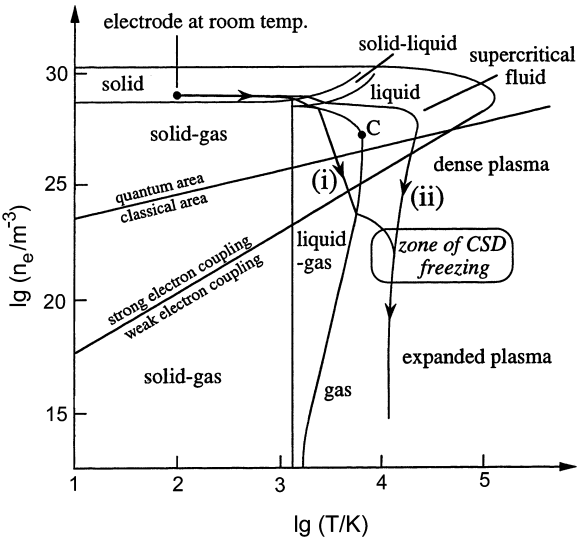

Fig. 3.47. Equilibrium phase diagram for copper using temperature–electron density presentation. One sees the classical phases as well as plasma at high temperature and low density. The two *straight lines* indicate degeneration of electrons and borderline of region with strong non-ideal coupling. The important information is in the path of cathode material. (Adapted from [45] and [211])

shown in Figure 3.47, copper is selected because many data are available (copper being the "guinea pig" material of arc physicists and electrical contact engineers). The figure shows two out of a large number of possible paths of the material when transitioning from solid to expanded plasma [45].

In the explosive stage of an emission site, comparable to a wire explosion, the material is heated so rapidly that its density initially remains almost constant. Therefore, the path in the diagram goes to the right almost horizontally. It is interesting to note that the temperature of the small volume under consideration can exceed the temperature of the critical point C, and hence the material can be a supercritical fluid that gradually transitions into a fully ionized plasma without ever having gone through the classical liquid and vapor phases. This transition is extremely fast, shorter than 1 ns, and likely to occur only at the beginning of the explosive stage of a new emission site. The material reaches a maximum temperature and, driven by the extreme pressure gradient to the surrounding vacuum or low-pressure plasma, it expands and cools down. Eventually, after some 10 ns, the plasma is not in equilibrium anymore and one needs to distinguish between the temperatures of electrons and ions.

In the later development stages of the emission site, processes are less violent, and the path is closer to what one would normally expect: the cathode material is still rapidly heated but expands slightly, melts, vaporizes, and becomes ionized in the vicinity of the spot. The plasma in the expanded plasma is different than the plasma produced from the supercritical fluid, which contributes to the rapid fluctuations seen in cathodic arc plasmas. In this later stage, the material is less ionized, and cathode erosion may become dominated by evaporation where the necessary energy is provided by ion bombardment from the plasma [220].

Due to the generally explosive nature of cathode processes, the path of material in the phase diagram is not constant but rapidly changing between the extremes located on both sides of the critical point.

3.9.2 Non-ideal Plasma

When the cathode material takes the path of explosive transformation from solid to plasma, circumnavigating the critical point (Figure 3.47), there is a certain, short-lived, high-density state that is best described as *non-ideal* plasma. For comparison, in the more common, ideal plasma, the kinetic energy of plasma particles is much greater than the interaction energy, which is mainly due to shielded Coulomb interaction. Equivalently, one can say that there are many charged particles in the Debye sphere, i.e., a sphere whose radius is the local Debye length. These properties allowed us to introduce the approximation of binary collisions between charged particles. In non-ideal plasmas, in contrast, the density is very high, and the interaction between charged particles is much stronger. The binary collision approximation is no longer a good approximation but one needs to consider multi-particle interactions, especially when the plasma density approaches solid-state density.

There are many texts on non-ideal plasmas [221–223], and here it should suffice to give the parameters that characterize the degree of coupling or non-ideality. A plasma is called non-ideal or strongly coupled if the potential energy of the plasma particles due to Coulomb interaction is not much smaller than the average kinetic energy. To quantify this, a dimensionless coupling parameter Γ_e can be defined as the ratio of potential to kinetic energy:

$$\Gamma_e = \frac{e^2}{4\pi\varepsilon_0 kT}\left(\frac{4\pi n_e}{3}\right)^{1/3}, \tag{3.94}$$

where the symbols have the usual meaning, like ε_0 is the permittivity of free space and k is the Boltzmann constant. The border between classical and quantum regions for the electron gas can be identified by the dimensionless degeneration parameter

$$\theta_e = n_e \Lambda_e^3, \tag{3.95}$$

where n_e is the electron density and Λ_e is a characteristic quantum length, the electron de Broglie wavelength:

$$\Lambda_e = \frac{h}{(2\pi m_e kT)^{1/2}}. \tag{3.96}$$

One of the features of non-ideal plasmas is the enhancement of the degree of ionization by *pressure ionization*, a multi-particle interaction effect observed at very high particle densities and pressure, as it exists during the explosive stage of an emission site [45]. The Coulomb interaction of the outer bound electrons of an atom or ion with the surrounding charged particles (ions and free electrons) and with polarizable particles (atoms and clusters) leads to a substantial lowering of their binding energy. For densities approaching solid-state density, this lowering is additionally strengthened by the quantum-mechanical exchange interaction between the bound-shell electrons of neighboring particles. With increasing density, the outer shells (bound electron states) become compressed and finally disappear. The mean ionization state continuously increases and is much higher in real plasmas at high pressure than one would expect on the basis of the more conventional theories which neglect such interactions. In the asymptotic limit of very high density, the high-pressure plasma is fully ionized, consisting only of free, bare nuclei and free electrons, whereas the ionization of an ideal model plasma (i.e., where interactions are neglected) tends to zero, with finally all charges bound in neutral atoms (Figure 3.48).

The cathode material in the explosive stage of an emission site follows a path from high to low density, which corresponds going from right to left in Figure 3.48 (putting aside, for a moment, that the temperature is not constant as assumed in that figure). The material transitions through a "valley of low ionization" for moderately non-ideal plasma conditions. This valley can be associated with a region where the conductivity is lowest (resistivity highest) and therefore power dissipation is highest. This can be understood taking into account that on the high-density side (right side of Figure 3.48), electrons

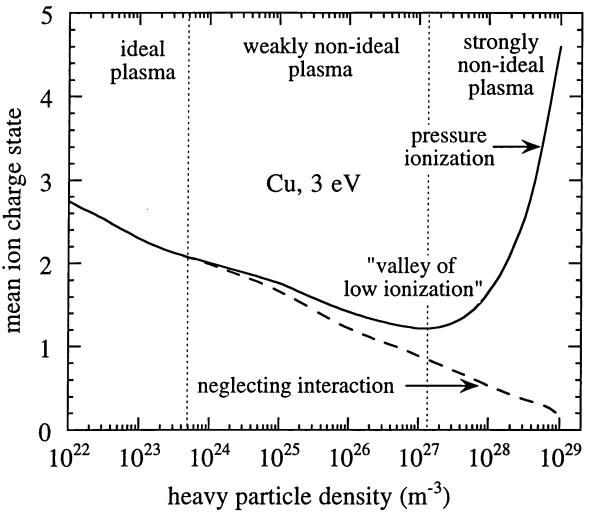

Fig. 3.48. Equilibrium calculations for ideal and non-ideal copper plasma at densities approaching solid state: for the ideal model plasma, the lowering of the ionization energy by multi-particle interaction was neglected, leading to unrealistically low ionization. The actual ionization curve describes a "valley of low ionization" in the region of weakly non-ideal parameters. (After [45])

degenerate, form conduction bands, and follow Fermi–Dirac statistics with a Fermi distribution (Section 3.2.1), hence there is good metallic conduction. On the low-density side, electrons are not degenerated and can therefore be described by Boltzmann statistics leading to a Maxwell distribution, and we have the high conductivity of a fully ionized plasma (the so-called Spitzer conductivity [224]). In the transition, the Fermi distribution asymptotically approaches the Boltzmann distribution. The now-free electrons in the dense plasma suffer many collisions due to the high density, which appear like "friction" to the transport of charge, hence the conductivity is reduced.

As the dense plasma expands, it moves through the region in the phase diagram where the curves of non-ideal and ideal calculation merge: this is the region of weakly non-ideal plasma. With further decreasing density, the frequency of collisions falls and therefore the condition for equilibrium are eventually violated: the plasma transitions into non-equilibrium, which plays an important role when considering plasma properties in the interelectrode space (Chapter 4).

One shortcoming of using Figure 3.48 is that it shows curves for constant temperature. In the explosive phase transition, matter is first rapidly heated followed by cooling during expansion. One could imagine a set of isothermal curves, each showing a valley of low ionization. The path of the plasma would intersect a number of those isothermals. Qualitatively, the physical picture remains the same.

Transient non-ideal plasma on the one hand and "holes" in the cathode sheath (Figure 3.13) on the other hand are intimately connected. The cathode metal transitions from solid to fully ionized plasma, i.e., circumnavigating the critical point, which requires that very high plasma densities exist. Both electrons and ions are present and can contribute to transport of the discharge current; however, the plasma is in the "valley of low ionization," as explained before. Under these transient conditions, which are spatially limited, the conductivity of the plasma is relatively low, and the voltage drop, which is normally associated with the cathode sheath, is in the non-ideal plasma, as opposed to that in the sheath. Cathode models throughout the literature focus on electron emission from a cathode surface, and various surface and emission conditions are assumed. The transient formation of holes in the sheath and the phase transition on the high-density side of the critical point are usually not considered. The relevance of this mechanism is still subject to further experimental diagnostics and theoretical modeling.

3.9.3 Ion Acceleration

This chapter is concluded by briefly considering ion acceleration near cathode spots because this will naturally lead to the next chapter in which the interelectrode plasma is discussed. In this section, only those acceleration processes are considered that are intimately related to plasma generation and electrode processes.

Ions "born" at cathode spots are known to have high velocity once they are observed or measured in distances that are large compared to the size of the spot. In fact, ion velocities are supersonic with respect to the ion sound velocity. Until now, there is no generally accepted theory of ion acceleration, which is in part due to the lack of reliable data on charge- and time-dependent velocity distribution functions. Although great progress was made, there are still questions on how much the electric field is contributing to ion acceleration. Another possible (or actually most likely and important) reason is that ion acceleration theories generally do not consider the very different stages of the emission site's life cycle. It is safe to assume that ions generated in the explosive stage experience different accelerating forces than ions generated in later stages. Due to the existence of non-stationary processes, one should *a priori* expect non-stationary velocity distribution functions. So far, only average velocities or kinetic energies or velocity distribution functions have been measured, although all researchers stress the great variability of velocity data.

Ion acceleration near emission sites (cathode spots or spot fragments) are thought to be due to the following forces: (i) pressure gradient of ions, (ii) pressure gradient of electrons, (iii) collective acceleration of ions by electron–ion coupling, and (iv) acceleration by an electric field if such field exists (potential hump). Explanation and theoretical modeling have been challenging and the subject of many papers over the years [114, 225–231].

The fractal model with explosive emission events as the short-time cutoff is best suited to (at least qualitatively) explain a range of experimental results, especially those obtained with high resolution, which show a wide spectrum of fluctuations. However, other models are also conceivable, and more tractable, by not considering the fluctuating features but rather by trying to explain the general, averaged trends.

In the simplest case one would use a stationary model in one dimension, keeping in mind that the results cannot explain any fluctuation or spatial variation other than on axis. Considering ions and electrons as two fluids led to a set of two-fluid equations that exhibit a saddle point at the ion sound velocity [227]. Transition to transonic flow velocities (i.e., ions become supersonic) is only possible through the directed friction force associated with electron–ion collisions. A small potential hump has only a minor effect for the momentum gain of the ions [226, 227].

Taking the multifluid equations that describe anisotropic plasma expansion in spherical coordinates, Hantzsche [229] found an analytical solution in the form of asymptotic power series. According to this model, the main force responsible for the high ion velocities is electron–ion friction, i.e., electrons move much faster and with greater quantities from the emission center; they transfer kinetic energy to the slower ions via Coulomb interaction. This mechanism provides roughly half of the kinetic energy given to the ions. The electrons, in turn, are accelerated by the electric field and the electron pressure gradient. The remaining ion acceleration is caused by the ion pressure gradient and the electric field force. Overall, most of the acceleration is completed in a space less than 10 μm from the emission center, and the velocities are approximately constant for distances greater than 100 μm. Those average ion velocities are further discussed in Chapter 4.

Other models are conceivable, too. For example, considering a mercury vacuum arc, Beilis [232] assumed that the near-cathode region consists of three layered regions, which – in the order of their distance from the cathode surface – can be called the first plasma region, the double sheath, and the second plasma region. Electrons emitted from the surface of the first plasma region are accelerated through the double sheath region (potential drop 10–15 V) into the second plasma region. Likewise ions flowing from the second ion region are accelerated through the double sheath into the first plasma region where they serve as a significant heat source. Two types of time-dependent solutions with characteristic times of 0.1–1 and 100 μs exist [232]. However, this model is difficult to bring into relation to the fractal structure of emission sites advocated in this chapter.

References

1. Hantzsche, E., "Über die Katodenmechanismen in Gasentladungen," Academy of Sciences, Berlin, Germany, 1978.
2. Hantzsche, E., "Theories of cathode spots," in *Handbook of Vacuum Arc Science and Technology*, Boxman, R.L., Martin, P.J., and Sanders, D.M., (Eds.). pp. 151–208, Noyes, Park Ridge, New Jersey, (1995).

3. Anders, A., The fractal nature of cathode spots, *IEEE Trans. Plasma Sci.* **33**, 1456–1464, (2005).
4. Schulze, G.E.R., *Metallphysik*, 2nd ed. Akademie-Verlag, Berlin, Germany, (1974).
5. Lide, D.R., (Ed.) *Handbook of Chemistry and Physics,* 81st ed. CRC Press, Boca Raton, New York, (2000).
6. Skriver, H.L. and Rosengaard, N.M., Surface energy and work function of elemental metals, *Phys. Rev. B* **46**, 7157, (1992).
7. Richardson, O.W., On the negative radiation from hot platinum, *Proc. Cambridge Phil. Soc.* **11**, 286–295, (1901).
8. Richardson, O.W., *Emission of Electricity from Hot Bodies*, 2nd ed. Longmans, Green & Co., New York, (1921).
9. Dushman, S., Electron emission from metals as a function of temperature, *Phys. Rev.* **21**, 623–636, (1923).
10. Dushman, S., Thermionic emission, *Rev. Mod. Phys.* **2**, 381–476, (1930).
11. Fowler, R.H. and Nordheim, L., Electron emission in intense electric fields, *Proc. Roy. Soc. (London)* **A119**, 173–181, (1928).
12. Good Jr., R.H. and Müller, E.W., "Field emission," in *Handbuch der Physik vol. 21.* pp. 176–231, Springer, Berlin, (1956).
13. Dobrogowski, J., Moscicka-Grzesiak, H., Seidel, S., and Zalucki, Z., *Foundations of Discharges and Electrical Insulation in Vacuum (in Polish).* Panstwowe Wydawnictwo Naukowe, Warsaw and Poznan, Poland, (1983).
14. Miller, H.C., "Values of Fowler-Nordheim field emission functions $v(y)$, $t(y)$ and $s(y)$," General Electric Company, Technical Information Series, No.66-C-148 (1966).
15. Hantzsche, E., The thermo-field emission of electrons in arc discharges, *Beitr. Plasmaphys.* **22**, 325–346, (1982).
16. Dolan, W.W. and Dyke, W.P., Temperature and field emission of electrons from metals, *Phys. Rev.* **35**, 327, (1954).
17. Murphy, E.L. and Good Jr., R.H., Thermionic emission, field emission, and the transition region, *Phys. Rev.* **102**, 1446, (1956).
18. Christov, S.G., General theory of electron emission from metals, *Physica Status Solidi* **17**, 11, (1966).
19. Coulombe, S. and Meunier, J.L., Thermo-field emission – a comparative study, *J. Phys. D: Appl. Phys.* **30**, 776–780, (1997).
20. Hudson, J.B., *Surface Science*. Wiley, New York, (1992).
21. Somorjai, G.A., *Introduction to Surface Chemistry and Catalysis*. John Wiley & Sons, New York, (1994).
22. Kaminsky, M., *Atomic and Ionic Impact Phenomena on Metal Surfaces*. Springer-Verlag, Berlin, (1965).
23. Knudsen, M., *The Kinetic Theory of Gases*. McGraw Hill, New York, (1927).
24. Lafferty, J.M., (Ed.) *Foundations of Vacuum Science and Technology*, John Wiley & Sons, New York, (1998).
25. Schottky, W., *Zeitschrift für Physik* **14**, 80, (1923).
26. Farrall, G.A., "Vacuum Arc Ignition," in *Handbook of Vacuum Arc Science and Technology*, Boxman, R.L., Sanders, D.M., and Martin, P.J., (Eds.). pp. 28–72, Noyes Publications, Park Ridge, New Jersey, (1995).
27. Little, R.P. and Whitney, W.T., *J. Appl. Phys.* **34**, 2430–2432, (1963).
28. Latham, R.V. and Wilson, D.A., The energy spectrum of electrons field emitted from carbon fibre micropoint cathodes, *J. Phys. D: Appl. Phys.* **16**, 455–463, (1983).

29. Cox, B.M., Variation of the critical breakdown field between copper electrodes in vacuo, *J. Phys. D: Appl. Phys.* **7**, 143–170, (1974).
30. Ecker, G. and Müller, K.G., Electron emission from the arc cathode under the influence of the individual field component, *J. Appl. Phys.* **30**, 1466–1467, (1959).
31. Jüttner, B. and Vasenin, Y.L., *Cathode Processes of the Metal Vapor Arc*. E.O. Paton Electric Welding Institute, Kiev, (2003).
32. Mueller, E.W., *Z. f. Physik* **106**, 541, (1937).
33. Dyke, W.P., Trolan, J.K., Martin, E.E., and Barbour, J.P., The field emission initiated vacuum arc. I. Experiments on arc initiation, *Phys. Rev.* **91**, 1043–1054, (1953).
34. Dyke, W.P. and Trolan, J.K., Field Emission: large current densities, space charge, and the vacuum arc, *Phys. Rev.* **89**, 799–808, (1953).
35. Mesyats, G.A. and Barengol'ts, S.A., Mechanism of anomalous ion generation in vacuum arcs, *Physics-Uspekhi* **45**, 1001–1018, (2002).
36. Beilis, I.I., "Theoretical modeling of cathode spot phenomena," in *Handbook of Vacuum Arc Science and Technology*, Boxman, R.L., Martin, P.J., and Sanders, D.M., (Eds.). pp. 208–256, Noyes, Park Ridge, New Jersey, (1995).
37. Honig, R.E. and Kramer, D.A., Vapor pressure data for the solid and liquid elements, *RCA Rev.* **30**, 285–305, (1969).
38. Nottingham, W.B., Remarks on the energy loss attending thermionic emission of electrons from metals, *Phys. Rev.* **59**, 906–907, (1941).
39. Swanson, L.W., Crouser, L.C., and Charbonnier, F.M., Energy exchanges attending field electron emission, *Phys. Rev.* **151**, 327, (1966).
40. Chandrasekhar, S., *Radiative Transfer*, 1960 Reprint of 1950 Edition. Dover, New York, (1960).
41. Mesyats, G.A., *Explosive Electron Emission*. URO Press, Ekaterinburg, (1998).
42. Mesyats, G.A., *Cathode Phenomena in a Vacuum Discharge: The Breakdown, the Spark, and the Arc*. Nauka, Moscow, Russia, (2000).
43. Bochkarev, M.B., "Ecton processes of low current vacuum arc imaged with streak technique," XXIth Int. Symp. Discharges and Electrical Insulation in Vacuum, Yalta, Ukraine, 241–244, (2004).
44. Prock, J., Solidification of hot craters on the cathode of vacuum arcs, *J. Phys. D: Appl. Phys.* **19**, 1917–1924, (1986).
45. Anders, A., Anders, S., Förster, A., and Brown, I.G., Pressure ionization: its role in metal vapor vacuum arc plasmas and ion sources, *Plasma Sources Sci. Technol.* **1**, 263–270, (1992).
46. Mackeown, S.S., The cathode drop in an electric arc, *Phys. Rev.* **34**, 611–614, (1929).
47. Neumann, W., *The Mechanism of the Thermoemitting Arc Cathode*. Akademie-Verlag, Berlin, (1987).
48. Gabovich, M.D. and Poritskii, V.Y., Nonlinear waves at the surface of a liquid metal in an electric field, *JETP Lett.* **33**, 304–307, (1981).
49. Puchkarev, V.F. and Bochkarev, M.B., Cathode spot initiation under plasma, *J. Phys. D: Appl. Phys.* **27**, 1214–1219, (1994).
50. Uimanov, I.V., A two-dimensional nonstationary model of the initiation of an explosive center beneath the plasma of a vacuum arc cathode spot, *IEEE Trans. Plasma Sci.* **31**, 822–826, (2003).
51. Bugaev, S.P., Litvinov, E.A., Mesyats, G.A., and Proskurovskii, D.I., Explosive emission of electrons, *Sov. Phys. Usp.* **18**, 51–61, (1975).

52. Litvinov, E.A., Mesyats, G.A., and Proskurovskii, D.I., Field emission and explosive emission processes in vacuum discharges, *Sov. Phys. Usp.* **26**, 138, (1983).
53. Mesyats, G.A. and Proskurovsky, D.I., *Pulsed Electrical Discharge in Vacuum*. Springer-Verlag, Berlin, (1989).
54. Mesyats, G.A., Ecton mechanism of the vacuum arc cathode spot, *IEEE Trans. Plasma Sci.* **23**, 879–883, (1995).
55. Mesyats, G.A., Ecton or electron avalanche from metal, *Sov. Phys. Usp.* **38**, 567–590, (1995).
56. Barengolts, S.A., Mesyats, G.A., and Shmelev, D.L., Structure and time behavior of vacuum arc cathode spots, *IEEE Trans. Plasma Sci.* **31**, 809–816, (2003).
57. Kesaev, I.G., *Cathode Processes of an Electric Arc (in Russian)*. Nauka, Moscow, (1968).
58. Jüttner, B., Cathode spots of electrical arcs (Topical Review), *J. Phys. D: Appl. Phys.* **34**, R103–R123, (2001).
59. Seydel, U., Schöfer, R., and Jäger, H., Temperatur und Druck explodierender Drähte beim Verdampfungsbeginn, *Z. Naturforsch.* **30a**, 1166–1174, (1975).
60. Klein, T., Paulini, J., and Simon, G., Time-resolved description of cathode spot development in vacuum arcs, *J. Phys. D: Appl. Phys.* **27**, 1914–1921, (1994).
61. Chace, W.G. and More, H.K., *Exploding Wires*. Plenum Press, New York, (1962).
62. Kotov, Y.A., Sedoi, V.S., and Chemezova, L.I., "The integral of action and the energy for electrically exploded wires," Institute of High Current Electronics, Tomsk, Russia (1986).
63. Beilis, I.I., Mechanism for small electron current fraction in a vacuum arc cathode spot on a refractory cathode, *Appl. Phys. Lett.* **84**, 1269–1271, (2004).
64. Coulombe, S. and Meunier, J.-L., Arc-cold cathode interactions – parametric dependence on local pressure, *Plasma Sources Sci. Technol.* **6**, 508–517, (1997).
65. Jüttner, B., Erosion craters and arc cathode spots, *Beitr. Plasmaphys.* **19**, 25–48, (1979).
66. Tonks, L., A theory of liquid surface rupture by a uniform electric field, *Phys. Rev.* **48**, 562–568, (1930).
67. Forbest, R.G., Understanding how the liquid-metal ion source works, *Vacuum* **48**, 85–97, (1997).
68. Gamero-Castano, M. and de la Mora, J.F., Direct measurement of ion evaporation kinetics from electrified liquid surfaces, *J. Chem. Phys.* **113**, 815–832, (2000).
69. Rossetti, P., Paganucci, F., and Andrenucci, M., Numerical model of thermoelectric phenomena leading to cathode-spot ignition, *IEEE Trans. Plasma Sci.* **30**, 1561–1567, (2002).
70. Vogel, N. and Skvortsov, V.A., Plasma parameters within the cathode spot of laser-induced vacuum arcs: Experimental and theoretical investigations, *IEEE Trans. Plasma Sci.* **25**, 553–563, (1997).
71. Shmelev, D.L. and Litvinov, E.A., The computer simulation of the vacuum arc emission center, *IEEE Trans. Plasma Sci.* **25**, 533–537, (1997).
72. Shmelev, D.L. and Litvinov, E.A., Computer simulation of ecton in a vacuum arc, *IEEE Trans. Dielec. Electr. Insul.* **6**, 441–444, (1999).
73. Abbaoui, M., Lefort, A., and Clain, S., "Influence of the material nature (Ag, Cu, Al, Fe, W, C) on the arc root characteristics at the cathode," XXIth Int. Symp. Discharges and Electrical Insulation in Vacuum, Yalta, Ukraine, 233–236, (2004).
74. Vogel, N. and Höft, H., Cathode spot energy transfer simulated by a focused laser beam, *IEEE Trans. Plasma Sci.* **17**, 638–640, (1989).

75. Mandelbrot, B.B., *The Fractal Geometry of Nature*. W.H. Freeman and Company, New York, (1983).
76. Schroeder, M., *Fractals, Chaos, Power Laws: Minutes from an Infinite Paradise*, 8th Ed. W.H. Freeman and Company, New York, (2000).
77. Hantzsche, E., Jüttner, B., and Pursch, H., On the random walk of arc cathode spots in vacuum, *J. Phys. D: Appl. Phys.* **16**, L173–L179, (1983).
78. Daalder, J.E., Random walk of cathode arc spots in vacuum, *J. Phys. D: Appl. Phys.* **16**, 17–27, (1983).
79. Smeets, R.P.P. and Schulpen, F.J.H., Fluctuations of charged particle and light emission in vacuum arcs, *J. Phys. D: Appl. Phys.* **21**, 301–310, (1988).
80. Anders, S. and Jüttner, B., Influence of residual gases on cathode spot behavior, *IEEE Trans. Plasma Sci.* **19**, 705–712, (1991).
81. Schülke, T. and Siemroth, P., Vacuum arcs cathode spots as a self-similarity phenomenon, *IEEE Trans. Plasma Sci.* **24**, 63–64, (1996).
82. Siemroth, P., Schülke, T., and Witke, T., Investigations of cathode spots and plasma formation of vacuum arcs by high speed microscopy and spectrography, *IEEE Trans. Plasma Sci.* **25**, 571–579, (1997).
83. Peitgen, H.-O. and Richter, P.H., *The Beauty of Fractals*. Springer, Berlin, (1986).
84. Osborne, A.R. and Pastorello, A., Simultaneous occurrence of low-dimensional chaos and colored random noise in nonlinear physical systems, *Phys. Lett. A* **181**, 159–171, (1993).
85. Bak, P., Tang, C., and Wiesenfeld, K., Self-organized criticality: An explanation of $1/f$ noise, *Phys. Rev. Lett.* **59**, 381–384, (1987).
86. Anders, A., Lichtenberg Figures on Dielectrics in Gases and in Vacuum, *Beitr. Plasmaphys.* **25**, 315–328, (1985).
87. Meakin, P., Coniglio, A., Stanley, H.E., and Witten, T.A., Scaling properties for the surfaces of fractal and nonfractal objects: An infinite hierarchy of critical exponents, *Phys. Rev. A* **34**, 3325, (1986).
88. Anders, S., Anders, A., and Jüttner, B., Brightness distribution and current density of vacuum arc cathode spots, *J. Phys. D: Appl. Phys.* **25**, 1591–1599, (1992).
89. Hantzsche, E., Jüttner, B., and Ziegenhagen, G., Why vacuum arc cathode spots can appear larger than they are, *IEEE Trans. Plasma Sci.* **23**, 55–64, (1995).
90. Jüttner, B., The dynamics of arc cathode spots in vacuum, *J. Phys. D: Appl. Phys.* **28**, 516–522, (1995).
91. Anders, A., Oks, E.M., Yushkov, G.Y., Savkin, K.P., Brown, I.G., and Nikolaev, A.G., Measurements of the total ion flux from vacuum arc cathode spots, *IEEE Trans. Plasma Sci.* **33**, 1532–1536, (2005).
92. Beilis, I., Djakov, B.E., Jüttner, B., and Pursch, H., Structure and dynamics of high-current arc cathode spots in vacuum, *J. Phys. D: Appl. Phys.* **30**, 119–130, (1997).
93. Anders, A., Oks, E.M., and Yushkov, G.Y., Cathodic arcs: Fractal voltage and cohesive energy rule, *Appl. Phys. Lett.* **86**, 211503-1-3, (2005).
94. Puchkarev, V.F. and Murzakayev, A.M., Current density and the cathode spot lifetime in a vacuum arc at threshold currents, *J. Phys. D: Appl. Phys.* **23**, 26–35, (1990).
95. Hantzsche, E., Arc spot ignition caused by sheath instability, *IEEE Trans. Plasma Sci.* **25**, 527–532, (1997).
96. Niemeyer, L., Pietronero, L., and Wiesmann, H.J., Fractal dimension of dielectric breakdown, *Phys. Rev. Lett.* **52**, 1033–1036, (1984).

97. Batrakov, A., Popov, S., Vogel, N., Jüttner, B., and Proskurovsky, D.I., Plasma parameters of an arc cathode spot at the low-current vacuum discharge, *IEEE Trans. Plasma Sci.* **31**, 817–826, (2003).
98. Batrakov, A.V., Juettner, B.J., Popov, S.A., Proskurovsky, D.I., and Vogel, N.I., "Time resolved resonant laser diagnostics of the low-current vacuum arc cathode spot," XXIth Int. Symp. Discharges and Electrical Insulation in Vacuum, Yalta, Ukraine, 205–208, (2004).
99. Tsuruta, K., Nakajima, M., Kitaura, M., and Yanagidaira, T., "Effect of magnetic field on sustainment of low-current DC vacuum arcs," XXIth Int. Symp. Discharges and Electrical Insulation in Vacuum, Yalta, Ukraine, 261–264, (2004).
100. Schneider, D., Witke, T., Schwarz, T., Schöneich, B., and Schultrich, B., Testing ultra-thin films by laser-acoustics, *Surf. Coat. Technol.* **126**, 136–141, (2000).
101. Laux, M. and Pursch, H., Sound emission from an arc cathode, *IEEE Trans. Plasma Sci.* **29**, 722–725, (2001).
102. Harris, L.P., Transverse forces and motions at cathode spots in vacuum, *IEEE Trans. Plasma Sci.* **11**, 94–102, (1983).
103. Anders, A., Anders, S., Jüttner, B., Bötticher, W., Lück, H., and Schröder, G., Pulsed dye laser diagnostics of vacuum arc cathode spots, *IEEE Trans. Plasma Sci.* **20**, 466–472, (1992).
104. Anders, A., Anders, S., Jüttner, B., and Lück, H., High-resolution imaging of vacuum arc cathode spots, *IEEE Trans. Plasma Sci.* **24**, 69–70, (1996).
105. Vogel, N., The cathode spot plasma in low-current air and vacuum break arcs, *J. Phys. D: Appl. Phys.* **26**, 1655–1661, (1993).
106. Jüttner, B., The dynamics of arc cathode spots in vacuum. Part III: Measurements with improved resolution and UV radiation, *J. Phys. D: Appl. Phys.* **31**, 1728–1736, (1998).
107. Jüttner, B., The dynamics of arc cathode spots in vacuum: new measurements, *J. Phys. D: Appl. Phys.* **30**, 221–229, (1997).
108. Kleberg, I., "Dynamics of cathode spots in external magnetic field (in German)," Humboldt University, Berlin, Germany, 2001.
109. Jüttner, B., Nanosecond displacement times of arc cathode spots in vacuum, *IEEE Trans. Plasma Sci.* **27**, 836–844, (1999).
110. Jüttner, B. and Kleberg, I., The retrograde motion of arc cathode spots in vacuum, *J. Phys. D: Appl. Phys.* **33**, 2025–2036, (2000).
111. Dryvesteyn, M.J., Electron emission of the cathode of an arc, *Nature* **137**, 580, (1936).
112. Suits, C.G. and Hocker, J.P., Role of oxidation in arc cathodes, *Phys. Rev.* **53**, 670, (1938).
113. Cobine, J.D., Effects of oxides and impurities on metallic arc reignition, *Phys. Rev.* **53**, 911, (1938).
114. Lyubimov, G.A. and Rakhovsky, V.I., The cathode spot of a vacuum arc, *Sov. Phys. Uspekhi* **21**, 693–718, (1978).
115. Achtert, J., Altrichter, B., Jüttner, B., Pech, P., Pursch, H., Reiner, H.-D., Rohrbeck, W., Siemroth, P., and Wolff, H., Influence of surface contaminations on cathode processes of vacuum discharges, *Beitr. Plasmaphys.* **17**, 419–431, (1977).
116. Jüttner, B., On the variety of cathode craters of vacuum arcs, and the influence of the cathode temperature, *Physica* **114C**, 155–261, (1982).
117. Bushik, A.I., Jüttner, B., and Pursch, H., On the nature and the motion of arc cathode spots in UHV, *Beitr. Plasmaphys.* **19**, 177–188, (1979).

118. Jakubka, K. and Jüttner, B., The influence of surface conditions on the initiation, propagation and current density of unipolar arcs in fusion devices, *J. Nucl. Mat.* **102**, 259–266, (1980).
119. Szente, R.N., Munz, R.J., and Drouet, M.G., Effect of the arc velocity on the cathode erosion rate in argon-nitrogen mixtures, *J. Phys. D: Appl. Phys.* **20**, 754–756, (1987).
120. Szente, R.N., Munz, R.J., and Drouet, M.G., Arc velocity and cathode erosion rate in a magnetically driven arc burning in nitrogen, *J. Phys. D: Appl. Phys.* **21**, 909–916, (1988).
121. Szente, R.N., Munz, R.J., and Drouet, M.G., The influence of the cathode surface on the movement of magnetically driven electric arcs, *J. Phys. D: Appl. Phys.* **23**, 1193–1200, (1990).
122. Laux, M., Schneider, W., Wienhold, P., et al., Arcing at B_4C-covered limiters exposed to a SOL-plasma, *J. Nuclear Materials* **313**, 62–66, (2003).
123. Beilis, I.I., Application of vacuum arc cathode spot model to graphite cathode, *IEEE Trans. Plasma Sci.* **27**, 821–826, (1999).
124. Kandah, M. and Meunier, J.-L., Vacuum arc cathode spot movement on various kinds of graphite cathodes, *Plasma Sources Sci. Technol.* **5**, 349–355, (1996).
125. Richter, F., Flemming, G., Kühn, M., Peter, S., and Wagner, H., Characterization of the arc evaporation of a hot boron cathode, *Surf. Coat. Technol.* **112**, 43–47, (1999).
126. Buttolph, L.J., The Cooper Hewitt mercury vapor lamp, *General Electric Review* **23**, 741–751, (1920).
127. Karpov, D.A. and Nazikov, S.N., Multicomponent electric-arc source of metallic plasma, *Plasma Devices and Operations* **1**, 230–246, (1991).
128. Ding, C. and Yanabu, S., Effect of parallel circuit parameters on the instability of a low-current vacuum arc, *IEEE Trans. Plasma Sci.* **31**, 877–883, (2003).
129. Chandrasekhar, S., Stochastic problems in physics and astronomy, *Rev. Mod. Phys.* **15**, 1–89, (1943).
130. Erwin, S., Untersuchungen über die Bewegung des Brennflecks auf der Kathode eines Quecksilberdampf-Niederdruckbogens, *Annalen der Physik (Leipzig)* **439**, 246–270, (1949).
131. Jüttner, B., Puchkarev, V.F., Hantzsche, E., and Beilis, I., "Cathode Spots," in *Handbook of Vacuum Arc Science and Technology*, Boxman, R.L., Sanders, D.M., and Martin, P.J., (Eds.). pp. 73–281, Noyes, Park Ridge, New Jersey, (1995).
132. Jüttner, B., Pursch, H., and Shilov, V.A., The influence of surface roughness and surface temperature on arc spot movement in vacuum, *J. Phys. D: Appl. Phys.* **17**, L31–L34, (1984).
133. Daalder, J.E., Random walk of cathode spots: a random walk of definitions?, *J. Phys. D: Appl. Phys.* **16**, L177–L179, (1983).
134. Coulombe, S., Probabilistic modelling of the high-pressure arc cathode spot displacement dynamic, *J. Phys. D: Appl. Phys.* **36**, 686–693, (2003).
135. Anders, A. and Anders, S., Emission spectroscopy of low-current vacuum arcs, *J. Phys. D: Appl. Phys.* **24**, 1986–1992, (1991).
136. Kraft, V.V. and Stuchenkov, V.M., Effect of nonmetallic inclusions in cathodes on vacuum breakdown, *Sov. Phys.-Tech. Phys.* **17**, 66–70, (1972).
137. Lawler, G.F., *Intersections of Random Walks*. Birkhäuser, Boston, MA, (1991).
138. Lawler, G.F., *Introduction to Stochastic Processes*. Chapman & Hall/CRC, New York, (1995).
139. Takeda, K. and Sugimoto, M., Effects of active elements on oxide removal by a vacuum arc, *IEEE Trans. Plasma Sci.* **31**, 983–986, (2003).

140. Jüttner, B., "Personal communication," (2004).
141. Stark, J., Induktionserscheinungen am Quecksilberlichtbogen im Magnetfeld, *Zeitschrift für Physik* **4**, 440–443, (1903).
142. Weintraub, E., Investigation of the arc in metallic vapours in an exhausted space, *Phil. Mag*. **7** (of Series 6), 95–124, (1904).
143. Minorsky, M.N., La rotation de l'arc électrique dans un champ magnétique radial, *Le Journal de Physique et Le Radium* **9**, 127–136, (1928).
144. Longini, R.L., Motion of low pressure arc cathode spots in magnetic fields, *Phys. Rev*. **71**, 184, (1947).
145. Longini, R.L., A note concerning the motion of arc cathode spots in magnetic fields, *Phys. Rev*. **71**, 642–643, (1947).
146. Gallagher, C.J. and Cobine, J.D., Retrograde motion of an arc cathode spot in a magnetic field, *Phys. Rev*. **71**, 481, (1947).
147. Smith, C.G., Arc motion reversal in transverse magnetic field by heating cathode, *Phys. Rev*. **73**, 543, (1948).
148. Gallagher, C.J., The retrograde motion of the arc cathode spot, *J. Appl. Phys*. **21**, 768–771, (1950).
149. Yamamura, S., Immobility phenomena and reverse driving phenomena of the electric arc, *J. Appl. Phys*. **21**, 193–196, (1950).
150. Rothstein, J., Holes and retrograde arc spot motion in a magnetic field, *Phys. Rev*. **78**, 331, (1950).
151. Smith, C.G., Retrograde arc motion of supersonic speed, *Phys. Rev*. **84**, 1075, (1951).
152. Miller, C.G., Motion of the arc cathode spot in a magnetic field, *Phys. Rev*. **93**, 654, (1954).
153. Robson, A.E. and von Engel, A., Origin of retrograde motion of arc cathode spots, *Phys. Rev*. **93**, 1121–1122, (1954).
154. John, R.M.S. and Winans, J.G., The motion of arc cathode spot in a magnetic field, *Phys. Rev*. **94**, 1097–1102, (1954).
155. John, R.M.S. and Winans, J.G., Motion and spectrum of the arc cathode spot in a magnetic field, *Phys. Rev*. **98**, 1664–1671, (1955).
156. Hernqvist, K.G. and Johnson, E.O., Retrograde motion in gas discharge plasmas, *Phys. Rev*. **89**, 1576–1583, (1955).
157. Robson, A.E. and von Engel, A., Motion of a short arc in a magnetic field, *Phys. Rev*. **104**, 15–16, (1956).
158. Smith, C.G., Motion of an arc in a magnetic field, *J. Appl. Phys*. **28**, 1328–1331, (1957).
159. Ecker, G. and Müller, K.G., Theory of the retrograde motion, *J. Appl. Phys*. **29**, 1606–1608, (1958).
160. Guile, A.E. and Secker, P.E., Arc cathode movement in a magnetic field, *J. Appl. Phys*. **29**, 1662–1667, (1958).
161. Zei, D. and Winans, J.G., Motion of high speed arc spots in magnetic fields, *J. Appl. Phys*. **30**, 1814–1819, (1959).
162. Lewis, T.J. and Secker, P.E., Influence of the cathode surface on arc velocity, *J. Appl. Phys*. **32**, 54–64, (1961).
163. Hermoch, V. and Teichmann, J., Cathode jets and the retrograde motion of arcs in magnetic field, *Zeitschrift für Physik* **195**, 125–145, (1966).
164. Carter, R.P. and Murphree, D.L., Arc motion reversal in crossed electric and magnetic fields in an argon atmosphere from 200 to 900 Torr, *J. Appl. Phys*. **44**, 5190–5191, (1973).

165. Hermoch, V., On the retrograde motion of arcs in magnetic field by heating cathode, *IEEE Trans. Plasma Sci.* **PS-1**, 62–64, (1973).
166. Auweter-Ming, M. and Schrade, H.O., Explanation of the arc spot motion in the presence of magnetic fields, *J. Nucl. Mat.* **93–94**, 799–805, (1980).
167. Sethumraman, S.K. and Barrault, M.R., Study of the motion of vacuum arcs in high magnetic fields, *J. Nucl. Mat.* **93–94**, 791–798, (1980).
168. Fang, D.Y., Cathode spot velocity of vacuum arcs, *J. Phys. D: Appl. Phys.* **15**, 833–844, (1982).
169. Fang, D.Y., Temperature dependence of retrograde velocity of vacuum arcs in magnetic fields, *IEEE Trans. Plasma Sci.* **11**, 110–114, (1983).
170. Agrawal, M.S. and Holmes, R., Cathode spot motion in high-current vacuum arcs under self-generated azimuthal and applied axial magnetic fields, *J. Phys. D: Appl. Phys.* **17**, 743–756, (1984).
171. Drouet, M.G., The physics of the retrograde motion of the electric arc, *IEEE Trans. Plasma Sci.* **PS-13**, 235–241, (1985).
172. Sanochkin, Y.V., Velocity of retrograde motion and thermocapillary convection during local heating of a liquid surface, *Sov. Phys.-Tech. Phys.* **30**, 1052–1056, (1985).
173. Schrade, H.O., Arc cathode spots: their mechanism and motion, *IEEE Trans. Plasma Sci.* **17**, 635–637, (1989).
174. Moizhes, B.Y. and Nemchinskii, V.A., On the theory of the retrograde motion of a vacuum arc, *J. Phys. D: Appl. Phys.* **24**, 2014–2019, (1991).
175. Barengol'ts, S.A., Litvinov, E.A., Sadowskaya, E.Y., and Shmelev, D.L., Motion of cathode spot of vacuum arc in an external magnetic field, *Zh. Tekh. Fiz.* **68**, 60–64, (1998).
176. Beilis, I.I., Vacuum arc cathode spot grouping and motion in magnetic fields, *IEEE Trans. Plasma Sci.* **30**, 2124–2132, (2002).
177. Zabello, K.K., Barinov, Y.A., Logatchev, A.A., and Shkol'nik, S.M., "Cathode spot motion and burning voltage of low-current vacuum arc with electrodes of copper-chromium composition in magnetic field," Proc. of XXIth Int. Symp. Discharges and Electrical Insulation in Vacuum, Yalta, Ukraine, 280–281, (2004).
178. Zabello, K.K., Barinov, Y.A., Chaly, A.M., Logatchev, A.A., and Shkol'nik, S.M., Experimental study of cathode spot motion and burning voltage of low-current vacuum arc in magnetic field, *IEEE Trans. Plasma Sci.* **33**, 1553–1559, (2005).
179. Ehiasarian, A.P., Hovsepian, P.E., New, R., and Valter, J., Influence of steering magnetic field on the time-resolved plasma chemistry in cathodic arc discharges, *J. Phys. D: Appl. Phys.* **37**, 2101–2106, (2004).
180. Care, C.M., Stochastic model for the random motion of a vacuum arc in the presence of driving and confining fields, *J. Phys. D: Appl. Phys* **25**, 1841–1843, (1992).
181. Arapov, S.S. and Volkov, N.B., The formation and structure of current cells in a vacuum arc cathode spot, *Tech. Phys. Lett.* **29**, 1–4, (2003).
182. Alexandrov, A.F., Bogdankevich, L.S., and Rukhadze, A.A., *Principles of Plasma Electrodynamics*. Springer-Verlag, Berlin, (1984).
183. Laux, M., Schneider, W., Jüttner, B., Balden, M., Lindig, S., Beilis, I., and Djakov, B., "Ignition and burning of vacuum arcs on tungsten layers," XXIth Int. Symp. Discharges and Electrical Insulation in Vacuum, Yalta, Ukraine, 253–256, (2004).
184. Elenbaas, W., *High Pressure Mercury Discharge Lamps*. Philips Gloeilampenfabrieken, Eindhoven, The Netherlands, (1965).

185. Waymouth, J.F., *Electric Discharge Lamps*. MIT Press, New York, (1971).
186. Sampath, S. and Herman, H., Rapid solidification and microstructure development during plasma spray deposition, *Journal of Thermal Spray Technology* **5**, 445–456, (1996).
187. Mattox, D.M., Fundamentals of ion plating, *J. Vac. Sci. Technol.* **10**, 47–52, (1973).
188. Dearnley, P.A., "Ion Plating," Conf. on Ion Plating and Implantation, Atlanta, 31–38, (1985).
189. Benilov, M.S., Nonlinear heat structures and arc-discharge electrode spots, *Phys. Rev. A* **48**, 506–515, (1993).
190. Vasin, A.I., Dorodnov, A.M., and Petrosov, V.A., Vacuum arc with a distributed discharge on an expendable cathode, *Sov. Tech. Phys. Lett.* **5**, 634–636, (1979).
191. Dorodnov, A.M., Kuznetsov, A.N., and Petrosov, V.A., New anode-vapor vacuum arc with permanent hollow cathode, *Pis'ma Zh. Tekhn. Fiz.* **5**, 1101–1106, (1979).
192. Dorodnov, A.M., Zelenkov, V.V., and Kuznetsov, A.N., A stationary vacuum arc with two evaporable electrodes, *Teplofizika Vysokikh Temperatur* **35**, 983–984, (1997).
193. Ehrich, H., The anodic vacuum arc. I. Basic construction and phenomenology, *J. Vac. Sci. Technol. A* **6**, 134–138, (1988).
194. Ehrich, H., Hasse, B., Mausbach, M., and Müller, K.G., Plasma deposition of thin films utilizing the anodic vacuum arc, *IEEE Trans. Plasma Sci.* **18**, 895–903, (1990).
195. Ehrich, H., Hasse, B., Mausbach, M., and Müller, K.G., The anodic vacuum arc and its application to coatings, *J. Vac. Sci. Technol. A* **8**, 2160–2164, (1990).
196. Meassick, S., Chan, C., and Allen, R., Thin film deposition techniques utilizing the anodic vacuum arc, *Surf. Coat. Technol.* **54**, 343–348, (1992).
197. Musa, G., Ehrich, H., and Schuhmann, J., Pure metal vapor plasma source with controlled energy of ions, *IEEE Trans. Plasma Sci.* **25**, 386–391, (1997).
198. Beilis, I.I., Boxman, R.L., Goldsmith, S., and Paperny, V.L., Radially expanding plasma parameters in a hot refractory anode vacuum arc, *J. Appl. Phys.* **88**, 6224–6231, (2000).
199. Miller, H.C., A review of anode phenomena in vacuum arcs, *IEEE Trans. Plasma Sci.* **13**, 242–252, (1985).
200. Miller, H.C., "Anode Phenomena," in *Handbook of Vacuum Arc Science and Technology*, Boxman, R.L., Martin, P.J., and Sanders, D.N., (Eds.). pp. 308–364, Noyes Publications, Park Ridge, New Jersey, (1995).
201. Anders, A., Energetics of vacuum arc cathode spots, *Appl. Phys. Lett.* **78**, 2837–2839, (2001).
202. Anders, A., Yotsombat, B., and Binder, R., Correlation between cathode properties, burning voltage, and plasma parameters of vacuum arcs, *J. Appl. Phys.* **89**, 7764–7771, (2001).
203. Kesaev, I.G., Laws governing the cathode drop and the threshold currents in an arc discharge on pure metals, *Sov. Phys.-Techn. Phys.* **9**, 1146–1154, (1965).
204. Grakov, V.E., Cathode fall of an arc discharge in a pure metal, *Sov. Phys.-Techn. Phys.* **12**, 286–292, (1967).
205. Nemirovskii, A.Z. and Puchkarev, V.F., Arc voltage as a function of cathode thermophysical properties, *J. Phys. D: Appl. Phys.* **25**, 798–802, (1992).
206. Brown, I.G., Feinberg, B., and Galvin, J.E., Multiply stripped ion generation in the metal vapor vacuum arc, *J. Appl. Phys.* **63**, 4889–4898, (1988).
207. Brown, I.G. and Godechot, X., Vacuum arc ion charge-state distributions, *IEEE Trans. Plasma Sci.* **19**, 713–717, (1991).

208. Krinberg, I.A. and Lukovnikova, M.P., Application of a vacuum arc model to the determination of cathodic microjet parameters, *J. Phys. D: Appl. Phys.* **29**, 2901–2906, (1996).
209. Brown, I.G., Vacuum arc ion sources, *Rev. Sci. Instrum.* **65**, 3061–3081, (1994).
210. Krinberg, I.A. and Lukovnikova, M.P., Estimating cathodic plasma jet parameters from vacuum arc charge state distribution, *J. Phys. D: Appl. Phys.* **28**, 711–715, (1995).
211. Anders, A., Ion charge state distributions of vacuum arc plasmas: The origin of species, *Phys. Rev. E* **55**, 969–981, (1997).
212. Anders, A. and Yushkov, G.Y., Ion flux from vacuum arc cathode spots in the absence and presence of magnetic fields, *J. Appl. Phys.* **91**, 4824–4832, (2002).
213. Kittel, C., *Introduction to Solid State Physics*. John Wiley & Sons, New York, (1986).
214. Anders, A., "Cohesive energy rule for vacuum arcs," in *Emerging Applications of Vacuum-Arc-Produced Plasma, Ion and Electron Beams*, *NATO Science Series II. Mathematics, Physics and Chemistry vol. 88*, Brown, I. and Oks, E., (Eds.). pp. 1–14, Kluwer Academic Publishers, Dordrecht, (2002).
215. Rosén, J. and Anders, A., Material and time dependence of the voltage noise generated by cathodic vacuum arcs, *J. Phys. D: Appl. Phys.* **38**, 4184–4190, (2005).
216. Kimblin, C.W., Erosion and ionization in the cathode spot region of a vacuum arc, *J. Appl. Phys.* **44**, 3074–3081, (1973).
217. Daalder, J.E., Components of cathode erosion in vacuum arcs, *J. Phys. D: Appl. Phys.* **9**, 2379–2395, (1976).
218. Daalder, J.E., Erosion and the origin of charged and neutral species in vacuum arcs, *J. Phys. D: Appl. Phys.* **8**, 1647–1659, (1975).
219. Anders, S., Anders, A., Yu, K.M., Yao, X.Y., and Brown, I.G., On the macroparticle flux from vacuum arc cathode spots, *IEEE Trans. Plasma Sci.* **21**, 440–446, (1993).
220. Beilis, I.I., Transient cathode spot operation at a microprotrusion in a vacuum arc, *IEEE Trans. Plasma Sci.* **35**, 966–972, (2007).
221. Fortov, V.E. and Yakubov, I.T., *Physics of Nonideal Plasma*. Hemisphere, New York, (1990).
222. Ebeling, W., Förster, A., and Radtke, R., *Physics of Nonideal Plasmas*, Teubner Texte zur Physik vol. 26. Teubner Verlagsgesellschaft, Stuttgart and Leipzig, (1992).
223. Günther, K. and Radtke, R., *Electric Properties of Weakly Nonideal Plasmas*. Akademie-Verlag, Berlin, (1984).
224. Spitzer Jr., L., *Physics of Fully Ionized Gases*, preprint of the 2 nd revised edition, originally published by Wiley, 1962 ed. Dover, New York, (1990).
225. Lyubimov, G.A., Dynamics of cathode vapor jets, *Sov. Phys.-Techn. Phys.* **23**, 173–177, (1978).
226. Wieckert, C., A multicomponent theory of the cathodic plasma jet in vacuum arcs, *Contrib. Plasma Phys.* **27**, 309–330, (1987).
227. Wieckert, C., The expansion of the cathode spot plasma in vacuum arc discharges, *Phys. Fluids* **30**, 1810–1813, (1987).
228. Hantzsche, E., A revised theoretical model of vacuum arc spot plasmas, *IEEE Trans. Plasma Sci.* **21**, 419–425, (1993).
229. Hantzsche, E., Two-dimensional models of expanding vacuum arc plasmas, *IEEE Trans. Plasma Sci.* **23**, 893–898, (1995).

230. Beilis, I.I., Zektser, M.P., and Lyubimov, G.A., *Sov. Phys. Techn. Phys.* **33**, 1132–1137, (1988).
231. Beilis, I.I. and Zektser, M.P., *High Temp.* **29**, 501–504, (1991).
232. Beilis, I.I., Current continuity and instability of the mercury vacuum arc cathode spot, *IEEE Trans. Plasma Sci.* **24**, 1259–1271, (1996).

4

The Interelectrode Plasma

While the electric arc is one of the most common things of modern life, an understanding of it is not common.

Clement D. Child, in: *Electric Arc*, 1913

Abstract After plasma production at non-stationary cathode spots, the plasma expands into the interelectrode space. Plasma properties such as local density, temperature, streaming velocity, and ion charge state distribution are described for the expanding plasma. We are interested in the subject because it is one way to look back at cathode process and learn about plasma generation. Knowledge about the interelectrode plasma is also relevant to the application. Much of the information on arc plasmas is based on averaging over extended periods of time (DC arcs) or many pulses (pulsed arcs). In doing so, correlations between the solid-state cathode properties and the plasma properties can be established, which allowed us to formulate empirical rules. One section is dedicated to discuss the sources and effects of neutrals in the interelectrode plasma.

4.1 Plasma Far from Cathode Spots

The cathodic arc plasma expands from the spot region into vacuum or region of low gas pressure. In contrast to most other plasma systems, the cathodic arc plasma generator can be approximated by a *point source*. Even when the cathodes are very large, like the up to 2-m-long cathodes used in some commercial arc coaters, the plasma comes only from one (or several) single point(s) *at a given moment*. Over time, however, the locations of spots are distributed over the cathode surface, and therefore large-area coating is possible.

In this chapter, we consider macroscopic distances of tens of centimeters between cathode and substrate, and therefore we can neglect that the spot has

A. Anders, *Cathodic Arcs*, DOI: 10.1007/978-0-387-79108-1_4,

a structure and that several emission centers may be active. Uniform coatings require plasma expansion and the motion of the spot and, additionally, motion of the to-be-coated substrates. As mentioned in Chapter 3, spot motion can be random, or it can be controlled via magnetic fields or via the voltage drop in the cathode. While the cathode processes have been dealt with in Chapter 3, here we focus on the development of the plasma after its initial formation and after ion acceleration at the cathode spot.

The initial plasma expansion and ion acceleration are governed by pressure gradients and electron–ion coupling. These forces continue to act as the plasma moves away from the spot. However, additional effects are important, especially the location, shape, and size of the anode, external magnetic fields, if present, and the magnetic self-field generated by the arc current, and, last not least, the concentration of neutrals. The latter is often overlooked but requires special attention.

We consider first the case in which no external magnetic field is present, the anode is perfectly symmetric with respect to the spot location, and the arc current is relatively low so that the self-magnetic field is not important. Since there is much lower pressure everywhere around the dense plasma location, and the electrons do not have a preferred path to the anode, plasma expansion can be expected to be about spherically symmetric, except the directions affected by the cathode. This is indeed the case, as was experimentally shown using a large cylindrical anode with the cathode placed in the center of symmetry [1]. Plasma expansion was relatively symmetric in flux (Figure 4.1) and energy (Figure 4.2). The effect of the cathode can be approximated by a cosine distribution:

$$n \sim \cos^{\alpha} \vartheta, \tag{4.1}$$

where ϑ is the angle to the surface normal. The exponent α describes how much the plasma "plumes" along the surface normal. For $\alpha \to 0$ one would get a spherical distribution, while $\alpha > 1$ is sometimes reported. Alternatively, one may approximate the angular distribution by an exponential function [2]:

$$n \sim F_{\max} \exp(-\omega^2 / k^2), \tag{4.2}$$

where $F_{\max}$ is the maximum value (about 2.5%/sr for copper arcs of 100 A), ω is the solid angle, and k is the shape factor (about 4.6 sr for the example of an annular anode with 11-mm diameter and copper arc of 100 A [2]).

The distributions of Figures 4.1 and 4.2 can be significantly altered when the anode is not large and not symmetric. For example, when only a small anode is available, or the anode is placed quite remotely from the cathode, electrons need to drift to it, carrying the discharge current. A small voltage drop in the plasma and at the anode sheath affects the electron drift path and the overall plasma flow via electron–ion coupling. Furthermore, the self-magnetic field of the arc current tends to pinch the plasma flow. The plasma flow can appear as a jet

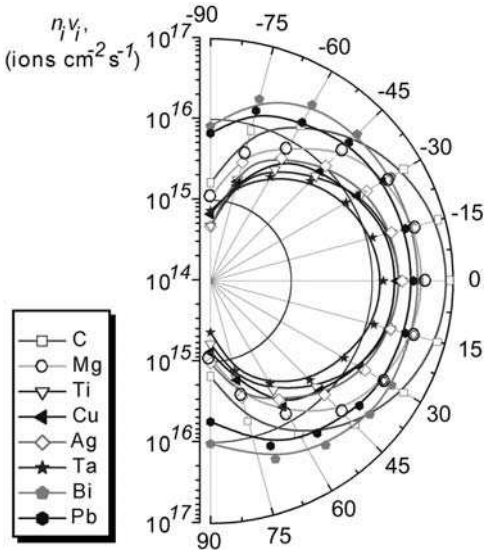

Fig. 4.1. Plasma ion flux from a cathode placed in the center of a symmetric anode (for selected materials), as a function of angle to the surface normal

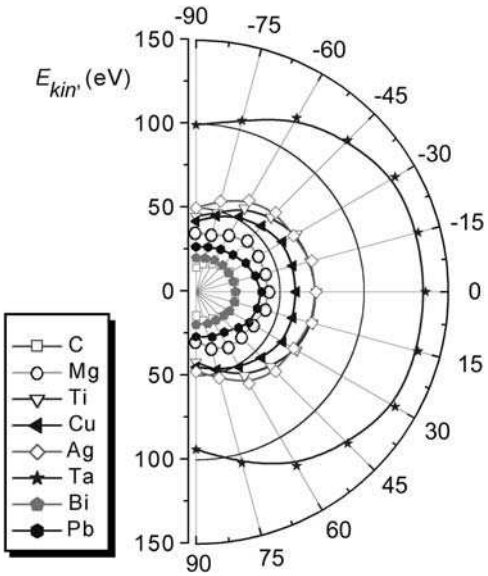

Fig. 4.2. Average kinetic energy of ions emitted from a cathode (for selected materials), as a function of angle to the cathode surface normal

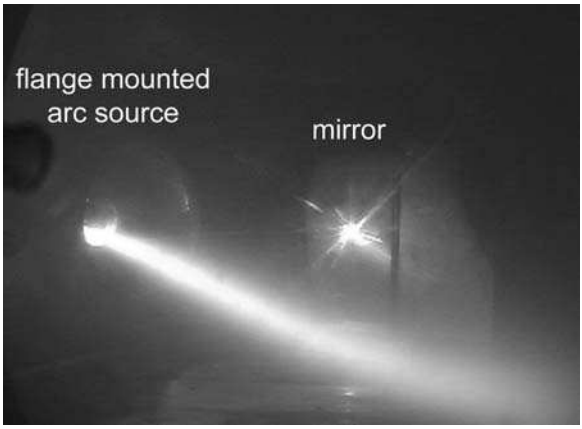

Fig. 4.3. Example of plasma jet formation in the case of limited anode area

rather than a symmetrically expanding plasma. Figure 4.3 shows an extreme example of a plasma jet emanating from a magnetically steered arc source into a chamber.

Plasma jet formation can be affected by the "disappearing anode" effect in the reactive deposition of insulating coatings such as aluminum oxide. The anode, "hidden" behind the insulating coating, disappears electrically as the coating grows, and therefore the electrons emitted from the cathode need to find whatever anode area is still available, i.e., the areas not coated. These areas are often in the shadow of the designated anode or other components, and plasma jet formation toward these shadowed areas can be observed. In extreme cases, the discharge becomes unstable due to the lack of available anode area.

Modeling of plasma jets is difficult mainly due to the feedback that is typical for plasmas: motion of electrically charged particles generates electromagnetic fields, and electromagnetic fields affect their motion. A common approach is to apply plasma models of magnetohydrodynamics [3, 4, 5, 6, 7, 8].

4.2 Special Cases of Plasma Expansion

4.2.1 Plasma Expansion into Vacuum

We assume that the plasma went through an initial rapid acceleration very close to the cathode spot, e.g., by a generalized hydrodynamic mechanism, as described at the end of Chapter 3. Let us further assume that expansion originates from a point source (the cathode spot) and that it is not dominated by external magnetic fields and interaction with gas. Using the continuity equation and assuming constant velocity after the initial acceleration, the expanding plasma should exhibit a quadratic drop in density from the spot center. Such

relationship was indeed found by careful probe measurements. Using very small probes, Ivanov, Jüttner, and others [9, 10] confirmed experimentally that the plasma density drops according to the point source law

$$n = C\frac{I_{arc}}{r^2} \tag{4.3}$$

along the surface normal, where C is a constant related to the ion erosion rate specific to the cathode material, I_{arc} is the arc current, and r is the distance from the spot. For copper, $C \approx 10^{13}\mathrm{A}^{-1}\mathrm{m}^{-1}$. The constants for other cathode materials can be estimated from ion erosion data provided in Chapter 3. Taking the angular dependence into account, a more general expression can be written as

$$n = C\frac{I_{arc}}{r^2}\cos^{\alpha}\vartheta, \tag{4.4}$$

with α and ϑ as defined in Section 4.1.

4.2.2 Plasma Expansion Dominated by an External Magnetic Field

An external magnetic field will strongly affect plasma expansion. In the most common configuration, the magnetic field lines intersect the cathode surface such as (i) to break the symmetry of plasma distribution around the emission site and thereby provide a preferred direction for spot ignition (so-called "steered arc") and (ii) to guide the plasma from the cathode to the substrate ("enhanced arc," "filtered arc," etc.). In any case, the plasma does not expand freely and therefore its density drops less than quadratic with increasing distance from the spot. An axial magnetic field is generally used to make the plasma plume in the forward direction [11, 12], which is used for improved plasma injection into macroparticle filters (see [13, 14] and Chapter 7).

The motion of electrons becomes greatly affected as soon as the density has dropped such that electrons become magnetized in the external field, i.e., their motion becomes governed by gyration in the magnetic field rather than the frequent collisions during a gyration cycle. One way of estimating the situation is to compare the kinetic plasma pressure:

$$p_{kin} \approx \sum_{\alpha} n_{\alpha} k T_{\alpha} \approx 2\overline{Q}\, C\frac{I_{arc}}{r^2} k T_e, \tag{4.5}$$

with the magnetic pressure

$$p_{mag} = \frac{B^2}{2\mu_0}. \tag{4.6}$$

In Eq. (4.5), the summation is over all plasma species, and the condition of quasi-neutrality $n_e = \overline{Q} n_i$ and Eq. (4.3) were used; $\overline{Q}$ is the mean ion charge state number, k is the Boltzmann constant, T_e is the electron temperature, μ_0 is the permittivity of free space, and B is the magnetic induction.

At the extremely high density near the spot, kinetic pressure is dominant, while the external field is governing plasma motion far from the spot. The characteristic radius of the transition zone (measured from the spot center) can be found by setting $p_{kin} \approx p_{mag}$, leading to

$$r_0 \approx \frac{1}{B}\sqrt{4\,\overline{Q}\,C\mu_0 I_{arc} k T_e}. \tag{4.7}$$

For a rough estimate, one can take $kT_e \approx 3\,\mathrm{eV}$, $\overline{Q} \approx 2$, $C \approx 10^{13}\mathrm{A}^{-1}\mathrm{m}^{-1}$ and obtains (units in parenthesis)

$$d_0(\mathrm{mm}) \approx 7\frac{\sqrt{I_{arc}(\mathrm{A})}}{B(\mathrm{mT})}. \tag{4.8}$$

For example, considering an arc of 100 A and an external field of 20 mT, the external field starts to dominate plasma motion for distances larger than 3.5 mm from the spot. Although these arguments are grossly simplified, the main conclusion is that plasma is already "magnetized" very close the cathode spot. With "magnetization" we mean that charged particle motion is governed by gyration (rotation around magnetic field lines). The mobility parallel to the magnetic field is unchanged while the mobility perpendicular to the field is drastically reduced and motion is only possible via collisions or collective phenomena (turbulence). There is a very large body of literature on the subject of plasmas in magnetic fields, mainly stimulated by research on thermonuclear fusion, for example [15, 16, 17, 18, 19].

At this point it should be stressed that the field strength is typically high enough to "magnetize" the electrons but not the ions: the gyration radius of ions is larger than the characteristic system size such as the characteristic length or diameter of the cathodic arc system. The radius of the gyration motion (Larmor radius) is directly proportional to the mass the charged particle:

$$r_L = \frac{v_\perp m}{|Q|eB}, \tag{4.9}$$

where Q is the charge state number (for electrons, $Q = -1$) and $v_\perp$ is the velocity component perpendicular to the magnetic field vector. To estimate $v_\perp$, one may use the thermal velocity.

Even when the ions are not magnetized, their motion is greatly affected via electron–ion coupling. As the electrons drift to the anode, the ions will move along, keeping the plasma quasi-neutral. The plasma will plume from the cathode spot and preferentially flow along the direction given by the magnetic field lines [20, 21]. This collective motion will also play a major role when discussing plasma transport in macroparticle filters (Chapter 7).

4.2.3 Plasma Expansion for High-Current Arcs

High-current arcs (of kiloamperes or more) are characterized by a large number of cathode spots. The approximation that the plasma is produced at a point

source at a given moment can be replaced by the approximation that plasma is produced uniformly [22, 23]. In that case, one neglects the "granular" or fractal structure of the emission and considers distances from the cathode surface that are much larger than the characteristic distances between emission sites.

The plasma density falls much slower than the inverse quadratic drop of Eq. (4.3), which is an immediate consequence of not having spherical expansion from a point source. The plasma density drops because the anode and walls are sinks of particles, i.e., the plasma condenses there. The rate of drop is a function of the specific geometry.

For high-current arcs, the influence of the self-magnetic field generated by the high current is large. It leads to jet formation and pinching, and may also lead to a number of plasma instabilities such as the Buneman instability [9].

To affect and assist current transport, an external axial magnetic field can be employed, which is used, for example, in vacuum circuit breakers [24]. The external magnetic field is superimposed on the self-field and thereby can largely determine the density distribution and plasma flow direction.

4.2.4 Plasma Expansion into Background Gas

The pressure near the cathode spot exceeds atmospheric pressure by a large factor and therefore it is not surprising that the arc can also exist in gases in a wide range of pressures, including atmospheric and higher. The arc can even burn with its electrodes immersed in liquids. For coating applications, one usually utilizes the arc either in vacuum or with a low-pressure background of argon, and in the case of reactive deposition with a reactive gas such as oxygen or nitrogen. Practitioners of arc coating often add some argon background gas, and this applies to both non-reactive and reactive deposition.

The original motivation of adding a *noble* gas may have originated from sputter deposition [25, 26], a widely used kind of physical vapor deposition (PVD), where a noble gas such as argon is essential to the process. In the case of cathodic arc deposition, the addition of a noble background gas is not necessary because the plasma can be exclusively formed from the cathode material. However, having a low background of argon or other noble gases has the beneficial effect of stabilizing the arc discharge. In light of the fractal spot ignition model, a possible interpretation is that the presence of gas increases the likelihood of spot ignition. This may be due to enhanced ion bombardment, an increase in pre-cathode plasma density, and a reduction of the cathode sheath thickness outside the active, emitting spot location.

The introduction of *reactive* gas in the system has two main effects. First, it will change the cathode surface by "poisoning," i.e., compound formation, which can greatly promote the ignition of type 1 spots (Chapter 3). Second, the eroded plasma will interact with the gas while expanding. For both noble and reactive background gases, the ions produced at the cathode emission centers interact with the much slower background gas atoms and molecules. Ionization of

background gas and a reduction of the metal ion charge state and kinetic energy depend on the kind of metal ions and the pressure and type of gas. As a rule of thumb, when the background pressure approaches $\sim 10^{-4}$ Torr ($\sim$10 mPa), the mean free path becomes comparable to the size of the coating system, and thus an influence of the gas on the metal plasma can be expected.

The interaction between an expanding arc plasma and neutral background gas has been described theoretically using different approaches. Meunier and Drouet found that the plasma and background gas occupy quite distinct volumes [27], which could be associated with the formation of a shock front [28]. In a series of studies, Gidalevich and co-workers [7, 29, 30] suggested that the front of the explosively formed cathode plasma compresses the background gas, accelerating the neutral gas while decelerating the plasma, until mixing occurs. The process was described as a "porous snowplough."

The shockwave and snowplough model is not universally used or accepted; the reduction of metal ion energies and charge state pointed to elastic and charge exchange collisions without the assumption of a shock front [31, 32, 33].

4.3 Ion Charge State Distributions

4.3.1 Experimental Observations

The charge state distributions (CSDs) of ions at high vacuum conditions have been extensively studied using mass-to-charge spectrometry [34, 35, 36, 37, 38, 39, 40, 41, 42, 43, 44]. The most complete table of experimental charge state distributions of vacuum arcs was given by Brown [42] and more recently by Anders and Yushkov [44]. While most investigations are limited to elemental cathodes, there are also a few studies on multi-element plasmas from alloy cathodes [45, 46]. It has been found that ion charge states are shifted to higher values by external magnetic fields [39, 40, 47] and by high discharge currents [48]; the latter effect is likely due to the self-magnetic field.

All of the ion charge state measurements were done in very large distances from the cathode spot, as viewed on the length scale of the cathode spot size. As the plasma expands into vacuum, density changes by expansion are much larger than density changes caused by inelastic collisions (like ionization and recombination). Therefore, it is reasonable to adopt a model in which those changes by inelastic collisions are neglected altogether, i.e., the charge state distribution is considered to be "frozen."

Since the CSD is originally established by frequent collisions in the vicinity of the spot, the freezing assumption suggested that freezing occurs when the plasma expands, i.e., when the plasma density and temperature drop and the collision rates between particles are dramatically reduced. In the most simplified picture, the plasma transitions from equilibrium near the spot to non-equilibrium far from the spot in a rather abrupt manner ("instantaneous freezing"), which will be considered in the next section. However, as will be shown later, the presence

of neutrals (from sources other than the cathode spot) can significantly "skew" the charge state and ion energy distributions as expansion progresses. Therefore, while the Saha freezing model is a helpful tool in understanding distribution functions, it oversimplifies reality.

Over the past decades, several attempts [43, 49, 50, 51, 52] have been made to reproduce the observed charge state distributions by modeling the plasma near the cathode spot using Saha equations, which are the ionization–recombination balance equations under equilibrium conditions. Baksht et al. [49] spectroscopically investigated nanosecond discharges of aluminum in vacuum and found that a transition to non-equilibrium occurs rapidly when the plasma expands into the vacuum ambient. Pustovit and co-workers [43] used mass spectrometry for In, Ga, and Sn cathodes; their conclusions are in agreement with the physical picture established by Baksht et al. [49]. Radic and Santic [50] and Hantzsche [52] used the Saha approach to determine reasonable ranges of density and temperature near the cathode spot for Cd, Mg, Al, Ni, Mo, and Cu. All authors found very high values for plasma density (of order 10^{26} m^{-3}) and temperature values up to 5 eV. Interestingly, all of the investigators concluded that there is reasonable agreement between experiment and theory but pointed out that further research is needed. Radic and Santic as well as Hantzsche noted that the Saha-determined temperatures are higher for higher-charged ions than for just single or double charged ions, indicating that the assumption of equilibrium is not quite adequate. In the next sections, the Saha approach is presented in greater detail, followed by a generalization and discussion of conditions when the Saha freezing model is not applicable.

4.3.2 Local Saha Equilibrium: The Instantaneous Freezing Model

In the model of "instantaneous freezing," one assumes that the transition from equilibrium near the spot to non-equilibrium far from the spot occurs very rapidly. As with all models, there are advantages and limitations. The main advantage is that the observable charge state distributions far from the spot can be reduced to *equilibrium* distributions that can relatively easily be calculated. It is the simplest model for calculating charge state distributions.

The following assumptions are made that allow calculations of charge state distributions for all metallic elements of the Periodic Table:

(i) Local thermodynamic equilibrium can be assumed in the vicinity of cathode spots, specifically the ionization and recombination reactions are balanced and can therefore be described by Saha equations (named after the Indian physicist Meghnad N. Saha).
(ii) The plasma expands and – at a certain distance from the spot center – transitions rapidly into non-equilibrium.
(iii) The plasma's transition into non-equilibrium occurs almost instantaneously, and therefore "frozen" charge state distributions far from the spot reflect the plasma conditions at the freezing location.

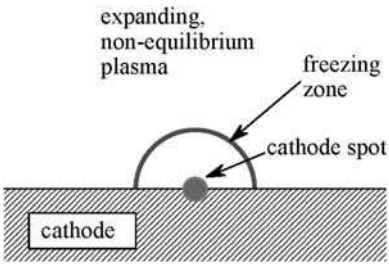

Fig. 4.4. Schematic illustration of the instantaneous freezing model

(iv) At the freezing location, the plasma is already sufficiently expanded that it can be treated as ideal or weakly non-ideal plasma, and therefore the Saha equations can be written in Debye–Hückel approximation.
(v) The fluctuations of plasma temperature and density at freezing can be averaged allowing us to introduce an "effective freezing temperature" and an "effective freezing density" for each element. The ratios of differently charged ions freeze almost simultaneously, and therefore only *one* effective freezing temperature and *one* effective freezing density are needed.

The last assumptions will be relaxed in the next section. Figure 4.4 illustrates the situation: the line indicating a half-sphere is the zone of "instantaneous freezing."

Ion charge state distributions are the result of inelastic, ionizing, or recombining collisions of electrons with "heavy" plasma particles, i.e., neutral atoms, singly charged ions, doubly charged ions, etc. In equilibrium, collisions are sufficiently frequent so as to cause numerous ionizing and recombining events per unit time. As a result, the ionization rate equals the recombination rate; the ratios between the fractions of various charged particles become time independent. The dense spot plasma provides the conditions for equilibrium (sufficiently frequent collisions). Ionization and recombination events can be treated like chemical reactions, and the corresponding steady-state reaction rate equations are known as Saha equations [53, 54, 55]:

$$S_Q \equiv \frac{n_e\, n_{Q+1}}{n_Q} = \Lambda_B^{-3}\, \frac{2\,\Sigma_{Q+1}(T)}{\Sigma_Q(T)}\, \exp\left(-\,\frac{E_Q - \Delta E_Q}{kT}\right), \tag{4.10}$$

where n_e and n_Q are the densities of free electrons and ions of charge state Q, respectively, $Q = 0$ for neutral atoms, $Q = 1$ for singly ionized ions, etc., with $Q_{\max}$ the maximum charge state present in the plasma; $\Sigma_Q(T)$ is the temperature-dependent partition function of ions of charge state Q, k is the Boltzmann constant, T is the temperature, and

$$\Lambda_B = h \Big/ (2\pi\, m_e\, kT)^{1/2} \tag{4.11}$$

is the thermal De Broglie wavelength, and E_Q is the ionization energy of the Q-fold charged ion. The lowering of the ionization energy, ΔE_Q, reflects the particle interaction or non-ideal nature of the plasma. For weakly non-ideal plasmas, the lowering of the ionization energies can be described in Debye-Hückel approximation [54] by

$$\Delta E_Q = \frac{(Q+1)\, e^2}{4\pi\, \varepsilon_0\, (\lambda_D + \Lambda_B/8)}, \tag{4.12}$$

where

$$\lambda_D = \left[\varepsilon_0\, kT/e^2 \left(n_e + \sum_Q Q^2\, n_Q \right) \right]^{1/2} \tag{4.13}$$

is the generalized Debye length and ε_0 is the permittivity of free space. The lowering of the ionization energy can be neglected for expanded plasmas but is significant for dense plasmas. The Debye-Hückel approximation becomes invalid when the plasma is extremely dense (strongly non-ideal, when ΔE_Q is comparable to E_Q).

The partition function reflects the structure of the electron shells and is defined by the equation [56]

$$\Sigma_Q(T) = \sum_{s=1}^{s=s_{\max}} g_{Q,s}\, \exp\left(-\frac{E_{Q,s}}{kT} \right), \tag{4.14}$$

where s is the level index ($s = 1$ is the ground state, $s_{\max}$ is the highest excited level which is bound), $g_{Q,s}$ and $E_{Q,s}$ are the statistical weight and the energy of level s of an ion with charge state Q, respectively. The statistical weight $g_{Q,s} = 2J_{Q,s} + 1$ can be obtained using the total angular momentum $J_{Q,s}$ given in spectroscopic tables. The system of Eqs. (4.10), (4.11), (4.12), (4.13) and is completed by the charge-neutrality condition:

$$n_e = \sum_Q^{Q_{\max}} Q\, n_Q. \tag{4.15}$$

The percentages of ion charge states are expressed as particle fractions of the total *ion* density (i.e., without neutrals):

$$f_Q = \frac{n_Q}{\sum_{Q'=1}^{Q'_{\max}} n_{Q'}} \cdot 100\%, \tag{4.16}$$

allowing us a direct comparison with the experimental results. The mean ion charge state is defined by

$$\overline{Q} = \sum_{Q=1}^{Q_{\max}} Q\, n_Q \Big/ \sum_{Q=1}^{Q_{\max}} n_Q. \tag{4.17}$$

This model can be used to assume specific combinations of temperature and total density at the freezing zone, calculate the charge state distribution, and compare the result with the experiment. In this approach, the measurements of the ion charge state distribution far from the spot can be used as a diagnostic tool for the plasma parameters at the freezing zone. The freezing zone is an "event horizon" beyond which we cannot probe the plasma using charge state distribution information. Provided the freezing assumption is good, the observable vacuum arc charge state distributions can be understood as relics of microexplosions, not unlike the cosmic three-Kelvin radiation is a relic of the Big Bang. We realize that the concept of "instantaneous freezing" is equivalent to a sharp, well-defined event horizon of "micro bangs."

Using the experimental data from Brown's work [42] (Table B5), and the ionization energies of Table B3 (both Appendix B), best fits were made for most metals of the Periodic Table, giving the effective temperature and density at the freezing zone [57]. The results are arranged in a Periodic Table (Table B6). For most elements, a relatively good self-consistent fit of calculated distributions and experimental data could be found, justifying the approach. However, in some cases, the observed distributions are substantially broader than any fit that can be constructed based on the instantaneous freezing model. There is a need to refine or replace the model, as discussed in the next sections.

4.3.3 Partial Saha Equilibrium: The Stepwise Freezing Model

So far it was assumed that the ratios of all ion charge states freeze at the same time. A more realistic assumption is that the Saha equilibrium is gradually lost as the plasma transitions into non-equilibrium. In the model of partial local Saha equilibrium (PLSE), the various ion charge state ratios are assumed to freeze stepwise at different plasma conditions, that is, at different distances from the spot center [58].

Partial local Saha equilibrium can be explained in analogy to the well-known model of partial local thermodynamic equilibrium (PLTE), which is often used in optical emission spectroscopy [53]. Griem [59] defines a homogeneous, steady-state plasma system in *complete* thermodynamic equilibrium (CTE) when all distributions of the various bound states and ionization stages are in equilibrium and the velocities of atoms, ions, and electrons are determined by Boltzmann distributions of the same temperature. The parameters may change gradually in space and time, which leads to the concept of complete *local* thermodynamic equilibrium (CLTE).

Real plasma systems are rarely in CLTE, and thus more complicated models must be employed. One approach is to consider only part of the system, for instance a group of energy levels for optical transitions when performing plasma spectroscopy. Here, the relations between the electron population densities of the various bound states of an atom or ion are of interest. The energy level structure of bound states of an atom or ion is shown schematically on the left of

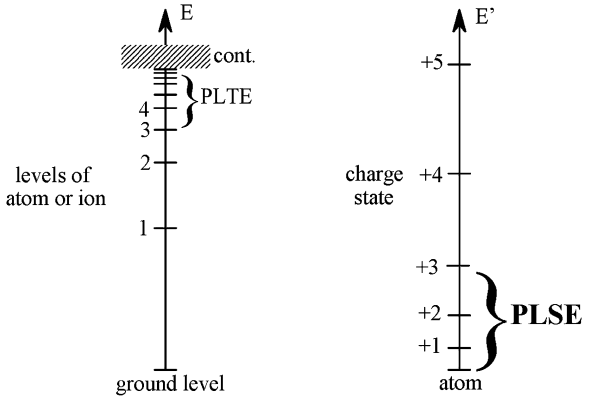

Fig. 4.5. The energy level structure of bound states of an atom or ion is shown schematically on the *left*, and the sequence of ionization energies on the *right*. Closely spaced energy levels can be in partial local thermodynamic equilibrium (PLTE), and charge states separated by a relatively small ionization energy can be in partial local Saha equilibrium (PLSE)

Figure 4.5. The largest energy gap is usually between the ground state and the first excited state. The energy gaps between levels decrease as the free electron continuum is approached. The populations of all energy levels are in equilibrium if the electron density is sufficiently high due to high rates of collisions [55, 59]. As the electron density decreases, the energy level with the largest gap (usually the ground state) will not have enough transitions to balance population and depopulation of this level, and therefore that level will not be in equilibrium with the remaining system. The remaining system, i.e., the excited bound states and the electron continuum, is still in *partial* local thermodynamic equilibrium (PLTE). With further decreasing electron density, more and more levels will not be in PLTE, until only the highest, closely spaced levels remain in PLTE with the electron continuum.

According to the *Principle of Detailed Balancing*, one can readily balance the forward and reverse reactions if collisional processes are more important than radiative decay and recombination. A modified Boltzmann formula for excited states and a modified Boltzmann–Saha equation relate the densities of ions with charge state Q to the upper levels of ions with charge state Q–1 [55].

Now, looking at charge state spectrometry, the Principle of Detailed Balancing can be used to consider ionization and recombination reactions in analogy to excitation and de-excitation reactions in optical spectroscopy. The PLTE concept allowed us to calculate the population ratios of excited states in the absence of CLTE. Analogously, the concept of PLSE gives the ratio of charge states in the absence of complete Saha equilibrium.

The ionization–recombination balance equations are

$$\frac{\partial n_Q}{\partial t} = n_{Q+1}\, n_e^2\, \alpha_{Q+1,Q} - n_Q\, n_e\, \beta_{Q,Q+1} \quad \text{for } Q = 0, \tag{4.18}$$

$$\begin{aligned}\frac{\partial n_Q}{\partial t} = {} & n_{Q-1}\, n_e\, \beta_{Q-1,Q} + n_{Q+1}\, n_e^2\, \alpha_{Q+1,Q} - n_Q\, n_e\, \beta_{Q,Q+1} \\ & - n_Q\, n_e^2\, \alpha_{Q,Q-1} \text{ for } Q \geq 1,\end{aligned} \tag{4.19}$$

where β and α are the ionization and recombination coefficients, respectively. We follow here the notation of Biberman et al. [60] who defined the coefficients in such a way that they are density independent (except for the non-ideal plasma correction). This is convenient since it shows, for example, that recombination is determined by three-body collisions; inelastic two-body collisions are unlikely to satisfy energy *and* momentum conservation. According to the Principle of Detailed Balancing, radiative ionization and recombination are neglected. The first two terms on the right-hand side of (4.19) describe the increase of ion density of charge state Q by ionization (from Q–1) and recombination (from $Q+1$), and the other two terms describe the decrease by ionization (to $Q+1$) and recombination (to Q–1). From (4.19), the characteristic time of change by ionization and recombination reactions is

$$\Delta t = \frac{\Delta n_Q}{n_{Q-1}\, n_e\, \beta_{Q-1,Q} + n_{Q+1}\, n_e^2\, \alpha_{Q+1,Q} - n_Q\, n_e\, \beta_{Q,Q+1} - n_Q\, n_e^2\, \alpha_{Q,Q-1}}. \tag{4.20}$$

As long as the plasma is in Saha equilibrium (near the spot), we can use the Saha factors S_Q defined in (4.10) and obtain

$$\Delta t = \frac{\Delta n_Q}{n_Q} \left(\frac{n_e^2}{S_{Q-1}} \beta_{Q-1,Q} + S_Q\, n_e\, \alpha_{Q+1,Q} - n_e\, \beta_{Q,Q+1} - n_e^2\, \alpha_{Q,Q-1} \right)^{-1}. \tag{4.21}$$

From this expression we can derive the characteristic times of the individual processes and their dependence on the charge state Q if we know the charge state dependence of the ionization and recombination coefficients. Following Biberman [60] we have

$$\beta_{Q,Q+1}(E_Q, T) \sim \frac{\Sigma_{Q+1}}{g_Q} \exp\left(- \frac{E_Q - \Delta E_Q}{kT} \right) \Big/ (kT)^3, \tag{4.22}$$

and

$$\alpha_{Q,Q-1} \sim (kT)^{-9/2}. \tag{4.23}$$

The first term in the denominator of (4.21) is independent of Q, the second and third terms are proportional to $\exp\left(-\left(E_Q - \Delta E_Q\right)/kT\right)$, and the last term is independent of Q. One can conclude that the characteristic times for recombination *to* charge state Q and for ionization *from* charge state Q increase with Q. Therefore, ions of higher charge will tend to be in non-equilibrium sooner than ions of lower charge state.

When we apply this result to the expanding spot plasma we realize that the highest ion charge states (such as +5 and +4) will leave the Saha equilibrium system first, while lower charge states (such as +3, +2, +1, and 0) are still in

equilibrium. This situation of PLSE is illustrated on the right side of Figure 4.5. With decreasing density and temperature, the states +3, +2, +1 will successively drop out of PLSE until "freezing" is completed. The freezing zone has now a finite, non-zero thickness because the ion charge states do not freeze simultaneously but successively. This is one explanation why for some materials one cannot find a single combination of temperature and total density for which the set of Saha equations reproduces the experimental charge state distribution.

Because freezing density and temperature cover a *range* of values, more input information is required than the ion charge state distribution to find unique solutions. A quantitative analysis of PLSE has, for instance, to deal with the energy balance, i.e., the rate at which the temperature drops while the plasma is expanding. The concept of PLSE can be tested by comparing Saha calculations for different temperatures with experimental charge state distribution data, as was done for hafnium [58]. Reasonable ranges of temperature and density of the freezing zone could be identified ($3.6 \rightarrow 2.6\,\text{eV}$ and $8\times10^{25}\,\text{m}^{-3} \rightarrow 1\times10^{24}\,\text{m}^{-3}$), cf. Figure 4.6. Additionally, charge state distributions of not-yet-used cathode elements can be predicted in an approximate manner [61]. Since the development of the model in the mid-1990s, the charge state distributions of previously not measured elements, boron [62] and thallium [63], have been measured, and good agreement with the predictions has been found.

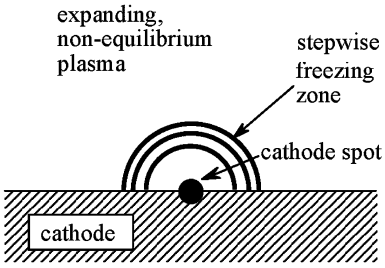

Fig. 4.6. Illustration of stepwise freezing and finite thickness of the freezing zone in accordance with the PLSE model

4.3.4 Plasma Fluctuations

Due to the explosive nature of plasma generation it is not surprising that all plasma parameters are "noisy," i.e., they fluctuate around average values. The "noise" of plasma parameters can be greater than the effects under investigation. Therefore, literature data are usually based on measurements that have been repeated many times and results were presented for *average* values. For example, data for the burning voltage [64], plasma density [65, 66], electron temperature [57], ion velocity [44], ion charge state distribution [42, 67], and ion erosion rate [68] are cathode material and arc current-dependent average data.

A few studies focus on the fluctuations themselves and give information on possible instantaneous deviations from average values. As an example of fluctuating plasma parameters, one may look at the instantaneous ion charge state distribution observed at a fixed distance from the cathode spot. The distribution can be conveniently recorded using a vacuum arc ion source [58]: Ions were extracted from the flowing plasma and analyzed using a time-of-flight spectrometer [69]. The measured sample is obtained by putting a rectangular voltage pulse to a system of gate plates, allowing us to take a 200-ns sample of the ion beam, which is directed to the detector.

It is important to stress that these sample-to-sample fluctuations are not due to uncertainties of the measuring principle but due to the inherently fluctuating nature of the plasma from which the ions are extracted. Strictly speaking, even the sample measurement represents an average, too, taken over the finite time resolution, which is determined by the gate pulse duration of 200 ns.

Figures 4.7 and 4.8 show some result of the experiment for Ag and Au plasma. One can see that gold exhibits relatively small scattering of mean ion charge state data while the data for silver scatter significantly. Scattering of mean ion charge state is the result of processes affected by many specific parameters and the statistics of spot ignition. Since spot parameters have been correlated with the cathode material parameters (see Cohesive Energy Rule, Chapter 3), one might also look for correlations of cohesive energy and fluctuation statistics. In Figure 4.9 the standard deviations of the measured mean ion charge states are plotted as a function of the cohesive energy of the cathode

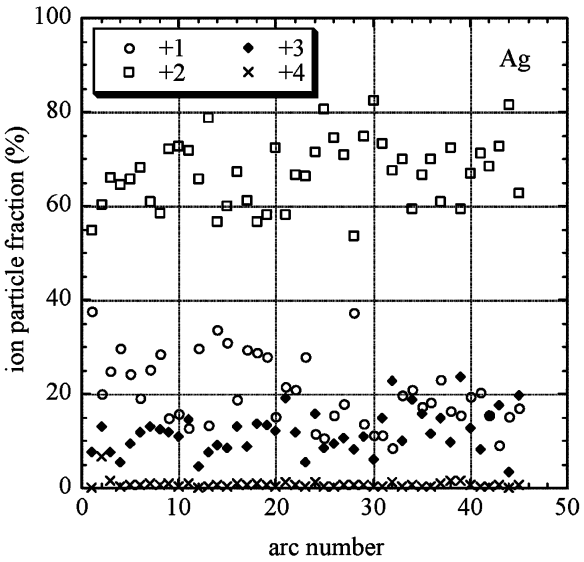

Fig. 4.7. Determination of the mean ion charge state of silver plasma by time-of-flight spectroscopy: Each data point is one measurement with an integration time of only 200 ns

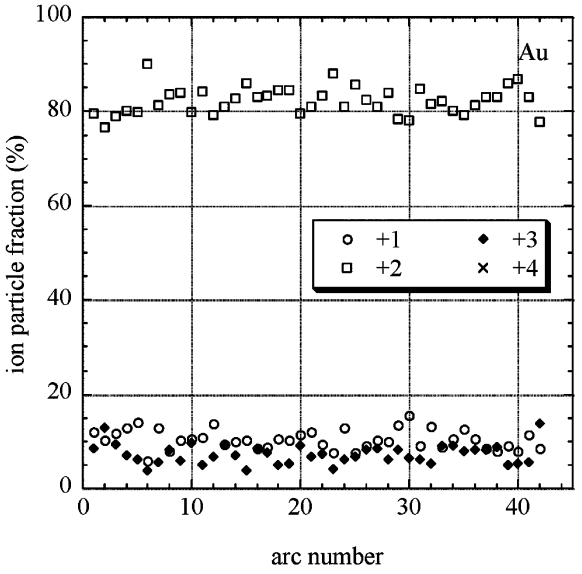

Fig. 4.8. As Figure 4.7 but with gold plasma

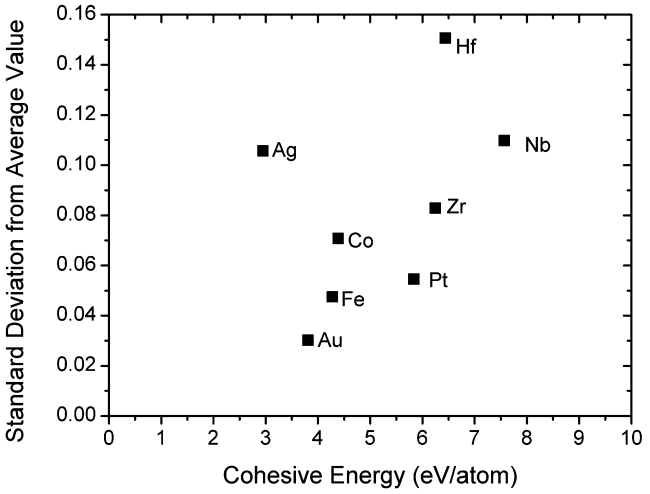

Fig. 4.9. Standard deviation of the mean ion charge state as a function of cohesive energy for some cathode materials. (Data from [58])

material. One can see some correlation, although the result is clearly affected by other parameters.

For coating applications, one may argue that the fluctuations are of minor concern because the coating process is integrating over the deposition time. Indeed, one can obtain rather reproducible coatings using the cathodic arc

process. Yet, for precision coatings, the fluctuations represent an issue. This refers not only to obtaining precise thickness but also to the energetics of the process, especially when bias is involved. The energy gain in the substrate's sheath is directly proportional to the charge state (Chapter 8). When ions are extracted from the plasma to form a beam, the plasma fluctuations directly translate to fluctuations of the ion beam [70, 71, 72, 73].

4.3.5 Effect of an External Magnetic Field

A magnetic field impedes the motion of charged "magnetized" particles perpendicular to the field lines (see Section 4.2.2), and therefore the dense plasma does not transition rapidly into non-equilibrium. When a magnetic field is present, the PSE/freezing model is not a good approximation; rather, the interaction between charged particles is reduced in a more gradual way as they move away from the spot. Ionization and recombination reactions occur in rather large distances from the spot. Since plasma expansion is much reduced, the electron temperature reduction will not occur like it did in the adiabatic expansion case. Consequently, higher ion charge states are observed in the presence of magnetic fields [40, 41, 44, 67, 74, 75].

Figure 4.10 illustrates that magnetization of the electrons has an immediate effect on the enhancement of charge states, whereas very strong magnetic fields do not enhance the charges much further. Figure 4.11 provides a closer look at

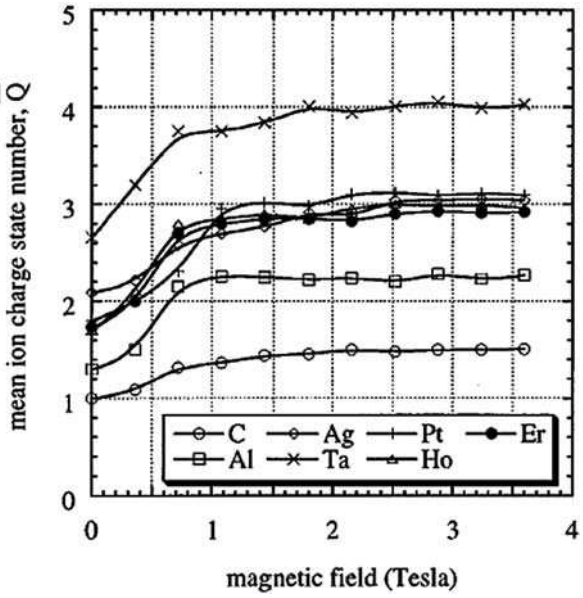

Fig. 4.10. Enhancement of the average ion charge states for cathodic arcs in vacuum (arc current 300 A), charge states measured with a time-of-flight spectrometer. (From [74])

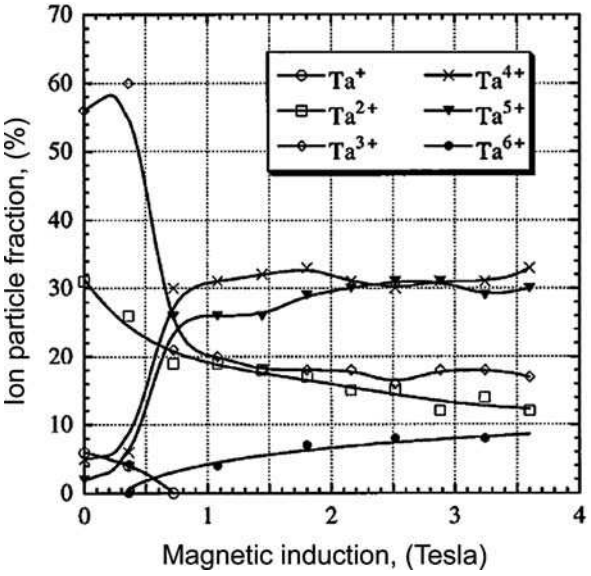

Fig. 4.11. Ion charge state distribution for tantalum arc plasma at 300 A as a function of the magnetic field. (From [74])

one of the elements, tantalum, by giving detailed information on the individual charge states as a function of magnetic field. Also here one can see that the greatest effect is already obtained for field strength less than 1 T. One should note, however, that even 1 T is a rather high field strength. The region of high field strength is accessible by either going to pulsed operation, as done in the cited work, or by using superconducting coils.

The arc itself generates a magnetic field which starts to affect plasma expansion and plasma composition when the arc current exceeds about 300 A. It was experimentally found that the ion charge state distributions are independent of arc currents as long as the current is low [41], while very high arc currents ($>$ 1 kA) shift the charge distribution to higher values [67]. Figure 4.12 shows the average charge state for copper plasma, measured at 60 and 200 μs after arc ignition, as a function of arc current in the absence of an external magnetic field. Self-field effects are apparent only at high arc currents. Oks and co-workers [67] used the arc current to drive a magnetic field coil. At high currents, both the "external" magnetic field (via the coil) and the self-field (generated by current in the discharge) contribute to the magnetic field effect. Also in this experiment, the greatest effects were already seen at moderate currents (Figure 4.13).

The enhancement in charge states must of course be related to the energy balance in the cathodic arc plasma. Since the arc current was kept constant (determined by the impedance of the power supply circuit), it was clear that the arc burning voltage, measured directly between cathode and anode, might be higher such as to provide greater power to the discharge. Equivalently, one may

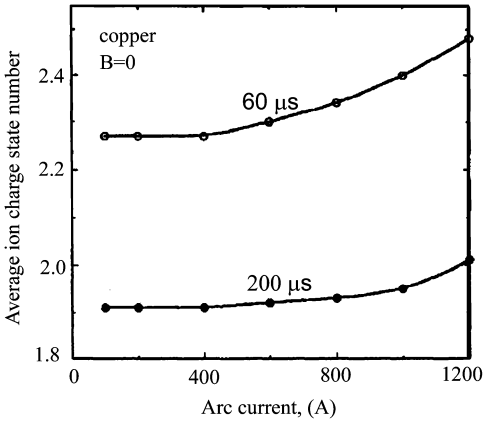

Fig. 4.12. Average charge state for copper plasma, measured at 60 and 200 μs after arc triggering, as a function of arc current in the absence of an external magnetic field. (From [67])

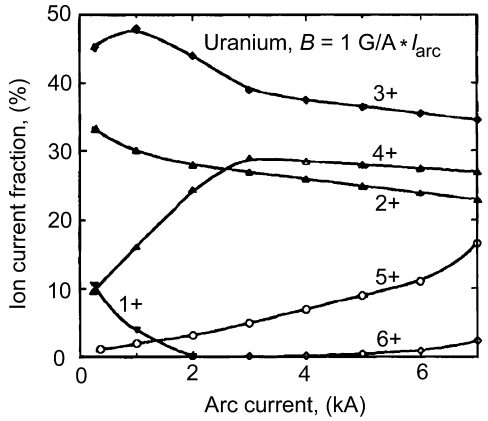

Fig. 4.13. Ion charge state distribution of uranium plasma as a function of arc current and "external" magnetic field: the discharge current was used to drive a magnetic field coil with 10^{-4} T/A (10^{-4} T/A = 1 kG/kA). (From [67])

say that the impedance of the plasma is increased. Figure 4.14 shows the charge state distribution for carbon ions as a function of arc current (coupled with an external magnetic field). Remarkably, the mean ion charge state of carbon ions can be greater than one under these conditions (Figure 4.15). A correlation between mean ion charge state and impedance can be established (Figures 4.15 and 4.16).

Krinberg [76] calculated that the electron temperature in the near-cathode region is proportional to the arc current and inversely proportional to the coefficient of erosion of the cathode material, in good agreement with observation.

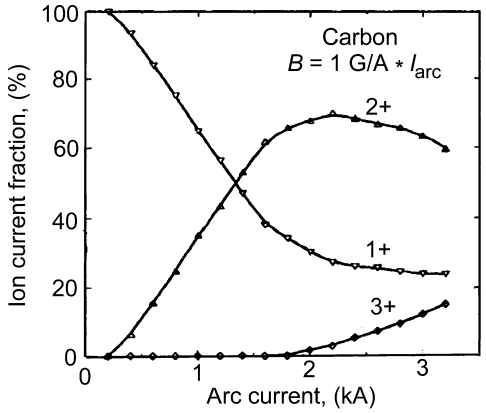

Fig. 4.14. As Figure 4.13 but for carbon plasma

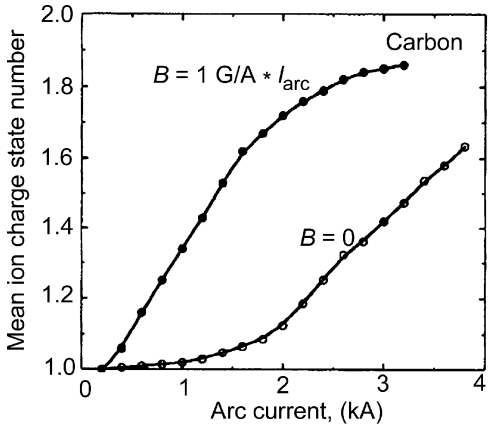

Fig. 4.15. Average carbon ion charge state as a function of arc current. *Upper curve*: arc current was connected to a magnetic field coil of 10^{-4} T/A. *Lower curve*: magnetic field coil was disconnected; only the self-field played a role in changing the impedance

4.3.6 Effect of Processing Gas

The plasma–gas interaction leads to a reduction in the average ion charge state through several processes as soon as the pressure is increased, and the mean free path is comparable or shorter than a characteristic system length, such as the distance between cathode and substrate. Figure 4.17 shows the example of aluminum plasma expanding in either argon or oxygen. Charge exchange collisions between multiply charged ions and neutrals are most relevant for the reduction of

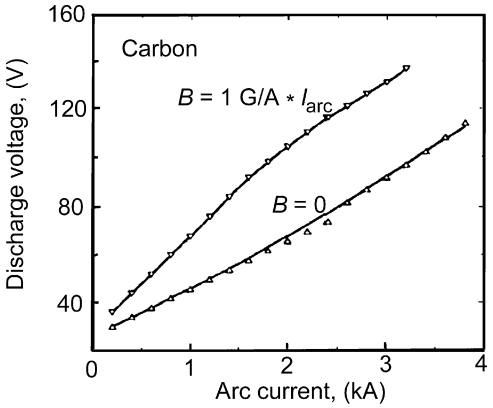

Fig. 4.16. Arc voltage, as measured between anode and cathode, for the carbon arc as shown in Figure 4.15. (From [67]. Note: the voltage drop inside the carbon cathode rod is included, that is, not all of the measured voltage is related to the impedance of the carbon plasma, see discussion in [64])

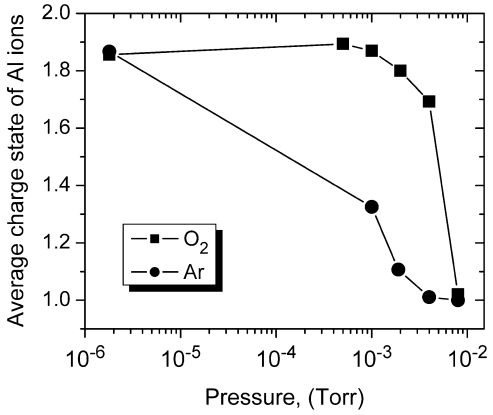

Fig. 4.17. Example of metal plasma–gas interaction: the decrease of the average charge state depends on the gas, here argon or oxygen. (From [87])

the mean charge state of metal ions. Higher-charged ions are especially affected. The other main collisional process is electron–ion recombination, which is important at higher pressures because gas atoms serve as the third body in three-body recombination. A third body is generally needed to simultaneously satisfy energy and momentum conservation in the collisional process [77].

While the ion charge of the metal plasma is reduced, partial ionization of the processing gas occurs, either via direct electron impact ionization, which is especially relevant in the presence of a magnetic field, or via the above-mentioned charge exchange collisions.

The interaction of the arc plasma with background gas has been investigated by several researches [78, 79, 80, 81, 82, 83, 84, 85, 86, 87]; the effects on ion charge states and energies are so important that a larger section will be devoted to a more detailed discussion (Section 4.5).

4.4 Ion Energies

At the end of Chapter 3, a correlation was established between the mean ion energy and the cohesive energy of the cathode material (Table B8). Most of the ion acceleration was accomplished very close to the cathode spot, and that the local energy balance at the spot greatly influences the ion energies observed far from the spot, provided we consider plasma expansion into vacuum. The ion energies can be greatly altered when a magnetic field is present or when ions collide with background gas molecules. In this section, we first further explore ion energy distribution functions and move on to the cases of magnetic field and background gas effects.

4.4.1 Ion Energy Distribution Functions for Vacuum Arcs

The cathodic arc plasma plumes from the cathode spot into the processing chamber. The flow can be described as mesosonic because it is subsonic for electrons:

$$v_{e,drift} < (kT_e/m_e)^{1/2}, \tag{4.24}$$

and, conversely, supersonic for ions:

$$v_{i,drift} > (kT_e/m_i)^{1/2}. \tag{4.25}$$

When using the term *sound velocity* it should be remarked (a) that the electron sound waves are exponentially damped for low frequencies, $\omega < \omega_{pl}$, where ω_{pl} is the plasma frequency, and undamped for $\omega > \omega_{pl}$; and (b) that the *electron* temperature appears in the formula for the *ion* sound velocity (for a more general derivation see text books on plasma waves such as [88, 89]). Since electrons and ions stream approximately with the same drift velocity, one can see that the distinction in subsonic versus supersonic is rooted in the difference of electron and ion mass.

Electrons are generally treated as having a thermal distribution. The fact that they drift with the plasma could be taken into account by a small shift of their Maxwell distribution. Such shift is generally neglected and one can write

$$f(v) = 4\pi\left(\frac{m}{2\pi kT_e}\right)^{3/2} v^2 \exp\left(-\frac{mv^2}{2kT_e}\right). \tag{4.26}$$

The situation is much more complicated for ions. One may assign a temperature or thermal energy, kT_i, to the ions using a frame of reference moving with

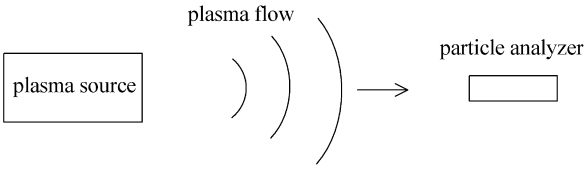

Fig. 4.18. Schematic of plasma flow and detector position for energy measurements

the center of mass of the plasma. The description of ion motion can be thought of as being composed of a thermal motion and a drift as seen in a laboratory frame of reference. In practice, one looks at the distribution functions measured in one direction, usually with the detector facing the incoming plasma flow (Figure 4.18), thereby getting information on the drift and thermal spread. The ion distribution functions are then shifted Maxwellian distributions which can be expressed as [83, 87, 90, 91]

$$\phi_i(E) = C_s\, E \exp\left[-\left(\sqrt{E} - \sqrt{E_{dir}}\right)^2 \Big/ kT_i\right], \tag{4.27}$$

where C_s is a scaling constant and E_{dir} is the kinetic energy of the directed motion.

Some studies just deal with the determination of the most-likely velocity for a given cathode material, v_i^*, i.e., the peak value of the ion velocity distribution function, which can readily be converted into the most-likely ion energy according to $E_{kin}^* = m_i\left(v_i^*\right)^2 \Big/ 2$. As Rosén and co-workers pointed out [92], the most-likely values of velocity and energy are not the average values because the distribution functions are usually not symmetric but have a long tail. More information is provided by those studies that deal with the complete velocity or kinetic ion energy *distribution functions* [35, 36, 91, 93, 94, 95]. Distribution functions of kinetic energy $\phi(E)$ or directed velocity $f(v)$ are equivalent and can be converted [96]:

$$\phi(E) = \frac{v(E)}{m} f[v(E)], \tag{4.28}$$

with $v(E) = (2E/m)^{1/2}$.

To determine the kinetic ion energies or drift velocities, one usually employs either (i) time-of-flight (TOF) techniques [44, 97, 98, 99, 100, 101] or (ii) electrostatic field methods [35, 36, 83, 91]. While TOF measurements deliver velocity information, electrostatic field methods provide information on energy.

The simplest case of TOF measurements does not use charge and mass resolution. The drift time of the plasma flow over a given macroscopic distance is measured. To create time markers, the plasma production can either be kept short [97], or be modulated by oscillating the arc current [44] or superimposing

short current spikes [102]. Because peaks in the ion signal are used, the information obtained is about the most-likely drift velocity (the maximum of the velocity distribution).

By using rapid arc termination by a crowbar (arc bypass) switch, the derivative of the ion current signal can be used to determine the charge-state-averaged velocity distribution function in the flow direction [95]. Using a 2-m-long plasma drift TOF section, a comprehensive collection of charge-state-averaged velocity distributions was created. Some of them are displayed in Figure 4.19. Each of these distributions was derived by averaging 100 measurements under the same conditions, capturing 50,000 data points per measurement [95]. Because the TOF principle does not depend on the plasma potential, the error associated with ion acceleration at the detector sheath is negligible (in contrast to electrostatic energy measurements, as discussed below).

A striking feature is that there is *one* distinct peak in the distribution functions, even as there was no resolution of charge states in these measurements. This shows that most ions drift with approximately the same velocity. This is true for many elements, even as they have very different charge state distributions. This supports the notion that ions are hydrodynamically accelerated at cathode spots, as opposed to acceleration by the electric field of a potential hump. Hence, the hump is small or non-existent. Acceleration by the hump would have manifested itself through the appearance of peaks in the velocity distribution when different charge states are present in the plasma. The distributions have a large error at high velocity (kinetic energy) because they are obtained by using the first derivative of a signal that is noisy despite the fact that an average over 100 measurements was used [95]. Therefore, the individual peaks seen at high energy should not be over-interpreted: they only indicate that a high-energy tail may exist.

Charge-state-resolved information on the most-likely velocities of ions in the flow direction can be obtained by combining the plasma drift with an ion beam time-of-flight system [94, 100]. Such experiments indicated that all ions, regardless of their charge state, drifted with about the same velocity.

Electrostatic field techniques come in various embodiments such as the retarding field analyzer (RFA) [103], or curved sector analyzer (like the EQP by HIDEN Ltd), or cylindrical mirror analyzer (CMA, like the PPM422 by Pfeiffer Vacuum). The RFAs have the disadvantage that they cannot discriminate between ions of different masses and charges, and the energy distributions are therefore averaged over charge and mass of all charged species. The so-called plasma monitors combine the electrostatic energy analyzer with a mass spectrometer. Strictly speaking, these devices measure energy/charge and mass/charge of the selected particle species. Typically, there is an entrance mesh (for RFAs) or a single, small entrance aperture (for plasma analyzers).

The housing and entrance aperture of the energy analyzer are commonly grounded, whereas the plasma potential is very likely not exactly at ground. Therefore, a sheath forms right at the entrance of the analyzer such that positive

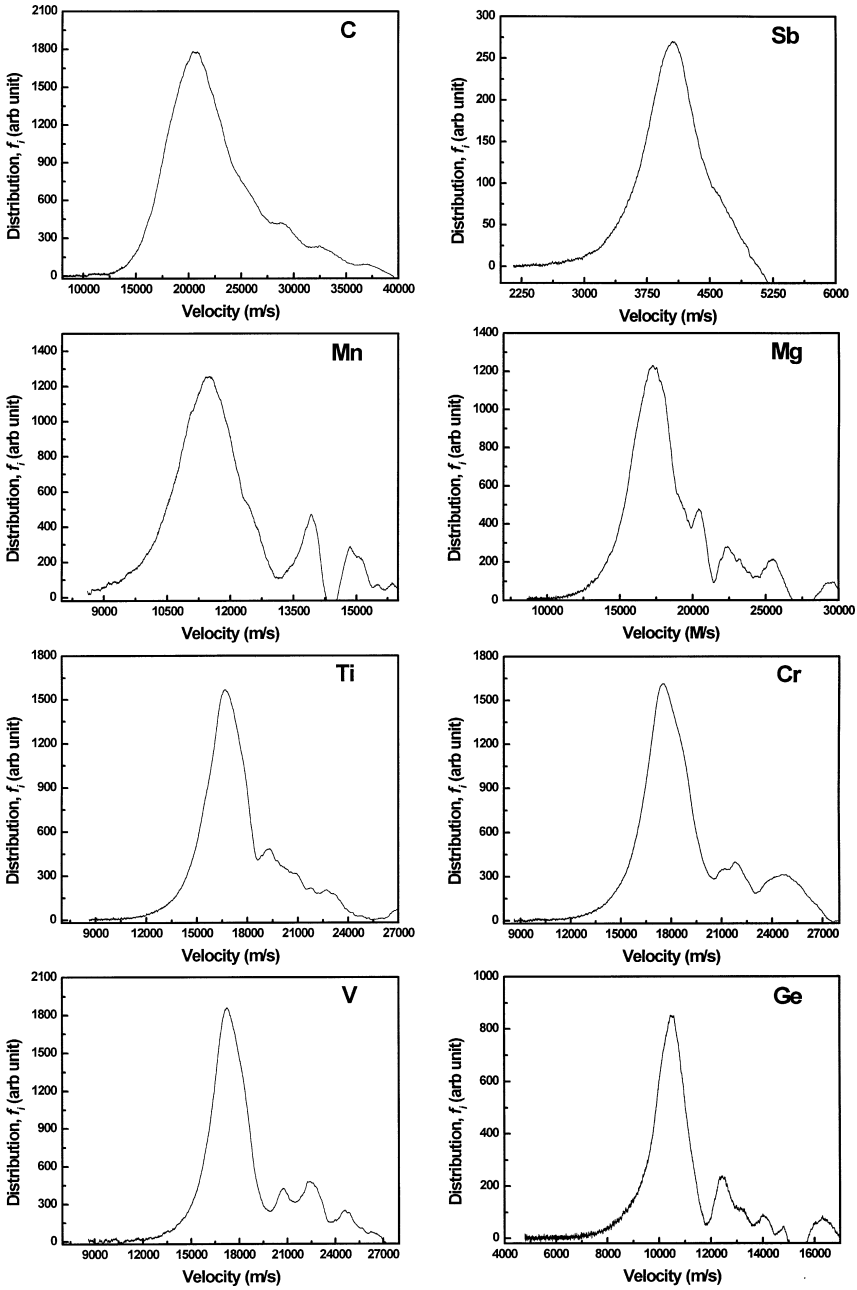

Fig. 4.19. Ion velocity distributions functions obtained by the time-of-flight method using rapid arc termination (for more details see [95]). Vacuum arc, 100 A, base pressure 4×10^{-4} Pa, no charge state resolution. The principle used implies a small error at low energies but increasingly greater error at high energy; peaks at high energy can be artifacts of the measurement

ions will be accelerated for $V_{pl} > V_{entrance}$, or decelerated for $V_{pl} < V_{entrance}$. For $V_{pl} > V_{entrance}$ the gain in the kinetic energy at the analyzer is

$$\Delta E_{kin}(Q) = Qe\left(V_{pl} - V_{entrance}\right), \tag{4.29}$$

provided there are no collisions in the sheath; Q is the charge state number and e is the elementary charge. The charge-state-dependent gain of the energy can be described as a change of the ion's potential energy to kinetic energy. Taking into account this gain in the kinetic energy at the analyzer entrance, Eq. (4.27) should be written as

$$\phi_i(E) = C_s[E - \Delta E_{kin}] \exp\left[-\left(\sqrt{E - \Delta E_{kin}} - \sqrt{E_{dir}}\right)^2 \Big/ kT_i\right]. \tag{4.30}$$

The situation $V_{pl} < V_{entrance}$ is not as simple because the sheath may not be stable, especially when the sheath voltage is driven to high values [104, 105]. This applies to the situation when the entrance is grounded and the plasma potential is negative. The fact that energy analyzers measure a kinetic energy that is composed of the kinetic energy of the drifting plasma plus a potential-dependent gain at the analyzer entrance may account for the rather wide spread of results reported in the literature. One needs to have information on the plasma potential to fully interpret measured raw data. In one recent publication [101], the plasma potential was measured and its influence clearly demonstrated by intentional "plasma biasing." The results obtained are in general agreement with TOF results.

For the case of expansion into vacuum and in the absence of significant magnetic fields, the two-fluid plasma model (ions, electrons) works fairly well: assuming that all energy is deposited in a small volume at the cathode spot and considering adiabatic expansion, the expression

$$\overline{v_i} \approx \frac{2}{\gamma - 1}\sqrt{\gamma \frac{kT_i^* + \bar{Q}\, kT_e^*}{m_i}} \tag{4.31}$$

can be derived for the final ion velocity [106, 107], where $\gamma \approx 5/3$ is the adiabatic coefficient and the star indicates the initial temperature in the cathode spot. Similarly, considering the equations of energy and motion for a multi-component plasma, the relatively simple approximate expression

$$\overline{v_i} \approx 3.5\sqrt{\overline{Q}\, kT_e^*/m_i} \tag{4.32}$$

can be derived, where T_e^* denotes the electron temperature at the point where the ion velocity becomes supersonic [108, 109, 110]. To evaluate these expressions, one may use the temperature data [57] that have been derived from measured ion charge state distributions [42]. The charge state distributions "froze" very close to the cathode spot, and therefore the electron temperature at the charge state freezing zone is approximately the temperature when ions reach supersonic velocity. The result is shown in Figure 4.20. Figure 4.21 shows the average ion

velocity, converted to ion energy, the electron temperature at the freezing zone, and cohesive energy of the cathode material. These results have been obtained by several research groups, including Pluytto et al. [36], Davis and Miller [35], and Lunev et al. [34] (Figure 4.22).

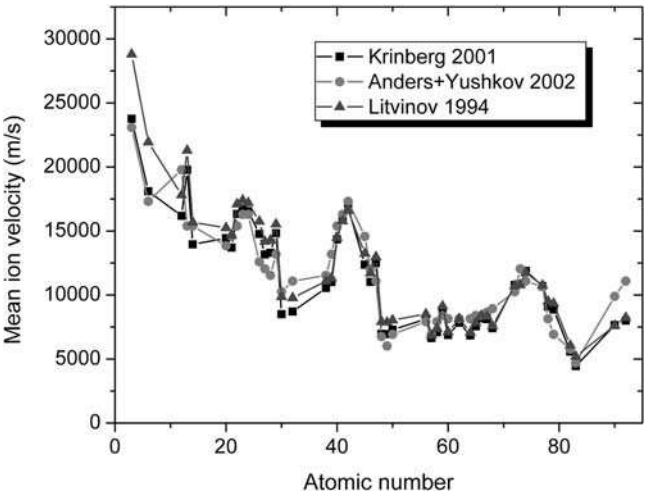

Fig. 4.20. Mean ion velocity, as calculated by Litvinov [106] and Krinberg [110], compared to data from Anders and Yushkov [44]

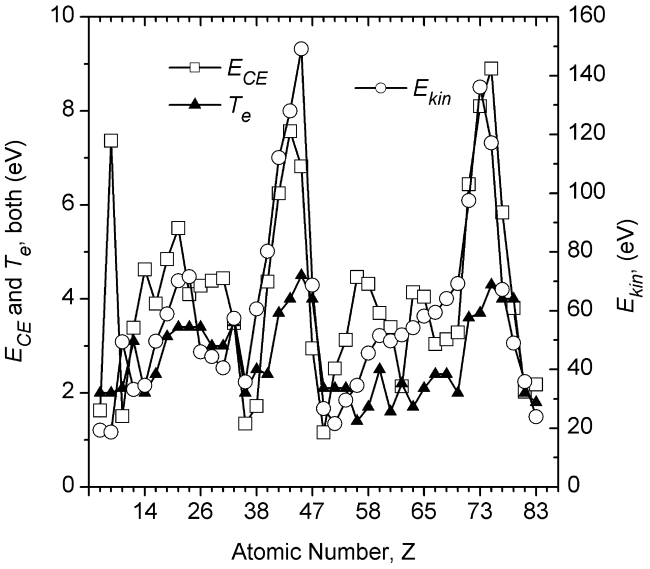

Fig. 4.21. Most-likely ion velocity for vacuum arc plasma, converted to ion energy, the electron temperature at the freezing zone, and the cohesive energy of the cathode material. (From [44])

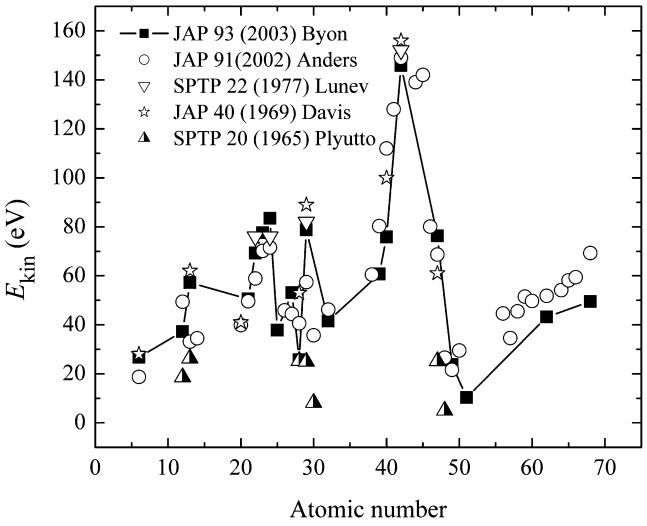

Fig. 4.22. Compilation of most-likely ion energies observed in vacuum arc experiments: one can clearly see the correlation as determined by the material's place in the Periodic Table; data from [34, 35, 36, 44, 95]. (Adapted from [95])

4.4.2 Ion Energies in the Presence of Magnetic Fields

In Section 4.3.5, it was shown that an external magnetic field can significantly shift the ion charge states to higher values. It can be expected that a magnetic field also influences the kinetic energy of ions. The effects, however, depend not just on the field strength but on the field distribution, and especially on the field gradient in the direction of the plasma plume motion. There is a general tendency to higher ion velocities with increasing field strength, which is especially pronounced when the plasma is generated in a strong magnetic field and expanding into a region of lower magnetic field strength. Conversely, if the plasma is moving into a region of higher field, the drift is slowed down.

First, let us consider the effect of absolute field strength. The field impedes the motion of electrons perpendicular to the field lines, which is immediately clear by an enhancement of the plasma impedance (higher burning voltage at given constant current). Higher burning voltage implies greater power input, higher electron temperature, higher pressure gradients from the spot, and finally greater ion velocities (Figure 4.23). The increase in burning voltage in these experiments is quite substantial (Figure 4.24). The increase in ion charge states is approximately proportional to the increase in arc burning voltage or power input.

Second, we will now have a closer look at the magnetic field gradient. Plasma confinement by a "magnetic bottle" is very well known since the late 1950s when

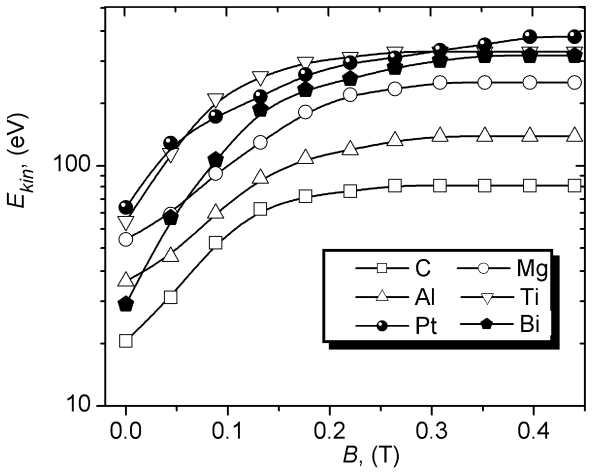

Fig. 4.23. Ion kinetic energy of selected cathode materials as a function of magnetic field strength; the arc current was 250 A and magnetic field was created by a small coil through which the plasma from the spot has to flow through before expanding to vacuum. (From [44])

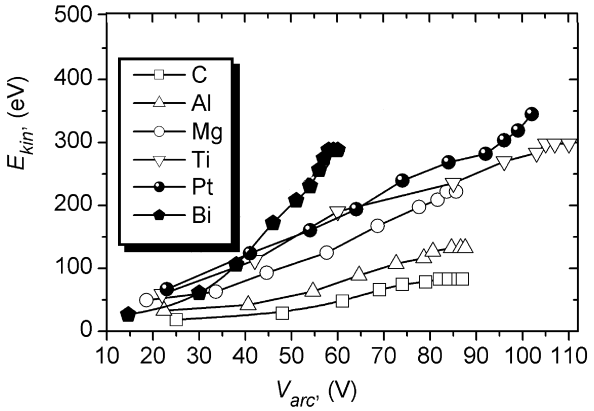

Fig. 4.24. Ion kinetic energy of Figure 4.23 but plotted against the burning voltage measured during the experiments. (From [44])

magnetic mirror machines were developed for thermonuclear fusion [15]. The simplest way to describe the acceleration or deceleration of ions is to consider the motion of individual charged particles in a magnetic field. In the absence of collisions, the magnetic moment of a charged particle

$$\mu = \frac{mv_{\perp}^2}{2\,B} \tag{4.33}$$

is an adiabatic invariant, $v_\perp$ is the previously introduced (Eq. (4.9)) velocity component perpendicular to the magnetic field vector. That means, depending on whether B decreases or increases, $v_\perp$ decreases or increases, respectively, in a quadratic manner. In the absence of collisions, the kinetic energy is conserved and thus the velocity component parallel to the field line increases or decreases, respectively. The force acting on the particle is

$$\mathbf{F}_{||} = -\mu \frac{\partial B}{\partial \mathbf{s}}, \tag{4.34}$$

where $\partial \mathbf{s}$ is a line element along $\mathbf{B}$. In the case of cathodic arc plasmas, only the electrons are typically magnetized; therefore, only electrons would slow down when moving along the field lines into a region of stronger field. However, electron–ion coupling via the electric field has an effect on the ions, too, and therefore the plasma as a whole will slow down when streaming into a region of stronger magnetic field, and accelerate when expanding into a region of lower B-field.

This general picture is well supported by experiments. For example, the ion drift velocity can be greatly affected when using two different field coils [44]. The results of experiments are shown in Figure 4.25: The arc plasma was accelerated by the field gradient of a short coil placed near the cathode, whereas it was slowed down when it was streaming into a 0.5-m-long coil.

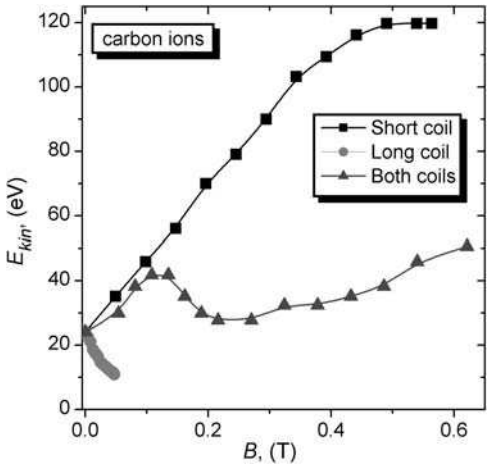

Fig. 4.25. Kinetic energy of carbon ions as determined by a detector placed at the end of a 0.5-m-long magnetic field coil: in one case, only a short but strong field coil was activated, resulting in ion acceleration; in another case only the long coil was used, resulting in a deceleration of the plasma; in the case with both coils activated, the effects of the coils approximately cancel and no very significant change is observed. (From [44])

4.4.3 Ion Energy Distribution Functions for Cathodic Arcs in Processing Gas

The interaction of the expanding arc plasma with background gas will affect not only the ion charge states but also the ion energy distribution functions. Here, only a summary will be given. The interaction will be further discussed in Section 4.5, where a distinction will be made between interactions with process gas and metal neutrals.

It is clear that collisions of the fast plasma ions with slow gas ions will transfer energy and momentum to the gas, and therefore it is not surprising that significant shifts of the ion energy distribution functions to lower values are observed as the gas pressure is increased [33, 83, 86, 87, 111, 112]. The most significant changes occur when the mean free path becomes comparable with the path length of the ions traveling from the cathode to the substrate or detector. Figure 4.26 shows that the energy distribution function is changed from a shifted Maxwellian distribution in the vacuum case to a more complicated distribution when gas interaction becomes important. One can clearly discern particles that have not (yet) collided with the background gas, while others have lost a good fraction of their original energy. Ions that have undergone collisions contribute to a new peak at much lower energy, and it is common to find a distribution that is a superposition of two or more particle groups formed in the collisions with gas particles.

While metal ions become slower, the particles of the processing gas can gain much higher than thermal energy. In addition to binary collisions, collective plasma effects (instabilities, turbulence) can contribute to this energy transfer [113].

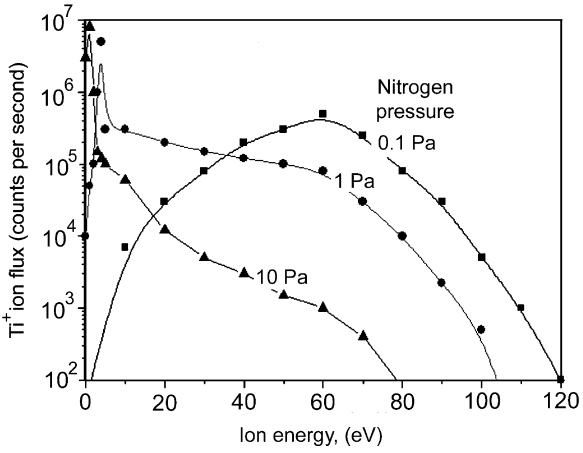

Fig. 4.26. Energy distribution function for Ti^+ as a function of gas nitrogen gas pressure; the measurements were done with a mass-selective ion energy analyzer placed 20 cm from the Ti cathode; arc current 85 A. (Data courtesy of Georg N. Strauss, PhysTech Coating Technology GmbH, Austria)

4.5 Neutrals in the Cathodic Arc Plasmas

4.5.1 Sources and Sinks of Neutrals

The concentration of neutrals in vacuum arc plasmas is a relatively unexplored field. This is mainly due to the difficulty that neutral atoms or molecules are not detected by ion detectors (they rely on the charge brought to the detector). In the literature, the fraction of neutrals is often described as "relatively small," which may be referring to several percent or tens of percent of all heavy particles. The notion of *fully ionized* plasma becomes prevalent because the plasma dynamics is governed by the charged particles (electrons and ions) as soon as their concentration exceeds a few percent of the total heavy particle (i.e., ion and atom) density [18, 114]. Because cathodic vacuum arc plasmas are commonly dominated by multiply charged ions, the argument was made that the amount of neutrals *directly produced in explosive plasma formation* is negligibly small [57]. This, however, does not mean that there are only few neutrals in the vacuum arc plasma. Rather, the concentration of neutrals in the chamber is increasing after the arc was started until it reaches a fluctuating, steady-state density determined by supply and removal. That density may be surprisingly high.

The following sources of neutrals have been identified:

(i) in the case of oblique angle condensation, low sticking of energetic metal ions;
(ii) self-sputtering [115];
(iii) evaporating macroparticles [116];
(iv) vapor from cooling, yet still-hot craters of previously active emission sites [117];
(v) neutrals formed by recombining ions;
(vi) neutrals desorbed from surfaces by the interaction of plasma with the surface.

The order of this list is not necessarily the order of relevance, and it may indeed depend on the specifics of the cathode material and geometry of the system. Sources (i)–(iv) are sources of neutral *metal* atoms, while source (vi) produces mainly water and hydrogen molecules.

There are three sinks removing neutrals from the plasma:

(i) vacuum pumps,
(ii) condensation on walls and other components,
(iii) ionization.

Among the ionization processes, several channels can be distinguished:

(iiia) charge exchange reaction of the neutral with a multiply charged ion,
(iiib) electron impact ionization,
(iiic) Penning ionization (transfer of sufficiently high excitation energy, e.g., from a level of a noble gas, to cause removal of a bound electron from a metal atom).

While macroparticle filtering (Chapter 7) removes neutrals from the plasma, even the filtered plasma can contain significant amounts of neutrals because the sources (i), (ii), (v), and (vi) are associated with the plasma flow, rather than with the processes at cathode spots. The processes of self-sputtering, low sticking, desorption, etc., are also considered in the chapter on energetic condensation (Chapter 8). Neutrals may have a great effect on a number of plasma parameters as well as on the properties of the coatings produced by energetic condensation.

4.5.2 The Effects of Metal Neutrals on the Ion Charge States

Experimentally observed charge states are higher at the beginning of each arc discharge than during steady-state operation. While cathode surface effects may play a role, such as an increase of the overall temperature, change in chemical composition, and spot mode due to the erosive action of the spot, neutrals can "skew" the steady-state charge state and energy distributions [118].

Once produced, neutrals travel through the discharge volume where they may interact with ions of the plasma flow. The flux of neutrals will gradually fill the volume enclosed by the surfaces onto which the plasma is condensing. The velocity of atoms, v_a, is much lower than the velocity of ions coming from the cathode. The characteristic filling time of the discharge system with neutrals is

$$t_{a1} \approx s/v_a, \tag{4.35}$$

where s is a characteristic length, such as the cathode–anode distance. For an order-of-magnitude estimate one may use $s \approx 0.1$ m and $v_a \approx 100 - 1000$ m/s to obtain $t_{a1} \approx 0.1 - 1$ ms, which is about the time needed for the plasma parameters to reach their steady-state (yet fluctuating) values.

The interaction of metal ions with metal atoms is dominated by charge exchange collisions [119, 120], which can be written as

$$\mathrm{Me}^{Q+} + \mathrm{Me} \Rightarrow \mathrm{Me}^{(Q-1)+} + \mathrm{Me}^{+}, Q = 1, 2, 3, \ldots, \tag{4.36}$$

where Me^{Q+} stands for the Q-fold charged metal ion. Charge exchange reactions with multiply charged ions will lead to ionization of the atom and to a reduction of the population of highly charged ions. Therefore, even as total charge is conserved in individual collisions of the type (4.36), the average charge state number is not conserved because previously neutral particles are now included in the averaging of *ion* charge states. Neutral particles are conventionally not included in the averaging procedure mainly for practicality reasons, i.e., because the concentration of neutrals is not known.

The relevance of ion–atom interaction can be estimated by considering the likelihood of an ion of the plasma flow interacting with a neutral atom before it arrives at the substrate or detector. The mean free path of the projectile (i.e., the ion of charge state Q),

$$\lambda_{Qa} = \left(n_a \sigma_{Qa}\right)^{-1}, \tag{4.37}$$

is determined by the density of targets (i.e., of atoms, n_a) and the ion–atom collision cross-section, σ_{Qa}. The cross-sections for charge exchange reactions depend on the internal energy defect:

$$\Delta E = \left(\sum E_{pot}\right)_{before} - \left(\sum E_{pot}\right)_{after}, \tag{4.38}$$

which is the difference in potential energies (ionization, excitation energy) between pre-collision and after-collision particles. If the energy defect is negative, $\Delta E < 0$, the cross-section is negligibly small. Charge exchange with $Q = 1$ has zero energy defect and its cross-section is very large. This reaction, known as resonant charge exchange, creates fast neutrals and slow singly charged ions, although the number of singly charged ions and the mean ion charge state are not changed.

Charge transfer collisions between multiply charged ions and gas atoms or molecules are facilitated by the capture of an electron from the target atom by the multiply charged ion into a specific excited level. This takes place at a rather well-determined inter-nuclear distance, which is typically between 0.3 and 0.6 nm, where the potential energy for the initial channel matches the potential energy for the final channel, i.e., where $\Delta E \approx 0$. The absolute values of resonant charge exchange ($Q = 1$) cross-sections for low-energy ions ($\sim$ 10–100 eV) are in the range $(1 - 4) \times 10^{-19}\mathrm{m}^{-2}$, which is very large compared to cross-sections of other collisional processes in the plasma [121]. While there is a general lack of experimental data for charge exchange cross-sections involving multiply charged ions at the low kinetic energies relevant for cathodic arcs, various model calculations indicate that the cross-sections increase with the charge of the projectile [120, 122, 123, 124, 125, 126]. Therefore, the higher the charge state the faster these ions will be removed from the plasma composition.

To evaluate the relevance of non-sticking and self-sputtering, one may look at experiments with Zr and Au plasmas which indicated a yield of about $\gamma \approx 0.05$ in the absence of bias, and much greater values when bias was applied [115]. The flux of metal atoms from the surface is

$$n_a v_a = \gamma n_i v_i, \tag{4.39}$$

where the ion density n_i can be estimated using Eq. (4.4). The ratio of the characteristic length of the discharge volume and mean free path can be defined as the collisionality or the non-normalized collision probability:

$$P = s/\lambda_{Qa}. \tag{4.40}$$

Using Eqs. (4.4) and (4.37) – (4.40), one arrives at

$$P = \sigma_{Qa} C I_{arc} \gamma \frac{v_i}{s\, v_a} \cos^{\alpha} \vartheta, \tag{4.41}$$

giving numerically about $P \approx (1 - 10)\%$. This means that neutrals from non-sticking and self-sputtering alone could cause a relevant rate of charge exchange. As a consequence, the ion charge state distributions measured at large distance

from the spot do not really represent the charge state distributions that were established in the freezing process. The charge state "freezing" concept is a helpful approach to understanding the physics of expanding plasmas; however, charge exchange skews the distribution, especially for large distances from the cathode spot.

Looking now at cathode materials that have a high vapor pressure, the effects should be amplified because evaporation from macroparticles and cooling craters on the cathode surface can be substantial sources of neutrals. This was shown, for example, for Pb and Bi plasmas [127]. Both metals have high vapor pressure, and indeed both show a strong decay of the charges as the neutrals fill the volume between cathode and the grid system that was used for ion analysis. Because the thermal conductivity of Bi is much smaller than that of Pb, the thermal energy dissipated in cathode spots is not effectively removed for Bi, and therefore its surface temperature stays higher for a longer time, leading to greater evaporation. The experiment showed that the mean charge state of Bi is much more reduced than the mean charge state of Pb (Figure 4.27(a) and (b)).

Evaporation can also play a role for refractory metals. Even as they generally have low vapor pressure, the temperature of the pool of molten material in craters is high and the resulting evaporation can be significant. This has been demonstrated for Mo, among other materials (Figure 4.28) [128].

The role of charge exchange involving multiply charged ions, and the resulting reduction of the mean charge state as the plasma flows from the cathode spot, has been shown by systematically increasing the distance between the cathode and the analyzing mass/charge spectrometer (Figure 4.29) [128].

The reduction of the mean ion charge state can be very well fitted using an exponential decay of first order, i.e.,

$$\overline{Q}(t) = A \exp(-t/\tau) + \overline{Q}_{ss}, \tag{4.42}$$

where A is a factor that describes the relevance of the decay, τ is the characteristic decay time, and $\overline{Q}_{ss}$ is the steady-state average charge state number which is approached for $t \gg \tau$. The fit parameters for the example shown in Figure 4.29 are given in Table 4.1. The table also contains the correlation parameter R^2 which approaches unity as the fit is perfect. The data in the table describe a few interesting properties that agree well with the concept that charge exchange collisions are the main reason for the decay. We can see that the parameter A increases as the plasma flows from the cathode region, i.e., the further the plasma is away from the origin of plasma production, the greater the number of charge-reducing collisions. The characteristic time is associated with the time of neutrals reaching their steady-state density after arc ignition; one could expect that it would take longer far from the cathode. The first data point does not show that, which is associated with the difficulty of measuring there due to the very large fluctuations of plasma density and composition near the cathode. The steady-state mean ion charge state, $\overline{Q}_{ss}$, is systematically reduced as the plasma moves away from the cathode because ions have a greater likelihood to experience one or more charge-reducing

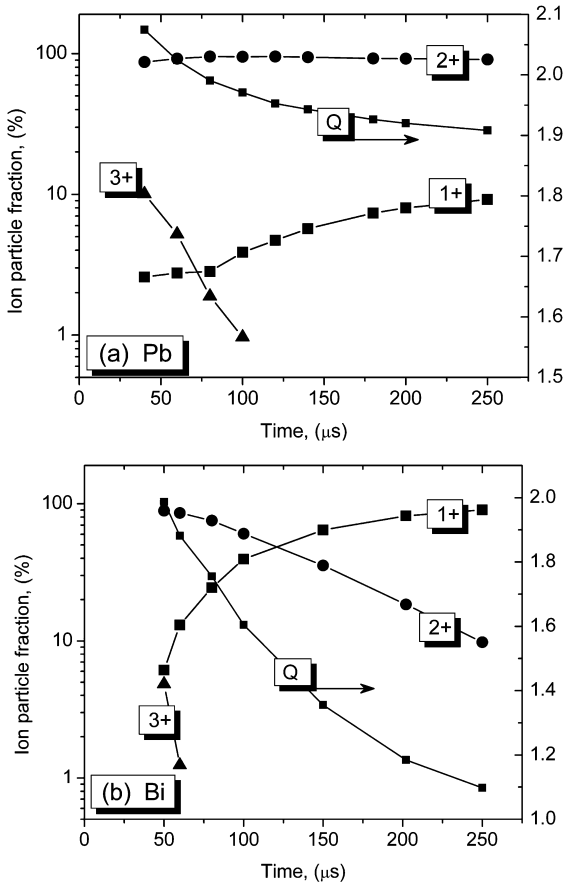

Fig. 4.27. Evolution of the ion charge state distribution of cathodic vacuum arcs for (**a**) lead plasma, (**b**) bismuth plasma. Arc current 300 A, ion extraction about 10 cm from the cathode, 7 pulses per second. (From [127])

collisions. Finally, the table also contains the extrapolated mean ion charge state as produced at that very beginning of the arc discharge, $\overline{Q}(t \to 0)$, i.e., when ions expand into vacuum and not into a region already filled with plasma and neutrals. Ideally, these values should be the same, however, large fluctuations of individual data cause deviations.

With the desire to obtain high ion charge states, one may take the above result and design a discharge system that exclusively works with short pulses by minimizing the interaction with neutrals. Even higher charge states can be obtained by dissipating more energy per plasma particle, which can be done using the transient stage of a vacuum spark, characterized by high current (kA) *and* high burning voltage (kV). The spark is characterized by its high burning

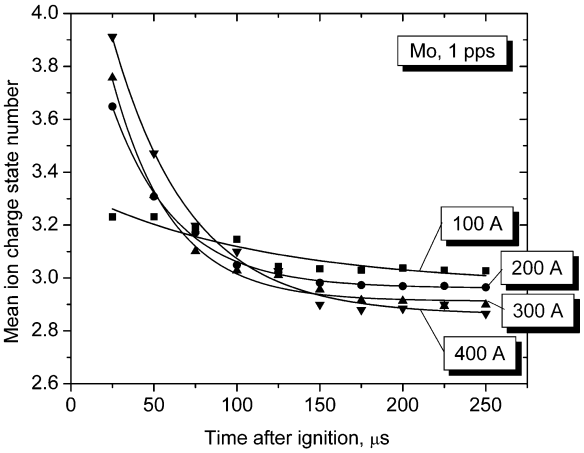

Fig. 4.28. Mean ion charge state number for molybdenum as a function of time after arc ignition with the arc current as a parameter. (From [128])

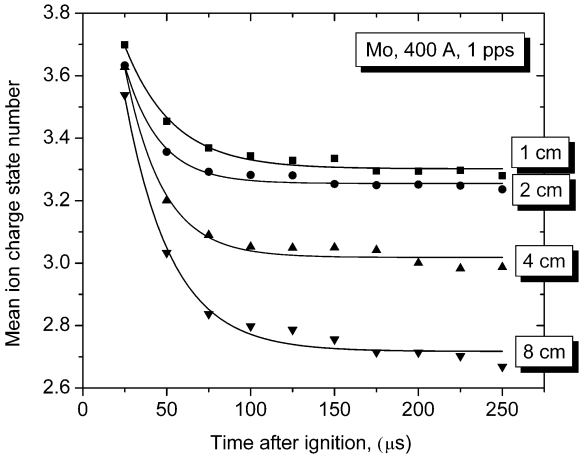

Fig. 4.29. Mean ion charge state number for molybdenum as a function of time for different distances between cathode surface (location of ion production) and extraction grid (location of ion analysis). The data points were fitted with an exponential decay first order, and the fit parameter are given in Table 4.1. (From [128])

voltage, much higher than the typical arc values of 15–30 V. The voltage, not current, is the key difference between spark and arc. A high-current discharge may operate with low voltage (arc) or high voltage (spark). The latter is typically transient and cannot be maintained for times exceeding some microseconds (or tens of microseconds, at most). Using a simple setup of a high-voltage capacitor

Table 4.1. Fit parameters A, τ, and $\overline{Q}_{ss}$ for the decay of the average molybdenum ion charge state (cf. Figure 4.29), as a function of distance between ion production and analysis; the indicated errors describe the quality of the fit relative to the exponential decay law, and they do not fully reflect the noisy nature of the data. The mean ion charge state $\overline{Q}(t \to 0)$ is extrapolated for the very beginning of an arc, when the plasma expands into vacuum. R^2 is a correlation coefficient of the data relative to a perfect exponential decay. (After [128])

Distance (cm)	A	τ (μs)	$\overline{Q}_{ss}$	$\overline{Q}(t \to 0)$	R^2
1	0.94 ± 0.10	28.6 ± 3.0	3.30 ± 0.01	4.24 ± 0.11	0.986
2	1.28 ± 0.17	20.4 ± 2.1	3.25 ± 0.01	4.53 ± 0.18	0.989
4	1.87 ± 0.27	22.2 ± 2.6	3.02 ± 0.01	4.89 ± 0.28	0.985
8	2.01 ± 0.20	27.8 ± 2.7	2.72 ± 0.01	4.73 ± 0.21	0.987

discharge in vacuum, the values of ion charge states can be much higher than what is obtained for vacuum arcs. Table B7 (Appendix B) gives a systematic overview for values measured 3 μs after discharge initiation. Going to higher currents and shorter pulses delivers even higher charge states, up to 10+ for 4-kA pulses (Figure 4.30) [129]. From that spectrum we can also see that a large amount of non-metallic contamination is present, and one has to be careful to not falsely identifying such peaks as very high charge states of the metal. From Figure 4.31, we see how quickly the spark charge state distribution decays into the more familiar distribution for vacuum arcs.

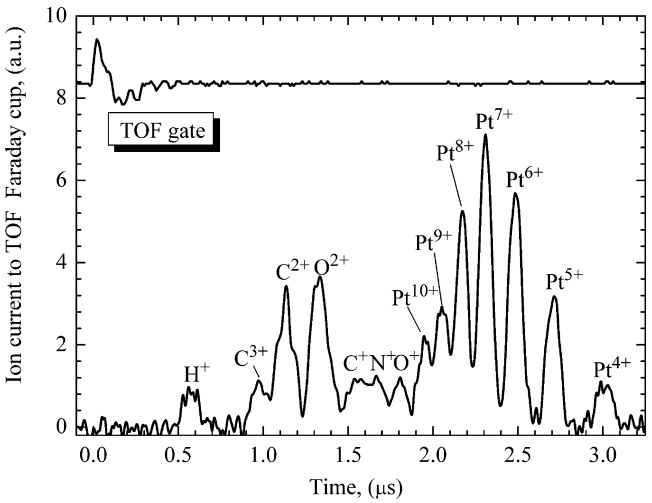

Fig. 4.30. Ion charge state distribution of a 4-kA, 8-μs vacuum spark: the *top curve* is the gating voltage of the time-of-flight spectrometer, and the bottom is the electric current to the magnetically shielded Faraday cup. (From [129])

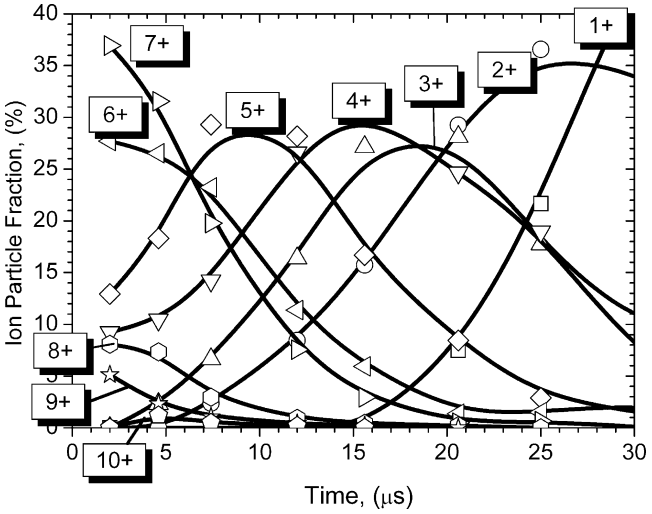

Fig. 4.31. Evolution of the Pt ion charge state distribution in the transition from vacuum spark to vacuum arc, as measured with the time-of-flight method. The time "zero" is defined here as the arrival time of the first (fastest) ions at the Faraday cup detector. (From [129])

4.5.3 The Effects of Gas Neutrals on the Ion Charge States

Introduction of gas neutrals also shifts metal ion charge states to lower values. The situation is similar to metal neutrals but has the following differences:

- The electronic structure of the metal ion and the gas atom or molecule are different in all cases, making it unlikely that the potential energies of the initial matches that of the final channel, i.e., where the condition $\Delta E \approx 0$ is fulfilled.
- The sources of gas are the externally controlled backfill of the process chamber as well as the surfaces with which the plasma interacts; the externally controlled pressure is usually dominant at high pressure ($p > 10^{-2}$ Pa).

The model of charge state freezing is not applicable, especially when the pressure is high and ions experience many collisions. Table 4.2 gives some examples of experimental observations of metal plasma–gas background interaction.

The interaction of metal plasma with nitrogen is of special interest because of its relevance for the deposition of nitrides. The successive reduction of metal ion charge states could be caused by charge transfer reactions, similar to (4.36) but the neutral in this case is a nitrogen molecule:

$$\mathrm{Me}^{Q+} + \mathrm{N}_2 \Rightarrow \mathrm{Me}^{(Q-1)+} + \mathrm{N}_2^+. \tag{4.43}$$

The molecular ion may dissociate in these processes. The cross-sections for reactions of this type are vastly different for different charge states because of

Table 4.2. Changes of metal ion charge states due to interaction with background or process gas

Metal plasma	Background gas	Specific conditions, Main findings	Reference
Cu, Ag, C	N_2, Ar, He	Systematic study of the effects of increasing gas pressure up to atmospheric pressure; demonstrate that spot processes in vacuum and at high pressure are similar; no charge state measurements	[134]
Al	O_2	Higher Al charge states are reduced with increasing pressure, beginning at 5×10^{-3} Pa, oxygen ions appear and dominate the plasma for $p > 0.5$ Pa; this study also includes axial magnetic field, showing non-monotonic dependencies of species' fractions on field strength	[82]
Al	O_2	Development of a pulsed aluminum plasma stream in oxygen at various pressures: Charge states are high at the beginning of each pulse and approach steady state only for $t > 100$ μs; hydrogen detected even when operating in pure O_2: indication of walls being a source of water vapor	[84]
Zr, Cr	N_2	Plasma has the typical vacuum arc ion charge distribution as long as the pressure is less than 10^{-2} Pa Presence of reactive gases does not prohibit elevated charge states at the beginning of an arc pulse Higher charge states are eliminated first as the pressure is increased beyond 10^{-2} Pa	[85]
Al, Cu, Fe, Mo, Ta, Ti, Ni	H_2, He, N_2, O_2, Ar, Xe	With increasing gas pressure, higher charge states are reduced first while lower charge states increase, followed by a decrease. Gas ionization can be substantial. Influence of gas can be seen for $p > 10^{-4}$ Pa. Metal plasma flow is completely blocked for about $p > 10^{-1}$ Pa, details depend on metal–gas combination	[135]
Ti, Mo	N_2	N_2^+ ions are produced primarily by charge exchange of Ti^{2+} or Mo^{2+} on N_2. The properties of the nitride coatings are correlated with the production of nitrogen ions	[79]

(*Continued*)

Table 4.2. *(Continued)*

Metal plasma	Background gas	Specific conditions, Main findings	Reference
Ti	N_2	Optical and mass spectrometry: effects are small for $p < 10^{-3}$ Pa; Ti^{2+} are drastically reduced for $p > 10^{-2}$ Pa; charge exchange and nitrogen ion are dominant at high pressure ($p > 10^{-2}$ Pa)	[80]
Ti	N_2	50-A arc in pressure range 0.13–26.6 Pa; optical emission spectroscopy shows: Ti^{2+} is much reduced for $p > 10^{-1}$ Pa, the intensity of Ti^{+} has maximum at 1 Pa, Ti neutrals dominate spectrum for $p > 10$ Pa	[81]
Ti, Al	N_2, O_2	Successive reduction of charge states with increasing pressure is consistent with both charge exchange and electron impact ionization and recombination	[83]

the internal energy defect (4.38). As described for metal–metal collisions, the cross-section is large for multiply charged ions. If the energy defect is negative, $\Delta E < 0$, the cross-section is negligibly small [77, 119, 121, 130].

Nitrogen ion formation through the interaction with metal plasma was discussed by Bilek et al. [83, 131], Chhowalla [132], and Rosén et al. [86]. Different channels of nitrogen ion production were identified: electron impact ionization, dissociation of N_2^{+}, and erosion of a nitrogen-containing compound at the cathode surface.

Whereas metal neutrals need time to establish a (noisy) steady-state density, background gas neutrals are supplied to the chamber prior to the arc ignition. As measurements with background gas showed [128], the charge states are indeed smaller right from the very start and do not decay with time (Figure 4.32). In extreme cases, one can even observe a slight *increase* of the mean ion charge state with time, which can be associated with a reduction of the neutral density. This gas rarefaction effect is well known in ionized sputtering [133].

Charge exchange leads to partial ionization of the background gas. The ionization of background gas is greatly enhanced if a magnetic field is present because the likelihood of an energetic electron colliding with a gas molecule is greatly enhanced due to the electron's gyro-motion. The magnetic field can therefore serve different functions, namely not only to guide the plasma toward the substrate, or to facilitate macroparticle filtering, but also to enhance gas ionization. Magnetic macroparticle filters commonly show this usually welcome side effect.

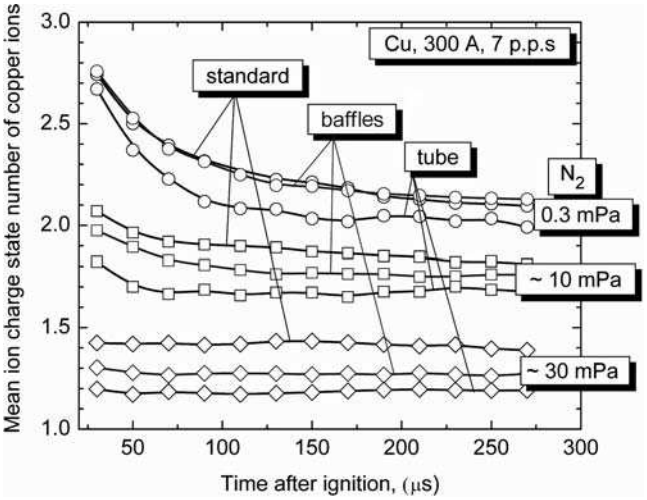

Fig. 4.32. Compilation of results of charge state measurements for copper ions under various conditions: "standard" refers to vacuum arc where the plasma can expand in an undisturbed manner; "baffles" and "tube" refer to measurements when additional baffles and a tube were inserted in the expansion zone, respectively. Additionally, three pressure conditions were considered, as indicated, for each of the three geometries. One can see that both background gas and plasma–surface interaction influence the measured mean ion charge state. When the background gas pressure is high, the reduction of charge states occurs right from the start of the arc discharge. (From[128])

4.5.4 The Effects of Neutrals on the Ion Energy

This section is an extension of Section 4.4.3. The topic is reconsidered here because now the effects of neutrals on the ion charge state have been discussed, and information was provided of how metal and gas neutrals evolve in the interelectrode volume. With this additional background information, it is easy to see that the energy distribution functions are likely to show time dependence after arc triggering similar to the time dependence of the charge state distributions.

Measuring ion energy distribution functions with charge and time resolution is a challenging task. Reports in the literature are limited to average or most-likely ion velocities or energies as a function of time, or some integration over time was done. For example, arc pulses of different lengths were used to investigate the charge-state-resolved ion energy distributions of magnesium plasma [101]. By considering different pulse lengths, some information about the time evolution is revealed. From Figure 4.33 one can see that the average energy of Mg^{2+} ions is high at the beginning of each arc pulse and that state-steady values are approached for arc durations longer than 100 μs. Using a time-of-flight technique, similar observations were made for tantalum ions [44]. In all

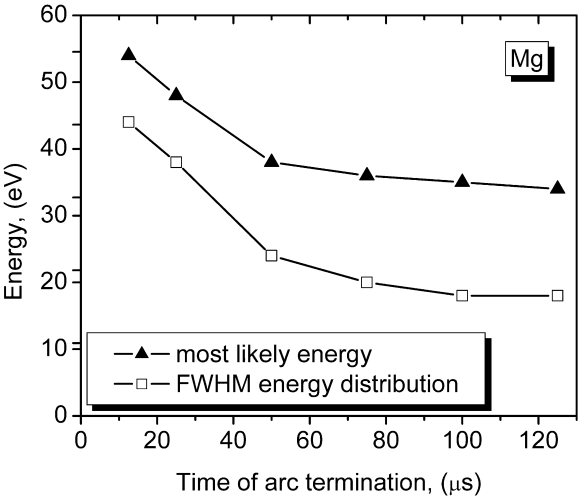

Fig. 4.33. Peak and full width at half maximum (FWHM) of the energy distribution function for vacuum arc Mg^{2+} ions; arc current 220 A, 2 pulses per second, the distribution functions were integrated over the duration of the arc pulses, which were terminated by a bypass crowbar such as to terminate the discharge rapidly and reproducibly. (After [101])

of these cases, the decay times to steady state are comparable to the times observed for the settling of the average ion charge state. Other factors than the evolution of the neutral particle density play a role, too, such as a non-constant energy input – the relative importance of these factors is still subject to research.

As mentioned in Section 4.4.3, the ion energy distribution functions of continuously operating arcs are shifted to lower energies as compared to pulsed arcs. They are more asymmetric: they exhibit a longer high-energy tail. This could be attributed to the collisions, which shift many particles to the low-energy end of the distribution, while those with less or no collisions populate the high-energy tail. This is the general picture that can be applied to unfiltered or filtered arc systems.

References

1. Anders, A. and Yushkov, G. Y., Angularly resolved measurements of the ion energy of vacuum arc plasmas, *Appl. Phys. Lett.* **80**, 2457–2459, (2002).
2. Kutzner, J. and Miller, H. C., In flux from the cathode region of a vacuum arc, *IEEE Trans. Plasma Sci.* **17**, 688–694, (1989).
3. Sutton, G. W. and Sherman, A., *Engineering Magnetohydrodynamics*, reprint of the 1965 first edition by McGraw-Hill ed. Dover, Mineola, NY, (2006).
4. Wieckert, C., A multicomponent theory of the cathodic plasma jet in vacuum arcs, *Contrib. Plasma Phys.* **27**, 309–330, (1987).

5. Keidar, M., Beilis, I.I., Anders, A., and Brown, I.G., Free-boundary vacuum arc plasma jet expansion in a curved magnetic field, *IEEE Trans. Plasma Sci.* **27**, 613–619, (1999).
6. Keidar, M., Beilis, I.I., Boxman, R.L., and Goldsmith, S., 2D expansion of the low-density interelectrode vacuum arc plasma jet in an axial magnetic field, *J. Phys. D, Appl. Phys.* **29**, 1973–1983, (1996).
7. Gidalevich, E., Goldsmith, S., and Boxman, R.L., Modeling of nonstationary vacuum arc plasma jet interaction with a neutral background gas, *J. Appl. Phys.* **90**, 4355–4360, (2001).
8. Beilis, I.I., The vacuum arc cathode spot and plasma jet, Physical model and mathematical description, *Contrib. Plasma Phys.* **43**, 224–236, (2003).
9. Ivanov, V.A., Jüttner, B., and Pursch, H., Time-resolved measurements of the parameters of arc cathode plasmas in vacuum, *IEEE Trans. Plasma Sci.* **13**, 334–336, (1985).
10. Jüttner, B., Characterization of the cathode spot, *IEEE Trans. Plasma Sci.* **PS-15**, 474–480, (1987).
11. Aksenov, I.I., Padalka, V.G., and Khoroshykh, V.M., Investigation of a flow of plasma generated by a stationary erosion electric arc accelerator with magnetic confinement of the cathode spot, *Sov. J. Plasma Phys.* **5**, 341, (1979).
12. Cohen, Y., Boxman, R.L., and Goldsmith, S., Angular distribution of ion current emerging from an aperture anode in a vacuum arc, *IEEE Trans. Plasma Sci.* **17**, 713–716, (1989).
13. Anders, S., Anders, A., and Brown, I.G., Focused injection of vacuum arc plasmas into curved magnetic filters, *J. Appl. Phys.* **75**, 4895–4899, (1994).
14. Anders, A. and MacGill, R.A., Asymmetric injection of cathodic arc plasma into a macroparticle filter, *J. Appl. Phys.* **95**, 7602–7606, (2004).
15. Chen, F.F., *Plasma Physics and Controlled Fusion*. Plenum Press, New York, (1984).
16. Goldston, R.J. and Rutherford, P.H., *Introduction to Plasma Physics*. Institute of Physics, Bristol, (1997).
17. Golant, V.E., Zhilinsky, A.P., and Sakharov, I.E., *Fundamentals of Plasma Physics*. Wiley, New York, (1980).
18. Cap, F., *Introduction to Plasma Physics I. Theoretical Foundation*, 2nd ed. Akademie-Verlag, Berlin, (1975).
19. Krall, N.A. and Trivelpiece, A.W., *Principles of Plasma Physics*. McGraw-Hill, New York, (1973).
20. Heberlein, J.V.R. and Porto, D., The interaction of vacuum arc ion currents with axial magnetic fields, *IEEE Trans. Plasma Sci.* **11**, 152–159, (1983).
21. Nemchinskii, V.A., Focusing of the plasma jet of a vacuum arc by a magnetic field, *Sov. Phys. Tech. Phys.* **35**, 518–519, (1990).
22. Beilis, I.I., "Theoretical modeling of cathode spot phenomena," in *Handbook of Vacuum Arc Science and Technology*, Boxman, R.L., Martin, P.J., and Sanders, D.M., (Eds.). pp. 208–256, Noyes, Park Ridge, NJ, (1995).
23. Beilis, I., Djakov, B.E., Jüttner, B., and Pursch, H., Structure and dynamics of high-current arc cathode spots in vacuum, *J. Phys. D, Appl. Phys* **30**, 119–130, (1997).
24. Chaly, A.M., Logatchev, A.A., Zabello, K.K., and Shkol'nik, S.M., High-current vacuum arc appearance in nonhomogenous axial magnetic field, *IEEE Trans. Plasma Sci.* **31**, 884–889, (2003).
25. Westwood, W.D., *Sputter Deposition*, AVS Education Committee Book Series, vol. 2. AVS, New York, (2003).

26. Shah, S.I., "Sputtering: Introduction and General Discussion," in *Handbook of Thin Film Processing Technology*, Glocker, D.A. and Shah, S.I., (Eds.). pp. A3.0:1–A3. 0:18, IOP Publishing, Bristol, UK, (1995).
27. Meunier, J.-L. and Drouet, M.G., Experimental study of the effect of gas pressure on arc cathode erosion and redeposition in He, Ar, and SF_6 from vacuum to atmospheric pressure, *IEEE Trans. Plasma Sci.* **15**, 515–519, (1987).
28. Meunier, J.-L., Pressure limits for the vacuum arc deposition technique, *IEEE Trans. Plasma Sci.* **18**, 904–910, (1990).
29. Gidalevich, E., Goldsmith, S., and Boxman, R.L., *J. Phys. D: Appl. Phys.* **33**, 2598, (2000).
30. Gidalevich, E., Goldsmith, S., and Boxman, R.L., *Plasma Sources Sci. Technol.* **10**, 24, (2001).
31. Kelly, H., Márquez, A., and Minotti, F.O., A simplified fluid model of the metallic plasma and neutral gas interaction in a multicathode spot vacuum arc, *IEEE Trans. Plasma Sci.* **26**, 1322–1329, (1998).
32. Grondona, D., Kelly, H., Márquez, A., Minotti, F., and Zebrowski, O.J., Experimental investigation of ion parameters in a cathodic arcplasma operated with nitrogen gas, *IEEE Trans. Plasma Sci.* **28**, 1280–1286, (2000).
33. Grondona, D., Kelly, H., and Minotti, F.O., Hydrodynamic model for a vacuum arc operated with background gas: Theory and experimental validation, *J. Appl. Phys.* **99**, 043304–7, (2006).
34. Lunev, V.M., Padalka, V.G., and Khoroshikh, V.M., Plasma properties of a metal vacuum arc. II, *Sov. Phys. Tech. Phys.* **22**, 858–861, (1977).
35. Davis, W.D. and Miller, H.C., Analysis of the electrode products emitted by dc arcs in a vacuum ambient, *J. Appl. Phys.* **40**, 2212–2221, (1969).
36. Plyutto, A.A., Ryzhkov, V.N., and Kapin, A.T., High speed plasma streams in vacuum arcs, *Sov. Phys. JETP* **20**, 328–337, (1965).
37. Brown, I.G., Feinberg, B., and Galvin, J.E., Multiply stripped ion generation in the metal vapor vacuum arc, *J. Appl. Phys.* **63**, 4889–4898, (1988).
38. Brown, I.G. and Godechot, X., Vacuum arc ion charge-state distributions, *IEEE Trans. Plasma Sci.* **19**, 713–717, (1991).
39. Anders, A., Anders, S., Jüttner, B., and Brown, I.G., Time dependence of vacuum arc parameters, *IEEE Trans. Plasma Sci.* **PS-21**, 305–311, (1993).
40. Oks, E., Brown, I.G., Dickinson, M.R., MacGill, R.A., Spädtke, P., Emig, H., and Wolf, B.H., Elevated ion charge states in vacuum arc plasmas in a magnetic field, *Appl. Phys. Lett.* **67**, 200–202, (1995).
41. Paoloni, F.J. and Brown, I.G., Some observations of the effect of magnetic field and arc current on the vacuum arc charge state distribution, *Rev. Sci. Instrum.* **66**, 3855–3858, (1995).
42. Brown, I.G., Vacuum arc ion sources, *Rev. Sci. Instrum.* **65**, 3061–3081, (1994).
43. Pustovit, A.N., Zhila, V.I., and Sikharulidze, G.G., Mass spectral diagnostics of plasma formed at cathode tip explosion, *Sov. Phys. Tech. Phys.* **31**, 496–497, (1986).
44. Anders, A. and Yushkov, G.Y., Ion flux from vacuum arc cathode spots in the absence and presence of magnetic fields, *J. Appl. Phys.* **91**, 4824–4832, (2002).
45. Sasaki, J. and Brown, I.G., Ion spectra of vacuum arc plasma with compound and alloy cathodes, *J. Appl. Phys.* **66**, 5198–5203, (1989).
46. Sasaki, J., Sugiyama, K., Yao, X., and Brown, I., Multiple-species ion beams from titanium-hafnium alloy cathodes in vacuum arc plasmas, *J. Appl. Phys.* **73**, 7184–7187, (1993).

47. Brown, I.G., Galvin, J.E., MacGill, R.A., and West, M.W., Multiply charged metal ion beams, *Nucl. Instrum Meth. Phys. Res. B* **43**, 455–458, (1989).
48. Anders, A., Brown, I., MacGill, R., and Dickinson, M., High ion charge states in a high-current, short-pulse, vacuum arc ion source, *Rev. Sci. Instrum.* **67**, 1203–1204, (1996).
49. Baksht, R.B., Kudinov, A.P., and Litvinov, E.A., Cathode plasma in the initial stage of a vacuum discharge, *Sov. Phys. – Techn. Phys.* **18**, 94–97, (1973).
50. Radic, N. and Santic, B., "Composition of vacuum arc plasma," Int. Symp. on Discharges and Electrical Insulation in Vacuum, Paris, pp. 217–219, (1988).
51. Anders, S. and Anders, A., Frozen state of ionization in a cathodic plasma jet of a vacuum arc, *J. Phys. D: Appl. Phys.* **21**, 213–215, (1988).
52. Hantzsche, E., Consequences of balance equations applied to the diffuse plasma of vacuum arcs, *IEEE Trans. Plasma Sci.* **17**, 657–660, (1989).
53. Griem, H.R., *Plasma Spectroscopy*. McGraw-Hill, New York, (1964).
54. Ebeling, W., Kremp, W.-D., and Kraeft, D., *Theory of Bound States and Ionization Equilibrium in Plasmas and Solids*. Akademie-Verlag, Berlin, (1976).
55. Richter, J., "Radiation of Hot Gases," in *Plasma Diagnostics*, Lochte-Holtgreven, W., (Ed.). pp. 1–65, AIP Press, New York, (1995).
56. Drawin, H.-W. and Felenbok, P., *Data for Plasmas in Local Thermodynamic Equilibrium*. Gauthier-Villars, Paris, (1965).
57. Anders, A., Ion charge state distributions of vacuum arc plasmas: The origin of species, *Phys. Rev. E* **55**, 969–981, (1997).
58. Anders, A., Plasma fluctuations, local partial Saha equilibrium, and the broadening of vacuum-arc ion charge state distributions, *IEEE Trans. Plasma Sci.* **27**, 1060–1067, (1999).
59. Griem, H.R., Validity of local thermal equilibrium in plasma spectroscopy, *Phys. Rev.* **131**, 1170–1176, (1963).
60. Biberman, L.M., Vorobev, V.S., and Yakubov, I.T., *Kinetics of the Non-Equilibrium and Low-Temperature Plasma (in Russ.)*. Nauka, Moscow, (1982).
61. Anders, A. and Schülke, T., "Predicting ion charge state distributions of vacuum arc plasmas," XVIIth Int. Symp. on Discharges and Electrical Insulation in Vacuum, Berkeley, pp. 199–203, (1996).
62. Richter, F., Flemming, G., Kühn, M., Peter, S., and Wagner, H., Characterization of the arc evaporation of a hot boron cathode, *Surf. Coat. Technol.* **112**, 43–47, (1999).
63. Yushkov, G.Y. and Anders, A., Cathodic vacuum arc plasma of thallium, *IEEE Trans. Plasma Sci.* **35**, 516–517, (2007).
64. Anders, A., Yotsombat, B., and Binder, R., Correlation between cathode properties, burning voltage, and plasma parameters of vacuum arcs, *J. Appl. Phys.* **89**, 7764–7771, (2001).
65. Puchkarev, V.F. and Murzakayev, A.M., Current density and the cathode spot lifetime in a vacuum arc at threshold currents, *J. Phys. D: Appl. Phys.* **23**, 26–35, (1990).
66. Jüttner, B., On the plasma density of metal vapour arcs, *J. Phys. D: Appl. Phys.* **18**, 2221–2231, (1985).
67. Oks, E.M., Anders, A., Brown, I.G., Dickinson, M.R., and MacGill, R.A., Ion charge state distributions in high current vacuum arc plasma in a magnetic field, *IEEE Trans. Plasma Sci.* **24**, 1174–1183, (1996).
68. Anders, A., Oks, E.M., Yushkov, G.Y., and Brown, I.G., "Measurement of total ion flux in vacuum arc discharges," Proc. of XXIth Int. Symp. on Discharges and Electrical Insulation in Vacuum, Yalta, Ukraine, pp. 272–275, (2004).

69. Brown, I.G., Galvin, J.E., MacGill, R.A., and Wright, R.T., Improved time-of-flight charge state diagnostic, *Rev. Sci. Instrum* **58**, 1589–1592, (1987).
70. Anders, A. and Hollinger, R., Reducing ion-beam noise of vacuum arc ion sources, *Rev. Sci. Instrum.* **73**, 732–734, (2002).
71. Lunev, V.M., Padalka, V.G., and Khoroshikh, V.M., Use of a monopole mass spectrometer for investigating the ion component of a plasma stream generated by a vacuum arc, *Instrum. Exp. Tech.* **19**, 1465–1467, (1976).
72. Oks, E., Spädtke, P., Emig, H., and Wolf, B.H., Ion beam noise reduction method for the MEVVA ion source, *Rev. Sci. Instrum.* **65**, 3109–3112, (1994).
73. Brown, I.G., Spädtke, P., Rück, D.M., and Wolf, B.H., Beam intensity fluctuation characteristics of the metal vapor vacuum arc ion source, *Nucl. Instrum. Meth. Phys. Res. A* **295**, 12–20, (1990).
74. Anders, A., Yushkov, G., Oks, E., Nikolaev, A., and Brown, I., Ion charge state distributions of pulsed vacuum arc plasmas in strong magnetic fields, *Rev. Sci. Instrum.* **69**, 1332–1335, (1998).
75. Krinberg, I.A., On the mechanism of the external magnetic field action on the electron temperature and ion charge state distribution in a vacuum arc plasma, *Techn. Phys. Lett.* **29**, 504–506, (2003).
76. Krinberg, I.A., The ion charge-current strength relationship in stationary and pulsed vacuum discharges, *Tech. Phys. Lett.* **27**, 45–48, (2001).
77. McDaniel, E.W., *Collision Phenomena in Ionized Gases*. Wiley, New York, (1964).
78. Kimblin, C.W., A review of arcing phenomena in vacuum and in the transition to atmospheric pressure arcs, *IEEE Trans. Plasma Sci.* **10**, 322–330, (1971).
79. Demidenko, I.I., Lomino, N.S., Ovcharenko, V.D., Padalka, V.G., and Polyakova, G.N., Ionization mechanism for nitrogen in a vacuum arc discharge, *Sov. Phys-Tech. Phys.* **29**, 895–897, (1984).
80. Martin, P.J., McKenzie, D.R., Netterfield, R.P., Swift, P., Filipczuk, S.W., Müller, K.-H., Pacey, C.G., and James, B., Characteristics of titanium arc evaporation processes, *Thin Solid Films* **153**, 91–102, (1987).
81. Sakaki, M. and Sakakibara, T., Excitation, ionization, and reaction mechanism of a reactive cathodic arc deposition of TiN, *IEEE Trans. Plasma Sci.* **22**, 1049–1054, (1994).
82. Oks, E. and Yushkov, G., "Some features of vacuum arc plasmas with increasing gas pressure in the discharge gap," XVIIth Int. Symp. on Discharges and Electrical Insulation in Vacuum, Berkeley, CA, pp. 584–588, (1996).
83. Bilek, M.M.M., Martin, P.J., and McKenzie, D.R., Influence of gas pressure and cathode composition on ion energy distributions in filtered cathodic vacuum arcs, *J. Appl. Phys.* **83**, 2965–2970, (1998).
84. Schneider, J.M., Anders, A., Brown, I.G., Hjörvarsson, B., and Hultman, L., Temporal development of the plasma composition of a pulsed aluminum plasma stream in the presence of oxygen, *Appl. Phys. Lett.* **75**, 612–614, (1999).
85. Rosén, J., Anders, A., Hultman, L., and Schneider, J.M., Temporal development of the composition of Zr and Cr cathodic arc plasma streams in a N_2 environment, *J. Appl. Phys.* **94**, 1414–1419, (2003).
86. Rosén, J., Anders, A., Hultman, L., and Schneider, J.M., Charge state and time resolved plasma composition of a pulsed zirconium arc in a nitrogen environment, *J. Appl. Phys.* **96**, 4793–4799, (2004).
87. Rosén, J., Anders, A., Mráz, S., Atiser, A., and Schneider, J.M., Influence of argon and oxygen on charge-state-resolved ion energy distributions of filtered aluminum arc, *J. Appl. Phys.* **99**, 123303-1-5, (2006).

88. Ginzburg, V.L., *Propagation of Electromagnetic Waves in Plasma*. Pergamon, Oxford, (1964).
89. Stix, T.H., *Waves in Plasmas*. American Institute of Physics, New York, (1992).
90. Kutzner, J. and Miller, H.C., Integrated ion flux emitted from the cathode spot region of a diffuse vacuum arc, *J. Phys. D: Appl. Phys.* **25**, 686–693, (1992).
91. Rosén, J., Anders, A., Mráz, S., and Schneider, J.M., Charge-state-resolved ion energy distributions of aluminum vacuum arcs in the absence and presence of a magnetic field, *J. Appl. Phys.* **97**, 103306-1-6, (2005).
92. Rosén, J., Schneider, J.M., and Anders, A., Charge state dependence of cathodic vacuum arc ion energy and velocity distributions, *Appl. Phys. Lett.* **89**, 141502-1-3, (2006).
93. Rusteberg, C., Lindmayer, M., Jüttner, B., and Pursch, H., On the ion energy distribution of high current arcs in vacuum, *IEEE Trans. Plasma Sci.* **23**, 909–914, (1995).
94. Yushkov, G., "Measurements of directed ion velocity in vacuum arc plasmas by arc current perturbation methods," Proc. of XXth Int. Symp. on Discharges and Electrical Insulation in Vacuum, Xi'an, P.R. China, pp. 260–263, (2000).
95. Byon, E. and Anders, A., Ion energy distribution functions of vacuum arc plasmas, *J. Appl. Phys.* **93**, 1899–1906, (2003).
96. Lieberman, M.A. and Lichtenberg, A.J., *Principles of Plasma Discharges and Materials Processing*. John Wiley & Sons, New York, (1994).
97. Tsuruta, K., Skiya, K., and Watanabe, G., Velocities of copper and silver ions generated from an impulse vacuum arc, *IEEE Trans. Plasma Sci.* **25**, 603–608, (1997).
98. Bugaev, A.S., Gushenets, V.I., Nikolaev, A.G., Oks, E.M., and Yushkov, G.Y., Influence of a current jump on vacuum arc parameters, *IEEE Trans. Plasma Sci.* **27**, 882–887, (1999).
99. Bugaev, A.S., Oks, E.M., Yushkov, G.Y., Anders, A., and Brown, I.G., Enhanced ion charge states in vacuum arc plasmas using a "current spike" method, *Rev. Sci. Instrum.* **71**, 701–703, (2000).
100. Yushkov, G.Y., Anders, A., Oks, E.M., and Brown, I.G., Ion velocities in vacuum arc plasmas, *J. Appl. Phys.* **88**, 5618–5622, (2000).
101. Anders, A. and Oks, E., Charge-state-resolved ion energy distribution functions of cathodic vacuum arcs, A study involving the plasma potential and biased plasmas, *J. Appl. Phys.* **101**, 043304-1-6, (2007).
102. Yushkov, G.Y., Oks, E.M., Anders, A., and Brown, I.G., Effect of multiple current spikes on the enhancement of ion charges states of vacuum arc plasmas, *J. Appl. Phys.* **87**, 8345–8350, (2000).
103. Kelly, H., Minotti, F., Marquez, A., and Grondona, D., Kinetic model for the evaluation of spatial charge effects in retarding field analysers applied to vacuum arc devices, *Measurement Sci. Technol.* **13**, 623–630, (2002).
104. Stenzel, R.L., Instability of the sheath-plasma resonance, *Phys. Rev. Lett* **60**, 704–707, (1988).
105. Iizuka, S., Michelsen, P., Rasmussen, J.J., Schrittwieser, R., Hatakeyama, R., Saeki, K., and Sato, N., Dynamics of a potential barrier formed on the tail of a moving double layer in a collisionless plasma, *Phys. Rev. Lett* **48**, 145–148, (1982).
106. Litvinov, E.A., "Kinetic of cathode jet at explosive emission of electrons," in *High Current Nanosecond Pulsed Sources of Accelerated Electrons (in Russian)*, Mesyats, G.A., (Ed.), Nauka, Novosibirsk, (1974).
107. Mesyats, G.A. and Proskurovsky, D.I., *Pulsed Electrical Discharge in Vacuum*. Springer-Verlag, Berlin, (1989).

108. Krinberg, I.A. and Lukovnikova, M.P., Application of a vacuum arc model to the determination of cathodic microjet parameters, *J. Phys. D: Appl. Phys.* **29**, 2901–2906, (1996).
109. Yushkov, G.Y., Bugaev, A.S., Krinberg, I.A., and Oks, E.M., On a mechanism of ion acceleration in vacuum arc-discharge plasma, *Doklady Physics* **46**, 307–309, (2001).
110. Krinberg, I.A., Acceleration of multicomponent plasma in the cathode region of vacuum arc, *Techn. Phys.* **46**, 1371–1378, (2001).
111. Tarrant, R.N., Bilek, M.M.M., Oates, T.W.H., Pigott, J., and McKenzie, D.R., Influence of gas flow and entry point on ion charge, ion counts and ion energy distribution in a filtered cathodic arc, *Surf. Coat. Technol.* **156**, 110–114, (2002).
112. Lepone, A., Kelly, H., and Marquez, A., Role of metallic neutrals and gaseous molecular ions in a copper cathodic arc operated with oxygen gas, *J. Appl. Phys.* **90**, 3174–3181, (2001).
113. Aksenov, I.I., Konovalov, I.I., Padalka, V.G., Sizonenko, V.L., and Khoroshikh, V.M., Instabilities in the plasma of a vacuum arc with gas in the discharge: I., *Sov. J. Plasma Phys.* **11**, 787–791, (1985).
114. Spitzer Jr., L., *Physics of Fully Ionized Gases*, preprint of the 2 nd revised edition, originally published by Wiley, 1962 ed. Dover, New York, (1990).
115. Anders, A., Observation of self-sputtering in energetic condensation of metal ions, *Appl. Phys. Lett.* **85**, 6137–6139, (2004).
116. Lins, G., Evolution of copper vapor from the cathode of a diffuse vacuum arc, *IEEE Trans. Plasma Sci.* **15**, 552–556, (1987).
117. Prock, J., Solidification of hot craters on the cathode of vacuum arcs, *J. Phys. D: Appl. Phys.* **19**, 1917–1924, (1986).
118. Anders, A., Time-dependence of ion charge state distributions of vacuum arcs: An interpretation involving atoms and charge exchange collisions, *IEEE Trans. Plasma Sci.* **33**, 205–209, (2005).
119. Smirnov, B.M., Atomic structure and the resonant charge exchange process, *Uspekhi Fizicheskikh Nauk* **171**, 233–266, (2001).
120. Janev, R.K. and Gallagher, J.W., Evaluated theoretical cross-section data for charge exchange of multiply charged ions with atoms. III. Nonhydrogenic target atoms, *J. Phys. Chem. Reference Data* **13**, 1199–249, (1984).
121. Smirnov, B.M., Tables for cross sections of the resonant charge exchange process, *Physica Scripta* **61**, 595–602, (2000).
122. Grozdanov, T.P. and Janev, R.K., Charge-exchange collisions of multiply charged ions with atoms, *Physical Review A* **17**, 880, (1978).
123. Bransden, B.H. and McDowell, M.R.C., *Charge Exchange and the Theory of Ion-Atom Collisions*. Clarendon Press, Oxford, UK, (1992).
124. Presnyakov, L.P. and Ulantsev, A.D., Charge exchange between multiply charged ions and atoms, *Sov. J. Quantum Electronics* **4**, 1320–1324, (1975).
125. Beuhler, R.J., Friedman, L., and Porter, R.F., Electron-transfer reactions of fast Xe^{n+} ions with Xe in the energy range 15 keV to 1.6 MeV, *Phys. Rev. A* **19**, 486–494, (1979).
126. McDaniel, E.W., Mitchell, J.B.A., and Rudd, M.E., *Atomic Collisions: Heavy Particle Projectiles*. Wiley, New York, (1993).
127. Anders, A. and Yushkov, G.Y., Puzzling differences in bismuth and lead plasmas: evidence for the significant role of neutrals in cathodic vacuum arcs, *Appl. Phys. Lett.* **91**, 091502, (2007).

128. Anders, A., Oks, E.M., and Yushkov, G.Y., Production of neutrals and their effects on the ion charge states in cathodic vacuum arc plasmas, *J. Appl. Phys.* **102**, 043303, (2007).
129. Yushkov, G.Y. and Anders, A., Extractable, elevated ion charge states in the transition regime from vacuum sparks to high current vacuum arcs, *Appl. Phys. Lett.* **92**, 201501, (2008).
130. Hasted, J.B., *Physics of Atomic Collisions*, 2 nd ed. Butterworths, London, (1972).
131. Bilek, M.M.M., Chhowalla, M., and Milne, W.I., Influence of reactive gas on ion energy distribution in filtered cathodic vacuum arcs, *Appl. Phys. Lett.* **71**, 1777–1779, (1997).
132. Chhowalla, M., Ion energy and charge state distributions in zirconium nitride arc plasma, *Appl. Phys. Lett.* **83**, 1542–1544, (2004).
133. Hopwood, J.A., (ed.) *Ionized Physical Vapor Deposition*, Academic Press, San Diego, CA, (2000).
134. Kimblin, C.W., Cathode spot erosion and ionization phenomena in the transition region from vacuum to atmospheric pressure arcs, *J. Appl. Phys.* **45**, 5235–5244, (1974).
135. Spädtke, P., Emig, H., Wolf, B.H., and Oks, E., Influence of gas added to the MEVVA discharge on the extracted ion beam, *Rev. Sci. Instrum.* **65**, 3113–3118, (1994).

5

Cathodic Arc Sources

Gera's Rule: *The arc discharge does not run well when the anode cable is disconnected.*

Abstract The chapter on arc sources and systems is somewhat unusual because it focuses on technology and engineering, rather than on physics. Here, practical designs for DC and pulsed arc sources are presented. Many details are covered such as how to trigger the arc and how to steer the apparent spot motion. From source design we move on and consider the whole system, which is generally either a batch coater or, less often, an in-line coater.

5.1 Continuous Versus Pulsed: Advantages and Disadvantages of Arc Switching and Pulsing

Practically all commercial cathodic arc systems operate in the continuous direct current (DC) mode. Continuous DC systems are characterized by a high deposition rate and reasonably low equipment cost. This is true for non-filtered and filtered systems (for filters see Chapter 7). The typical arc current is between 40 and 150 A. The lower limit of this current range is determined by arc chopping (i.e., the spontaneous extinguishing of the cathodic arc discharge), whereas the upper limit is determined by cooling considerations. In principle, the arc current can be much higher than 150 A, leading to proportionally higher plasma production and deposition rate, but one quickly runs into the issues of cooling problems of plasma source and substrate, increased cost for the power supply, and a higher macroparticle content of the coatings.

For some applications, deposition with pulsed arcs can have advantages over DC operation. The average power consumption can be easily regulated via the arc duty cycle rather than the arc current. Spot steering is not an issue since the arc spots travel only a limited distance from the point of ignition. Ignition can be designed to occur in the center of a disk cathode with the arc spots "repelling" each other. In this approach, the pulse is conveniently chosen to end when the

A. Anders, *Cathodic Arcs*, DOI: 10.1007/978-0-387-79108-1_5,

spots arrive at the cathode rim, ensuring rather uniform cathode erosion. Pulsed arcs can be operated with very high pulsed currents, and therefore the average plasma production may approach those of DC arcs.

Due to their relative simplicity in terms of power and cooling demands, pulsed arcs are frequently used in R&D systems. Results obtained in pulsed systems (charge states, ion velocity, etc.) can generally be scaled or transferred to DC arcs because the cathode processes are non-stationary regardless of pulsed or DC operation. However, there are differences between pulsed and DC arcs and one has to be careful with such generalizations. First, as discussed in Chapter 4, DC arc plasmas contain greater amounts of neutrals, such as from evaporating macroparticles and cooling spot craters. Therefore, DC arcs have

Table 5.1. Considerations for continuously operating (DC) and pulsed arc coating systems

	DC	Pulsed
Deposition rate	High	Typically only a few percent of DC, though can be scaled to DC values
Cost	Low, especially if normalized to deposition rate and part throughput	Wide range, from very low for small experimental system to moderate for high rate systems
Macroparticle production and incorporation in film (assuming no filter)	Moderate to high, especially when operating in the absence of reactive gas, cathodes of low melting temperature, and less than perfect cathode cooling	Less than DC under otherwise comparable conditions
Incorporation of hydrogen and other contamination	Very low	Can be high, especially for low duty cycle system and substrates near room temperature
Power consumption and cooling requirements	1 kW or greater per arc source, cooling must match this input power	Small for low duty systems (may not even need water cooling) to high for system that match DC deposition rates (high current, high duty cycle)
Trigger requirements	Mechanical trigger is adequate	Electronic trigger system, often involving higher voltage (>1 kV)
Scaling options	Can be scaled to elongated cathodes, or ganged for large area coatings	Typically used as point sources, may be ganged for large area coatings

generally somewhat lower mean ion charge states and ion energy, which may have consequences for the film properties. Second, coatings produced by pulsed arcs tend to have greater incorporation of hydrogen and oxygen (which is usually unwanted). While coatings with very little hydrogen (and other contaminations) can routinely be obtained with DC arcs, the hydrogen content of films can be surprisingly high when deposited in pulsed mode, especially when using short pulses, arcs with low duty cycle, and non-heated substrates [1, 2]. This will be further explored in the chapter on energetic condensation.

A comparison between DC and pulsed arcs is given in Table 5.1. In the remainder of this chapter we will explore DC and pulsed arc sources in greater detail and include a separate section on trigger methods.

5.2 DC Arc Sources

5.2.1 Random Arc Sources

DC arc sources are the workhorses of most industrial arc coaters. Some relevant patents are quite old, and hence have expired. The early commercially used designs go back to developments done in the Soviet Union (see Chapter 2). For example, the group of Leonid P. Sablev and co-workers of Kharkov, Ukraine, experimented with a number of designs. Much of the early work was only described in patents not accessible to the rest of the world, like the 1966 patent USSR N235523. In 1971, Sablev and co-workers filed for a patent in the United States, which was granted in 1974 [3]. Before we look at that particular one, we need to consider another important patent, filed in 1968 and granted in 1971 to Alvin A. Snaper [4].

Snaper's arc patent contains many elements of typical arc sources. Figure 5.1 shows the basic arrangement, here with a high-voltage spark trigger. Another version of a similar source is shown with greater detail in Figure 5.2, here with a magnetically actuated mechanical trigger. The field coil has the dual function of removing the trigger from the cathode and to "increase the directivity of the

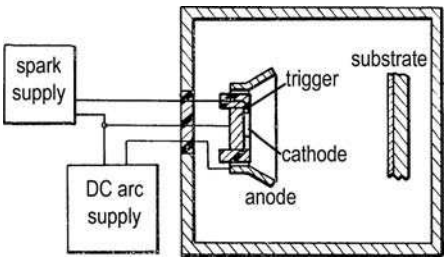

Fig. 5.1. Basic coating setup with random arc plasma source after Snaper [5]. This particular plasma gun had a high voltage trigger and the cathode's working area was limited by an insulator

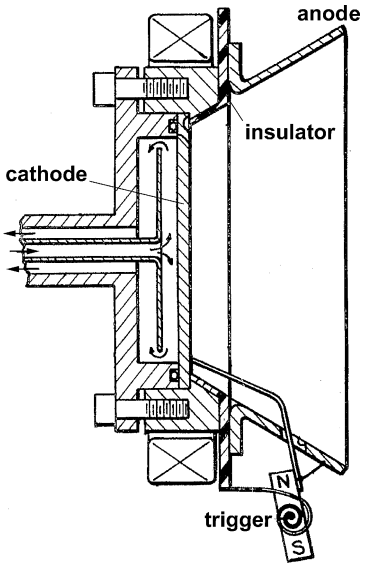

Fig. 5.2. Snaper's arc source with magnetically actuated trigger and field enhancement. (Adapted from [5])

ionized beam." Snaper does not disclose spot steering. An important feature of these arc sources is the determination of the working part of the cathode by an enclosing insulator. This solution implies that the spot(s) may operate at the cathode–insulator interface, thereby eroding the insulator material over time, which could contaminate the plasma and limit the lifetime of the insulator. Of additional concerns are the coating of the insulator by the metal plasma, which could lead to an electric short of cathode and anode, and possible cracking of the ceramic under the stress caused by the thermal load. Boron nitride has been identified as a preferred insulator material.

These problems were addressed by Sablev's patent which may be considered the prototype of "random arc" sources: a disk cathode enclosed by a floating shield, such that arc spots can only burn on the front face. Should the arc spot move into the narrow gap between cathode and shield, the impedance goes up and the operation of another spot on the front face is favored, hence the operation on the front surface is reestablished. Other features of Sablev's source included a discrete anode (as opposed to using the chamber as grounded anode) and a mechanical trigger that was connected to the anode via a resistor (Figure 5.3).

The insulator separating the cathode and the floating shield could also be coated over time and it is desirable to prevent such coating through a clever design of the gap. An example is the "labyrinth gap" by Hovsepian [7] (Figure 5.4).

In some designs, the clamping parts are exposed to the plasma, which is not a problem if the arc source is to be exclusively used with materials that arc "easily," i.e., materials of low cohesive energy. The issue of possible arcing on the cathode clamp or shields is much less critical as long as they are made of a material with

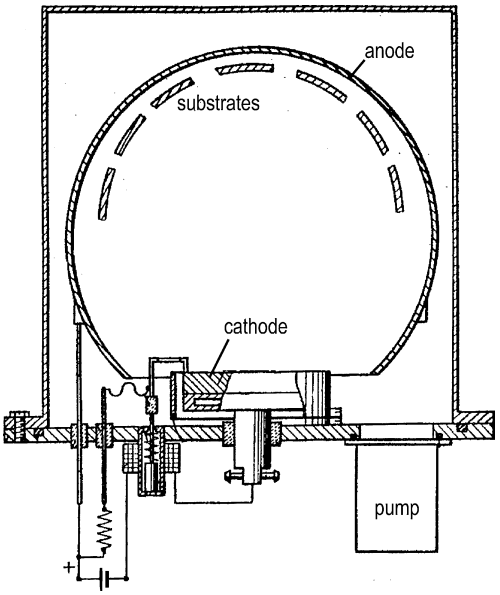

Fig. 5.3. Random arc source as disclosed by Sablev and co-workers. (Adapted from [6])

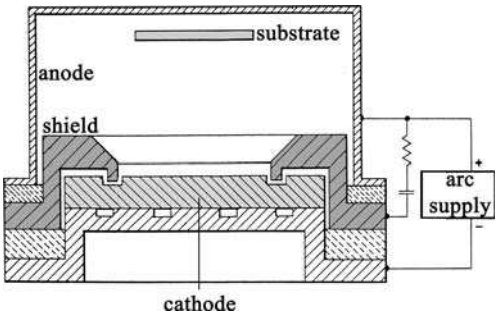

Fig. 5.4. Labyrinth design of a gap between cathode and shield. (Adapted from [7])

high cohesive energy. For example, an aluminum or titanium cathode may be held with a clamp of tungsten, molybdenum, or tantalum.

Figure 5.5 shows a "worn" titanium cathode that was used in a random arc. Typically, material erosion occurs preferentially in the center of the cathode, leading to a bowl-shaped cathode. In the case of Figure 5.5, erosion was a bit stronger on one side, perhaps due to the presence of the trigger pin on that side.

Generally, one may distinguish between random and steered arc sources, named after whether or not the apparent spot motion (Chapter 3) is controlled

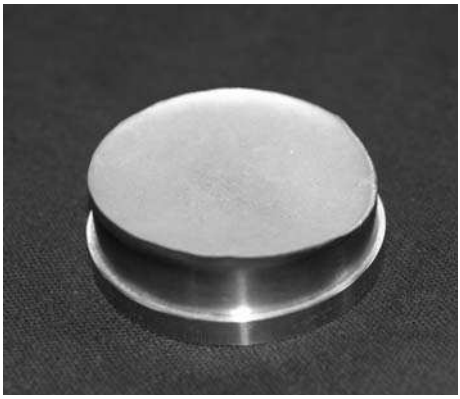

Fig. 5.5. Titanium cathode of 3 in. (7.62 cm) diameter used in a random arc source. The erosion on the right side was slightly larger because the trigger was located at that side. (Berkeley Lab, 1990s)

by electric or magnetic means. Random arc sources are a simple, low-cost approach which is reasonable for not-too-large cathodes (typically less than 10 cm in diameter). There are perhaps two reasons for considering the more-involved steered arc sources. One is related to scaling: on a larger cathode one wants to have better control of the spot location than "random," and furthermore the macroparticle content is lower if the spot is driven to higher apparent velocities (or, more physically speaking, if the ignition probability in one direction is enhanced and the spot lifetime at a given location is reduced).

5.2.2 Steered Arc Sources

Most commercial sources have some kind of spot steering, either by magnetic or by electric means. The underlying reasons for spot motion are related to the non-isotropic distribution of ignition probabilities of new emission centers, which was discussed in Chapter 3. With "spot motion" we actually refer to a virtual motion, because it is not the spot that moves but the location of related ignition events.

Let us first look at the more common magnetic steering. Generally, one may formulate two rules that govern the apparent spot motion: (i) the *retrograde motion rule* and (ii) the *acute angle rule*.

According to the retrograde motion rule, the spot tends to move in the direction of $-\mathbf{j} \times \mathbf{B}$, where $\mathbf{j}$ is the vector of current density (per engineering definition from plus to minus, i.e., pointing into the cathode) and $\mathbf{B}$ is the vector of the magnetic induction, which is in most cases given by the presence of permanent magnets or magnetic field coils. The rule is called "retrograde" because the minus sign in $-\mathbf{j} \times \mathbf{B}$ indicates a motion opposite to the Amperian force $\mathbf{j} \times \mathbf{B}$ that would act on a conductor. It is often asked why the spot motion does not follow the

Amperian force but goes in the opposite direction. The answer is simply that the virtual spot motion is not determined by the Amperian force on a conductor, rather it is related to the non-isotropic probability distribution of ignition, which in turn is related to the time-dependent local electric field strength on the cathode surface, influenced by the sheath, cathode surface layers, ion bombardment and surface temperature, and field enhancement by roughness (Chapter 3).

The *acute angle rule* says that apart from the $-\mathbf{j} \times \mathbf{B}$ motion, the spot tends to move toward the direction given by the acute angle between the magnetic vector **B** and the normal of the cathode surface [8]. This will be illustrated in several examples below.

Following the steered arc source classification by Karpov [9], one may distinguish two basic magnetic field configurations: (i) the "through-field," where magnetic field lines are essentially normal to the cathode surface (Figure 5.6), and (ii) the "arched field," where field lines arch over the cathode, forming a magnetic "tunnel," very much like in sputtering magnetrons (Figure 5.7). In fact, ordinary magnetrons, designed for deposition by sputtering, can be used as steered arc sources, though one should be careful to not arc through the rather thin targets; the arc spots tend to erode the same area that normally is preferably sputtered, also known as the *racetrack*.

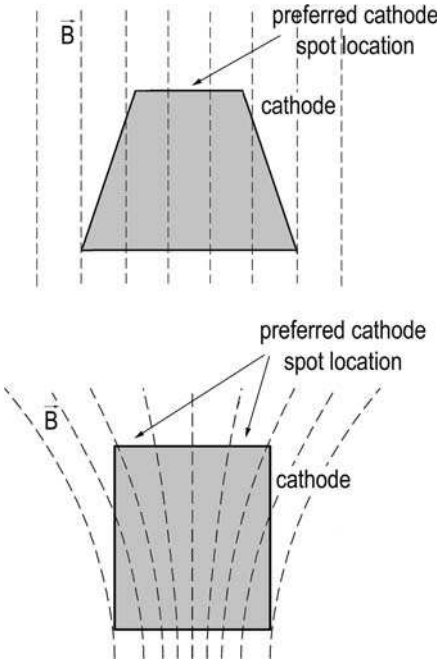

Fig. 5.6. Magnetic "through-field" used for spot steering; *top*: cone-shaped cathode and axial field; *bottom*: cylindrical cathode and diverging field

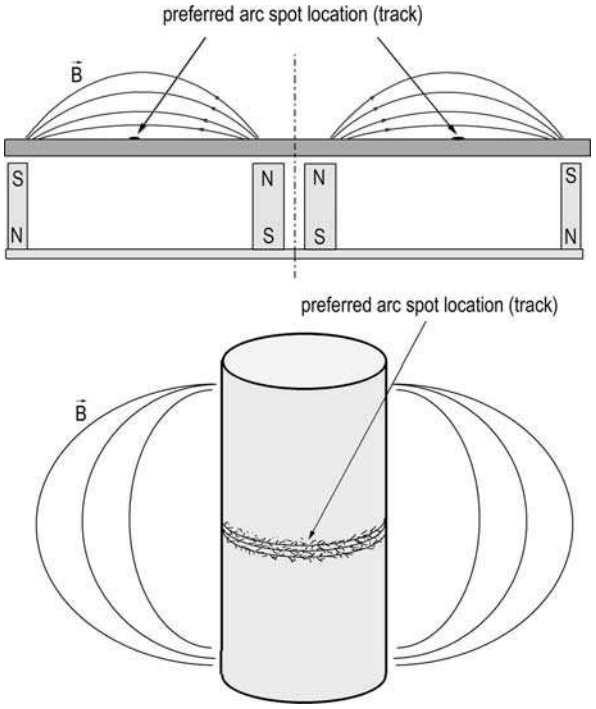

Fig. 5.7. Magnetic arched or "tunnel"-field, used for spot steering; *top*: geometry like in a planar magnetron (cross-section view); *bottom*: geometry like in a cylindrical magnetron

If we apply the acute angle rule to the through-field geometry we see that the spots tend to move to the edge region of the blunt cone or cylinder cathode (Figure 5.6). Applying the rule to the arched geometry, it is clear that the spots tend to move where the magnetic field is parallel to the cathode surface (Figure 5.7). In both cases, the spots continue to follow the retrograde motion when they have reached the optimum position according to the acute angle rule. For example, in the arched geometry, the spots tend to follow the "tunnel" formed by the arched field.

Most steered arc sources use the through-field configuration because this type of field promotes the transport of plasma to the substrate. The arched field can "trap" plasma near the cathode, which can have interesting effects on the plasma composition, but generally one would prefer a "leaky" field, as used in unbalanced magnetrons, to promote plasma drift to the substrate [10].

Magnetic spot steering was already industrially used in the Bulat arc sources developed in the 1970s (Chapter 2) [11]. The basic design of the Bulat source served as a prototype for generations of copies and improvements (Figure 5.8). Spot steering of the through-field type was accomplished by using an external magnetic field coil around the cathode that produced an essentially axial field which was normal to the front face of the blunt cone. The tilt of the cone's side

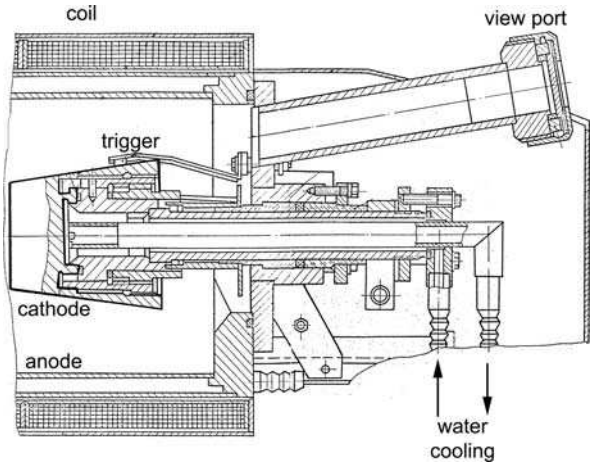

Fig. 5.8. Schematic drawing of the "grandfather" of steered arc sources, the Bulat source

surface (as opposed to using a straight cylinder) ensured that the spots were driven to the front surface (acute angle rule). A careful look at the photograph Figure 2.24 reveals the crater traces left by the spots: they indicate the screw-like path from the trigger location on the side surface toward the front edge of the blunt cone, which is the result of retrograde motion and acute angle rule.

A similar magnetic field can be achieved using a permanent ring magnet that produces an axial but diverging magnetic field. Figure 5.9 shows a conical

Fig. 5.9. Graphite cathode of conical shape used in a magnetically steered arc source; the trigger was placed on the side surface – one can see the screw-like traces indicating how the spots moved to the tip. The magnetic field was produced by a permanent ring magnet behind the cathode

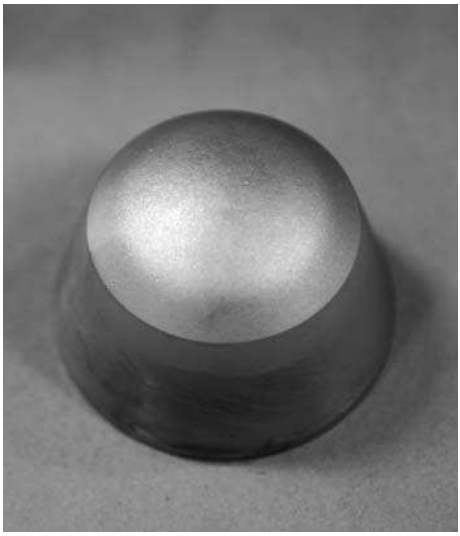

Fig. 5.10. Chromium cathode, originally a blunt cone, used in the same arc source as the cathode shown in Figure 5.9

cathode where a permanent magnet was placed behind it: one can see the arc traces winding to the tip of the cone. This geometry delivers a stable plasma flow that is exceptionally well suited for plasma injection in filters (Chapter 7) and where a well-defined spot location is desired. However, the cone shape implies that the tip, where most of the energy dissipates, is far from the cooled surface, i.e., the base surface of the cone. The material must be of high heat conductivity, like copper, or be able to handle high temperature without melting, such as graphite (Figure 5.9), or made from a refractory metal. The cone tip of other metals tends to melt, especially when the current is high. When a cone or blunt cone is used, the preferential erosion by the spot results in a dome shape after some time (Figure 5.10).

Spot steering was adopted to many other arc source designs [12]. In the following we look at a few examples and apply the above-mentioned rules.

An interesting case is the addition of a coil placed behind a cylindrical cathode. Using the labyrinth gap-limited cathode design of Figure 5.4, the coil creates a through-field that helps to collimate plasma and promote flow from source to substrate [13] (Figure 5.11). However, the effect on spot steering is small because $-\mathbf{j} \times \mathbf{B}$ is small ($\mathbf{j}$ and $\mathbf{B}$ are almost parallel), and the acute angle rule indicates a weak driving of spots toward the edges of the cathode. Therefore, the design of Figure 5.11 essentially remains a random arc but with improved cathode erosion compared to what is shown in Figure 5.5.

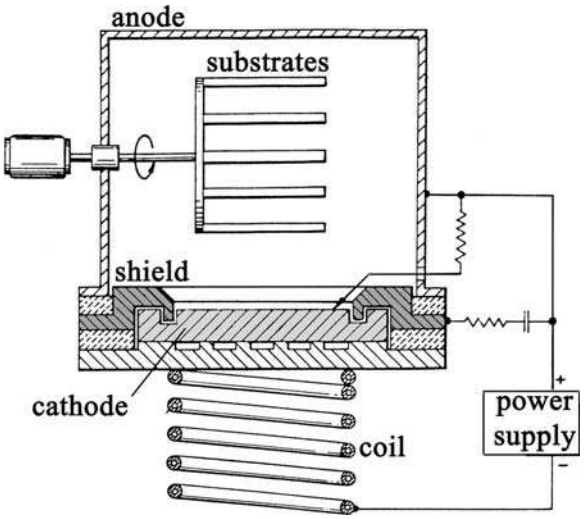

Fig. 5.11. Addition of a field coil to the labyrinth gap source, primarily for plasma collimation; the spots are slightly driven to the edges and the system is only weakly steered. (Adapted from [13])

If the field coil is small in diameter compared to the diameter of the cathode, one arrives at a geometry shown in Figure 5.12, which is characterized by a field where the normal component reaches zero [14]. Again, the acute angle rule promotes spot motion to the side but this time the spot anchors when the location of zero normal field is reached: here, only the $-\mathbf{j} \times \mathbf{B}$ drives the spot in circles and causes a "racetrack." This is in fact the tunnel-field situation of Figure 5.7. The two previous cases illustrate that the physics of through-field and tunnel-field is of course the same and just the geometry of field lines with respect to cathode and anode determines the distinction.

The coil-behind-the-cathode case can be expanded by using a *pair* of coils that produces a tunnel-field (Figure 5.13). With this arrangement, the cathode utilization and coating uniformity can be improved by changing the current in the two field coils [15].

Another idea is to use a permanent magnet behind and a field coil around the cathode. By periodically varying the coil current, the preferred location of cathode spots is varied, leading to very efficient utilization of the cathode material [16].

Yet another approach is to only use a permanent magnetic field, as mentioned earlier. Going a step further, Ramalingam [17] adopted an idea practiced with large planar magnetrons, namely to physically *move* permanent magnets behind the cathode to create a cycloidal path of the spot (corresponding to a cycloidal racetrack of a magnetron) on the working surface of the cathode (Figure 5.14).

The magnetic fringe field of macroparticle filters, which will be extensively discussed in Chapter 7, can have a noticeable effect on spot steering. In extreme

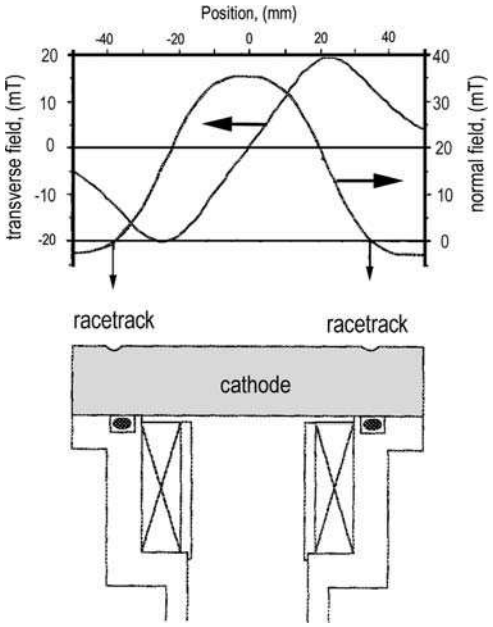

Fig. 5.12. System similar to the previous but with small-diameter coil such that the normal component of the field reaches zero – hence a tunnel-field. (Adapted from [14])

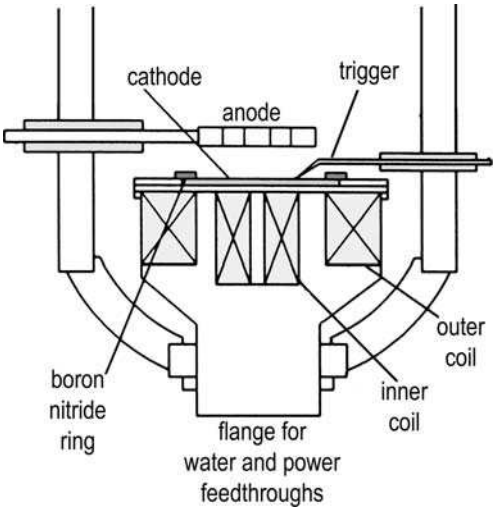

Fig. 5.13. Magnetic steering configuration with adjustable magnetic field. (Adapted from [15])

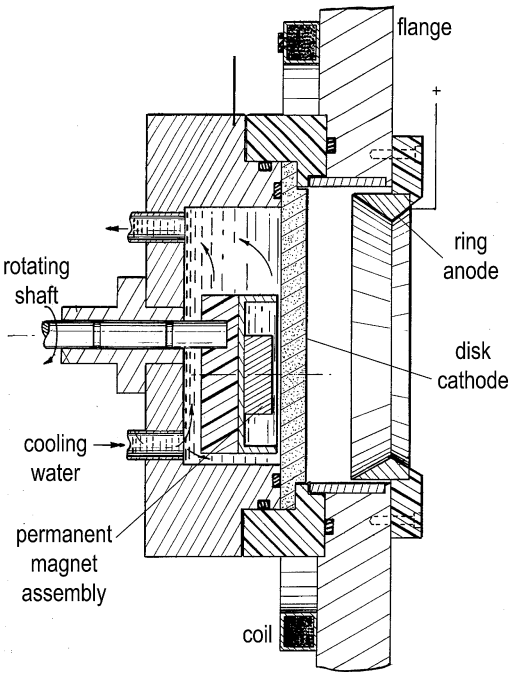

Fig. 5.14 Magnetic steering configuration in which the magnetic field is changed by physical motion of a permanent magnet. (Adapted from [17])

cases, the filter field can disrupt the desired steering altogether [18]. Therefore, the design of the *combined* magnetic steering and filter field is critical.

Some DC systems operate in a switched mode which is designed to facilitate a certain magnetic or electric type of spot steering and enhancement of the apparent spot velocity (thereby reducing macroparticle production, see Chapter 6). Examples of such switched arcs are systems developed by Vergason Technology, Inc., [19] and Vapor Technologies, Inc. [20]. In one of Vergason's designs, for example, the cathode is a long rod where the negative contact is on one end (Figure 5.15). A spot sensor (sensing the spot current's magnetic field, or light, etc.) provides information on the arrival of the spot to a switch box which connects the power contact to the other end of the cathode, thereby reversing the spot's travel direction. By adding a magnetic field [21], the arc spot appears to travel in a helix around and along the rod (Figures 5.16 and 5.17).

5.2.3 Sources with Challenging Cathodes

Some cathode materials represent special challenges and limitations: (i) cathodes that are not stable in air, (ii) cathodes that are toxic or form toxic compounds, (iii) cathodes of very low melting point, and (iv) cathodes that are metalloids or

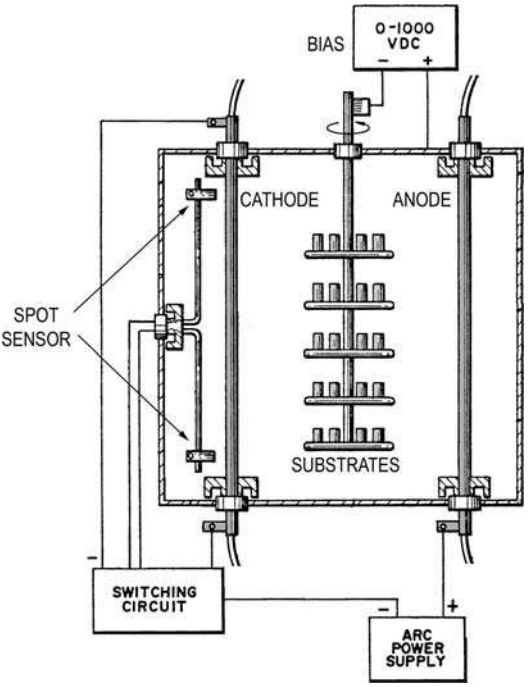

Fig. 5.15. Switched arc with long, water-cooled cathodes and anodes: the spot is steered by minimizing the voltage drop, i.e., the spot tends to move toward the end that is connected to the negative of the arc power supply. Once the spot arrives in the vicinity of the cathode end, a sensor triggers the switching of the power contact to the other end, and the spot direction reverses. (Adapted from [19])

semiconductors. Examples of cathodes belonging to group (i) are those that react readily with oxygen and/or water, especially the alkali and alkali earth metals, i.e., group IA and IIA elements of the Periodic Table, and some rare earth elements like praseodymium (Pr). An example of group (ii) cathode materials is lead (Pb). Those materials can in principle be used but require special handling, usually mounting under inert gas in a glove box.

Low-melting-point materials can be operated in a liquid form in vessels or crucibles. Ironically, the toxic, low-melting-point material mercury (Hg) was the best investigated cathode material until about the 1960s. Materials like tin (Sn) can be used in solid form provided the arc current is kept as small as possible and cooling is adequate. Tin is an important material to make SnO_2 for optical thin films. To utilize Sn, Boxman and co-workers constructed a plasma source with a copper cathode/crucible such that they can be filled with Sn ingots, which are melted into place using a hot plate. After cool-down, the copper–tin assembly cathode is part of the source as shown in Figure 5.18.

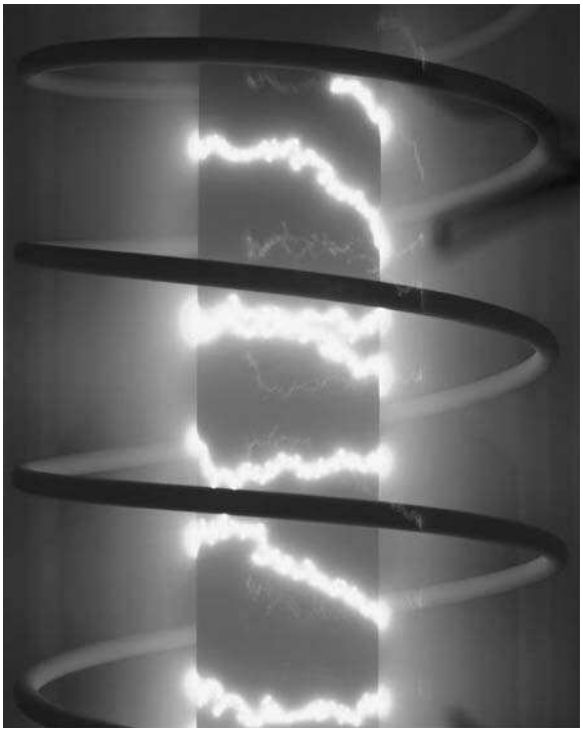

Fig. 5.16. Arc spot steering on rod cathode in a magnetic field. (Photo courtesy of Garry Larson, Vapor Technologies)

Metalloids (e.g., boron) and semiconductor cathodes (e.g., highly doped silicon, germanium) present their own challenges. Ohmic heating through the arc current often leads to expansion that the brittle materials cannot accommodate; they fracture or shatter. If the current is too low, the arc tends to be unstable and extinguishes and if it is high, high open-circuit voltages are required and significant Ohmic heating occurs inside the cathode body. The apparent spot motion is much slower compared to metals, which in part is due to the resistivity decreasing with temperature, $d\rho/dT < 0$. For these reasons, cathodic arc sources are usually operated only with "well-behaving" metals.

However, since it is highly desirable to have high fluxes of ions of such materials, serious attempts have been made to overcome the obstacles. In one approach to produce silicon plasma [22], the cathode was allowed to crack but was kept together with a holding ring; the heat by the spot fused the parts of the cathode together so deposition could continue.

In another approach, the cathode is heated before arc ignition, and one utilizes the Ohmic heating to maintain a very high temperature of the part where cathode spots are supposed to operate. This concept was successfully

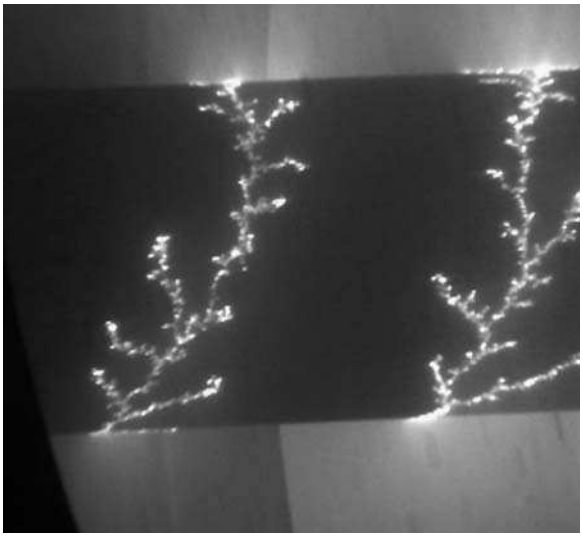

Fig. 5.17. Open-shutter photograph of cathode spots eroding an aluminum rod (diameter 2.5 cm) cathode in vacuum with an axial magnetic field present; the apparent spot motion toward one end of the rod is determined by the electrical contact made to that end of the cathode; one can see the superposition of random branching and steered motion (Berkeley Lab, 2002)

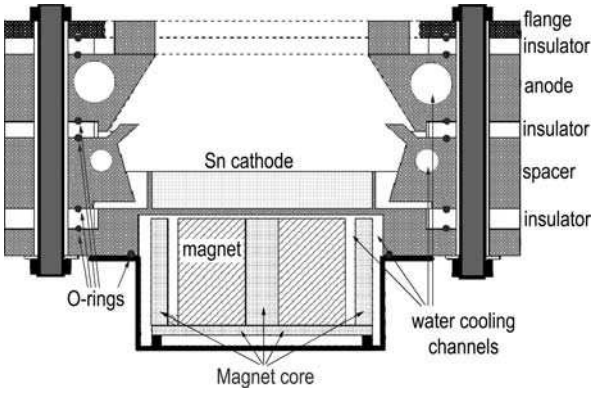

Fig. 5.18. Cross-section of the Sn arc plasma source constructed at Tel Aviv University (about 2002); the source is elongated and to be used with the linear S-shaped filter (see Chapter 7) for the deposition of large-area SnO_2 coatings

introduced for boron by pre-heating to about 800°C and operating in Ar/N_2 gas mixture in a pressure range of 0.08–1.2 Pa [23]. Operation in vacuum has been demonstrated with boron and boron compound cathodes [24] made by a special microwave-assisted sintering process [25]. Figure 5.19 shows such a boron cathode after it has been used in a cathodic arc source.

Fig. 5.19. Boron cathode produced by the microwave sintering process [25], shown here after arc operation. (Courtesy of C.C. Klepper, HY-Tech Corporation)

5.2.4 Sources with Multiple Cathodes

For advanced coatings it is desirable to have more than one metal available. A straightforward solution is to use an alloy or sintered multi-element cathode. This has the advantage of simplicity but the disadvantage of not being able to change the metal atom ratio of the coating. Therefore, some groups have opted to use individual arc sources and combine their plasma flows [26, 27], for example to study $Ti_xCr_{1-x}N$ of variable composition with (200) preferred orientation [28]. For systems that require macroparticle filtering (cf. Chapter 7), it is, however, desirable to produce the different metals at practically the same location, and so the solution is an arc source that has more than one cathode. The group in Tel Aviv [29] demonstrated exactly that using a triple-cathode arc source coupled to a straight plasma duct. The three cathodes were located in a circle centered on the system axis. There was a common anode but with three apertures, each located opposite to one of the cathodes. Each cathode had a separate trigger ignition system and the cathodes could be operated simultaneously or separately. A figure is provided in Chapter 7 when plasma filters and steering coils are discussed.

5.3 Pulsed Arc Sources

5.3.1 Miniature Sources

Pulsed operation of an arc source allows us to design miniature source versions that have a small "footprint" in several respects: size, cost, power consumption, cooling requirement, flexibility of mounting, etc. Another reason is that the duty

cycle can be chosen to be arbitrarily small, and thereby the thermal load on temperature-sensitive materials (like plastics) can be kept as low as needed. Yet another reason for using a miniature source is that the working area of the cathode can be made small, even down to a few square millimeters if needed, and thereby the location of the plasma production can be point-like and well defined. In contrast, for thermal management reasons, DC arc sources need to have a rather large cathode, often a cone or disk of at least 5- to 10-cm diameter, on which the cathode spots can burn.

Miniaturized arc sources need to be designed to match the desired average power,

$$\overline{P} = \int I_{arc} V_{arc} dt \Big/ \left(t_{on} + t_{off}\right), \tag{5.1}$$

to the cooling capabilities. In (5.1), the integral is over the pulse period. If the current is approximately constant during the pulse on-time, the integral can simply be approximated by $\int I_{\mathrm{arc}} V_{\mathrm{arc}} \mathrm{d}t \approx I_{\mathrm{arc}} V_{\mathrm{arc}} t_{\mathrm{on}}$ and (5.1) can be re-written as

$$\overline{P} = \delta I_{arc} V_{arc}, \tag{5.2}$$

where δ designates the duty cycle,

$$\delta = t_{on} \Big/ \left(t_{on} + t_{off}\right). \tag{5.3}$$

In the absence of water cooling, the duty cycle must be kept very small, typically $\delta < 1\%$. The implication is, naturally, that the deposition rates that can be achieved with these miniaturized sources are generally much smaller than the rates obtained with DC arc sources.

Due to the pulsed nature, miniature arc sources are commonly equipped with an electric (as opposed to mechanical) trigger system, or the simple "triggerless" approach is applied (Section 5.4.4). MacGill and co-workers [30] described a number of miniature arc sources that were designed around small cathode rods whose diameter ranged from 1/2 in. (12.5 mm) to 1/8 in. (3.12 mm) (Figures 5.20 and 5.21).

Miniaturization may also include the power supply such as to minimize the weight of the total system. This has been done to develop so-called microthrusters that can be utilized to control the attitude of satellites in space [31].

5.3.2 High-Current Pulsed Arc Sources

In contrast to general perception, pulsed arc sources can reach or even exceed the deposition rate of DC arc sources. This can be achieved when using high arc current pulses (> 1 kA) at high pulse duty cycle. The plasma production was shown to be approximately proportional to the power of the arc discharge. Since the discharge voltage does not increase very much when higher currents are used, it is common to refer to the arc current (not power) as the output scaling parameter.

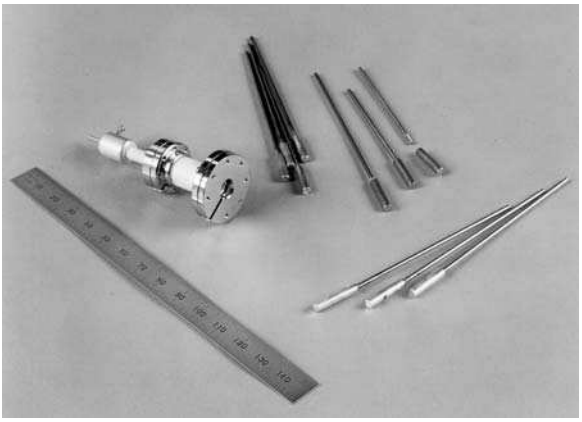

Fig. 5.20. Miniature cathodic arc source ("microgun") with sets of spare cathodes and a ruler for size comparison; this source was made from ceramic and metal only and used in the study of catalytic ultrathin films in ultra-high vacuum (Berkeley Lab, about 1995); it was manufactured under license by RHK Technology, Inc.

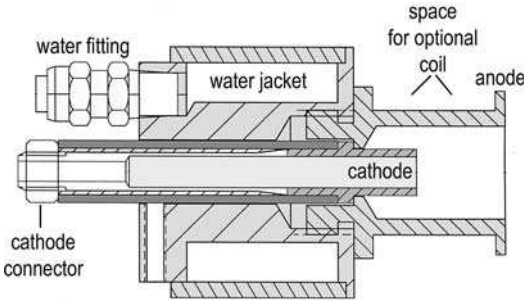

Fig. 5.21. Miniature cathodic arc source ("minigun"), a popular low-cost choice for small-scale R&D applications (Berkeley Lab, about 1995); for scale: the cathode rod has a diameter of a ¼ in. (6.25 mm)

In high-current arcs, multiple cathode spots form on the cathode. Based on the retrograde motion rule and taking into account the magnetic field produced by the current path to a spot, simultaneously existing cathode spots tend to "repel" each other (Figure 5.22). Therefore, it is convenient to use this feature with a centrally located trigger, as realized in the high-current arc (HCA) of the Fraunhofer Institute [32, 33] and very similar incarnations [34, 35]. The trigger pin is located in the center of the cathode. The spots appear to be steered away from the initial central trigger location (Figure 5.23). Therefore, the pulsed high-current arc can be considered as a special case of a steered arc. For a limited time, the HCA is capable of operating with very high currents (peak up to 5 kA) at

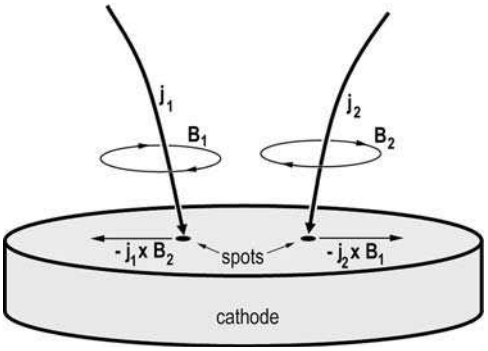

Fig. 5.22 Illustration of simultaneously existing arc spots of a high-current arc: the spots tend to repel each other following the same retrograde motion rule and acute angle rule as arc spots on DC cathodes with external magnetic field. Note that the retrograde rule applies in such a way that the current **j** of one spot is in the field **B** created by the current of the neighboring spot

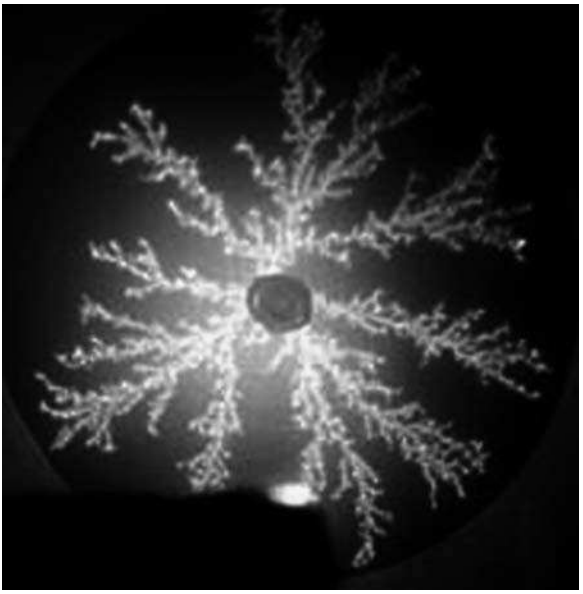

Fig. 5.23. Arc spots moving away from the central trigger of a high-current arc; also here one sees the superposition of random and steered spot motion. (Photo courtesy of Thomas Schülke)

high arc pulse repetition frequencies (up to 300 pulses per second) such that the average plasma production and deposition rate can exceed typical DC values.

The HCA system can be combined with a macroparticle filter. Also here, the *combined* filter and high-current self-field need to be taken into account. The filter typically operates continuously because the coil current rise and fall times

would be too long when operating the arc with very high repetition rates. (More about the filtered HCA is described in Chapter 7.)

In the absence of intentional and varying steering fields, an erosion pattern appears that amplifies itself: the spot trains tend to carve valleys into the cathode when used for more than 10^5 pulses [35] (Figure 5.24).

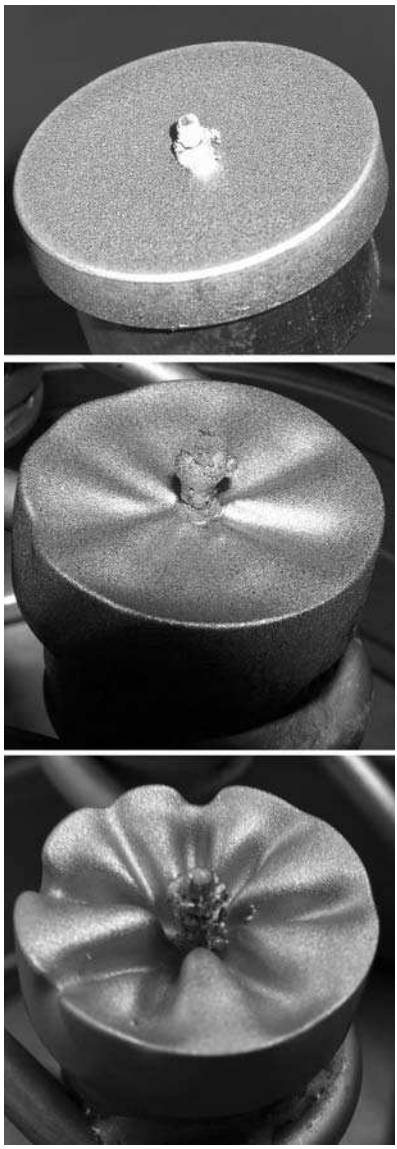

Fig. 5.24. Arc erosion pattern as carved into the cathode by repeated action high-current pulse arcs: after 10,000 pulses (*top*), after 450,000 pulses (*center*), after 10^6 pulses. (Photo courtesy of Marcela Bilek and Luke Ryves, Sydney University)

5.3.3 Sources with Multiple Cathodes

Cathodic arc sources with multiple cathodes were already mentioned in Section 5.2.3, and here we look at their smaller cousins suitable for pulsed operation. The group in Sydney took the basic design of the high-current arc (HCA), introduced in Section 5.3.2, and built a source with two cathodes [36]. Figure 5.25 shows its cathode assembly with the cylindrical anode removed.

A similar approach based on the minigun design (Section 5.3.1) was done in Berkeley where two cathodes were integrated into a single anode body [37] (Figure 5.26). In this source, no trigger electrodes are needed (see section on triggering) but the arc power is switched on the cathode side. As illustrated in Figure 5.27, the purpose of the compact dual-cathode source is to inject plasma into a single filter and, additionally, to allow for selective cathode operation, which enables the operator to apply bias in synchronization with the desired

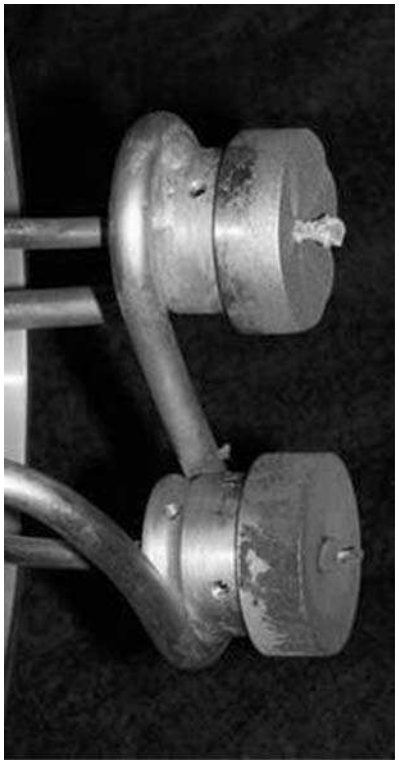

Fig. 5.25. Cathode assembly of the two-cathode version of a miniaturized high-current pulsed arc source; the anode is removed for better visibility. The cathodes, titanium (*top*) and graphite (*bottom*), are heavily used and so the central trigger pins are clearly visible. (Photo courtesy of Marcela Bilek and Luke Ryves, Sydney University, see also [36])

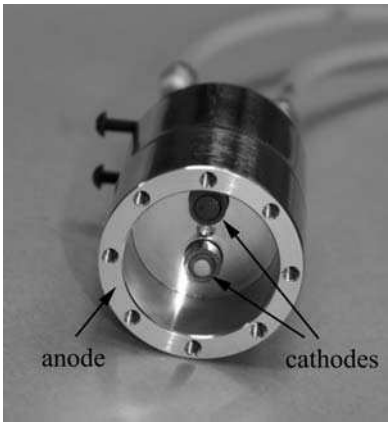

Fig. 5.26. Photograph of a miniature pulsed cathodic arc plasma source with two cathodes in a common, water-cooled anode body; each of the cathode is a rod with ¼-in. (6.25-mm) diameter. (Photo Berkeley Lab, about 2004, see also [37])

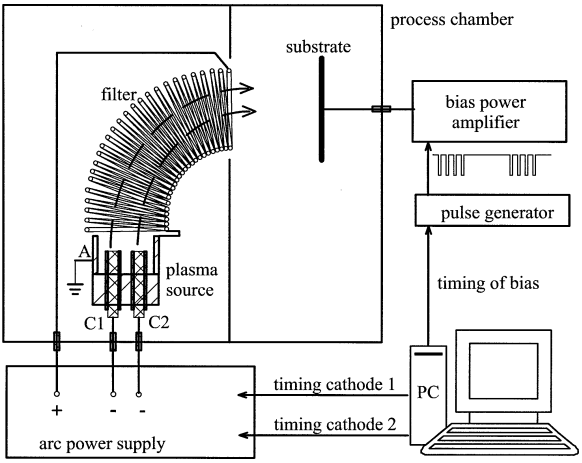

Fig. 5.27. Integration of a dual-cathode plasma source in a filtered arc system; the setup allows the operator to selectively synchronize arc pulses and bias pulses. (After [37])

material. For example, if the material is graphite and molybdenum, one may wish to selectively apply bias to the flux of carbon to optimize the diamond-like properties of the coating but does not use bias for the molybdenum flux because that would cause graphitization [38].

5.4 Arc Triggering

> The simplest way to make a cathode active is that used in all arcs, i.e. separating the two electrodes after having brought them into contact.
>
> E. Weintraub, 1904

5.4.1 Contact Separation

The oldest and most reliable technique of starting an arc is by electrode separation. This applies to both the cathodic and thermionic arc modes. One can find examples of this method back to the earliest reports and patents on arcs. For example, Weintraub in 1904 explains this and refers to "Eug. Pat. 211 (1879)" by Rapieff ([39] p. 96). Electrode separation works even in the case of the mercury arc, i.e., using the liquid metal. As Buttolph writes in 1920, arc triggering was "easily produced by bringing the mercury cathode into contact with the anode and then breaking the circuit thus formed" ([40] p. 745).

The arc separation method requires that at least one of the electrodes is movable, for instance by mounting it on bellows. Vacuum circuit interrupters [41, 42] work this way. The instant the electrodes separate, the contact area is reduced to one or two microscopic points with very high current density. The mechanism of initial plasma production is similar to a wire explosion (the "wire" now being very short).

5.4.2 Mechanical Trigger

A straightforward extension of the contact separation method is using a third electrode, the movable trigger, which is at anode potential and touching the cathode. The cathode and anode are stationary (Figure 5.28). This is a very

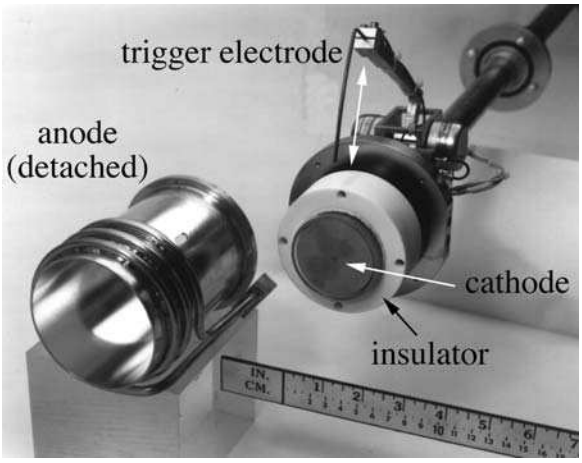

Fig. 5.28. DC arc source with a mechanical trigger pin, which – in this case – is actuated by an electromagnetic solenoid (Berkeley Lab, early 1990s)

reliable method that has been widely adopted for DC arc systems. The actuator of the mechanical trigger can be electromagnetic, spring-loaded, pneumatic, manual, or a combination of these methods. The trigger pin approaches the cathode, touches it, and is removed so as to allow the same processes of cathode–anode contact separation to occur.

The trigger electrode is usually and conveniently connected to the anode via a resistor. The resistance should be small to allow arc initiation at sufficiently high current (i.e., higher than the chopping current). However, very low resistance would imply an enhanced likelihood of welding of the trigger pin to the cathode. Values of about 2–10 Ω have been found to be practical.

Disadvantages of a mechanical trigger are its low repetition rate, the problem of welding pin and cathode, and pin erosion. The first disadvantage is not an issue for DC operation where the number of trigger events is small. The welding problem can be mitigated by choosing suitable trigger pin materials. Tungsten, tantalum, and molybdenum are often used, and welding is completely avoided when using graphite. Graphite pins, however, show high mechanical abrasion and tend to fail after a small number of trigger events unless an adjustment mechanism is employed.

Mechanical triggers have been used in industrial batch coaters since their introduction in the 1980s [43].

5.4.3 High-Voltage Surface Discharge

Pulsed arc systems require a large number of trigger events and, in some cases, with rather high repetition rate ($\sim$ 100 pulses per second). Clearly, mechanical triggers are not well suited. Repetitively pulsed electrical systems are clearly favored. One common approach is to utilize a pulse discharge between a (stationary) trigger electrode and the cathode, with the trigger being positive and the cathode negative, hence the initial spot forms at the cathode [44–47]. Generally, a ceramic insulator is placed between trigger electrode and cathode, and the discharge may be described as surface flashover (Figure 5.29).

For reliable triggering, the amount of plasma produced in the trigger discharge must not be too small. This can be assured by making trigger pulse current and duration sufficiently high and long, respectively. For example, a

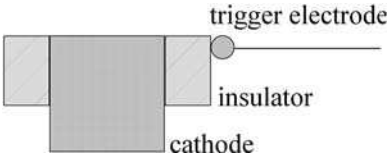

Fig. 5.29. Schematic of a surface flashover trigger: a positive high-voltage pulse is applied to the trigger electrode with respect to the cathode potential

current pulse should be at least a few tens of amperes, with a duration of at least a few microseconds, preferably tens of microseconds [47, 48].

Such trigger pulses can be readily achieved with common high-voltage equipment based on thyratrons or thyristors (also known as silicon-controlled rectifiers, SCRs). Recent development in IGBTs (insulated gate bipolar transistors) expanded their use into the kilovolt range, and therefore IGBT-based semiconductor pulse generators become increasingly popular. A step-up transformer is sometimes used to obtain higher voltages with inexpensive semiconductor switches, though one should keep in mind that stepping up the voltage implies stepping down the current. Hence, the current in the transformer's primary circuit must be rather high to ensure that the current in the secondary, i.e., the trigger current, is greater than the chopping current.

A popular approach to avoid very high voltages is to intentionally "contaminate" the surface of the ceramic such that it becomes slightly conducting (in the simplest case, one can use the "pencil mark trick").

Possible drawbacks of the surface discharge approach are the contamination of the plasma with erosion products from the insulator surface and the possible ceasing of the trigger discharge if the insulator gets coated with a conducting layer. In that case, the trigger current will flow through the conducting coating without trigger plasma production. A good insulator design or partial shielding of the insulator from the arc plasma can solve this issue.

The trigger–ceramic geometry can be such that the ceramic is at the side of the cathode or it may be placed in the center (e.g., used for the HCA, Section 5.3.2).

5.4.4 Low-Voltage and "Triggerless" Arc Ignition

An elegant extension of the previous approach is to utilize, not avoid, a rather conducting coating on the insulator. The trigger current is used to produce a "hot spot" at the interface where the coated ceramic touches the cathode. Ohmic heating causes thermal runaway: the hotter the contact spot the greater the voltage drop and power dissipation at that location, leading to even greater temperature, and eventually (and quickly) to plasma. The current through the coating does not need high driving voltage when its resistance is relatively low. One may simply use the open-circuit voltage of the arc power supply (typically 80 V or greater). In this case, the trigger electrode can simply be connected to the anode via a resistor. The electric circuit looks similar to the one for the previously described mechanical trigger. Yet another simplification is to not even use the third electrode (the trigger electrode) but coat the insulator that separates the cathode and anode. The coating itself is the trigger resistor (Figure 5.30). In such an approach, neither a trigger power supply nor a trigger electrode is used, which led to the label "triggerless" arc ignition [49]. The arc plasma is utilized to "repair" the eroded contact area, and $\sim 10^6$ pulses have been demonstrated. Such "self-triggering" system requires that the arc power is switched. The principle not only is applicable to repetitively pulsed systems with trigger

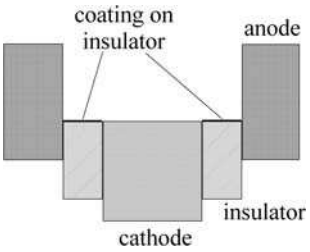

Fig. 5.30. Principal geometry for initiation of a cathodic arc in the "triggerless" scheme, using a conducting coating on the ceramic that separates cathode and anode

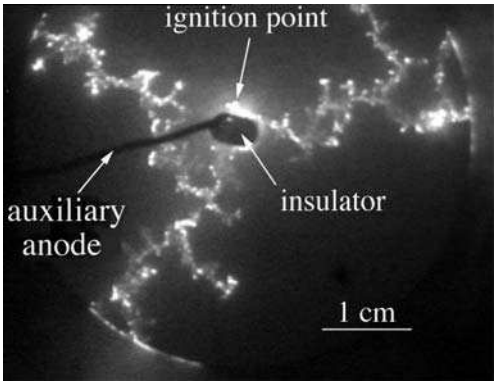

Fig. 5.31. Central trigger approach using a stationary pin touching a coated ceramic; the pin is at anode potential via a resistor. The application of the arc voltage leads to the formation of a hot spot and plasma. In the case shown here, the current is high such that about three arc spots operate simultaneously, repelling each other

locations on the side of the cathode (like the minigun design) or in the center of the cathode (Figure 5.31), but can also be used with steered DC arcs, and in fact some Bulat systems and systems with elongated cathodes have implemented it.

5.4.5 Laser Trigger

Early experiments of laser-triggered vacuum discharges were carried out shortly after the laser became available [50]. Usually, CO_2–TEA lasers ($\lambda = 10.6$ μm) with pulse duration 100–200 ns and power 1–10 MW were used [51], and those proved too expensive to be of any practical relevance.

This assessment changed when Siemroth and Scheibe [52] found that a peak power of 40 kW was sufficient for repetitive arc triggering (Nd-YAG laser, $\lambda = 1.06$ μm, pulse duration 90 ns). The laser beam was focused to a spot size of 150-μm diameter and the cathode was rotated to provide a fresh surface for

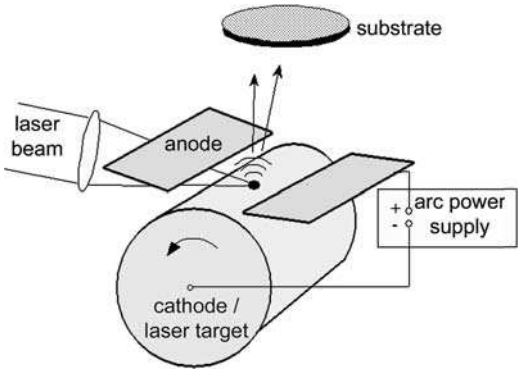

Fig. 5.32. Schematic of a laser-triggered cathodic arc

every pulse (Figure 5.32). The arc ignition probability was greater than 50% for a titanium cathode when the power exceeded $8 \times 10^{11} \mathrm{W/m^2}$. Vogel and Höft [53] came to a similar result using a Q-switched ruby laser at $\lambda = 694$ nm with pulse duration of only 20 ns. They found that crater formation on the laser-irradiated surface starts when the laser power density exceeds 2×10^{11} W/m^2 for Pt, 0.9×10^{11} W/m^2 for tungsten, and 1.3×10^{11} W/m^2 for silver. The depth of the produced craters was about 10 μm, thus the volume power density was of the order 10^{16} W/m^3. With the availability of affordable pulsed lasers, the concept seems increasingly acceptable. Indeed, the "Laser-Arc," developed by the Fraunhofer Institute in Germany, has become a well-established, repetitively pulsed arc system especially for the deposition of hard coatings [54] and multilayers [55].

5.4.6 Plasma Injection

Triggering is generally achieved when the local electric field strength at the cathode surface is high enough to facilitate thermal runaway of the thermo-field electron emission (explosive emission, see Chapter 3). The high field is generally obtained when some sort of plasma is provided such that the sheath shrinks: with the cathode voltage dropping in a very thin sheath, the resulting field strength is high right at the cathode surface.

Various ways other than the already described have been used to produce initial plasma that triggers the main arc discharge. For example, the initial plasma could be injected using a separate plasma injector. However, one really shifts the issue to triggering the injector.

Lafferty [56] used a high-voltage surface discharge between hydrogen-loaded titanium electrodes to inject plasma into the main vacuum arc gap. Bernadet and

co-workers [57, 58] investigated the parameters of the injected plasma needed for reliable triggering. They found that the arc trigger probability had a sharp threshold, which is a function of the main gap distance. For example, using a short 4-μs trigger pulse, the current producing the injected plasma needs to be 300 A for a main gap of 2 cm and 500 A for a gap of 4 cm. The dependence on the gap distance can be related to the greater plasma expansion for the larger gap: greater expansion gives lower plasma density, thicker sheath, and therefore lower electric field strength at the cathode.

5.4.7 Trigger Using an ExB Discharge

An interesting approach to the trigger issue was found by Nikolaev et al. [59] who employed a discharge in crossed electric and magnetic fields. This approach is applicable to cathodic arcs operating with background gas (as opposed to vacuum arcs). Two configurations have been explored: a Penning discharge and a magnetron discharge. The gas discharges are fed by a high-voltage (several kV), low-current (about 0.1 A) power supply via a capacitor whose capacity is sufficient to maintain a current pulse of many amperes for at least 10 μs, allowing the formation of a cathode spot. In contrast to all other schemes, not the applied voltage but the *magnetic field* is pulsed. The gas pressure can be as low as 10^{-5} Torr (1 mPa) when the pulsed field is very strong, i.e., of the order of about 1 T. The pressure needs to be somewhat higher for lower fields. At the low pressure of 1 mPa, the arc plasma composition and ion charge states are practically the same as with a "pure" vacuum arc.

5.5 Arc Source Integration in Coating Systems

> Half of all problems are due to bad electrical contacts.
>
> (a professor of experimental physics, about 1980)

5.5.1 Batch Systems

Almost all industrial arc coating systems are batch coaters. This may be promoted by the fact that the cathodic arc plasma is naturally produced at point-like emission sites, even when using large or elongated cathodes. DC arc sources with a typical cathode size of 10 cm can be considered technical point sources. It is common to implement more than one DC "point" source in order to improve coating uniformity, or to coat a large number of parts simultaneously, and to improve the average deposition rate. An example of a very large batch coater with several arc "point" sources is shown in Figure 5.33.

For a number of applications, such as the coating of batches of drill bits, somewhat smaller chambers are more practical. Figure 5.34 shows schematically a popular design: the set or "gang" of sources is arranged to fill the deposition

Fig. 5.33. Very large batch coater using a "gang" of point-like arc sources. (Photo courtesy of Dmitry Karpov)

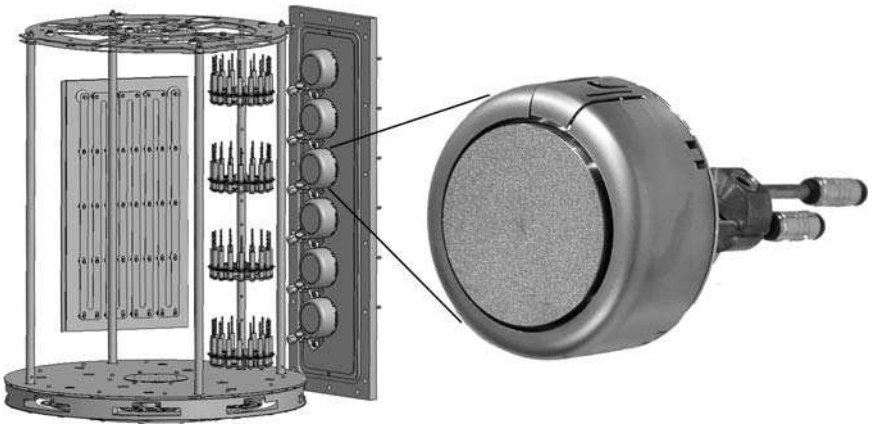

Fig. 5.34. A common approach to batch coating of tools or similar workpieces: the deposition chamber is uniformly filled with metal plasma by a set of vertically aligned plasma sources; one source is shown on the *right* side, and the rectangle on the *left* side is the substrate heater. (Illustration courtesy of Inovap GmbH, Germany)

chamber uniformly with metal plasma; the substrates are attached to movable fixtures, often based on a planetary rotational system (Figure 5.35). Figure 5.36 shows a similar commercial batch coater but this time equipped with an elongated cathode, replacing the gang of sources. The spot is steered and therefore the plasma is uniformly distributed along the length of the cathode in the time-averaged sense, as is evident from the erosion pattern seen on the cathode (Figure 5.37).

From an industrial and economical point of view it is important to consider the whole process, not just the actual coating phase. Other phases are critical

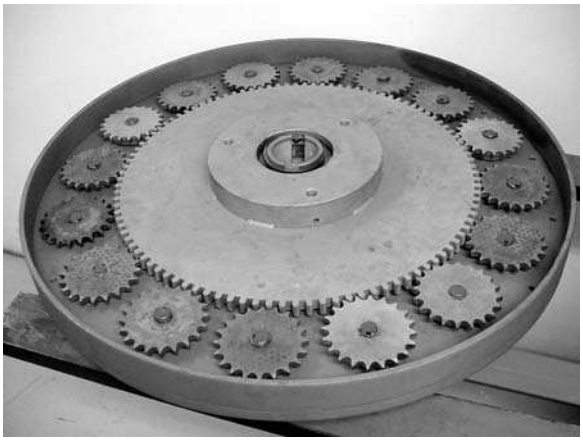

Fig. 5.35. Part of the planetary substrate rotation system, often mounted above the floor of a batch coater; rotating rods with fixtures are mounted on top of each gear. (Photo courtesy of Vergason Technologies, Inc.)

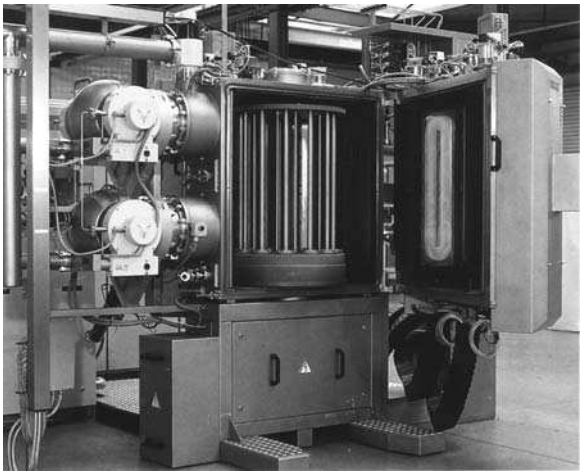

Fig. 5.36. Example of a smaller batch coater using a long cathode, visible on the inside of the open chamber door. The substrates are mounted to the planetary rotational systems in the center of the chamber. The two units on the left side are large turbo-molecular pumps. (Photo courtesy of Hauzer Techno Coatings)

such as loading and unloading the fixtures, positioning, pumpdown, and pre-heating. In Figure 5.38, a batch system is shown with its customized loading equipment: a forklift-style holder positions a fixture system into the chamber. This kind of approach is especially important when the weight and size and fixtures and parts are much larger than a human could possibly handle (Figure 5.39).

Fig. 5.37. Long (1 m) titanium cathode showing uniform erosion along its length, indicative for uniform plasma production averaged over time. (Photo courtesy of Vergason Technologies, Inc.)

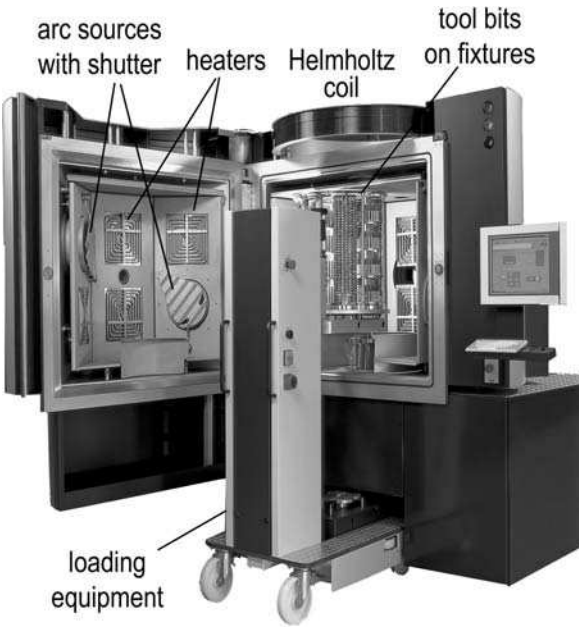

Fig. 5.38. Modern batch coater (Balzers RCS) with custom forklift-like loading system; the chamber is wide open and one can see the arc sources (with shutter) and heaters built in the door and side wall of the chamber. (Courtesy of Balzers Ltd., Liechtenstein)

5.5.2 In-Line Systems

While most of the commercial coating tools are batch coaters, some in-line coaters make use of arc coating [60]. Figure 5.40 shows an in-line coater: such a coating system has a sequence of adjacent chambers designed to handle specific process steps such as loading, heating, cleaning, arc coating, cooling, unloading.

Fig. 5.39. Very large batch coater capable of coating large batches or very large individual parts. (Photo courtesy of Hauzer Techno Coatings)

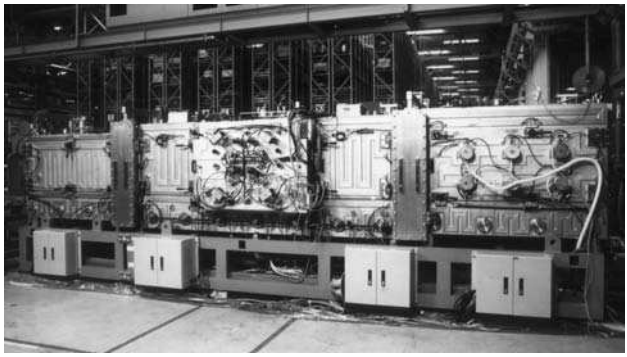

Fig. 5.40. In-line coater, characterized by sequence of subchambers, each designed to accommodate each process step: loading, heating, coating, etc.; note that this is a vertical system with the sources on the side walls. (Photo courtesy of Kobelco, Japan)

In-line coaters can have large production throughput, often for large, flat substrates. In-line coaters depend on the full operation of all subchambers – therefore they require careful design and components of high reliability. It is preferred that each process step requires about the same time, which maximizes throughput. Generally one distinguishes horizontal and vertical in-line systems, depending on the positioning of samples and sources. In the vertical version shown in Figure 5.40, the sources are mounted on the side walls, pluming plasma horizontally onto the vertically extended substrates.

References

1. Schneider, J.M., Anders, A., Hjörvarsson, B., and Hultman, L., Magnetic-field-dependent plasma composition of a pulsed arc in a high-vacuum ambient, *Appl. Phys. Lett.* **76**, 1531–1533, (2000).
2. Schneider, J.M., Anders, A., Hjörvarsson, B., Petrov, I., Macak, K., Helmerson, U., and Sundgren, J.-E., Hydrogen uptake in alumina thin films synthesized from an aluminum plasma stream in an oxygen ambient, *Appl. Phys. Lett.* **74**, 200–202, (1999).
3. Sablev, L.P., Dolotov, J.I., Getman, L.I., Gorbunov, V.N., Goldiner, E.G., Kirshfeld, K.T., and Usov, V.V., "Apparatus for vacuum evaporation of metals under the action of an electric arc," patent US 3,783,231 (1974).
4. Snaper, A.A., "Arc deposition process and apparatus," patent US 3,836,451 (1974).
5. Snaper, A.A., "Arc deposition process and apparatus," patent US 3,625,848 (1971).
6. Sablev, L.P., Atamansky, N.P., Gorbunov, V.N., Dolotov, J.I., Lutseenko, V.N., Lunev, V.M., and Usov, V.V., "Apparatus for metal evaporation coating," patent US 3,793,179 (1974).
7. Hovsepian, P., "Lichtbogen-Verdampfungsvorrichtung," patent DE 4220588 (1994).
8. Aksenov, I.I. and Andreev, A.A., Motion of the cathode spot of a vacuum arc in an inhomogeneous magnetic field, *Sov. Tech. Phys. Lett.* **3**, 525–526, (1977).
9. Karpov, D.A., Cathodic arc sources and macroparticle filtering, *Surf. Coat. Technol.* **96**, 22–33, (1997).
10. Ehiasarian, A.P., Hovsepian, P.E., New, R., and Valter, J., Influence of steering magnetic field on the time-resolved plasma chemistry in cathodic arc discharges, *J. Phys. D: Appl. Phys.* **37**, 2101–2106, (2004).
11. Aksenov, I.I., Padalka, V.G., and Khoroshykh, V.M., Investigation of a flow of plasma generated by a stationary erosion electric arc accelerator with magnetic confinement of the cathode spot, *Sov. J. Plasma Phys.* **5**, 341, (1979).
12. Falabella, S. and Karpov, D.A., "Continuous cathodic arc sources," in *Handbook of Vacuum Science and Technology*, Boxman, R.L., Martin, P.J., and Sanders, D.M., (Eds.). pp. 397–412, Noyes, Park Ridge, (1995).
13. Hovsepyan, P. and Hensel, B., "Lichtbogen-Verdampfungsvorrichtung," patent DE 4223592 (1994).
14. Swift, P.D., McKenzie, D.R., Falconer, I.S., and Martin, P.J., Cathode spot phenomena in titanium vacuum arcs, *J. Appl. Phys.* **66**, 505–512, (1989).
15. Walke, P.J., New, R., and Care, C.M., Behavior of steered cathodic arc as a function of steering magnetic field, *Surf. Coat. Technol.* **59**, 126–128, (1993).

16. Kim, J.K., Lee, K.R., Eun, K.Y., and Chung, K.H., Effect of magnetic field structure near cathode on the arc spot stability of filtered vacuum arc source of graphite, *Surf. Coat. Technol.* **124**, 135–141, (2000).
17. Ramalingam, S., Qi, C.B., and Kim, K., "Controlled vacuum arc material deposition, method and apparatus," patent US 4,673,477 (1987).
18. Zhitomirsky, V.N., Boxman, R.L., and Goldsmith, S., Unstable arc operation and cathode spot motion in a magnetically filtered vacuum-arc deposition system, *J. Vac. Sci. Technol. A* **13**, 2233–2240, (1995).
19. Vergason, G.E., "Electric arc vapor deposition device," patent US 5,037,522 (1991).
20. Brondum, K. and Larson, G., "Low-temperature arc vapor deposition as a hexavalent chrome electroplating alternative," Technical Report Vapor Technologies Inc., Longmont, CO, May 13 (2005).
21. Welty, R.P., "Apparatus and method for coating a substrate using vacuum arc evaporation," patent US 5,269,898 (1993).
22. Bilek, M.M.M. and Milne, W.I., Filtered cathodic vacuum arc (FCVA) deposition of thin film silicon, *Thin Solid Films* **291**, 299–304, (1996).
23. Richter, F., Krannich, G., Hahn, J., Pintaske, R., Friedrich, M., Schmidbauer, S., and Zahn, D.R.T., Utilization of cathodic arc evaporation for the deposition of boron nitride thin films, *Surf. Coat. Technol.* **90**, 178–183, (1997).
24. Klepper, C.C., Hazelton, R.C., Yadlowsky, E.J., Carlson, E.P., Keitz, M.D., Williams, J.M., Zuhr, R.A., and Poker, D.B., Amorphous boron coatings produced with vacuum arc deposition technology, *J. Vac. Sci. Technol. A* **20**, 725–732, (2002).
25. Morrow, M.S., Schechter, D.E., Tsai, C.-C., Klepper, C.C., Niemel, J., and Hazelton, R.C., "Microwave processing of pressure boron powders for use as cathodes in vacuum arc sources," patent US 6,562,418 (2003).
26. Uglov, V.V., Anishchik, V.M., Zlotski, S.V., Abadias, G., and Dub, S.N., Stress and mechanical properties of Ti-Cr-N gradient coatings deposited by vacuum arc, *Surf. Coat. Technol.* **200**, 178–181, (2005).
27. Uglov, V.V., Anishchik, V.M., Zlotski, S.V., and Abadias, G., The phase composition and stress development in ternary Ti-Zr-N coatings grown by vacuum arc with combining of plasma flows, *Surf. Coat. Technol.* **200**, 6389–6394, (2006).
28. Anischik, V.M., Uglov, V.V., Zlotski, S.V., Konarski, P., Cwil, M., and Ukhov, V.A., SIMS investigation of nitride coatings, *Vacuum* **78**, 545–550, (2005).
29. Ben-Ami, R., Zhitomirsky, V.N., Boxman, R.L., and Goldsmith, S., Plasma distribution in a triple-cathode vacuum arc deposition apparatus, *Plasma Sources Sci. Technol.* **8**, 355–362, (1999).
30. MacGill, R.A., Dickinson, M.R., Anders, A., Monteiro, O.R., and Brown, I.G., Streaming metal plasma generation by vacuum arc plasma guns, *Rev. Sci. Instrum.* **69**, 801–803, (1998).
31. Schein, J., Qi, N., Binder, R., Krishnan, M., Ziemer, J.K., Polk, J.E., and Anders, A., Inductive energy storage driven vacuum arc thruster, *Rev. Sci. Instrum.* **73**, 925–927, (2002).
32. Siemroth, P., Schülke, T., and Witke, T., High-current arc – a new source for high-rate deposition, *Surf. Coat. Technol.* **68**, 314–319, (1994).
33. Witke, T. and Siemroth, P., Deposition of droplet-free films by vacuum arc evaporation-results and applications, *IEEE Trans. Plasma Sci.* **27**, 1039–1044, (1999).
34. Büschel, M. and Grimm, W., Influence of the pulsing of the current of a vacuum arc on rate and droplets, *Surf. Coat. Technol.* **142–144**, 665–668, (2001).
35. Oates, T.W.H., Pigott, J., McKenzie, D.R., and Bilek, M.M.M., A high-current pulsed cathodic vacuum arc plasma source, *Rev. Sci. Instrum.* **74**, 4750–4754, (2003).

36. Ryves, L., Bilek, M.M.M., Oates, T.W.H., Tarrant, R.N., McKenzie, D.R., Burgmann, F.A., and McCulloch, D.G., Synthesis and in-situ ellipsometric monitoring of Ti/C nanostructured multilayers using a high-current, dual source pulsed cathodic arc, *Thin Solid Films* **482**, 133–137, (2005).
37. Anders, A., Pasaja, N., and Sansongsiri, S., Filtered cathodic arc deposition with ion-species-selective bias, *Rev. Sci. Instrum.* **78**, 063901-1-5, (2007).
38. Pasaja, N., Sansongsiri, S., Intarasiri, S., Vilaithong, T., and Anders, A., Mo-containing tetrahedral amorphous carbon deposited by dual filtered cathodic vacuum arc with selective pulsed bias voltage, *Nucl. Instrum. Meth. Phys. Res. B* **259**, 867–870, (2007).
39. Weintraub, E., Investigation of the arc in metallic vapours in an exhausted space, *Phil. Mag.* **7** (of Series 6), 95–124, (1904).
40. Buttolph, L.J., The Cooper Hewitt mercury vapor lamp, *General Electric Review* **23**, 741–751, (1920).
41. Greenwood, A., "Vacuum switching of high current and high voltage at power frequencies," in *Handbook of Vacuum Arc Science and Technology*, Boxman, R.L., Martin, P.J., and Sanders, D.M., (Eds.). pp. 590–624, Noyes Publications, Park Ridge, New Jersey, (1995).
42. Slade, P.G., (ed.) *Electrical Contacts: Principles and Applications*, Marcel Dekker, Inc., New York, (1999).
43. Bergman, C., Vergason, G.E., Clark, R., and Bosak, S., "Arc-initiating trigger apparatus and method for electric arc vapor deposition coating systems," patent US 4,448,799 (1984).
44. Boxman, R.L., Triggering mechanisms in triggered vacuum gaps, *IEEE Trans. Electron Devices* **ED-24**, 122–128, (1977).
45. Gilmour, A. and Lockwood, D.L., Pulsed metallic-plasma generator, *Proc. IEEE* **60**, 977–992, (1972).
46. Kamakshaiah, S. and Rau, R.S.N., Delay characteristics of a simple triggered vacuum gap, *J. Phys. D: Appl. Phys.* **8**, 1426–1429, (1975).
47. Watt, G.C. and Evans, P.J., A trigger power supply for vacuum arc ion sources, *IEEE Trans. Plasma Sci.* **21**, 547–551, (1993).
48. Evans, P.J., Watt, G.C., and Noorman, J.T., Metal vapor vacuum arc ion source research at ANSTO, *Rev. Sci. Instrum.* **65**, 3082–3087, (1994).
49. Anders, A., Brown, I.G., MacGill, R.A., and Dickinson, M.R., "Triggerless" triggering of vacuum arcs, *J. Phys. D: Appl. Phys.* **31**, 584–587, (1998).
50. Clark, R.J. and Gilmour, A.S., "Studies on a laser-triggered, high-voltage, high-vacuum switch tube," 3rd Int. Symp. Disch. Electr. Insul. Vacuum, Paris, pp. 367–372, (1968).
51. Hirschfield, J.L., Laser-initiated vacuum arc for heavy ion sources, *IEEE Trans. Nucl. Sci.* **NS-23**, 1006–1007, (1976).
52. Siemroth, P. and Scheibe, H.-J., The method of laser-sustained arc ignition, *IEEE Trans. Plasma Sci.* **18**, 911–916, (1990).
53. Vogel, N. and Höft, H., Cathode spot energy transfer simulated by a focused laser beam, *IEEE Trans. Plasma Sci.* **17**, 638–640, (1989).
54. Scheibe, H.J., Schultrich, B., and Drescher, D., Laser-induced vacuum arc (Laser Arc) and its application for deposition of hard amorphous carbon films, *Surf. Coat. Technol.*, 813–818, (1995).
55. Scheibe, H.J., Pompe, W., Siemroth, P., Buecken, B., Schulze, D., and Wilberg, R., Preparation of multilayers films structures by laser arcs, *Surf. Coat. Technol.* **193–194**, 788–798, (1990).
56. Lafferty, J.M., Triggered vacuum gaps, *Proc. IEEE* **54**, 23–32, (1966).

57. Bernardet, H., Godechot, X., and Jarjat, F., "A highly reliable trigger for vacuum arc plasma sources," Workshop on Vacuum Arc Ion Sources, Berkeley, CA, pp. 67–80, (1995).
58. Bernardet, H., Godechot, X., and Riviere, C., "Investigation of firing properties of vacuum arcs triggered by plasma injection," Workshop on Vacuum Arc Ion Sources, Berkeley, CA, pp. 81–101, (1995).
59. Nikolaev, A.G., Yushkov, G.Y., Oks, E.M., MacGill, R.A., Dickinson, M.R., and Brown, I.G., Vacuum arc trigger based on **E**x**B** discharges, *Rev. Sci. Instrum.* **67**, 3095–3098, (1996).
60. Tamagaki, H., Tsuji, K., Komuro, T., Kiyota, F., and Fujita, T., The in-line arc ion plating system for high throughput processing of automotive parts, *Surf. Coat. Technol.* **54–55**, 594–598, (1992).

6

Macroparticles

. . .As quick advances seem to have been made of late years, as in many equal periods of time past whatever. Nay, it appears to me, that the progress is really accelerated.

Joseph Priestley, in: *History and Present State of Electricity*, 1767

Abstract The infamous macroparticle problem is the main reason why cathodic arc plasma deposition is not broadly used in high-tech applications. Macroparticles are formed at cathode spots, together with electrons and ions. They are commonly called "macroparticles" because they are very massive compared to ions and electrons. The formation and transport of macroparticles are considered, having in mind that we want to reduce, and possibly eliminate them. The size distributions can be fit by power laws, which is another indication for the self-similar nature of cathode processes. In one section, we contemplate whether macroparticles could be destroyed, e.g., by heating or by the interaction with plasma particles.

6.1 Macroparticle Generation of Random Arcs

The generation of macroparticles is the most severe issue in cathodic arc plasma deposition. Therefore, a whole chapter is devoted to describe the generation and properties of macroparticles and to touch briefly on the kinds of coating defects they can cause. At the end of this chapter, mitigation measures will be reviewed briefly. A separate chapter is specifically dedicated to macroparticle filtering, which represents to date the most complete approach to macroparticle removal.

Macroparticles are liquid or solid debris particles that are produced at cathode spots along with the plasma. Macroparticles are named this way to emphasize their very massive nature compared to electrons and ions. The term "macroparticle" is commonly used, although some authors refer to "droplets" or "microparticles," or "nanoparticles" when considering the sub-micron part of the size distribution.

A. Anders, *Cathodic Arcs*, DOI: 10.1007/978-0-387-79108-1_6,

It is commonly acknowledged that macroparticle generation is related to the formation of a pool of liquid cathode material formed as a result of thermal runaway and the explosive plasma formation (Chapter 3), though there may be special cases such as carbon or sintered cathodes where additional mechanisms may play a role.

Let us consider the typical case of a metal cathode. As explained in Chapter 3, all phases of matter (solid, liquid, gas, plasma) can be found in the explosive processes on the cathode surface. It is intuitively clear that a thin transition zone must exist between the region of dense plasma (having a temperature of a few 10,000 K) and the much colder solid cathode. The liquid metal in this transition zone is subject to the time-varying plasma pressure, which will cause a rather complicated motion of the liquid. The ejection of droplets from such liquid under varying pressure is to be expected. Images taken of spot craters using scanning electron microscopes bring ample evidence of the violent nature of arc plasma and macroparticle formation (Figure 6.1). The generation of plasma and macroparticles is intimately related to the explosive crater formation – they are both characteristic of cathodic arcs. Therefore, one may state that if an arc discharge does not emit macroparticles it is not a cathodic arc but a thermionic arc, or another form of discharge.

A schematic illustration of macroparticle generation is shown in Figure 6.2. Macroparticles form when the layer of liquid cathode material (in black) yields to the plasma pressure. As the illustration suggests, many macroparticles are preferentially ejected under 5–30° angle to the cathode surface. Just-ejected macroparticles or nonlinear waves of the liquid may rapidly cool down and freeze

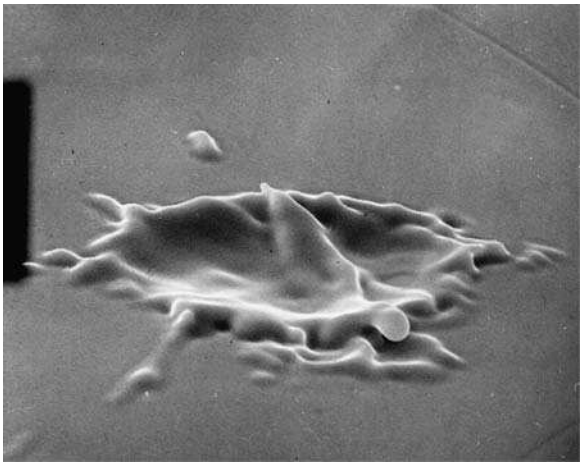

Fig. 6.1. Example of macroparticle and erosion crater formation by a cathode spot; scanning electron microscope image taken after a 10-ns arc on molybdenum. (Photo courtesy of Burkhard Jüttner, Berlin)

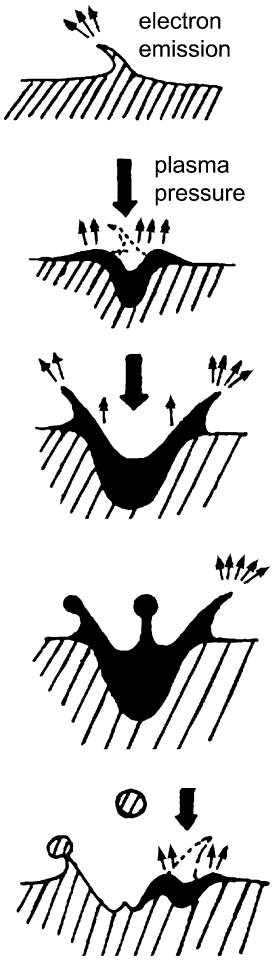

Fig. 6.2. Cartoon illustrating macroparticle generation as a result of plasma pressure on the liquid cathode material. (Adapted from on original by Burkhard Jüttner)

at the crater rim, forming microprotrusions that can serve as field-enhancing objects for the ignition of the next emission site.

There are some considerations indicating that this intuitive picture is oversimplified. For example, the explosive stage in the evolution of the emission site is likely to be shorter than the characteristic time of motion of the metallic liquid. Daalder [1, 2] observed that the angular distribution of macroparticles has a maximum in the range of 10–30° from the cathode surface; however, there is also a large fraction of macroparticles ejected in a direction close to the surface normal. The latter observation can be qualitatively consolidated with the impulse nature of the plasma pressure. In the explosive phase, a layer of liquid metal is formed, which is subject to large plasma pressure. In the next phase,

when the plasma pressure drops rapidly, the surface of the liquid may respond similarly to water when a stone has been thrown into it: a transient central column of liquid forms at the impact location in response, from which a droplet detaches. Figure 6.1 shows such a central cone and one may imagine that the macroparticle on the top left was ejected from the center before it solidified. It is remarkable that crater formation is possible when the arc duration exceeds just 10 ns. This is much shorter than assumed in most studies. For example, considering a model for arcs of a few amperes, Coulombe and Meunier [3] determined typical times for reaching the melting temperature in the range of a few microseconds, i.e., much longer than experimentally observed, which is perhaps another indicator that the power density is fractal with much higher peak values at the small-scale cutoff (Chapter 3).

Among the systematic studies on cathode erosion and macroparticle generation is the pioneering work done by Udris [4], Davis and Miller [5], Daalder [1, 2], Utsumi and English [6], and Tuma et al. [7], followed by others [8, 9, 10, 11, 12, 13, 14, 15, 16, 17, 18].

The most-often-used approach to quantify macroparticles is to analyze macroparticles caught by collecting probes placed near the cathode. An underlying assumption is that the distribution of macroparticles sticking to the surface represents the distribution as emitted from the cathode spot. That assumption is hardly justified, and in fact photographic images show that many macroparticles do not stick but "bounce" off, at least in the cases of carbon and refractory metals (Figure 6.3). Macroparticles can in fact be reflected several times before they come to rest on a surface. Keeping this in mind, distributions described in the literature have an error that is usually not specified. Yet deposition probes

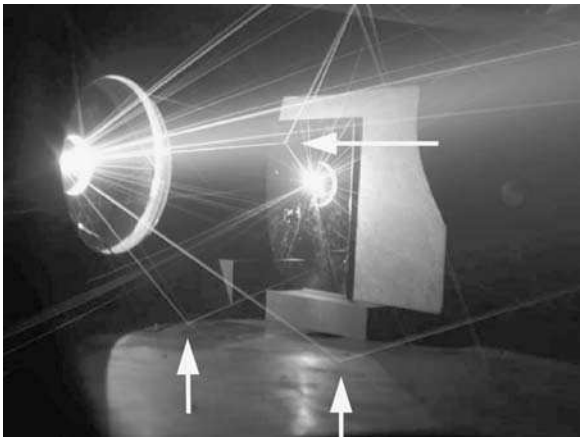

Fig. 6.3. Macroparticle emission from a cathodic arc on graphite; arc current 100 A, exposure time about 100 ms. Macroparticles are incandescently glowing and their trajectories are therefore visible as white lines. Thick arrows indicate where macroparticles are reflected from the chamber wall or other components

represent the most straightforward, generally accepted approach for the determination of macroparticles.

When quantifying macroparticles, one should always use normalized values in order to give useful and reproducible data. For example, one could describe the number of macroparticles per size class (e.g., an interval of macroparticle diameter), area, and film thickness. Another normalization could be the number of macroparticles of size class, area, and cumulative charge transferred through the cathode, $\int I_{\text{arc}} \mathrm{d}t$.

For coating applications, most relevant are macroparticles emitted in the direction close to the normal direction of the cathode surface, i.e., those ejected along with the useable plasma. Figure 6.4 gives examples of macroparticle distributions collected on axis of a pulsed cathodic arc plasma source using Pb, W, Ag, Ni, Pt, and Cu cathodes. One can see, as a rule, that materials of low melting point, or of low cohesive energy, produce more and larger macroparticles. Comparing macroparticles emitted from copper and cadmium cathodes, Daalder [1] came to the same conclusion.

It was outlined in Chapter 3 that a higher arc current would increase the *number* of active cathode spots or emissions sites, rather than a change in their character. Therefore, one could expect that the distribution of macroparticles is not changed much when the arc current is increased, at least as long as the arc operates in the diffuse anode mode, i.e., when current and plasma concentration

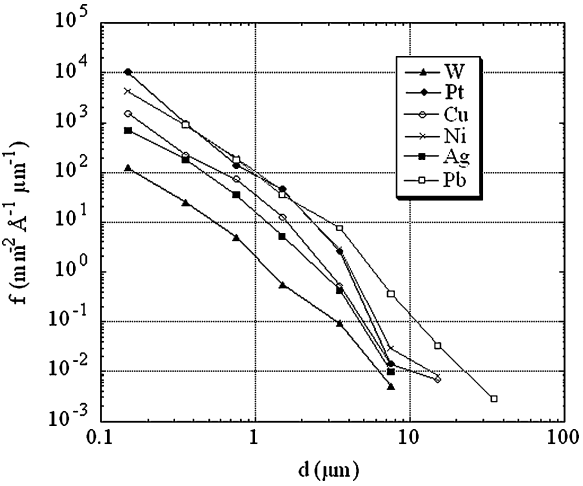

Fig. 6.4. Size distribution functions for macroparticles collected on axis of a pulsed cathodic arc source in vacuum. The macroparticles were collected on a silicon wafer chip that was located 6.5 cm from the cathode on axis of the cathodic arc plasma source, and analysis was done using imaging of a scanning electron microscope. The functions are normalized as number in size class per area and film thickness; the arc current was 200 A. (After [17])

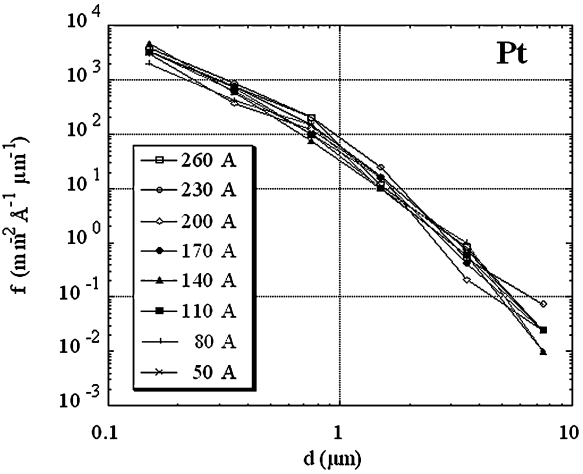

Fig. 6.5. Macroparticle size distribution for a platinum cathode as a function of arc current; all other details as with Fig. 6.4

due to the magnetic self-field and anode spots are not yet important. Figure 6.5 shows that this is indeed the case. In that experiment, a platinum cathode was chosen to make sure that no secondary effects due to oxide and other layers would play a role. Studying a range of very small arc current, 2–6 A, Utsumi and English [6] also found an independence of the macroparticle distribution on the arc current. Going to a much higher current range, 2–5 kA, Gellert and Schade [13] found a strong dependence of the macroparticle distribution on the current level, which they associated with anode activities.

In many studies, the reported lower limit of macroparticle size was about 0.1 μm. As pointed out, for example in [17], this lower limit is related to the resolution of the imaging tool, most often a scanning electron microscope, rather than a physically relevant limit, and it is not a priori clear whether a lower limit exists. Some studies claim macroparticles down to the nanometer range [7, 19].

In a study by Siemroth et al. (unpublished), the statistical errors were carefully analyzed. They found that the measuring technique has a systematic error at the lower limit of the size distribution. Figure 6.6 shows the macroparticle size distribution for a 50-nm copper film. What appears as a "small" macroparticle at low magnification will look like a "large" macroparticle at higher magnification. Because large macroparticles are much less frequent, it is possible that at any given magnification, very large particles are not in the area of view. Therefore, the statistical error of the method is large at the large-size end of the distribution. At the small-size end of the distribution, there are many macroparticles. The issue here is that very small macroparticles may not be well recognized, given the limited resolution of the microscope, camera, and counting system at the particular magnification. Therefore, the data points indicating a drop for the smallest macroparticles are actually an artifact. This becomes clear when considering Figure 6.7,

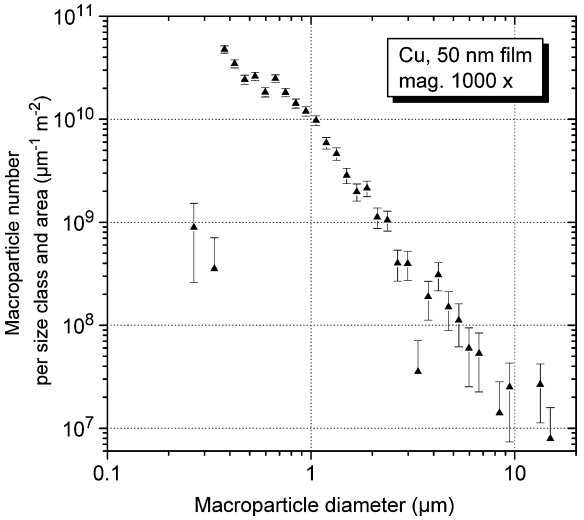

Fig. 6.6. Macroparticle size distribution measured on a 50-nm-thick copper film deposited on silicon. Magnification ×1,000. (Data courtesy of Peter Siemroth and co-workers)

where a higher resolution was used on the same sample investigated in Figure 6.6. One might therefore conclude that the drop seen in Figure 6.7 for the very small macroparticles is likely to be also an artifact. The observation and interpretation are not specific to copper but applies to other materials as well, see Figure 6.8.

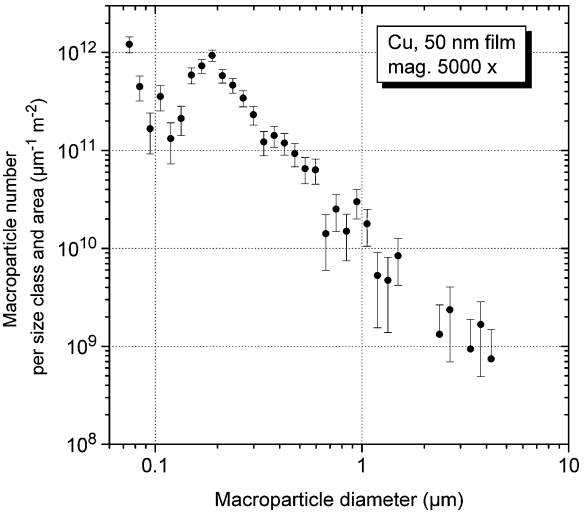

Fig. 6.7. Macroparticle size distribution of the same sample as in Fig. 6.5 but measured with magnification ×5,000. (Data courtesy of Peter Siemroth and co-workers, Dresden, Germany)

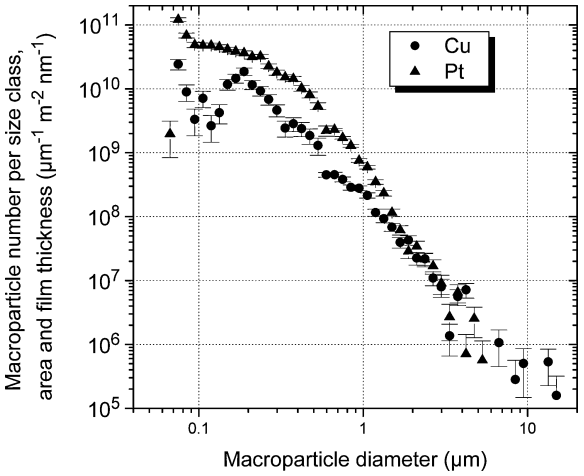

Fig. 6.8. Macroparticle size distributions for copper and platinum, normalized as number per size class, area, and film thickness. (Data courtesy of Peter Siemroth and co-workers, Dresden, Germany)

In all of the previously mentioned figures, the size distribution is a power law,

$$f(d_{\mathrm{MP}}) = A\, d_{\mathrm{MP}}^{-\alpha}, \tag{6.1}$$

which is represented by a straight line in log–log presentation, where d_{MP} is the diameter of the macroparticle. The power law characteristic is another feature supporting the fractal model of cathode spot processes (see discussion on power laws and self-similarity, Chapter 3).

Macroparticles that stick to the substrate or collector surface are usually deformed by the impact. They often have a donut-like shape like shown in Figure 6.9. It is clear that those macroparticles were still in the liquid phase

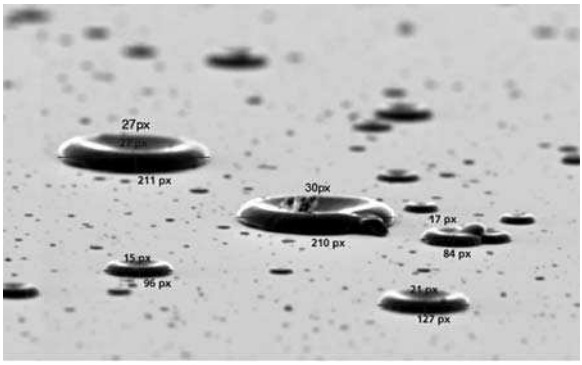

Fig. 6.9. Copper macroparticles on silicon: they are deformed when they impact the surface still being in the liquid phase (image taken under 10° angle to the surface, data courtesy of Peter Siemroth and co-workers, Dresden, Germany)

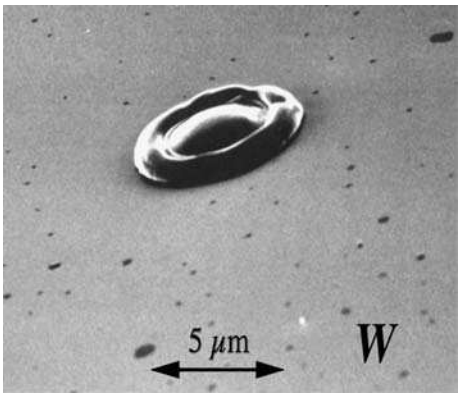

Fig. 6.10. A large tungsten macroparticle shows the same deformation, indicating that it also arrived on the surface as a liquid droplet (image taken under 20° angle to the surface, after [17])

when impacting the collector surface, and they must have rapidly solidified. Flattened macroparticles are quite common, not just for low-melting-point materials but also for refractory metals (Figure 6.10). However, not all macroparticles are deformed, quite the contrary: most macroparticles smaller than 0.5 μm tend to be spherical, indicating that they have been cooled down and solidified before impact. Besides the very large macroparticle, Figure 6.10 also shows numerous small dark spots, indicating defects caused by the impact of small macroparticles. The low resolution of Figure 6.10 does not allow us to determine whether the small macroparticles are still there or not.

Using images of collector probes, one can estimate the volume and mass of macroparticles. In Figure 6.9, for example, the imaging software put pixel numbers on macroparticles, and such data can be used for quantitative macroparticle statistics. The analysis can provide an answer to the question what *size* classes of macroparticles contribute most to cathode erosion. There are two competing trends: large-sized macroparticles have larger mass but they are rare, while small macroparticles are much more frequent but each carries only a small mass. By convoluting the macroparticle size distribution with corresponding volume and mass density, the *mass* erosion function can be determined, as shown in Figure 6.11. One can see that all macroparticle size classes contribute to the total cathode erosion, with medium-sized macroparticles (of about 1 μm diameter) contributing most.

By integrating over the mass distribution function, the cathode's macroparticle erosion rate can be determined. This is relevant for deposition of films and also for other application of cathodic arcs, such as space thrusters. Table 6.1 compares mass deposition in the form of macroparticles versus condensation of metal ions. One can see that macroparticles may constitute a large or even the dominating fraction of the coating mass. This is especially true for materials of low melting point. However, as mentioned before, a significant fraction of

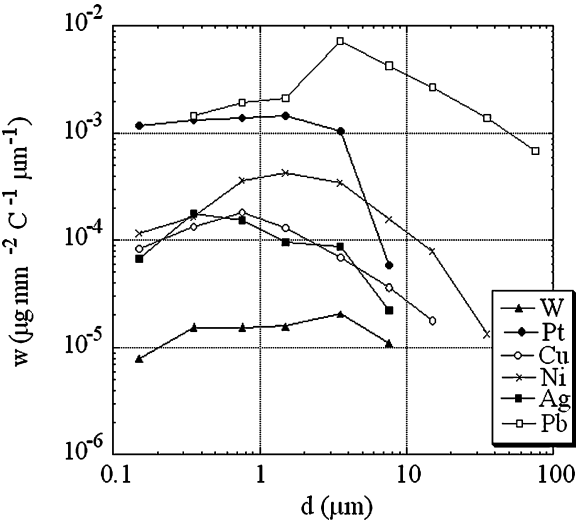

Fig. 6.11. Mass distribution of macroparticles, obtained by convoluting size distribution function, shape factor, and mass density. (After [17])

Table 6.1. Mass deposited in the form of macroparticles compared to mass deposited by condensing ions. The tungsten data (and possibly others) are lower limits because many already solidified macroparticles "bounce" and they are therefore not taken into account (After [17])

Cathode material	Mass fraction of macroparticles for a coating made on axis (%)
W	3.5
Pt	43
Ni	61
Cu	21
Ag	10
Pb	90

macroparticles does not stick to the collector, especially for refractory metals; therefore, the data present a lower limit of the true macroparticle erosion.

6.2 Macroparticle Generation of Steered Arcs

As pointed out in Chapter 5, one may distinguish between cathodic arc sources with random spots and steered spots. In "steered arcs," the ignition probability for the next spot location is greatly affected by a transverse magnetic field, mainly via the anisotropic plasma density, which in turn locally enhances the electric field via

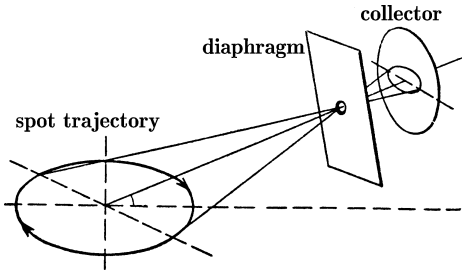

Fig. 6.12. Macroparticle imaging technique by Udris [4]: the spot is magnetically steered in a circular path; macroparticles are passing through a 1-mm hole and project themselves on a soot-coated glass collector. Because not the macroparticles themselves but their impact traces are recorded; this technique is free of the questionable sticking assumption used in many other studies

a locally thinner sheath. Spot "steering," or "driving," reduces the average spot residence time and enhances the apparent spot velocity. As a result, less and smaller macroparticles are ejected, as will be evident by a number of experiments mentioned.

One of the first systematic investigations of macroparticle generation was done by Udris in the 1950s, when investigations of spots on liquid mercury were still the focus of cathodic arc research [4]. To catch macroparticles from a steered arc, Udris used an ingenious imaging technique shown in Figure 6.12. The spot was magnetically steered in a circular path. A small fraction of macroparticles passed through a 1-mm diameter diaphragm beyond which a soot-coated glass plate was placed. The mercury macroparticles hit the surface and left a trace (Figure 6.13). After controlled exposure, the glass with traces was removed and evaluated under a microscope. In this way, Udris found that at relatively low

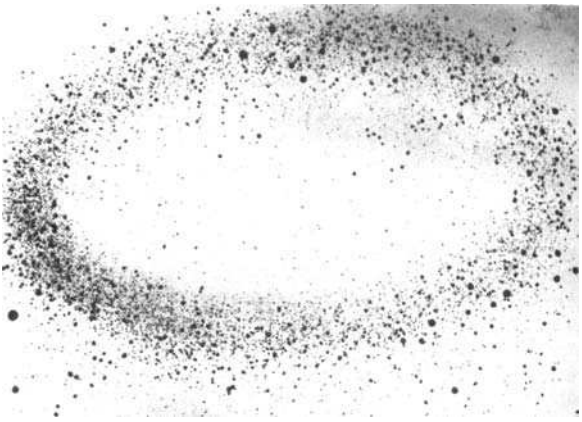

Fig. 6.13. Macroparticle traces left by a 8.5-A mercury arc, obtained in the projection geometry shown in Fig. 6.12

spot velocities of less than 30 m/s, the number of macroparticles ejected in the direction of motion was much less than the number ejected in the back direction. With increasing field and apparent spot velocity, the number in the forward direction remained about constant while the number in the back direction decreased. Overall, he concluded that as the spot velocity is increased, the number and size of the macroparticles decrease monotonically (see also [20], Appendix 4). This realization is the basis for one of the macroparticle mitigation measures where driving of spots is increased as much as possible (Section 6.8). As already found in the 1980s, the reduction of macroparticles when going from a random arc to a steered arc showed immediate improvements in the scratch resistance and wear performance of nitride coatings [21].

Even as the macroparticle emission seems to be reduced, the overall cathode erosion rate, as normalized by the charge transferred, remained rather independent of the magnetic induction, or related speed of the apparent spot motion [22]. This has been shown up to a high induction of 0.9 T. The total erosion rate was also independent of the arc current (in the range 300–750 A), which is not surprising given the spot-splitting feature and provided the cathode is well cooled. At high cathode temperature, exceeding 400°C for stainless steel for example, the erosion rate starts to increase [22], which is consistent with observations that high temperatures lead to larger craters [23].

Using a relatively small steered DC arc source and a titanium cathode, Swift [24] observed that the apparent spot velocity saturated at a relatively low transverse magnetic induction of 15 mT . Such saturation was seen before but at a much higher induction of about 600 mT [22]. Swift measured that the product of apparent spot velocity and number of macroparticles deposited per area is

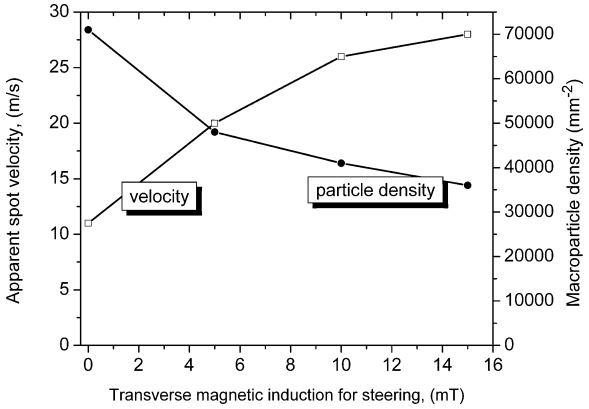

Fig. 6.14. Apparent speed of cathode spots and the number density of macroparticles deposited on a glass collector plate, placed 130 mm from the cathode center and under an angle of 10° with respect to the cathode surface plane, as a function of the transverse magnetic inductance driving the steered spot motion. The cathode was made from Ti, and the arc current was running at 100 A for 30 s. (Data from [24])

approximately constant (Figure 6.14). The spot velocity was determined optically [25], and the macroparticle density by using a collection probe positioned under an angle of 10° to the surface, where the maximum angular emission was expected.

6.3 Macroparticle Generation of Pulsed Arcs

In pulsed arcs, the arc current is often much higher than in DC arcs, and thus several cathode spots are simultaneously emitting plasma and macroparticles. Despite higher instantaneous currents, the time-averaged power of pulsed arcs is usually lower than the power of continuous arcs, and therefore the temperature of the cathode surface zone might be lower. The interaction of simultaneously operating spots tends to cause faster spot motion, similar to steered arcs in the previous section. Ignition tends to occur on "fresh" location of the cathode surface, with the result that less and smaller macroparticles are produced compared to the DC case (Figure 6.15). This conclusion was particularly evident for the centrally triggered high current arc (HCA) [26] that was described in Chapter 5 as a special case of a steered arc ("self-steered arc" might be a good term).

Based on data shown in Figure 6.15 one might suspect that the total cathode erosion rate is reduced because less macroparticles are collected when the spot is magnetically steered by the pulsed self-field. However, the presence of a magnetic field does not necessarily reduce the total cathode mass loss, as cathode weighing experiments showed [17]. A pulsed cathodic arc source was used that

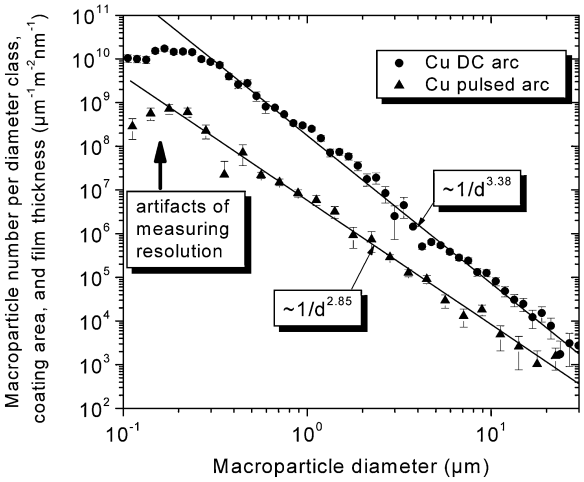

Fig. 6.15. Comparison of copper macroparticle distribution functions for DC arcs and pulsed high-current arcs. The number of macroparticles is normalized to size class, deposition area, and film thickness. (Data courtesy of Peter Siemroth and co-workers, Dresden, Germany)

Table 6.2. The total mass erosion rate (mass loss per charge transferred) of the cathode determined by weighing the cathodes; pulsed arc of 250 μs duration, with an external axial magnetic field of $B = 170$ mT (after [17])

Element	Erosion rate (μC/C) without external field	Erosion rate (μC/C) with 170 mT external field	Relative change in erosion rate (%)
Pb	807	975	21
Ag	76	84	10
Cu	51	56	10
Au	86	101	17
Ni	38	49	28
Pt	111	116	5
Mo	31	39	26
W	44	50	13

can run with or without magnetic field. The cathode was weighed before and after the deposition experiment. The results shown in Table 6.2 indicate that the total mass erosion from a cathode in a magnetic field is not reduced but rather slightly increased. This is in contrast to most other findings using DC arc operation.

In order to interpret this result, one needs to recall that the cathode erosion is conventionally measured as cathode mass loss per charge transferred through the arc current, in units of μg/As. However, the burning voltage is also enhanced when the magnetic field was used, suggesting that cathode erosion might be better normalized by the *energy* dissipated rather than the *charge* transferred. Interestingly, such normalization was quite common in the 1950s and earlier work [20] but unfortunately replaced by normalization to charge transferred, perhaps because such charge normalization is simpler to do because it requires only measurement of the current.

6.4 Macroparticles from Poisoned Cathodes

Cathode "poisoning" is associated with the formation of a non-metallic layer on the cathode surface, which leads to type 1 cathode spots (Chapter 3). Because spot ignition is much promoted by such layer, the average time of operation is shorter, and additionally the current per spot is drastically reduced compared to spots burning on clean metal (type 2 spots). Therefore, it is not surprising that fewer macroparticles are observed. Intentionally or unintentionally, this effect is widely used in reactive arc deposition of nitrides and oxides. While there are many studies on macroparticles for vacuum arcs (or cathodic arcs with type 2 spots), only few systematic data are available for the industrially more relevant case of reactive deposition. Fewer particles are produced on poisoned cathodes,

and macroparticle deposition may be further reduced due to the particle interaction with the background gas.

For example, a hot titanium macroparticle traveling in a nitrogen background atmosphere is likely to form a TiN surface, which has a much higher melting point (2930°C) than the metallic surface (1668°C). As a result, the macroparticle arriving at the substrate is more likely in the solid phase and thus more likely to "bounce" than the liquid particle. This example is especially relevant since titanium or titanium-containing cathodes operating in nitrogen or nitrogen–argon mixtures are widely used for hard and decorative coatings.

Studying the titanium–nitrogen system for a total gas pressure from vacuum up to 133 Pa (1 Torr), Kim and co-workers [27] found, as they anticipated, that the erosion rate decreased as the cathode surface was poisoned. Higher cathode temperatures resulted in enhanced nitriding (poisoning), leading to reduced erosion. The erosion rate dropped sharply when the gas pressure reached about 10 Pa (1 mTorr). Steered arcs showed lower erosion rates of 38 and 15 μg/C for argon and nitrogen, respectively, compared to random arc values of 45 and 35 μg/C. Erosion rate studies on TiN-coated cathodes showed low erosion rates of about 22 μg/C.

6.5 Macroparticle–Plasma Interaction

6.5.1 Plasma Effects on Macroparticles

Once a macroparticle becomes "airborne," it is subject to intense interaction with the surrounding plasma. It is floating (electrically isolated) and thus behaves like a floating probe immersed in a streaming, fully ionized plasma. A macroparticle too cold to emit electrons will be negatively charged with respect to the plasma potential in order to balance the electric current of the very mobile plasma electrons and less mobile ions condensing on its surface [28, 29, 30]. Along with the electron and ion currents goes a flux of mass, energy, and momentum, and the flux of neutrals may also contribute to those balances. The macroparticles are usually very hot (and even liquid), and therefore mass can be lost by evaporation, and electrons can be emitted by thermionic emission. An electron-emitting macroparticle will charge up positively if it is in vacuum [31], which can happen for short arc pulses such that the plasma decays much faster than the time the macroparticle travels away from the cathode. The net charge is not so obvious when the emitting macroparticle travels in plasma due to the many factors that influence the balance of emission and arrival of charged particles from and to the surface of the macroparticle, respectively. In extreme cases, electron emission and evaporation can lead to dense plasma near a departing macroparticle, as was measured by high-speed resonant laser interferometry and shadowgraphy [32].

Detailed balances of mass, energy, momentum, and charge have been considered in the literature [28, 29, 31, 33, 34, 35]. Depending on which processes

have been included and which assumptions have been made, various, sometime conflicting, results were obtained. There are arguments that there must be a cut-off in the size distribution function for very small macroparticles due to thermal instabilities associated with plasma electron heating [33], but it has also been argued that interaction with the plasma cannot lead to complete particle destruction by evaporation or other mechanisms within the short time a macroparticle moves from the cathode to the substrate [29].

This conclusion has been challenged by considering vacuum arc plasma in an external magnetic field in a "reflex geometry" (Penning cell) [35]. Here, the heating of the macroparticle by the plasma can lead to dense plasma near the macroparticle, which in turn intensifies the plasma heating; the resulting run-away is believed to cause complete evaporation of macroparticles.

Mass, energy, and momentum balance are coupled and discussed in greater detail in the following sections. As we will see, the physical processes are rather involved. For the sake of clarity, these balances are separately described and discussed.

6.5.2 Mass Balance

Large macroparticles are not likely to have changed very much since ejection from the pool of a cathode spot. This conclusion can be drawn when comparing the size of large macroparticles with size of craters on the cathode. However, the rate of change for small macroparticles is unknown. Modeling and simulations seem to be the most efficient ways of studying the issue. When considering macroparticle–plasma interaction, probe theories [36] as well as the theories of dusty plasmas [37, 38, 39] and plasma spraying [33] are valuable resources.

When the macroparticle travels from the spot to the substrate, it will be subject to competing mass gain and loss processes. The gain processes are mostly associated with the arrival and condensation of atoms and ions, while mass losses are dominated by evaporation. Very large macroparticles may also serve as condensation sites for smaller macroparticles (coalescence). Mass loss by sputtering via impact of sufficiently energetic ions is possible but likely to be small because the self-sputter yields are low in the energy range of interest.

Yet another effect might be a mechanical instability of the liquid macroparticle (droplet): it may make large oscillations whose forces exceed surface tension and therefore it could break up into two or more smaller droplets. Ultimately, each droplet will assume spherical shape due to surface tension.

Let us assume that droplet break-up and droplet coalescence can be neglected. The mass balance equation can be written in its simplest from as

$$\frac{\mathrm{d}m_{MP}}{\mathrm{d}t} \approx \overline{S_i} \int\limits_{A_{MP}} \frac{j_i\, m_i}{\overline{Q} e}\, \mathrm{d}A - \int\limits_{A_{MP}} \Gamma_a\, \mathrm{d}A, \tag{6.2}$$

where the first term on the rhs. is the mass gain by condensation of ions and the second term is the mass loss by evaporation. The symbols in (6.2) have the

following meaning: $\overline{S_i}$ is the sticking probability for ions, $j_i/\overline{Qe}$ is the ion current density divided by the average charge; hence this expression is the flux of ions, Γ_a is the net flux of atoms, and the integration is over the surface of the macroparticle, A_{MP}. The ion and atom flux contributions are now considered with some greater detail.

Since the macroparticle is immersed in a stream of plasma where the directed ion velocity is much greater than the macroparticle velocity, one could consider that the ion flow occurs only from the side facing the cathode spot; therefore

$$\int_{A_{MP}} \frac{j_i\, m_i}{\overline{Q}e}\, \mathrm{d}A \approx n_i(d)\, \overline{v_i}\, m_i \pi r_{MP}^2, \tag{6.3}$$

where $n_i(d)$ is the local ion density, which for relatively large distances from the spot can be approximated by

$$n_i(d) \approx C\frac{I_{arc}}{d^2}, \quad d > 100\mu\mathrm{m} \tag{6.4}$$

due to the expansion of plasma (see Chapter 4, equation (4.3)). The average ion velocity $\overline{v_i}$ is approximately known for practically all cathode materials. The expression πr_{MP}^2 is the geometric macroparticle cross-section. The effective cross-section for ion–macroparticle interaction, however, is larger than the geometric cross-section, as illustrated in Figure 6.16. Ions entering the sheath surrounding the macroparticle will be affected in their trajectories by the sheath electric field, but not all of them will reach the macroparticle surface, as known from orbital motion theory [40, 41]. The centrifugal force associated with the angular momentum prevents ions with an impact parameter larger than R_{cap}

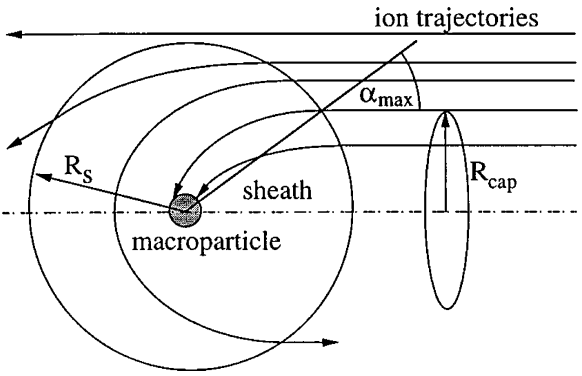

Fig. 6.16. Illustration of effective cross-section for ion–macroparticle interaction. Not all ions entering the sheath arrive at the macroparticle surface. Note the simplification of the sheath thickness; in reality, the sheath side facing the ion flux from the spot is thinner than the sheath on the opposite side

from reaching the surface of a spherical probe; R_{cap} is the radius of the ion-capture cross-section. Using the conservation equations of energy and angular momentum,

$$\frac{m_i\, v_{i@MP}^2}{2} = \frac{m_i\, v_i^2}{2} - Q\, e\, U_s, \tag{6.5}$$

$$R_s\, \mathrm{v}_i\, \sin\alpha = r_{MP}\, \mathrm{v}_{i@MP}\, \sin\alpha_{MP}, \tag{6.6}$$

one may derive a maximum angle of capture. In these equations, and using a frame of reference tight to the macroparticle, v_i is the velocity of an ion arriving at the sheath edge, $v_{i@MP}$ is the velocity of an ion when it arrives at the surface of the macroparticle, α_{MP} is the angle of the trajectory to the axis of symmetry (see Figure 6.16). The radius of the spherical sheath, R_s, contains the radius of the macroparticle, r_{mp}, and the sheath thickness, s:

$$R_s = r_{MP} + s. \tag{6.7}$$

In order for the ion to arrive at the macroparticle surface, the angle α_{MP} must not be too great. At the maximum angle, $\alpha_{\max}$, ions arrive at the macroparticle surface at grazing angle. The maximum angle is given by

$$\sin\alpha_{\max} = \frac{r_{MP}\, v_{i@MP}}{R_s\, v_i} = \frac{r_{MP}}{R_s}\sqrt{1 - \frac{2\, Q\, eU_s}{m_i\, v_{\mathrm{i}}^2}}. \tag{6.8}$$

Note that the sheath voltage $U_s < 0$ and therefore the maximum angle is greater for high ion charge states. The macroparticle has an ion-capture cross-section which is greater for higher charge states. From Figure 6.16 we see that

$$R_{cap} = R_s \sin\alpha_{\max}, \tag{6.9}$$

and the capture cross-section becomes

$$A_{cap} = \pi\, R_{cap}^2 = \pi\, r_{MP}^2 \left(1 - \frac{2\, Q\, e\, U_s}{m_i\, v_i^2}\right), \tag{6.10}$$

again, because $U_s < 0$, we have $R_{cap} > r_{MP}$. With this approximation one can improve estimate (6.3) by the expression

$$\int_{A_{MP}} \frac{j_i\, m_i}{\overline{Q}e}\, \mathrm{d}A \approx n_i(d)\, \overline{v_i}\, m_i \pi R_{cap}^2. \tag{6.11}$$

In this derivation, a gross simplification was adopted from orbital motion theory, namely that the sheath has a spherical shape surrounding the macroparticle. Because the macroparticle is immersed in fast plasma flow, the sheaths facing the spot and the opposite side (facing the substrate) are very different, at variance to the simplified cartoon of Figure 6.16. A more comprehensive treatment of the macroparticle sheath remains to be developed and is beyond the scope here.

Returning to the mass balance equation (6.2), we need to discuss the contribution of atoms condensing and evaporating. The term containing Γ_a is written to include both condensing and evaporating fluxes. In equilibrium, the net mass evaporation rate is given by the Hertz–Knudsen equation [42, 43]:

$$\Gamma_a = \alpha_v \left(\frac{m_a}{2\pi k T_{MP}} \right)^{1/2} [p^*(T_{MP}) - p], \tag{6.12}$$

where α_v is the sticking coefficient for vapor atoms on the surface of the macroparticle, $p^*(T_{MP})$ is the equilibrium vapor pressure of the evaporating material, which depends on the macroparticle surface temperature T_{MP}. As already found by Hertz [42], the net evaporated flux depends on the pressure *difference* between the vapor pressure and the hydrostatic pressure. In vacuum, $p = 0$. The situation for a macroparticle is complicated by the fact that there is no equilibrium. Pressures and incoming fluxes depend strongly on the direction, e.g., other evaporating macroparticles that happen to be nearby. Evaporating macroparticles have been identified as a major source of neutral vapor present in the vacuum arc plasma [44].

One should note that the vapor pressure $p^*(T_{MP})$ is a very strong function of temperature and material [45]. Therefore, there is a need to address the energy balance of a macroparticle before any conclusions on its mass balance can be drawn.

6.5.3 Energy Balance

The energy balance equation of a macroparticle can be written as

$$\begin{aligned} m_{MP}\, C \frac{\mathrm{d}T_{MP}}{\mathrm{d}t} = {} & P_{e,pl} + P_{i,pl} + P_{rad,pl} - P_a(T_{MP}) - P_{e,th}(T_{MP}) \\ & - P_{rad}(T_{MP}), \end{aligned} \tag{6.13}$$

where C is the specific heat capacity (unit in SI: J/kg K), $P_{e,pl}$, $P_{i,pl}$, and $P_{rad,pl}$ is the heating power of electrons, ions, and plasma radiation, respectively, and $P_a(T_{MP})$, $P_{e,th}(T_{MP})$, and $P_{rad}(T_{MP})$ is the energy loss per time due to evaporation of atoms, emission of electrons, and radiation, respectively. While the heating terms depend mainly on the plasma parameters, the loss mechanisms depend explicitly on the macroparticle temperature T_{MP}. In the following, the relative importance of these terms will be evaluated.

Energy Fluxes Related to Electron Currents

The macroparticle is electrically floating; therefore the net electric current must be zero:

$$I_{i,pl} - I_{e,pl} + I_{e,th} + I_{e,SE} = 0, \tag{6.14}$$

where

$$I_{i,pl} = \sum_{Q=1}^{Q_{\max}} I_{i,Q} \tag{6.15}$$

is the ion current from the plasma (sum over all partial ion currents of charge state Q, with $Q_{\max}$ the maximum charge state present in the plasma), $I_{e,pl}$ is the electron current from the plasma, $I_{e,th}$ is the thermionic emission current, and

$$I_{e,SE} = \gamma_{i,SE}\, I_{i,pl} + \gamma_{e,SE}\, I_{e,pl} \tag{6.16}$$

is the secondary electron emission current caused by the impact of primary ions (yield $\gamma_{i,SE}$) and primary electrons (yield $\gamma_{e,SE}$). Additionally, one could consider photoemission of electrons caused by UV radiation of the plasma. Generally, secondary electron currents are smaller than incoming ion and electron currents. When we consider macroparticles with relatively low temperature, such that thermionic electron emission can be neglected, the balance equation is simplified to

$$I_{i,pl} - I_{e,pl} = 0, \tag{6.17}$$

which says that the electron current is supplied such as to provide enough recombining charge for condensing ions. Because of the high electron thermal velocity, the electron current to the macroparticle can be assumed to come from all directions to the sheath edge. As above, the sheath is roughly approximated by a sphere of radius R_S, see Figure 6.16. Because the thermal velocity of electrons is much greater than the average ion velocity, the macroparticle potential is negative with respect to the plasma potential and

$$I_{e,pl} = \int j_{e,pl}\, \mathrm{d}A_S \approx j_{e,pl}\, 4\pi\, R_S^2 = e\, n_e\, v_{e,th}\, \pi\, R_S^2\, \exp\, \eta, \tag{6.18}$$

where

$$v_{e,th} = \sqrt{\frac{8kT_e}{\pi\, m_e}} \tag{6.19}$$

is the average electron thermal velocity, and

$$\eta = \frac{eU_s}{kT_e} < 0 \tag{6.20}$$

is the normalized sheath voltage. The density n_e is to be taken at the sheath edge. The current is large when the plasma density is high, i.e., near the cathode spot. The electron current leads to heating, dissipating its kinetic and potential energies:

$$P_{e,pl} = I_{e,pl} \left(\left[\frac{2\, kT_e}{e} + U_s \right] + \phi \right). \tag{6.21}$$

The sheath voltage U_s was introduced as the macroparticle potential with respect to the plasma potential; hence $U_s < 0$. Electrons are decelerated and

thus lose kinetic up to eU_s before they arrive at the macroparticle surface. The factor $\exp \eta$ appearing in (6.18) describes the reduction of the *number* of electrons reaching the macroparticle, while U_s in (6.21) describes the reduction in *kinetic energy* for those electrons that actually make it to the surface. The potential energy is associated with the work function, ϕ, which is typically about 4 eV.

While arriving electrons lead to heating, emitted electrons carry away energy, as was extensively discussed in Chapter 3. Thermionic electron emission is described by the Richardson–Dushman equation:

$$I_{e,th} = 4\pi\, r_{MP}^2\, A_R\, T_{MP}^2\, \exp\left(-\frac{e\phi}{kT_{MP}}\right), \tag{6.22}$$

where A_R is the Richardson constant. Thermionic emission cannot be neglected when the temperature of the macroparticle is about 2000 K or higher. Similar to (6.21) , electrons emitted from a macroparticle have a cooling effect described by

$$P_{e,th}(T_{MP}) = I_{e,th}(T_{MP})\left(\frac{2\,kT_{MP}}{e} + \phi\right). \tag{6.23}$$

Energy Fluxes Related to Ion Currents

Each ion arriving at the surface of the macroparticle delivers kinetic and potential energies. The *kinetic* energy consists of the kinetic energy when it reached the sheath edge plus the kinetic energy gained by acceleration in the sheath:

$$E_{kin} = E_0 + Q\, e\, |U_s|, \tag{6.24}$$

where

$$E_0 = \frac{m_i}{2}\,(v_i - v_{MP})^2 \approx \frac{m_i}{2}\, v_i^2 \tag{6.25}$$

is the kinetic energy associated with the directed motion of ions relative to the macroparticle. The *potential* energy brought by an ion to the macroparticle includes the enthalpy of sublimation, excitation, and ionization energies minus the work function times the charge state. These terms are discussed in greater detail in the chapter on energetic condensation (Chapter 8). An ion with charge state Q arriving at the macroparticle heats the macroparticle with

$$E_{eff}(Q) = E_0 + Q\, e\, |U_s| + E_{sub} + E_{exc} + E_{ion}(Q) - Q\, e\phi. \tag{6.26}$$

The power associated with the ion current is

$$P_{i,pl} = \sum_{Q=1}^{Q_{\max}} \frac{I_{i,Q}\, E_{eff}(Q)}{Q\, e}. \tag{6.27}$$

The contribution of ions with high charge states to heating is greater than their percentage in the particle fraction, which is mainly due to their higher

ionization energy. The evaluation of (6.27) requires calculating the ion current via the current balance of the macroparticle. This is more difficult to do than for electrons because ions have a high directed velocity, which is faster than the ion sound speed, the ion thermal velocity, and the macroparticle velocity, i.e.,

$$v_{MP} << \sqrt{\frac{kT_i}{m_i}} < 2\sqrt{\frac{kT_e}{m_i}} < v_i. \tag{6.28}$$

The issue was already considered in the framework of mass balance. In a simple approximation, the ion current is determined by the flux of ions hitting the capture cross-section of the macroparticle as illustrated in Figure 6.16:

$$I_{i,Q} = Q\ e\ n_i\ v_i\ \pi\ R_{cap}^2. \tag{6.29}$$

Summing over all charge states, and using (6.10), gives the total ion current to the macroparticle:

$$I_{i,pl} = \sum_{Q=1}^{Q_{\max}} I_{i,Q} = \sum_{Q=1}^{Q_{\max}} \left[n_{i,Q}\ v_i\ Q\ e\ \pi\ r_{MP}^2 \left(1 - \frac{2\ Q\ e\ U_s}{m_i\ v_i^2} \right) \right]. \tag{6.30}$$

Since ion and electron current compensate each other, we obtain, using the quasi-neutral condition for plasma (outside the sheath),

$$n_e = \sum_{Q=1}^{Q_{\max}} Q\ n_{i,Q}, \tag{6.31}$$

an implicit equation for the sheath voltage,

$$U_s = \frac{kT_e}{e} \ln \left(\frac{v_i}{v_{e,th}} \left(1 - \frac{2\ e\ U_s}{m_i\ v_i^2} \frac{\sum_{Q=1}^{Q_{\max}} Q^2\ n_{i,Q}}{n_e} \right) \right). \tag{6.32}$$

This is an expression describing the floating potential of a relatively cold (non-emitting) macroparticle immersed in flowing multi-charge-state plasma in the cold ion approximation ($kT_i << m_i v_i^2/2$). Using the approximation $\overline{Q^2} \approx \overline{Q}^2$ we can simplify (6.30) to

$$I_{i,pl} = n_e\ v_i\ e\ \pi\ r_{MP}^2 \left(1 - \frac{2\ \overline{Q}\ e\ U_s}{m_i\ v_i^2} \right) \tag{6.33}$$

and (6.32) to

$$U_s = \frac{kT_e}{e} \ln \left(\frac{v_i}{v_{e,th}} \left(1 - \frac{2\ e\ \overline{Q}\ U_s}{m_i\ v_i^2} \right) \right). \tag{6.34}$$

Note that the sheath voltage depends mainly on the electron temperature, and only weakly on the plasma velocity, ion mass, and charge state. The result does not explicitly depend on the density (but the validity of the model does).

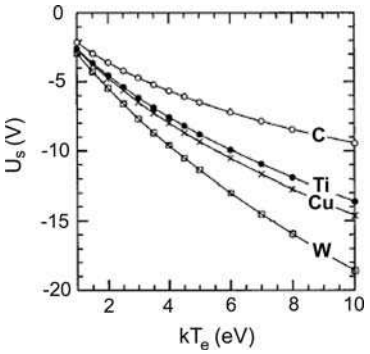

Fig. 6.17. Voltage drop in sheath of a macroparticle as a function of electron temperature; it is assumed that the macroparticle has a diameter of 1 micrometer, and the plasma velocity is 10^4 m/s. (Adapted from [29])

To illustrate the result, (6.34) was iteratively solved for carbon, titanium, copper, and tungsten macroparticles of 1-μm radius (Figure 6.17).

The total heating power of plasma ions and electrons can be found from (6.21) and (6.27) :

$$P_{pl} = P_{i,pl} + P_{e,pl}. \tag{6.35}$$

The two largest contributions to heating come from the kinetic energy and the ionization energy of ions. The power is proportional to the ion and electron currents, which are in turn proportional to the plasma density. The macroparticle is usually immersed in an expanding plasma during its flight from the cathode to the substrate, and the rate of decrease of plasma density depends on whether the expansion is free or governed by a magnetic field (e.g., plasma flow in a magnetic filter). In any case, the plasma is densest close to the cathode spot, and thus most heating by plasma particles will occur immediately after the macroparticle has left the cathode surface.

Using known materials data and reasonable estimates, it was concluded that ion and electron bombardment under typical cathodic arc conditions cannot heat macroparticles sufficiently to cause significant evaporation [29]. Worse, even when neglecting coalescence, estimates of the total mass balance indicate that macroparticles are more likely to "gain weight" after takeoff.

Energy Fluxes Related to Atom Fluxes

The flux and energy of (neutral) atoms condensing on a macroparticle are smaller than the corresponding values for ions, which is due to the high degree of ionization of cathodic arc plasmas, a smaller atom-collecting area (the macroparticle cross-section, πr_{MP}^2, as opposed to πR_{cap}^2), and the absence of ionization energy.

The flux of atoms evaporating from the macroparticle, $\varphi_a(T_{MP})$, carries away the latent heat of sublimation and thermal energy; and the power loss by evaporation cooling is

$$P_a(T_{MP}) = \left(E_{sub} + \frac{3}{2}\, kT_{MP}\right)\, \varphi_a(T_{MP})\; A_{MP}, \tag{6.36}$$

where A_{MP} is again the surface area of the macroparticle. Numerical evaluation shows that evaporation cooling is much smaller than radiative cooling [29].

Energy Fluxes Related to Radiation

The plasma of a vacuum arc is optically transparent, with the exception of the micron vicinity of the cathode spot [47, 48, 49]. The power irradiating a macroparticle is therefore much smaller than the black body radiation of optically thick plasmas. A precise determination of the radiative power requires the knowledge of the distribution of plasma species, density, and electron temperature, i.e., data not easily available. However, from plasma spraying technology, it is known that micron-size metal particles immersed in atmospheric argon plasma are not significantly heated by plasma radiation [33], and thus radiative heating can be neglected. In contrast, cooling of a macroparticle by radiation is significant. Cooling by radiation is described by black body radiation:

$$P_\nu = \varepsilon\, 4\pi\, r_{MP}^2\, \sigma_{SB}\, T_{MP}^4, \tag{6.37}$$

where $\sigma_{SB} = 5.67 \times 10^{-8}\mathrm{W/m^2K^4}$ is the Stefan–Boltzmann constant, and ε is the emissivity ($\varepsilon = 1$ for the ideal black body). The emissivity of metals at high temperatures depends on the material and wavelength but can be approximated by $\varepsilon \approx 0.1$ [50]. Evaluation showed that radiation cooling dominates over all other cooling processes at relatively low and medium macroparticle temperatures but not necessarily at very high temperatures. In particular, evaporation cooling can be greater than radiation cooling for materials of high vapor pressure at high temperature. However, this statement does not take into account that many materials of high vapor pressure have low melting and boiling temperatures (Table B1 of Appendix B). A more realistic balance for this situation still remains to be developed.

6.5.4 Momentum Balance

The velocity distribution of macroparticles immediately after takeoff is not known but can be estimated by considering the response of a liquid to highly localized, transient high pressure. The situation is corroborated by crater images taken in scanning electron microscopes.

Velocities of macroparticles have been measured but only in distances of millimeters or centimeters, i.e., at distances exceeding spot dimensions by a factor 10^3 or greater. Macroparticle velocity distributions may have changed between particle takeoff from the cathode surface and arrival at distances far

from the cathode. As indicated earlier, vapor and plasma particles condensing on the macroparticle surface will change not only the macroparticle mass but also its velocity and temperature.

Considering macroparticle acceleration due to momentum transfer from ions, one may start by writing the momentum conservation law for a collision of a single ion with a macroparticle:

$$m_i v_i + m_{MP} v_{MP,0} = (m_{MP} + m_i) v_{MP}, \tag{6.38}$$

where the subscript 0 refers to the velocity before collision. For simplicity, it was assumed that the ion condenses on the macroparticle, although it may be leaving the surface like an evaporated atom. Due to the vastly different masses of ion and macroparticle, one can write

$$v_{MP} = \frac{m_i}{m_{MP}} v_i + v_{MP,0}. \tag{6.39}$$

Obviously "ion wind" can only be of significance if a large number of ions interact with the macroparticle. This number can be introduced by multiplying (6.39) with the ion density and capture cross-section (6.10) . The gain in macroparticle velocity starts right near the cathode spot and extends all the way to the point of observation or arrival at the substrate. One may integrate along the macroparticle path:

$$\int_{R_0}^{R_1} \left(v_{MP}(R) - v_{MP,0}\right) n_i(R) \pi R_{cap}^2 \mathrm{d}R = \int_{R_0}^{R_1} \frac{m_i}{m_{MP}} v_i n_i(R) \pi R_{cap}^2 \mathrm{d}R, \tag{6.40}$$

where the lhs represents the total velocity gain from all ion impacts. Considering free plasma expansion (no magnetic field), the plasma density falls quadratically, as mentioned in Chapter 4:

$$n_i(R) \approx C \, \frac{I_{arc}}{R^2}, \tag{6.41}$$

with $C \approx 10^{13} \mathrm{A}^{-1}\mathrm{m}^{-1}$ and I_{arc} in Ampere, and the distance R in meters. With this relation, the rhs of (6.40) can be analytically solved, giving the total velocity gain of a macroparticle on its way from R_0 to R_1:

$$\Delta v_{MP} = \frac{m_i}{m_{MP}} v_i \pi R_{cap}^2 C \, I_{arc} \left(\frac{1}{R_0} - \frac{1}{R_1}\right). \tag{6.42}$$

Because $R_0 << R_1$, the expression in parenthesis can be simplified to $1/R_0$, indicating that only acceleration in the dense plasma near the spot is important. Furthermore, one can see the velocity gain increases with ratio of ion mass and macroparticle mass, in agreement with observations that smaller macroparticles are faster than larger ones.

It is important to point to a weakness of the above derivation, namely the somewhat arbitrary introduction of a minimum distance, R_0, where acceleration starts. The velocity result critically depends on the value of R_0. The relation of expansion (6.41) refers to a point source and is only justified and experimentally

confirmed for $R_0 > 100\,\mu m$, considering arcs with small current operating with a single spot. For smaller distances, one would need to know the plasma distribution. Here, the fractal structure of a spot comes into play. One could speculate that a macroparticle ejected from a crater associated with one spot fragment (emission site) becomes subject to the plasma generated by another spot fragment. Taking the fragments life or operational time into consideration, the macroparticle would be hit by a plasma stream that is most likely not perpendicular to the surface. This process could happen several times as the macroparticle is moving away from the surface pushed by plasma bursts coming from a sequence of microexplosions. The initial part of the macroparticle trajectory would not be straight but determined by the mechanical forces of plasma bursts. In larger distances from the spot, (6.42) is applicable. In that sense, R_0 represents the distance from which a macroparticle would not distinguish anymore bursts from various fragments but see the aggregation of fragments as one single spot. This distance is of the order 100 μm.

Finally, (6.42) can be illustrated by an example. Let us assume a copper macroparticle whose ion-capture radius is 1 μm is embedded in a copper plasma flow with an arc current of 100 A. With the average copper ion velocity of 1.3×10^4 m/s one can estimate $\Delta v_i \approx 5$ m/s, which is less than the typical velocity observed, leading us to the conclusion that most acceleration must have happened in the ejection process or at a distance less than 100 μm from the cathode.

A related problem is the interaction of positive ions drifting in a glow discharge plasma and encountering isolated particles, causing "ion drag," which is an important subject in "dusty plasmas" [39, 51, 52]. Charged particles in dusty plasma can interact and form Coulomb crystals [38, 53], but this subject is beyond the scope considered here.

The bombardment of macroparticles with charged particles from the plasma is asymmetric and therefore a tiny voltage difference (~10 nV) and cross-particle current may arise. The interaction of this current with the magnetic field can lead to fast rotation of the macroparticle. Gidalevich and co-workers [54] calculated at rotation rate of $\sim 10^5\ s^{-1}$ assuming a magnetic field of 20 mT.

6.6 Interaction of Macroparticles with Surfaces

As mentioned earlier, not all macroparticles arriving at a substrate will stick to it. The probability of sticking depends to a large degree on the phase that a macroparticle has before impact. Scanning electron micrographs (such as Figure 6.9) suggest that liquid macroparticles tend to stick, while solidified (spherical) macroparticles tend to "bounce." For some materials such as graphite, macroparticles can shatter and fracture into two or more pieces upon impact (Figure 6.18).

Since macroparticles are negatively charged by the interaction with the surrounding plasma, an electric force may influence the macroparticle interaction with the substrate. Keidar and co-workers predicted and detected a reduction of macroparticles when the substrate was negatively biased [55, 56]. Yin and

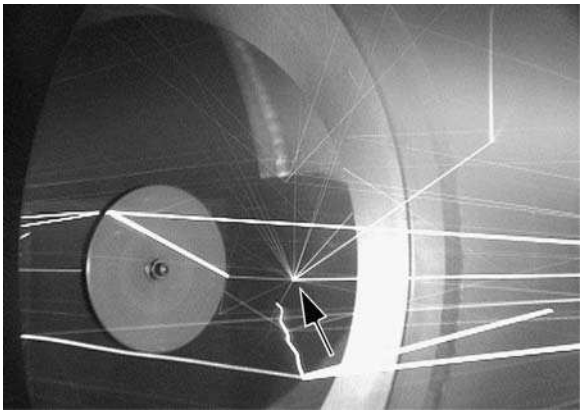

Fig. 6.18. Illustration of macroparticle reflection and fracture: the cathodic arc carbon source is on the *right*, emitting plasma and macroparticles to the *left*; deposition is done on a fast rotating disk of mirror finish. The stylized *arrow* indicates where a macroparticle fractures into several pieces upon impact. (Adapted from [46])

McKenzie [57] deposited CuCr on negatively biased silicon wafers that were aligned with the flux of plasma showing that the macroparticle density in the coating can be dramatically reduced by this configuration; this will be again considered in conjunction with macroparticle filters, cf. Figure 7.31.

6.7 Defects of Coatings Caused by Macroparticles

Macroparticles can be comparable to, or even larger than the coating thickness. They always significantly reduce the quality of a coating, which is true for all kinds of cathodic arc coatings, including nitrides (Figure 6.19),

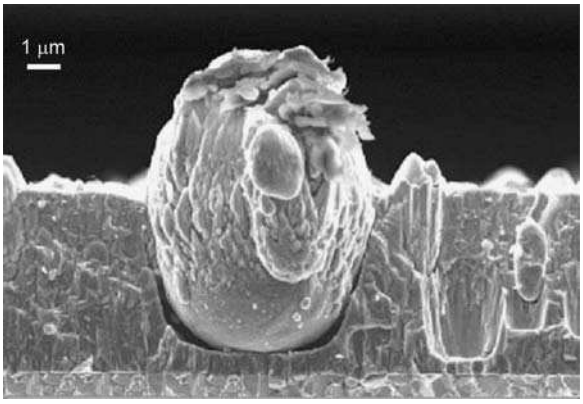

Fig. 6.19. Incorporation of a large titanium macroparticle in a titanium nitride film. (Photo courtesy of Andreas Schütze, Liechtenstein)

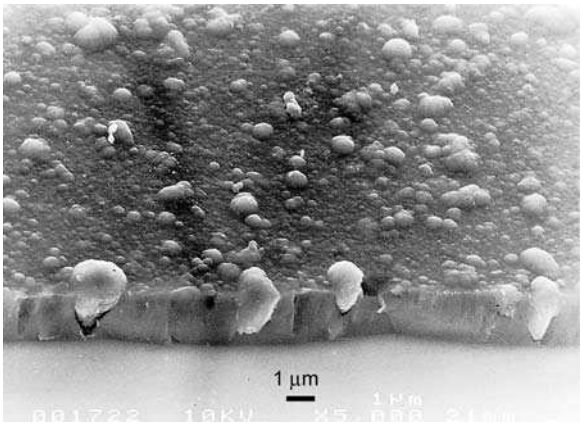

Fig. 6.20. Incorporation of graphite macroparticles in a diamond-like carbon coating. (Photo courtesy of Hans-Joachim Scheibe, cf. [58])

diamond-like carbon (Figure 6.20), or pure metals (Figure 6.21). Figures 6.19 to 6.21 reveal interesting details of the deposition history, such as the moment of macroparticle arrival in relation to the duration of the coating process. Usually, the macroparticle itself becomes coated, and it shadows the immediate vicinity of the coating. The resulting defect is deleterious for mechanical, tribological, optical, and other properties of the coating. In some cases, especially in reactive deposition, macroparticle incorporation is tolerated because macroparticles are small and the degradation of properties is within acceptable limits. Removal of macroparticles is technically difficult and usually associated with a reduction in deposition rate, which may not be acceptable in terms of process economics.

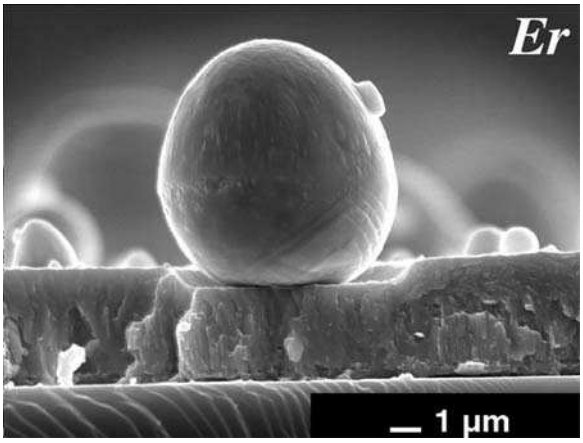

Fig. 6.21. Incorporation of an erbium macroparticle in an erbium coating. (Photo courtesy of B. Wood, Los Alamos, NM)

6.8 Mitigation Measures

There were and still are many efforts to reduce and hopefully completely eliminate the amount of macroparticles incorporated in coatings. Here, a few different attempts and concepts are described, and the most important of them, the application of curved macroparticles filters, is discussed in much greater detail in Chapter 7.

The very first step toward improved coatings is to utilize the natural separation of plasma and macroparticle fluxes (Figure 6.22). Generally, the plasma tends to plume in the normal direction from the cathode surface, toward the anode, whereas macroparticles are preferably ejected under a small angle to the cathode surface [1]. Therefore, one would position the substrate in the maximum of the plasma plume and avoid the solid angle close to the cathode surface. However, the macroparticle content of the plasma in the direction normal to the cathode surface is still large.

The next level of improving the situation is to influence the plasma flow by an axial magnetic field because this enhances the plasma arrival at the substrate compared to the arrival of macroparticles. The plasma density distribution, which in the absence of an external magnetic field is approximately proportional to the cosine of the angle to the discharge axis [59, 60], is more peaked in the axial direction when an axial magnetic field is applied; the plasma appears like a plume, or even a jet [61] (Figure 6.23). The macroparticle content, normalized by coating thickness, could be reduced by 40–50% for titanium [62] and diamond-like carbon [63]. The company Multi-Arc Inc. commercialized this approach as "Enhanced Arc."

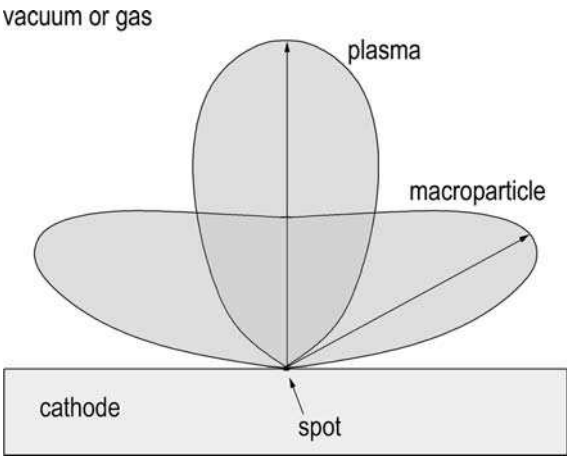

Fig. 6.22. Schematic presentation of the spatial (angular) distribution function of plasma and macroparticles: the plasma tends to plume along the cathode normal, whereas macroparticles are more likely to be ejected into the solid angle near the surface

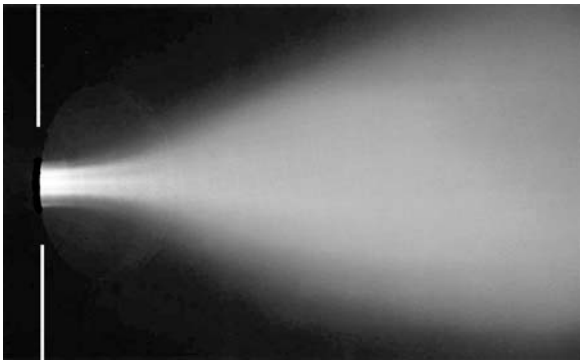

Fig. 6.23. Plasma pluming from the flange-mounted source (*left*) into the chamber (substrates to the *right*); the plume is guided by a magnetic field and therefore the coating is improved due to relatively reduced incorporation of macroparticles

Kang and co-workers [64] suggested enhancing the natural separation by rotating the cathode at high speeds (4200 rpm). Indeed, they found that most particles can be centrifuged, and plasma deposition with much less particles was demonstrated. However, this method is impractical because it is difficult to reliably transfer the arc current to a very fast rotating cathode.

A similar idea could be applied to the substrate: provided the rotational speed of a disk or wafer substrate is very high, the sticking probability may be greatly reduced. This is indeed the case for the periphery of the wafer but less so near the center where the centrifugal force is small [46]. Also here, the approach does not seem to be practical nor satisfying the requirements.

Much more successful are approaches that drive the spot to high velocities, either magnetically or electrically, as explained before. More physically speaking, the high virtual speeds imply that the ignition conditions for emission sites are favorably affected, which reduces the dwell or "activity" time of the active emission site. Thus, less cathode material is locally heated and less is available to form macroparticles.

This concept was optimized by increasing the spot motion through electrical switching [65, 66]. It is evident from Figure 6.24 that the size and depth of craters left of the spot action are smaller when the spot motion is driven faster. Spot driving is improved when discrete, dedicated anodes are used, as opposed to using the chamber wall as anode. The reduction in crater size is immediately reflected in a reduction of size and number of macroparticles.

The most pronounced effect of macroparticle reduction is when spot driving is combined with "poisoning" of the cathode surface, i.e., the formation of a surface layer that additionally promotes spot ignition (type 1 spots). In many cases of commercial application, such as hard coatings on tools, the quality of coatings obtained by steered arcs operating with reactive gases is quite acceptable, and no macroparticle filtering system is needed.

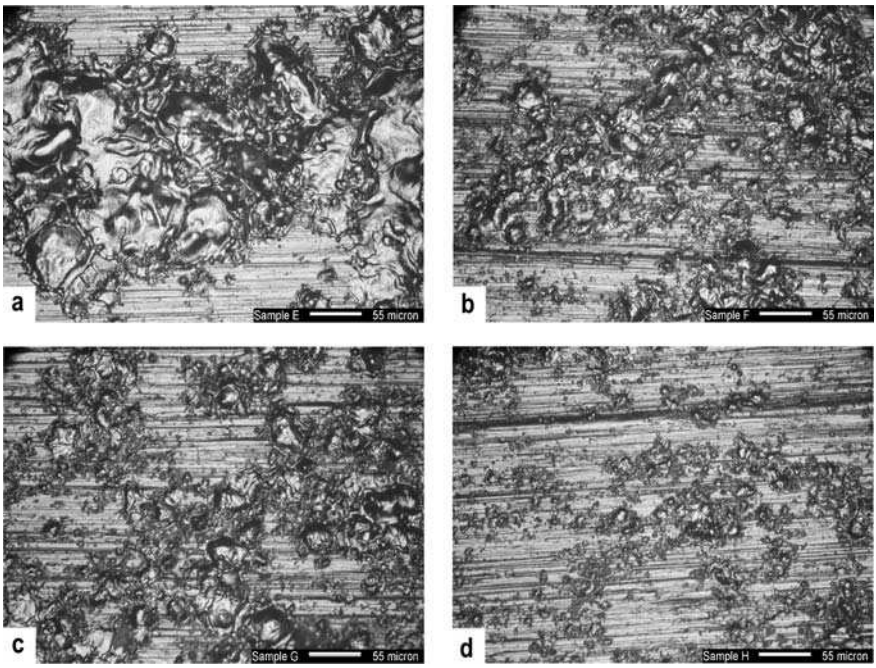

Fig. 6.24. Arc craters left by a single 120-A, 250-ms arc on a Ti cathode operating in low-pressure argon (10^{-2} Pa): (**a**) random arc, chamber wall is anode; (**b**) random arc using discrete anode; (**c**) switched arc with discrete anode, switching 4 times per second; (**d**) switched arc with discrete anode, switching 16 times per second. (Photo courtesy of Gary Vergason, Van Etten, NY, for more details see [66])

However, for highest quality, more draconian technical means are needed, and those usually involve filtering of the arc plasma even if that implies significant losses of arc plasma. Filtering techniques are explained in the following chapter.

References

1. Daalder, J.E., Components of cathode erosion in vacuum arcs, *J. Phys. D: Appl. Phys.* **9**, 2379–2395, (1976).
2. Daalder, J.E., Cathode spots and vacuum arcs, *Physica C* **104C**, 91–106, (1981).
3. Coulombe, S. and Meunier, J.-L., Theoretical prediction of non-thermionic arc cathode erosion rate including both vaporization and melting of the surface, *Plasma Sources Sci. Technol.* **9**, 239–247, (2000).
4. Udris, Y.Y., *Investigation in the field of electric discharges in gases (in Russian)*, Trudy VEI (All-Union Order of Lenin Institute of Electric Engineering) vol. 63. Gosenergoizdat, Moscow, Russia, (1958).
5. Davis, W.D. and Miller, H.C., Analysis of the electrode products emitted by dc arcs in a vacuum ambient, *J. Appl. Phys.* **40**, 2212–2221, (1969).

6. Utsumi, T. and English, J.H., Study of electrode products emitted by vacuum arcs in form of molten metal particles, *J. Appl. Phys.* **46**, 126–131, (1975).
7. Tuma, D.T., Chen, C.L., and Davis, D.K., Erosion products from the cathode spot region of a copper vacuum arc, *J. Appl. Phys.* **49**, 3821–3831, (1978).
8. Gellert, B., Schade, E., and Dullni, E., *IEEE Trans. Plasma Sci.* **PS-15**, 545–551, (1987).
9. Disatnik, G., Boxman, R.L., and Goldsmith, S., Characteristics of macroparticle emission from a high-current-density multi-cathode spot vacuum arc, *IEEE Trans. Plasma Sci.* **PS-15**, 520–523, (1987).
10. Shalev, S., Goldsmith, S., Boxman, R.L., Einav, S., and Avidor, J.M., Laser Doppler anemometry: a tool for studying macroparticle dynamics in a vacuum arc, *J. Phys. E: Sci. Instrum.* **17**, 56–61, (1984).
11. Shalev, S., Boxmann, R.L., and Goldsmith, S.J., Velocities and emission rates of cathode-produced molybdenum macroparticles in a vacuum arc, *J. Appl. Phys.* **58**, 2503–2507, (1985).
12. Shalev, S., Boxman, R.L., and Goldsmith, S., *IEEE Trans. Plasma Sci.* **PS-14**, 59–62, (1986).
13. Gellert, B. and Schade, E., "Optical investigation of droplet emission in vacuum interrupters to improve contact materials," XIVth Int. Symp. on Discharges and Electrical Insulation in Vacuum, Santa Fe, pp. 450–454, (1990).
14. Boxman, R.L. and Goldsmith, S., Macroparticle contamination in cathodic arc coatings: Generation, transport and control, *Surf. Coat. Technol.* **52**, 39–50, (1992).
15. Kandah, M. and Meunier, J.-L., Study of microdroplet generation from vacuum arcs on graphite cathodes, *J. Vac. Sci. Technol. A* **13**, 2444–2450, (1995).
16. Kandah, M. and Meunier, J.-L., Erosion study on graphite cathodes using pulsed vacuum arcs, *IEEE Trans. Plasma Sci.* **24**, 523–527, (1996).
17. Anders, S., Anders, A., Yu, K.M., Yao, X.Y., and Brown, I.G., On the macroparticle flux from vacuum arc cathode spots, *IEEE Trans. Plasma Sci.* **21**, 440–446, (1993).
18. Schülke, T. and Anders, A., Velocity distribution of carbon macroparticles generated by pulsed vacuum arcs, *Plasma Sources Sci. Technol.* **8**, 567–571, (1999).
19. Monteiro, O. and Anders, A., Vacuum-arc-generated macroparticles in the nanometer range, *IEEE Trans. Plasma Sci.* **27**, 1030–1033, (1999).
20. Kesaev, I.G., *Cathode Processes in the Mercury Arc (authorized translation from the Russian)*. Consultants Bureau, New York, (1964).
21. Boelens, S. and Veltrop, H., Hard coatings of TiN, (TiHf)N and (TiNb)N deposited by random and steered arc evaporation, *Surf. Coat. Technol.* **33**, 63–71, (1987).
22. Sethumraman, S.K., Chatterton, P.A., and Barrault, M.R., A study of the erosion rate of vacuum arcs in a transverse magnetic field, *J. Nucl. Mat.* **111/112**, 510–516, (1982).
23. Jüttner, B., On the variety of cathode craters of vacuum arcs, and the influence of the cathode temperature, *Physica* **114C**, 155–261, (1982).
24. Swift, P.D., Macroparticles in films deposited by steered cathodic arc, *J. Phys. D: Appl. Phys.* **29**, 2025–2031, (1996).
25. Swift, P.D., McKenzie, D.R., Falconer, I.S., and Martin, P.J., Cathode spot phenomena in titanium vacuum arcs, *J. Appl. Phys.* **66**, 505–512, (1989).
26. Siemroth, P., Schülke, T., and Witke, T., High-current arc – a new source for high-rate deposition, *Surf. Coat. Technol.* **68**, 314–319, (1994).
27. Kim, G.E., Meunier, J.L., and Ajersch, F., Experimental study of the effect of nitrogen on titanium-arc cathode erosion, *IEEE Trans. Plasma Sci.* **23**, 1001–1005, (1995).

28. Boxman, R.L. and Goldsmith, S., The interaction between plasma and macroparticles in a multi-cathode-spot vacuum arc, *J. Appl. Phys.* **52**, 151–161, (1981).
29. Anders, A., Growth and decay of macroparticles: A feasible approach to clean vacuum arc plasmas?, *J. Appl. Phys.* **82**, 3679–3688, (1997).
30. Beilis, I.I., Keidar, M., Boxman, R.L., and Goldsmith, S., Nonequilibrium macroparticle charging in low-density discharge plasmas, *IEEE Trans. Plasma Sci.* **25**, 346–352, (1997).
31. Delzanno, G.L., Lapenta, G., and Rosenberg, M., Attractive potential around a thermionically emitting microparticle, *Phys. Rev. Lett.* **92**, 035002–4, (2004).
32. Batrakov, A.V., Jüttner, B., Proskurovsky, D.I., and Pryadko, E.L., Light emission of droplet spots at vacuum arc and after arc extinction, *IEEE Trans. Plasma Sci.* **33**, 1476–1480, (2005).
33. Chen, X., Chen, J., and Wang, Y., Heat transfer from a rarefied plasma flow to a metallic particle with high surface temperature, *J. Phys. D: Appl. Phys.* **27**, 1637–1645, (1994).
34. Froebrich, P., On the decay of hot metallic clusters by evaporation, *Annalen der Physik* **6**, 403–21, (1997).
35. Proskurovsky, D.I., Popov, S.A., Kozyrev, A.V., Pryadko, E.L., Batrakov, A.V., and Shishkov, A.N., Droplets Evaporation in Vacuum Arc Plasma, *IEEE Trans. Plasma Sci.* **35**, 980–985, (2007).
36. Schott, L., "Electrical Probes," in *Plasma Diagnostics*, Lochte-Holtgreven, W., (Ed.). pp. 668–705, AIP, New York, (1995).
37. Daugherty, J.E., Porteous, R.K., Kilgore, M.D., and Graves, D.B., Sheath structure around particles in a low-pressure discharge, *J. Appl. Phys.* **72**, 3934–3942, (1992).
38. Fortov, V.E., Ivlev, A.V., Khrapak, S.A., Khrapak, A.G., and Morfill, G.E., Complex (dusty) plasmas: Current status, open issues, perspectives, *Phys. Rep.-Rev. Sect. Phys. Lett.* **421**, 1–103, (2005).
39. Khrapak, S.A., Ivlev, A.V., Morfill, G.E., and Thomas, H.M., Ion drag force in complex plasmas, *Phys. Rev. E* **66**, (2002).
40. Mott-Smith, H.M. and Langmuir, I., The theory of collectors in gaseous discharges, *Phys. Rev.* **28**, 727–763, (1926).
41. Bernstein, I.B. and Rabinowitz, I.N., Theory of electrostatic probes in a low-density plasma, *Phys. Fluids* **2**, 112–121, (1959).
42. Hertz, H., Über die Verdunstung der Flüssigkeiten, insbesondere des Quecksilbers, im luftleeren Raume, *Annalen der Physik und Chemie* **17**, 177–193, (1882).
43. Knudsen, M., Die maximale Verdampfungsgeschwindigkeit des Quecksilbers, *Annalen der Physik, IV. Folge* **47**, 697–708, (1915).
44. Hayess, E., Jüttner, B., Lieder, G., Neumann, W., Pursch, H., and Weixelbaum, L., Measurements of the behavior of neutral atom density in a diffuse vacuum arc by laser-induced fluorescence (LIF), *IEEE Trans. Plasma Sci.* **17**, 666–671, (1989).
45. Honig, R.E. and Kramer, D.A., Vapor pressure data for the solid and liquid elements, *RCA Rev.* **30**, 285–305, (1969).
46. Anders, A., Approaches to rid cathodic arc plasma of macro- and nanoparticles: a review, *Surf. Coat. Technol.* **120–121**, 319–330, (1999).
47. Anders, A., Anders, S., Jüttner, B., Bötticher, W., Lück, H., and Schröder, G., Pulsed dye laser diagnostics of vacuum arc cathode spots, *IEEE Trans. Plasma Sci.* **20**, 466–472, (1992).

48. Batrakov, A., Vogel, N., Popov, S.E., Proskurovsky, D., Kudimov, D., and Nikitine, D., Interferograms of a cathode spot plasma obtained with a picosecond laser, *IEEE Trans. Plasma Sci.* **30**, 106–107, (2002).
49. Batrakov, A.V., Jüttner, B., Popov, S., Proskurovsky, D.I., and Vogel, N.A., Refraction and absorption shadow imaging of the vacuum arc cathode spot at an atomic resonance line of cathode vapors, *IEEE Trans. Plasma Sci.* **33**, 1465–1469, (2005).
50. Brandes, E.A. and Brook, G.B., *Smithells Metals Reference Book*, 7th ed. Butterworth-Heinemann, Oxford, (1992).
51. Kilgore, M.D., Daugherty, J.E., Porteous, R.K., and Graves, D.B., Ion drag on an insulated particulate in a low-pressure discharge, *J. Appl. Phys.* **73**, 7195–7202, (1993).
52. Kilgore, M.D., Daugherty, J.E., Porteous, R.K., and Graves, D.B., Transport and heating of small particles in high-density plasma sources, *J. Vac. Sci. Technol. A* **12**, 486–493, (1994).
53. Thomas, H., Morfill, G.E., Demmel, V., Goree, J., Feuerbacher, B., and Mohlmann, D., Plasma crystal -Coulomb crystallization in a dusty plasma, *Phys. Rev. Lett.* **73**, 652–655, (1994).
54. Gidalevich, E., Goldsmith, S., and Boxman, R.L., Macroparticle rotation in the vacuum arc plasma jet, *J. Appl. Phys.* **95**, 2969–2974, (2004).
55. Keidar, M., Beilis, I., Boxman, R.L., and Goldsmith, S., Macroparticle interaction with a substrate in cathodic vacuum arc deposition, *Surf. Coat. Technol.* **86/87**, 415–420, (1996).
56. Aharonov, R. and Keidar, M., "Influence of an electric field on the macroparticle size distribution in a vacuum arc," Int. Conf. Metal. Coat. & Thin Films, San Diego, paper B1-6, (1999).
57. Yin, Y. and McKenzie, D.R., Electric field control of plasma and macroparticles in cathodic arc deposition as a practical alternative to magnetic fields in ducts, *J. Vac. Sci. Technol. A* **14**, 3059–3064, (1996).
58. Drescher, D., Koskinen, J., Scheibe, H.-J., and Mensch, A., A model for particle growth in arc deposited amorphous carbon films, *Diamond Rel. Mat.* **7**, 1375–1380, (1998).
59. Daalder, J.E. and Wielders, P.G.E., Proc. 12th Int. Conf. Phenom. Ionized Gases, Eindhoven, The Netherlands, p. 232, (1975).
60. Heberlein, J.V.R., Proc. 30th Gaseous Electronics Conf., Palo Alto, CA, p. 44, (1977).
61. Heberlein, J.V.R. and Porto, D., The interaction of vacuum arc ion currents with axial magnetic fields, *IEEE Trans. Plasma Sci.* **11**, 152–159, (1983).
62. Martin, P.J., McKenzie, D.R., Netterfield, R.P., Swift, P., Filipczuk, S.W., Müller, K.-H., Pacey, C.G., and James, B., Characteristics of titanium arc evaporation processes, *Thin Solid Films* **153**, 91–102, (1987).
63. Coll, B.F., Sathrum, P., Aharonov, R., and Tamor, M.A., Diamond-like carbon films synthesized by cathodic arc evaporation, *Thin Solid Films* **209**, 165–173, (1992).
64. Kang, G.H., Uchida, H., and Koh, E.S., Macroparticle-free TiN films prepared by arc ion-plating, *Surf. Coat. Technol.* **68/69**, 141–145, (1994).
65. Vergason, G.E., "Electric arc vapor deposition device," patent US 5,037,522 (1991).
66. Vergason, G.E., Lunger, M., and Gaur, S., "Advances in arc spot travel speed to improve film characteristics," Annual Technical Conference of the Society of Vacuum Coaters, Philadelphia, pp. 136–140, (2001).

7

Macroparticle Filters

Mistakes lead to discovery and that can produce delight. . .you should try it!

Chef Alice Broke, made famous in Arlo Guthrie's song "Alice's Restaurant"

Abstract The most common and successful approach to deal with the infamous macroparticle issue is to utilize curved macroparticle filters. The principles of guiding arc plasma in filters are explained. A filter can be considered as a plasma optical system that takes the source plasma and transports it to a substrate, where an "image" of the source is produced. A solenoid is the simplest example of such a plasma optical system. The chapter contains a rather comprehensive review of plasma transport models as well as filter geometries. Many examples are illustrated. The different approaches are grouped. One way of classification is to consider filters using a duct with the magnetic filter coils surrounding it and filters of "open architecture," characterized by openings through which the macroparticles can escape from the filter volume. In the open architecture, we utilize the fact that macroparticles tend to "bounce" from surfaces.

7.1 Introduction to Macroparticle Filtering

Filters are used to separate and remove macroparticles from the cathodic arc plasma, thereby greatly improving the quality of cathodic arc thin films and coatings. In fact, some high-tech applications are enabled by the use of macroparticle filters. Coatings without filters have macroparticles incorporated, therefore they are rough and structurally and chemically not uniform, especially when considering reactive deposition because unreacted metal is embedded in the compound film.

The general idea of most macroparticle filters is to electromagnetically guide the cathodic arc plasma to a substrate that is not in line of sight with the cathode. This can be done, for example, by bending a solenoid serving as the

A. Anders, *Cathodic Arcs*, DOI: 10.1007/978-0-387-79108-1_7,

electromagnetic guiding structure. Due to their large inertia and relatively small charge, the trajectories of macroparticles are practically not influenced by electric and magnetic fields, and therefore macroparticles are assumed to be lost in the filter. For straight filters, macroparticles are not eliminated but their number is reduced relative to the plasma flow arriving at the substrate. The large inertia of macroparticles is also used in the stroboscopic filter concept for pulsed arcs; here, however, separation of macroparticles and plasma is achieved via a time-of-flight effect.

Macroparticle filtering is typically done with curved magnetic filters. Plasma guiding in such filters is accomplished by a combined magnetic field and electric field mechanism. Details of the transport mechanism are discussed in Section 7.3. In essence, the electron gyration radius is much smaller than the inner filter radius, while ion motion is only marginally affected by the magnetic field. Under these conditions, magnetic field lines are approximately equipotential lines forming an electric potential "valley" or "channel" whose minimum is near the curved filter axis. The potential channel guides ions through the filter. The plasma moves as a whole, remaining quasi-neutral.

Various designs of filters have been described in the literature. It seems obvious that tighter filter curvature and longer filters would reduce the amount of macroparticles; however, long or tightly curved filters have greater plasma losses. It is important to realize that the ratio of plasma to macroparticles is decisive for the quality of a coating, rather than the absolute reduction in macroparticle particle number or density.

Most filter designs are variations of the now-classic 90° filter duct, which was developed by Aksenov, Belous, Padalka, and Khoroshikh [1, 2] in the 1970s. More information on historical aspects can be found in Chapter 2. Various filter designs are shown and discussed in Section 7.4, and additional information may be found in reviews [3–7].

7.2 Figures of Merit

7.2.1 Filter Efficiency

Not all ions entering a filter will be available for coating. Some, or perhaps most of them, may be lost to the filter wall by diffusion and other mechanisms and therefore it is important to consider parameters that characterize the performance of a filter. The plasma transport efficiency of a filter can be quantified by determining the ratio of the number of ions leaving the filter to the number of ions entering the filter, both numbers taken per time unit, which cancels in this definition, hence

$$\kappa_{eff} = N_{i,exit} / N_{i,enter}. \tag{7.1}$$

The efficiency defined this way has values between 0 and 1, or 0 and 100%, as is common with efficiencies. The definition is straightforward; however, it is

usually difficult or impractical to measure these quantities. Furthermore, such efficiency would characterize only the filter, although the efficiency of the complete source and filter system is more relevant to the performance of a filtered arc system. Therefore, other quantities are useful and frequently used, as discussed in the following sections.

7.2.2 System Coefficient

A useful figure of merit, called the *system coefficient*, can be defined as the ratio of filtered ion current to arc current [6]:

$$\kappa = I_i / I_{arc} \tag{7.2}$$

This ratio is reasonable because the amount of plasma produced at the cathode spots is known to be approximately proportional to the arc current: the system coefficient measures ion output with respect to ion generation as quantified by the arc current. Note that κ is not a conventional efficiency like the previously defined filter efficiency because κ can never reach 100% since electrons, not ions, transport most of the arc current. Looking at reports in the literature, typical system coefficients for filtered arcs are about 0.5–1%, and values of 2–5% should be considered very high, as discussed later.

For pulsed systems, one may use the charge transported per pulse, rather than current, because sufficiently constant current values may not exist. For pulsed systems we thus have

$$\kappa_{pulse} = \int_0^{t_{pulse}} I_i(t)dt \Big/ \int_0^{t_{pulse}} I_{arc}(t)dt, \tag{7.3}$$

where the integration is over the pulse duration t_{pulse}.

The system coefficient makes easy the comparison of various filter and source configurations because measurements of arc current and ion current of the filtered plasma are simple.

7.2.3 Particle System Coefficient

The above-defined system coefficients (7.2) and (7.3) are most useful when different configurations for the *same* cathode material are considered. For configuration with *different* cathode materials, however, there are shortcomings because each material has its characteristic ion erosion rate and ion charge state distribution. While the ion charge state distributions and their mean ion charge states are generally known [8, 9], at least in the sense of time-averaged values in the absence of external magnetic fields, the ion erosion rates may vary not only with cathode material but also depending on the thermal, geometric, and electrical specifics of the discharge system, which makes comparison of systems with different materials difficult. Therefore, a *particle system coefficient* can be used

as a figure of merit, which at least eliminates the influence of the various ion charge states from the measurement. The particle system coefficient is similar to the system coefficient but we consider the particle current rather than the electric ion current. This can be done by dividing the measured ion current by the mean ion charge state, $\overline{Q}$, of the material used:

$$\kappa^{part} = I_i / \left(\overline{Q}\, I_{arc} \right). \tag{7.4}$$

For pulsed systems one can define, in analogy to (7.3),

$$\kappa_{pulse}^{particle} = \int_0^{t_{pulse}} I_i(t)dt \Bigg/ \left[\overline{Q} \int_0^{t_{pulse}} I_{arc}(t)dt \right]. \tag{7.5}$$

In this way we eliminate the "artificial" enhancement in measured ion current, which occurs when the mean ion charge state is greater than unity. Integration of currents can easily be done using modern data acquisition such as the integral function on a digital oscilloscope.

It is generally accepted that the amount of plasma produced is proportional to the arc current. This is indeed a good approximation because the arc voltage is of order 20 V and almost constant [10] as long as the arc current does not exceed about 1 kA. When refinements become necessary, one should normalize not to the arc current but to the arc power, $I_{\mathrm{arc}} V_{\mathrm{arc}}$, or for pulsed systems to the arc energy per pulse, $\int I_{\mathrm{arc}} V_{\mathrm{arc}} \mathrm{d}t$. One should also note that the average ion charge states are well known only in the absence of external magnetic field. The effects of the filter field or other, additional fields may enhance the average charge state, introducing another source of error. For simplicity, though, one may use the particle system coefficient as defined in (7.5) with tabulated mean ion charge states or even ignore charge state effects and choose the system coefficient (7.2) or (7.3).

7.2.4 Attenuation Length

When investigating plasma transport in straight and curved filters, Storer and co-workers [11] found that losses are approximately exponential (Figure 7.1), and therefore an *attenuation length* can be defined as the length where the plasma density has fallen to 1/e of its original value. For the filters used by Storer and co-workers, the attenuation length of the straight filter was about twice as large as that of the curved filter (Figure 7.2). Cluggish [12] suggested to use the attenuation length normalized by the inner radius of the filter,

$$\kappa_{atten} = L_{atten} / r_{filter}, \tag{7.6}$$

as a physically meaningful figure of merit. This normalization takes into account that filters of larger inner radius may have less plasma losses to the wall but may be less beneficial in terms of macroparticle reduction.

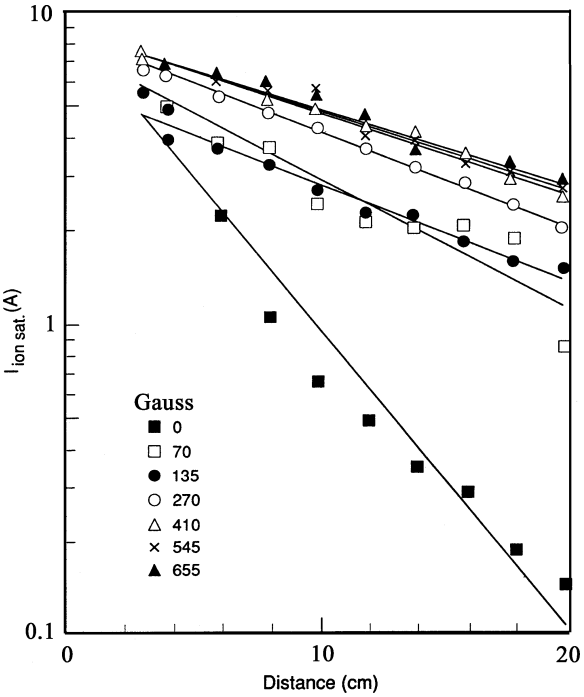

Fig. 7.1 Example of the ion saturation current to a probe inside a straight filter as a function of distance from the filter entrance, with the magnetic field strength as a parameter. (Adapted from Figure 4 of [11])

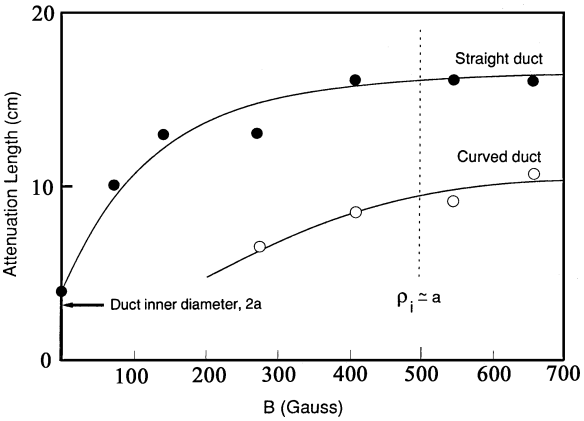

Fig. 7.2 Attenuation length of the ion saturation current to a probe inside a straight and 90°-curved filter coil, as a function of magnetic field strength. (Adapted from Figure 6 of [11])

7.2.5 Normalized Macroparticle Reduction Factor

So far, all attempts to introduce a figure of merit have concentrated on the quantification of plasma losses. It was usually implicitly assumed that all macroparticles are removed by the filter. However, and especially when straight filters are included in the discussion, macroparticles are not completely removed but their number is only more or less reduced. A good figure of merit must therefore include both macroparticle reduction and plasma losses. One may define the normalized macroparticle reduction factor as

$$\eta_{MP} = \frac{\rho_{filtered}}{\rho_0}. \tag{7.7}$$

In this definition, the symbol ρ_{filtered} is the number of macroparticles per area and film thickness when deposition is done with the filter, while ρ_0 denotes the number of macroparticles per area and film thickness if the deposition was done without filter. One should note that by normalizing the macroparticle density to the film thickness one actually includes the plasma transmission efficiency in the definition. A filter with less plasma losses will reach the targeted film thickness faster and therefore relatively less macroparticles will have a chance to reach the substrate within the deposition time. The definition emphasizes that it is not the absolute number of particles that is important but the density of macroparticles in relation to the film thickness deposited.

One weakness of the above definition of η_{MP} is that no clear statement is made about the macroparticle size distribution. Obviously, one would count all large macroparticles, but uncertainty may arise where to set a lower boundary for very small "macroparticles" (i.e., nanoparticles!). This may actually depend on the instrumental capabilities to measure very small macroparticles or the relevance of very small macroparticles to the application in mind.

One possible approach to deal with this issue is to determine the area of defects caused by macroparticles, e.g., one could use a modified macroparticle reduction factor such as

$$\tilde{\eta}_{MP} = \frac{\tilde{\rho}_{filtered}}{\tilde{\rho}_0}, \tag{7.8}$$

where the symbol $\tilde{\rho}_{\text{filtered}}$ denotes the defect area of macroparticles per area and film thickness when deposition is done with the filter and $\tilde{\rho}_0$ is the corresponding value without filter. Very small macroparticles, although most frequent in the macroparticle size distribution function, may cause negligible defects and damage for the applications under consideration. Very demanding applications, such as protective overcoats on magnetic storage media or metallization layers for integrated semiconductor circuits, may require further, more detailed considerations which clearly address the role of very small macroparticles.

7.3 Theory of Plasma Transport in Filters

7.3.1 Motion of Charged Particles and Plasma Models

In the following we focus on the most common geometry, where a plasma stream is injected into a curved magnetic filter. Much of the theory can be extended to other geometries. The plasma stream contains electrons, ions, neutral atoms, and macroparticles. We are interested in maximizing the transport of ions through the filter because ions are the condensing, film-forming particles. Ideally, all macroparticles are lost in the filter. The transport of ions is coupled to the transport of space-charge-compensating electrons. Without electrons, electrostatic repulsion of ions, i.e., their space charge, would "blow up" the flow of ions. Hence, the desired motion of ions is a plasma transport problem, not just a transport problem for ions or electrons.

The motion of charged particles, i.e., electrons and ions, in electromagnetic fields is governed by the equation of motion

$$m\frac{d^2\mathbf{r}}{dt^2} = Qe(\mathbf{E} + \mathbf{v} \times \mathrm{B}), \tag{7.9}$$

where $\mathbf{v}$ is the velocity vector of the particle, m and Q are its mass and charge state number, and e is the elementary charge. The general difficulty of plasma physics is that the electric field, $\mathbf{E}$, and the magnetic induction, $\mathbf{B}$, are not only composed of external fields but also self-consistently affected by the presence and motion of all charged particles. Therefore, even in the absence of collisions, motion of charged particles in a plasma has collective character. Hydrodynamic and kinetic models have been developed to adequately describe plasma motion in macroparticle filters (see later in this chapter).

The physics of plasma flow in a filter can be qualitatively described using an over-simplified model, but more sophisticated models have been developed for quantitative calculations. For example, one can, in the simplest case, try to determine the structure of electric and magnetic fields in a filter and then consider the motion of electrons and ions in such fields neglecting the self-consistent nature of particle motion and field distribution.

7.3.2 Magnetization and Motion of Guiding Center

At magnetic field strengths typical for filters, $B \approx 10 - 100$ mT, the electrons of the cathodic arc plasma are magnetized, but ions are usually not magnetized, as will be shown below. The term *magnetization* means that one can average over the gyration motion and consider only the motion of the gyration or *guiding center*. Averaging over the gyration greatly simplifies the treatment of the transport problem [13].

Magnetization implies that two conditions are fulfilled. One is that the gyration or Larmor radius is much smaller than the inner radius (or similar

characteristic size) of the filter, and the other is that the gyrating particle can complete at least a few gyrations without collisions with particles of other types.

The first condition can be written as

$$r_L = \frac{v_\perp}{\omega_c} << r_{filter}, \tag{7.10}$$

where r_L is the Larmor radius of the gyrating particle,

$$\omega_c = |Q|eB/m \tag{7.11}$$

is the gyration or cyclotron frequency, $v_\perp$ is the velocity perpendicular to the magnetic vector **B**, and r_{filter} is the characteristic filter size, often the inner radius or minor radius of a quarter torus, for example. For electrons, the velocity distribution function can be approximated by a Maxwell distribution with a temperature T, and one can write

$$\overline{|v_\perp|} = \int_{-\infty}^{\infty} |v_\perp| f_{Maxwell}(v)\, d^3v = \sqrt{\frac{2kT}{\pi m}}, \tag{7.12}$$

and hence condition (7.10) can be written for a Maxwellian ensemble of particles as

$$\overline{|r_L|} = \sqrt{\frac{2kTm}{\pi}} \Big/ |Q|eB << r_{filter}. \tag{7.13}$$

For electrons, $|Q| = 1$, $m = m_e$, and $T = T_e$. The situation is more complicated for ions. First, ions have a supersonic drift velocity (acquired at the cathode spot), and therefore the distribution of the velocity component perpendicular to the magnetic field is not Maxwellian. It cannot be simply expressed by a temperature. Instead, the ion velocity component perpendicular to **B** is a component of the supersonic flow velocity. Second, most cathode materials produce ions with several charge states (charge state and velocities of cathodic arc ions have been discussed in Chapters 3 and 4). Most important, however, is that the ion mass is much larger than the electron mass and therefore the gyration radius is correspondingly greater, usually exceeding the filter's characteristic length (for example, the inner or minor radius of a torus geometry). From Figure 7.3 one can see that electrons readily fulfill condition (7.13), whereas ions have a gyration radius smaller than the filter size only in the presence of a strong magnetic field.

When considering example data as shown in Figure 7.3 one must not forget that in reality the gyration radii are distributed, as is the velocity component perpendicular to the magnetic field. There will always be some energetic particles whose perpendicular velocity component is large and therefore their gyration radius is large, possibly exceeding the characteristic size of the filter.

The second condition for magnetization was that the gyrating particle can complete a few gyrations without collisions, otherwise the ion trajectory is

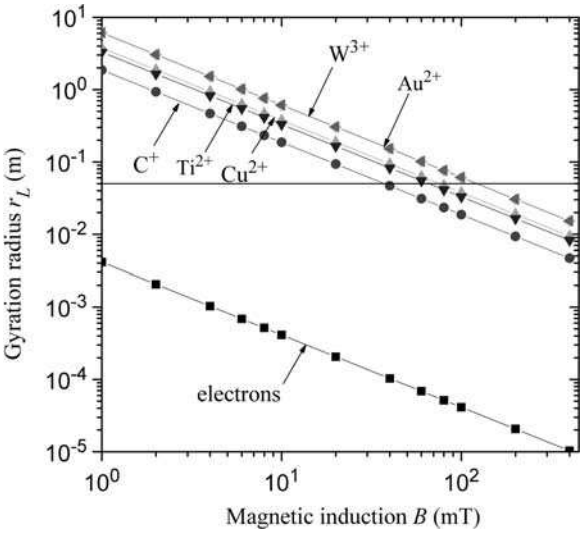

Fig. 7.3 Gyration radius of electrons and selected ions as a function of magnetic field strength. The most probable velocity of a Maxwellian distribution with a temperature of 3 eV was selected for electrons. For ions, the measured average velocity (as published in [16]) of selected ions was arbitrarily multiplied by cos 30° to derive typical values for illustration; actual gyration radii vary with velocity and angle to the magnetic field. The *horizontal line* in the center indicates a typical minor radius of a curved filter

dominated by collisions rather than by the magnetic field. This condition can be written as

$$2\pi\omega_c >> v_{coll}, \tag{7.14}$$

where the collision frequency, v_{coll}, includes collisions with all other kinds of particles:

$$v_{coll}(u) = \sum_f n_f \, u \, \sigma_f(u). \tag{7.15}$$

Like-particle collisions are not important since the motion of the center of mass of like-particles is not affected by such collisions [13]. In (7.15), u is the relative velocity between the gyrating particle of interest and the particle of type f with whom it could potentially collide, and $\sigma_f(u)$ is the velocity-dependent cross-section for such collision.

Both conditions for magnetization can be expressed as conditions for the strength of the magnetic field. The first condition, (7.14), leads to

$$B >> \frac{\sqrt{2kTm}}{\sqrt{\pi}|Q|e \, r_{filter}}, \tag{7.16}$$

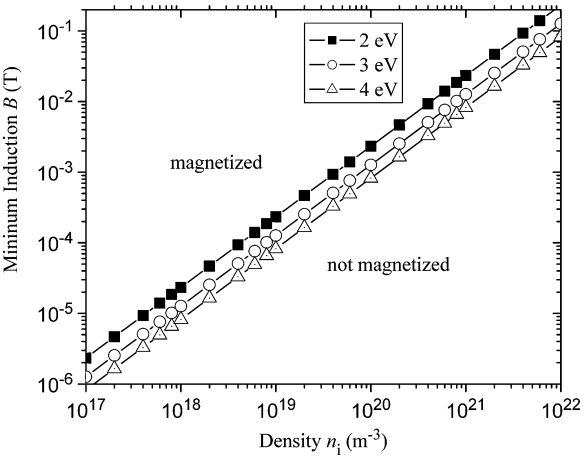

Fig. 7.4 Illustration of the additional condition of magnetization, as defined by (7.17), indicating that at typical magnetic induction in a filter, $B > 10\,\mathrm{mT}$, electrons can make many gyration rotations before colliding

and the second condition, (7.14), is

$$B >> \frac{m\, v_{coll}}{2\pi |Q| e} \,. \tag{7.17}$$

In a curved filter with streaming cathodic arc plasma, most neutral atoms, if present, are quickly lost to the wall, and one only needs to consider collisions between electrons and ions [14]:

$$v_{coll} = v_{ei} = \frac{Q^2 e^4 \ln \Lambda}{3(2\pi)^{3/2} \varepsilon_0^2} \frac{n_i}{(kT_e)^{3/2}}, \tag{7.18}$$

where Q is the ion charge state number, and $\ln \Lambda \approx 10$ is the Coulomb logarithm. Expressions (7.18) and (7.17) can be readily evaluated for electrons. The result is shown in Figure 7.4, indicating that at typical magnetic induction in a filter, $B > 10\,\mathrm{mT}$, electrons can make many gyrations before colliding, unless the density is extremely high, e.g., greater than $10^{21}\ \mathrm{m}^{-3}$.

7.3.3 Existence of an Electric Field in the Magnetized Plasma

In the absence of magnetic fields, significant electric fields usually do not exist in plasmas over distances large compared to the Debye length due to the high mobility of electrons. The situation is different when magnetic fields are applied because the mobility of electrons perpendicular to magnetic field lines is much reduced compared to the mobility parallel to magnetic field lines. To express the condition mathematically one may use the hydrodynamic equation of motion (momentum conservation) of the electron "fluid" [13, 15],

$$\frac{m_e}{e}\left(\frac{\partial \mathbf{v}_e}{\partial t} + \nabla \mathbf{v}_e\right) = -\left(\mathbf{E} + \mathbf{v}_e \times \mathbf{B} + \frac{\nabla p_e}{n_e} + \frac{\mathbf{j}}{\sigma}\right), \tag{7.19}$$

where $p_e = n_e k T_e$ is the electron pressure and $\mathbf{v}_e$ is the velocity vector of an electron fluid element; the net current term $\mathbf{j}/\sigma$ considers average electron motion relative to average ion motion and thus contains electron–ion friction; all other particle interactions are neglected. From this equation one reads that an electric field can be produced in a plasma by four factors: inertia (the term containing m_e), the Lorentz force ($\mathbf{v}_e \times \mathbf{B}$ term), the gradient of the electron pressure, and a net electrical current. The inertia term is very small due to the small electron mass, and also the current or ohmic term is usually small, which leads to

$$\mathbf{E} = -\left(\mathbf{v}_e \times \mathbf{B} + \frac{\nabla p_e}{e\, n_e}\right). \tag{7.20}$$

For the relatively low electron temperatures of a few eV, as are typical in cathodic arc plasmas (see Table B6 of Appendix B), the electron pressure term is also small, and hence the remaining two terms must approximately balance:

$$\mathbf{E} \approx -(\mathbf{v}_e \times \mathbf{B}). \tag{7.21}$$

This relation shows that in order for an electric field to exist in a plasma of low electron temperature and small net current, there must exist a transverse magnetic induction, **B**, and also an electron drift across **B**. Because **E** is transverse to **B**,

$$\mathbf{B} \cdot \mathbf{E} = -\mathbf{B} \cdot \nabla \varphi = 0 \tag{7.22}$$

where φ is the electrostatic potential. Therefore, the electrostatic potential is a constant along a magnetic field line if the above conditions (such as low electron temperature and pressure) are fulfilled. This statement is very important in understanding ion guiding, especially in the framework of plasma optics and other models.

7.3.4 An Over-Simplified but Intuitive Interpretation of Ion Transport in Curved Filters

As shown in Figure 7.5, the experimentally found depth of the electric potential channel is typically only 10–20 V. It is surprising, at first sight, how such relatively shallow potential channel is able to guide ions having kinetic energies in the range 20–150 eV (see Chapters 3 and 4).

An answer can be derived from the following over-simplified picture. Consider a curved solenoid filter and assume that the potential channel is given. The potential minimum is approximately along the curved axis of the filter. Ions having entered the filter will gradually move up the outside wall of the potential channel due to their inertia. They become subject to the force of the radial

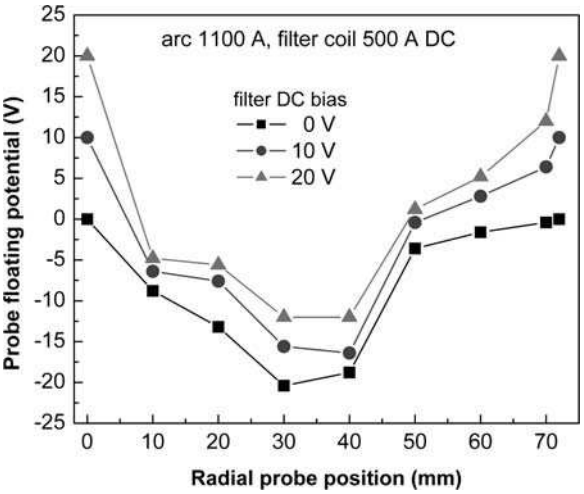

Fig. 7.5 Illustration of electric potential distribution across a curved solenoid filter, as determined by the potential of a movable floating probe. Although the local plasma potential is not the same as the floating potential, one can assume that the shapes of the spatial distributions are similar. Additional to the floating potential, the intentional bias potentials of the filter (0, 10, and 20 V) are also shown. Here, the curves are for illustration only (for more details see [108] or [107])

electric field, which accelerates them back in the direction of the channel's minimum, i.e.,

$$\mathbf{F}_{\mathrm{E}} = Qe\mathbf{E} = -Qe\frac{\partial}{\partial R}\varphi(R), \tag{7.23}$$

where R is the curvature radius of the filter (if a quarter torus filter is used, R is the major torus radius). It is known that ions are indeed transported through a curved filter, and therefore the radial electric force must have turned the straight motion into a motion with a curved path (laboratory frame). The force caused by the electric field must at least have compensated the centrifugal force:

$$\mathbf{F}_{\mathbf{E}} \geq -\mathbf{F}_R = \frac{m_i v_i^2}{R^2}\mathbf{R}. \tag{7.24}$$

Considering the radial component one obtains from Eqs.(7.23) and (7.24)

$$\frac{m_i}{2}v_i^2 \leq \frac{1}{2}Qe\frac{\partial\varphi}{\partial R}\ R. \tag{7.25}$$

One may re-write this as

$$|\mathbf{E}_R| = \frac{\partial\varphi}{\partial R} \geq \frac{m_i\ v_i^2}{QeR}. \tag{7.26}$$

Table 7.1 Minimum radial electric field strength required to compensate the centrifugal force acting on ions (selected examples) while moving through a curved filter of 0.1-m major radius

Material	Typical Charge State, Q	Minimum Radial Field (V/m)
C	1	373
Ti	2	586
Cu	2	573
W	3	776
Au	2	486

This expression is a condition for the minimum radial field that must exist. The quantities on the rhs are all known. For illustration, taking $R = 0.1$ m and published ion data (for example [16]), one finds typical values as shown in Table 7.1. One may compare these values with approximate experimental data from Figure 7.5, where there is about 10 V drop radially across 1–2 cm, leading to $E \approx 500 - 1000\text{V/m}$, which is indeed about the field strength required by (7.26). Note that much more refined theories will be described later in this chapter.

7.3.5 Kinetic Models: Rigid Rotor Equilibria

Kinetic plasma models are useful when effects need to be described which are associated with the species' distribution function, i.e., where the much simpler fluid models may not be adequate. Kinetic theory is usually much more involved than fluid models. However, some theoretical papers on plasma transport in filters refer to a rigid rotor theory, a special class of kinetic model, based on Vlasov equilibria, and it is appropriate to mention some aspects of this approach here.

The Vlasov equation describes the changes of the distribution function, $f(\mathbf{r}, \mathbf{v}, t)$, for particles of mass, m, and electrical charge, Qe, for the special case that collisions can be neglected [13]:

$$\frac{\partial f}{\partial t} + \mathbf{v} \cdot \nabla f + \frac{Qe}{m}(\mathbf{E} + \mathbf{v} \times \mathbf{B}) \cdot \frac{\partial f}{\partial \mathbf{v}} = 0. \tag{7.27}$$

Considering electrostatic perturbations of a spatially non-uniform cylindrical plasma column, Davidson [17] performed an analysis of a class of radially confined plasma. Each kind of plasma particles is considered to rotate around the plasma cylinder's axis in such a way that the average rotation frequency does not depend on the particle's distance from the axis (hence, *rigid rotor*). In confinement equilibrium, each kind of particle is assumed to have a distribution function of the type

$$f^0(\mathbf{r}, \mathbf{v}) = \frac{nm}{2\pi T} F\left(\frac{\varepsilon_\perp - \omega P_\theta}{T}, v_z\right), \tag{7.28}$$

where n, T, and ω are constants, v_z is the axial velocity, and P_θ is the canonical angular momentum,

$$P_\theta = r\left[mv_\theta + (Qe/c)A_\theta^0(r)\right]. \tag{7.29}$$

$\varepsilon_\perp$ is the perpendicular energy defined as

$$\varepsilon_\perp = \frac{m}{2}\left(v_r^2 + v_\theta^2\right) + eQ\ \varphi_0(r), \tag{7.30}$$

where $\varphi_0(r)$ is the electrostatic potential for the equilibrium radial electric field,

$$E_r^0(r) = -\partial\varphi/\partial r, \tag{7.31}$$

and A_θ^0 is the azimuthal component of the vector potential for the total equilibrium axial magnetic field. It is an important feature of the equilibrium distribution functions that they depend on P_θ and $\varepsilon_\perp$ exclusively through the linear combination $\varepsilon_\perp - \omega P_\theta$, which means that the mean azimuthal motion corresponds to a rigid rotor with angular frequency ω.

Other assumptions in Davidson's analysis were as follows: the equilibrium properties are independent of the axial coordinate, $\partial/\partial z = 0$; they are also azimuthally symmetric, $\partial/\partial\theta = 0$; and finally the plasma pressure is much smaller than the magnetic pressure, where the equilibrium vector potential can be approximated by

$$A_\theta^0(r) = rB_0/2 \tag{7.32}$$

and B_0 is the external magnetic field. Introducing the symbols e_j (that is, $e_\mathrm{e} = -e$ for electrons and $e_\mathrm{i} = +Qe$ for ions), and $\varepsilon_j = \mathrm{sgn}\ e_j$, the canonical angular momentum can be expressed as

$$P_\theta = \left[v_\theta + \varepsilon_j r\omega_{cj}/2\right]m_j r, \tag{7.33}$$

where ω_{ce} and $_{ci}$ are the electron and ion cyclotron frequencies.

The physical idea is that an external magnetic field provides magnetic confinement of a cylindrical plasma column. The electron ensemble rotates such that the magnetic restoring force balances the electron centrifugal force. The ion ensemble may or may not rotate. In the latter case, ions are purely confined by the radial electric force, $E_r^0(r) < 0$.

With the above assumptions Davidson derived that the equilibrium potential is *quadratic* in the radial coordinate:

$$\varphi_0(r) = \frac{1}{2\overline{Q}e}\ \frac{T_e T_i}{T_e + T_i}\left[\frac{m_e}{T_e}\left(\omega_e\omega_{ce} - \omega_e^2\right) + \frac{m_i}{T_i}\left(\omega_i\omega_{ci} - \omega_i^2\right)\right] r^2, \tag{7.34}$$

where the mean ion charge state, $\overline{Q}$, is derived from the quasi-neutrality condition

$$n_i = \overline{Q}n_e. \tag{7.35}$$

The symbols $\omega_e = \text{const}$ and $\omega_i = \text{const}$ describe the mean azimuthal motion of electrons and ions: the motion is that of a rigid rotor with a constant angular velocity

$$v_{j\theta}(r) = \omega_j r \tag{7.36}$$

with $j = e, i$. Using the equilibrium $\mathbf{E} \times \mathbf{B}$ rotation frequency

$$\omega_{E\times B} = \frac{cT_eT_i}{eB_0(QT_e + T_i)}\left[\frac{m_e}{T_e}\left(\omega_e\omega_{ce} - \omega_e^2\right) + \frac{m_i}{T_i}\left(\omega_i\omega_{ci} - \omega_i^2\right)\right], \tag{7.37}$$

one can write (7.34) in the compact form

$$\varphi_0(r) = \frac{1}{2e_j}\,\frac{m_j}{e_j}\varepsilon_j\,\omega_{cj}\,\omega_{ExB}\,r^2. \tag{7.38}$$

The quantity $(\omega_{ci}\omega_{E\times B})^{1/2}$ is the frequency of ion oscillations in the equilibrium potential $\varphi_0(r)$.

In the special case that the distribution function (7.28) has the form

$$F\left(\frac{\varepsilon_\perp - \omega_j P_\theta}{T_j}, v_z\right) = \exp\left(\frac{\varepsilon_\perp - \omega_j P_\theta}{T_j}\right) G_j(v_z), \tag{7.39}$$

with the normalization condition $\int_{-\infty}^{+\infty} G_j(v_z)\mathrm{d}z = 1$, the density profile can be shown to be *Gaussian*:

$$n_e^0(r) = \overline{Q}\, n_i^0(r) = n_{\max}\exp\left(-\frac{r^2}{R_0^2}\right), \tag{7.40}$$

where $n_{\max}$ is the maximum density on axis ($r = 0$). The square of the characteristic radius of the plasma column is

$$R_0^2 = \frac{2\left(\overline{Q}\,T_e + T_i\right)}{\overline{Q}\,m_e\left(\omega_e\omega_{ce} - \omega_e^2\right) - \,m_i(\omega_i\omega_{ci} + \omega_i^2)}. \tag{7.41}$$

In the limiting case where ions do not rotate, $\omega_i = 0$, the characteristic plasma equilibrium radius R_0 is simply related to the equilibrium $\mathbf{E} \times \mathbf{B}$ rotation frequency:

$$R_0^2 = \frac{2T_i}{m_i(\omega_{E\times B}\omega_{ci})} \tag{7.42}$$

and

$$\omega_{E\times B} = \frac{T_i}{\overline{Q}\,T_e + T_i}\,\frac{\omega_e\omega_{ce} - \omega_e^2}{\omega_{ce}}. \tag{7.43}$$

Experiments with vacuum arc plasma centrifuges have confirmed that at least near the axis of a 1-m-long cylindrical device the potential is quadratic and the density profile Gaussian [18, 19]. More recently, Giuliani and co-workers considered the onset of rotation of the vacuum arc plasma flux when it enters a straight duct [20, 21].

While these considerations on Vlasov equilibria of plasma rotation are quite fundamental, their application to the important case of curved filters is not trivial. Furthermore, in order to perform a rigorous theory, a number of other assumptions were made, such as the form of the distribution function. One may also note that in this approach, emphasis was put on average values for each kind of plasma particles, and in this sense a transition to simpler hydrodynamic theories was indicated. For more practical calculations, other model approaches are needed, as outlined in the following sections.

7.3.6 Plasma Optics

The *plasma optics* model [15] formalizes the previously mentioned, over-simplified model and puts it on a more solid theoretical basis. It is assumed that electrons are strongly magnetized while ions are not:

$$r_{L,e} << r_{filter} < r_{L,i}, \tag{7.44}$$

i.e., the electron Larmor radius is much smaller than the inner radius of a filter or similar characteristic length, and the ion Larmor radius is larger than such characteristic length. Other assumptions are (a) the collisions of ions with other ions and other particles can be neglected in a first approximation, (b) the electron temperature is much lower than the average ion kinetic energy

$$kT_e << \frac{1}{2} m_i \overline{v_i^2}, \tag{7.45}$$

and (c) the magnetic field produced by moving charged particles (ions and electrons) is much smaller than the external magnetic field and therefore can be neglected in a first approximation. The last two conditions imply that the dynamic pressure of the beam is smaller than the magnetic pressure of the external field:

$$\frac{\rho_i}{2} \overline{v_i^2} << \frac{B^2}{2\mu_0}, \tag{7.46}$$

where ρ_i is the mass density of the ion fluid element and μ_0 is the permeability of free space.

With these assumptions, a class of phenomena related to fully neutralized ion beams can be described. Indeed, a cathodic arc plasma flow with its supersonic ion velocities can be considered, in a first approximation, as a fully neutralized ion beam. If a neutralized ion beam moves in a magnetic field and the electron temperature is low, the beam behaves like a stream of single ions with the exception of instabilities [15].

The field of plasma optics can be related to the field of plasma electronics. The latter is the study of processes of electron beams propagating in the background of ions and plasma. In plasma optics, the propagation of ions is studied in a

background of electrons and plasma. Due to the very different relative masses of electrons and ions, plasma electronics and plasma optics are not the same.

The term *plasma optics* was chosen having in mind that transport of neutralized ion beams can conceptually be described like ion optics, i.e., the focusing and defocusing of non-neutralized, low-density beams of ions. Magnetic field structures in plasma optics correspond to electrostatic lenses in ion optics. In this way it is possible to "project" a source of neutralized ion beams to a target by means of a plasma-optical system (Figure 7.6).

An important concept of plasma optics is that magnetic field lines are equipotential lines, as derived in Section 7.3.3. By designing magnetic field configurations in relation to electrodes, a variety of electric fields can be produced, characterized by equipotential surfaces, $\varphi = \text{const}$, along which electrons can drift. (One should recall, strictly speaking, that it is the guiding center of the gyrating electron that drifts.)

Following Morozov and Lebedev [15], one can distinguish two classes of systems, namely those with open drift contours and those with closed drift contours. Systems with open drift contours have magnetic field lines connecting an electron emitter (cathode) with electron collector (anode). Since cathode and anode have different potentials, there must be potential drops near the electrodes: a cathode fall near the cathode surface, which is typically $|U_c| > kT_e/e$, and an anode fall, typically $|U_a| \leq kT_e/e$. Systems with closed drift contours have potential surfaces with $\varphi = \text{const}$ not intersecting electrodes; electrons in the plasma volume will remain in the volume. An example of an open contour system is a cathodic arc plasma source in the presence of an external magnetic field, and examples of closed contour systems are end-hall plasma sources, which were originally developed as thrusters for the space satellite program and later adapted for plasma-assisted deposition [22]. A curved solenoid filter is essentially a closed contour system with the exception of its entrance and exit

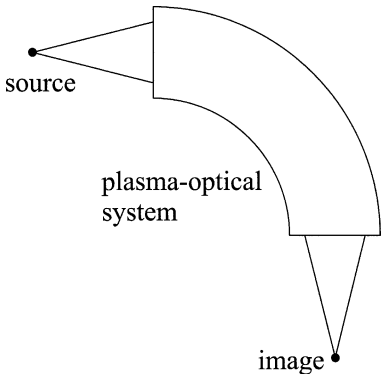

Fig. 7.6 A schematic representation of a plasma-optical system. The point source could be a cathodic arc source with cathode spot, the plasma-optical system could be a bent solenoid, and the image area corresponds to the substrate

regions. A curved solenoid filter can be thought of as composed of a number of plasma lenses, which are magnetic field-generating, current-carrying loops. Plasma lenses have been investigated both theoretically [23] and experimentally [24, 25].

Taking potential jumps near electrodes into account, the magnetic lines are equipotential lines whose potential is essentially determined by the electrode potential intersected by the magnetic field line. In this way, apart from a small potential jump, the electrode potential "propagates" throughout the plasma-optical system and determines the electric field distribution. This concept is the key to plasma optics, and it can be used to explain the effect of biasing the filter wall on ion transport (Section 7.5.1).

The simplest application of plasma optics to ion transport in a quarter torus was already described in a 1978 publication by Aksenov and co-workers [1]. They assumed that the effect of the magnetic field is purely to provide the electric field structure. The electric potential is assumed to be parabolic:

$$\varphi(r) = \varphi_0 \frac{r^2}{r_{filter}^2}, \tag{7.47}$$

where φ_0 is the wall potential and r_{filter} is the minor radius of the quarter torus. Assuming further that the electric field does not depend on the z-coordinate, they considered the Lagrangian of an ion of mass m_{i},

$$L = \frac{m_i}{2}\left(\dot{r}^2 + \dot{r}^2\dot{\phi}^2 + \dot{z}^2\right) - Qe\varphi, \tag{7.48}$$

to derive an equation for ion trajectories inside the torus. Ions oscillate radially on their way through the filter, therefore a criterion for transport is that the maximum amplitude of oscillation is smaller than r_{filter}.

A more advanced model was later developed by the same group [26] and further analyzed through a numerical solution by Davis and Donelly [27]. Two different regions were considered, namely a source or input region and the region of the quarter torus itself. To explore the effect of the input geometry, two different input situations were analyzed: (a) the plasma flow from the source is flowing into a converging magnetic field, thus plasma is "funneled" into the quarter torus and (b) the source is placed in a constant axial magnetic field of the same strength as assumed to exist inside the filter.

Aksenov and co-workers pointed out that ions can be lost either by reflection in the converging field region or by hitting the filter wall. One may define a critical angle θ_{c} as the maximum angle between source axis and initial ion velocity vector at which ions still transit the input region and enter the torus filter. Analysis of the input region is concerned with the determination of θ_{c} in relation to the ion angular distribution. The equation of ion motion is again considered in (r, ϕ, z) geometry. To discuss the situation (a), the converging magnetic field, normalized parameters are introduced:

$$\Phi = Qe\varphi_0 / \left(m_i v_i^2 / 2\right), \tag{7.49}$$

$$\Omega = \frac{QeB_0}{m_i} \frac{r_{filter}}{v_i}, \tag{7.50}$$

$$\kappa = \frac{\pi}{2} \frac{r_{filter}}{L}, \tag{7.51}$$

where L is the length between arc source and filter entrance. One can express the Lagrangian of ion motion as

$$L = \left(\dot{r}^2 + \dot{r}^2\dot{\phi}^2 + \dot{z}^2\right) - \left(\Phi - \frac{2I_1(\kappa)}{\kappa}\Omega\dot{\phi}\right)\frac{rI_1(\kappa r)}{I_1(\kappa)}\sin(\kappa z). \tag{7.52}$$

Here it was assumed that the converging magnetic field in the input region can be expressed by

$$B_r(r,z) = -B_0 I_1(kz)\cos(kz), \tag{7.53}$$

$$B_z(r,z) = B_0 I_0(kz)\sin(kz), \tag{7.54}$$

where $k = \pi/(2L)$ and I_0 and I_1 are the modified Bessel functions. The electric potential in the input region with converging magnetic field is given by

$$\varphi(r,z) = \varphi_0 \frac{rI_1(kr)\sin(kz)}{r_{filter} I_1\left(kr_{filter}\right)}. \tag{7.55}$$

The analysis of these expressions shows that ions with large radial velocities will be lost to the wall (which is somewhat arbitrarily set in the case of a converging field); ions with small radial velocities will oscillate in the (r, ϕ) plane, with v_z approaching zero when the ion emission angle approaches the critical angle θ_c. The transmission of the input region will be largest for small values of L/r_{filter}. Detailed results are given by Davis and Donnelly [27]. One should note that the critical angle θ_c is in the range 15°–30° for the relevant confining normalized potentials in the range $\Phi = 0.3 - 0.5$.

The situation (b), the source placed in a uniform magnetic field, is easier to describe. Ions move in the effective potential

$$U_{eff} = \left[\Phi + (\Omega/2)^2\right] r^2 \tag{7.56}$$

and will be confined when $\left[\Phi + (\Omega/2)^2\right] > 1$. The critical angle is

$$\theta_c = \sin^{-1}\left(\left(\Phi + (\Omega/2)^2\right)^{1/2}\right). \tag{7.57}$$

Moving on to the toroidal region, a new cylindrical coordinate system is used, (ρ, ψ, ζ), where ρ is the radius coordinate from the torus' major axis and ψ is the angle of filter curvature (i.e., ψ starts at zero and ends at 90° for a quarter torus). The magnetic field is assumed constant along the torus, i.e., $B_\psi = (R/\rho)B_0$, hence entrance and exit divergence of the solenoid field are ignored.

$R = R_0/r_{\text{filter}}$ is the radius of curvature of the toroidal filter normalized by the torus minor radius. The Lagrangian reads in normalized form

$$L = \left[\dot{\rho}^2 + \rho^2\dot{\psi}^2 + \dot{\zeta}^2\right] - \Phi\left[(\rho - R)^2 + \zeta^2\right] + 2\Omega R \ln\left(\frac{\rho}{R}\right)\dot{\zeta}. \tag{7.58}$$

The analysis shows that in the case of small Ω (corresponding to large ion Larmor radius), a condition for transport can be derived such that the dynamic boundary of trajectories does not touch the torus wall. This leads to

$$\theta_c = \sin^{-1}\left(\left[\Phi - \left(2R^{-1} + R^{-2}\right)(1 - \Phi)\right]^{1/2}\right). \tag{7.59}$$

From this equation one finds that there is a minimum potential below which there is no transmission:

$$\Phi_{\min} = 1 - \left[\frac{R}{R+1}\right]^2. \tag{7.60}$$

For a given confining potential, φ_0, $\Phi_{\min}$ gives the maximum kinetic energy of an ion that can be transmitted through the quarter filter. Analyzing 10^4 ion trajectories, Davis and Donnelly [27] pointed out further that ion motion in the filter is inherently three-dimensional but curvature and ∇B drifts were found to be important only for very small normalized potential Φ. In most cases of reasonably large Φ, it was found that ions spend similar time above and below the $\zeta = 0$ plane, and only little displacement from the average position off $\zeta = 0$ was observed. Other effects such as periodic focusing and defocusing were found in the computation and associated with the periodic nature of ion motion in the essentially parabolic guiding potential.

7.3.7 Drift Models

Although the plasma optics model could reproduce some important features of curved filters, it also had shortcomings such as the assumption of a certain, not self-consistent electric field structure. Particle collisions were neglected. The shortcomings of the kinetic model using Vlasov equilibrium were already mentioned. Therefore, various researchers have developed other models such as drift and hydrodynamic approximations.

The development of guiding center, drift, and hydrodynamic models of plasma flow in a curved solenoid can be traced back to many years before curved plasma filters were used for macroparticle filtering. Schmidt [28] developed a guiding center approximation where the motion of charged particles is self-consistently simulated for the case of collisionless plasma. In a zero-order approximation, a charged particle would follow the magnetic field line it gyrates around. In first-order approximation it would experience centrifugal and $\nabla_\perp B$ drift. He developed expressions for the perpendicular drift of guiding centers.

At this point one should note that in Schmidt's and other guiding center approximations, both electrons and ions are assumed to be magnetized, which is

not the case in most filter situations. The electron gyration radius is much smaller than the filter (minor) radius or similar characteristic filter dimension, while the ions gyration radius usually exceeds the filter radius. In these cases, ions do not experience $\mathbf{E} \times \mathbf{B}$ or $\nabla_{\perp} B$ or any other magnetic-field-related drift. However, ion trajectories are always indirectly affected via the electric field (which exists due to the magnetic field, see Section 7.3.3) and directly affected to some degree by magnetic fields, especially light ions in stronger magnetic filter fields, i.e., in situations where ions are not quite magnetized. Therefore, there is justification for including all terms of the equations.

Taking electron–ion collisions into account, the equations of motion for electrons and ions can be written as

$$m_e \frac{d\mathbf{v}_e}{dt} = -e(\mathbf{E} + \mathbf{v}_e \times \mathbf{B}) + m_e \nu_{ei}(\mathbf{v}_i - \mathbf{v}_e), \tag{7.61}$$

$$m_i \frac{d\mathbf{v}_i}{dt} = eQ(\mathbf{E} + \mathbf{v}_i \times \mathbf{B}) + m_i \nu_{ie}(\mathbf{v}_e - \mathbf{v}_i), \tag{7.62}$$

where ν_{ei} is the collision frequency of electrons with ions and ν_{ie} is the collision frequency of ions with electrons. Assuming a Maxwellian distribution for electrons, Spitzer [14] derived

$$\nu_{ei} = \frac{Q^2 e^4 n_i \ln \Lambda}{3 \cdot 2^{3/2} \pi^{7/8} \varepsilon_0^2 m_e^{1/2} (kT_e)^{3/2}}, \tag{7.63}$$

where $\ln \Lambda \approx 10$ is the Coulomb logarithm resulting from the treatment of many small-angle Coulomb collisions. Note that

$$\nu_{ie} = \nu_{ei} \frac{m_e}{m_i} \tag{7.64}$$

to satisfy momentum conservation. In early drift models [28–30], the electric field is considered to be the polarization field that arises from the opposite z-drift of the guiding centers of ions and electrons. Since ions are often not magnetized, the polarization field may not be relevant. The non-magnetized ions can cross magnetic field lines but electrons cannot follow: their motion is bound to the field lines (neglecting collisions for the moment). As a result, a radial electric field is setup such as to confine ions and limit their loss to the wall. The plasma as a whole is therefore affected even in cases when ions are not magnetized.

Still using the symbol $\mathbf{E}$ for the polarization field, Shi and co-workers [31] added an ad hoc term to the equations of motion that introduces the radial electric field:

$$m_e \frac{d\mathbf{v}_e}{dt} = -e(\mathbf{E} + \mathbf{v}_e \times \mathbf{B}) + m_e \nu_{ei}(\mathbf{v}_i - \mathbf{v}_e) - e\mathbf{E}_{\phi}, \tag{7.65}$$

$$m_i \frac{d\mathbf{v}_i}{dt} = eQ(\mathbf{E} + \mathbf{v}_i \times \mathbf{B}) + m_i \nu_{ie}(\mathbf{v}_e - \mathbf{v}_i) + e\mathbf{E}_{\phi}. \tag{7.66}$$

This radial electric field is explicitly assumed to be linked to a parabolic potential,

$$\mathbf{E}_\phi = -e\nabla\left(\frac{r_\phi^2}{r_{filter}^2}\varphi_0\right) = -2e\frac{\varphi_0}{r_{filter}^2}\mathbf{r}_\phi, \tag{7.67}$$

which makes this approach not self-consistent. The justification for this assumption is based on the previously discussed rigid rotor approximation and the vacuum arc centrifuge experiments supporting it. The symbol φ_0 describes here the potential difference between the potential minimum at the filter axis, $r_\phi = 0$, and the filter wall, $r_\phi = r_{\text{filter}}$. Shi and co-workers [31] derived a set of differential equations that were numerically evaluated and compared with experiments by Storer et al. [11]. Although good agreement between simulation and experiment is found, the approach is not quite satisfactory since the electric field is not self-consistently treated. There is still a need for improvement, and perhaps hydrodynamic models can satisfy that need best, as outlined in the next section.

7.3.8 Magneto-hydrodynamic Models

In magneto-hydrodynamic models, which are often simply called hydrodynamic models, the plasma is treated as a single fluid or as a mixture of two (or more) fluids of charged particles. The trajectories of individual particles are not considered but the motion of small fluid elements containing many particles. In most cases, two interacting fluids are considered, namely electrons and ions. More sophisticated models could contain more fluids, e.g., treating each ion charge state as a separate fluid. For simplicity and transparency of the treatment, let us consider two-fluid theory. One should always keep in mind that when we speak of ion or electron motion we actually mean motion of fluid elements, not individual particles.

Alterkop and co-workers have developed a hydrodynamic theory for curved macroparticle filters derived for the case that ions are not magnetized [32] or both electrons and ions are magnetized [33, 34], and their treatment includes analytical [32, 34] and numerical [33, 35] solutions. The following summary roughly follows their work. One can start by writing down the general system of magneto-hydrodynamic equations, i.e., we allow for both ions and electrons to be magnetized. The case of non-magnetized ions will be discussed later in this section. The general hydrodynamic equations of motion are

$$m_i n_i(\mathbf{v}_i\nabla)\mathbf{v}_i + \nabla p_i - n_i\overline{Q}e\mathbf{E} + n_i\nu_{ie}m_i(\mathbf{v}_i - \mathbf{v}_e) + n_i\omega_i m_i\frac{\mathbf{v}_i\times\mathbf{B}}{B} = 0, \tag{7.68}$$

$$m_e n_e(\mathbf{v}_e\nabla)\mathbf{v}_e + \nabla p_e + n_e e\mathbf{E} + n_e\nu_{ei}m_e(\mathbf{v}_e - \mathbf{v}_i) + n_e\omega_e m_e\frac{\mathbf{v}_e\times\mathbf{B}}{B} = 0, \tag{7.69}$$

where $\overline{Q}$ is the average ion charge state number, ω is the electron gyration frequency, and m and n are the mass and density, with the index e and i referring to electrons and ions. The electron and ion densities are linked by the quasi-neutrality condition,

$$n_e = \overline{Q} n_i. \tag{7.70}$$

This last condition is valid in the plasma but not in the thin sheath region near the filter wall or other objects. The system of equation is supplemented by the ideal plasma state equations, which link pressure, density, and temperature:

$$p_\alpha = n_\alpha k T_\alpha, \tag{7.71}$$

where $\alpha = \mathrm{e}, \mathrm{i}$ and k is the Boltzmann constant. The system of hydrodynamic equations is closed by the equations of continuity

$$\nabla(n_i \mathbf{v}_i) = 0, \tag{7.72}$$

$$\nabla(n_e \mathbf{v}_e) = 0, \tag{7.73}$$

which in this form imply that ionization and recombination in the filter are neglected.

The terms in the equations of motion (7.68) and (7.69) have the following physical meaning. The first terms represent the inertia terms. For ions in a curved filter it becomes the centrifugal force term:

$$n_i m_i (\mathbf{v}_i \nabla)\mathbf{v}_i \approx n_i m_i \mathbf{g} = n_i m_i \frac{v_0^2}{R} \mathbf{e}_R \tag{7.74}$$

where $\mathbf{g}$ is the centrifugal acceleration, R is the curvature radius of the toroidal filter, and $\mathbf{e}_R$ is the unit vector of the curvature radius of the magnetic field, perpendicular to the field lines and in the plane of toroidal symmetry. The corresponding electron inertia term can be neglected because the thermal electron velocity (of order 10^6 m/s) is much greater than the plasma streaming velocity (of order 10^4 m/s) due to the small electron mass:

$$n_e m_e (\mathbf{v}_e \nabla)\mathbf{v}_e \approx 0. \tag{7.75}$$

The next terms in (7.68) and (7.69) describe the force due to the pressure gradient. Often it is assumed that the temperature variation is negligible, and one can write

$$\nabla p_\alpha \approx k T_\alpha \nabla n_\alpha. \tag{7.76}$$

The following terms in (7.68) and (7.69) are the force by the electrostatic field. Since (7.68) refers to ions and (7.69) to electrons, these terms have different charge signs. The next terms consider the interaction between electrons and ions, where ν_{ei} and ν_{ie} are the collision frequencies between electrons and ions and ions and electrons, respectively, see Eqs. (7.63) and (7.64). The collision terms are sometimes called the friction terms or drag force terms. The last expressions in

(7.68) and (7.69) consider the Lorentz force, which is perpendicular to both velocity vector and magnetic field vector.

The goal is to find steady-state density and potential distributions, i.e., a solution where all partial time derivatives are zero. The approach is to determine the velocity and current density vectors, which can be thought of as being composed of longitudinal and perpendicular (to the magnetic field) components:

$$\mathbf{j} = n_i Q e \mathbf{v}_i - n_e e \mathbf{v}_e = n_e e(\mathbf{v}_i - \mathbf{v}_e) = \mathbf{j}_\parallel + \mathbf{j}_\perp. \tag{7.77}$$

The parallel and perpendicular components can be obtained by the scalar product and cross product of the current density with $\mathbf{b} \equiv \mathbf{B}/B$:

$$\mathbf{j}_\parallel = \mathbf{b}(\mathbf{b} \cdot \mathbf{j}) \text{ and } \mathbf{j}_\perp = \mathbf{b} \times (\mathbf{j} \times \mathbf{b}). \tag{7.78}$$

The ion and electron velocities across the magnetic field are

$$\mathbf{v}_{i\perp} = \frac{1}{B}\left(\mathbf{E}_\perp + \frac{m_i}{Qe}\mathbf{g} - \frac{\nabla_\perp p_i}{Qen_i} - \frac{\mathbf{j}_\perp}{\sigma_\perp}\right) \times \mathbf{b}, \tag{7.79}$$

$$\mathbf{v}_{e\perp} = \frac{1}{B}\left(\mathbf{E}_\perp + \frac{\nabla_\perp p_e}{en_e} - \frac{\mathbf{j}_\perp}{\sigma_\perp}\right) \times \mathbf{b}, \tag{7.80}$$

where we see again that the electron inertia term was omitted. The first terms on the rhs of (7.79) and (7.80) describe the well-known $\mathbf{E} \times \mathbf{B}$ drift, which is independent of the charge sign and mass of particles. The terms associated with the pressure gradients are also known as diamagnetic drift terms [13]; they have opposite signs for electrons and ions, and hence they will lead to electron–ion charge separation and the setup of a polarization field. Again, one should keep in mind that this statement applies only when both electrons and ions are magnetized. The role of the polarization field will depend on whether the filter has a conducting wall or not. In the case of a conducting wall, the polarization field will cause a short-circuit current in the filter wall, which needs to be taken into account. The last terms in (7.79) and (7.80) are the electron–ion drag terms. The symbol $\sigma_\perp$ is the perpendicular conductivity, which is a little less than half of the parallel conductivity:

$$\sigma_\perp \approx 0.4\,\sigma_\parallel = 0.4\,\frac{e^2 n_e}{m_e \nu_{ei}}. \tag{7.81}$$

Note that the parallel conductivity contains the density-dependent electron–ion collision frequency, which was introduced earlier (7.63).

To solve the system of hydrodynamic equations, appropriate boundary conditions for the torus wall and entrance need to be added. The physical meaning of various force and drift contributions can be more readily recognized when using analytical solutions, but additional simplification and assumptions will be needed to manage the complexity of the task.

We first consider the case when the magnetic field is very strong such that both electrons and ions are magnetized. A right-hand cylindrical coordinate

system (R, θ, z) can be introduced, with its origin on the main torus axis, the z-axis. The radial coordinate R is directed along the centrifugal vector $\mathbf{g}$, and the azimuthal coordinate θ is in the direction from the entrance to the exit of torus. The magnetic field is

$$\mathbf{B} = \frac{R_{filter}}{R} B_0 \mathbf{e}_\theta, \tag{7.82}$$

where R_{filter} is the major torus radius, i.e., distance from the z-axis to the curved axis inside the torus and $\mathbf{e}_\theta$ is the unit vector in the θ-direction. Assuming that the density inside the filter depends only on the azimuthal coordinate,

$$n(R, \theta, z) \approx \eta(\theta) n_0, \tag{7.83}$$

where n_0 is the initial density at the filter entrance, Alterkop and co-workers [35] found that the filter efficiency, $\eta(\theta) = n/n_0$, depends on the effects of the polarization field, which in turn depends on the magnetic field strength and the possible shorting of the polarization field by a conducting filter wall.

In the case that the polarization field is short-circuit, the efficiency of a 90°-torus can be expressed by [35]

$$\eta = \frac{1}{1 + \dfrac{\theta}{\theta_{crit}}} \quad \text{or} \quad \eta = \frac{1}{1 + \dfrac{B^2}{B_{crit}^2}}, \tag{7.84}$$

where

$$\theta_{crit} = \frac{\omega_{ce,0}\omega_{ci,0} R_{filter}}{2\nu_{ei,0} v_0} \quad \text{and} \quad B_{crit} = \left(\frac{m_i \Gamma_0}{\sigma_\perp R_{filter} r_{filter}^2} \right)^{1/2}, \tag{7.85}$$

where, as above, the index 0 refers to a value at the filter entrance, e.g., v_0 and Γ_0 are the ion flow velocity and ion particle flux at the filter entrance.

In the other case, when a significant polarization field E_z exists, the efficiency of a 90° filter depends exponentially on the magnetic field [35]:

$$\eta_{90} \sim \exp\left(-\frac{E_{z,90}}{v_0 B} \right), \tag{7.86}$$

where $E_{z,90}$ is the polarization field at the filter exit.

We now consider the more common case when the magnetic field is not that strong. Electrons are assumed to be magnetized but ions are not: the ion gyration radius is larger than the minor radius of the torus. In this case one can neglect the Lorentz force on the ions,

$$n_i \omega_i m_i \frac{\mathbf{v}_i \times \mathbf{B}}{B} \approx 0, \tag{7.87}$$

and hence no electron–ion drift polarization and no polarization field will exist. Ions are not confined by the magnetic field and therefore move initially according to their inertia. In contrast, electrons are magnetized and their inertia terms

could be neglected: electrons follow approximately the curved magnetic field lines. This different behavior of electrons and ions will quickly lead to a small charge separation which sets up an electric field, as was explained in the over-simplified model, Section 7.3.4.

If one assumes that the electron mean-free-path is greater than the filter's inner radius, the drag force term can be neglected [32]. At this point it is advantageous to introduce the non-dimensional variables $\rho = R\omega_{Li}/u_{sound}$ and $\zeta = z\omega_{\mathrm{Li}} z\omega_{\mathrm{Li}}/u_{\mathrm{sound}}$, so the coordinates would become (ρ, θ, ζ). In this normalization, $\omega_{\mathrm{ci}} = QeB/m_{\mathrm{i}}$ is the ion cyclotron frequency and $u_{\mathrm{sound}} = \sqrt{(kT_{\mathrm{e}} + \gamma_{\mathrm{i}} kT_{\mathrm{i}})/m_{\mathrm{i}}}$ is the ion sound velocity, with $\gamma_{\mathrm{i}} \approx 3$ for plane ion acoustic waves [13]. The density distribution in the filter is approximately [32]

$$n(\rho, \theta, \zeta) \approx n_0 f(\rho) \exp\left\{-k\left[(\mathrm{sgn}(\mathbf{B} \cdot \mathbf{e}_\theta))\,\zeta + \left(\frac{v_0}{u_{sound}} + \frac{u_{sound}}{v_0}\right)\right]\theta\right\}, \qquad (7.88)$$

where k is a positive parameter, $f(\rho)$ is a function that satisfies the boundary condition, n_0 and v_0 are the density and velocity distribution at the filter entrance plane. The term containing sgn takes into account whether the magnetic field is parallel or antiparallel to the plasma flow. In a similar approach [33], the same group derived the filter efficiency as

$$\frac{\Gamma_i(\theta)}{\Gamma_0} = \exp\left(-\sqrt{\frac{m_i v_\parallel^2}{QkT_e}}\,\theta\right). \qquad (7.89)$$

For a 90° filter, the efficiency is thus

$$\eta_{90} = \frac{\Gamma_i(\pi/2)}{\Gamma_0} = \exp\left(-\frac{\pi}{2}\sqrt{\frac{m_i v_\parallel^2}{QkT_e}}\right). \qquad (7.90)$$

Interestingly, in the framework of this model and as long as the assumptions are fulfilled, the efficiency does not depend on the magnetic field strength or the absolute size of the filter.

Numerical solutions of the system of hydrodynamic equations have the advantage that one does not need to make certain simplifying assumptions. The usual approach is to find a suitable coordinate system and to introduce normalized variables and parameters of similarity. All equations and boundary conditions will be expressed in dimensionless form, which thus become suitable for numerical methods such as Runge–Kutta routines and finite element methods.

For example, Alterkop, Gidalevich and co-workers have executed numerical calculations for a 90° filter [33, 35]. They considered the transport of a model plasma with doubly charged titanium ions with an initial velocity of 1.2×10^4 m/s. They found that for the case of relatively weak magnetic fields of 20 mT or less, i.e., when ions are not magnetized, the filter efficiency does not exceed 10%. The plasma is displaced from the torus axis by the centrifugal acceleration and

also in the direction $-\mathbf{g} \times \mathbf{b}$. When the magnetic field is much stronger and ions are magnetized, the radial ion motion is determined by the electron diffusion across the magnetic field. A transverse electric current appears that is perpendicular and proportional to the centrifugal force, i.e., the previously mentioned polarization field, which can cause currents in the conducting filter wall, if such wall is present.

7.4 Experimental and Industrial Filter Designs

7.4.1 Filters of Closed and Open Architecture

Plasma and macroparticles can be separated in curved filters, as described theoretically in the previous section; however, the loss of macroparticles in the filter is non-trivial because macroparticles do not always stick to the filter wall. In fact, it is quite likely that they are more or less elastically reflected when hitting the duct wall or other filter component. Macroparticle "bouncing" is most likely when the macroparticle is solid, as opposed to a liquid drop of molten cathode material.

To address the "bouncing" issue, two fundamentally different filter designs have been developed, which may be called filters of closed and open architecture. Both design types have their advantages and disadvantages.

Closed filters usually consist of a duct surrounded by a magnetic field coil. The duct is usually made of metal and also serves as part of the vacuum chamber. The magnetic field coil is in air, and cooling of the coil is therefore relatively easy. This type of filter is relatively large, with the path length of the plasma being typically 0.3–1.5 m. The duct diameter is typically 10–20 cm and can easily accommodate the plasma flux from a large cathode operating in DC mode or in high-current pulsed mode. The early filters described by Aksenov and coworkers [1, 2] are of this type. Closed filters have baffles inserted inside the duct so as to direct reflected macroparticles back to the source area, where they may accumulate. Macroparticles may suffer not just one but several reflections [6, 36] in the baffle structure. They will move until they have lost all of their kinetic energy in collisions with the wall and baffle structure. They will accumulate as loose debris at the "floor" surface, unless they stick to a surface. Multiple reflections in the baffle structure may also cause a significant number of macroparticles reaching the substrate, where they may cause defects or may even be incorporated into the growing coating.

Loose macroparticles, although filtered during deposition, may become an issue again when the chamber is vented: they represent a dust that may be blown to the substrate, and they may also present a health hazard, depending on the material and concentration.

Open filters have been developed to better address the risk of macroparticles being scattered forward, i.e., in the direction of plasma flow. As mentioned above, single or multiple macroparticle reflections prevent complete macroparticle

removal in closed filters, even when the substrate is not in line of sight with the cathode. In contrast, open filters utilize reflection rather than considering them a nuisance. Openings in the filter are provided so that reflected macroparticles can leave the filter volume. In most cases, an open filter is a freestanding solenoid. Macroparticles can leave the filter volume after they have hit a turn of the filter coil. In this sense, the turns of the coil correspond to the baffles in the closed filter architecture. Because they are open, these filters cannot be part of the vacuum chamber; instead, they are placed inside the vacuum chamber [37–39]. Macroparticles that have left the filter enter a designated collecting area near the source, usually the floor space of the vacuum chamber under the open filter. It is essential to the design of open filters that the macroparticle-contaminated source and filter area are carefully separated from the clean substrate area. This is done by introducing a "macroparticle firewall," i.e., a mechanical barrier that has only one designated opening through which the cleaned plasma, exiting the filter, enters the substrate region.

Open filters are usually more compact than their closed counterparts. They have to be accommodated in the source area of a vacuum chamber, and therefore they have a relatively small path length and cross-section. The latter implies a limitation on the cathode size, hence only cathodes of relatively small diameter (e.g., less than 5 cm) are suitable, which are most often used in pulsed arc systems. In contrast to closed filters, open filters have a magnetic coil with just a few turns per length unit. To generate a sufficiently strong magnetic field, each turn must carry a relatively high coil current, usually hundreds of amperes. The arc current may by utilized as filter coil current by switching the arc and filter coil electrically in series. The relatively high coil current may lead to excessive heating of the coil, unless it is water cooled. Even with water cooling, the high coil currents are more easily implemented when using a pulsed system because the average power load can be kept much smaller than the instantaneous load during each pulse. However, open systems have also been used with DC arc systems.

7.4.2 Filters for Circular and Linear Plasma Source Areas

In the previous section, filters have been classified as of either closed or open architecture. Another way of classifying filters is to look for the shape of their cross-section. Typical cross-sections are either *circular* or rectangular with very large aspect ratio, which one may consider *linear*. The latter can be used for large area coating, provided the substrate is slowly moved perpendicular to the filter's linear dimension.

The cross-section of a filter is of course not arbitrarily chosen but matches the shape and design of the arc source producing the plasma. Plasma is produced on the *plasma source area*, i.e., the area on which cathode spots are "allowed" to operate. This area is usually defined and limited by mechanical members of the

cathode assembly, like ceramic clamping rings, or by a gap to a floating shield and/or by the spot-steering magnetic field.

Most cathodic arc sources have a cathode of circular cross-section, and therefore most filters have a circular cross-section that can accommodate the plasma flow from the circular plasma source area.

Some industrial applications require coatings of large area, and therefore linear cathodic arc sources have been developed, where the plasma source area is approximately rectangular. One should keep in mind, even with very large cathodes, that the actual plasma production occurs at point-like sources, i.e., at cathode spots; however, the time-averaged output can be approximately linear if the spots burn on all of the cathode surface. This is most effectively achieved with controlled spot motion along the cathode. Any filter that is mated to a linear cathodic arc source will approximately match the linear extension of the plasma source area.

In the following, a wide range of geometric filter designs are compiled, some of them have industrial relevance, and others are more of academic interest. The grouping was done such that *closed* filter designs are mentioned first, starting from the simplest, straight filters, and proceeding to other, sometimes "exotic" designs, and eventually focusing on a variety of open designs.

7.4.3 Straight Filter

In the theoretical section it was stressed that the primary function of filters is the separation of plasma and macroparticles, which is achieved by guiding the plasma to a substrate location that is not in line of sight with the cathode. Obviously, straight filters (Figure 7.7) would not prevent line of sight, and therefore the number of macroparticles is reduced, at best, but they are not eliminated. Still, straight filters are of theoretical and even practical value as argued below.

Straight filters amplify the "natural" plasma–macroparticle separation because they guide the plasma to the substrate and improve the plasma to macroparticle ratio or, said differently, the number of macroparticles normalized by the film thickness is reduced. As pointed out in Section 7.2.5, not the absolute number of particles but the density of macroparticles in relation to the film thickness deposited is important.

Research in straight filters is of theoretical interest because plasma losses are less than in curved filters, and one can thus distinguish between plasma losses

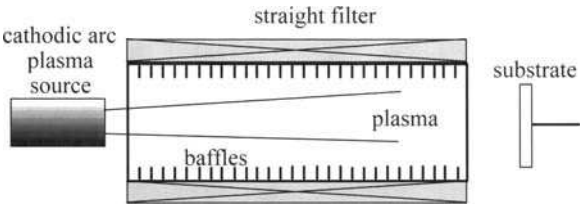

Fig. 7.7 Schematic of a plasma source with straight filter

occurring with plasma flow in general, and losses specifically related to curvature. Especially noteworthy research in straight filters was done by Aksenov and co-workers [40], Storer and co-workers [11], and Cluggish [12]. The plasma density in straight filters decays exponentially with attenuation lengths typically between 10 and 25 cm, which is typically 2–4 times longer than with comparable curved filters. This implies that straight filters have generally a higher plasma transmission than curved filters, and normalized particle reduction may be adequate for a number of coating applications. Therefore, straight filters are quite often used in industrial cathodic arc apparatus, although the fact is often not explicitly acknowledged. For example, Tamagaki and Kaisha [41] of Kobe Steel placed a magnetic guiding field between cathode and substrate and claim reduced macroparticle contamination and smaller surface roughness on tools and other coated substrates. Sathrum and Coll [42, 43] of Multi-Arc developed the "Enhanced Arc," where, among other effects, macroparticles were reduced by letting the cathodic arc plasma stream through a couple of apertures and an electromagnetic field coil. Plasma transport properties for a similar system were recently reported using Sn and Al plasma [44].

As already mentioned in the chapter on history, guiding of plasma from the cathode to the substrate has been suggested in the 1930s [45], much earlier than generally known.

7.4.4 Straight Filter with Axial Line-of-Sight Blockage

The greatest disadvantage of a straight filter is that there is a line of sight between cathode and substrate. Aksenov[1] and co-workers [46] proposed to insert an additional electromagnetic structure inside a straight filter such that a line of sight is prevented while plasma is still efficiently guided (magnetic island filter, Figure 7.8). This configuration is well suited for relatively small substrates, as is obvious from simple geometric, line-of-sight considerations.

A simpler geometry was proposed and tested by Miernik and co-workers [47]. In contrast to the previous approach [46], the central blocking shield did not house an electromagnetic coil but was simply an anode made from titanium. Since this part was not water-cooled its temperature exceeded 600°C ("red hot"). This was not detrimental since the system was designed for the deposition of TiN. Note that this central "additional" anode [47] carried 90% of the total arc current, the rest was collected by the grounded chamber wall.

A yet simpler setup, though much less efficient, is to use a blocking shield that does not have a magnetic field and is not electrically connected, hence the shield is simply a mechanical blockage. The idea was patented in the 1980s [48] and has been used in other works [49–51].

---

[1] The patent spells I.I. Axenov; he is the same researcher from Kharkov, Ukraine, often transliterated as I.I. Aksenov.

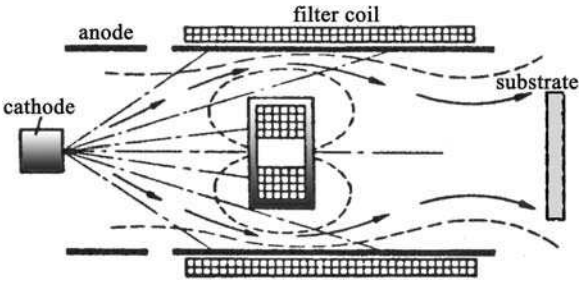

Fig. 7.8 The "magnetic island filter" is a straight filter in which a central shield is inserted; the shield is a magnetic structure that helps guiding the plasma around it [46]. Although straight, this filter does not have a line of sight between cathode and substrate

7.4.5 Straight Filter Combined with Annular-Cathode Plasma Source

To address the same issue as just mentioned in the previous section, Treglio [52] developed a different geometrical solution. A cathodic arc plasma source with an annular cathode (Figure 7.9) was combined with a short, annular magnetic field coil which has a macroparticle blocking function as well as plasma guiding function. One may consider such design as a special case of a straight filter.

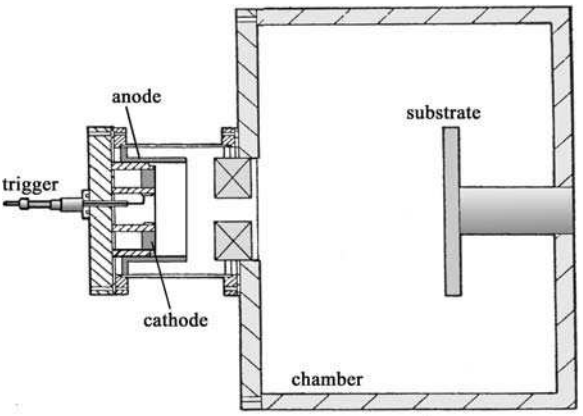

Fig. 7.9 Arc plasma source with an annular cathode combined with a short, annular magnetic field coil which has a macroparticle blocking function as well as plasma guiding function. (After [52])

7.4.6 Straight Filter with Off-Axis Substrate

Lossy and co-workers [53] used a straight duct filter with a DC arc source to deposit diamond-like carbon films. In contrast to a simple straight filter, the

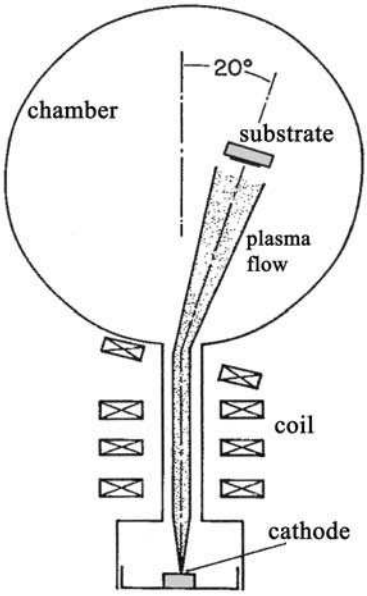

Fig. 7.10 Straight duct filter with tilted exit coil; macroparticles are allowed to enter the deposition chamber but the substrate is not in line of sight with the cathode. (After [53])

magnetic field coil at the filter's exit was tilted by 20° in order to redirect the plasma plume toward the substrate, which was mounted off-axis with respect to the axis of the linear filter (Figure 7.10). Macroparticles were allowed to enter the deposition chamber but their amount on the substrate was small since there was no line of sight to the cathode.

7.4.7 Classic 90° Duct Filter

At this point it is about time to finally introduce what could be considered the classic filter. It is a 90°-curved duct filter (Figure 7.11), i.e., a filter of closed architecture as defined in Section 7.4.1. Often termed *quarter torus* or Aksenov filter, it has been widely used in research and development, see, e.g., [5, 54–58], and therefore it should be considered a classic filter indeed. The duct filter consists of a curved tube, a 90°-elbow, the "duct," which is surrounded by a magnetic field coil generating the curved axial field, i.e., the toroidal field of a quarter torus.

Devices of this kind have been investigated for other than cathodic arc plasmas in the 1960s [29], that is, some years before Aksenov and co-workers introduced the concept to macroparticle removal in the 1970s. As pointed out in Chapter 2, the group in Kharkov deserves recognition for the pioneering work in

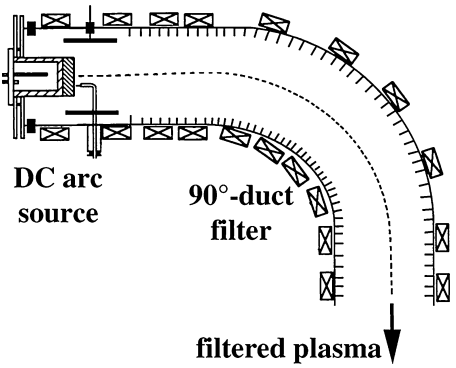

Fig. 7.11 Schematic of the now-classic 90°-duct filter developed in the 1970s (after Aksenov and co-workers [1, 2]); for the original see Figures 2.26 and 2.27

the field of cathodic arc filtering in general, and for the "classic" duct filter in particular [1, 2, 26, 40, 59]. The group has also introduced a number of improvements, such as the insertion of baffles to reduce macroparticle transport by multiple reflections and the application of positive bias to the duct leading to improved plasma transport and filter efficiency.

7.4.8 Modular Filter

Many experiments showed that the plasma losses increase exponentially with filter path length, which led to the suggestion of using the attenuation length as a length characterizing the particular filter design (Section 7.2.4). This dependence also suggests to design compact filters having minimal path length. Depending on the demands of macroparticle removal, one may use a modular filter design, where several, short, curved duct segments are coupled so as to satisfy the filtering demands of the specific application. Witke and co-workers [60, 61] developed 30°-duct segments (of closed architecture) that could be combined to 30°, 60°, or 90°, etc., filters (Figure 7.12). They used this concept with their pulsed, high-current arc (HCA) system [60], which operates with high pulsed arc currents (peak up to 5 kA) and high arc repetition frequency (up to 300 Hz). At maximum settings, the time-averaged plasma flow from a filtered HCA can reach, or even exceed, typical DC values.

7.4.9 Knee-Filter

Because plasma losses become greater for larger curvature angle of the filter, it is reasonable to design a non-line-of-sight filter that has a small bending angle and is otherwise straight. This concept has been realized by Falabella and Sanders [62] with their knee-filter, which consists of two straight filter sections

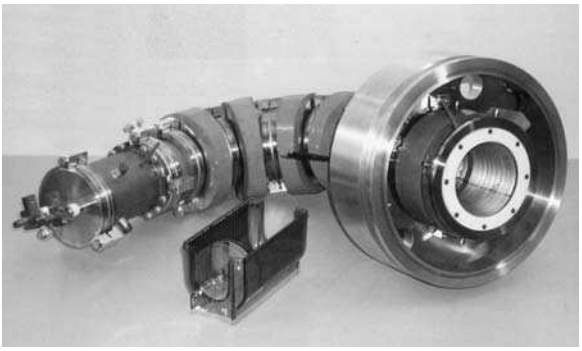

Fig. 7.12 The modular filter is a variation of the classic 90° filter: modules of 30° can be arbitrarily mounted to 30° or 60° or other angles, as best suited for the application. (After [60, 61])

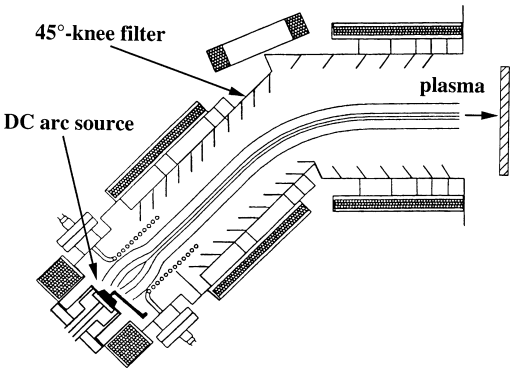

Fig. 7.13 The knee-filter consists of two straight filter sections with a 45° angle (after [62]); a commercial version is later shown in Figure 7.41

with a 45° angle (Figure 7.13). Such filter was commercially available in the 1990s from Commonwealth Scientific Corporation, Alexandria, VA [63]. As in the classic 90°-duct filter, macroparticle reflection is reduced by baffles. The commercial knee-filter was designed for DC operation and was used, among other materials, with graphite cathodes in the arc source for the deposition of diamond-like carbon coatings. A characteristic of this system was the AC magnetic sweeping system at the exit of the filter which caused the plasma flow to sweep over the substrate area like a paint brush. The usable coating area was increased to about $(300\,\mathrm{mm})^2$.

7.4.10 Large-Angle, Ω- and S-Duct Filters

In an effort to further reduce the flux of residual macroparticles, filters have been developed whose bending angle exceeds 90°. For instance, one could continue to

bend the filter to 180° or any other large angle [64]. Plasma losses in such filters may become severe, and these filters seem to be practicable only for applications in which film thickness is small or moderate. For certain high-tech applications, such as protective films on magnetic media and metallization of semiconductors, a filter angle greater than 90° might be chosen to minimize the normalized macroparticle contamination (for normalization see discussion in Section 7.2.5). An example of such an approach is the 120° filter developed by Siemroth and co-workers (Figure 7.14, [65]).

It was often observed that the plasma stream in a curved filter is offset from the filter axis, which is caused by several reasons such as asymmetry in the magnetic field structure, electron drift in crossed **E-** and **B-**fields, and action of the centrifugal force. In any case, rather than increasing the angle beyond 90°, one may try offsetting these shifts by bending the plasma back into an S-shaped filter (Figure 7.15). This has been done with some success, and a system coefficient of 0.6% has been reported [66]. The residual macroparticle flux to the substrate was reduced to the limits of detection. Filters of S-shape and Ω-shape have been mentioned in the early Soviet patents of the Kharkov group [67] and used more recently in the deposition of high-quality TiN coatings [68].

7.4.11 Off-Plane Double Bend Filter

Research at the Nanyang Technical University Singapore [69–71] led to the development of a modified S-filter. The second bend is not in the same plane

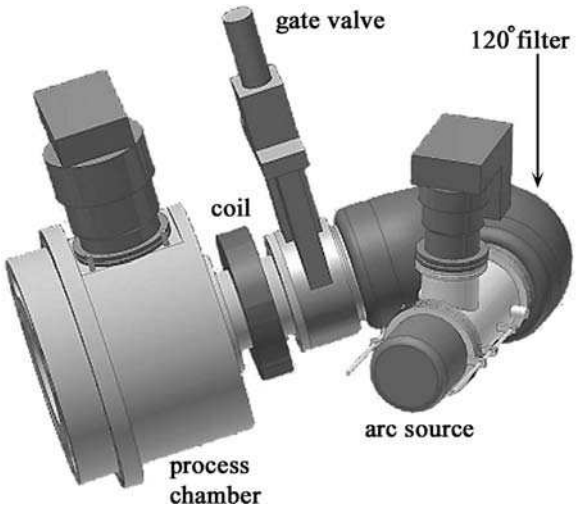

Fig. 7.14 A 120° filter developed for the high-current pulsed arc by Siemroth and co-workers for demanding applications and in the microelectronics and data storage industry. (Photo courtesy of Peter Siemroth [65])

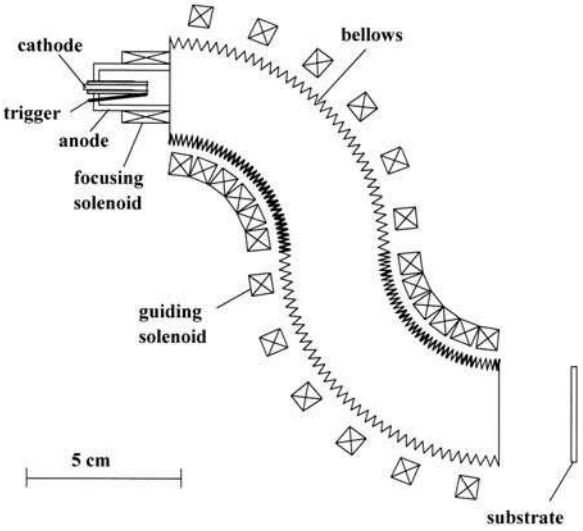

Fig. 7.15 S-filter as a special example for filters having more than 90° bending angle. (After [66])

as the first bend, which has a few advantages. One is that it is easier to prevent line of sight between filter entrance and exit than with an in-plane S-filter, and second, one may be able to better utilize off-axis shifts because they may occur perpendicular to the bending plane. The "off-plane double bend" (OPDB) filters (Figure 7.16) developed in Singapore have usually a bending angle of less than 70° per bend. A large number of arc systems with OPDB filter have been sold by Nanofilm Ltd in Singapore.

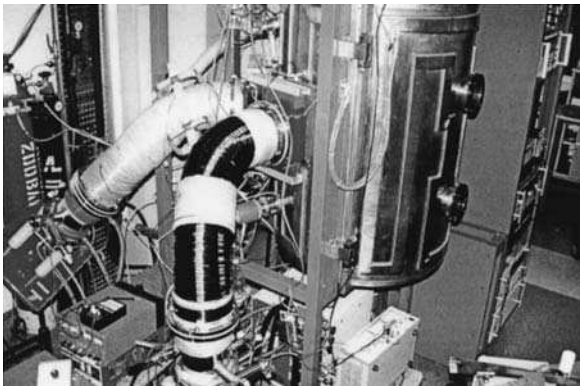

Fig. 7.16 Vacuum system with two off-plane double bend (OPDB®) filters developed at the Nanyang Technical University Singapore [69–71]. (Photo from [69])

7.4.12 Duct Filter for Linear Arc Source

Early versions of a rectangular 90°-duct filter were developed in the 1980s in the Soviet Union as part of the Cold War weapons and technology effort (Secret Soviet Author Certificate, unpublished [72]). A version of such linear filtered arc source was later patented in the United States by Gorokhovsky [73]. By using very elongated rectangular filters, the possibilities of macroparticle removal are expanded toward industrially relevant large-area coatings, as was explained in Section 7.4.2. Welty [74, 75] developed a similar design of a duct filter with a rectangular cross-section (Figure 7.17). Interestingly, this filter also utilizes magnets other than solenoids. These magnets, either electromagnets or permanent magnets, are located outside the duct wall. The shape and cross-section of a rectangular duct filter are matched to the size of the rectangular cathode, with one of its dimensions much longer than the other. The spot can be magnetically steered back and forth along the length of the cathode. Very large area coatings are possible when the substrate is moved perpendicular to the long extension of the filter.

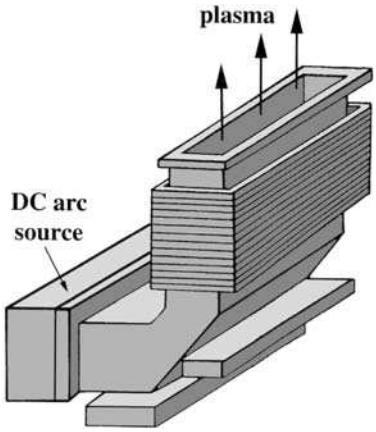

Fig. 7.17 Elongated rectangular filter for large-area coatings. (After [74, 75])

7.4.13 Rectangular S-Filter for Linear Arc Source

Combining the S-shape (though not necessarily with two 90° bends but smaller bending angle) and the need to filter plasma from an elongated or linear arc source provides the opportunity to deposit films of optical quality on large areas. In terms of illustrations, one may think of merging the geometries of the S-filter, Figure 7.15, and the elongated duct filter, Figure 7.17. A prototype in-line coater has been developed at Tel Aviv University and the spin-off company Transarc Ltd to produce transparent conducting coatings on glass [76, 77]. The figure showing this system was already introduced in Chapter 2, see Figure 2.29: it has

two arc and filter systems in deposition-up geometry: this ensures that gravity helps keeping bouncing macroparticles away from the surface of the substrate. The geometry was also chosen to allow operation with low-melting-point cathode materials such as tin (Sn). (A source design for Sn was mentioned in Section 5.2.3 and shown in Figure 5.18.)

7.4.14 Dome Filter

The idea of the dome filter is to insert a line-of-sight blocking shield between cathode and substrate and to guide the plasma around it with a dome-shaped magnetic field (Figure 7.18). There is some similarity with the linear filter that houses a central blocking member, as described in Section 7.4.4; however, the shape and position of the cathode assembly are different. In contrast to the linear filter, the eroding cathode surface is parallel to the plasma flow direction. The central shield can also serve as the anode. One may also consider that in the dome filter design, source and substrate are located in the same processing chamber. The idea was first documented in a Soviet patent by Aksenov and Bren [78], and years later described by others [79, 80]. A very high source–filter system coefficient of 3.5% is claimed [79, 80].

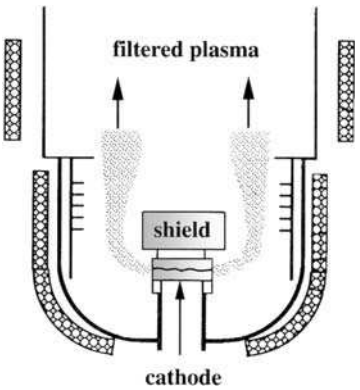

Fig. 7.18 Filter with dome-shaped magnetic field ("dome filter," after [78–80])

7.4.15 Magnetic Reflection Configuration

One of the earliest filter configurations (publication submitted in August 1977) was the magnetic reflection configuration by Osipov and co-workers [81] who used an $\mathbf{E} \times \mathbf{B}$ field as shown in Figure 7.19. The researchers drew from the knowledge of so-called end-hall plasma accelerators; they guided the plasma from the cathode to the substrate in a curved, annular fashion, where substrate and cathode are not in line of sight.

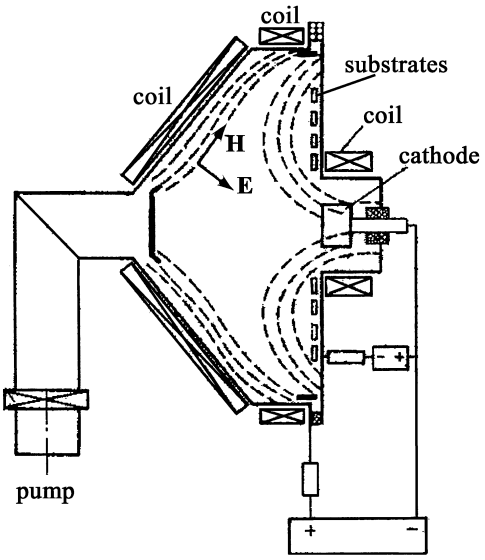

Fig. 7.19 Magnetic reflection configuration by Osipov and co-workers [81]

7.4.16 Bi-directional Linear Filter

While the original dome filter has a cylindrical cathode with the plasma generated in an axially symmetric fashion, the geometry can be modified in such a way as to obtain two "linear" plasma flows streaming in opposite directions [82]. The basic geometry of a "bi-directional linear arc and filter" is shown in Figure 7.20. It can be understood as an "elongated" or "linear" dome filter, rotated by 90° when compared to Figure 7.18. In contrast to the dome filter, the plasma streams along both directions of the magnetic field lines. Also here, the arc spots are magnetically driven along the cathode periphery. The longer the cathode the smaller the plasma losses at the ends of the cathode bar. The setup is suitable as an axial source in a batch system or as a source for a linear dual substrate system.

7.4.17 Radial Filter

A modified arrangement of cathode, anode, and magnetic fields leads to the design of a radial filter by Buhl [83], where cathode and substrate are not in line of sight but in planes that may be perpendicular to each other. The plasma is guided with a curved magnetic field; however, more than one cathode and anode may be involved. Plasma can be thought of as being transported radially. Aksenov and co-workers [84] described a similar kind of geometry involving

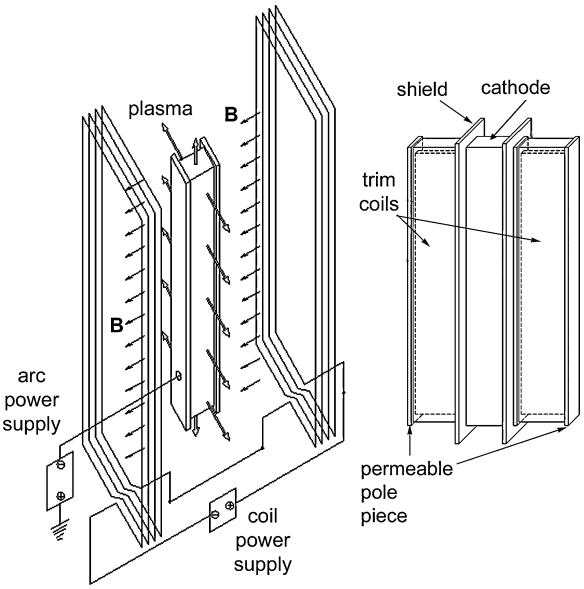

Fig. 7.20 Bi-directional linear arc and filter, which can be understood as an "elongated" or "linear" version of the dome filter shown in Figure 7.18.; the *left* side shows the two elongated field coils, and the *right* side an advanced version of the cathode assembly with two "trim coils" next to the elongated cathode. (Figures courtesy of Richard Welty, Boulder, CO)

an axially symmetric magnetic filter configuration (Figure 7.21). Deposition occurs on the inside of a substrate holder of large diameter. Both mirror and ring-cusp magnetic geometries (adding and opposing magnetic field coils, respectively) were investigated. Good efficiency and high film deposition rates were demonstrated (10 μm/h of TiN over 0.2-m^2 substrate area).

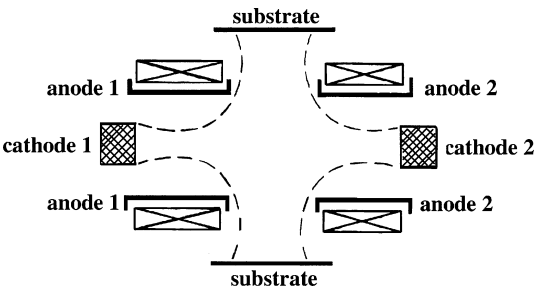

Fig. 7.21 Axially symmetric magnetic filter configuration where deposition occurs on the inside of a substrate holder of large diameter. Both mirror and ring-cusp magnetic geometries (adding and opposing magnetic field coils, respectively) were investigated. (After [84])

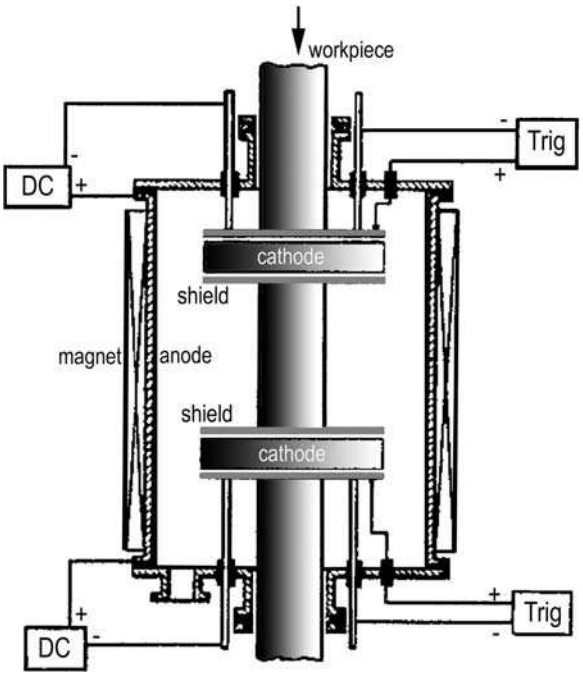

Fig. 7.22 Kljuchko and colleagues positioned a substrate (tube) inside two annular cathodes and guided the plasma magnetically to the substrates. (Adapted from [85])

7.4.18 Annular Cathode Apparatus

In their search for alternative geometries and principles to the classic 90° filter duct, the Ukrainian researchers Kljuchko et al. [85] positioned substrates inside annular cathodes and guided the plasma magnetically to the substrates. Figure 7.22 shows the setup with two cathodes. The substrate surface does not face the annular cathode surface; plasma streams to the enclosure which serves as the anode. The magnetic field prevents some of the plasma from arriving at the anode; part of the plasma is deposited onto the substrate. This geometry does not prevent macroparticles from being reflected onto the substrate. No data are available on the quality of coating and system efficiency or coefficient. This geometry also limits the substrate to certain shapes and sizes.

7.4.19 Annular Venetian Blind Filter

In another step from the dome filter, Ryabchikov and co-workers made the blocking shield partially transparent to the plasma by designing the shield as concentric, nested, vanes of a Venetian blind (Figure 7.23) [86, 87]. A reduction

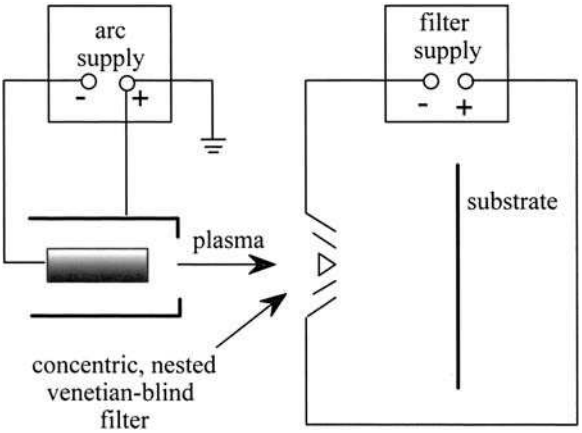

Fig. 7.23 Annular Venetian blind filter, consisting of a set of concentric, nested vanes. (After [86, 87] and adapted from review [6])

of two orders of magnitude in the macroparticle fraction was reported. The plasma transport efficiency was claimed to be up to 70% (system coefficient about 7%).

7.4.20 Linear Venetian Blind Filter

Ryabchikov also proposed and built a linear version of a Venetian blind filter but only few details were provided in the original publication [88]. The linear version, Figure 7.24, has the advantage that it can easily be scaled for large-area coatings, similar to the rectangular 90°-duct filter. Based on Ryabchikov's design, a linear Venetian blind filter was built and tested by Bilek and co-workers [89]. It was found that the filter efficiency dramatically increased when high

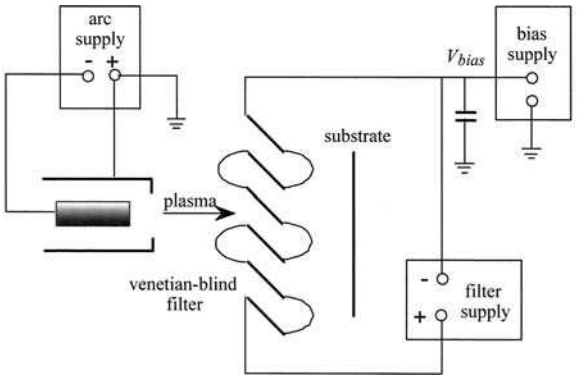

Fig. 7.24 Linear Venetian blind filter, consisting of a set of straight vanes tilted relative to the plasma flow. (After [86, 87] and adapted from review [6])

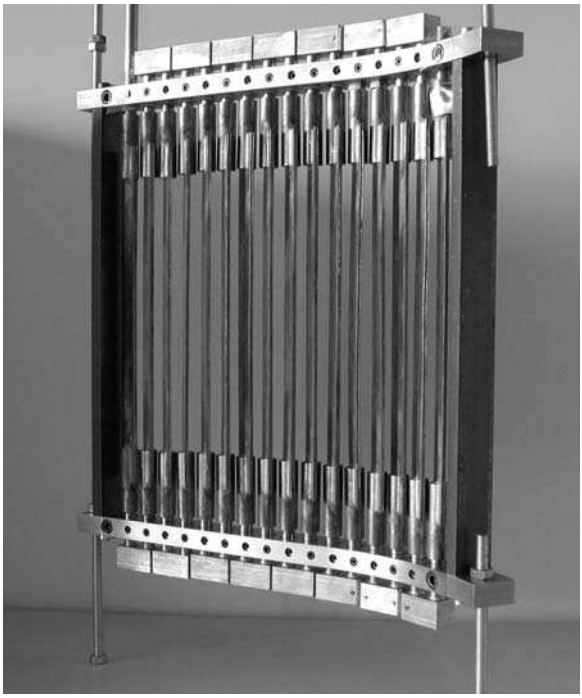

Fig. 7.25 Dresden version of a linear Venetian blind filter; the usable filter cross-section is about 30 cm × 30 cm. (Photo courtesy of Otmar Zimmer, IWS Dresden)

current was flowing through the filter vanes, which generated the necessary magnetic field. Under optimum conditions (filter vane current greater than 1 kA), the system coefficient was found to be as high as 2.5%. More recently, a somewhat larger version with a useable area of 30 cm × 30 cm was tested in Dresden, Germany (Figure 7.25) [90].

7.4.21 Open, Freestanding 90° Filter

In contrast to the closed, classic 90°-duct filter, a freestanding, open solenoid 90° filter can improve the issue of macroparticle reflection by letting particles escape from the filter volume (Figure 7.26). As explained in Section 7.4.1, open filters do not have a duct or other wall, and the magnetic field is produced by only a few turns of a solenoid. Therefore, each turn must carry a relatively large current to produce a satisfactorily high magnetic field. Often the arc current is conveniently used for generating the magnetic field [6, 11, 37]. Macroparticles may either leave the filter through openings between the turns of the field coil, or they may stick to the turns. There is still a small but

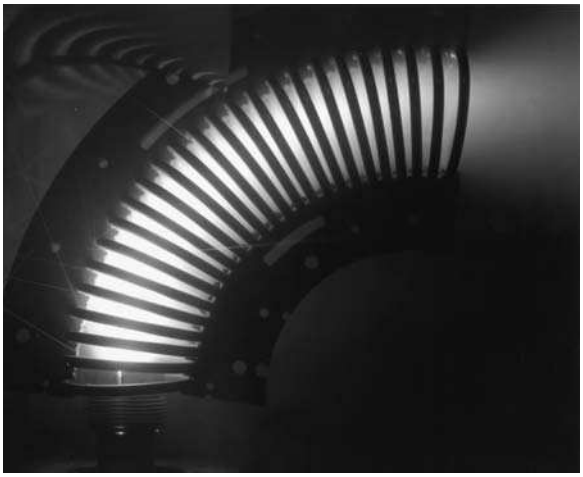

Fig. 7.26 Compact open filter, essentially consisting of a curved solenoid that produces the magnetic field using the arc current. The pulsed arc source is at the *lower left*, and the filtered plasma at the *upper right*, and the curvature (major torus radius) is about 15 cm. In the original photo one can clearly see glowing macroparticles leaving the filter volume through the opening between turns (open shutter photograph through vacuum window, Berkeley Lab, about 1994)

non-zero probability that a macroparticle will be reflected from a turn of the coil into the direction of the substrate, which leads to the need to further improve the open design.

7.4.22 Open, Freestanding S-Filter

The same argument that leads from a classic 90°-duct filter to a freestanding 90° filter can also be applied to make the step from a closed S-filter (i.e., with duct) to a freestanding, open S-filter (without duct) [6]. An open filter is an excellent research tool because deposition probes can easily be inserted for recording the plasma position and density as a function of various parameters [91]. Also, open filters are nicely accessible for optical diagnostics. Figure 7.27 shows a free-standing S-filter with well-collimated plasma, illustrating that the plasma indeed tends to follow magnetic field lines.

7.4.23 Twist Filter

A variation of the open S-filter is to twist the "S" out of plane, hence the name "twist filter" [38]. The twist filter can also be seen as the open-architecture analogy to the closed-architecture OPDB-filter described in Section 7.4.11. Again, the open filter is much more compact (Figure 7.28) than its closed-architecture counterpart. It is therefore better suited for pulsed plasma

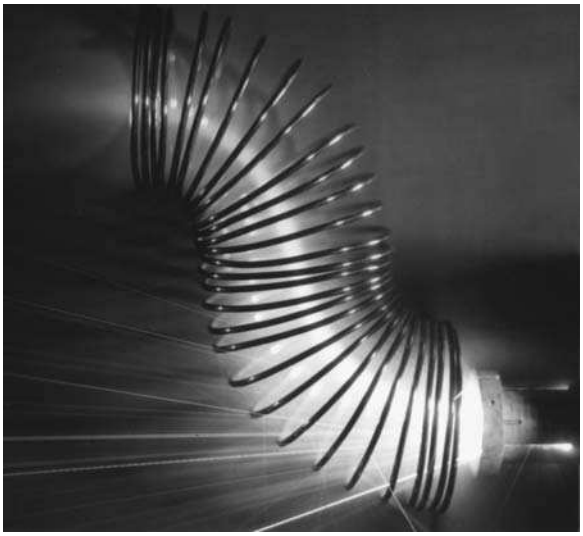

Fig. 7.27 Compact, freestanding S-filter; the filter coil current is the arc current (pulsed, about 1 kA, 1 ms); the arc source with a carbon cathode is at the *lower right* and the filtered plasma at the *upper left*; one can see a large number of small, glowing macroparticles leaving the filter volume. (Photo 1998, Berkeley Lab)

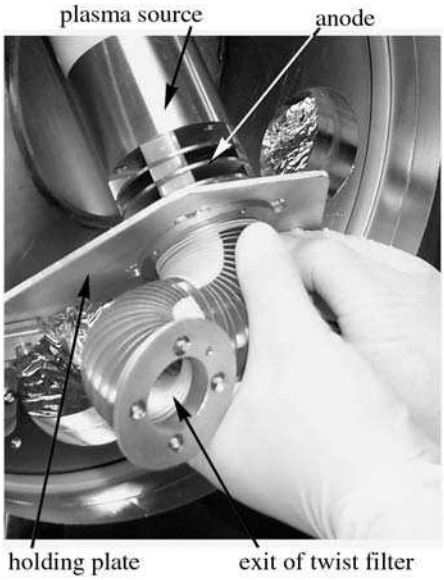

Fig. 7.28 Compact twist filter for the pulsed deposition of ta-C films; the system offers a source with advancing graphite cathode (only the source body is visible here) operating with pulses of about 1 kA, 1 ms, up to 5 pulses per second; this version of the twist filter has flat-shaped turns to promote the reflection of macroparticles from the filter volume. The hands mounting the source give an impression of the extreme compactness of the system, (Photo 2001, Berkeley Lab)

operation, although DC operation is also possible, provided cooling of the filter coil is sufficient. One should keep in mind that the few turns of the open filter may carry rather high currents, typically in the 1-kA range. The twist filter was developed for the deposition of ultrathin tetrahedral amorphous carbon (ta-C) films used as protective layers on magnetic multilayers of read–write heads and possibly also on magnetic storage media [92, 93].

7.4.24 Stroboscopic Filter

The concept of a stroboscopic filter was mentioned in a review on filters [6] but no experimental results have been reported yet. A possible issue may be, surprisingly at a first glance, the presence of *slow* macroparticles. Namely, one can show that the slow macroparticles may still be present when the shutter opens for the next discharge plasma pulse (Figure 7.29).

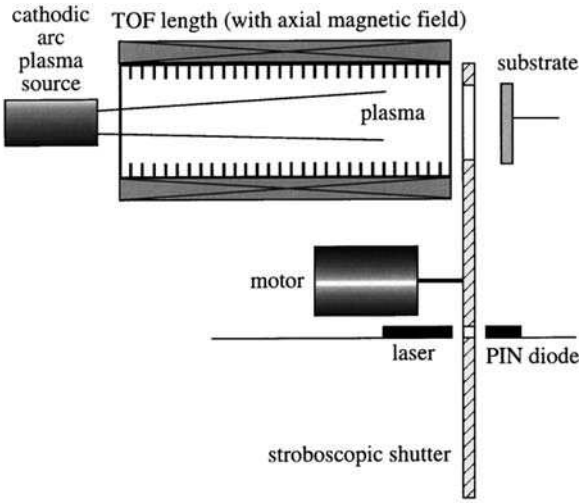

Fig. 7.29 Stroboscopic filter: the different velocities of plasma ions and macroparticles are used to obtain spatial separation in the time-of-flight drift tube; after the plasma pulse has arrived at the substrate, the path is temporarily blocked for the later-arriving macroparticles. The laser and light diode are used to synchronize gate rotation and arc pulsing. (After [6])

7.4.25 Rotating Blade Filter

In the early 1970s, Utsumi and English [94] developed a rotating blade device that they used to measure macroparticle velocities from Au, Pd, and Mg cathodic arcs (Figure 7.30). This device may also be considered to be a macroparticle filter, although no practical use has been reported. One of the reasons is perhaps

that devices relying on fast-moving parts in vacuum are expensive, difficult to maintain, and prone to failure. One should note though that, in contrast to a stroboscopic filter, the rotating blade filter is well suited for operation with DC arcs. The principle of operation is clear from Figure 7.30: if the blades rotate fast enough, macroparticles are deflected on their way to the substrate by colliding with the fast-moving blades. Utsumi and English operated this filter with rotational speeds up to 3,100 rotations per minute, eliminating all macroparticles with velocities less than 300 m/s.

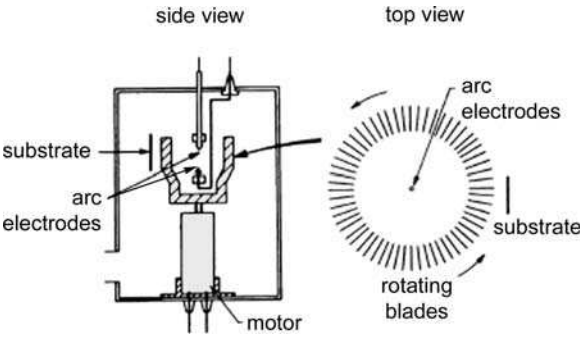

Fig. 7.30 Rotating blade filter: plasma and particles are emitted from a cathode located inside a fast rotating blade system. (Adapted from [94])

7.4.26 Parallel Flow Deposition

The flowing arc plasma is relatively dense compared to many other low-temperature plasmas, and even as the ionizing and recombining collisions are considered negligible (Chapter 4), there are still plenty of elastic collisions that can alter the direction of ion trajectories. This leads to the idea of aligning the substrate with the flow, rather than using the conventional normal incidence (Figure 7.31). The application of negative bias helps positive ions to reach the substrate because a sheath forms that accelerates them toward the surface. Taking the average kinetic energy of the directed flow, E_{kin}, and the energy ions gain in the sheath, QeV_{bias}, the average angle of incidence is about $\alpha = \arctan(\sqrt{E_{\text{kin}}/QeV_{\text{sheath}}})$. Best results in the sense of absence of macroparticles are obtained when the plasma is prefiltered, as in the arrangement shown in Figure 7.31.

High deposition rates have been observed, with good film quality in terms of the absence of macroparticles, even without prefiltering. One should be cautious: oblique angle deposition can have an impact on the microstructure, which has been very well researched for evaporation and sputter-deposited films, showing strongly tilted columns [95], and which can lead to impressively sculptured films [96] when the substrate is slowly moved with respect to the arriving flux of condensing particles. In the cathodic arc case though, the energetics of

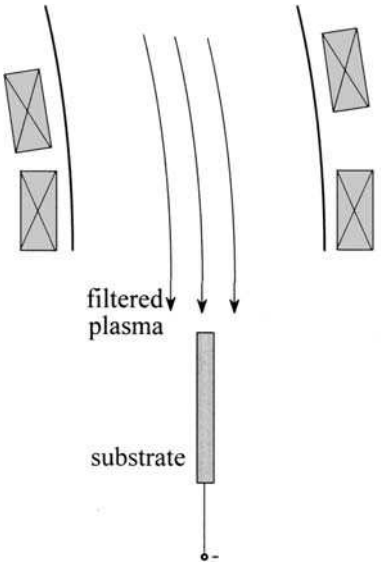

Fig. 7.31 Deposition onto the surface parallel to the arc plasma flux: there are enough elastic collisions that plasma ions can reach the surface, where they condense. For a more complete reduction of macroparticles one could use a (pre-)filtered arc plasma

arriving ions will lead to a modification (densification) of the nucleation and growth process, which is further considered in Chapter 8. Looking at the directed flow, researchers are often surprised to find coatings on surface areas that are not in line of sight, and that is true even without the application of bias. Pushing this observation to the extreme and using the MePIIID technique, metal ions can be implanted into surface areas that are in the "shadow" or wake of the plasma flow [97].

7.5 Filter Optimization

7.5.1 Biasing

The detailed theoretical explanation on plasma transport showed that plasma transport involves a coupled magnetic and electric mechanism, where the magnetic field acts on electrons, which in turn allows magnetic field lines to become equipotential lines, setting up an electric field for ion transport. The idea of biasing is now to enhance the electric potential of magnetic field lines near the filter wall or boundary, thereby deepening the electric potential channel that guides ions. Ions moving in a deeper potential channel are less likely to be lost.

Already in their pioneering work [1], Aksenov and co-workers used positive filter wall bias, and they demonstrated a significant improvement of plasma

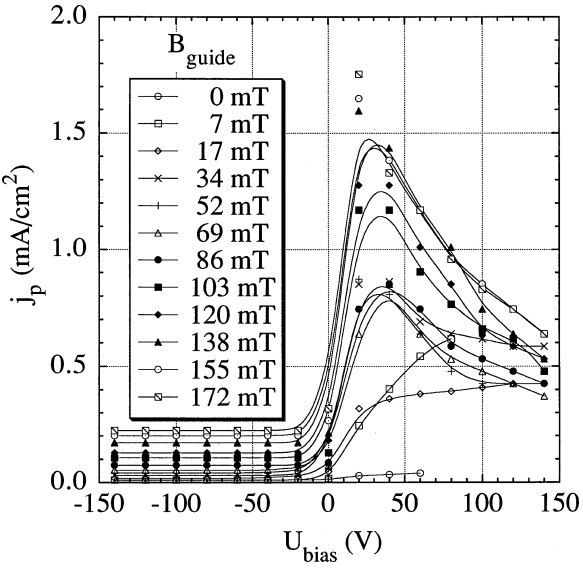

Fig. 7.32 Plasma output, as measured by the ion saturation current density to a large-area ion collector, as function of filter bias, with the magnetic field strength as a parameter. (From [98])

transport when bias values in the range + 10 to + 25 V were used. This effect was subsequently investigated and utilized by many researchers, e.g., [98–109].

Using a very compact version of a classic 90° filter, the data for a large filter [1] could be confirmed and extended [98]. Figure 7.32 shows the results of parametric magnetic field and potential variations. One can recognize that there is an optimum, and excessive bias voltage will reduce plasma transport. One may assign this reduction to the breakdown of the assumption used in the plasma optics model that electrons are magnetized and not further influenced by macroscopic electric fields. At very high positive bias, large electron currents are drawn to the filter wall, causing a loss of electrons in the streaming plasma, the potential channel becomes shallower, followed by increased ion losses.

To determine the optimum bias of a classic 90°-duct filter, Zhang and coworkers [100, 110, 111] measured the filtered ion current as a function of cathode material (C, Ti, Mo, and W) and arc current (50, 100, 150 A). They found that the optimum bias, as defined by the bias condition leading to a maximum system coefficient, depends on the cathodic material (i.e., ion mass, and possibly mean charge state) as well as on the arc current, i.e., the plasma density. The experiments showed that the optimum bias decreases with increasing field until at about $B \approx 40$ mT and is approximately constant for higher magnetic field. Figure 7.33 shows that the optimum bias is higher for the heavy elements (that also happen to have higher mean ion charge state). Interestingly, carbon, as so

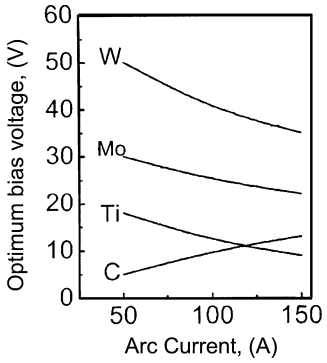

Fig. 7.33 Optimum bias voltage for a filter duct, giving the maximum ion saturation for a fixed magnetic field of 40 mT, as a function of arc current, with the cathode material as a parameter. (Adapted from [99])

often observed with other features, is different in its dependence. The determination of "optimum" plasma transport was based on maximizing the ion current to a negatively biased collector plate, assuming the ion charge states were unchanged. While carbon ions are almost exclusively of charge state $1+$, the mean ion charge state of ions in the filtered plasma becomes reduced when the magnetic field [112] and duct bias [113] are increased, indicating that ion collector measurements should only be interpreted when the charge state measurements are included.

It is interesting to note that at very weak magnetic fields, the potential of a floating wall is negative, whereas at strong fields it is positive [1, 98]. This can easily be explained by considering the cross-field mobility of ions and electrons and recalling that the net current of ions and electrons must vanish, i.e., $I_i + I_e = 0$. In the absence of a magnetic field, electrons are much more mobile than ions due to their small mass. Thus, in order to balance the arrival of electrons and ions for net-zero current of the floating wall, the wall needs to assume a negative potential, whose value is self-adjusting so as to deflect excess electrons. At very weak magnetic field, electrons gyrate but their gyration radius is still large; the cross-field mobility starts to be restricted and hence a less negative floating potential is needed for balancing the electron and ion currents. As the magnetic field increases, the flux of ions crossing the field lines becomes larger than the flux of electrons, and the wall will become positive to deflect ions for balancing the net current to zero. One can recognize that with strong fields and appropriate geometry, the duct does not necessarily need external bias but will naturally assume a positive potential if kept floating.

In the framework of the over-simplified model (Section 7.3.4), the centrifugal force is balanced by the electric force, therefore the bias effect is especially important on the outside curvature. Bilek and co-workers recognized this feature and applied positive bias to only a strip electrode located near the outer wall

of the interior of the duct, as opposed to biasing the whole filter wall [106]. The bias plate has the advantage that the filter wall can be kept at ground potential, which is highly desirable to satisfy safety requirements when the filter wall is also part of the vacuum chamber, even when the effect produced is not quite as good as biasing the whole duct wall [114, 115].

7.5.2 Arc Source–Filter Coupling

While most attention usually focuses on filter design and plasma transport mechanisms, some research addressed the performance of the complete source–filter–substrate system. The subject was mentioned when the system coefficient was introduced in Section 7.2.2. There, filter output normalization was done not with respect to filter input but rather with respect to plasma production at the cathodic arc source, as measured by the arc current.

Several theoretical approaches recognized the importance of optimized source–filter coupling because the result of calculations strongly depended on the way plasma is provided to the filter entrance. In the plasma optics model, where ion particle motion is simulated in a given magnetic structure and potential distribution (Section 7.3.6), assumptions had to be made on the field configuration, e.g., converging field or constant field structure [26, 27].

The calculated optimum performance, as defined by maximum ion transport to the substrate, may imply conditions where the anode is magnetically insulated. The arc discharge may become unstable, which experimentally shows as enhanced noise in the burning voltage and plasma output. In extreme cases, the arc discharge extinguishes altogether. Zhitomirsky and co-workers [58,116] showed the effect of the filter field on the spot motion and related arc instabilities. They showed that the magnetic field of the filter can disrupt steered spot motion on the cathode, leading to arc instabilities.

Magnetic insulation of the dedicated anode implies that the plasma in the filter carries a large net current, perhaps even approaching the magnitude of the discharge current, because electrons "seek" a suitable anode surface beyond the filter exit. Depending on the electrical discharge circuit used, such "suitable" anode could be the grounded chamber wall. Large currents in the plasma flow streaming through the filter may cause drift instabilities of the Kelvin–Helmholtz type, leading to kinks and deflections of the plasma stream, which may aperiodically or periodically hit the filter wall. For example, regular oscillations of the filter output have been observed when the arc source anode was magnetically insulated [117] (Figure 7.34).

Kim and co-workers [118] addressed the issue of instabilities by placing a permanent magnet behind the cathode such that the magnetic field counteracted the filter field. Additionally there was an adjustable electromagnet whose current amplitude oscillated to allow for varying spot locations, leading to maximum cathode utilization.

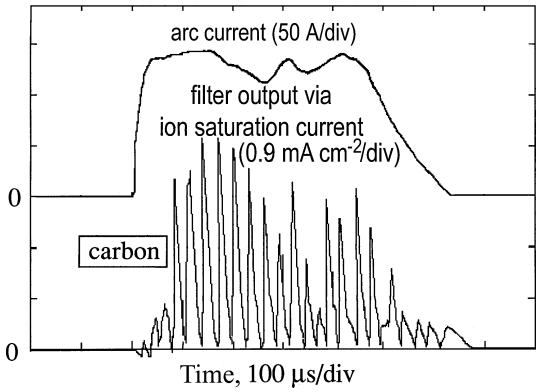

Fig. 7.34 Plasma oscillations, as measured by the ion saturation current to a collector downstream of the macroparticle filter, are induced by excessive magnetic insulation of the arc anode. (After [117])

7.6 Effects of Filtering on Ion Charge State and Energy Distribution

While the main purpose of a macroparticle filter is the reduction or removal of macroparticles from the cathodic arc plasma, it is clear that atoms, if present, are also removed since electromagnetic transport mechanisms do not apply to electrically neutral particles. However, some atoms or clusters may be transported with the plasma flow via collisions. As discussed before, the actual transport is rather complex and it is by no means given that the ions of different charge states and energy have the same transport probability. Quite contrary, the electric and magnetic fields acting on the magnetized plasma should be expected to change the ion charge state distribution and energy distribution. There are a few investigations on that matter so far, and more research can be expected in coming years. One difficulty is that there is a great variety of filter geometries and conditions, as compiled earlier in this chapter, and therefore findings for one geometry may not apply to other conditions.

When the issue of plasma source–filter coupling was discussed, it was pointed out that the magnetic field affects the burning voltage and hence power input and plasma conditions. This will lead to a shift toward higher charge states and greater kinetic energies with increasing magnetic field. In this way, the filter field has an effect on the ion charge state and velocities at the time of plasma production, not just when the plasma is transported.

For ion transport, however, optimal bias and increasing magnetic field help to transmit lower charge states through the filter, and, contrary to their influence on ion charge state production, higher fields can lead to *lowering* of the mean ion charge state of the plasma leaving the filter. Kwok and co-workers have indeed observed such a tendency for a 90° filter and pulsed Ti arcs [113]. In their case,

the mean charge state was slightly reduced from 2.12 to 1.98. These changes are indeed minor and therefore, for rough estimates, one may consider the ion charge state approximately constant. Another experiment by Bilek and Brown [112] also showed the lowering of the mean charge state with increasing magnetic field, measured for Ti and Ta. In their experiment, the distance between cathode and filter entrance was varied. It was shown that the mean ion charge state also depends on relatively minor changes of this distance, confirming that the coupling of plasma source and filter depends sensitively on the field geometry.

If the plasma is "born" outside the filter in a relatively weak magnetic field, the plasma flow enters a region of stronger field and will be decelerated. This effect can be associated with the magnetic mirror effect [13] for magnetized electrons. The usually non-magnetized ions cannot directly "experience" the magnetic mirror effect since their trajectories are only indirectly affected by the magnetic fields. However, as discussed before, magnetization of electrons leads to the existence of electric fields in the magnetized plasmas, and ion distributions can be influenced via this mechanism. In the same sense, electrons leaving the filter see the inverse mirror effect, i.e., a longitudinal acceleration. Ions may also experience acceleration, which would be direct via inverse mirror effect if magnetized or indirect if not magnetized. In any case, both ion acceleration and deceleration can be expected when filters are used, and such changes have indeed been observed [16].

7.7 Plasma Density Profile and Coating Uniformity

The plasma flux leaving a macroparticle filter approximately reflects the size and shape of the cathode (plasma optics). For larger area coating, it is therefore straightforward to use larger size cathodes, such as implemented in all sources with elongated or "linear" cathodes. If we were able to take a snapshot of the plasma output, for example by looking at a picture from a high-speed framing camera, we could see that the plasma is concentrated due to the generation at cathode spots, i.e., at each given moment the plasma is very non-uniform, and so is the instantaneous deposition rate. Via the apparent spot motion on the cathode, the non-uniform profile smears out, resulting in a greater uniformity of the coating.

For many applications, it is desirable to improve the uniformity. Apart from using larger cathodes, a natural improvement can be accomplished by increasing the distance between the filter exit (or the plasma source for unfiltered systems) and the substrate. The plasma expands into the vacuum or low-pressure ambient, and therefore the uniformity for a fixed size of substrate is improved at the cost of lower deposition rate and reduced plasma utilization because more plasma is lost to the sides next to the substrate.

Another approach to improving uniformity is to actively shape the plasma density profile. This can be done using the same principles as used for plasma

flux guiding in a macroparticle filter, and therefore this topic is a good conclusion of this chapter on filters.

Plasma trapping, or confinement, is a topic extensively researched in the field of thermonuclear fusion [13] and has early been adapted to low-temperature plasmas, especially to confining and shaping plasma in broad-beam ion sources [119, 120]. An example is the so-called plasma bucket, formed by a set of alternating permanent magnets [121, 122].

The idea of a plasma bucket was adopted to shape the flowing cathodic arc plasma: the plasma streams through a finite length bucket, also called a magnetic cusp homogenizer, and the resulting density profile becomes flatter. This effect is observed because the charged particle motion is suppressed across the magnetic field lines near the bucket "wall" [123–126], while it is not affected near the center of the bucket where the field is very weak. Of course, as with all plasma-shaping elements, plasma is lost as it streams through magnetic elements, even as the losses to the wall are suppressed.

The magnetic multipole can be made from strong permanent magnets (like SmCo, Figure 7.35) [123] or it can be constructed from a set of alternating current-carrying wires [125, 126]. In the latter case, if pulsed systems are considered, the high arc current may be used to also generate the field of the multipole cusp field (Figure 7.36).

In order to evaluate the effect of the magnetic multipole homogenizer one may place a deposition probe after the homogenizer. A deposition probe works best when the deposited material is absorbing or reflecting, and one simply

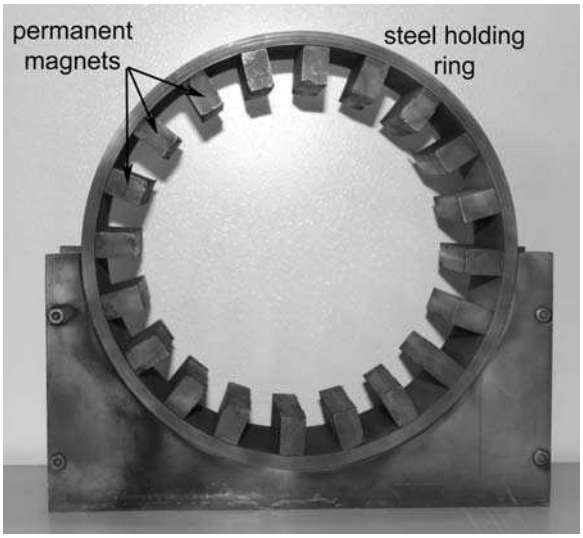

Fig. 7.35 Permanent magnet multipole homogenizer for flattening the plasma profile; the inner diameter of the steel ring is 8 in. (about 20 cm) (Berkeley Lab, mid 1990s)

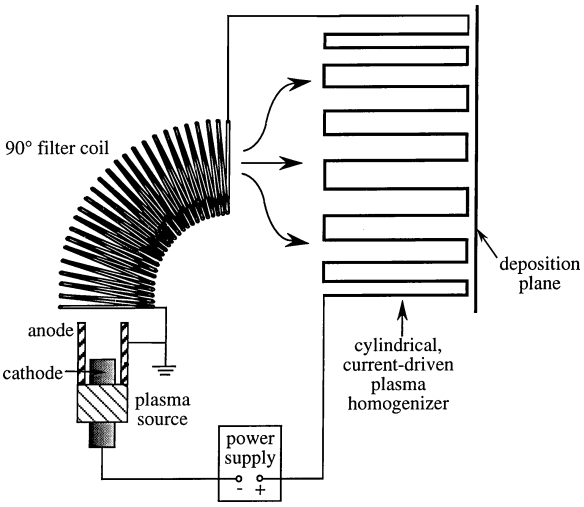

Fig. 7.36 Schematic of implementing an electromagnetic plasma homogenizer with a pulsed arc: the arc current is electrically in series with the filter and homogenizer so only one pulsed high-current power supply is needed

deposits a thin film whose local transmittance can be used to estimate the film thickness. That can be readily done by scanning the probe sheet in a conventional scanner. Quantitative evaluation is done best using an algorithm that converts light intensity (grey level) into equidensity contours. Figure 7.37 shows such a density profile which is obtained 11 cm from the exit of a filter in the absence of any homogenizer. The cathode in this example was a rod of 6.25-mm diameter, i.e., it acted like a point source for this 20-cm (8-in.) diameter deposition probe. After placing the homogenizer before the deposition probe, the density distribution is completely changed (Figure 7.38). A similar effect can be obtained with the electromagnetic homogenizer provided the current is high (Figure 7.39). In both Figures 7.38 and 7.39 we can see that the magnetic field structure is not perfect, which leads to interesting, though generally unwanted, density patterns. To improve the situation, the magnetic field as well as the positioning of the homogenizer with respect to the plasma flow must be optimized (Figure 7.40). Generally, it is highly desirable to move (rotate) the substrate. Using a nominal 8-in. homogenizer and substrate rotation, a film uniformity better than 3% (3σ) has been demonstrated for 4-in. (10-cm) wafers (unpublished).

Another way of addressing the need for better uniformity for large (300-mm) wafers is to raster the plasma "beam" horizontally and vertically over the coating area. The sweeping occurs through magnetic deflection, that is, the constant axial magnetic field (z-component) is supplemented by a time-varying radial (x and y) component that steers the plasma column off-axis. This steering results in

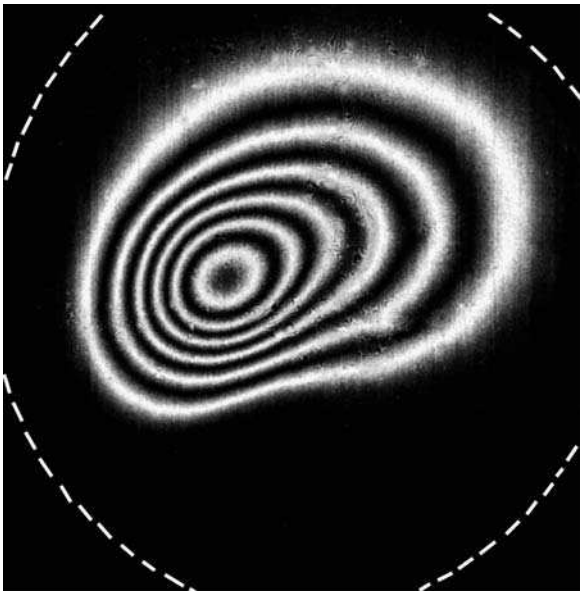

Fig. 7.37 Equidensity contours on a deposition probe obtained at 11-cm distance from a 90° filter without homogenizer: one can clearly see the strongly peaked plasma profile leading to a very non-uniform film (40 pulses of titanium plasma, 1.4 kA, 500 μs)

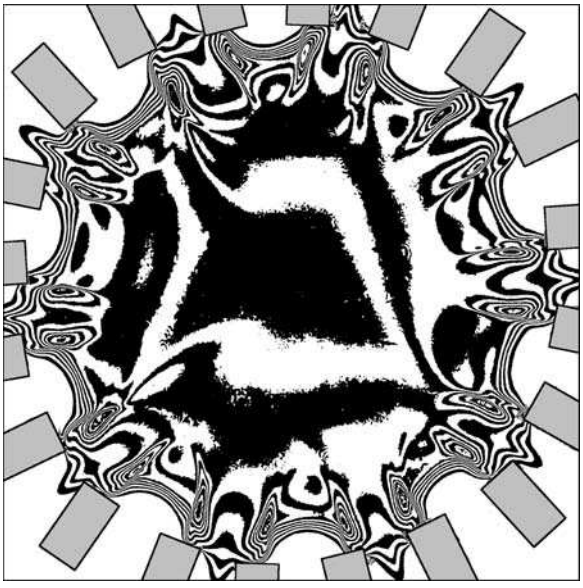

Fig. 7.38 Plasma density profile when a permanent magnetic homogenizer is added to the flow; the *rectangles* indicate the position of the permanent magnets

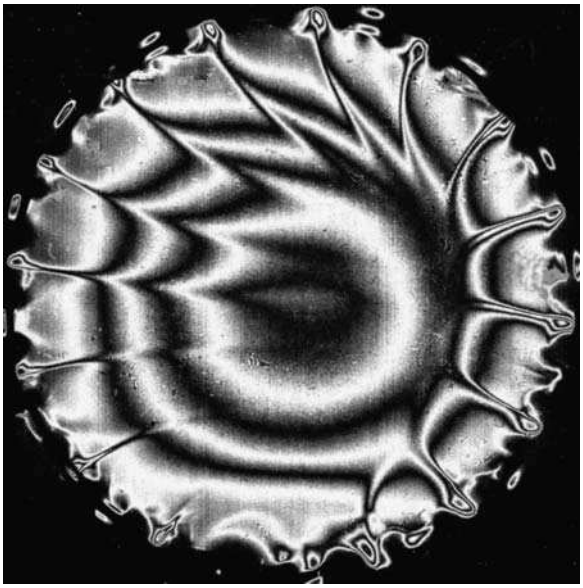

Fig. 7.39 Plasma density profile using a wire magnetic homogenizer; the strange little islands and patterns at periphery are caused by plasma drifting near the wires, where the field is strongest. There can be an unwanted pattern throughout the homogenizer caused by an asymmetric field structure – its effect can be mitigated by substrate motion

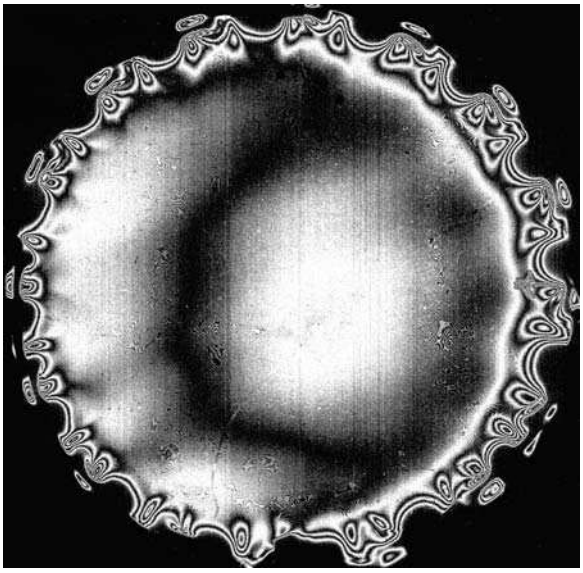

Fig. 7.40 Plasma density as before but with carefully improved plasma injection and alignment of the homogenizer's wires

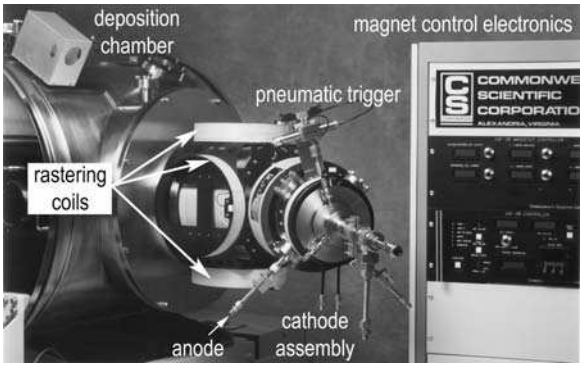

Fig. 7.41 Two sets of deflection or raster coils at the exit of the 45° knee-filter, completing the CAF-38 filtered arc system by Commonwealth Scientific. (Photo about 1997, courtesy of David Baldwin, then Commonwealth Scientific Corporation, Alexandria, VA)

a "paint-brush-style" covering of the to-be-coated area. The generation of the x and y components can be obtained by pairs of magnetic field coils aligned perpendicular to the axis of the filter (Figure 7.41). The coils are typically driven by medium-frequency AC power supplies, for example up to 10 kHz in the CAF-38 system by Commonwealth Scientific Corporation. It is also used in many other filtered DC arcs such as Singapore's OPDB filter system for ta-C coatings and in the three-cathode system with a straight filter at Tel Aviv University [127].

References

1. Aksenov, I.I., Belous, V.A., Padalka, V.G., and Khoroshikh, V.M., Transport of plasma streams in a curvilinear plasma-optics system, *Sov. J. Plasma Phys.* **4**, 425–428, (1978).
2. Aksenov, I.I., Belous, V.A., Padalka, V.G., and Khoroshikh, V.M., Apparatus to rid the plasma of a vacuum arc of macroparticles, *Instrum. Exp. Tech.* **21**, 1416–1418, (1978).
3. Boxman, R.L. and Goldsmith, S., Macroparticle contamination in cathodic arc coatings: Generation, transport and control, *Surf. Coat. Technol.* **52**, 39–50, (1992).
4. Boxman, R.L., Zhitomirsky, V., Alterkop, B., Gidalevitch, E., Beilis, I., Keidar, M., and Goldsmith, S., Recent progress in filtered vacuum arc deposition, *Surf. Coat. Technol.* **86–87**, 243–253, (1996).
5. Brown, I.G., Cathodic arc deposition of films, *Annual Rev. Mat. Sci.* **28**, 243–269, (1998).
6. Anders, A., Approaches to rid cathodic arc plasma of macro- and nanoparticles: a review, *Surf. Coat. Technol.* **120–121**, 319–330, (1999).
7. Martin, P.J. and Bendavid, A., Review of the filtered vacuum arc process and materials deposition, *Thin Solid Films* **394**, 1–15, (2001).
8. Brown, I.G., Vacuum arc ion sources, *Rev. Sci. Instrum.* **65**, 3061–3081, (1994).

9. Anders, A., Ion charge state distributions of vacuum arc plasmas: the origin of species, *Phys. Rev. E* **55**, 969–981, (1997).
10. Anders, A., Yotsombat, B., and Binder, R., Correlation between cathode properties, burning voltage, and plasma parameters of vacuum arcs, *J. Appl. Phys.* **89**, 7764–7771, (2001).
11. Storer, J., Galvin, J.E., and Brown, I.G., Transport of vacuum arc plasma through straight and curved magnetic ducts, *J. Appl. Phys.* **66**, 5245–5250, (1989).
12. Cluggish, B.P., Transport of a cathodic arc plasma in a straight, magnetized duct, *IEEE Trans. Plasma Sci.* **26**, 1645–1652, (1998).
13. Chen, F.F., *Plasma Physics and Controlled Fusion*. Plenum Press, New York, (1984).
14. Spitzer, Jr., L., *Physics of Fully Ionized Gases*, preprint of the 2nd revised edition, originally published by Wiley, 1962 ed. Dover, New York, (1990).
15. Morozov, A.I. and Lebedev, S.V., "Plasma Optics," in *Reviews of Plasma Physics, Vol. 8*, Leontovich, M.A., (Ed.). pp. 301–460, Consultants Bureau, New York, (1980).
16. Anders, A. and Yushkov, G.Y., Ion flux from vacuum arc cathode spots in the absence and presence of magnetic fields, *J. Appl. Phys.* **91**, 4824–4832, (2002).
17. Davidson, R.C., Vlasov equilibrium and nonlocal stability properties of an inhomogeneous plasma column, *Phys. Fluids* **19**, 1189–1202, (1976).
18. Krishnan, M., Geva, M., and Hirshfield, J.L., Plasma centrifuge, *Phys. Rev. Lett.* **46**, 36–38, (1981).
19. Prasad, R.R. and Krishnan, M., Rigid rotor equilibria of multifluid, neutral plasma columns in crossed electric and magnetic fields, *Phys. Fluids* **30**, 2496–3501, (1987).
20. Giuliani, L., Minotti, F., Grondona, D., and Kelly, H., On the dynamics of the plasma entry and guiding in a straight magnetized filter of a pulsed vacuum arc, *IEEE Trans. Plasma Sci.* **35**, 1710–1716, (2007).
21. Giuliani, L., Grondona, D., Kelly, H., and Minotti, F.O., On the plasma rotation in a straight magnetized filter of a pulsed vacuum arc, *J. Phys. D: Appl. Phys.* **40**, 401–408, (2007).
22. Kaufman, H.R., Robinson, R.S., and Seddon, R.I., End-Hall ion source, *J. Vac. Sci. Technol. A* **5**, 2081–2084, (1987).
23. Morozov, A.I., Focussing of cold quasineutral beams in electromagnetic fields, *Sov. Phys. Doklady* **10**, 775–777, (1966).
24. Demidenko, I.I., Lomino, N.S., Morozov, A.I., and Padalka, V.G., Focusing of a neutralized ion beam by a plasma-optics system, *Sov. Phys.-Tech. Phys.* **19**, 347–350, (1974).
25. Goncharov, A.A., Protsenko, I.M., Yushkov, G.Y., and Brown, I.G., Focusing of high-current, large-area, heavy-ion beams with an electrostatic plasma lens, *Appl. Phys. Lett.* **75**, 911–913, (1999).
26. Aksenov, I.I., Belokhvostikov, A.N., Padalka, V.G., Repalov, N.S., and Khoroshikh, V.M., Plasma flux motion in a toroidal plasma guide, *Plasma Phys. Controlled Fusion* **28**, 761–770, (1986).
27. Davis, C.A. and Donelly, I.J., Simulation of ion transport through curved-solenoid macroparticle filters, *J. Appl. Phys.* **72**, 1740–1747, (1992).
28. Schmidt, G., Plasma motion across magnetic fields, *Phys. Fluids* **3**, 961–965, (1960).
29. Khizhniyak, N.A., Motion of a plasmoid in the magnetic field of a toroidal solenoid, *Sov. Phys. Tech. Phys.* **10**, 655–661, (1965).
30. Veerasamy, V.S., Amaratunga, G.A.J., and Milne, W.I., Plasma motion in a filtered cathodic vacuum arc, *IEEE Trans. Plasma Sci.* **21**, 322–328, (1993).

31. Shi, X., Tu, Y.Q., Tan, H.S., and Tay, B.K., Simulation of plasma flow in toroidal solenoid filters, *IEEE Trans. Plasma Sci.* **24**, 1309–1318, (1996).
32. Alterkop, B., Zhitomirsky, V.N., Goldsmith, S., and Boxman, R.L., Propagation of a vacuum arc plasma beam in a toroidal filter, *IEEE Trans. Plasma Sci.* **24**, 1371–1377, (1996).
33. Alterkop, B., Gidalevich, E., Goldsmith, S., and Boxman, R.L., Vacuum arc plasma jet propagation in a toroidal duct, *J. Appl. Phys.* **79**, 6791–6802, (1996).
34. Alterkop, B., Gidalevich, E., Goldsmith, S., and Boxman, R.L., Propagation of a magnetized plasma beam in a toroidal filter, *J. Phys. D: Appl. Phys.* **31**, 873–879, (1998).
35. Alterkop, B., Gidalevich, E., Goldsmith, S., and Boxman, R.L., The numerical calculation of plasma beam propagation in a toroidal duct with magnetized electrons and unmagnetized ions, *J. Phys. D: Appl. Phys.* **29**, 3032–3038, (1996).
36. Anders, A., Interaction of vacuum-arc-generated macroparticles with a liquid surface, *Appl. Phys. Lett.* **73**, 3199–3201, (1998).
37. Koskinen, J., Anttila, A., and Hirvonen, J.-P., Diamond-like carbon coatings by arc-discharge methods, *Surf. Coat. Technol.* **47**, 180–187, (1991).
38. Anders, A. and MacGill, R.A., Twist filter for the removal of macroparticles from cathodic arc plasmas, *Surf. Coat. Technol.* **133–134**, 96–100, (2000).
39. Bilek, M.M.M. and Anders, A., Designing advanced filters for macroparticle removal from cathodic arc plasmas, *Plasma Sources Sci. Technol.* **8**, 488–493, (1999).
40. Aksenov, I.I., Padalka, V.G., Tolok, V.T., and Khoroshikh, V.M., Motion of plasma streams from a vacuum arc in a long, straight plasma optics system, *Sov. J. Plasma Phys.* **6**, 504–507, (1980).
41. Tamagaki, H. and Akari, U., "Apparatus and method of cathodic arc deposition," patent US 5,126,030 (1992).
42. Sathrum, P.E. and Coll, B.F., "Plasma enhanced apparatus and method for physical vapor deposition," patent US 5,458,754 (1995).
43. Sathrum, P.E. and Coll, B.F., "Plasma enhancement apparatus and method for physical vapor deposition," patent US 6,139,964 (2000).
44. Zhitomirsky, V.N., Zarchin, O., Boxman, R.L., and Goldsmith, S., Transport of a vacuum-arc produced plasma beam in a magnetized cylindrical duct, *IEEE Trans. Plasma Sci.* **31**, 977–982, (2003).
45. Burkhardt, W. and Reinecke, R., "Method of coating articles by vaporized coating materials," patent US 2,157,478 (1939).
46. Axenov, I.I., Belous, V.A., Padalka, V.G., and Khoroshikh, V.M., "Arc plasma generator and a plasma arc apparatus for treating the surface of work-pieces, incorporating the same arc plasma generator," patent US 4,452,686 (1984).
47. Miernik, K. and Walkowicz, J., Design and performance of the microdroplet filtering system used in cathodic arc coating deposition, *Plasmas & Ions* **3**, 41–51, (2000).
48. Brandolf, H., "Vapor deposition method and apparatus," patent US 4,511,593 (1985).
49. Kimura, K., Izumi, K., Takikawa, H., and Sakakibara, T. Preparation of metal nitride and oxide thin films using shielded reactive vacuum arc deposition, *Vacuum* **59**, 159–167, (2000).
50. Takikawa, H., Miyano, R., Sakakibara, T., Bendavid, A., Martin, P.J., Matsumuro, A., and Tsutsumi, K. Effect of substrate bias on AlN thin film preparation in shielded reactive vacuum arc deposition, *Thin Solid Films* **386**, 276–280, (2001).
51. Mändl, S. and Rauschenbach, B., Plasma stream homogeneity in metal plasma immersion ion implantation and deposition, *IEEE Trans. Plasma Sci.* **31**, 968–972, (2003).

52. Treglio, J.R., "Magnetically filtered cathodic arc plasma apparatus," patent US 5,317,235 (1994).
53. Lossy, R., Pappas, D.L., Roy, R.A., Cuomo, J.J., and Sura, V.H., Filtered arc deposition of amorphous diamond, *Appl. Phys. Lett.* **61**, 171–173, (1992).
54. Vyskocil, J. and Musil, J., Cathodic arc evaporation in thin film technology, *J. Vac. Sci. Technol. A* **10**, 1740–1748, (1992).
55. Martin, P.J., Falabella, S., and Karpov, D.M., "Coatings from the vacuum arc deposition," in *Handbook of Vacuum Arc Science and Technology*, Boxman, R.L., Martin, P.J., and Sanders, D.M., (Eds.). pp. 367–551, Noyes, Park Ridge, (1995).
56. Martin, P.J., Bendavid, A., and Kinder, T.J., The deposition of TiN thin films by filtered cathodic arc techniques, *IEEE Trans. Plasma Sci.* **25**, 675–679, (1997).
57. Boxman, R.L. and Goldsmith, S., Principles and applications of vacuum arc coatings, *IEEE Trans. Plasma Sci.* **17**, 705–712, (1989).
58. Zhitomirsky, V.N., Boxman, R.L., and Goldsmith, S., Influence of an external magnetic field on cathode spot motion and coating deposition using filtered vacuum arc evaporation, *Surf. Coat. Technol.* **68/69**, 146–151, (1994).
59. Aksenov, I.I., Vakula, S.I., Padalka, V.G., Strel'nitskii, V.E., and Khoroshikh, V.M., High-efficiency source of pure carbon plasma, *Sov. Phys. Techn. Phys.* **25**, 1164–1166, (1980).
60. Witke, T., Schuelke, T., Schultrich, B., Siemroth, P., and Vetter, J., Comparison of filtered high current pulsed arc deposition (ϕ-HCA) with conventional vacuum arc methods, *Surf. Coat. Technol.* **126**, 81–88, (2000).
61. Witke, T. and Siemroth, P., Deposition of droplet-free films by vacuum arc evaporation-results and applications, *IEEE Trans. Plasma Sci.* **27**, 1039–1044, (1999).
62. Falabella, S. and Sanders, D.M., "Filtered cathodic arc source," patent US 5,279,723 (1994).
63. Baldwin, D.A. and Fallabella, S., "Deposition processes utilizing a new filtered cathodic arc source," Proc. of the 38th Annual Techn. Conf., Society of Vacuum Coaters, Chicago, 309–316, (1995).
64. Hakovirta, M., Salo, J., Anttila, A., and Lappalainen, R., Graphite particles in the diamond-like a-C films prepared with the pulsed arc-discharge method, *Diamond and Rel. Mat.* **4**, 1335–1339, (1995).
65. Siemroth, P., "personal communication on 120-degree filter," Dresden, Germany, (2003).
66. Anders, S., Anders, A., Dickinson, M.R., MacGill, R.A., and Brown, I.G., S-shaped magnetic macroparticle filter for cathodic arc deposition, *IEEE Trans. Plasma Sci.* **25**, 670–674, (1997).
67. Aksenov, I.I., Belous, V.A., and Padalka, V.G., A device for producing coatings in vacuum, patent USSR 605425 (1976).
68. Zhang, Y.J., Yan, P.X., Wu, Z.G., Zhang, W.W., Zhang, G.A., Liu, W.M., and Xue, Q.J., Effects of substrate bias and argon flux on the structure of titanium nitride films deposited by filtered cathodic arc plasma, *Physica Status Solidi (a)* **202**, 95–101, (2005).
69. Shi, X., Tay, B.K., Tan, H.S., Liu, E., Shi, J., Cheah, L.K., and Jin, X., Transport of vacuum arc plasma through an off-plane double bend filtering duct, *Thin Solid Films* **345**, 1–6, (1999).
70. Shi, X., Tay, B.G., and Lau, S.P., The double bend filtered cathodic arc technology and its applications, *Int. J. Mod. Phys. B* **14**, 136–153, (2000).

71. You, G.F., Tay, B.K., Lau, S.P., Chua, D.H.C., and Milne, W.I., Carbon arc plasma transport through different off-plane double bend filters, *Surf. Coat. Technol.* **150**, 50–56, (2002).
72. Gorokhovsky, V.I., "Personal communication," 1999.
73. Gorokhovsky, V.I., "Apparatus for application of coatings in vacuum," patent US 5,435,900 (1995).
74. Welty, R.P., "Rectangular vacuum-arc plasma source," patent US 5,480,527 (1996).
75. Welty, R.P., "Rectangular vacuum-arc plasma source," patent US 5,840,163 (1998).
76. Boxman, R.L., Zhitomirsky, V., Goldsmith, S., David, T., and Dikhtyar, V., "Deposition of SnO_2 coatings using a rectangular filtered vacuum arc source," 46th Annual Technical Meeting of the Society of Vacuum Coaters, San Francisco, CA, 234–239, (2003).
77. Zhitomirsky, V.N., Boxman, R.L., and Goldsmith, S., Plasma distribution and SnO_2 coating deposition using a rectangular filtered vacuum arc plasma source, *Surf. Coat. Technol.* **185**, 1–11, (2004).
78. Aksenov, I.I. and Bren', V.G., Vacuum arc plasma apparatus patent USSR 913744 (1981).
79. Boercker, D.B., Falabella, S., and Sanders, D.M., Plasma transport in a new cathodic arc ion source: theory and experiment, *Surf. Coat. Technol.* **53**, 239–242, (1992).
80. Falabella, S. and Sanders, D.M., Comparison of two filtered cathodic arc sources, *J. Vac. Sci. Technol. A* **10**, 394–397, (1992).
81. Osipov, V.A., Padalka, V.G., Sablev, L.P., and Stupak, R.I., Unit for depositing coatings by precipitation of ions extracted from a vacuum-arc plasma, *Instrum. Exp. Tech.* **21**, 1650–1652, (1978).
82. Welty, R.P., "Linear magnetron arc cathode and macroparticle filter," Int. Conf. Metal. Coat. & Thin Films, San Diego, paper B1-5, (1999).
83. Buhl, R., "Method and apparatus for coating workpieces," patent US 4,929,321 (1990).
84. Aksenov, I.I. and Khoroshikh, V.M., "Radial ion flows in a vacuum-arc plasma," 17th International Symposium on Discharges and Electrical Insulation in Vacuum, Berkeley, California, 900–903, (1996).
85. Kljuchko, G.V., Padalka, V.G., Sablev, L.P., and Stupka, R.I., "Plasma arc apparatus for applying coatings by means of a consumable cathode," patent US 4,492,845 (1985).
86. Ryabchikov, A.I. and Stepanov, I.B., Investigations of forming metal-plasma flows filtered from microparticle fraction in a vacuum arc evaporator, *Rev. Sci. Instrum.* **69**, 810–812, (1998).
87. Ryabchikov, A.I., Stepanov, I.B., Dektjarev, S.V., and Sergeev, O.V., Vacuum arc ion and plasma source Raduga 5 for materials treatment, *Rev. Sci. Instrum.* **69**, 893–895, (1998).
88. Ryabchikov, A.I., Repetitively pulsed vacuum arc ion and plasma sources and new methods of ion and ion plasma treatment of materials, *Surf. Coat. Technol.* **96**, 9–15, (1997).
89. Bilek, M.M.M., Anders, A., and Brown, I.G., Characterization of a linear Venetian-blind macroparticle filter for cathodic vacuum arcs, *IEEE Trans. Plasma Sci.* **27**, 1197–1202, (1999).
90. Zimmer, O., Vacuum arc deposition by using a Venetian blind particle filter, *Surf. Coat. Technol.* **200**, 440–443, (2005).

91. Bilek, M.M.M. and Brown, I.G., Deposition probe technique for the determination of film thickness profiles, *Rev. Sci. Instrum.* **69**, 3353–3356, (1998).
92. Anders, A. and Ryan, F.R., "Ultrathin ta-C films on heads deposited by twist-filtered cathodic arc carbon deposition (invited)," Symposium on Interface Tribology Towards 100 Gbit/in^2 and Beyond, Seattle, WA, 43–50, (2000).
93. Anders, A., Fong, W., Kulkarni, A., Ryan, F.R., and Bhatia, C.S., Ultrathin diamondlike carbon films deposited by filtered carbon vacuum arcs, *IEEE Trans. Plasma Sci.* **29**, 768–775, (2001).
94. Utsumi, T. and English, J.H., Study of electrode products emitted by vacuum arcs in form of molten metal particles, *J. Appl. Phys.* **46**, 126–131, (1975).
95. Robbie, K. and Brett, M.J., Sculptured thin films and glancing angle deposition: growth mechanics and applications, *J. Vac. Sci. Technol. A* **15**, 1460–1465, (1997).
96. Lakhtakia, A. and Messier, R., *Sculptured Thin Films: Nanoengineered Morphology and Optics*. SPIE – The International Society for Optical Engineering, Bellingham, WA, (2005).
97. Bilek, M.M.M., Evans, P., Mckenzie, D.R., McCulloch, D.G., Zreiqat, H., and Howlett, C.R., Metal ion implantation using a filtered cathodic vacuum arc, *J. Appl. Phys.* **87**, 4198–4204, (2000).
98. Anders, A., Anders, S., and Brown, I.G., Effect of duct bias on transport of vacuum arc plasmas through curved magnetic filters, *J. Appl. Phys.* **75**, 4900–4905, (1994).
99. Zhang, T., Zhang, Y.C., Chu, P.K., and Brown, I.G., Wall sheath and optimal bias in magnetic filters for vacuum arc plasma sources, *Appl. Phys. Lett.* **80**, 365–367, (2002).
100. Zhang, T., Chu, P.K., Kwok, D.T.K., and Brown, I.G., Optimal duct bias for transport of cathodic-arc plasmas, *IEEE Trans. Plasma Sci.* **30**, 1602–1605, (2002).
101. Zhang, T., Tang, B.Y., Chen, Q.C., Zeng, Z.M., Chu, P.K., Bilek, M.M.M., and Brown, I.G., Vacuum arc plasma transport through a magnetic duct with a biased electrode at the outer wall, *Rev. Sci. Instrum.* **70**, 3329–3331, (2002).
102. Keidar, M. and Beilis, I.I., Plasma-wall sheath in a positive biased duct of the vacuum arc magnetic macroparticle filter, *Appl. Phys. Lett.* **73**, 306–308, (1998).
103. Beilis, I.I., Keidar, M., Boxman, R.L., and Goldsmith, S., Macroparticle separation and plasma collimation in positively biased ducts in filtered vacuum arc deposition systems, *J. Appl. Phys.* **85**, 1358–1365, (1999).
104. Keidar, M. and Beilis, I.I., Hydrodynamic model of vacuum arc plasma flow in a positively biased toroideal macroparticle filter, *Plasma Sources Sci. Technol.* **8**, 376–383, (1999).
105. Zhang, T., Tang, B.Y., Chen, Q.C., Chu, P.K., Bilek, M.M.M., and Brown, I.G., Vacuum arc plasma transport trough a magnetic duct with a biased electrode at the outer wall, *Rev. Sci. Instrum.* **70**, 3329–3331, (1999).
106. Bilek, M.M.M., McKenzie, D.R., Yin, Y., Chhowalla, M.U., and Milne, W.I., Interactions of the directed plasma from a cathodic arc with electrodes and magnetic field, *IEEE Trans. Plasma Sci.* **24**, 1291–1298, (1996).
107. Bilek, M.M.M., Yin, Y., and McKenzie, D.R., A study of filter transport mechanisms in filtered cathodic vacuum arcs, *IEEE Trans. Plasma Sci.* **24**, 1165–1173, (1996).
108. Byon, E. and Anders, A., Bias and self-bias of magnetic macroparticle filters for cathodic arc plasmas, *J. Appl. Phys.* **93**, 8890–8897, (2003).
109. Kim, J.-K., Kim, D.-G., Byon, E., Lee, S., Kim, K.-H., and Lee, G.-H., Effect of plasma duct bias on the plasma characteristics of a filtered vacuum arc source, *Thin Solid Films* **444**, 23–28, (2003).

110. Zhang, T., Chu, P.K., and Brown, I.G., Effects of cathode materials and arc current on optimal bias of a cathodic arc through a magnetic duct, *Appl. Phys. Lett.* **80**, 3700–3702, (2002).
111. Zhang, T., Chu, P.K., Fu, R.K.Y., and Brown, I.G., Plasma transport in magnetic duct filter, *J. Phys. D: Appl. Phys.* **35**, 3176–3177, (2002).
112. Bilek, M.M.M. and Brown, I.G., The effects of transmission through a magnetic filter on the ion charge state distribution of a cathodic vacuum arc plasma, *IEEE Trans. Plasma Sci.* **27**, 193–198, (1999).
113. Kwok, D.T.K., Chu, P.K., Bilek, M.M.M., and Brown, I.G., Ion mean charge state in a biased vacuum arc plasma duct, *IEEE Trans. Plasma Sci.* **28**, 2194–2201, (2000).
114. Zhang, T., Tang, B.Y., Chen, Q.C., Chu, P.K., Bilek, M.M.M., and Brown, I.G., Mechanism of enhanced plasma transport of vacuum arc plasma through curved magnetic ducts, *J. Vac. Sci. Technol. A* **17**, 3074–3076, (1999).
115. Zhang, T., Kwok, D.T.K., Chu, P.K., and Brown, I.G., Guiding effect of electric and magnetic fields on the plasma output of a cathodic arc magnetic filter, *J. Appl. Phys.* **89**, 672–675, (2001).
116. Zhitomirsky, V.N., Boxman, R.L., and Goldsmith, S., Unstable arc operation and cathode spot motion in a magnetically filtered vacuum-arc deposition system, *J. Vac. Sci. Technol. A* **13**, 2233–2240, (1995).
117. Anders, A., Anders, S., and Brown, I.G., Transport of vacuum arc plasmas through magnetic macroparticle filters, *Plasma Sources Sci. Technol.* **4**, 1–12, (1995).
118. Kim, J.K., Lee, K.R., Eun, K.Y., and Chung, K.H., Effect of magnetic field structure near cathode on the arc spot stability of filtered vacuum arc source of graphite, *Surf. Coat. Technol.* **124**, 135–141, (2000).
119. Forrester, A.T. and Busnardo-Neto, J., Magnetic fields for surface containment of plasmas, *J. Appl. Phys.* **47**, 3935–3941, (1976).
120. Forrester, A.T., *Large Ion Beams*. Wiley, New York, (1988).
121. Leung, K.N., Samec, T.K., and Lamm, A., Optimization of permanent magnet plasma confinement, *Phys. Lett. A* **51**, 490–492, (1975).
122. Leung, K.N., Taylor, G.R., Barrick, J.M., Paul, S.L., and Kribel, R.E., Plasma confinement by permanent magnet boundaries, *Phys. Lett. A* **57**, 145–147, (1976).
123. Anders, S., Raoux, S., Krishnan, K., MacGill, R.A., and Brown, I.G., Plasma distribution of cathodic arc deposition systems, *J. Appl. Phys.* **79**, 6785–6790, (1996).
124. Bilek, M.M.M., Monteiro, O.R., and Brown, I.G., Optimization of film thickness profiles using a magnetic cusp homogenizer, *Plasma Sources Sci. Technol.* **8**, 88–93, (1999).
125. Bilek, M.M.M., Anders, A., and Brown, I.G., Magnetic system for producing uniform coatings using a filtered cathodic arc, *Plasma Sources Sci. Technol.* **10**, 606–613, (2001).
126. Machima, P., Bilek, M.M.M., Monteiro, O.R., and Brown, I.G., Simple and inexpensive current-driven magnetic multipole plasma homogenizer, *Rev. Sci. Instrum.* **71**, 3373–3376, (2000).
127. Ben-Ami, R., Zhitomirsky, V.N., Boxman, R.L., and Goldsmith, S., Plasma distribution in a triple-cathode vacuum arc deposition apparatus, *Plasma Sources Sci. Technol.* **8**, 355–362, (1999).

8

Film Deposition by Energetic Condensation

In all sciences there are many truths for the reception of which it is absolutely necessary that men's minds, even those of the higher order, be suitably prepared. . .If these truths are discovered before this time, they will be contended, smothered at birth and forgotten. They appear as flashes of light, piercing the gloom of a cavern, illuminating it for one brief moment, only to abandon it once more to the darkness of night.

Pierre Sue, in *Histoire du Galvanisme*, 1802

Abstract When the plasma ions arrive at a surface, they do so with considerable kinetic energy, which is typically in the range 20–150 eV without bias. A bias voltage can increase this energy even further. Energetic condensation involves subsurface processes when the arriving ions displace surface and near-surface ions to come to rest below the surface. Shallow ion implantation or "subplantation" occurs, leading to dense and hard coatings that are generally under high compressive stress. Hardness and compressive stress are related. Excessive compressive stress is detrimental because it can lead to catastrophic failure of the coating by delamination. Stress control becomes paramount for high-performing coatings. This can be addressed by utilizing the high degree of ionization: biasing the substrate is very efficient in giving ions controlled, high energy capable of generating small collision cascades in the subsurface layer of the solid. Stress can be relieved through atom rearrangement facilitated by the short period of high mobility. This is best controlled by sophisticated biasing techniques, such as pulsed biasing with optimized pulse duration and duty cycle. One can maximize stress relief while maintaining an overall high level of hardness and elastic modulus.

A. Anders, *Cathodic Arcs*, DOI: 10.1007/978-0-387-79108-1_8,

8.1 Energetic Condensation and Subplantation

Energetic condensation can be defined as a deposition process where a significant fraction of the condensing (film-forming) species have hyperthermal energies [1, 2, 3, 4], which, in most cases, imply energies of about 10 eV and greater. Energetic condensation is characterized by a number of surface and subsurface processes that are activated or enabled by the energy of the particles arriving at the surface such as desorption of adsorbed molecules, enhanced mobility of surface atoms, and the stopping of arriving ions under the surface.

Let us start by looking at growth and nucleation for conventional (lower energy) physical vapor deposition [5]. Depending on whether or not the bonding between like adatoms is stronger than between adatom and substrate atoms, one can distinguish three basic growth modes: (i) three-dimensional or island growth mode, also known as Volmer–Weber mode, (ii) two-dimensional or layer-by-layer growth, also known as Frank–van der Merve mode, and (iii) a mixed mode that starts with two-dimensional growth that switches into island mode after one or more monolayers; this mode is also known as the Stranski–Krastanov mode. In the two-dimensional growth mode, the condensing particles have a strong affinity for the substrate atoms: they bond to the substrate rather than to each other. When the opposite is true, the adatoms build three-dimensional islands that grow in all directions, including the direction normal to the surface. The growing islands eventually coalesce and form a contiguous and later continuous film. In the mixed mode, finally, the relation of bond strength between like atoms and dislike atoms is more subtle. The bonding environment is changed once the surface atoms are covered and hidden by the first one or two monolayers such that islands start to form. To explain this one needs to carefully take into account the energy of the whole system, which includes contributions of strain energy caused by lattice mismatch and the surface free energy. This has been the subject of many good texts and the reader is referred to them [5, 6, 7, 8, 9].

Of great interest is the low-energy end of energetic condensation, i.e., an energy regime where the condensing particles have enough energy to promote high surface mobility but do not cause ion damage to the growing film. The kinetic energy of condensing particles is here in the range 5–25 eV.

More often, however, energetic condensation is considered as a process in which higher kinetic energies are involved, and one may even define energetic condensation as a process in which most film-forming ions or atoms exceed the displacement energy [10], E_d, allowing them to penetrate the subsurface region. Film growth can therefore occur *under* the surface rather than *on* the surface. Film growth by such *subplantation* [11, 12, 13] has been associated with dense and hard films which show high intrinsic stress. Due to film–substrate intermixing and with the formation of chemical bonds, these films can be well adherent unless the intrinsic stress is excessive, driving delamination. Methods of stress management are discussed later in this chapter. Film growth by subplantation does not mean that surface processes could be neglected. Quite contrary,

energetic condensation at subplantation energies causes a loss of atoms from the surface (desorption and sputtering) and provides energy to surface atoms, thereby promoting their surface migration to thermodynamically preferred places, which contributes to the minimization of the system's free energy.

A conventional approach to implementing energetic condensation is to utilize streaming metal plasma from a cathodic arc plasma source. Accelerated by extreme pressure gradients and electron–ion coupling, ions reach supersonic velocity not very far from the cathode spot (Chapters 3 and 4). This "natural" ion velocity shall be designated with v_{i0}, and the corresponding kinetic energy of a cathodic arc ion is

$$E_{i0} = m_i v_{i0}^2/2. \tag{8.1}$$

This kinetic energy may be modified before the ion reaches the substrate region by collisions with neutrals or other interactions within the plasma flow (Chapter 4). If the substrate surface potential is lower than the plasma potential, for example when negative bias is applied, positive ions experience an additional "boost" in the substrate sheath before they impact the substrate surface. The ion charge state, Q, which is often +2 or +3 for many cathode materials (Chapter 3 and Appendix B), is a multiplier for the kinetic energy gain determined by the sheath voltage, V_s. The total kinetic energy at impact can be written as

$$E_{i,kin} = E_{i0} + QeV_s, \tag{8.2}$$

where e is the elementary charge and where we assumed that there are no collisions within the sheath. Ions gain some additional small amount of kinetic energy by image charge acceleration, E_{ic}, which is discussed below.

Condensing ions from a cathodic arc plasma have not only kinetic but also potential energy, which includes the cohesive energy, E_c, the cumulative ionization energy, E_{ion} (Table B4 of Appendix B), and also excitation energy of bound electrons, E_{exc}, in case bound electrons are in excited states. The potential energy can be written as

$$E_{pot}(Q) = E_c + E_{ion} + E_{exc}. \tag{8.3}$$

While *all* ions carry ionization energy, the excited states may be Boltzmann-distributed (equilibrium assumption, which is only valid for the dense plasma relatively close to cathode spot) or under-populated (excitational non-equilibrium plasma far from the cathode spot). The contribution of the electronic excitation energies is relatively small and can therefore be neglected in the rest of this discussion.

The ionization energies are very significant, especially for multiply charged ions. The ionization energy E_Q is defined as the energy needed to remove a bound electron from an ion of charge state Q, forming an ion of charge state $Q+1$ [14, 15]. Therefore, when calculating the cumulative ionization energy being supplied to the film by, for example, a triply charged ion, one needs to add the ionization energies of

all three ionization steps. Table B8 includes the cohesive energies and Table B4 the cumulative ionization energies as calculated by

$$E_{ion} = E_{Q+}^{sum} = \sum_{Q'=0}^{Q-1} E_{Q'}. \tag{8.4}$$

For example, E_{2+}^{sum} represents the cumulative ionization energy that a doubly charged ion brings to the surface.

To better understand energetic deposition, one needs to study in greater detail the physical events that occur when an ion approaches the substrate surface. The situation is similar to the one when plasma ions bombard the cathode outside the active emission site, and therefore some of the processes have been mentioned in Chapter 3. The main differences between the cathode situation and a substrate are in the sheath voltage which, in the case of a substrate, can be much higher than the cathode fall of ~20 V, and in the plasma density, which is much smaller at the substrate compared to the density of the near-spot plasma.

Let us consider a *metal* substrate first. When the ion approaches and is within few nanometers of the surface, an image charge of opposite polarity is induced in the substrate, exerting the force

$$F = (eQ)^2 \Big/ \left(4\pi\varepsilon_0 (2d)^2\right) \tag{8.5}$$

on the ion, where d is the distance between the ion and the surface (Figure 8.1). This force causes acceleration toward the surface and therefore provides an extra "kick" to the approaching ion, slightly enhancing its kinetic energy. With decreasing distance, the electric field of the ion reduces the potential barrier that

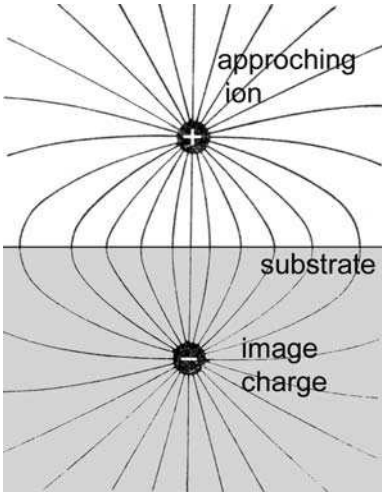

Fig. 8.1. Schematic presentation of the ion acceleration and image charge prior to ion impact on the substrate surface

normally keeps electrons from escaping into the vacuum. Electrons near the Fermi edge of the metal can transfer resonantly into an excited level of the incident ion when the potential barrier between metal and the ion reaches the Fermi level, i.e., when the transfer becomes classically allowed (classical "over-the-barrier" (COB) model [16]). The electron transfer occurs at a critical distance

$$d_c(Q) \approx a_B E_H \Big/ e\phi\sqrt{8Q+2}, \tag{8.6}$$

where a_B is the Bohr radius, E_H is the ionization energy of hydrogen, and $e\phi$ is the work function [16]. After the transfer, the ion charge and the image charge are reduced and the barrier height increased. In the case of a multiply charged ion, a second, smaller critical distance exists where a second electron transition is classically allowed. Multiply charged ions reduce their charge stepwise in a staircase fashion. In the staircase approximation, the kinetic energy gain by image charge is [16]

$$E_{ic} = \frac{e\phi}{2}\sum_{i=0}^{Q-1}\frac{2(Q-i)-1}{\sqrt{8(Q-i)+2}}. \tag{8.7}$$

For example, a gold ion of charge state $Q=3$ approaching a gold surface ($e\phi \approx 5.4$ eV) will gain kinetic energy by image charge acceleration of $E_{ic} \approx 5.4$ eV.

The situation is different when the ion approaches an *insulating* surface because there are no electrons in the conduction band. One may consider an effective image charge $Q_{eff} = \chi Q$ where χ is a dielectric response function [17] with $0 < \chi < 1$. The energy gain is determined by the image energy gain at the distance d_{c1} of the *first* electron capture:

$$E_{ic,insul} = \chi(d_{c1})\frac{e^2Q^2}{4d_{c1}}. \tag{8.8}$$

After the first electron has been captured, the surface is locally charged positively. Image charge acceleration is partially offset by deceleration by the newly formed surface charge and thus no further energy gain is relevant for film formation [17].

When the ion captures an electron, energy may be emitted as radiation or via Auger electrons. For geometry reasons, statistically, half of the radiation energy illuminates the substrate and growing film. The captured electrons are in excited states because there is not enough time between capture and surface impact to cascade down to the ground state, hence we deal with a "hollow atom" [18]. The time between electron capture and surface impact is of the order of a few tens of femtosecond.

When the ion (now a hollow atom) arrives at the surface, the projected range of penetration is determined by its momentum or *kinetic* energy. The loss rate of kinetic energy is determined by (i) nuclear elastic collisions, involving large, discrete energy losses with significant angular deflection of the ion trajectory in the solid, and (ii) electronic inelastic collisions where the moving ion excites or ejects electrons of the substrate, involving small energy losses per collision and

negligible deflections of the ion trajectory [10]. With the loss rate of order 100 eV/nm, ions in energetic deposition penetrate just a few monolayers (subplantation). The *kinetic* energy can be associated with short collision cascades and atom displacements. Each displaced atom will come to rest with large amplitude vibrations around its new site, a process far from thermodynamic equilibrium. Atoms involved in cascades represent an atomic scale volume of hot material whose thermal energy is rapidly quenched by thermal conduction. One has to be cautious when using the terms "heat" and "temperature" because of the non-equilibrium nature of the energetic ion deposition process.

The release of *potential* energy and its effects on film properties is less studied and often neglected because most studies consider the condensation of vapor and not multiply charged ions. In the case of cathodic arc plasmas, the potential energy is important. The ionization energy is released in two steps. The first step is above the surface via radiation and Auger processes, and the second step is in the solid. Part of the potential energy is transferred to the solid via electronic excitation [19]. Electron–phonon coupling leads to local heating of the lattice; the timescale to reach equilibrium between electron and lattice temperature is of order 1 ps [20]. The high potential energy of the arriving ion can cause surface atoms to be emitted (potential sputtering [18]). For insulating surfaces, surface charge-up will attract electrons from the plasma. The ionization energy can be considered released to the solid when a charge-compensating electron is actually supplied. The cohesive energy becomes available (turns into heat) when the arriving ion has become a film atom, i.e., its electrons have established bonds with neighboring atoms.

In energetic deposition of cathodic arc plasma, each ion delivers significant kinetic *and* potential energy, and both contribute to what may be called *atomic scale heating* (ASH). Kinetic energy and potential energy are usually greater than the binding energy, surface binding energy, and activation energy for surface diffusion, and therefore both kinetic and potential energies can be expected to have a significant effect on film evolution and resulting film properties. The total energy that an ion of charge state Q brings to the substrate can be calculated by adding kinetic and potential energies, reduced by the energy required to capture Q electrons from the substrate, hence

$$E_{total}(Q) = E_{kin,0} + QeV_{sheath} + E_{ic} + E_c + E_{exc} + \sum_{Q'=0}^{Q-1} E_{Q'} - Qe\phi. \quad (8.9)$$

In filtered cathodic arc deposition, the majority of condensing species are ions, therefore, each of the atoms in the growing film was subject to ASH several times, namely, once when it arrived and again when neighboring atoms arrived. Musil [21] pointed out that ASH can replace conventional heating and so produce dense films via enhanced surface mobility at generally low bulk temperature. Of course, ASH eventually gives rise to temperature elevation of the substrate and the growing film as a whole [3]. If the substrate is attached to a heat sink, its bulk may stay close to the original temperature, for instance close to room temperature for water-cooled holders.

Even without intentional bias, the kinetic ion energies are already high enough to insert the ions (atoms after neutralization) into the surface, i.e., into the uppermost monolayers of the substrate, which causes densification and appearance of high compressive stress. The relation of ion energy to stress generation and relief (at high ion energy) is further discussed in Section 8.4.

The impact of ions with kinetic energies in the range 10 eV–10 keV leads to subplantation processes far from thermodynamic equilibrium, and hence metastable amorphous or nanocrystalline phases can be formed on timescales of femtoseconds to picoseconds [13]. Film growth by energetic condensation and ion-assisted deposition are affected by both kinetic and thermodynamic factors [22]. This makes modeling challenging. One approach to bridging kinetic and thermodynamic regimes of growth is using kinetic Monte Carlo simulations taking self-consistently into account the strain field generated during the growth process [23]. Later, in Section 8.4, we will consider ion effects on preferred orientation and the generation and relief of stress.

8.2 Secondary Electron Emission

Energetic condensation of ions can cause emission of secondary electrons. Secondary electron emission (SEE) was already mentioned when considering operational mechanisms of cathodes (Chapter 3). SEE is relevant for processes in the near-substrate plasma, and therefore it needs to be mentioned here, too. One generally distinguishes kinetic emission (KE) and potential emission (PE) based on the kind of energy most responsible for the emission process. Kinetic emission is relevant when the kinetic energy of the primary ion is greater than about 1 keV, and it becomes dominant at a few keV. If we assume, for example, that we have a cathodic arc plasma with a mean charge state of 2, any bias greater than 500 V would cause significant kinetic emission of electrons, with a yield greater than 0.1 (the yield is defined as the average number of secondary particles – here electrons – emitted per incident primary particle). At very high bias energies, in the regime used for ion etching and plasma immersion ion implantation, the yield of kinetic emission can grow to large values. Figure 8.2 shows the example of emission caused by zirconium ions impacting an aluminum substrate, charge state resolved, and Figure 8.3 shows the charge-state-averaged yield for a number of metal ions impacting a stainless steel substrate [24].

At lower kinetic energies, the kinetic emission yield becomes negligibly small and potential emission is dominant (though small in absolute terms). Potential emission is characterized by an Auger-type process in which at least two conduction band electrons are involved, one neutralizing the arriving ion into the ground state and the other being excited into the continuum above the filled band [25]. The yield by PE is generally small, typically much less than unity. Figure 8.4 illustrates that clearly, and it also shows that singly charged metal ions at low kinetic energy have a negligibly small total yield because both kinetic and potential emission yields are very small [26, 27, 28].

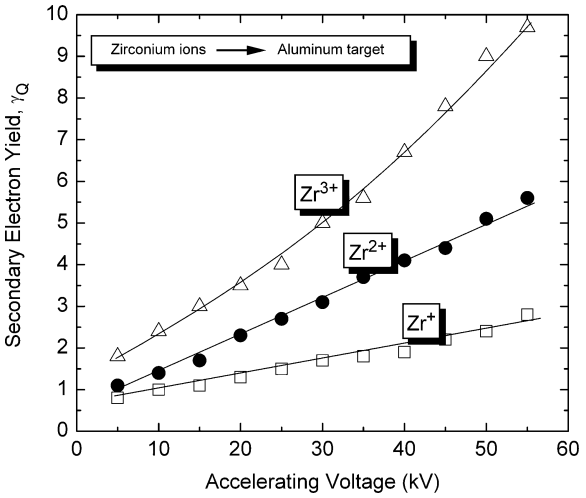

Fig. 8.2. Secondary electron yield obtained by impact of singly, doubly, and triply charged zirconium ions arriving on an aluminum substrate; the accelerating voltage is very high, as it is typical for plasma immersion ion implantation processes. The values are measured data obtained using a vacuum arc metal ion source. (Data from [24])

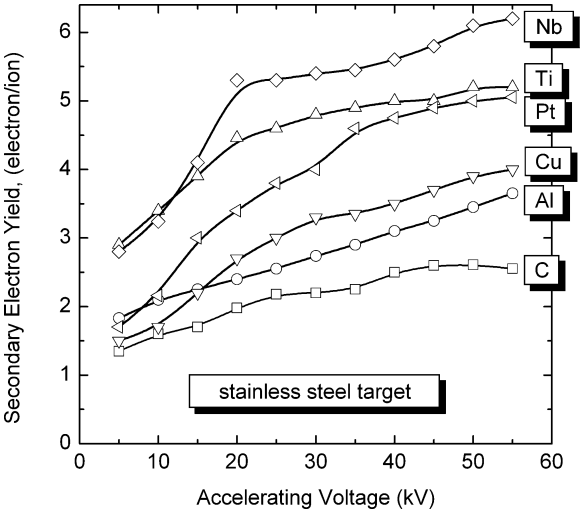

Fig. 8.3. Secondary electron yield from stainless steel, averaged over the charge state distribution of the impacting ions, for various metal plasma at high applied voltages. (Data from [24])

Secondary electrons, once emitted, are in the same electric field of the sheath that accelerated the (positive) ions, but now it accelerates the (negative) electrons in the opposite direction. The electrons may interact with the arc plasma, especially with the colder plasma electrons, as well as with the background

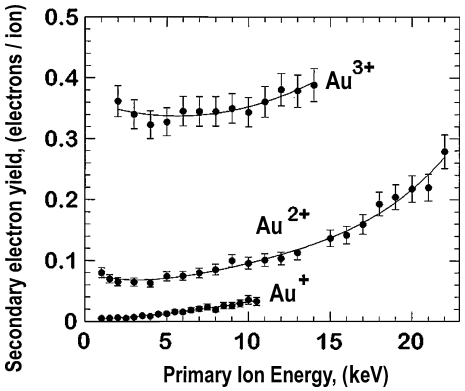

Fig. 8.4. Secondary electron yield from gold upon gold ion impact: with decreasing energy, the kinetic emission is reduced and becomes negligible whereas potential emission remains relevant with the exception of singly charged gold, because the potential energy of singly charged gold ions is less than twice the work function of gold. (Adapted from [26])

gas, if present, and thereby enhance the plasma density. This additional ionization may or may not be important, depending on the mean free path, which in turn is a function of the electron energy (corresponding to the sheath voltage), the density of "target" particles, and the cross-section of interaction. In many cases, the additional ionization is not important and so we can move on to look at the next secondary particles, namely the atoms that come from the substrate's surface.

8.3 Neutrals Produced by Self-Sputtering and Non-sticking

When an energetic ion approaches the surface it is likely that it comes to rest on or under the surface, and therefore it contributes to deposition. However, not all ions are incorporated into the substrate, rather, depending on the energy and incident angle of the arriving ion and the kind of substrate material, some ions may "bounce" back as neutralized atoms and therefore contribute to the density of neutral atoms rather than to film growth. Generally, one may introduce a sticking probability for arriving, energetic ions. Again, it should be stressed that a sticking probability less than unity contributes to an increase of the density of neutrals in the plasma leading to a reduction of the high charge states (cf. Chapter 4).

Another mechanism of generating neutrals is that the arriving atom becomes incorporated into the substrate; however, the collision cascade under the surface can lead to the expulsion of one (or more) surface atoms. The process is generally called sputtering, and in case the arriving ion and the sputtered atom are of the same material, one speaks of self-sputtering. Clearly, self-sputtering reduces the effective film deposition rate, and in case the yield exceeds unity, no film is grown.

Only little experimental information is available on self-sputtering yields for the case of condensing cathodic vacuum arc plasmas at low energy, i.e., with no or low bias voltage. In one study, the case of energetic condensation of zirconium and gold on stainless steel and silicon substrates was studied [29]. Self-sputtering will of course depend on the specifics of the material considered, and one should expect that self-sputtering is especially important for materials of high ion mass and small surface binding energy, such as Zr and Au. In the experiment with gold, the effect was immediately visible because the sample at ground potential showed the characteristic gold color, whereas the gold color disappeared on samples of increasingly higher bias [29]. Almost no film was discernable on samples whose bias exceeded −50 V. There was noticeable metal coating on parts and components that did not have a line of sight with the plasma source, indicating that scattering in the plasma and/or sputtering from the substrate surface must have occurred. Film thickness was found to be a strong function of bias. Thickness data can be converted to approximate self-sputtering yields (Figure 8.5). Taking kinetic and potential energies into account [22], the ion energy exceeds 100 eV for all Zr and a fraction of Au ions even at zero bias.

Molecular dynamics [30, 31] (MD) and binary collision theory [32, 33] (BCT) have been used to model the energetic interaction of ions with solids. A very popular group of BCT codes are derived from TRIM (transport and range of ions in matter), Monte Carlo codes originally developed to simulate high-energy ion implantation [34]. These codes are computationally very effective because they use the universal ZBL (Ziegler–Biersack–Littmark) interaction potential

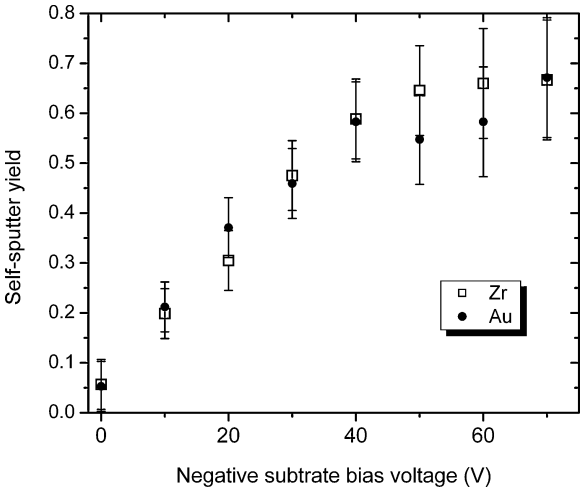

Fig. 8.5. Effective self-sputtering yields derived from gold and zirconium vacuum arc coating experiments on biased substrates. It should be stressed that the energy of arriving ions does not simply correspond to the voltage due to the presence of multiple charge state, image charge acceleration, enhancement by potential sputtering, etc., see text. (Data from [29])

(see also [10, 35]). The ZBL potential can be used to quickly show a stopping rate of order 100 eV/nm. Versions of the TRIM or SRIM code can be downloaded from http://www.SRIM.org/.

Summarizing the results of molecular dynamics simulation for self-sputtering and sticking probability in the relevant energy range [30, 31, 36, 37], one may consider the generic energy and angle dependences shown in Figures 8.6 and 8.7. For details of the embedded atom method (EAM), the reader is referred to examples of copper [30] and aluminum and nickel [31]. For normal incidence, the sticking coefficients were determined to be close to unity for all materials, and self-sputtering yields at 100 eV were 0.2 for Al, 0.3 for Ni, and 0.5 for Cu. Taking potential and kinetic energies of ions into account, experimental self-sputter data are in reasonable agreement with MD and BCT simulations. As it is already intuitively clear, the sticking probability at normal incidence is usually close to unity because ions of cathodic vacuum plasmas have sufficient kinetic energy to displace near-surface atoms and come to rest in the subsurface region. At oblique angle, however, penetration is much reduced; rather, the ion interacts with surface atoms, becomes neutralized by "absorbing" a number of electrons according to its pre-impact charge state number, and transfers energy and momentum. As a result, a neutral atom may be produced whose kinetic energy is reduced compared to the pre-impact kinetic energy, though it still may have hyperthermal energy.

Another deviation from the general rule of high sticking probability at normal incidence occurs when very light ions impact on a substrate of heavy lattice atoms with high displacement energy. The light atoms are not very effective to displace those atoms, and a rather high probability of backscattering

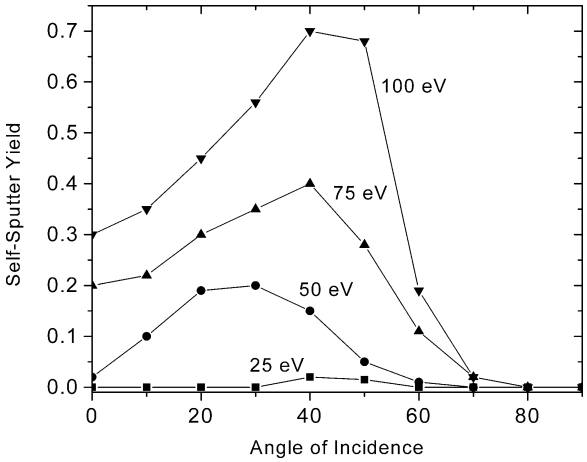

Fig. 8.6. Self-sputter yield as a function of impact angle (with respect to the surface normal), with the primary ion energy as a parameter. The data are for nickel but other materials behave qualitatively in a similar way. (Adapted from [31])

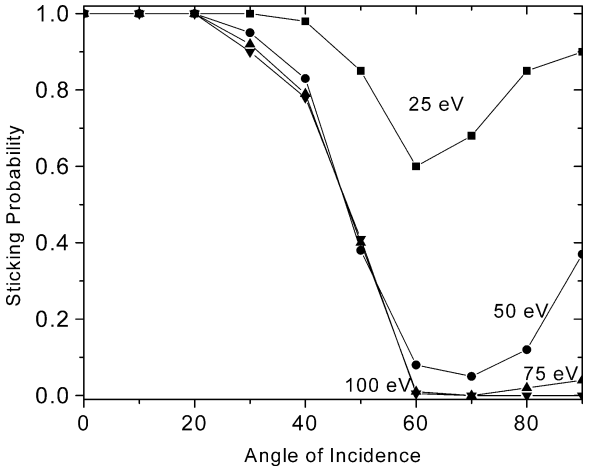

Fig. 8.7. Sticking probability as a function of impact angle (with respect to the surface normal), with the primary ion energy as a parameter. The data are for nickel but other materials behave qualitatively in a similar way. (Adapted from [31])

exists even at normal incidence. For example, TRIM calculations suggest that the backscattering probability of aluminum ions impacting on a tungsten surface is about 50% for the interesting energy range of 30–100 eV. Indeed, aluminum film growth from arc plasma on tungsten was not successful, i.e., the ions were practically completely backscattered, unless either the aluminum ions were slowed by argon gas or the surface was changed by adding oxygen [38].

The formation of neutrals by sputtering and non-sticking leads to an enhanced concentration of such neutrals above the surface. Indeed, one can readily observe an enhancement of emission lines from neutrals above a surface hit by the vacuum arc plasma flow. Tarrant and co-workers [39] spectroscopically measured those "optical flares."

8.4 Film Properties Obtained by Energetic Condensation

8.4.1 Structure Zone Diagrams

Energetic condensation of ions from cathodic arc plasmas is known to lead to dense films even at relatively low substrate temperature [2, 3]. This can be traced back to the above-described atomic scale heating (ASH) associated with the impact of ions having relatively high kinetic and potential energies. Generally, deposition can be done in a wide range of substrate temperature, and in many cases an elevated substrate temperature is highly desirable in order to control (reduce) the incorporation of hydrogen from water and to promote a desirable crystalline phase and orientation. Deposition at room (or near) temperature has

the advantage that temperature-sensitive substrates like polymers can be used, and the process is more economical due to the elimination of the heating and cooling steps.

The effect of process parameters on coating properties can be more generally visualized by a structure zone diagram, a concept introduced by Movchan and Demchishin [40]. Considering films made by evaporation, their original diagram had only the substrate temperature as a process variable. This temperature was normalized to the melting temperature of the coating material, T/T_m, also known as the *homologous temperature*, to obtain a relation valid for most materials.

Expanding the concept to sputtered films, Thornton added the sputter pressure as an additional axis [41]. In Thornton's diagram, Figure 8.8, the axis of process pressure can also be interpreted as an axis for energy, with lower pressure corresponding to higher energy. The pressure–energy relationship is due to the sputter voltage increase and the smaller likelihood of collisions with the background gas at reduced pressure.

The ion energies involved in energetic condensation from cathodic arcs are higher than the corresponding kinetic energies of atoms in sputtering. The ion energies are about one order of magnitude or even higher with biasing, and therefore an extended structure zone diagram needs to be developed. A step in this direction was taken by Messier [42], who explicitly replaced the sputter pressure by the energy of bombarding ions (Figure 8.9). Still, Messier had a sputter process in mind, and more detailed structure zone diagrams for film formation by energetic condensation remain to be developed. The challenge is to find the common features and trends for an increasingly wide range of materials, which now often include ternary and quaternary compounds with a host of phases, textures, and nanostructures.

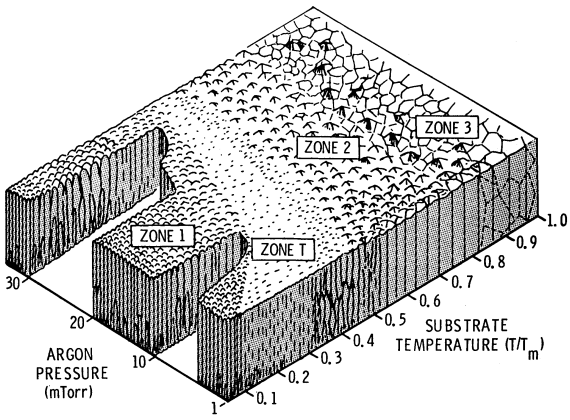

Fig. 8.8. Classic structure zone diagram by Thornton ([41]); the substrate temperature, T, is normalized by the melting temperature of the coating material, T_m

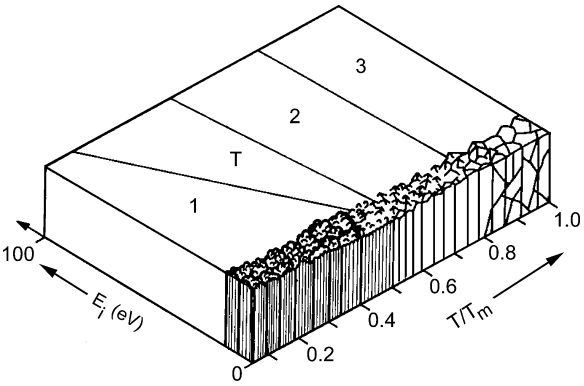

Fig. 8.9. Structure zone diagram by Messier and co-workers, now explicitly including the ion energy (the original work – Figure 5 of [42] – displays the bias voltage)

Deposition at low (e.g., room) temperature and high ion fluxes produces special challenges due to the non-equilibrium nature of the growth process. For example, Mausbach [43] investigated copper films of 1 μm deposited by a vacuum arc with a consumable anode, i.e., anodic arc, with substrate temperatures of 50–500°C. In his setup, the degree of ionization could be adjusted by the discharge parameters (1–30%), and the energy of the ions by biasing (2–150 eV). When deposited at room temperature, the copper films are metastable and recrystallize at room temperature within a few days. Mausbach proposed to use the product of ion energy and degree of ionization in the condensing flux as a characteristic parameter that determines how much the system is formed away from equilibrium and therefore subject to change. He states that below a homologous temperature of 0.3, a metastable film structure exists if the mean ion energy exceeded about 1 eV. The grain size was determined by an athermal growth process and no activation energy for the grain growth could be found, whereas grain growth occurs at elevated temperatures in a thermally activated manner.

8.4.2 Stress and Stress Control

One generally distinguishes extrinsic and intrinsic stresses of a coating. The extrinsic or thermal stress is caused by the differences in thermal expansion between substrate and coating materials, and it develops when substrate and coating cool down from the deposition temperature T_{dep} to room temperature, T_{RT}. The extrinsic stress can be compressive or tensile, depending on the coefficients of thermal expansion, α_{sub} and α_{coat} [44]:

$$\sigma_{extr} = -(\alpha_{sub} - \alpha_{coat})(T_{dep} - T_{RT})\frac{Y}{1-\nu}, \tag{8.10}$$

where Y and ν are the elastic (Young's) modulus and Poisson's ratio of the coating material, respectively. The extrinsic stress rarely exceeds 1 GPa [44, 45] and therefore we can proceed to consider intrinsic or growth stress, which can reach much higher values in energetic condensation.

We will especially consider the effects of the energy of ions arriving at the surface. In the extreme of low energy, observed for deposition by thermal evaporation, the energy of condensing atoms is very low indeed, generally $kT < 1$eV, where T is the temperature of the evaporation source. The resulting films are of low density; they have voids and a columnar microstructure, and they exhibit tensile stress. When going to higher energies by considering sputter deposition techniques, the films are denser and show compressive stress, especially at low sputtering pressure. With the much higher energies typical for cathodic arc deposition, the intrinsic stress can be very high, and therefore the issue deserves detailed consideration.

Densification is desirable for many (but not all) applications. It is known that film densification can be obtained when a few percent of the arriving particles have higher energy, i.e., energies greater than the displacement energy. This has extensively been used in ion beam assisted deposition (IBAD) [46, 47] and plasma immersion ion implantation and deposition [48]. Along with densification one has observed two effects: the formation or change of a preferred orientation (in the case of crystalline films) and an increase in compressive stress. Stress causes strain energy which can drive delamination processes [49]. In the following we will follow the work by Bilek and co-workers [49, 50, 51] who provided the most comprehensive discussion of the relationship of ion bombardment and stress evolution, which will directly lead to strategies for the reduction of intrinsic stress. This is especially important for hard and superhard (> 40 GPa) materials such as tetrahedrally bonded carbon (see last section of this chapter), transition metal nitrides, and boron nitride.

With the typical energies of cathodic arc ions (Chapter 4), displacement of surface and subsurface atoms is possible. The arriving ions are inserted in the subsurface region, just a few atoms below the surface. If the substrate is biased, the subplantation depth may be many monolayers deep, and at higher bias (many kV) may reach a depth that qualifies the process as ion implantation. Insertion of ions causes densification of the region where the ion comes to rest. Densification of the local phase causes compressive stress. If the material is a metal it can yield to the stress by plastic deformation. However, if the material is covalently bonded it will resist plastic deformation and exhibit a higher density than the normal density. This material is metastable and tends to show a high coordination of bonds if more than one phase can exist (most famously, carbon establishes sp^3 bonds, diamond bonds, as opposed to the sp^2 bonds of the less dense graphitic material).

Davis [52] developed a model in the early 1990s to qualitatively describe the evolution of stress by a competition of stress generation by knock-on

implantation (or subplantation) and atomic scale annealing in a thermal spike volume. For a thin film the stress σ is related to the strain ε by [53]

$$\sigma = \frac{Y}{1-\nu}\varepsilon. \tag{8.11}$$

In Davis' model [52] one obtains

$$\sigma(E_i) \propto \frac{Y}{1-\nu}\frac{E_i^{1/2}}{\left(J\Big/j + \kappa E_i^{5/3}\right)}, \tag{8.12}$$

where E_i is the energy of arriving ions, J is the net condensing flux, j is the ion bombarding flux, and κ is a material-dependent parameter.

While Davis' model reproduces well the characteristic curve (Figure 8.10), Bilek and McKenzie's recent model [49, 50] gives a better fit to experimental data. They point out that the time for energy removal from thermal spike volume around the point of insertion (the "quench time") determines whether the material is densified (compressive stress increases) or atoms have time to rearrange their bonding structure, allowing the heated volume to expand toward the surface (stress is relieved). The quench time depends on the size of the heated volume, which in turn depends on the energy of the inserted ion.

To make the problem tractable, one could assume that the region affected by the thermal spike is spherical with the radius R_{th}. Then the quench time is proportional to the square of the thermal spike or to the 2/3-power of the ion energy [54]:

$$t_{quench} \propto R_{th}^2 \propto E_i^{2/3}. \tag{8.13}$$

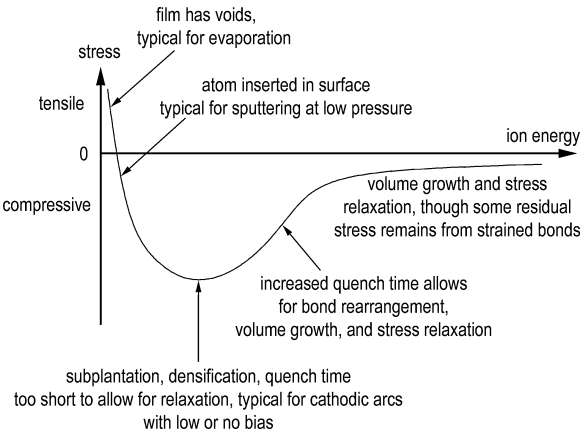

Fig. 8.10. Schematic presentation of stress evolution as a function of the kinetic energy of ions impacting the surface. (Adapted from [49] and other sources)

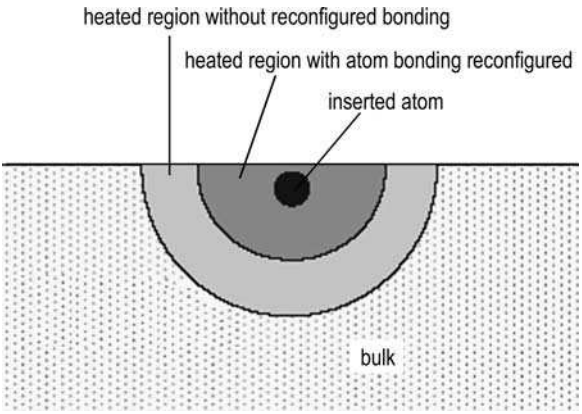

Fig. 8.11. Simplified geometry for developing a model for stress generation and relaxation: the thermal spike volume is assumed to be spherical with the inserted atom in the center. The stress is accumulated in the *light gray* region, the size of which is proportional to $E_{\mathrm{i}}^{2/3}$. (Adapted from Figure 1 of [49])

For $E_{\mathrm{i}} \sim 100$ eV, the quench time was calculated to be less than 1 ps, which is too short for significant rearrangement of atoms; rather, the atoms will use a high bond coordination with the available neighbors to *minimize the total system energy under constraints* (Figure 8.11).

The volume of the thermal spike is proportional to $\kappa(E_{\mathrm{i}} - E_{\mathrm{B}}) = (2/3)\pi R_{\mathrm{th}}^3$, where E_{B} is the energy barrier for the ion to be inserted into the surface (as opposed to staying on the surface). The volume of the light gray region (Figure 8.11) can be calculated as

$$V_{stressed} = 2\pi R_{th}^2 \, d\tau = 2\pi \left(\frac{\kappa}{2\pi}\right)^{2/3} E_i^{2/3} \, d\tau, \tag{8.14}$$

where $d\tau$ is the thickness of the interfacial region where atom movement is restrained by bonds to unaffected atoms in the bulk; the thickness $d\tau$ is about one bond length and remains that way even as the thermal spike volume grows at higher ion energies. The number of stressed sites is proportional to the volume V_{stressed} and one can write a parametric equation for the stress:

$$\sigma = C(E_i - E_B)^{2/3}, \tag{8.15}$$

where C and E_{B} are material constants.

Looking now at ions of greater energy, i.e., those that are inserted below the surface, with a kinetic energy clearly exceeding the 100–200 eV level, the effect on stress is quite different. The impacting ion creates a larger volume of a thermal spike, i.e., a transient melt shown in dark gray in Figure 8.11, allowing the atoms of this temporary liquid to access many possible bonding configurations. Those atoms can remain in a thermodynamically preferred configuration, i.e., one that minimizes the bond energy and strain energy. This is

often not the phase of highest density; rather, the thermal spike volume can expand and raise the level of the free surface. The possibility of raising the surface, thereby minimizing the strain energy without constraint, is the basis for ion-induced stress relief by energetic ion bombardment. Experimentally it has been observed that only a small fraction of high-energy ions is needed to relieve stress, and that saturation of such stress relief occurs when the percentage of the energetic ions is still small. Saturation of stress relief occurs when the volume regions of unconstrained rearrangement start to overlap.

The model described above can be expressed analytically. Assuming that the film growth occurs with both low-energy ions and atoms and high-energy ions (of energy E_i), the volume V still untreated by a thermal spike is reduced exponentially [49]:

$$\frac{V}{V_0} = \exp\left(-\frac{V_{spike}N}{V_0}\right), \tag{8.16}$$

where V_0 is the volume of a film slab under consideration, $V_\mathrm{spike} = E_\mathrm{i}/(E_\mathrm{A}n_\mathrm{a})$ is the volume of each thermal spike, E_A is the average energy given to atoms of the thermal spike volume, $N = n_\mathrm{a}V\delta$ is the number of high-energy impacts before the slab is covered by more condensing atoms, n_a is the atom density of the slab, $\delta = wf$ is the duty cycle of high-energy ions, produced by pulsed biasing, for example, with w being the pulse width of the bias and f the bias pulse repetition frequency. Alternatively, δ could be the fraction of energetic ions produced by other means such as an external ion source. While these considerations are developed with the plasma immersion technique [48] in mind, the underlying physics and derivations are rather general. Using the above expressions, Eq. (8.16) becomes

$$\frac{V}{V_0} = \exp\left(-\frac{E_i f w}{E_A}\right). \tag{8.17}$$

The stress can be assumed to vary with the volume fraction treated by high-energy ions, from the as-deposited value, σ_0, to the relaxed, residual value after ion treatment, σ_res, leading to

$$\sigma = \sigma_0 \frac{V}{V_0} + \sigma_{res}. \tag{8.18}$$

Using (8.17) gives

$$\sigma = \sigma_0 \exp\left(-\frac{E_i f w}{E_A}\right) + \sigma_{res}. \tag{8.19}$$

Now, if we use Eq. (8.15) to express the stress generated by the moderately energetic ions (those with energy E_G, inserted into or just below the surface) and replace the stress-relieving ion with energy $E_\mathrm{i} = E_R$, one obtains

$$\sigma = C(E_G - E_B)^{\chi} \exp\left(-\frac{E_R \delta}{E_A}\right) + \sigma_{res}, \tag{8.20}$$

where the exponent χ could be 2/3, as suggested by (8.15), but other exponents such a $\chi = 1$ or $\chi = 1/2$ also give a good fit to experimental data for a number of materials such as TiN [55], AlN [52], BN [56], a-SiH [57], SiBCN [58], and hard amorphous carbon [59]. The different exponents can be interpreted to deviations from the idealized spherical shape of the thermal spike; for example, one could consider a cylindrical geometry of the thermal spike volume [60]. It turns out that the choice of the exponent χ is not very critical for the quality of the fit [49]. The approach will be illustrated by the special case of carbon, see Section 8.10.

8.4.3 Preferred Orientation

Energetic condensation has a profound effect on the nucleation, growth, and the resulting microstructure. The first observation perhaps was made by Krohn, Meyer, and Bethge in 1983 [61] who experimented with different methods of metallization for electron microscopy. They compared thin films of gold, silver, and platinum obtained by thermal evaporation and by pulsed cathodic arc deposition on NaCl substrates at 150°C. They found that in both cases the initial growth occurred in island mode, though the islands were much smaller for the cathodic arc films and coalescence occurred at smaller nominal film thickness. The most important finding, though, was that the electron diffraction pattern in the case of cathodic arc gold indicated that the islands had a preferred orientation, namely an epitaxial relation to NaCl, (001)Au||(001) NaCl, and [100]Au||[100]NaCl.

Nucleation and growth under the conditions of energetic condensation was studied for the pure metal case, i.e., when the cathodic arc operates in vacuum or low-pressure inert gas. In situ conductivity measurements showed that the contribution of kinetic energy leads to smaller, more frequent islands (Figure 8.12), as compared to sputtering, and the coalescence occurs at smaller nominal film thickness, which can be detected by a sharp increase of conductivity (or equivalently, sharp decrease of resistivity) by several orders of magnitude [62]. This and other observations are further discussed when considering ultrathin metal films in Chapter 10, Applications. A more sophisticated and powerful investigation compared to simple in situ resistivity measurements is the use of in situ ellipsometry. Investigating ultrathin titanium films made by a pulsed cathodic arc, Oates and co-workers [63] determined the percolation threshold using a method by Arwin and Aspnes [64] by locating the thickness at which the real part of the dielectric function first becomes negative. The value for titanium on silicon is in the range 2.7–3.1 (± 0.1 nm). Ellipsometry is generally recognized as a preferred method for ultrathin film measurements and has become a routine tool, for example in determining the thickness of ultrathin ta-C protective films.

The observation of preferred orientation turns out to be a rather general trend: films made by energetic condensation tend to grow with a preferred

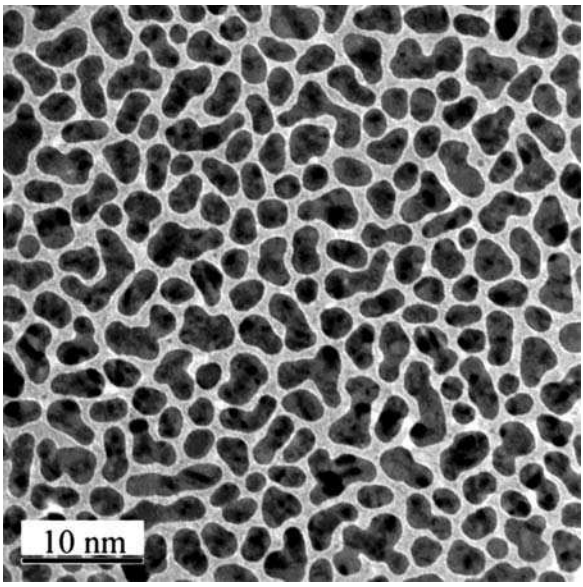

Fig. 8.12. Transmission electron microscope image of an ultrathin film of silver deposited by filtered pulsed cathodic arc on Si_3N_4 at room temperature: this film consists clearly of islands while the same nominal thickness of about 8 nm gives a contiguous, conducting film on ZnO-coated glass substrate (see also [62])

orientation, the specifics depending on the ion bombardment parameters. The growing film tends to prefer an orientation that is thermodynamically stable at low levels of biaxial stress [50]. Examples for TiN and AlN are given in Table 8.1. Figures 8.13 and 8.14 show high-resolution transmission electron microscopy (HRTEM) examples of epitaxial growth for TiN.

There is a direct link between microstructure and ion-generated stress, and ultimately the thermodynamic driving force of minimizing the system's energy affects both stress and preferred orientation [55].

In case of amorphous films, one cannot speak of preferred orientation, though also here one can see the effect on the microstructure, mostly via the density and the formation of different hybridizations, if applicable. For example, highly stressed carbon films tend to be rich in sp^3 bond, whereas stress-relaxed films are much more graphitic, i.e., rich in sp^2 bonds (more about this in Section 8.10).

Table 8.1. Preferred orientation obtained by energetic condensation. (Adapted from [49])

	High-stress material	Low-stress material
TiN	(111) orientation	(200) orientation
AlN	c-axis in plane	c-axis normal

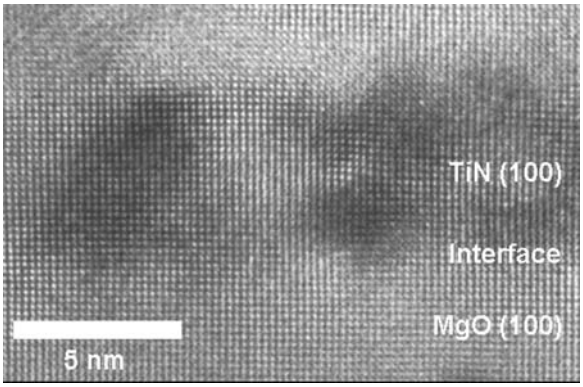

Fig. 8.13. High-resolution TEM image showing the epitaxial growth of TiN layer on MgO(100) obtained by energetic condensation; the titanium arc was operated in nitrogen at 7×10^{-2} Pa with the substrate at room temperature. (Courtesy of Jürgen Gerlach (experiment) and Thomas Höche (TEM), both IOM Leipzig)

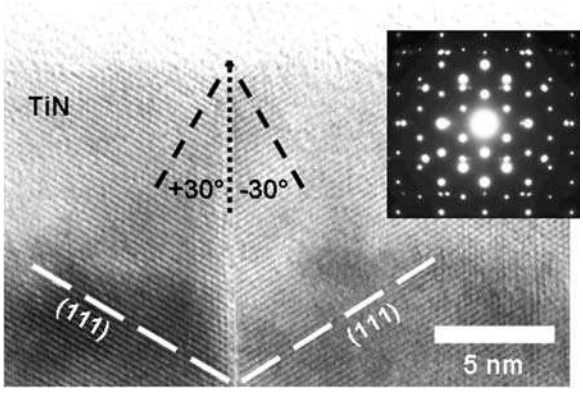

Fig. 8.14. High-resolution TEM image showing an epitaxial twin layer of TiN on r-plane sapphire obtained by energetic condensation; the titanium arc was operated in nitrogen at 7×10^{-2} Pa with the substrate at 700°C; on the right the corresponding electron diffraction pattern. (Courtesy of Jürgen Gerlach (experiment) and Thomas Höche (TEM), both IOM Leipzig)

8.4.4 Adhesion

Adhesion of coatings made by energetic condensation can range from excellent to poor depending on the film–substrate material combination and on the stresses involved. Film materials that can form strong chemical bonds to the substrate tend to be highly adherent. For example, carbon films can show excellent adhesion on carbide-forming materials such as silicon. This is especially true

when the materials form a gradient interface due to ion-induced intermixing. Energetic bombardment generally leads to compressive stress, especially when the ion impact energy is in the range of 100 eV, as explained in Section 8.4.2. The stress may become excessively high, often greater than 5 GPa. The related strain energy limits the thickness of coating because it may be greater than the interface energy: the film cracks and delaminates. Using the force picture, the stress may exceed the adhesion strength. In some cases, the interface is stronger than the cohesive strength of the substrate; cracking may occur in the substrate below the interface rather than at the interface.

Delamination can be quite forceful; for example, thick nitride coatings on steel can delaminate with audible noise when parts are cooled. Flakes of the delaminating coating can form dangerous projectiles (safety goggles are a good idea). In other cases, stress relief by delamination can propagate slowly, on the scale of minutes, hours, or even days. The cracking and delaminating film shows a characteristic periodic hill and valley structure (Figure 8.15). Often, the propagation of delamination and pattern formation can be observed in the optical microscope.

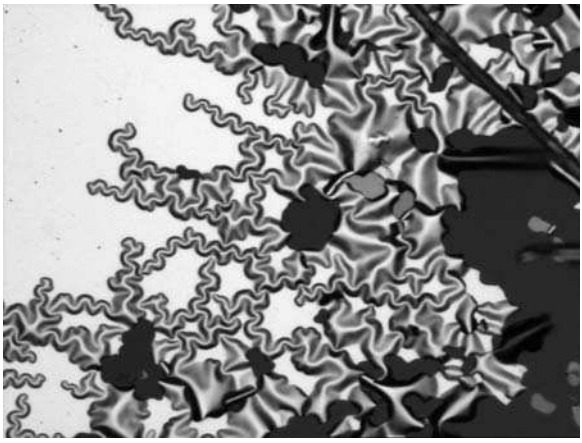

Fig. 8.15. Characteristic hill and valley structure of a delaminating film (optical micrograph of an arc-deposited Ti film on glass)

8.4.5 Hall–Petch Relationship

There is a well-established relationship between grain size and the yield point of a material: the classic Hall–Petch relation says that the larger the grain size of a crystalline material, d, the smaller its yield strength, σ_y. The relation can be expressed as

$$\sigma_y = \sigma_0 + k_y d^{-1/2} \tag{8.21}$$

where k_y is a material constant, and σ_0 is a material constant describing the starting stress for dislocation movement. This relation is based on the concept

that grain boundaries are barriers to dislocation glide, i.e., dislocations require greater amounts of energy to overcome the barrier to motion [65].

However, for very small grains, in the range of about 20 nm and smaller, the classic Hall–Petch relation reverses because the deformation mechanism is different. Plastic deformation is no longer determined by dislocation glide but by atomic sliding of grain boundaries. This leads to an inverse or reverse Hall–Petch relation: both material hardness and yield stress decrease with decreasing grain size.

Ion bombardment from cathodic arc plasma (or any other plasma or beam for that matter) brings energy and momentum to the growing film, thereby affecting its microstructure. For example, it is clear that the surface temperature is higher than the substrate temperature. Therefore, energetic condensation has a direct influence on the grain size – apart from the often-quoted substrate (bulk) temperature. Through energy and momentum transfer, the grain size is affected and with it the hardness and yield strength, where the direction of the change depends on the grain size, i.e., whether the classical or reverse Hall–Petch relationship is applicable.

8.5 Metal Ion Etching

At high negative DC bias voltage, typically −1,000 V or slightly greater, the sputter yield will clearly exceed unity (Figure 8.16) and therefore no film is deposited; rather, the removal of material by sputtering from the substrate surface exceeds the incoming flux of condensable ions and atoms. This process

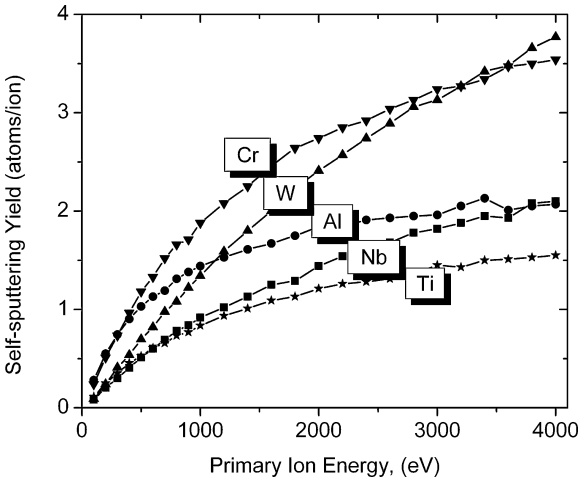

Fig. 8.16. Self-sputtering yield for selected metals as a function of ion energy (calculated by T-DYN Monte Carlo code; the apparent scatter is due to the statistics). The energy scale of up to 4 keV is quite appropriate considering the typical bias of 1 kV and the presence of multiply charged ions

is often labeled as ion etching. Using metal ions from a cathodic arc plasma has great advantages over the more common use of argon ions, as explained below.

The ions in a sputter cleaning process displace surface atoms and come to rest below the surface. When a noble gas like argon is used, the new atoms will not form bonds due to the closed electron shell. Most argon atoms will diffuse to the surface and leave the solid. However, some argon will remain and contribute to a defective, weak interface to the coating that is deposited after the sputter cleaning process. This can be particularly problematic when substrate and coatings are heated like in a typical cutting tool application. In this case, the argon atoms are mobile and coalesce to small bubbles, which greatly weaken the interface. Catastrophic delamination of the coating in the cooling process or later in the application may occur.

In contrast, etching with metal ions results in a superior interface that is characterized by an enhanced concentration of the kind of metal ions used for etching. For example, cleaning of stainless steel with chromium ions results in a surface layer with enhanced chromium content. Chromium can become part of the substrate because, according to the equilibrium phase diagram [66], it has unlimited solubility in Fe below 512°C. Toward the coating, chromium can readily form bonds to other metals or to nitrogen or oxygen, for example.

Etching with metal ions was already known in the 1970s: Aksenov and coworkers [67] measured the deposition and etching rates for aluminum arc plasmas as a function of bias voltage (Figure 8.17). The cleaning of parts to be coated with energetic metal ions was used in the early 1980s; especially Ti ions were used with −1,000 V bias prior to the cathodic arc deposition of TiN [68]. One should keep in mind that the charge states of metal ions are generally

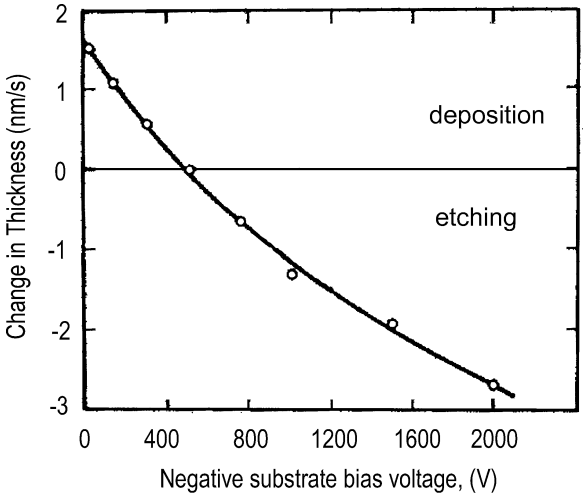

Fig. 8.17. Rate of deposition or etching as a function of bias voltage for aluminum arc plasma. (Adapted from [67])

greater than one (Chapter 4), and therefore a bias of −1,000 V translates into energies exceeding 2 or 3 keV, see Eq. (8.2).

The idea of replacing argon etching by metal ion etching prior to sputter deposition was later utilized in a patented process called *arc bond sputtering* (ABS) by Münz and co-workers [69]. This process was optimized using steered arcs and unbalanced sputter magnetrons in large batch coating systems [70, 71, 72]. For example, Schönjahn and co- workers used a chromium arc with reduced Ar background pressure (90 mPa) to etch the surface with up to 9 nm/min and to insert approximately 37% Cr into the near-surface region of high-speed steel substrates. The bias voltage in this etch phase was −1,200 V, followed by deposition of a $Ti_xAl_{(1-x)}N$ coating that showed a very high critical load of up to 85 ± 5 N.

One of the drawbacks of ABS is the presence of macroparticles produced in the etching process. They represent severe defects that compromise the performance of coatings in sliding wear [71, 73, 74], corrosion [75], and oxidation conditions [76]. Therefore, the next improvement was to utilize ions from *filtered* cathodic arc plasmas to do the etching step. This has been successfully demonstrated with Cr arc ion etching and subsequent CrN deposition [77]. In this example, a nanocrystalline interfacial layer was formed below the 3-μm-thick and smooth CrN. Due to the absence of large-scale defects, the coating exhibited very high adhesion with a critical load of 83 N, a very low wear coefficient of $2.3 \times 10^{-16}\,m^3/(N\,m)$, and a high resistance to corrosion with a pitting potential of +800 mV.

8.6 Metal Plasma Immersion Ion Implantation and Deposition (MePIIID)

In many cases it may be beneficial to involve metal ion etching and energetic condensation in one process. This leads to a range of new processing possibilities, with the specifics depending on the materials and energies involved. One may consider the combination of high- and low-energy ion processing as a special case of plasma-based ion implantation and deposition (PBII&D), also known as plasma immersion ion implantation and deposition (PIII&D) [48, 78, 79, 80] and other names, where ions are accelerated in the sheath of a biased substrate. The ion energies, and the related bias voltages, are typically quite high, e.g., tens of kilovolt, to obtain the acceleration necessary for ion implantation. In recent years though, the majority of research focused on much lower energies, down to a few kV, or even less, especially when the final result of the surface processing is a film, as opposed to a purely ion-implanted surface. In this sense, the original work in PIII converges with the more common plasma-assisted methods that use biasing of typically 1 kV or less.

In fact, the general idea of energetic condensation, facilitated by vapor ionization and substrate biasing, was invented several times. Most influential

was the "ion plating" approach introduced by Mattox in the 1960s [81]. Cathodic arc deposition with bias can be regarded as a version of ion plating.

One characteristic element of PIII is the use of *pulsed* bias, as opposed to DC or RF bias. When combining pulsed bias with the condensable metal plasma of a cathodic arc, the high- and low-bias phases correspond to phases of ion implantation and etching, and film formation, respectively. Main process parameters include the voltage levels of bias and the relative duration of implantation/etching and deposition (Figure 8.18). The rate of ion etching (by sputtering) can exceed the rate of deposition, and thereby a process of pure ion implantation can be obtained. The transition from net deposition to net etching and implantation is observed when the deposition rate equals the etching rate:

$$(\eta_i J_i + \eta_n J_n)(\tau_{on} + \tau_{off}) = \gamma_i J_i \tau_{on}, \tag{8.22}$$

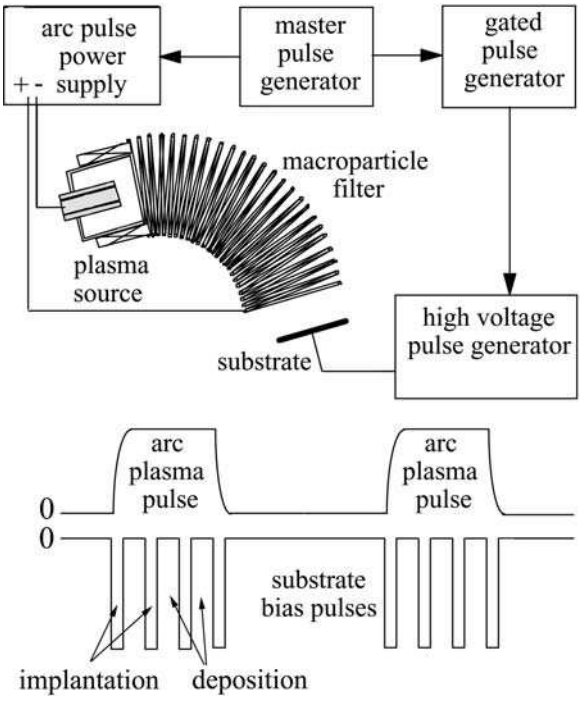

Fig. 8.18. Principle setup of MePIIID: a cathodic arc plasma source produces streaming metal plasma that, in the example, is going through a 90° macroparticle filter before arriving at the substrate; the substrate is pulse biased. In the example shown here, both the arc and bias systems are pulsed, with a burst of negative high-voltage bias pulses synchronized to each arc pulse. The burst mode gives the option of using a high-bias duty cycle while the arc plasma is produced, such that ion implantation without film formation can be realized. (Adapted from [82])

where η and J are the sticking coefficient and flux of ions and neutrals, respectively, τ_{on} is the on-time or duration of a high-voltage bias pulse, τ_{off} is the off-time between high-voltage bias pulses, and γ_{i} is the sputter yield (sputtered atoms per incident ion). Equation (8.22) can be written as a condition for the duty cycle:

$$\delta \equiv \frac{\tau_{on}}{\tau_{on} + \tau_{off}} = \frac{\eta_i J_i + \eta_n J_n}{\gamma_i J_i} \xrightarrow{\eta_i J_i \gg \eta_n J_n} \frac{\eta_i}{\gamma_i}. \tag{8.23}$$

We see that a film is formed only if

$$\delta < \frac{\eta_i J_i + \eta_n J_n}{\gamma_i J_i}. \tag{8.24}$$

The derivation above should be slightly modified if one considers that the ions during the bias pulses are inserted below the surface, whereas the insertion is into the very top surface layer in the absence of bias; hence, the use of a single accommodation coefficient η_{i} is over-simplified. The generalization of the balances is straight forward.

The discussion of sticking and insertion gains importance when considering coating of three-dimensional structures such as lithographically produced trenches for semiconductor processors and microelectromechanical systems (MEMS); this is further discussed in Chapter 10.

Returning to the issue of high compressive stresses and the possibility to obtain stress relief through ion-induced thermal spikes (Section 8.4.2), MePIIID offers the unique approach of using self-ion assisted deposition and stress relief via pulse biasing, which has been observed in the early 1990s (Figure 8.19) [83] but explained only recently [55]. The product of bias voltage and frequency (for constant pulse duration) or more generally the product of bias voltage and bias duty cycle can be used as parameters against which the effect of stress relief can be measured [50]. Physically, one considers the volume of the stress-relieving part of the ion-induced thermal spikes. The effect on stress relief reaches saturation when the thermal spike volumes overlap, as mentioned before. This has been observed for many materials, such as Ti-based alloys and compounds [84, 85], and will be illustrated for the case of carbon (Section 8.10).

PIII was originally introduced as a plasma technique that could modify the surface on all surfaces by immersing the part into the plasma and attracting ions from *all* sides by applying a negative pulsed bias [48, 78]. It became quickly clear that the ratio of the part's feature size and the sheath thickness is an important dimensionless parameter: only if that ratio is large, the treatment is about uniform [86, 87]. Of special interest is the treatment of trenches and holes, and an additional complication arises from the directed velocity of the arc plasma flow [88], in case cathodic arc plasma is used (i.e., MePIIID). Both extreme cases have been considered extensively, namely (i) where the trench or other feature size is large enough that – at least temporarily – it can accommodate at least two times the sheath thickness [87, 89, 90, 91] and (ii) very narrow trenches typical of integrated circuits [92, 93, 94]. The topic is revisited in Chapter 10 when the metallization of semiconductor circuits is considered.

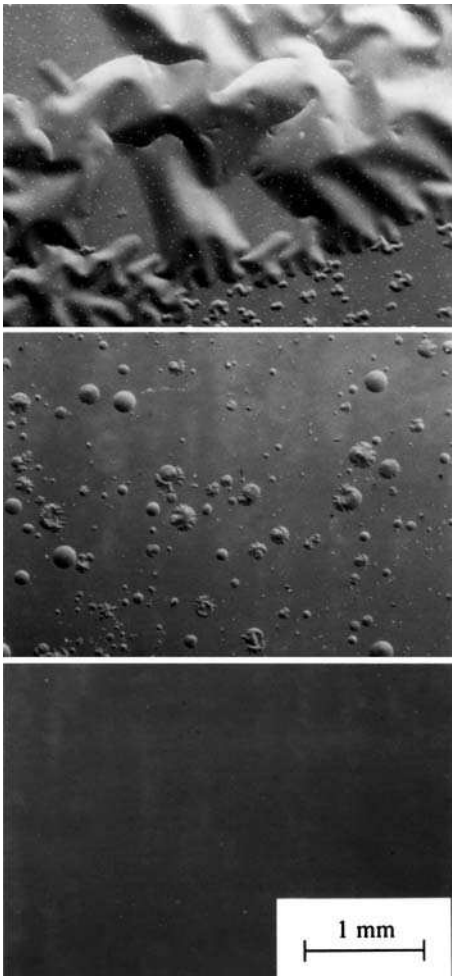

Fig. 8.19. Optical micrograph of $Ag/YBa_2Cu_3O_x$ films on Si deposited by filtered cathodic arc deposition, *top*: the substrate at ground potential shows extensive film delamination; *center*: the substrate was pulse biased to –200 V with much reduced areas of delamination; *bottom*: no signs of delamination can be detected when the pulse bias was increased to –2 kV. (From [83])

8.7 Processing with Bipolar Pulses – The Use of Ions and Electrons

Biasing is usually performed with negative polarity as to accelerate positive ions and repel electrons. For ion etching in the ABS process (Section 8.5), the bias is continuous (DC). Alternatively, one may connect the substrate to a radio-frequency (RF) supply via a matching network such that a negative self-bias establishes itself as a consequence of the mobility difference of the very

light electrons and the much more massive ions. In essence, one has a DC-like bias in that case, too. In the MePIIID process (Section 8.6), the negative bias is high and supplied in short, repetitive pulses.

In this section, we consider bipolar pulsing. We should recall that the physically relevant bias is always the potential difference between the substrate surface and the plasma, i.e., we consider the difference between surface potential and plasma potential, and this difference drops in a space-charge layer called the sheath. The electrical field, $\mathbf{E} = -\nabla V$, associated with the space charge ρ, is determined by the Poisson equation (cf. Chapter 3)

$$\frac{d^2V(z)}{dz^2} = -\frac{1}{\varepsilon\varepsilon_0}\rho(z), \tag{8.25}$$

where z is the coordinate along the surface normal, ε is the dielectric constant, and ε_0 is the permittivity of free space. While a negative substrate bias attracts ions to the surface, positive bias attracts electrons. In all cases, the energy supplied to the surface is the sum of potential and kinetic energies of the arriving particles. In the case of electrons, this is kT_e from the temperature of the plasma electrons plus the kinetic energy gained in the sheath, given by eV_{sheath}, and, last not least, the potential energy $e\phi$, which is determined by the work function $e\phi$ of the solid (the work function was discussed in Section 3.3.1). Sheath formation and stability was often considered in the literature (e.g., Bohm's classical work [95] and Riemann's review [96]), including specific considerations for the fast flowing vacuum arc plasma [88, 97].

The key motivation for using not only negative but positive bias is to also supply electrons, thereby providing a source of energy for *heating* the very surface of the solid or the growing film without incurring any large momentum transfer that could lead to "ion damage" of a crystalline structure. Additionally, in case of an insulating substrate surface, the flux of electrons can be used to neutralize the positive space charge that has accumulated during the negative phase of biasing. The process may be designed such that the coating is heated while the bulk of the substrate remains at a lower temperature, which can be important for temperature-sensitive materials. To obtain the heating effect, the positive bias does not need to be applied in a bipolar mode; rather, one may choose to utilize a rather extended electron-based substrate-heating phase before the main deposition starts [98]. The principle of heating by plasma electrons via positive bias can also be applied to other plasma-assisted deposition processes, such as the deposition of TiB_2 by sputtering, which has been shown to greatly reduce stress [99].

Bipolar bias techniques are usually asymmetric in voltage, current, and phase duration, and the process can be optimized by selecting these three parameters. The chosen asymmetry is to take into account the much smaller mass and higher mobility of electrons, compared to ions. When the surface does not show high conductivity, unipolar negative-pulsed substrate bias can be sufficient with the argument that the sheath collapses in the bias off

time and plasma electrons can reach the surface without the intentional positive bias because positive charge has accumulated during the negative pulse.

8.8 Substrate Biasing Versus Plasma Biasing

Biasing refers in general to the application of a potential difference between substrate surface and the plasma:

$$V_{bias} \equiv V_{substrate} - V_{plasma}. \tag{8.26}$$

The plasma potential can be defined in different ways, and perhaps the most descriptive is that if a small conducting object was immersed in the plasma, it has the plasma potential when it does not affect the fluxes of ions and electrons to its surface. One should note that the plasma potential is not the same as the floating potential; the latter is defined as the potential that an isolated object assumes when immersed in the plasma. An object at floating potential has by definition a zero net current, whereas an object at plasma potential has a net current because the flux of electrons will be larger than the flux of ions.

Biasing means one shifts the potential of the substrate with respect to the plasma potential. Biasing determines the fluxes and energies of particles arriving at the substrate. In most cases, one deals with negative substrate biasing, i.e., application of a negative bias to the substrate because one intends to accelerate positive ions in order to control their energy when they impact the substrate surface, with crucial consequences for the net deposition rate (arrival rate minus sputter rate) and properties of the coating.

The plasma potential is usually not exactly known. The fixed potential is the ground or earth potential, and therefore most potentials are referenced to ground. Strictly speaking, the applied voltage with respect to ground is not the bias voltage defined in Eq. (8.26); however, when the voltage amplitude is high, $V_{\text{applied}} \gg kT_e/e$, the deviation between ground and plasma potentials, which is often about $3kT_e/e \sim 10$ V, can be neglected. One should note, though, that the difference between ground and plasma potentials cannot be neglected when investigating the ion energy distribution function with a grounded energy analyzer: here, the difference will show up with the ion charge state as a factor [100, 101].

While the vast majority of biasing techniques makes use of negative substrate bias (with respect to ground or approximately with respect to the plasma potential), it is also conceivable that one can shift the plasma potential (with respect to ground or the grounded substrate). One may call this *plasma biasing*, as opposed to substrate biasing. Positive plasma biasing is equivalent to negative substrate biasing [102]. In extreme cases, to enhance the overall bias, one may

simultaneously shift both the substrate potential (negative) and the plasma potential (positive) [103].

Plasma biasing may be a suitable route when substrate biasing is not an option, for example when the substrates are mounted on permanently grounded chucks or holders that are loaded and unloaded by robots. This has been demonstrated for the deposition of hard, amorphous carbon [102], where even a small bias of order 100 V is very important (more on carbon in section 8.10).

There is, however, a general preference for substrate biasing because shifting the plasma potential to very high positive values can have undesirable side effects, namely unwanted sputtering from all grounded components, such as chamber walls. Moreover, there is the possibility that high positive plasma potential causes arcing from the relatively negative components of the system. Arc spots may appear on the chamber wall, producing metal plasma of the wall material, which could hardly be the intention of the operator.

8.9 Arcing and Arc Suppression

Let us pick up the remark on arcing in the last section. Arcing occurs when the local electrical field strength at the substrate or other negatively biased surface exceeds a threshold value of about 10^8 V/m. "Negatively biased" refers to the general understanding according to Eq. (8.26), and in that sense arcing may occur on grounded parts too.

The actual value of the critical surface field strength, at which arcing starts, depends on the material and surface conditions (cf. Chapter 3). Even a relatively low bias voltage can lead to arcing because the voltage drops across the thin sheath and is not evenly spread across the substrate–wall or substrate–source distance. In the presence of a dense plasma, the sheath can be very thin, e.g., a millimeter or much less (!), and therefore the surface field strength can be unexpectedly high. At the high surface field, field emission of electrons from local emission centers can run away, i.e., become unstable due to thermal enhancement of the emission. As a result, electron emission can switch into the explosive mode, and indeed the same spot processes as on the designated arc cathode can occur. Arcing is the unintentional formation of cathode spots on relatively negative parts such as a negatively biased substrate or probe.

The dense plasma expanding from the cathode spots causes an electric short of the sheath voltage; one often speaks of the "breakdown" of the bias voltage. A high current is observed, which is, together with a low voltage, a "fingerprint" of breakdown and arc spot formation. Substrate arcing can be avoided, or at least its likelihood can be reduced, by using pulsed bias, lower bias voltage, lower plasma density, or a combination thereof.

Modern bias supplies are usually equipped with fast arc suppression. That means, a fast internal circuit senses if the bias current has suddenly increased

and/or the voltage has dropped. If that is the case, the supply is briefly interrupted such that the arc spot can extinguish and the crater cool (typically some milliseconds), and the voltage is then reapplied to continue the process with as little disturbance and interruption to the overall process as possible.

8.10 Case Study: Tetrahedral Amorphous Carbon (ta-C)

All of the above-mentioned phenomena and properties can be found in the energetic condensation of carbon ions, which generally leads to hard, amorphous carbon (a-C) films. The case of carbon is, on the one hand, typical in terms of ion energy dependence of stress and stress-related properties and, on the other hand, special because carbon atoms can bond in various hybridizations (sp^1, sp^2, sp^3), leading to a variety of materials. Taking into account that carbon–carbon hybridization depends on the deposition conditions and that other elements can be incorporated, such as hydrogen, nitrogen, and metals, we realize that a whole family of diamond-like carbon (DLC) materials exists. DLC is indeed a term widely used and in many cases refers to hydrogenated carbon or a-C:H. The films with a dominance of sp^3 hybrids are referred to as tetrahedral a-C films, or ta-C [104], a term originally introduced by McKenzie[1] and co-workers in the early 1990s [104, 105].

Much has been published about DLC, see for example Robertson's review [106], and therefore we can here focus the discussion to materials formed by (filtered) cathodic arcs.

Historically, Heinz Schmellenmeier in Potsdam, in the 1950s of East Germany, studied discharges with acetylene and found that *a shiny black layer is formed on the cathode, which has initially great adherence but delaminates after hours or days . . .. This layer is extraordinarily hard. With low loads of 10 and 20 g, the layer will not be attacked by a sharp diamond tip. . .this material is X-ray amorphous* . . . [107]. He published his results in German only and they were largely ignored by the scientific community. Whereas Schmellenmeier very likely produced a-C:H, hydrogen-free carbon (a-C) was synthesized in the 1950s using "arc-evaporation" in vacuum [108, 109]. The goal was to fabricate thin conducting films supporting specimen for electron microscopy. A closer look at those publications [108, 109] reveals that the evaporation process most likely involved a thermionic arc, if any arc, and that the films must have contained significant

[1] Dave McKenzie wanted to use "amorphous diamond" to describe DLC with very high sp^3 content in a manuscript to *Physical Review Letters* but the reviewer insisted that diamond is always crystalline. So, there was a need to invent a new term, and "ta-C" was born (the reviewer would probably also have rejected manuscripts on liquid crystals). Today, both terms "ta-C" and "amorphous diamond" are used, the latter especially in the patent literature.

amounts of both sp^2 and sp^3 bonds. It took another 10 plus years to (re)discover diamond-like carbon [110], this time with widespread recognition.

Tetrahedral amorphous carbon, ta-C, is most readily produced using filtered cathodic arcs, as was shown in the late 1970s [111, 112, 113]. Using graphite as the feedstock material (cathode), carbon plasma is produced that contains mostly singly charged ions with a most-likely kinetic energy of about 20 eV (cf. Appendix B). Filtering reduces macroparticles and neutrals and may cause shifts of the ion energy distribution function [114]. The properties of the diamond-like material depend largely on the acceleration that carbon ions experience in the sheath to the substrate, which can be controlled via substrate bias [115] or plasma bias [102]. Deposition is generally done at room temperature because high temperature degrades the "diamond-likeness" of the material [116, 117, 118].

When processing occurs in high vacuum with relatively low partial pressure of water, the film material does not contain much hydrogen or any other elements, and one can speak of "hydrogen-free" amorphous carbon, a-C. It contains a mixture of carbon atoms with sp^3 and sp^2 hybridization. While the sp^3 hybrids determine the diamond-like properties such as high hardness and stress, high Young's modulus, chemical inertness, and a wide optical band gap [119], the sp^2 hybrids are largely responsible for the electronic and optical properties because the π states lie closest to the Fermi level [120].

The structure and properties of ta-C is mainly governed by the ratio of sp^3 to sp^2 bonds but additional features like the distortion of bond distances and angles compared to ideal graphite and diamond structures, distribution of ring sizes, and arrangement of the sp^2 hybrids also play a role [120, 121]. Films of ta-C can be deposited to thickness of only 2 nm, still preserving diamond-like and protective properties (cf. Chapter 10).

Even early investigations [104, 111, 112, 122, 123, 124, 125, 126, 127, 128, 129, 130, 131] showed that ta-C exhibits a maximum in many parameters such as hardness, Young's modulus, intrinsic stress , optical band gap, when the films were grown with the condensing ions having kinetic energy in the range 50–200 eV. This was shown to be correlated with a maximum of the sp^3/sp^2 ratio. Besides ion kinetic energy, the substrate temperature is critical for the sp^3 content: lower temperature leads to higher sp^3 content [123, 132], which was recently confirmed for ta-C films made by the pulsed high-current arc and by the laser-triggered pulsed arc ("Laser-Arc," Figure 8.20).

The theoretical interpretation on the formation conditions was subject to an intense debate (subplantation, ion pressure induced, density induced, compressive stress induced, etc.) which in part was a discussion on semantics rather than on physics. Much can be readily seen as directly related to the stress formation and relief model described in Section 8.4.2.

Molecular dynamics (MD) and high-resolution materials characterization have led to a general understanding of ta-C, or more generally a-C and other forms of DLC materials. Jäger and co-workers [134, 135] used the analytic hydrocarbon potential of Brenner with an increased C–C interaction cutoff

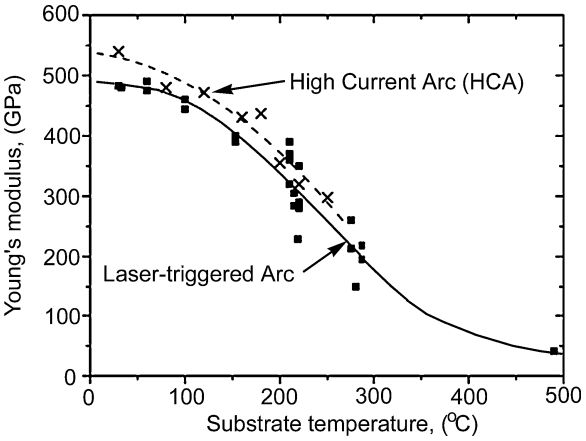

Fig. 8.20. Young's modulus of ta-C films as a function of the substrate temperature; films made by the high-current arc (HCA) and by the Laser-Arc of the of Fraunhofer Society's IWS institute. (Adapted from Scheibe [133])

value [136] to simulate the growth of films with a thickness of up to 10 nm for ion energies $E_{ion} = 10–80$ eV and for substrate temperatures T_s ranging from 100 to 900 K. Their results for the "bulk" properties of the computed ta-C films as well as structure and roughness of their sp^2-rich surface layers agreed qualitatively with experiment. The sp^3 fraction increased with ion energy, resulting in a highly sp^3-bonded ta-C with high compressive stress for $E_{ion} > 30$ eV as long as the substrate temperature was relatively low, up to room temperature.

Molecular-dynamics simulations by Uhlmann and co-workers [11] were based on interatomic forces derived from an efficient density-functional-based tight-binding scheme. In agreement with the work cited above, they found that surface processes are dominant for deposition below 30 eV, while subsurface processes govern the structure formation for higher energies, leading to an sp^3-rich, dense layer below a defective surface layer.

Extending Jäger's work [134], Gago and co-workers [120] focused on the role of sp^2 bond and bond clusters in the ta-C matrix. The simulation showed that the sp^2 hybrids are mainly arranged in chains or pairs. Coalescence of sp^2 clusters occurs for medium sp^2 fractions and the pronounced formation of rings when the sp^2 fraction exceeds 80%.

A critical part of MD simulations is the choice of interaction potential. To model ta-C growth, Marks [137] introduced an environment-dependent interaction potential suitable for studying disordered systems. He used ab initio data to parameterize the functional form, which includes environment dependence in the pair and triple terms, and generalized aspherical coordination describing dihedral rotation and non-bonded π-repulsion. These MD calculations are well suited to study film growth at relatively low energy of 40 eV, as discussed by Marks [137], and also at higher energy when numerous bonds are

broken and (re)established upon energetic ion impact (thermal spike), as mentioned before.

Experimentally it is known that ta-C is not stable at high temperature. The computation predicts a critical temperature T_c beyond which the kinetic energy of the atoms in the solid is sufficiently large to overcome the barrier in cohesive energy between the atoms in the ta-C matrix and the more stable graphite-like films. The transition between synthesizing ta-C and a rather graphitic material is relatively sharp; the simulation gave a growth temperature of about 200°C beyond which the material is graphitic. Most experiments are concerned with the thermal stability of the ta-C in air for films grown at low (room) temperature. It was found that ta-C is stable up to 400°C if the film had high sp^3 content at the beginning of the test, whereas a-C films with lower sp^3 content ($< 50\%$) already lost mass at lower annealing temperatures[2] [138]. Raman spectroscopy of films with different hydrogen content [118] showed clearly that the hydrogen-free ta-C is much more stable, up to 600°C in that study, than the hydrogenated material, a-C:H, which deteriorated at 400°C.

Repeated, rapid thermal annealing can be used to remove most of the compressive stress from ta-C films. Friedman and colleagues showed that when depositing a 100- to 200-nm-thick ta-C film, the high stress of typically 6–8 GPa can be relieved by heating to 600°C for 2 min [116]. Raman and electron energy-loss spectroscopy (EELS) from single-layer-annealed specimens showed only subtle changes from the as-grown films. Thick layers (> 1 μm) can be grown by using many subsequent deposition and annealing steps.

Thick hard carbon films can also be obtained using the effects of ions on stress generation and relief (Section 8.4.2). This point is important because a frequent failure mode for hard coatings is spontaneous delamination that occurs when the strain energy exceeds the adhesion energy. As the film grows thicker, the strain energy increases while the adhesion energy remains the same, inevitably leading to delamination when a certain thickness is reached. Tarrant and coworkers [139, 140] perfected the concept of stress relief by ion-induced thermal spikes and applied 20-keV bias pulses to the substrate that was exposed to carbon plasma from a filtered arc source, thereby creating a low-duty-cycle, high-energy ion bombardment of the growing hard carbon film. Films thicker than 4.5 μm have been obtained in this way.

Carbon shows both the common effects of stress generation (ion energy ~50–200 eV) and stress relief (ion energy > 500 eV). This can be nicely illustrated using the pulsed biasing (MePIIID) technique mentioned in Section 8.6. For example, keeping the bias pulses short and constant at 20 μs, Bilek and coworkers [141] varied the bias voltage amplitude and frequency, demonstrating that a smaller number of higher energy ions are equivalent to a higher number of

[2] A very early annealing study in 1957 showed that a-C of low sp^3 content is not stable as soon as the heating exceeded room temperature [109].

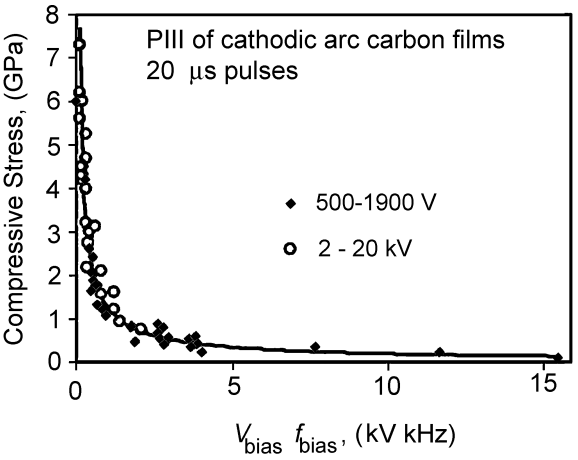

Fig. 8.21. Compressive stress of hard carbon films grown by a filtered DC cathodic arc with pulsed substrate bias: the bias pulse duration was constant at 20 μs, while the bias amplitude and frequency have been varied. The same curve can also be displayed as a function of the bias voltage times duty cycle. (Adapted from Figure 2 of [141], see also Figure 2 of [59])

lower energy ions as long as all of those ions are energetic enough to cause stress-relieving thermal spikes (Figure 8.21).

Stress of the as-deposited films can also be relieved by post-growth ion irradiation. Lee and co-workers at Los Alamos [142] used Xe, Ar, Ne, and C ion beams and monitored the stress relief in situ as a function of ion fluence via the curvature change of a thin substrate. Using Stoney's equation [143],

$$\Delta\sigma = \frac{Y_s}{1 - \nu_s} \frac{h_s^2}{6 h_f} \left(\frac{1}{R} - \frac{1}{R_0} \right), \tag{8.27}$$

the change of stress $\Delta\sigma$ can be readily calculated from the change of the curvature radius from R_0 to R. Y_s, ν_s, and h_s are Young's modulus, the Poisson ratio, and the thickness of the substrate, respectively, and h_f is the film thickness. They found that the samples initially showed a rapid decrease in compressive stress, with the rate of change being larger for the heavier ion species. The reduction in compressive film stress was correlated with a reduction in hardness and Young's modulus.

Another approach to reducing stress is to incorporate suitable elements, such as silicon. For example, Monteiro [144] introduced up to 6% Si and found crystalline metal carbides dispersed in an amorphous carbon matrix. Druz et al. [145] found similar effects for very thin, nitrogen-doped films.

Application of high-voltage pulses changes the sp^3/sp^2 ratio and of course all the properties that are based on or affected by that ratio. This is most vividly

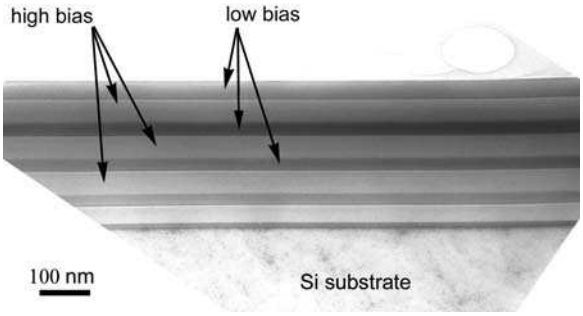

Fig. 8.22. Cross-section TEM of a carbon–carbon multilayer produced by pulsed cathodic carbon arcs with pulsed bias (i.e., MePIIID): the *dark*, *denser* layers were deposited with a pulsed bias of –100 V while the *lighter*, *less dense* layers were made with –2,000 V pulsed bias. (Adapted from [146])

illustrated by a deposition process where carbon ion generation is ongoing in a constant manner while the substrate bias is periodically enhanced and lowered. This leads to a carbon–carbon multilayer that is clearly visible in the TEM of Figure 8.22. In the multilayer structure, residual stress was reduced while hardness and Young's modulus were less affected, compared to a monolithic film of the same total thickness [146].

The Nanyang Technological University group [147] studied the various options brought forward to reduce stress (i.e., rapid thermal annealing, foreign atom incorporation, energetic ion bombardment via pulsed biasing, and multilayer formation) with the goal to make thick (> 1 μm) films suitable for microelectromechanical system (MEMS) applications. They concluded that about 80% of the as-deposited stress can be eliminated by rapid thermal annealing (RTA) to 200°C for 2 min in air; incorporation of 1.7 at.% of Al combined with RTA to 600°C for 2 min can reduce the stress to the low value of 200 MPa, while pulsed biasing is most effective in reducing [116, 117, 118] stress by over 90%. Therefore, pulsed biasing was recommended as the most effective and economical approach to stress relief.

Because of its great importance, we will revisit ta-C and related materials in Chapter 10, Applications.

References

1. Colligon, J.S., Energetic condensation: processes, properties, and products, *J. Vac. Sci. Technol. A* **13**, 1649–1657, (1995).
2. Brown, I.G., Cathodic arc deposition of films, *Ann. Rev. Mat. Sci.* **28**, 243–269, (1998).

3. Monteiro, O.R., Thin film synthesis by energetic condensation, *Ann. Rev. Mat. Sci.* **31**, 111–137, (2001).
4. Anders, A., Energetic deposition using filtered cathodic arc plasmas, *Vacuum* **67**, 673–686, (2002).
5. Greene, J.E., "Nucleation, film growth, and microstructural evolution," in *Handbook of Deposition Technologies for Films and Coatings*, Bunshah, R.F., (Ed.), 2 nd ed., pp. 681–739, Noyes, Westwood, NJ, (1994).
6. Hubler, G.K. and Sprague, J.A., Energetic particles in PVD technology: particle-surface interaction processes and energy-particle relationships in thin film deposition, *Surf. Coat. Technol.* **81**, 29–35, (1996).
7. Xu, S. and Evans, B.L., Nucleation and growth of ion beam sputtered metal films, *J. Mat. Sci.* **27**, 3108–3117, (1992).
8. Gill, S.P.A., Self-organised growth on strained substrates: the influence of anisotropic strain, surface energy and surface diffusivity, *Thin Solid Films* **423**, 136–145, (2003).
9. Petrov, I., Barna, P.B., Hultman, L., and Greene, J.E., Microstructural evolution during film growth, *J. Vac. Sci. Technol. A* **21**, S117–S128, (2003).
10. Nastasi, M., Mayer, J.W., and Hirvonen, J.K., *Ion-Solid Interactions*. Cambridge University Press, Cambridge, UK, (1996).
11. Uhlmann, S., Fraunheim, T., and Lifshitz, Y., Molecular-dynamics study of the fundamental processes involved in subplantation of diamondlike carbon, *Phys. Rev. Lett.* **81**, 641–644, (1998).
12. Lifshitz, Y., Kasai, S.R., Rabalais, J.W., and Eckstein, W., Subplantation model for film growth from hyperthermal species, *Phys. Rev. B* **41**, 10468–10480, (1990).
13. Ronning, C., Ion-beam synthesis and growth mechanism of diamond-like materials, *Appl. Phys. A* **77**, 39–50, (2003).
14. Carlson, T.A., Nestor, C.W., Wasserman, N., and McDowell, J.D., Calculated ionization potentials for multiply charges ions, *Atomic Data* **2**, 63–99, (1970).
15. Lide, D.R., (ed.) *Handbook of Chemistry and Physics, 81st Edition*, CRC Press, Boca Raton, New York, (2000).
16. Burgdörfer, J. and Meyer, F., Image acceleration of multiply charged ions by metallic surfaces, *Phys. Rev. A* **47**, R20–R22, (1993).
17. Hägg, L., Reinhold, C.O., and Burgdörfer, J., Energy gain of highly charged ions in front of LiF, *Nucl. Instrum. Meth. Phys. Res. B* **125**, 133–137, (1997).
18. Winter, H. and Aumayr, F., Interaction of slow HCI with solid surfaces, *Physica Scripta* **T92**, 15–21, (2001).
19. Schenkel, T., Barnes, A.V., Niedermayr, T.R., Hattass, M., Newman, M.W., Machicoane, G.A., McDonald, J.W., Hamza, A.V., and Schneider, D.H., Deposition of potential energy by slow, highly charged ions, *Phys. Rev. Lett.* **83**, 4273–4276, (1999).
20. Al-Nimr, M.A. and Arpaci, V.S., Picosecond thermal pulses in thin metal films, *J. Appl. Phys.* **85**, 2517–2521, (1999).
21. Musil, J., Hard and superhard nanocomposite coatings, *Surf. Coat. Technol.* **125**, 322–330, (2000).
22. Anders, A., Atomic scale heating in cathodic arc plasma deposition, *Appl. Phys. Lett.* **80**, 1100–1102, (2002).
23. Elsholz, F., Meixner, M., and Schöll, E., Kinetic Monte Carlo simulation of self-organized pattern formation in thin film deposition, *Nucl. Instrum. Meth. Phys. Res. B* **202**, 249–254, (2003).

24. Anders, A. and Yushkov, G.Y., Measurements of secondary electrons emitted from conductive substrates under high-current metal ion bombardment, *Surf. Coat. Technol.* **136**, 111–116, (2001).
25. Hagstrum, H.D., Auger ejection of electrons from tungsten by noble gas ions, *Phys. Rev.* **96**, 325–335, (1953).
26. Eder, H., Messerschmidt, W., Winter, H., and Aumayr, F., Electron emission from clean gold bombardment by slow Au^{q+} (q = 1–3) ions, *J. Appl. Phys.* **87**, 8198–8200, (2000).
27. Winter, H., Aumayr, F., and Lakits, G., Recent advances in understanding particle-induced electron emission from metal surfaces, *Nucl. Instrum. Meth. Phys. Res. B* **58**, 301–308, (1991).
28. Winter, H., Eder, H., Aumayr, F., Lorincik, J., and Sroubek, Z., Slow-ion induced electron emission from clean metal surfaces: "Subthreshold kinetic emission" and "potential excitation of plasmons", *Nucl. Instrum. Meth. Phys. Res. B* **182**, 15–22, (2001).
29. Anders, A., Observation of self-sputtering in energetic condensation of metal ions, *Appl. Phys. Lett.* **85**, 6137–6139, (2004).
30. Kress, J.D., Hanson, D.E., Voter, A.F., Liu, C.L., Liu, X.Y., and Coronell, D.G., Molecular dynamics simulation of Cu and Ar ion sputtering of Cu (111) surfaces, *J. Vac. Sci. Technol. A* **17**, 2819–2825, (1999).
31. Hanson, D.E., Stephens, B.C., Saravanan, C., and Kress, J.D., Molecular dynamics simulations of ion self-sputtering of Ni and Al surfaces, *J. Vac. Sci. Technol. A* **19**, 820–825, (2001).
32. Eckstein, W., *Computer Simulation of Ion-Solid Interactions*. Springer-Verlag, Berlin, (1991).
33. Hou, M. and Eckstein, W., Statistical properties of sputtering from individual atomic collisions cascades in solids, *J. Appl. Phys.* **71**, 3975–3980, (1992).
34. Ziegler, J.F., Biersack, J.P., and Littmark, U., *The Stopping and Range of Ions in Solids*. Pergamon Press, New York, (1985).
35. Nastasi, M., Möller, W., and Ensinger, W., "Ion implantation and thin-film deposition," in *Handbook of Plasma Immersion Ion Implantation and Deposition*, Anders, A., (Ed.). pp. 125–241, Wiley, New York, (2000).
36. Abrams, C.F. and Graves, D.B., Cu sputtering and deposition of off-normal, near-threshold Cu^{+} bombardment: Molecular dynamics simulation, *J. Appl. Phys.* **86**, 2263–2267, (1999).
37. Coronell, D.G., Hanson, D.E., Voter, A.F., Liu, C.L., Liu, X.Y., and Kress, J.D., Molecular dynamics-based ion-surface interaction models for ionized physical vapor deposition feature scale simulations, *Appl. Phys. Lett.* **73**, 3860–3862, (1998).
38. Burgmann, F.A., McCulloch, D.G., Ryves, L., Lim, S.H.M., McKenzie, D., and Bilek, M.M.M., Defects at interfaces are the key to enhancing the hardness in Al/W multilayers, *J. Appl. Phys.*, submitted, under review, (2008).
39. Tarrant, R.N., Bilek, M.M.M., Pigott, J., and McKenzie, D.R., Plasma transport and optical flares in high-density plasmas produced from a pulsed cathodic arc, *Surf. Coat. Technol.* **186**, 10–16, (2004).
40. Movchan, B.A. and Demchishin, A.V., Investigation of the structure and properties of thick vacuum-deposited films of nickel, titanium, tungsten, alumina and zirconium dioxide, *Fizika Metallov i Metallovedenie (Physics of Metals and Metallography)* **28**, 653–660, (1969).
41. Thornton, J.A., Influence of apparatus geometry and deposition conditions on the structure and topography of thick sputtered coatings, *J. Vac. Sci. Technol.* **11**, 666–670, (1974).

42. Messier, R., Giri, A.P., and Roy, R.A., Revised structure zone model for thin film physical structure, *J. Vac. Sci. Technol. A* **2**, 500–503, (1984).
43. Mausbach, M., Microstructure of copper films condensed from a copper plasma with ion energies between 2 and 150 eV, *Surf. Coat. Technol.* **74–75**, 264–272, (1995).
44. Oettel, H., Wiedemann, R., and Preiler, S., Residual stresses in nitride hard coatings prepared by magnetron sputtering and arc evaporation, *Surf. Coat. Technol.* **74–75**, 273–278, (1995).
45. Vlasveld, A.C., Harris, S.G., Doyle, E.D., Lewis, D.B., and Munz, W.D., Characterisation and performance of partially filtered arc TiAlN coatings, *Surf. Coat. Technol.* **149**, 217–223, (2002).
46. Bunshah, R.F., (ed.) *Handbook of Deposition Technologies for Films and Coatings: Science, Technology, and Applications*, Noyes, Park Ridge, N.J., (1994).
47. Mattox, D.M., *Handbook of Physical Vapor Deposition (PVD) Processing*. Noyes Publications, Park Ridge, N.J., (1998).
48. Anders, A., (ed.) *Handbook of Plasma Immersion Ion Implantation and Deposition*. John Wiley & Sons, New York, (2000).
49. Bilek, M.M.M. and McKenzie, D.R., A comprehensive model of stress generation and relief processes in thin films deposited with energetic ions, *Surf. Coat. Technol.* **200**, 4345–4354, (2006).
50. Bilek, M.M.M., Tarrant, R.N., McKenzie, D.R., Lim, S.H.N., and McCulloch, D.G., Control of stress and microstructure in cathodic arc deposited films, *IEEE Trans. Plasma Sci.* **31**, 939–944, (2003).
51. Lim, S.H.N., McCulloch, D.G., Bilek, M.M.M., and McKenzie, D.R., Minimisation of intrinsic stress in titanium nitride using a cathodic arc with plasma immersion ion implantation, *Surf. Coat. Technol.* **174–175**, 76–80, (2003).
52. Davis, C.A., A simple model for the formation of compressive stress in thin films by ion bombardment, *Thin Solid Films* **226**, 30–34, (1993).
53. Windischmann, H., An intrinsic stress scaling law for polycrystalline thin films prepared by ion beam sputtering, *J. Appl. Phys* **62**, 1800–1807, (1987).
54. Marks, N.A., Evidence for subpicosecond thermal spikes in the formation of tetrahedral amorphous carbon, *Phys. Rev. B* **56**, 2441, (1997).
55. Bilek, M.M.M., McKenzie, D.R., and Moeller, W., Use of low energy and high frequency PBII during thin film deposition to achieve relief of intrinsic stress and microstructural changes, *Surf. Coat. Technol.* **186**, 21–28, (2004).
56. Abendroth, B., Gago, R., Kolitsch, A., and Moller, W., Stress measurement and stress relaxation during magnetron sputter deposition of cubic boron nitride thin films, *Thin Solid Films* **447–448**, 131–135, (2004).
57. Yin, Y., McKenzie, D., and Bilek, M., Intrinsic stress induced by substrate bias in amorphous hydrogenated silicon thin films, *Surf. Coat. Technol.* **198**, 156–160, (2005).
58. Houska, J., Capek, J., Vlcek, J., Bilek, M.M.M., and McKenzie, D.R., Bonding statistics and electronic structure of novel Si–B–C–N materials: Ab initio calculations and experimental verification, *J. Vac. Sci. Technol. A* **25**, 1411–1416, (2007).
59. Bilek, M.M.M., Verdon, M., Ryves, L., Oates, T.W.H., Ha, C.T., and McKenzie, D.R., A model for stress generation and stress relief mechanisms applied to as-deposited filtered cathodic vacuum arc amorphous carbon films, *Thin Solid Films* **482**, 69–73, (2005).
60. Hofsäss, H., Feldermann, H., Merk, R., Sebastian, M., and Ronning, C., Cylindrical spike model for the formation of diamondlike thin films by ion deposition, *Appl. Phys. A: Mater. Sci. Process.* **66**, 153–181, (1998).

61. Krohn, M., Meyer, K.-P., and Bethge, H., Epitaxy by vacuum arc evaporation, *J. Crystal Growth* **64**, 326–332, (1983).
62. Byon, E., Oates, T.H., and Anders, A., Coalescence of nanometer silver islands on oxides grown by filtered cathodic arc deposition, *Appl. Phys. Lett.* **82**, 1634–1636, (2003).
63. Oates, T., McKenzie, D., and Bilek, M., Percolation threshold in ultrathin titanium films determined by in-situ spectroscopic ellipsometry, *Phys. Rev. B* **70**, 195406, (2004).
64. Arwin, H. and Aspnes, D.E., Unambiguous determination of thickness and dielectric function of thin films by spectroscopic ellipsometry, *Thin Solid Films* **113**, 101–113, (1984).
65. Veprek, S., The search for novel, superhard materials, *J. Vac. Sci. Technol. A* **17**, 2401–2420, (1999).
66. Andersson, J.-O. and Sundman, B., Thermodynamic properties of the Cr–Fe system, *Calphad* **11**, 83–92, (1987).
67. Aksenov, I.I., Belous, V.A., Padalka, V.G., and Khoroshikh, V.M., Producing coatings with aluminium oxide base from separated flow of vacuum arc plasma, *Fizika i Khimiya Obrabotki Materialov*, 89–93, (1977).
68. Bergman, C., "Arc plasma physical vapor deposition," 28th Annual SVC Technical Conference, Philadelphia, PA, 175–191, (1985).
69. Münz, W.-D., Schulze, D., and Hauzer, F.J.M., A new method for hard coatings – ABS (arc bond sputtering), *Surf. Coat. Technol.* **50**, 169–178, (1992).
70. Schönjahn, C., Ehiasarian, A.P., Lewis, D.B., New, R., Münz, W.-D., Twesten, R.D., and Petrov, I., Optimization of in-situ substrate treatment in a cathodic arc plasma: A study by TEM and plasma diagnostics, *J. Vac. Sci. Technol. A* **19**, 1415–1420, (2001).
71. Ehiasarian, A.P., Hovsepian, P.E., Hultman, L., and Helmersson, U., Comparison of microstructure and mechanical properties of chromium nitride-based coatings deposited by high power impulse magnetron sputtering and by the combined steered cathodic arc/unbalanced magnetron technique, *Thin Solid Films* **457**, 270–277, (2004).
72. Lewis, D.B., Reitz, D., Wüstefeld, C., Ohser-Wiedemann, R., Oettel, H., Ehiasarian, A.P., and Hovsepian, P.E., Chromium nitride/niobium nitride nano-scale multilayer coatings deposited at low temperature by the combined cathodic arc/unbalanced magnetron technique, *Thin Solid Films* **503**, 133–142, (2006).
73. Wang, H.W., Stack, M.M., Lyon, S.B., Hovsepian, P., and Munz, W.D., Preferential erosive wear of droplet particles for cathodic arc/unbalanced magnetron sputtering CrN/NbN superlattice PVD coatings, *J. Mat. Sci. Lett.* **20**, 547–550, (2001).
74. Wang, H.W., Stack, M.M., Lyon, S.B., Hovsepian, P., and Munz, W.D., Wear associated with growth defects in combined cathodic arc/unbalanced magnetron sputtered CrN/NbN superlattice coatings during erosion in alkaline slurry, *Surf. Coat. Technol.* **135**, 82–90, (2000).
75. Wang, H.W., Stack, M.M., Hovsepian, P., and Munz, W.D., Macroparticle induced corrosion for arc bond sputtering CrN/NbN superlattice coatings, *J. Mat. Sci. Lett.* **20**, 1995–1997, (2001).
76. Lembke, M.I., Lewis, D.B., and Münz, W.D., Localised oxidation defects in TiAlN/CrN superlattice structured hard coatings grown by cathodic arc/ unbalanced magnetron deposition on various substrate materials, *Surf. Coat. Technol.* **125**, 263–268, (2000).

77. Ehiasarian, A.P., Anders, A., and Petrov, I., Combined filtered cathodic arc etching pretreatment–magnetron sputter deposition of highly adherent CrN films, *J. Vac. Sci. Technol. A* **25**, 543–550, (2007).
78. Conrad, J.R., Radtke, J.L., Dodd, R.A., Worzala, F.J., and Tran, N.C., Plasma source ion-implantation technique for surface modification, *J. Appl. Phys.* **62**, 4591–4596, (1987).
79. Brown, I.G., Godechot, X., and Yu, K.M., Novel metal ion surface modification technique, *Appl. Phys. Lett.* **58**, 1392–1394, (1991).
80. Anders, A., From plasma immersion ion implantation to deposition: a historical perspective on principles and trends, *Surf. Coat. Technol.* **156**, 3–12, (2002).
81. Mattox, D.M., Film deposition using accelerated ions, *Electrochem. Technol.* **2**, 295–298, (1964).
82. Anders, A., Metal plasma immersion ion implantation and deposition: a review, *Surf. Coat. Technol.* **93**, 157–167, (1997).
83. Anders, A., Anders, S., Brown, I.G., Dickinson, M.R., and MacGill, R.A., Metal plasma immersion ion implantation and deposition using vacuum arc plasma sources, *J. Vac. Sci. Technol. B* **12**, 815–820, (1994).
84. Mukherjee, S., Reuther, H., Prokert, F., Richter, E., and Moeller, W., Substrate bias effects in plasma immersion ion implantation assisted deposition from a TiAl cathodic arc, *Surf. Coat. Technol.* **160**, 93–98, (2002).
85. Mukherjee, S., Prokert, F., Richter, E., and Moeller, W., Compressive stress, preferred orientation and film composition in Ti-based coatings developed by plasma immersion ion implantation-assisted deposition, *Surf. Coat. Technol.* **186**, 99–103, (2004).
86. Ensinger, W., Plasma immersion ion implantation for metallurgical and semiconductor research and development, *Nucl. Instrum. Meth. Phys. Res. B* **120**, 270–281, (1996).
87. Ikehata, T., Shioya, K., Araki, T., Sato, N.Y., Mase, H., and Yukimura, K., Sheath formation and ion flux distribution inside the trench in plasma-based ion implantation, *Nucl. Instrum. Meth. Phys. Res. B* **206**, 772–776, (2003).
88. Anders, A., Width, structure, and stability of sheaths in metal plasma immersion ion implantation: measurements and analytical considerations, *Surf. Coat. Technol.* **136**, 85–92, (2001).
89. Ma, X., Tang, G., Sun, M., and Yukimura, K., Characteristics of TiN films deposited on a trench-shaped sample prepared by plasma-based ion implantation and deposition, *Surf. Coat. Technol.* **196**, 100–103, (2005).
90. Yukimura, K., Ma, X., and Ikehata, T., Ion sheath evolution and current characteristics for a trench immersed in a titanium cathodic arc discharge, *Surf. Coat. Technol.* **186**, 73–76, (2004).
91. Tian, X.B., Yang, S.Q., Huang, Y.X., Gong, C.Z., Xu, G.C., Fu, R.K.Y., and Chu, P.K., Two-dimensional numerical simulation of non-uniform plasma immersion ion implantation, *Surf. Coat. Technol.* **186**, 47–52, (2004).
92. Qian, X.Y., Cheung, N.W., Lieberman, M.A., Brennan, R., Current, M.I., and Jha, N., Conformal implantation for trench doping with plasma immersion ion implantation, *Nucl. Instrum. Methods B* **55**, 898–901, (1991).
93. Chen, U.-S. and Shih, H.C., Characterization of copper metallization for interconnect by 90[deg]-bend electromagnetic filtered vacuum arc, *Nucl. Instrum. Meth. Phys. Res. B* **237**, 477–483, (2005).
94. Monteiro, O.R., Novel metallization technique for filling 100-nm-wide trenches and vias with very high aspect ratio, *J. Vac. Sci. Technol. B* **17**, 1094–1097, (1999).

95. Bohm, D., "Minimum ionic kinetic energy for a stable sheath," in *The Characteristics of Electrical Discharges in Magnetic Fields*, Guthrie, A. and Wakerling, R.K., (Eds.). pp. 77–86, McGraw-Hill, New York, (1949).
96. Riemann, K.-U., The Bohm criterion and sheath formation, *J. Phys. D: Appl. Phys.* **24**, 493–518, (1991).
97. Alterkop, B., On a sheath between a plasma and conducting surface, *J. Appl. Phys.* **95**, 1650–1655, (2004).
98. Vetter, J. and Perry, A.J., Advances in cathodic arc technology using electrons extracted from the vacuum arc, *Surf. Coat. Technol.* **61**, 305–309, (1993).
99. Berger, M., Karlsson, L., Larsson, M., and Hogmark, S., Low stress TiB_2 coatings with improved tribological properties, *Thin Solid Films* **401**, 179–186, (2001).
100. Richter, F., Peter, S., Filippov, V.B., Flemming, G., and Kühn, M., Characteristics of the cathodic arc discharge with a hot boron cathode, *IEEE Trans. Plasma Sci.* **27**, 1079–1083, (1999).
101. Anders, A. and Oks, E., Charge-state-resolved ion energy distribution functions of cathodic vacuum arcs: A study involving the plasma potential and biased plasmas, *J. Appl. Phys.* **101**, 043304-1-6, (2007).
102. Anders, A., Pasaja, N., Lim, S.H.N., Petersen, T.C., and Keast, V.J., Plasma biasing to control the growth conditions of diamond-like carbon, *Surf. Coat. Technol.* **201**, 4628–4632, (2007).
103. Anders, A., Brown, I.G., MacGill, R.A., and Dickinson, M.R., Vacuum-spark metal ion source based on a modified Marx generator, *IEEE Trans. Plasma Sci.* **25**, 718–721, (1997).
104. McKenzie, D.R., Muller, D., Pailthorpe, B.A., *et al.*, Properties of tetrahedral amorphous carbon prepared by vacuum arc deposition, *Diamond Rel. Mat.* **1**, 51–59, (1991).
105. Gaskell, P.H., Saeed, A., Chieux, P., and McKenzie, D.R., Neutron-scattering studies of the structure of highly tetrahedral amorphous diamondlike carbon, *Phys. Rev. Lett.* **67**, 1286–1289, (1991).
106. Robertson, J., Diamond-like amorphous carbon, *Mat. Sci. Eng.* **R 37**, 129–281, (2002).
107. Schmellenmeier, H., Die Beeinflussung von festen Oberflächen durch eine ionisierte Gasatmosphäre, *Experimentelle Technik der Physik* **1**, 49–68, (1953).
108. Bradley, D.E., Evaporated carbon films for use in electron microscopy, *Brit. J. Appl. Phys.* **5**, 65–66, (1954).
109. Blue, M.D. and Danielson, G.C., Electrical properties of arc-evaporated carbon films, *J. Appl. Phys.* **28**, 583–586, (1957).
110. Aisenberg, S. and Chabot, R., Ion-beam deposition of thin films of diamondlike carbon, *J. Appl. Phys.* **42**, 2953–2958, (1971).
111. Strel'nitskii, V.E., Aksenov, I.I., Vakula, S.I., Padalka, V.G., and Belous, V.A., Properties of diamond-like carbon coating produced by plasma condensation, *Sov. Techn. Phys. Lett.* **4**, 546–547, (1978).
112. Vakula, S.I., Padalka, V.G., Strel'nitskii, V.E., and Usoskin, A.I., Optical properties of diamond-like carbon films, *Sov. Techn. Phys. Lett.* **5**, 573–574, (1979).
113. Aksenov, I.I., Vakula, S.I., Padalka, V.G., Strel'nitskii, V.E., and Khoroshikh, V.M., High-efficiency source of pure carbon plasma, *Sov. Phys. Techn. Phys.* **25**, 1164–1166, (1980).
114. Anders, A. and Yushkov, G.Y., Ion flux from vacuum arc cathode spots in the absence and presence of magnetic fields, *J. Appl. Phys.* **91**, 4824–4832, (2002).

115. Pharr, G.M., Callahan, D.L., McAdams, D., et al., Hardness, elastic modulus, and structure of very hard carbon films produced by cathodic-arc deposition with substrate bias, *Appl. Phys. Lett.* **68**, 779–781, (1996).
116. Friedmann, T.A., Sullivan, J.P., Knapp, J.A., Tallant, D.R., Follstaedt, D.M., Medlin, D.L., and Mirkarimi, P.B., Thick stress-free amorphous-tetrahedral carbon films with hardness near that of diamond, *Appl. Phys. Lett.* **71**, 3820–3822, (1997).
117. Monteiro, O.R., Ager III, J.W., Lee, D.H., Lo, R.Y., Walter, K.C., and Nastasi, M., Annealing of nonhydrogenated amorphous carbon films prepared by filtered cathodic arc, *J. Appl. Phys.* **88**, 2395–2399, (2000).
118. Tang, Z., Zhang, Z.J., Narumi, K., Xu, Y., Naramoto, H., Nagai, S., and Miyashita, K., Effect of mass-selected ion species on structure and properties of diamond-like carbon films, *J. Appl. Phys.* **89**, 1959–1964, (2001).
119. Robertson, J., Mechanical properties and coordinations of amorphous carbons, *Phys. Rev. Lett.* **68**, 220–223, (1992).
120. Gago, R., Vinnichenko, M., Jager, H.U., Belov, A.Y., Jimenez, I., Huang, N., Sun, H., and Maitz, M.F., Evolution of sp^2 networks with substrate temperature in amorphous carbon films: Experiment and theory, *Phys. Rev. B* **72**, 014120–014129, (2005).
121. Robertson, J. and O'Reilly, E.P., Electronic and atomic structure of amorphous carbon, *Phys. Rev. B* **35**, 2946–2957, (1987).
122. Strel'nitskii, V.E., Padalka, V.G., and Vakula, S.I., Properties of the diamond-like carbon film produced by the condensation of a plasma stream with an RF potential, *Sov. Phys.-Techn. Phys.* **23**, 222–224, (1978).
123. Cuomo, J.J., Pappas, D.L., Bruley, J., Doyle, J.P., and Saenger, K.K., Vapor deposition process for amorphous carbon films with sp^3 fractions approaching diamond, *J. Appl. Phys.* **70**, 1706–1711, (1991).
124. Fallon, P.J., Veerasamy, V.S., Davis, C.A., Robertson, J., Amaratunga, G.A.J., Milne, W.I., and Koskinen, J., Properties of filtered-ion-beam-deposited diamond-like carbon as a function of ion energy, *Phys. Rev. B* **48**, 4777–4782, (1993).
125. Robertson, J., Deposition mechanism for promoting sp^3 bonding in diamond-like carbon, *Diamond Rel. Mat.* **2**, 984–989, (1993).
126. Anders, S., Anders, A., Brown, I.G., Wei, B., Komvopoulos, K., Ager, J.W., and Yu, K.M., Effect of vacuum arc deposition parameters on the properties of amorphous carbon thin films, *Surf. Coat. Technol.* **68/69**, 388–393, (1994).
127. McKenzie, D.R., Muller, D., and Pailthorpe, B.A., Compressive-stress-induced formation of thin-film tetrahedral amorphous carbon, *Phys. Rev. Lett.* **67**, 773–776, (1991).
128. McKenzie, D.R., Yin, Y., Marks, N.A., Davis, C.A., Kravtchinskaia, E., Pailthorpe, B.A., and Amaratunga, G.A.J., Tetrahedral amorphous carbon properties and applications, *J. Non-Cryst. Solids* **166**, 1101–1106, (1993).
129. Lifshitz, Y., Roux, C.D., Boyd, K., Eckstein, W., and Rabalais, J.W., Analysis of carbon film growth from low energy ion beams using dynamic trajectory simulations and auger electron spectroscopy, *Nucl. Instr. Meth. B* **83**, 351–356, (1993).
130. Lifshitz, Y., Lempert, G.D., Rotter, S., Avigal, I., Uzan-Saguy, C., Kalish, R., Marton, D., and Rabalais, J.W., The effect of ion energy on the diamond-like graphitic sp^3/sp^2 nature of carbon films deposited by ion beams, *Diamond Rel. Mat.* **3**, 542–546, (1994).
131. Lossy, R., Pappas, D.L., Roy, R.A., Cuomo, J.J., and Sura, V.H., Filtered arc deposition of amorphous diamond, *Appl. Phys. Lett.* **61**, 171–173, (1992).

132. Cuomo, J.J., Pappas, D.L., Doyle, J.P., Bruley, J., and Saenger, K.L., "Comparison of techniques for deposition of carbon thin films," in *Plasma and Laser Processing of Materials*, Upadhya, K., (Ed.). pp. 165–174, The Minerals, Metals & Materials Society, (1991).
133. Scheibe, H.-J. and Schultrich, B., "Laser-arc process and technology for deposition of hard amorphous carbon (ta-C)," 47th Annual Technical Conference, Society of Vacuum Coaters, Dallas, TX, 501–508, (2004).
134. Jäger, H.U. and Belov, A.Y., ta-C deposition simulations: Film properties and time-resolved dynamics of film formation, *Phys. Rev. B* **68**, 024201–0242013, (2003).
135. Belov, A.Y. and Jäger, H.U., Simulation of the non-equilibrium processes for tetrahedral amorphous carbon: Deposition and structural relaxation, *Nucl. Instrum. Meth. Phys. Res. B* **202**, 242–248, (2003).
136. Jäger, H.U. and Albe, K., Molecular-dynamics simulation of steady-state growth of ion-deposited tetrahedral amorphous carbon films, *J. Appl. Phys.* **88**, 1129–1135, (2000).
137. Marks, N., Modelling diamond-like carbon with the environment-dependent interaction potential, *J. Phys.: Condensed Matter* **14**, 2901–2927, (2002).
138. Anders, S., Ager III, J.W., Pharr, G.M., Tsui, T.Y., and Brown, I.G., Heat treatment of cathodic arc deposited amorphous hard carbon films, *Thin Solid Films* **308–309**, 186–190, (1997).
139. Tarrant, R.N., Montross, C.S., and McKenzie, D.R., Combined deposition and implantation in the cathodic arc for thick film preparation, *Surf. Coat. Technol.* **136**, 188–191, (2001).
140. Tarrant, R.N., Fujisawa, N., Swain, M.V., James, N.L., McKenzie, D.R., and Woodard, J.C., PBII deposition of thick carbon coatings from a cathodic arc plasma, *Surf. Coat. Technol.* **156**, 143–148, (2002).
141. Bilek, M.M.M., McKenzie, D.R., Tarrant, R.N., et al., Practical plasma immersion ion implantation for stress regulation and treatment of insulators, *Contrib. Plasma Phys.* **44**, 465–471, (2004).
142. Lee, D.H., Fayelle, S., Walter, K.C., and Nastasi, M., Internal stress reduction in diamond like carbon thin films by ion irradiation, *Nucl. Instrum. Meth. Phys. Res. B* **148**, 216–220, (1999).
143. Stoney, G.G., The tension of metallic films deposited by electrolysis, *Proc. Roy. Soc. A* **82**, 172, (1909).
144. Monteiro, O.R. and Delplancke-Ogletree, M.P., Investigation of non-hydrogenated DLC:Si prepared by cathodic arc, *Surf. Coat. Technol.* **163–164**, 144–148, (2003).
145. Druz, B., Yevtukhov, Y., Novotny, V., Zaritsky, I., Kanarov, V., Polyakov, V., and Rukavishnikov, A., Nitrogenated carbon films deposited using filtered cathodic arc, *Diamond Rel. Mat.* **9**, 668–674, (2000).
146. Anders, S., Callahan, D.L., Pharr, G.M., Tsui, T.Y., and Bhatia, C.S., Multilayers of amorphous carbon prepared by cathodic arc deposition, *Surf. Coat. Technol.* **94/95**, 189–194, (1997).
147. Tay, B.K., Sheeja, D., and Yu, L.J., On stress reduction of tetrahedral amorphous carbon films for moving mechanical assemblies, *Diamond Rel. Mat.* **12**, 185–194, (2003).

9

Reactive Deposition

Efim's Rule: *Never repeat an experiment – especially if it was successful.*

Abstract In this relatively short chapter, we consider energetic condensation in the presence of a reactive gas such as oxygen or nitrogen. This is very relevant because many of the industrial applications are based on reactive deposition in which compound coatings are synthesized on the substrate. Introduction of a reactive gas has a number of consequences, starting from the "poisoning" of the cathode surface to enhanced plasma–gas interaction, all of which affects arc erosion, particle transport, the chemistry of the plasma, and the ion velocity and charge state distribution functions. In recent years, multi-element compounds have become popular, like TiAlN, or compounds that consist of four or even more elements. The source of the material can be an alloy cathode, or a second cathode, and/or the reactive gas. Some ternary and quarternary compound films show superior performance due to their nanostructure.

9.1 Arc Operation in Vacuum and Gases: Introduction

Most industrial applications of cathodic arcs involve the presence of a reactive gas, and by far the most frequent industrial application is the formation of hard and/or decorative compound films such as TiN or TiAlN. The focus in this chapter is on the basic processes on the substrate as well as on the cathode in the presence of a reactive gas. Many other related subjects are dealt with in other parts of the book, such as hardware issues in Chapter 5, and the application aspects of compound layers and nanocomposites in Chapter 10. Therefore, this chapter will be relatively short.

Before going to the discussion of the *reactive* part, one should state that the cathodic arc is often operated in noble gas at low pressure ($\sim 10^{-2}$ Pa). The use of a noble gas is to stabilize the arc by assisting the ignition of emission centers on the arc cathode. The gas of choice is usually argon because of its relatively low

A. Anders, *Cathodic Arcs*, DOI: 10.1007/978-0-387-79108-1_9,

cost. Its noble (non-reactive) character implies that it is benign to the environment, the process equipment, and the operator. The choice of argon is perhaps also influenced because argon is generally used in sputtering – even as that technology is based on different processes.

Looking at the arc cathode processes, the presence of argon enhances the ion return flux to the cathode in the vicinity of emission centers, thereby increasing the probability that new emission centers can ignite. This ion return flux is composed of both metal and gas ions. Gas ions have enough potential energy (the ionization energy) to cause potential emission of secondary electrons, which are released, accelerated in the cathode sheath, though most of them to only ~20 eV because that is the typical voltage level of the arc voltage drop. Since the voltage is fluctuating, some may gain more kinetic energy. In any case, even a kinetic energy of 20 eV is much larger than the electron temperature of the arc plasma, which is typically in the range 2–4 eV. The energetic electrons can cause direct impact ionization but more likely they heat the electron gas and contribute to enhanced ionization that way. While this seems all reasonable, the effects of gas in the vicinity of emission centers is not well studied.

The presence of argon is not essential to cathodic arc operation: the spot processes can occur in high vacuum, and even in ultrahigh vacuum, provided the arc current is high (typically 100 A or greater) and the power supply has a high open-circuit voltage (typically 80 V or greater). The presence of argon can relax these qualifying limitations, making operation more stable, but the presence of gas will have consequences for the microstructure of the deposited films, as discussed in Chapter 8.

Because argon assistance is common, reactive deposition is usually done by adding the reactive gas to argon, although one may also use the reactive gas without mixing. The word "reactive" refers to the establishment of chemical bonds between the metal atoms, originating from cathode spot plasma, and the atoms and molecules of a reactive gas, most often nitrogen or oxygen, or hydrocarbons such as acetylene and methane. The role of water vapor also needs to be discussed.

The reactive gas does not only react with the metal condensing on the substrate but of course also form a compound layer on the chamber walls, the shields, fixtures, and the anode and cathode. Anode coating can lead to the infamous "disappearing anode" effect when the compound is electrically isolating. Cathode coating ("poisoning") leads to the formation of type 1 spots which are characterized by smaller craters and lower erosion rate compared to arc erosion from a pure metal surface (cf. Chapter 3).

9.2 Cathode "Poisoning": Effects on Spot Ignition and Erosion Rate

The formation of a thin compound layer on the cathode has profound implications on the arc spot type, erosion rate, plasma composition, etc. The situation is similar to reactive deposition by magnetron sputtering, where the sputter target

can be "poisoned." In sputter deposition, target poisoning is generally not desired because the sputter yield is dramatically reduced compared to the metal mode, leading to much smaller deposition rates and reduced productivity.

It is educational to compare the poisoned mode in sputtering with the reactive mode of cathodic arc deposition [1]. In sputtering, there is a balance between the formation of a compound layer on the target and the removal of such layer by sputtering via the impact of energetic ions, "chipping off" one or a few surface atoms at a time. Reactive sputter deposition [2, 3, 4, 5] is characterized by its well-known hysteresis in the relation of the sputter rate and the partial pressure of the reactive gas. The sputter *yield*, defined as the average number of atoms removed per incident ion, is strongly affected by the stronger chemical bond of the metal compound compared to the bonds of their parent metal. The surface binding energies of compound and pure metal need to be compared: the energetic ions impacting the compound surface of a poisoned target need to "chisel away" surface atoms that are tightly bonded to the solid. Besides exhibiting a lower sputter yield, another undesirable effect is associated with target poisoning: arcing on the target. In cathodic arc deposition, in contrast, arc spot ignition is desirable, or, to put it stronger, it is a prerequisite for the method itself. Therefore, what appears as an "issue" in sputtering technology is a "feature" in arc deposition.

In both reactive deposition methods, sputtering and arc deposition, there is a balance between formation and removal of the compound layer on the target and cathode, respectively. However, the mechanisms of material removal are completely different. While in sputtering the surface atoms are removed by the individual ion impacts and the small collision cascades created in the near-surface layer, cathodic arc processes are based on the explosive phase transformation at emission sites, including post-explosion evaporation, as explained in Chapter 3. The balance between compound formation and removal is affected by a number of factors, such as the partial pressure of the reactive gas, the "activation" (dissociation, excitation, ionization) of the reactive gas, the target or cathode temperature, the average power density, and whether or not the process is done in pulsed or DC mode.

Now, looking at pulsed arc processes, a compound layer will form on the cathode between each pulse and therefore the arc burns primarily with type 1 spots, as introduced in Chapter 3. In DC mode, or pulsed mode with very high duty cycle (long pulses and high repetition rate), the situation is more complicated because it depends on the rates of removal and formation of the compound layer. If the cathode surface area is small and the partial pressure of the reactive gas is low, or the compound has a small enthalpy of formation, the spot removes more material from the cathode than compound material is formed. In this case, the arc burns with type 2 spots, and the plasma composition is dominated by metal plasma, similar to the pure vacuum case. In the opposite case, when the cathode is large, the partial pressure of the gas is high, and the compound has a high enthalpy of formation; a compound layer will form on the cathode and the spot will burn with type 1 spots, leading to a plasma that contains both metal and

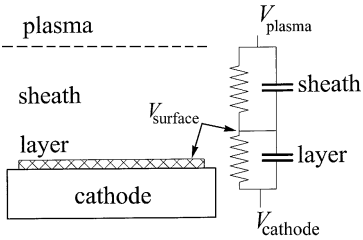

Fig. 9.1. One-dimensional schematic and equivalent circuit of sheath and compound layer placed between plasma and cathode

gas ion species [6]. In the transition region, a hysteresis can be observed, as discussed in Section 9.3.

Different cathode materials have of course a different affinity to the reactive gas. Additionally, the gas may diffuse below the cathode surface in the vicinity of hot craters. RBS measurements of samples cut from used arc cathodes showed that in the case of Ti and nitrogen the surface was moderately nitrided, whereas the surface of a Cr cathode remained metallic even at relatively high nitrogen pressures (0.1 Pa) [1].

In the presence of a compound layer, the ignition of a new spot is promoted by the local high electric field strength that results from charge-up of the compound layer, which is especially true when the compound layer is insulating because the conductivity of the compound layer determines the surface potential. Let us consider the equivalent circuit (Figure 9.1) consisting of a parallel resistor and capacitor for the layer in series with a resistor and capacitor for the cathode sheath [7, 8]. The balance of charge accumulated on the surface leads to an expression for the time-dependent insulator surface potential:

$$\frac{\mathrm{d}V_{\mathrm{surf}}}{\mathrm{d}t} = \frac{\mathrm{d}V_{\mathrm{c}}}{\mathrm{d}t} + \frac{d_{\mathrm{layer}}}{\kappa\varepsilon_0}\left(j_{\mathrm{i}} + j_{\mathrm{e}} + j_{\mathrm{displ}} + j_{\mathrm{leak}}\right) \tag{9.1}$$

where V_{c} is the potential of the cathode body, d_{layer} is the thickness of the compound layer, κ is the dielectric constant of the layer, and ε_0 is the permittivity of free space. The current densities in the parentheses designate ion and electron currents from the plasma sheath, displacement current, and leakage current through the compound layer. Note that some terms in the current balance are positive and others are negative.

If the compound layer is very thin, or it has an appreciable conductivity, the leakage current is large and the surface potential will be close to the cathode potential. In the opposite case, when a highly insulating layer is formed, the leakage current can be neglected, and the surface is floating. That means that the surface potential will adjust itself such as to balance the flow of electrons and ions from the plasma. This implies that a large fraction of the voltage is actually dropping in the insulating layer, which can readily lead to dielectric breakdown. For example, if we consider an aluminum cathode with an oxide layer of 10 nm, surface charging could cause a field of $\sim$1 V/nm, which is just in the breakdown range determined for aluminum oxide films [9].

When a compound layer is a highly insulating dielectric but only a few monolayers thick, charge transport through the layer may still occur via tunneling. Localized electronic states can hybridize with conduction electrons of the cathode. Field emission is enhanced through the shortened potential barrier, and the enhancement is exponential (see discussion of field emission and potential barrier in Chapter 3).

When the dielectric layer grows and approaches about 1 nm, charge transport is increasingly defined by localized states in the band gap and charge scattering. The layer is still thin enough to allow charges to move and therefore no significant charge-up is to be expected. The situation changes when the compound layer grows to several nanometers. Electrons can move via hopping but very strong fields can build up in the layer. These strong fields produce hot electrons that can lead to avalanches and dielectric breakdown. The consequence will be thermal runaway of the cathode material at the breakdown location, and hence a spot of type 1 is ignited. The likelihood of ignition is higher in the presence of dielectric layers than by nanoprotrusions because the local field enhancement factor caused by a dielectric layer is higher. Therefore, spot ignition is much more likely on cathode surfaces with dielectric layers and inclusions than on clean but rough surfaces. As experiments have shown, spots tend to burn on a remote contaminated (e.g., oxidized) area rather than on an arc-cleaned area close to the anode.

The above-described situation also applies to arcing in reactive magnetron sputtering [8], especially in systems with targets that readily react with oxygen like aluminum [10]. As it is typical for magnetron sputtering, sputtering is concentrated in a ring-like zone called the "racetrack" (Figure 9.2) defined by the arched shape of the magnetic field, resulting in a relatively well-defined

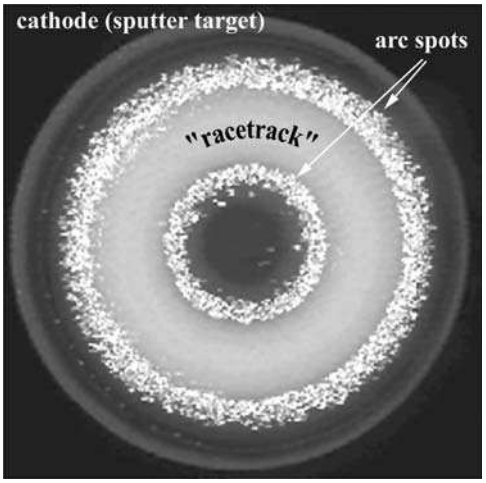

Fig. 9.2. Open-shutter photograph of a 2″ (5 cm) diameter aluminum magnetron target in argon–oxygen plasma; the ignition of arc spots is concentrated where the cathode is covered by a thin oxide film. (Photo courtesy of Roger De Gryse, Gent, Belgium)

closed zone of high plasma density that also defines the zone of most intense ion bombardment. Based on the local balance of compound formation and removal, the racetrack surface can stay metallic while the center and surrounding areas of the target are coated with an oxide layer. Using open-shutter photography, and low power settings, one can see that arc spot ignition occurs most likely in the transition zone between the racetrack and the areas coated with a relatively thick oxide [11]. In this transition zone, the field strength is highest because the voltage drop between the surface floating potential and cathode potential drops in a dielectric layer that is just thick enough to become insulating, causing a high field strength in the layer. Other factors may also play a role, such as flashover (i.e., a lateral surface discharge) from the charged surface to the racetrack area, due to a strong lateral electric field.

9.3 Cathode "Poisoning": Hysteresis

As the reactive gas is introduced, the erosion rate is lowered when type 1 spots form, which causes a lower consumption of reactive gas in the formation of the compound coating, which in turn can lead to a further increase in the partial pressure of the reactive gas. A hysteresis of cathode erosion rate and related deposition rate as a function of reactive gas flow can be observed, which is not unlike the hysteresis observed with reactive sputtering, although the erosion processes on the arc cathode are different than the sputter processes on the sputter target.

The hysteresis curves can be seen in various parameter relations such as pressure versus flow (Figure 9.3) or ion current to the substrate versus flow

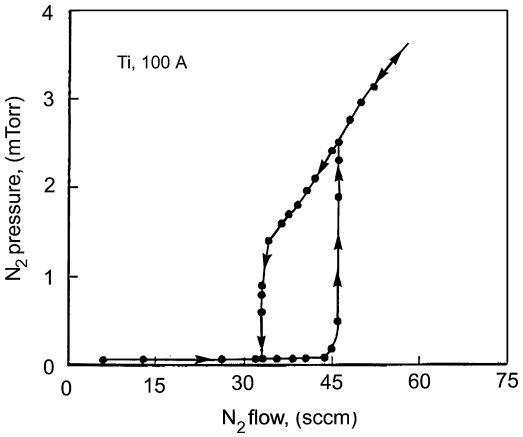

Fig. 9.3. Pressure versus flow in reactive deposition, where the compound film getters the reactive gas: The typical hysteresis loop indicates that the erosion from the cathode depends on the direction of the gas flow rate change. Ti arc in nitrogen, 100 A. (Adapted from Bergman [12], Figure 6)

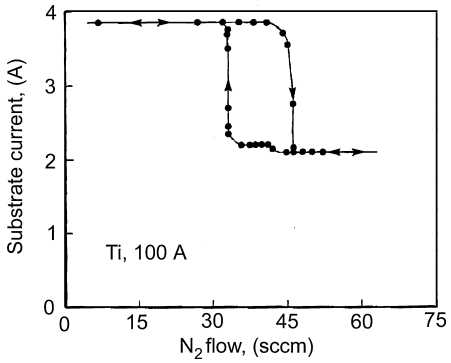

Fig. 9.4. Ion current to the substrate versus flow in reactive deposition, showing the same kind of hysteresis as in Figure 9.3. (Adapted from Bergman [12], Figure 7)

(Figure 9.4) [12]. The appearance of the hysteresis, i.e., the dependence of the curve on the direction of change, is caused by the feedback of gas consumption (the coating acts like a pump) and the balance of compound formation and removal on the cathode surface.

For example, let us consider Figure 9.3 and start at the low flow end on the left hand side. The cathode is metallic and the erosion rate is high, which produces a film on the substrate, walls, etc., that is ready to absorb all available reactive gas; hence the pressure remains low even as the flow is increased. The coating will still absorb (pump) the gas until a flow is reached that exceeds the pumping capacity of the coating. At that moment, an increase in pressure increases the bombardment of the cathode with reactive gas, promoting the formation of a compound layer on the cathode, which causes the spot type to switch to type 1, which has a lower erosion rate. Therefore, the amount of metal arriving on the substrate is reduced, further decreasing the film's pumping capacity. This feedback amplifies and one can see a very sharp increase in the pressure, at a flow of 45 sccm in the example. If the flow is further increased, one sees a proportional increase in pressure.

Now, starting from the high-flow side and the cathode operating with type 1 spots, we reduce the flow of reactive gas. The pressure reduces proportionally with the flow below the 45-sccm point because the erosion of the cathode is still low due to operation with type 1 spots. As the flow reaches about 33 sccm, the balance of compound formation and erosion on the cathode surface is changed because not enough gas atoms arrive at the cathode to form the compound as fast as removed by the spot. This switches the spots to type 2 with high erosion, and the increased rate causes the formation of strongly pumping films on substrate and walls, hence the sharp drop of pressure. The hysteresis shown in Figure 9.4 can be explained in a corresponding way.

The pumping (gettering) effect of the compound film can also be presented as a function of pressure, as shown in the TiN example of Figure 9.5.

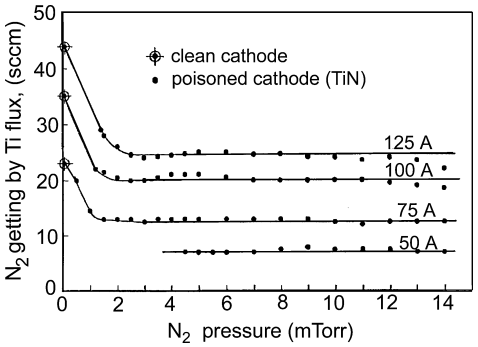

Fig. 9.5. Nitrogen gettering by a titanium film produced by a 100-A titanium arc, indicating the reduced titanium erosion rate when the cathode becomes "poisoned." (Adapted from Bergman [12], Figure 8)

9.4 Interaction of the Expanding Spot Plasma with the Background Gas

The presence of a reactive gas affects the cathodic arc plasma in several ways. The spot type and erosion conditions are strong functions of the gas-dependent surface conditions, as explained before. Furthermore, the metal plasma interacts with the background gas which affects the flux and energy of ions (see Chapter 4). The interaction will depend on the gas pressure, gas type, and other factors, and may lead to turbulent mixing, shockwaves, scattering and cooling of the plasma particles, among other effects. A multitude of plasma-chemical reactions may occur, including charge exchange and dissociation of molecules, which can activate the gas, thereby promoting the compound formation on the surface. "Activation" refers to all processes that promote the formation of compound formation, such as dissociation, ionization, and electronic excitation of gas atoms and molecules.

Gas phase reactions leading to compounds usually occur at pressures higher than what is customary used in reactive physical vapor deposition because such inelastic collisions require three particles to participate in the collision to simultaneously satisfy the conservation laws of energy and momentum. Three-particle collisions are very unlikely at lower pressures, compared to two-particle collisions. At very high gas pressures, though, more typical for chemical vapor deposition, condensation in the gas phase can occur, leading to the formation of nanoparticles; this is related to the field of "dusty plasmas" and of great concern to some semiconductor processing.

Interestingly, the first cathodic arc coatings in air at atmospheric pressure observed by Priestley in the mid-1700s (see Chapter 2) showed a peripheral zone of extremely fine black powder, which most likely constituted a deposition of oxidized particles, and perhaps even containing nanoparticles.

In many cases, operation with gas *mixtures* (argon plus reactive gas) is preferred, and this opens the possibility to inject the gases separately, as opposed to premix them. This is especially relevant when using a filtered system where the distance between cathode and substrate is rather large. Schemmel and colleagues [13] determined that it was advantageous for their 90° duct system to inject argon near the aluminum cathode while oxygen was injected near the substrate. Aluminum oxide films of "high optical quality" could be obtained for substrates between room temperature and 130°C at a rate of 80 nm/min using 110-A arc current and 35% oxygen in the mixture. At the low temperature, the films are amorphous with a refractive index of 1.68 over most of the visible spectrum.

Not all researchers follow this approach, rather many prefer gas injection in the arc source region, near the cathode, with the argument that the interaction of the dense plasma with the background gas contributes to gas activation and overall higher incorporation of the reactive gas species into the growing coating. In an extreme case, one may inject the gas through a hole in the cathode to promote the intentional poisoning of the cathode and to maximize gas activation. With this approach, poisoning of the zirconium cathode is observed for nitrogen pressures as low as 0.05 Pa, and this resulted in the synthesis of hard (36 GPa) stress-stabilized cubic Zr_3N_4, which is harder than the more common orthorhombic Zr_3N_4 and ZrN phases [14].

The popular combination of a titanium cathode and nitrogen gas was selected to study the effect of the gas entry point for a 90° duct filter system; one entry point was behind the cathode, the other near the substrate, or equivalently a mass–energy plasma analyzer [15]. Gas flow rate and pressure could be independently regulated by a mass flow controller and an adjustable gate valve. The plasma analyzer recorded that the Ti^+ and Ti^{2+} ion fluxes were high, and the N^+ and $N_2{}^+$ fluxes were low, when the gas was injected behind the cathode at a relatively low gas flow rate of 23 sccm. This was especially true when the pressure was low (2 mTorr or 0.27 Pa). Injecting the gas near the substrate reduces the Ti ion flux and increases the nitrogen ion flux at the substrate. At a higher gas flow rate, 71 sccm, the Ti ion flux is reduced even when the gas is injected behind the cathode. Titanium and nitrogen ions have higher energy when the gas is injected behind the cathode. Their charge state is little influenced by the gas entry point but the total pressure is important: high gas pressure leads to a reduction of the ion flux, as was already mentioned in Chapter 4.

Yet another reason to intentionally poison the cathode is to suppress the formation of large macroparticles, which are usually associated with type 2 cathode spots on clean metallic surfaces. The smaller craters produced by the type 1 spots cannot be the source of large particles, and this has an immediate effect on the quality of the coating even when no filtering is implemented. The company Multi-Arc pursued this line of thought in their reactive gas controlled arc (RGCA) process [16].

9.5 Nucleation and Growth

The basic ideas of nucleation and growth have been brought forward in Chapter 8. The classic growth modes, layer-by-layer (or two-dimensional mode), island mode (or three-dimensional mode), and layer followed by island growth (mixed or Stranski-Kastranov mode), were introduced and explained by the thermodynamic driving forces, especially the interface energy. We have also seen that the kinetic energy brought by the energetic condensation process modifies to some extent these modes, though thermodynamic forces remain important, especially when considering the long-term, thermodynamically preferred, stable configuration.

In *reactive* deposition, some further modifications occur. First, we need to consider that the different condensing (film-forming) species can arrive at the surface with a wide spread of kinetic energies. A typical case is where the metal component is supplied by the arc process, and hence has the high energy typical for energetic condensation. The metal ions may have collided with gas molecules and therefore have *less* kinetic energy than in the case of vacuum arc plasma deposition. They may have reduced ion charge states, which is yet another factor that reduces the kinetic energy because the final acceleration in the substrate's sheath is less effective. A fraction of the condensing species may come from the gas phase; hence such atoms never went through the acceleration at cathode spots as metal ions did.

On the other hand, compared to reactive deposition by sputtering or evaporation, the gas component is *more* energetic and activated due to the interaction with the energetic particle flux from the cathode spots. Activation is a very important factor in determining the stoichiometric composition of the compound. For example, the triple bond of the nitrogen molecule is very strong (945 kJ/mol), so most molecules hitting the surface will not participate in any chemical reaction but rather bounce back into the pre-surface volume. Activation implies dissociation, ionization, and excitation. The activated species (N, N^*, N^+, N_2^*, N_2^+ in the case of nitrogen) react much more readily than the N_2 molecule in its ground state. Reactions preferably occur on the surface: here, energy and momentum conservation are easily satisfied since the solid body of the substrate can accommodate any excess energy or momentum. In contrast, a two-particle collision rarely leads to a chemical bond – the particles often collide without reaction even if there was energy to overcome the energy barrier for a reaction.

Reactive deposition is not always related to using reactive gases. If more than one condensing material is provided they may react on the surface and form a compound layer. For example, using the dual-cathode arc source introduced in Chapter 5, a flux of titanium and carbon can be brought to the substrate, and those elements may react and form TiC. The groups at Sydney University, Sydney, and RMIT University in Melbourne, Australia, took the idea one step further and produced a multilayer of TiC and carbon (a-C) to study the

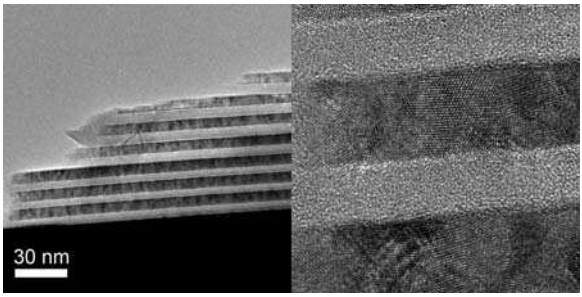

Fig. 9.6. Transmission electron microscopy image of a TiC/C multilayer deposited on a silicon wafer with a SiO_2 surface using a dual-cathode pulsed arc; *left*: lower resolution, showing sharp interfaces; *right*: high resolution, indicative of the amorphous character of the C layers and the nanocrystalline of TiC. The multilayers have a period of about 16 nm. The specimen was prepared by cleaving which preserves the original structure very well. (Image courtesy of Luke Ryves (deposition) and Per Persson (TEM) – work done at the University of Sydney)

formation and mechanical properties of such multilayer system. The corresponding TEM image is shown in Figure 9.6.

Another example involves the reaction of fluxes from two filtered cathodic arc sources and oxygen. Monteiro [17] used highly doped silicon for one cathode and aluminum for the other to synthesize amorphous films of silicon–aluminum oxide, which turn into aluminum silicate, $3Al_2O_3 \cdot 2SiO_2$, also known as mullite, upon annealing. The annealing was done at 1100°C for 2 h in air, and the films were tested by indentation (Figure 9.7) and pull testing. The adhesion on SiC

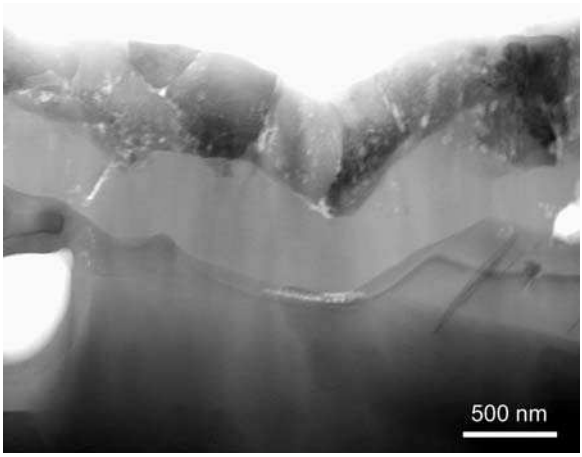

Fig. 9.7. Cross-section electron microscopy image showing the region of indentation of a mullite film on SiC: the film adheres well despite severe deformation by the indenter. (Photo courtesy of Othon Monteiro, Berkeley, now Houston)

substrates was excellent and reached the limits of the pull tester used, 70 MPa. Mullite is known for its excellent high-temperature properties such as thermal shock resistance due to low thermal expansion, high strength, and interlocking grain structure [18].

Many compound films are amorphous when deposited at room temperature, and they may become crystalline when annealed; this has been observed, for example, with arc-deposited TiO_2, WO_3, and TiC. However, energetic condensation promotes the formation of crystal grains of various sizes at or near room temperature, and even a preferred orientation may be established. This was already mentioned in Chapter 8 and is especially applicable to the compound films formed by reactive arc deposition. For example, Lim and co-workers [19] used a stoichiometric TiAl alloy cathode to deposit TiAlN in a cathodic arc process at 1 mTorr (0.13 Pa) of nitrogen without intentional substrate heating. The films were rich in Ti and N compared to the expected $Ti_{0.25}Al_{0.25}N_{0.5}$ films. The stress could be reduced from 6.5 to less than 2 GPa through application of pulsed high-voltage pulses, as explained in Chapter 8, when using the plasma ion immersion implantation process. The cubic structure was observed in both cases but for the highly stressed sample, different grain orientations can be seen from the diffraction pattern shown in Figure 9.8. With the application of high-voltage pulses (14 kV, 20 μs, 500 Hz) during film growth, a strong preferred orientation was found in the {200} planes aligning perpendicular to the substrate. Such results are exemplary, and similar results were found for other materials, e.g., for AlN [20, 21] and $Ti_{1-x}V_xN$ [22]. However, energetic condensation even without bias and at room temperature can give dense films with columnar, crystalline microstructure that has preferred orientation, as shown for TiN (Figure 9.9).

Another example of arc-based reactive deposition is the synthesis of nanocomposites such as ZrSiN, where the Zr stems from the arc cathode, Si comes

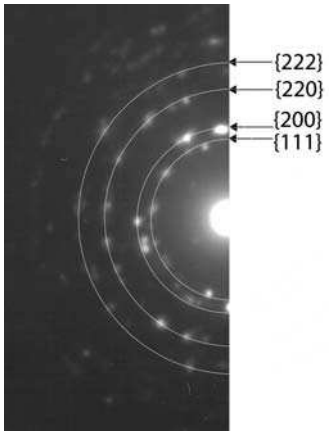

Fig. 9.8. Diffraction pattern of a $Ti_{0.22}Al_{0.20}N_{0.58}$ film deposited by a cathodic arc with the substrate at room temperature in the absence of pulse biasing. (Figure courtesy of Sunnie Lim, Melbourne, now Sydney, Australia)

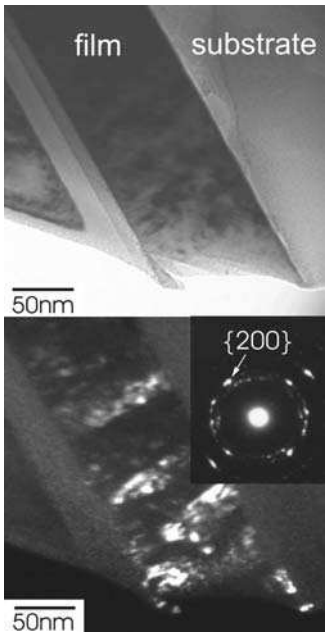

Fig. 9.9. Transmission electron images illustrating the formation of crystalline TiN films deposited by a cathodic arc at room temperature. *Top*: brightfield image, *bottom*: dark-field image showing the columnar structure whose diffraction pattern indicates preferred orientation with the {200} planes perpendicular to the surface. (Figure courtesy of Sunnie Lim, Melbourne, now Sydney, Australia)

from tetramethylsilane (TMS) liquid precursor, and nitrogen is provided by N_2 gas. This process may be labeled as a hybrid of physical vapor deposition (PVD) and chemical vapor deposition (CVD), the latter being characterized by the decomposition and condensation of a precursor liquid or gas. The supply of a liquid to vacuum processing is usually controlled by evaporation in a heated mass flow controller. Winkelmann and co-workers [23] used an arc current of 145 A and a TMS flow rate of 0–35 sccm, which led to a Si content in the resulting film of 0–18%. The flow rate of N_2 was 28 sccm, giving a process pressure of 0.8 Pa. The Si substrates were heated to 350°C and biased –150 V with respect to the grounded chamber. The resulting coating was a nanocomposite structure consisting of ZrN crystallites embedded in a thin layer of amorphous Si_3N_4 (nc-ZrN/a-Si_3N_4). Incorporation of Si increased the hardness compared to pure ZrN and reached a maximum at 3 at.% Si with 43 GPa. The grain size decreased with increasing Si content and was about 10 nm for the films having 3 at.% Si. TEM images identified the ZrN grains, and XPS spectra reveal the presence of phases other than ZrN and Si_3N_4, including ZrO, ZrC, and elemental Si, which appear to be incorporated into the amorphous Si_3N_4 phase.

This and other work support the science of nanostructure affecting hardness and residual stress [24, 25], as also mentioned in Chapter 8.

The effect of energetic ions on the growing film can also be illustrated by considering filtered arc deposition of copper oxide. There are generally two phases, cupric oxide (CuO) and cuprous oxide (Cu_2O), which coexist as evidenced by XRD, XPS, and Raman analyses [26]. Upon application of bias, the CuO phase became dominant and exhibited (020) texture. Apparently, bias promoted the activation and incorporation of oxygen. XRD analysis indicates that the energetic ions accelerated by biasing create defects in the crystalline structure, and the crystallites are smaller. In agreement with that, AFM imaging showed smoother films with very fine, evenly distributed crystallites when the bias was applied. Such observations are exemplary and apply to compound materials. An excellent review of those effects for a number of arc-deposited oxides was given by Tay, Zhao, and Chua [27].

9.6 Water Vapor and Hydrogen Uptake

Practically all reactive deposition is done in high-vacuum processing chambers. The residual gas in a typical high-vacuum chamber consists mostly of water vapor, assuming that there is no substantial leak (a leak would show as high nitrogen and correlated oxygen partial pressures). The water vapor is in thermodynamic equilibrium with an adsorbed water film on all surfaces, including chamber walls, fixtures, and substrates. The thickness of the water film mainly depends on temperature. Increasing the temperature shifts the equilibrium to thinner adsorbed layers – this is the basis for "baking" vacuum systems. Water can also be effectively removed by combining heating with UV radiation from internal lamps, and by flushing the system with heated nitrogen; the reader may consult the literature on vacuum [28, 29, 30, 31].

Coming back to our (non-baked) high-vacuum chamber and equipment at room temperature, we acknowledge that water is present. Desorption of the water film can be stimulated by various forms of energy brought to the surface, and this is most efficiently done when plasma impacts the surface. For example, in a pulsed cathodic arc system, the plasma stream interacts with all components and therefore water vapor becomes part of the plasma composition, especially immediately after arc triggering.

Once water is part of the plasma, it is not surprising that the growing film will incorporate hydrogen and oxygen. In the case of oxide deposition, when the process gas already contains oxygen, only the hydrogen incorporation may come as a "surprise." A compound film consisting of a mixture of oxide and hydroxide will of course show properties such as hardness, elastic modulus, and refractive index deviating from the expected properties of the oxide. In the case of nitride deposition, the films may contain oxygen and hydrogen at a surprisingly high level. While the metal–oxygen or metal–nitrogen content can be readily determined by various characterization techniques, it is relatively

difficult to measure the hydrogen content. Therefore, the coating's hydrogen content is often not known, mentioned, or even considered.

The case of alumina deposition is exemplary for the issue and especially prominent when using pulsed arcs [32]. Due to the time between pulses, there is ample opportunity for the water vapor to interact with the fresh surface made by one deposition pulse. Hydrogen *in the plasma* can be detected using quadrupole mass spectrometry or a time-of-flight mass-spectrometric technique [32]. Detection and quantification of hydrogen *in the coating* can be done by nuclear resonance absorption (NRA) using the nuclear reaction $^{1}H(^{15}N\alpha\gamma)^{12}C$. With this technique, nitrogen ions of the isotope ^{15}N with energy equal to or greater than the resonance energy $E_{res} = 6.385\,MeV$ penetrate the film, react with hydrogen ^{1}H, thereby producing α particles, γ rays, and the carbon isotope ^{12}C. The yield of the γ-rays is proportional to the hydrogen content. By increasing the ^{15}N ion energy, the hydrogen composition of the films can be profiled [33].

The hydrogen uptake by the coating not only is a function of the hydrogen concentration in the plasma but also depends on thermodynamic driving forces for the formation of the hydrogen-containing compounds. In the case of the aluminum–oxygen–hydrogen system, one should consider the standard enthalpy of formation for AlH_3 and AlOOH; the values are $\Delta H_f^0(AlH_3) = -46\,kJ/mol$ and $\Delta H_f^0(AlOOH) = -1970\,kJ/mol$ [34]. Therefore, the formation of aluminum hydroxide, AlOOH, is energetically favored. Table 9.1 gives the standard enthalpy of formation of some selected compounds indicating the driving force for the formation of the oxide versus a hydride or hydroxide.

For the case of pulsed arcs, it was found that the hydrogen uptake increased with increasing oxygen partial pressure, which could be attributed to increased "scrubbing" of water from source components and chamber walls, with subsequent formation and erosion of aluminum oxide hydroxide on the cathode surface [32]. Figure 9.10 shows that the hydrogen uptake of the coating could reach about 20%, and thus, strictly speaking, the film was not alumina (aluminum oxide) but a mixture of alumina and aluminum hydroxide. The mechanical film properties such as hardness and elastic modulus were shown to be greatly affected [35], and similar conclusions can also be drawn for films made by magnetron sputtering [35]. Not only the mechanical but also the electronic properties of arc-deposited materials are affected as well [36].

One should note that the presence of a magnetic field, for example caused by a macroparticle filter, enhances the probability that water is dissociated and ionized because the free electrons of the plasma have a much greater likelihood of colliding with gas molecules [37]. As a consequence, oxygen and hydrogen are especially strongly incorporated in the growing films when magnetic fields are present.

Mitigation measures for unwanted hydrogen uptake include (i) improving the vacuum quality of the deposition system, (ii) use of DC operation, as opposed to pulsed deposition, and (iii) substrate heating. Measure (i) is self-explanatory and can be done with higher pumping speed and "baking" of the chamber (caution: the baking temperature may be limited by the presence of O-rings of the high

Table 9.1. Standard enthalpy of formation at 298.15 K for selected metals that form compounds containing oxygen and/or hydrogen. (From [34])

Compound	ΔH_f^0 (kJ/mol)
AlH_3	–46.0
AlOOH	–1970.0
AlO_4P	–1733.8
Al_2O_3	–1675.7
BeH_2O_2	–902.5
BeO	–609.4
CdH_2O_2	–560.7
CdO	–258.4
CoH_2O_2	–539.7
CoO	–237.9
Co_3O_4	–891.0
MgO	–601.6
MgH_2	–75.3
MgH_2O_2	–924.5
Ni_2O_3	–489.5
NiH_2O_2	–529.7
SnH_2O_2	–561.1
SnO	–280.7
SnO_2	–577.6
SrH_2	–180.3
SrH_2O_2	–959.0
SrO	–592.0
Ta_2H	–32.6
Ta_2O_3	–2046.0
ThH_2	–139.7
ThO_2	–1226.4
ZnH_2O_2	–641.9
ZnO	–350.5
ZrH_2	–169.0
ZrO_2	–1100.6

vacuum system). Measure (ii), going to DC operation, is the most common way and implemented in practically all industrial systems. DC operation automatically implies high average deposition rates, and as a desired side effect, the ratio of desired material to water flux is large. Finally, measure (iii), substrate heating, is related to changing the sticking probability for water molecules. At very high temperature, it is also possible to decompose the hydride if it has formed. For example, in the aluminum–oxygen–hydrogen system, the hydride is less thermally stable than the oxide, and therefore deposition at high temperature (e.g., $>800^{\circ}$C) results in high-quality aluminum oxide. Of course, high temperature also greatly affects crystallinity and texture of the coating – and it is for that reason widely used, for example for nitride-based hard coatings.

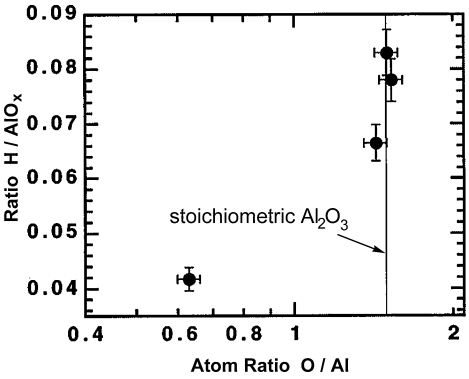

Fig. 9.10. Hydrogen uptake of an aluminum oxide coating synthesized by pulsed aluminum arc deposition in oxygen; the Al and O concentrations were measured by RBS, while the hydrogen content was measured by NRA; the *vertical line* indicates the stoichiometric ratio of O and Al for aluminum oxide. (Adapted from [32])

Hydrogen may not only come from water but may be intentionally introduced into the processing chamber, for example when using a hydrocarbon gas to produce a carbide coating. Hydrogen uptake depends greatly on the substrate temperature. For example, studying TiC and TiC_xN_{1-x} films using the cathodic arc plasma deposition process, Randhawa [38, 39] used a titanium cathode and CH_4 for TiC, and a mixture of CH_4 and N_2 for TiCN, respectively. Due to the decomposition of the hydrocarbon molecules, hydrogen was present in both processes. The most relevant result was that the films deposited at substrate temperatures of 500°C and below contained significant amounts of hydrogen whereas films deposited at a temperature exceeding 600°C were virtually free of hydrogen. The hydrogen-free coatings outperformed the hydrogen-containing coatings in wear and erosion tests.

Very high temperatures may not be an option for many substrates because undesirable changes in phase (like the softening of tool steel) or irreversible damage (like with polymers) will occur. Therefore, one has to consider on a case-by-case basis what oxygen and hydrogen levels are desirable or tolerable. The main point of this section was to make the reader aware of the often overlooked or underestimated water and hydrogen issue.

9.7 Arcs in High-Pressure Environments

Arc discharges can operate in high-pressure environments, and in fact the historically early research on arcs was done in air (cf. Chapter 2). As long as the cathode is cold, the arc operates in the cathodic mode regardless of the pressure [40, 41].

Interesting phenomena may occur at higher pressure such as the self-organized synthesis of nanostructures. For example, multiwall carbon nanotubes

are synthesized at cathode craters and on the surface of carbon macroparticles when the arc is operated in 0.5 Pa of helium or hydrogen [42]. In a later paper by the same group [43], multiwall carbon nanotubes were also found at the lower pressure of 20 mPa. Metal additives to the graphite cathode play an important role in catalyzing nanotube growth.

When the arc is operated at higher pressure, intense ion bombardment and ohmic heating are likely to allow a switch to the thermionic mode, especially when the cathode is not cooled but designed for high temperature. For example, high-pressure sodium or mercury discharge lamps used for outdoor illumination and super-high-pressure xenon lamps used in projectors work that way: they go through a very brief period of cathodic arc mode to enter the much less erosive thermionic mode [44].

Arcs may also burn in liquids such as water: this has generated quite some interest because again nanostructures can be formed. For example, Sano and co-workers [45] found carbon nano-onions. However, the source of the material was not the cathode but the anode, and the discharge should be classified as a thermionic arc from a cathode operation's point of view, and as an anodic arc considering the source of material. Many more results in the field of cathodic arcs at high pressure or in liquids can be expected in the coming years.

References

1. Kühn, M. and Richter, F., Characteristics in reactive arc evaporation, *Surf. Coat. Technol.* **89**, 16–23, (1997).
2. Vossen, J.L. and Kern, W., *Thin Film Processes II*. Academic Press, Boston, (1991).
3. Bunshah, R.F., (ed.) *Handbook of Deposition Technologies for Films and Coatings: Science, Technology, and Applications*. Noyes, Park Ridge, N.J., (1994).
4. Schneider, J.M., Rohde, S., Sproul, W.D., and Matthews, A., Recent developments in plasma assisted physical vapour deposition, *J Phys. D: Appl. Phys.* **33**, R173–R186, (2000).
5. Sproul, W.D., Christie, D.J., and Carter, D.C., Control of reactive sputtering processes, *Thin Solid Films* **491**, 1–17, (2005).
6. Yushkov, G.Y. and Anders, A., Effect of the pulse repetition rate on the composition and ion charge-state distribution of pulsed vacuum arcs, *IEEE Trans. Plasma Sci.* **26**, 220–226, (1998).
7. Barnat, E.V. and Lu, T.M., Transient charging effects on insulating surfaces exposed to a plasma during pulse biased dc magnetron sputtering, *J. Appl. Phys.* **90**, 5898–5903, (2001).
8. Anders, A., Physics of arcing, and implications to sputter deposition, *Thin Solid Films* **502**, 22–28, (2006).
9. Seino, T. and Sato, T., Aluminum oxide films deposited in low pressure conditions by reactive pulsed dc magnetron sputtering, *J. Vac. Sci. Technol. A* **20**, 634–637, (2002).
10. Schneider, J.M. and Sproul, W.D., "Reactive Pulsed DC Magnetron Sputtering and Control," in *Handbook of Thin Film Processing Technology*, Glocker, D.A. and Shah, S.I., (Eds.). pp. A5.1:1–A5.1:12, IOP Publishing Ltd, Bristol, UK, (1998).

11. Segers, A., Depla, D., Eufinger, K., Haemers, J., and De Gryse, R., "Reactive sputtering," Nouvelles Tendances en Procédés Magnetron et arc pour le Dépot de Couches Minces, Gent, Belgium, pp. 25–39, (2003).
12. Bergman, C., "Arc plasma physical vapor deposition," 28th Annual SVC Technical Conference, Philadelphia, PA, pp. 175–191, (1985).
13. Schemmel, T.D., Cunningham, R.L., and Randhawa, H., Process for high rate deposition of Al_2O_3, *Thin Solid Films* **181**, 597–601, (1989).
14. Chhowalla, M. and Unalan, H.E., Thin films of hard cubic Zr_3N_4 stabilized by stress, *Nat. Mater.* **4**, 317–322, (2005).
15. Tarrant, R.N., Bilek, M.M.M., Oates, T.W.H., Pigott, J., and McKenzie, D.R., Influence of gas flow and entry point on ion charge, ion counts and ion energy distribution in a filtered cathodic arc, *Surf. Coat. Technol.* **156**, 110–114, (2002).
16. Rogozin, A.F. and Fontana, R.P., Reactive gas-controlled arc process, *IEEE Trans. Plasma Sci.* **25**, 680–684, (1997).
17. Monteiro, O.R., Wang, Z., and Brown, I.G., Deposition of mullite and mullite-like coatings on silicon carbide by dual-source metal plasma immersion, *J. Mater. Res.* **12**, 2401–2410, (1997).
18. Martinon-Torres, M., Rehren, T., and Freestone, I.C., Mullite and the mystery of Hessian wares, *Nature* **444**, 437–438, (2006).
19. Lim, S.H.N., McCulloch, D.G., Bilek, M.M.M., McKenzie, D.R., Russo, S.P., Barnard, A.S., and Torpy, A., Characterization of cathodic arc deposited titanium aluminium nitride films prepared using plasma immersion ion implantation, *J. Phys.: Condensed Matter* **17**, 2791–2800, (2005).
20. Gan, B.K., Bilek, M.M.M., McKenzie, D.R., Taylor, M.B., and McCulloch, D.G., Effect of intrinsic stress on preferred orientation in AlN thin films, *J. Appl. Phys.* **95**, 2130–2134, (2004).
21. Gan, B.K., Bilek, M.M.M., McKenzie, D.R., Yang, S., Tompsett, D.A., Taylor, M. B., and McCulloch, D.G., Stress relief and texture formation in aluminium nitride by plasma immersion ion implantation, *J. Phys. Condensed Matter* **16**, 1751–1760, (2004).
22. Davies, K.E., Gan, B.K., McKenzie, D.R., Bilek, M.M.M., Taylor, M.B., McCulloch, D.G., and Latella, B.A., Correlation between stress and hardness in pulsed cathodic arc deposited titanium/vanadium nitride alloys, *J. Phys. Condensed Matter* **16**, 7947–7954, (2004).
23. Winkelmann, A., Cairney, J.M., Hoffman, M.J., Martin, P.J., and Bendavid, A., Zr-Si-N films fabricated using hybrid cathodic arc and chemical vapour deposition: Structure vs. properties, *Surf. Coat. Technol.* **200**, 4213–4219, (2006).
24. Veprek, S., The search for novel, superhard materials, *J. Vac. Sci. Technol. A* **17**, 2401–2420, (1999).
25. Veprek, S. and Veprek-Heijman, M.G.J., The formation and role of interfaces in superhard nc-MenN/a-Si3N4 nanocomposites, *Surf. Coat. Technol.* **201**, 6064–6070, (2007).
26. Gan, Z.H., Yu, G.Q., Tay, B.K., Tan, C.M., Zhao, Z.W., and Fu, Y.Q., Preparation and characterization of copper oxide thin films deposited by filtered cathodic vacuum arc, *J. Phys. D: Appl. Phys.* **37**, 81–85, (2004).
27. Tay, B.K., Zhao, Z.W., and Chua, D.H.C., Review of metal oxide films deposited by filtered cathodic vacuum arc technique, *Mat. Sci. Eng. R: Reports* **52**, 1–48, (2006).
28. Lafferty, J.M., (ed.) *Foundations of Vacuum Science and Technology*. John Wiley & Sons, New York, (1998).

29. Hoffman, D.M., Singh, B., and Thomas III, J.H., (eds.), *Handbook of Vacuum Science and Technology*. Academic Press, San Diego, CA, (1998).
30. O'Hanlon, J.F., *A User's Guide to Vacuum Technology*, 2 nd ed. John Wiley & Sons, New York, (1989).
31. Redhead, P.A., Hobson, J.P., and Kornelsen, E.V., *The Physical Basis of Ultrahigh Vacuum*. Chapman & Hall, London, (1968).
32. Schneider, J.M., Anders, A., Hjörvarsson, B., Petrov, I., Macak, K., Helmerson, U., and Sundgren, J.-E., Hydrogen uptake in alumina thin films synthesized from an aluminum plasma stream in an oxygen ambient, *Appl. Phys. Lett.* **74**, 200–202, (1999).
33. Hjörvarsson, B., Ryden, J., Karlsson, E., Birch, J., and Sundgren, J.E., Interface effects of hydrogen uptake in Mo/V single-crystal superlattices, *Phys. Rev. B* **43**, 6440–6445, (1991).
34. Lide, D.R., (ed.) *Handbook of Chemistry and Physics, 81st Edition*. CRC Press, Boca Raton, N.Y., (2000).
35. Schneider, J.M., Larsson, K., Lu, J., Olsson, E., and Hjörvarsson, B., Role of hydrogen for the elastic properties of alumina thin films, *Appl. Phys. Lett.* **80**, 1144–1146, (2002).
36. Bilek, M.M.M. and Milne, W.I., Electronic properties and impurity levels in filtered cathodic vacuum arc (FCVA) amorphous silicon, *Thin Solid Films* **308–309**, 79–84, (1997).
37. Schneider, J.M., Anders, A., Hjörvarsson, B., and Hultman, L., Magnetic-field-dependent plasma composition of a pulsed arc in a high-vacuum ambient, *Appl. Phys. Lett.* **76**, 1531–1533, (2000).
38. Randhawa, H., TiN-coated high-speed steel cutting tools, *J. Vac. Sci. Technol. A* **4**, 2755–2758, (1986).
39. Randhawa, H., Cathodic arc plasma deposition of TiC and TiC_xN_{1-x} films, *Thin Solid Films* **153**, 209–218, (1987).
40. Kimblin, C.W., A review of arcing phenomena in vacuum and in the transition to atmospheric pressure arcs, *IEEE Trans. Plasma Sci.* **10**, 322–330, (1971).
41. Anders, S. and Jüttner, B., Arc cathode processes in the transition region between vacuum arcs and gaseous arcs, *Beitr. Plasmaphys.* **27**, 223–236, (1987).
42. Takikawa, H., Yatsuki, M., Sakakibara, T., and Itoh, S., Carbon nanotubes in cathodic vacuum arc discharge, *J. Phys. D: Appl. Phys.* **33**, 826–830, (2000).
43. Takikawa, H., Minamisawa, S., Xu, G.C., Miyakawa, N., Sakakibara, T., and Shiina, Y., "Cathode erosion and carbon-nanotubed droplet in T-shape filtered arc deposition with various carbon cathodes," XXIth Int. Symp. on Discharges and Electrical Insulation in Vacuum, Yalta, Ukraine, pp. 484–487, (2004).
44. Anders, A. and Jüttner, B., Cathode Mode Transition in High-Pressure Discharge Lamps at Start-Up, *Lighting Res. Technol. (GB)* **22**, 111–115, (1990).
45. Sano, N., Wang, H., Alexandrou, I., Chhowalla, M., Teo, K.B.K., Amaratunga, G. A.J., and Iimura, K., Properties of carbon onions produced by an arc discharge in water, *J. Appl. Phys.* **92**, 2783–2788, (2002).

10

Some Applications of Cathodic Arc Coatings

The arc in vacuum has no great commercial value . . .

Clement D. Child, in: *Electric Arcs*, 1913

Abstract The choice of words "some applications" indicates that it is impossible to give a truly comprehensive account about all the films, coatings, multilayers, and nanostructures made by energetic condensation. Some important examples are selected, this time sorted and driven by the application rather than by the material or process. The range of applications includes hard coatings on tools, which are typically nitrides or carbides, corrosion-resistant and protective coatings such as ta-C (tetrahedral amorphous carbon), decorative coatings (nitrides, oxynitrides, carbides), optical coatings (oxides), metallization for the semiconductor industry, some wide band gap semiconductors (e.g., transparent conducting oxides), and bio-compatible coatings, and here we reconsider ta-C, among others.

10.1 Overview

Many applications of cathodic arcs make use of *reactive* deposition of various nitrides and oxides. In recent years, emphasis has shifted from monolithic coatings to higher performing multilayers and nanocomposites. For efficiency and cost reasons, most commercial coaters do not use macroparticle filters. Macroparticles are tolerated in many applications; however, coating requirements become more stringent every year, and therefore the interest in *filtered* cathodic arcs and other advanced arc coating methods is increasing.

Manufacturers became interested in cathodic arc coatings due to the technology's ability to produce dense compound coatings with high rates, which is valuable for applications that require hard and wear-resistant coatings, e.g., on cutting and forming tools, decorative and corrosion-resistant coatings on automotive parts and building supplies (doorknobs, faucets, showerheads, etc.). When

A. Anders, *Cathodic Arcs*, DOI: 10.1007/978-0-387-79108-1_10,

Table 10.1. Some commercial application and typical materials of cathodic arc coatings

Category	Application	Typical coating material
Hard coatings	Cutting tools	TiN, TiAlN, TiCN, TiAlYN, multilayers
Hard coatings with solid lubrication layer	Forming dies and punches	CrN, multilayers
	Cutting tools	TiAlN/W-C:H; TiAlN/WC/C; TiAlN/MoS_2
Decorative and protective coatings	Forming dies and punches	CrN/W-C:H
	Faucets, shower heads	ZrN, CrN, TiAlN
Functional coatings	Door hardware	ZrN
	Watch housing and wrist bands, jewelry	ZrN, TiN, Au, TiAlN
	Engine parts	CrN (pistons)
	Fuel injection	Metal-containing ta-C
	Automotive interior parts	Metal-containing ta-C, AlSn, CrN
	Textile machinery	TiCN, metal-containing DLC
	EMI/RFI shielding	Al, Cu, Ni–Cr, with sheet resistance $< 1\ \Omega$
	Reflective coatings, e.g., for automotive lights	Al, Cr, stainless steel, Ni–Cr
	Bio-compatible surfaces for medical tools and implants	Ti, ta-C, TiN, TICN, ZrN, and CrN, Ag, Au, Pt
	Bio-compatible surfaces with cytotoxic (antibacterial) properties	ta-C films with Ag doping
	Metallization and diffusion barrier layers for semiconductors	Ta, TaN, TiN, Cu
	Protection of magnetic disks and read–write heads	Ultrathin diamond-like carbon

the arc is operated in vacuum (or, for arc stability reasons, in a background of argon at low pressure), metallic coatings are produced for shielding against electromagnetic (EM) and radio-frequency (RF) interference, e.g., on the inside of the plastic housing of cell phones, or for light reflection, e.g., on automobile headlight reflectors. In recent years, the interest has shifted to higher value products, utilizing the electronic, optical, or magnetic properties of coatings. The most common applications and typical coatings are compiled in Table 10.1. Table 10.2 lists selected coating materials and their most important properties.

Table 10.2. Examples of cathodic arc compound coatings for tool or decorative applications, with thickness 2–10 μm; for comparison, some data of the pure parent metal also given. (Data from various sources including web pages of companies offering arc coatings)

Coating material*	Color	Hardness (HV 0.025–0.05, unless given in GPa)	Maximum working temp. (°C)	Typical coefficient of friction (against Al_2O_3, without lubrication)	Most important properties and application
Ti	Metallic /gray	3 GPa			Corrosion protection
TiN	Gold, brownish gold when high N-content	2,300–3,200, 30 GPa	600	0.65	Still most common arc coating due to its hardness, inertness, and color; cutting tools for iron-based materials
TiAlN	Bronze, brown	2,200–3,500	800	0.42	Excellent oxidation resistance at high temperature, multilayers for carbide and high-speed tools
AlTiN	Gray, black	4,100–4,800	800	0.42	High-temperature oxidation resistance because it produces Al_2O_3 when high temperatures are encountered, higher hardness and smoother surface finish compared to TiAlN; dry machining, machining titanium alloys, Inconel® (austenitic nickel-based superalloys), stainless alloys and cast iron
TiAlN/WC/C		2,600/1,000	800–1,000		High-temperature solid lubrication multilayers, for carbide and high-speed tools

(*Continued*)

Table 10.2. *(Continued)*

Coating material*	Color	Hardness (HV 0.025–0.05, unless given in GPa)	Maximum working temp. (°C)	Typical coefficient of friction (against Al_2O_3, without lubrication)	Most important properties and application
TiAlN/VN		3,000–3,200	850	0.3	
TiCN	Pink to dark gray, black	3,000–4,400 (softer at high temp.)	400–500	0.32–0.45	Lower coefficient of friction, high hardness, toughness, and wear resistance; superior to TiN when machining stainless steels, high nickel alloys, cast iron, non-ferrous materials and plastics
TiAlCN	Blue black				Decorative
TiAlYN		2,800	850	0.5	
TiAlCrYN		2,800	950	0.55	
TiO_x	Transparent when thin, indigo black				Optical, decorative
Cr	Metallic/gray	12 GPa			Corrosion protection, replacement for electroplated chromium
CrN	Silver gray	1,700–2,900/ 24 GPa	620–700	0.55	Excellent corrosion, oxidation resistance and high hardness at high temperature; machining of copper, molding tools

CrN/NbN		3,300–3,400	850	0.5	
CrC	Silver gray	2,300	650		Corrosion and oxidation resistance; Al and Mg die casting
Zr	Metallic/gray	9 GPa			Rarely used in pure metal form
ZrN	White gold to brass	2,600–3,000, 27 GPa	500–600	0.6	High hardness, excellent corrosion resistance, low coefficient of friction; decorative coating, coating for medical and surgical instruments
ZrO_x	Like stainless steel	18 GPa			Decorative coating, e.g., to make plastic appear like stainless steel
ZrOC	Dark gray to bronze	27 GPa			
ZrCN	Stainless steel and nickel to brass, gold and black				
WC/C	Black	1,000	300	0.2	Low friction in dry cutting

* Symbols like ZrCN do not necessarily imply that the stoichiometric ratio Zr:C:N of the compound is 1:1:1, rather they are written for convenience.

Of course it is impossible to be comprehensive in this rapidly changing and expanding field, and therefore this chapter is only to highlight the most important applications and material examples. A comprehensive treatment would fill a book of its own. Many coatings are multifunctional, and this presented a challenge how to organize the subject. In essence, the most relevant applications are mentioned, with selected examples of arc-deposited materials addressing the functional need. One may see a web of materials and applications evolving, even as the selection of examples and their explanation are necessarily incomplete. In all cases, the common thread is that the coatings or structures are made by energetic condensation of arc plasma.

10.2 Nitride Coatings for Wear Applications

10.2.1 TiN and Other Binary Nitrides

Although the advent of industrial arc coatings may have been Edison's coatings attempts, the actual development began in the Soviet Union in the 1960s and 1970s (see Chapter 2). The first and still popular material was TiN because it combines decorative gold color with excellent wear and corrosion properties. Arc coating machines were built in large numbers, and the development of macroparticle filters followed just a few years later. With the introduction of this technology to the West, TiN became quickly popular for both tool and decorative coatings applications [1, 2] (Figures. 10.1 and 10.2).

Even today, some research and development efforts are still concerned with this material and its deposition techniques. Macroparticle filters are often involved when improving TiN, such as the classic 90° filter [3] or the Venetian

Fig. 10.1. Examples of conventional TiN tool coatings made by the cathodic arc process (the objects have a golden-looking coating which, unfortunately, is not reproduced in this black-and-white illustration). (Photo courtesy of Balzers Ltd, Liechtenstein)

Fig. 10.2. Examples of decorative coatings on faucets, door handles, and other objects. (Photo courtesy of Balzers Ltd, Liechtenstein)

blind filter [4]. In order to further improve the quality and adhesion on GCr15-bearing steel, not only was the Ti plasma filtered but the nitrogen gas was ionized by an RF-generator, and the substrate was pulse biased using a plasma immersion ion implantation approach [5].

With the perfection of TiN, a natural extension of the technology was to investigate, test, and produce a range of other compounds, and in particular other binary nitrides such as CrN, ZrN, and HfN [6, 7]. CrN was found to exhibit a lower coefficient of friction than TiN [6]. Coating companies started to look into a wide range of various nitrides for industrial applications in the 1980s [8, 9]. ZrN was found superior to TiN for cutting of titanium alloys [9].

It was realized that the performance of a coating needs to be considered under actual environmental conditions. For a cutting tool, this means to consider hardness, friction, wear, and chemical stability at the very high temperature of the cutting edge, which depend on the friction pair, lubrication, and cutting speed. For example, the temperature may reach 1,000°C in high-speed cutting. TiN is not oxidation resistant at this temperature, and therefore the need for improved coatings was recognized and remains a field of intense research until today.

Before we go to those improved material systems it should be pointed out that the mechanical performance is really the result of the properties of all components of the tribological or protective systems, not just the coating. For example, it makes little sense to try to maximize the hardness of a coating when the substrate is substantially softer. One approach in this specific situation could be a pre-coating hardening step of the substrate, for example via plasma nitriding if the substrate is a steel or aluminum alloy. This could be done in the same chamber, for example using a plasma immersion ion implantation process [10, 11, 12, 13], or by using the arc-generated plasma itself [14].

10.2.2 $Ti_{1-x}Al_xN$

In the late 1980s, $Ti_{1-x}Al_xN$, sometimes labeled (TiAl)N, and often simply abbreviated as "AlTiN," has emerged as a superior tool coating. It is hard, dense, well adherent on cutting tool inserts and shows excellent wear resistance and oxidation resistance at high temperature. This material has enabled high-speed machining and dry cutting. A very large body of research has been published on arc-deposited TiAlN [15]. TiAlN is grayish in color and has therefore not completely replaced TiN. In many applications, the decorative character of the coating is surprisingly important, at least in the marketing phase of a product.

The Ti–Al ratio of the cathode is a major parameter that can be selected to tune film composition and microstructure. However, this ratio in the cathode is not exactly reproduced in the composition of film. Often, the aluminum content in the film is slightly (a few percent) lower than the corresponding content in the cathode, which is due to sputtering in the energetic condensation process. The difference between cathode composition and film composition depends on the different sputter yields (here on the Ti yield versus Al yield) and on the energy of sputtering ions. The latter is determined by the (negative) bias of the substrate relative to the plasma potential. High bias leads to higher yields and an increase in the difference between Ti–Al ratio of cathode and film [16].

The group of Hultman at Linköping University [17] selected $Ti_{1-x}Al_x$ cathodes of various aluminum percentages and studied the microstructure of as-deposited and isothermally annealed samples. Transmission electron micrographs revealed a dense and columnar microstructure of the as-deposited films, which exhibited metastable cubic structures for an aluminum content of $x \leq 0.66$, whereas films from cathodes of $x = 0.74$ yielded two-phase coatings consisting of cubic and hexagonal structures. Increasing aluminum content promoted a (200) preferred crystallographic orientation and had a large influence on the hardness of the as-deposited coatings (up to 32 GPa). This corroborated earlier findings [18] that indicated a cubic NaCl structure for the as-deposited films from a $x = 0.67$ cathode, and the presence of nanocrystallites of wurzite-structure hexagonal AlN in a cubic (c)-(Ti,Al)N matrix when a $x = 0.75$ cathode was used. All films were stable with respect to phase composition and grain size during annealing at 900°C for 120 min. When the temperature was increased to 1,100°C, films deposited from the 67 at.% cathodes showed phase separation forming c-TiN and h-AlN via spinodal decomposition of c-TiN and c-AlN [17]. In another work [19], the same group showed that the as-deposited $Ti_{1-x}Al_xN$ films are metastable: they initially undergo spinodal decomposition into coherent cubic-phase nanometer-size domains, causing an increase in hardness at elevated temperatures. These intermediate metastable domains transform into their stable phases TiN and AlN during further thermal treatment, which explains the observed age-hardening and thermal stability of this class of ceramics. It was proposed [17] that competing mechanisms are responsible for the effectively constant hardness: softening by residual stress relaxation through lattice defect annihilation is balanced by

hardening from formation of a coherent nanocomposite structure of c-TiN and c-AlN domains by spinodal decomposition.

Spinodal decomposition is generally considered as the central mechanism responsible for the high-temperature behavior of $Ti_{1-x}Al_xN$ and other multi-element nitrides. This kind of phase separation is known in equilibrium chemistry of materials when certain multi-element single-phase materials are cooled. A solubility or miscibility gap appears in the phase diagram, below which the material can spontaneously decompose into two new phases having the same crystal structure but different composition ([20] p. 171). In the spinodal region of the phase diagram, phase separation can spontaneously occur via small fluctuations because the Gibbs free energy of the system is lowered. In the case of $Ti_{1-x}Al_xN$ and similar coatings, the as-deposited material is not in equilibrium but metastable. At high temperature, for example when a tool coating is used in high-speed cutting, atoms are given activation energy so they can diffuse thereby bringing the material closer to equilibrium conditions, and spinodal decomposition can occur. The formation of two or more phases increases the strength of the material by impeding the motion of dislocations (spinodal hardening).

Figure 10.3 shows a cross-section scanning electron microscope (SEM) micrograph of an alloyed TiAlN coating deposited by cathodic arcs at a substrate temperature of about 500°C. The multilayered structure is a consequence of the threefold substrate rotation and periodic switch-on and -off of different sources. The substrate material was the common WC/Co cemented carbide.

The hardness of TiAlN can be influenced by the substrate bias, which determines the stress and microstructure as explained in Chapter 8. PalDey and Deevi [21] observed the highest hardness of 2783±25 HV at −75 V bias and a N_2 pressure of 0.66 Pa. The adhesion strengths on M2 steels were in the range of 44–92 N, with the highest values at −75 V and at 1.33 Pa of N_2. They observed that higher critical loads can be obtained for gradient (Ti,Al)N coatings by continuously varying the bias voltage during deposition, which, interestingly, worked for both increasing and decreasing bias. This may be related to the maximum of intrinsic stress: changing the bias in either direction may result in reduced stress, which clearly can lead to enhanced critical loads.

10.2.3 Other Ternary and Quaternary Nitrides, Carbides, and Nanocomposites

Ternary nitrides can be deposited using either an alloy cathode, or two cathodes in a single source, or two individual arc sources with different cathodes. The latter two options have the advantage that fabrication of costly sintered cathodes is avoided while composition control is possible by adjusting the current of the individual cathodes. This has been demonstrated with Ti, Al, and Cr arc sources, producing coatings within the systems Ti–Al–N, Ti–Cr–N and Cr–Al–N [22]. The underlying idea is to identify film material systems that show superior performance based on spinodal decomposition, similar to the

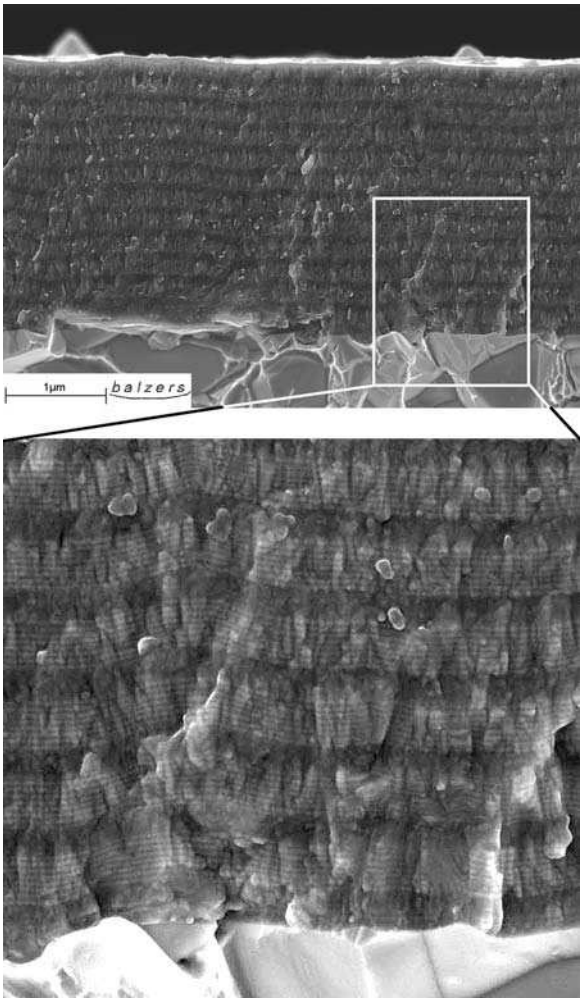

Fig. 10.3. SEM micrograph of a cross-section of an alloyed TiAlN coating on WC/Co cemented carbide; the multilayered structure, shown enlarged in the lower part of the figure, is a consequence of using several arc sources and substrate motion. (Photo courtesy of Balzers Ltd, Liechtenstein)

well-established TiAlN system. For the Ti–Cr–N system, only one phase, c-(TiCr)N, was identified as long as the chromium content was low (10 at.%) [23]. Coatings with higher chromium content (17–58 at.%) consisted of two phases: cubic (TiCr)N and hexagonal β-$(CrTi)_2N$. Due to preferential sputtering of Cr, the chromium content decreased with increasing substrate bias voltage (see Chapter 8). The two-phase coatings were nanocrystalline and showed high hardness with a maximum in the range 3,700–3,900 Vickers at a chromium content of about 25–30 at.% and a load of 0.5 N [23].

The ternary coating TiCrN can be modified by introducing carbon to the elemental composition, which could be done by using either an additional carbon (or carbon-containing) cathode or a carbon-containing process gas. For example, Chang and co-workers [24] used a mixture of nitrogen and acetylene and synthesized TiCrN and nanocomposite TiCr(C,N)/amorphous carbon (a-C) coatings with different carbon contents (9–27 at.%). As expected, increasing the acetylene fraction leads to greater carbon content. The coating contained a nanocomposite of metastable hard TiCr(C,N) crystallites and an amorphous carbon phase (a-C), which is not surprising because the carbon concentration exceeds the solubility of carbon in TiCrN. The nanocomposite TiCr(C,N)/a-C coatings exhibited higher hardness of about 30 GPa compared to the monolithic TiCrN coating (about 26 GPa).

Other examples of arc-deposited ternary nitrides are $Ti_{0.94}Hf_{0.06}N$ and $Ti_{0.92}Nb_{0.08}N$ that have been deposited on cemented carbide inserts using random and steered arc sources [8]. These coatings showed less flank and crater wear than conventional TiN and CVD-deposited TiC–TiN coatings.

The obstruction of dislocation movement has been recognized as a main approach to synthesize superhard materials. Arc-deposited TiC_xN_{1-x} materials have been carefully studied, with x ranging from zero (TiN) to unity (TiC) [25, 26]. In this case, the reactive deposition makes use of one cathode (Ti) and two reactive gases, N_2 and CH_4, and the film composition can be adjusted by the gas flow ratio. Because these coatings are relevant to cutting tools, cemented carbide inserts (WC-6 wt.% Co) were used as substrates. Negative bias is usually applied: it is a means to heat the substrates and also to affect the microstructure (Chapter 8). For example, a bias of –400 V resulted in a substrate temperature of 550°C. Cross-sectional transmission electron microscopy (XTEM) in combination with X-ray diffraction (XRD) showed that the films were single phase of the NaCl-type structure with a dense columnar microstructure. The intrinsic stress had a maximum of –5.9 GPa in the composition range $0.4 \leq x \leq 0.7$. Nanoindendation of the as-deposited films showed a maximum hardness of 45 GPa in the same composition range. For comparison, the hardness of TiN and TiC is 28 and 36 GPa, respectively. Compressive stress can be varied by adjusting composition and the bias voltage. High voltage (up to –820 V) reduced stress, while increasing the carbon content increased stress. Cracking of the films occurred when the compressive stress exceeded about –7 GPa.

Another approach to improvements of TiAlN coatings is by adding another metal to the metastable single-phase coating and thereby producing a quaternary compound. For example, adding chromium might promote the formation of a protecting chromium oxide surface layer. Yamamoto and co-workers [27] added chromium, forming $(Ti_xCr_yAl_z)N$, with $x{:}y \approx 1{:}2$, $z = 0.63$–0.73, $x + y + z = 1$. They found that this cathode material produces less macroparticles than conventional cathodes. Perhaps the ignition of emission centers is promoted on this material so that each emission center operates shorter at one location, overtaken by its successor. They also found that negative substrate bias greater than 50 V induced a phase change of the deposited films from hexagonal

to cubic, increasing the hardness up to 35 GPa (for ion-induced hardness increases and phase changes, see Chapter 8). Measurements with a thermal balance showed that the films started to oxidize when the temperature exceeded 1,000°C, which is slightly better than TiAlN.

The trend to adding one or more metals has recently become very popular: there is a vast range of possibilities; generally, combinations of the materials Ti-Al-Cr-Si-C-B-N are investigated, and additionally other transition metals are considered such as Nb, V, Mo, Ta, and Hf.

10.2.4 Multilayers, Nanolayers, and Nanolaminates

Multilayer structures have been recognized as superior to monolithic layers in several ways. With suitable deposition configurations, their fabrication is not much more involved than more conventional coatings, while their mechanical properties like toughness can be greatly improved and even better than the properties of each of the constituent materials used. Typically, multilayer structures for tool coatings are more than 1 μm thick, with each individual layer having a thickness of a few nanometers or tens of nanometers. When the individual layers of a multilayer system have ~10 nm or less thickness, one may speak of nanolayers.

For example, Lee and co-workers [28] deposited a nanolayered WC–CrAlN heterostructure on silicon and S45C steel with a bi-layer period of 2–10 nm. The multilayer structure facilitates a low residual stress of less than 2 GPa while the microhardness was very high, in the range 30–43 GPa. The adhesion strength could be enhanced to 50 N by depositing a buffer layer of WC-Cr.

Using their dual-arc LAFAD (large-area filtered arc deposition) facility [29], Gorokhovsky and co-workers deposited TiN/Ti multilayers and TiCrN/TiCr superlattice multilayer coatings on periodontal dental instruments [30]. They demonstrated that wear is reduced by approximately 90% compared to uncoated dental tools. Ultrasonic cleaning and sterilization cycles did not affect the wear resistance of the coating systems.

Nanolaminates may be defined as a series of alternating sublayers with different compositions and/or electron density distributions [31]. Not all nanolaminates are thin film superlattices but they can be single-phase materials like the famous MgB_2 or the so-called MAX phases [32], which consist of an early transition metal M, an element from the A groups of the Period Table, usually IIIA and IVA, and a third element, X, which is either nitrogen or carbon. The composition is $M_{n+1}AX_n$, where $n = 1$, 2, or 3. The classes of materials naturally form three groups, based on the number of atoms of the M, A, and X elements in each molecule; these groups are known as 211, 312, and 413 materials. Examples for the first group are M_2AlC, with M = Sc, Y, La, Ti, Zr, Hf, V, Nb, Ta, Cr, Mo, W. More than 50 MAX phases are known and more can be expected since this is a field of intense research. MAX phase materials have amazing properties because they combine high-temperature stability of ceramics with properties of metals such as good thermal and electrical conductivity. In contrast to

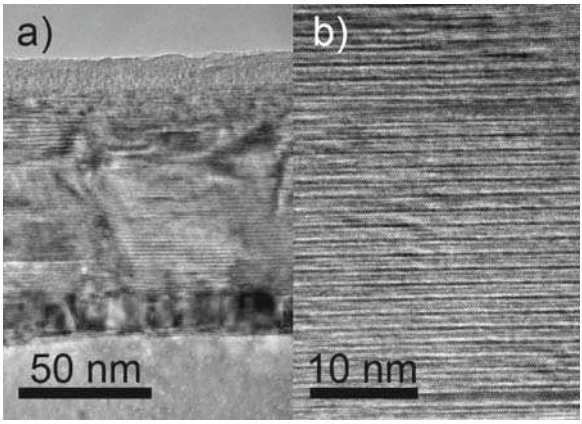

Fig. 10.4. Cross-sectional TEM image of a Ti_2AlC MAX phase coating synthesized by three-cathode pulsed arc deposition at 900°C: (**a**) low-resolution image, with the $\alpha - Al_2O_3(0001)$ substrate at the *bottom*, coating in *center*, and the amorphous-looking TEM-glue layer on *top*; (**b**) high-resolution image clearly showing the nano-laminate structure. (Image courtesy of Johanna Rosén (deposition) and Per Persson (TEM), work done at Sydney University)

conventional ceramics, like the binary transition carbides or nitrides, they are relatively soft and machinable. For an introduction the reader may resort to Barsoum and El-Raghy's paper [33], and consult the rapidly growing literature, which is beyond the scope of this book.

The synthesis of the Ti_2AlC MAX phase was successfully demonstrated using cathodic arc deposition with a triple-cathode pulsed arc system [34]. The Ti:Al:C pulse ratios were fine-tuned such as to obtain the necessary stoichiometric relation in the coating, which was deposited on $\alpha - Al_2O_3(0001)$ substrates at 900°C. TEM revealed epitaxial growth and the nanolaminated hexagonal structure with some rare cubic precipitates (Figure 10.4).

10.2.5 Replacement of Hexavalent Chromium

Many cathodic-arc-deposited hard coatings also provide excellent corrosion resistance, which is due to the chemical nature and high density of the coatings. For example, the later described ta-C films are actually multifunctional coatings. In fact, as ta-C films become thinner than 5 nm, their main function is corrosion protection of the magnetic layers.

A broad class of corrosion-resistant coatings includes chromium and chromium-containing alloys. These coatings work via the formation of a thin oxide layer, which is very inert (this is also the reason for the corrosion resistance of stainless steel). Chromium and chromium-containing alloys can be deposited by a number of techniques. Wet-chemical plating is popular because thick coatings

can be deposited at low cost, with high throughput. An additional advantage is that three-dimensional objects can be readily coated. While the plating process provides an excellent surface finish, which shows desirable color, high hardness, and good corrosion resistance, it is known to involve carcinogenic chromium hexavalent (CrVI) compounds, often called hexavalent chromium, or simply "hexavalent chrome." Examples are calcium chromate, chromium trioxide, lead chromate, potassium dichromate, strontium chromate, and zinc chromate. Reduction and eventual elimination of hexavalent chromium is mandated by law in many countries. In the United States, the Occupational Safety & Health Administration (OSHA) regulates the exposure (see http://www.osha.gov/SLTC/hexavalentchromium/).

Cathodic arc deposition is now used as an alternative process because arc-deposited chromium has similar, and in some cases even better properties than plating-produced chromium coatings. A study at Vapor Technologies in Colorado [35] showed that arc plasma deposition delivers coatings of indistinguishable color (compared to plating) and high hardness of 800–1,400 HV, compared to 600–700 HV for plated chromium. Usually, a relatively thick (25 μm) layer of nickel is deposited electrochemically and the surface finish is done with a relatively thin layer (0.25 μm) of arc-deposited chromium. The corrosion resistance was tested using CASS (copper accelerated salt spray) using standard ASTM B-368 and evaluation standard ASTM B-537-70. Most of the samples in this study passed rating 9, which means that less than 0.1% of the surface was attacked by corrosion.

10.2.6 Carbides

Besides oxides and nitrides, carbides can also have excellent wear and corrosion-resistance properties. As mentioned in Chapter 9, carbides can be synthesized either from metal and carbon plasma, or from metal plasma and using a carbon-containing gas as the source. In the latter case, to minimize hydrogen incorporation, the substrate is kept at high temperature.

Chromium carbide is an example of a coating used to enhance the performance and lifetime of forming and molding dies. The high mechanical strength, chemical resistance, and high-temperature stability of the Cr_3C_2 phase can be beneficial in severe abrasive wear and corrosion conditions. Using XRD and other characterization techniques, Esteve and co-workers [36] showed an evolution of the crystalline structure of the coatings from amorphous carbide to Cr_7C_3 and to the pure Cr_3C_2 phase as the C_2H_2 pressure in the deposition chamber decreases from 6.3 to 0.4 Pa. They also noticed that adhesion of the Cr_3C_2 coatings strongly increased by adding a CrN interlayer. The highest hardness of 22 GPa was obtained for the Cr_3C_2 coatings while the amorphous carbide showed the lowest hardness (10 GPa) and friction coefficient.

Boron carbide is another very attractive (yet challenging) coating – it will be dealt with in a later section of this chapter. For extensive information on the physical,

thermodynamic, chemical, and other properties and data of refractory nitrides, carbides, and borides, the reader is referred to the literature [37, 38, 39, 40, 41].

10.2.7 Multi-Element Coatings on Turbine Blades

Blades in aircraft and in land-based gas turbines are in an extremely hostile environment associated with hot combustion gases. The base material is optimized for the extreme mechanical demands. High creep strength and high cycle fatigue resistance is required. For example, the base material can be a nickel alloy such as NCK 18 TDA or a superalloy such as Inconel® 718, which have maximum operation temperatures of 850 and 650°C, respectively [42]. These nickel-based alloys require the oxidation resistance to be improved, which is addressed by applying a relatively thick coating. Low-pressure plasma spraying (LPPS) has been used to deposit such coatings, but cathodic arc deposition has emerged as an alternative process delivering a denser coating that provides better protection.

Arc cathodes containing five to seven elements have been investigated for "MCrAlY" coatings on turbine blades [43]. MCrAlY implies that the cathode and resulting coatings contain the elements Cr, Al, and Y, as well as other metals "M." The composition of the coating is different from that of the cathode material, but the difference is relatively small (within percents, see also comment on preferential sputtering in the TiAlN case, Section 10.2.2). For a selected and fixed bias voltage, the desired coating composition can be reached by proper adjustment of the cathode material. The MCrAlY coating showed a two- or three-phase structure with satisfactory adhesion strength. The use of the arc coating process suggests going to a multi-cathode system that allows the operator to deposit multilayers, which are known to exhibit superior performance, for example, in making high-temperature diffusion barriers.

Under certain conditions, for example when dust and sand particles are present, erosive wear is a major issue for turbine blades. In these cases, one can "borrow" from the experience in tool coatings and apply hard, abrasion-resistant coatings such as TiAlN or TiN/TiAlN multilayers [42]. The oxidation resistance for these coatings is due to the formation of a thin Al_2O_3 film that prevents diffusion of oxygen to the bulk of the coating and underlying base material.

10.2.8 Cubic Boron Nitride and Boron-Containing Multi-Component Coatings

The interest in boron and boron-containing coatings is due to some extraordinary properties of the element as well as its compounds. In particular, cubic boron nitride, c-BN, is the second hardest material after diamond (not counting some recent man-made materials such as ta-C and certain nanostructures). Cubic-BN is superior to diamond in polishing and cutting applications in oxidizing atmospheres. It combines very high hardness, low coefficient of friction, and inertness to many chemicals. Unlike diamond or diamond-like carbon, it does not react with iron in tribological contact and is therefore a material of great interest for

coating of tools and wear parts. Several methods have been used to synthesize films with considerable amounts of the cubic phase; all have in common that the substrate is kept at elevated temperature during deposition and bombarded by an intense flux of ions. High compressive stress is typical, often limiting adhesion of the coating.

It is difficult to use boron as a cathodic arc cathode because it is not a true metal but rather a *metalloid* (semi-metal, semiconductor); its electrical resistivity is $1.5 \times 10^4\ \Omega$ m at room temperature. Several concepts are used to utilize boron in a cathodic arc process: (i) using a conducting boron-containing sintered compound or alloy cathode [44, 45], (ii) heating a boron cathode to become sufficiently conducting ($T > 800^\circ$C) [46, 47, 48], (iii) get boron from a boron-containing gas or vapor (reactive deposition), or (iv) combine arc deposition with other techniques such as sputtering.

Richter and co-workers [46] did pioneering work using a filtered cathodic arc with a hot boron cathode in a nitrogen atmosphere aiming to synthesize c-BN films. Materials characterization with FTIR (Fourier transform infrared) spectroscopy and cross-section transmission electron microscopy (XTEM) and electron diffraction revealed that the BN phase was mainly hexagonal (not cubic, as needed).

In another line of work by Werner and co-workers [49], boron-containing, multi-component coatings were deposited on high-speed steel HSS SW7M (AISI M2) using a two-step process. In the first step, a titanium adhesion layer was deposited, followed by cathodic arc deposition using $Ti_{55.2}B_{24.8}Si_{20}$, $Ti_{60}B_{40}$, $Ti_{50}Al_{50}$, and $Ti_{80}Si_{20}$ cathodes. For simplicity, the resulting coatings were labeled Ti–B–Si–N, Ti–B–N, Ti–Al–N, and Ti–Si–N, respectively. According to this study, the Ti–B–N coatings exhibited the highest hardness, exceeding by 15–20% the hardness of similar layers at lower B concentration, which was interpreted as due to a high content of the TiB_2 phase. The Ti–B–Si–N coatings showed the highest adhesion with a critical load of 130 N. Overall, the Ti–Si–N coatings exhibited the best wear resistance.

Much work on boron-containing coatings by cathodic arc deposition was done at HY-Tech Research Corporation for applications in the tool and automotive industry, protective coatings on thermonuclear fusion devices (walls, RF antennas), and on biomedical implants. Using a sintered B_4C cathode, Klepper and co-workers [50, 51] operated the arc in long pulse mode (up to 0.5 s) depositing amorphous boron carbide films with deposition rates greater than 10 nm/s. Using substrate bias up to –500 V [52], the hardness and elastic modulus were tuned, much as explained in Chapter 8 on energetic condensation.

Going to a pure boron cathode (see Figure 5.19) operating in vacuum (without background gas), the group demonstrated amorphous boron/boron suboxide coatings on various metal alloy substrates. For example, nanoindentation of a 400-nm-thick film on steel showed a microhardness of up to 27 GPa, a modulus of 180 GPa, and hence a high H/E ratio, which suggests good impact resistance (toughness) of the coating.

One application for pure boron coatings on steel is the wetting protection of aluminum die cast molds. Experiments [53] confirmed that the as-deposited

boron films adhere well to steel while they would not be wetted by aluminum. Coated areas without macroparticles had superior performance, whereas areas with macroparticle-related defects showed some unwanted adhesion of aluminum. The avoidance of wetting is of great importance to the automotive industry where molding dies are used to produce light-weight parts from aluminum alloys.

10.2.9 Tetrahedral Amorphous Carbon (ta-C)

The growth of ta-C films by subplantation has been discussed in Chapter 8. Here we consider some properties and applications of this material.

Tetrahedral amorphous carbon (ta-C) is the most diamond-like material in the family of diamond-like carbon (DLC) materials. Using filtered cathodic arc deposition, more than 80% sp^3 bonds have been demonstrated [54, 55, 56]. Some researchers prefer to call this material amorphous diamond, or a-D [57, 58, 59, 60], to stress the dominance of the tetrahedral (sp^3) bonds, but some others object to this name, and so ta-C seems to be the preferred name in recent years.

Similar to diamond, ta-C is superhard, has a very high elastic modulus, is chemically inert, and optically transparent. The combination of these outstanding properties makes this material very interesting for many applications. However, there are also limitations: ta-C films have often high intrinsic stress, which can lead to cracking and delamination. This is especially a problem when thicker films (>300 nm) are needed. For thicker films, bias techniques for stress relief should be applied (Chapter 8), or atoms other than carbon should be incorporated (see later this section).

Films of ta-C, which commonly have very low hydrogen content, are characterized by a relatively high coefficient of friction (about 0.6) under dry conditions, e.g., in vacuum or dry argon. However, the coefficient of friction can be drastically reduced, to about 0.1 or even less, when surface adsorbates such as hydrogen, oxygen, and especially water molecules are present [61], see also Erdemir's review [62].

An important application of filtered-arc-deposited ta-C is in the magnetic storage industry, where ultrathin (about 5 nm in 2002, down to about 2 nm in 2008) films are used to protect magnetic media and read–write heads. The storage industry and its technologies have remarkably developed over the last two decades, as manifested by the astonishing increase of storage capacity in computer hard drives. This development has also enabled new hand-held music, gaming, and communication devices.

The issues of overcoats, including filtered-arc-deposited ta-C, have been discussed in a number of papers and reviews [63, 64, 65, 66, 67, 68, 69]. A significant contribution to the industry's success was the reduction of overcoat thickness down to about 2 nm, with current attempts to reduce this even further. In order to further increase the density of stored information, which currently already exceeds 100 Gbit/in.^{2}, the "magnetic spacing" between storing layer and read–write head needs to be reduced as much as possible. If we consider a typical

hard disk situation, the magnetic spacing includes the magnetically dead layer formed at the interface between protective coating and magnetic material, the protective coatings of head and disk, a lubricant layer on the disk, and the flying height of the slider (head carrier).

For applications of cathodic arc films in the storage and semiconductor industry, requirements on macroparticle filtering are very stringent. Singh Bhatia, a lead engineer at IBM in the late 1990s, compared the slider flying over the hard disk to a 747 jumbo jet just before touchdown: If there was a macroparticle present it would correspond to the pilot seeing a building in the middle of the runway! Therefore, for most of the last two decades, the industry preferred sputtering and later ion beam technology to fabricate ultrathin protective films. In recent years, however, the requirements led to the development of improved filter schemes, which are characterized by filter bending angles greater than 90° ([65, 68, 70, 71, 72, 73], see Chapter 7).

Ultrathin ta-C films are required to be well adherent to the magnetic material or an ultrathin adhesion layer (Si). They need to be smooth at the atomic level, pinhole-free, hard, inert, and they need to wet the lubricant. Hardness becomes less of an issue since such extremely thin films cannot withstand great mechanical forces: such films serve mainly as a corrosion protection coating. Corrosion can occur as part of the tribological use of the coating, and therefore specific investigations have been made characterizing the abrasion and corrosion behavior in controlled tribological environments [74, 75, 76].

Assuming that macroparticle filtering is not an issue, research focuses on properties such as continuity (i.e., lack of pinholes) of ultrathin ta-C films, which is a challenge not only to deposition technology but to metrology. Special instrumentation was developed to evaluate films of less than 5-nm thickness. For example, atomic force microscopy (AFM) was used for nano-scratching. By combining AFM and X-ray reflectivity measurements it could be established that scratch resistance of ultrathin carbon films correlates with the mass density [65], confirming an earlier result found for 300-nm films [77]. This is one of the arguments why hydrogen-free filtered-arc-deposited films are superior to ion-beam-deposited or sputtered films.

For a storage density exceeding 200 Gbit/in.^{2}, the ta-C film thickness should be less than 2 nm and the roughness well below 1 nm. Atomic force microscopy (AFM) showed that the surface roughness of filtered ta-C is almost constant at about 0.12 nm [66] and likely related to the roughness of the substrate surface. In general, roughness, r, evolves during film growth following a fractal scaling law with increasing thickness, h, according to $r = ah^{\beta}$, where β is the growth exponent. For a fixed film thickness and scan length l, the roughness varies as l^{α}, where α is the roughness exponent. Casiraghi and co-workers [66] found $\alpha = 0.39$ and $\beta = 0 - 0.1$ for ta-C films. Despite the extremely small thickness, these films appear to be of very low pinhole density, of high sp^3 content (about 50%), and show a Young's modulus of about 100 GPa. The pinhole density is determined by corrosion tests involving corrosive solutions or salt fog spraying, with subsequent inspection in an optical microscope. The extremely small

roughness, inertness, and other properties mentioned suggest that filtered-arc-deposited overcoats for storage densities approaching 1 Tbit/in.^{2} are possible.

A very different application of ta-C coatings by filtered arc is on razor blades, as commercialized by the Gillette Company [78, 79]. Here, the combination of low wear, low friction, and the chemical inertness (compatibility with skin and tissue) is utilized. The filtered arc coating process ensures that adhesion to steel is excellent even without the application of an adhesion layer. The ta-C films of 45-GPa hardness and 400-GPa modulus preserve the sharp edge and impart stiffness and rigidity of the thin blade.

On the other end of the spectrum of carbon film applications, very *thick* ta-C films are desired, namely for the fabrication of MEMS and NEMS (microelectromechanical systems and nanoelectromechanical systems). Usually those structures are made from silicon using lithographic techniques; however, diamond-like carbon could be a superior material due to its excellent tribological properties, low stiction,[1] chemical inertness, and high elastic modulus.

The reduction or even elimination of intrinsic stress is the key to fabrication and wider application of ta-C or related materials. Methods of stress reduction were discussed in Chapter 8, and so here we only mention the growth of thick (>1 μm) films. Using 3-kV negative pulsed bias, Sheeja and co-workers [80] succeeded in reducing the stress to about 1 GPa for a 3.1-μm-thick film deposited by filtered arc. Wear testing against a sapphire ball gave a low friction coefficient of 0.084 and a low wear rate of 6.7×10^{-8} mm^3/N m. By improving the stress relief technique and using a slightly higher pulsed bias voltage of 5 kV with 25 μs at 600 Hz, the intrinsic compressive stress was further reduced to 300 MPa, which allowed them to fabricate large, 2 mm $\times$ 2 mm freestanding amorphous carbon (a-C) films [81] as well as cantilever structures using photolithography with anisotropic wet etching [82]. The carbon films can be etched using oxygen plasma or oxygen ion beams, techniques known as reactive ion etching (RIE), and reactive ion beam etching (RIBE) [83].

10.2.10 Hydrogen, Nitrogen, and Metal-Doped Tetrahedral Amorphous Carbon

The filtered cathodic arc process can also be used to incorporate other elements in the amorphous carbon film. Operating in a background of hydrocarbon gases (like acetylene) or nitrogen, hydrogenated or nitrogenated films can be made, respectively.

For example, Lemoine and co-workers [84] used a double bent filtered arc system to fabricate ta-C and a-C:H films of 10- to 50-nm thickness on floating Al_2O_3–TiC substrates. They studied the adhesion and wear properties by

[1] The term *stiction* refers to sticking or "static friction" (a force is applied but no motion occurs), whereas friction usually involves a force to keep the object moving. Here, low stiction means a low force threshold to the onset of motion, which is related to the hydrophobic properties of diamond-like carbon.

nanoindentation, nano-scratching, and other techniques. As expected, the ta-C films are harder (max. 51 GPa for the 50-nm film), they have a higher critical load, and showed wear rates of 1.8×10^{-4} mm^3/N m at an initial contact pressure of 37 GPa. The critical loads and wear rates are smaller than those of hydrogenated films. The ta-C is in fact so hard that it blunted the diamond tip, which required recalibration of measurements in which the tip area plays a role. For nanoindentation of very thin and hard films, the reader is referred to the much-cited work by Oliver and Pharr [85].

One motivation to hydrogenate the hard carbon films is to make them less brittle but softer, more stretchable and bendable so they are more compatible to plastic and rubber substrates [86]. As a side effect, operation of a filtered carbon arc in acetylene slightly increases the deposition rate compared to the carbon arc in vacuum. The structure of the hydrogenated film on rubber, however, is very different from the structure of ta-C films on silicon wafers. The former appears as "meshed islands," with the islands cracking into smaller pieces as the substrate was bent [87].

Nitrogen-doped, or "nitrogenated" ta-C films, also designated as ta-C:N or a-C:N films, can have hardness and modulus close to the undoped material but at reduced stress. Ultrathin film can be deposited by using the filtered arc in a nitrogen background gas, and such films were considered for the demanding applications in the magnetic storage industry [88]. With high hardness in the range 40–65 GPa, Young's modulus 200–285 GPa, the material had excellent elastic recovery, a high critical pressure for scratch formation, and very low wear rates.

At a high percentage of nitrogen incorporation, however, one can clearly see a deterioration of the extreme properties of ta-C [89]: hardness and elastic modulus are reduced (Figure 10.5), which was ascribed to the clustering of sp^2 sites [90].

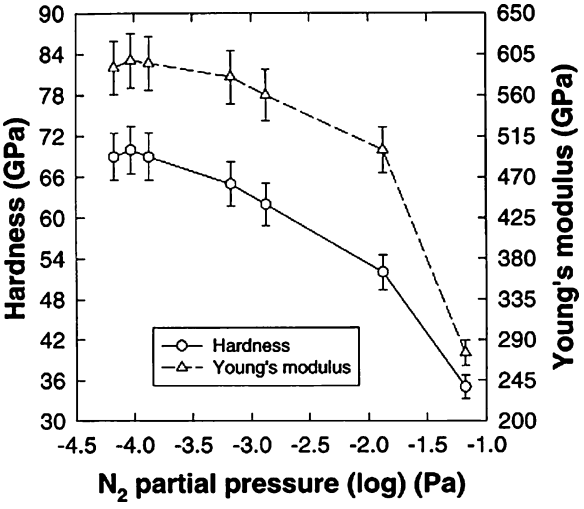

Fig. 10.5. Hardness and Young's modulus of ta-C:N films deposited by a filtered cathodic arc at different N_2 partial pressures. (From [89])

The nitrogen molecule has a strong triple bond and therefore it is not very reactive unless it is "activated." As mentioned in Chapter 9, activated nitrogen species include atoms, excited or ionized atoms or molecules. In a study of the effects of assisting nitrogen ions, Kühn and co-workers [91] tested various ion and plasma sources to find that a low energy supply of nitrogen is beneficial for the mechanical properties of the coating, whereas energetic beams are detrimental, which can readily be explained by the ion damage and graphitization of the arc-deposited ta-C films.

Facing the challenge of having several factors influencing the properties of a-C:N films produced by filtered cathodic vacuum arc deposition, Tan and co-workers [92] used a design-of-experiment (DOE) approach to optimize the wear and corrosion protection properties. They considered four factors: negative substrate bias voltage, arc current, Ar flow, and the N_2/Ar ratio. This ultimately gave the optimum wear-corrosion properties using a –20-V substrate bias, 30-A arc current, 30-sccm Ar flow, and 1/6 N_2/Ar ratio, leading to a low wear-corrosion current density of 5.6 nA/cm^2 , and a very low coefficient of friction of only 0.025 against a sintered Al_2O_3 ring with roughness 0.3 μm, with an applied force of 70 mN in 3.5% NaCl aqueous solution.

Apart from gaseous species (like N, H), one may also incorporate metal atoms in the amorphous carbon matrix. The source of metal typically is from a cathodic arc, although one may also consider a magnetron or metalorganic gases. The carbon source is generally the cathodic arc operating with a graphite cathode, but also here alternatives are possible: the metal arc could be operated in a hydrocarbon background (such as C_2H_2). The latter was done by Fu and co-workers [93, 94, 95], who operated a molybdenum arc in acetylene at various flow rates. Using XRD and TEM for film characterization, they found that the film material consists of molybdenum carbide grains embedded in an amorphous carbon matrix. The surface was smooth (∼0.1 nm), and the material was stable up to 500°C, which is comparable to ta-C films made by filtered arcs. A similar approach was done by Vetter and co-workers [96] to produce a-C:H:Me coatings (where Me stands for a metal) that exhibit low friction in dry and lubricated tests, high critical load, and high wear resistance as needed in hydraulic systems.

Yet another way of incorporating carbon and a metal is to use a graphite/metal composite cathode in a filtered cathodic arc system [73, 97]. The doped or composite films are typically investigated using X-ray-induced photoelectron spectroscopy (XPS), Raman spectroscopy, atomic force microscopy, and nanoindentation. Using iron in the composite cathode, Chen and co-workers [97] found that the Fe concentration in the films was always higher than in the cathode, and small amounts of oxygen could be found. The stress was reduced compared to undoped ta-C films. The intensity ratio of the Raman D and G peaks increased with an increase in Fe content, suggesting that the sp^2 content and the size of the sp^2-bonded clusters increase with an increase in the Fe content.

A rather comprehensive study was done by B.K. Tay and his group [73, 98] using various composite cathodes that included up to 10% of Si, Al, Ti, Fe, Ni,

or Co. Incorporating those metals leads to significantly decreased stress, increased surface roughness, an increase in the sp^2 content, and a clustering of sp^2-bonded carbon when the metal content is high. For small metal content, hardness and elastic modulus remain almost as high as for pure ta-C materials, but reductions are observed as the film contains more and more metal. If the metal is a carbide former, like titanium, this reduction is not as pronounced compared to when non-carbide formers are used, such as aluminum. The latter are therefore not recommended for wear applications.

A pure ta-C film has surface energy of about 0.0428 N/m, and this value can be increased by incorporating Ni, or decreased when using Fe or Al. In a related publication [99] dedicated to the surface energy of doped ta-C films, Zhang reports that the highest contact angle with water is observed with Al doping, reaching 101°. The Si-containing films showed the lowest contact angle of 64°. The contact angles of Ni- and Ti-containing ta-C were 80° and 97°, respectively.

Another way of producing metal-containing ta-C films is by using a pulsed filtered arc with two cathodes [100, 101, 102]. The amount of metal in the film can easily be adjusted by selection of the metal to carbon pulse ratio. An interesting twist in the work [101, 102] was that the substrate was biased when carbon ions arrived at the substrate while no bias was applied at the time of metal ion arrival. In this way, the ratio of sp^3 and sp^2 bonds could be affected independently of the concentration of metal. As in the previous work, a greater metal content led to more conductive films, which was ascribed to greater sp^2 content and sp^2 cluster size.

All of the above properties are important when using metal-containing ta-C films for MEMS fabrication. For example, films need to have several microns of thickness before they could be considered viable for those applications. Stress control is paramount, and roughness, surface energy, and the mechanical properties will affect friction and wear.

10.3 Decorative Coatings

10.3.1 Appearance of Color

Decorative coatings are multifunctional coatings whose color and appearance are of great importance to the end user. These properties are determined when visible light interacts with the coating. One may distinguish extrinsic and intrinsic optical properties [103]. Extrinsic properties alter the light direction of different wavelengths, for example surface roughness determines glossy or matte appearance. Intrinsic interaction is determined by reflection and absorption of light by electrons in the material. Following the work by Niyomsoan and co-workers [103] on TiN and ZrN, intrinsic interaction shall be discussed in greater detail because it is important for the color of numerous hard and decorative coatings made by cathodic arc deposition.

When light falls on an object, it is reflected and absorbed, and a fraction may be transmitted. If we designate the intensity of incident light as I_0, the intensities of the reflected and transmitted light are $I_0\rho$ and $I_0\tau$, respectively, where ρ is the reflectance and τ is the transmittance. From energy conservation follows the radiation distribution equation:

$$\rho + \tau + \alpha = 1, \tag{10.1}$$

where α is the absorbance [104].

It is the reflected light that gives us the color impression of the coating. Therefore, we need to consider interference of multiply reflected waves in the case of transparent or slightly absorbing film materials, and the absorbing properties for spectrally absorbing coatings of materials having free charge carriers. These two cases will be discussed in the next two sections.

10.3.2 Color by Interference

Interference colors established by multiple reflection from thin transparent films on reflecting bodies (substrates) or air gaps between transparent bodies were already described by Robert Hooke in 1664 and explained by Isaac Newton in 1670 ("Newton's rings"). The details are discussed in all textbooks on optics, and therefore a brief summary will suffice here.

When light is incident on a transparent or slightly absorbing film, the waves are multiply reflected as shown in Figure 10.6. The superposition of the reflected waves leads to amplification (constructive interference) when the optical length is $\lambda/2$, $3\lambda/2$, $5\lambda/2$, etc. The optical length is defined as the geometric length times the refractive index, n, of the medium. Additionally, a phase shift of $\lambda/2$ needs to be taken into account, which occurs upon reflection, where λ is the wavelength of the light. For normal incidence, the condition for constructive interference can be written as

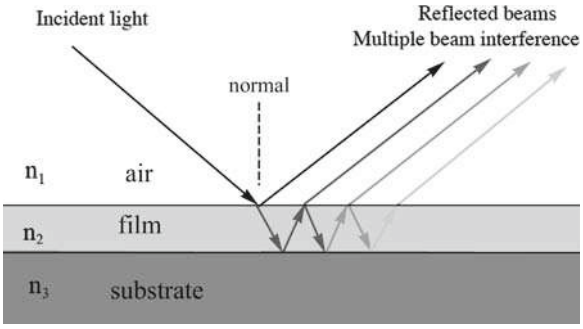

Fig. 10.6. Schematic of multiple reflections from a transparent film and interference of the reflected beams

$$2dn_{film} = \left(m - \frac{1}{2}\right)\lambda, \quad m = 1, 2, 3, ..., \tag{10.2}$$

where d is the film thickness and n_{film} is the refractive index of the film; the factor 2 comes from the fact that the light travels through the film from front to back and then back to the front surface. For oblique angle incidence, as shown in Figure 10.6, the optical path in the film is longer and Eq. (10.2) should be written in the more general form:

$$\frac{2dn_{film}}{\cos\vartheta} = \left(m - \frac{1}{2}\right)\lambda, \quad m = 1, 2, 3, ..., \tag{10.3}$$

where ϑ is the angle of incidence relative to the surface normal. This equation contains all the necessary information to answer questions like the following: What thinnest film would give the appearance of green ($\lambda = 540$ nm) at normal incidence? Assuming a refractive index of 1.65 (for aluminum oxide at about 550 nm), and taking $m = 1$, we obtain $d = 81.8$ nm. From Eq. (10.3) we also see that if we looked at the same coating under an oblique angle of, say, 40° with white light illumination, we would see a red film (constructive interference at $\lambda = 705$ nm). The color of interference coatings depends on the film thickness as well as on the angle of view, which may or may not be desirable. If one wants to obtain an angle-independent colored coating, one needs to work with spectrally selective absorbing coatings.

A final comment before we deal with those spectrally selective absorbing coatings. The order of the interference, $m = 1, 2, 3, ...$, can be used to quickly and rather accurately determine film thickness, provided one knows the refractive index. For thicker films, typically several 100 nm thick, one could simply count the number of repeating interference fringes which may be visible at edges of three-dimensional parts, or at the transition to an uncoated area. For estimates one may use tabulated refractive index values. The colors of the first and second interference are usually more vivid (greater saturation in the color space, see Section 10.3.4) than higher orders due to some absorption occurring in the film.

If the films are moderately absorbing and thick, most of the light will be absorbed and the coating appears black (e.g., thick diamond-like coatings).

Absorption can be quantified by the extinction coefficient, k, which is often introduced as the imaginary part of the complex refractive index:

$$N = n + \mathrm{i}k, \tag{10.4}$$

where n is the real part of the refractive index, typically in the range 1.4–2.7 for most transparent materials. The real part n describes the phase velocity of light in matter, $n = c_0/c$, where c_0 is the speed of light in vacuum. These expressions will come in handy when discussing absorption.

10.3.3 Color by Spectrally Selective Absorption

A coating shows color when incident white light is spectrally selectively reflected, which is closely related to the light being spectrally selectively absorbed,

see Eq. (10.1). Absorption mechanisms can be categorized into four types (in the order of importance):

- free carrier absorption (intraband transitions),
- interband transitions,
- absorption due to impurities,
- reststrahlen absorption.

Free carrier absorption or intraband transition refers to electron excitation from partially filled valence bands to unfilled states just above the Fermi level. These carriers absorb a broad range of photon energies, including photons in the visible part of the spectrum. Excited electrons may interact with lattice vibrations (phonons) and dissipate their energy as heat. Other electrons return to lower energy states by emission of photons, which may leave the material and can then be observed as reflected or scattered light. Quantum-mechanical selection rules for electron transitions can force electrons to return to lower levels via different levels than their excitation paths, and the color of the emitted light may not correspond to the absorbed light.

Materials with a filled valence band and an empty conduction band, separated by an energy gap, will absorb photon energy greater than the gap, leading to electron transition from the valence band into the conduction band (interband transitions). Color results from the remaining, not absorbed, visible light. Materials whose band gap is wider than the ultraviolet limit of the visible spectrum, $E_g > 3.5\,\text{eV}$, are transparent to the eye, since photons of the visible part of the spectrum have less energy then the threshold absorption given by the band gap. Narrow band gap materials, whose band gap is smaller than the infrared limit of the visible spectrum, $E_g < 1.7\,\text{eV}$, appear black since all of the visible light photons are sufficiently energetic to excite electrons into the conduction band. The intermediate region, materials with a band gap in the interval $1.7\,\text{eV} < E_g < 3.5\,\text{eV}$, can show a characteristic color depending on the energy of the band gap.

Color can also be caused by defects present in the material, e.g., in the form of impurities which may occupy an energetic state in the energy gap. Valence electrons can be excited into these states which are normally forbidden. The transition into these states is accompanied by absorption of photons with energy corresponding to the transition into this energy state, giving rise to spectrally selective absorption, or color. Famous examples of this mechanism are the coloration of corundum (Al_2O_3) and diamond (C) by doping.

Reststrahlen (German for "residual ray") absorption is due to excitation of optical phonons in response to the electromagnetic waves; this absorption occurs generally in the infrared part of the spectrum and does therefore not contribute to color. It is not further discussed.

In the following we consider a coating material that has free charge carriers, such as electrons in a metal or in conducting nitrides such as ZrN and TiN. It is well known that light can be described as an electromagnetic wave with angular

frequency ω. Putting the coordinate system such that the wave propagates in the x-direction, we can write for the electric field in the medium:

$$\mathfrak{E} = \mathfrak{E}_0 \exp\left(\mathrm{i}\omega\left(\frac{nx}{c} - t\right)\right) \exp\left(\omega\frac{kx}{c}\right). \tag{10.5}$$

The first of the exponential factors describes the periodic nature of the wave in space and time, and the second describes the exponential dampening of the wave in the medium; $\mathfrak{E}_0$ is the electric field strength when the wave enters the medium. Electromagnetic waves interact with the free charge carriers in the medium, and therefore their concentration and mass are important to what happens to the wave.

In the well-known Drude model (after Paul Drude, 1863–1906), the classical kinetic theory of gases is applied to electrons. The Drude model is relatively simple and allows us to interpret many electrical and optical properties despite the quantum nature of electron–electron and electron–matter interaction. In the framework of this classical model, the basic relationship between wave and carriers is summarized in the complex refractive index:

$$N = n + \mathrm{i}k = 1 - \frac{n_e e^2}{\varepsilon_0 m_e \omega^2}, \tag{10.6}$$

where n_e is the free carrier (electron) density, m_e is here the effective electron mass (note: the effective mass may deviate from the actual electron mass, a concept to account for the interaction with lattice atoms), and $\varepsilon_0 = 8.854 \times 10^{-12}\mathrm{As/Vm}$ is the permittivity of free space. The frequency at zero complex refractive index is called the plasma frequency:

$$\omega_{pl} = \left(\frac{n_e e^2}{\varepsilon_0 m_e}\right)^{1/2}, \tag{10.7}$$

which we have encountered before in Chapter 4 when describing the properties of arc plasma. The plasma frequency separates the frequency domains that are either reflecting and absorbing ($\omega \ll \omega_{pl}$) or transparent ($\omega \gg \omega_{pl}$) for electromagnetic waves of frequency ω. The region around the plasma frequency is often called the plasma edge. Because the free carrier density of solids is rather high, typically about 10^{28} m^{-3}, the corresponding plasma frequency is about 5×10^{15} s^{-1}, which corresponds to waves in the ultraviolet (UV) region. Therefore, as expected, metals are reflecting and absorbing for all wavelengths longer than the UV spectral region, including the visible.

The color is dependent on the spectral distribution of reflected and absorbed light. With normal incidence, the frequency (or wavelength) dependent reflectance (also known as reflectivity) can be expressed as

$$\rho = \left|\frac{1-N}{1+N}\right|^2 = \frac{(n-1)^2 + k^2}{(n+1)^2 + k^2}, \tag{10.8}$$

and, using equations (10.6) and (10.7), we arrive at

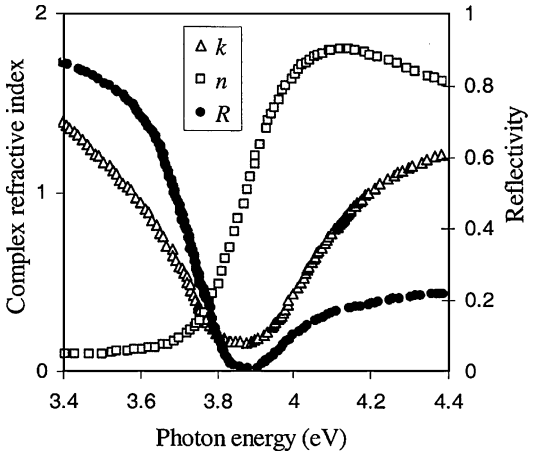

Fig. 10.7. Reflectance, the real refractive index n, and extinction coefficient k, for silver as a function of the photon energy. The photon energy of 3.85 eV corresponds to $\omega = 5.8 \times 10^{15}$ s^{-1} which is in the UV spectral region. (From [105])

$$\rho = \frac{\omega_{pl}^2 \Big/ \omega^2}{2 + \omega_{pl}^2 \Big/ \omega^2}. \tag{10.9}$$

The reflectance has a minimum at about the plasma frequency. Based on the previous discussion, this minimum is not symmetric but ρ is much greater for lower frequencies (or, equivalently, longer wavelength). This is clearly illustrated for the case of silver, which is a much-studied reflecting material. We see this in Figure 10.7, where the reflectance, the real refractive index n, and extinction coefficient k are shown as a function of photon energy. The relation between photon energy E and frequency ν is given by

$$E = h\nu = \hbar\omega, \tag{10.10}$$

where h is the Planck constant, $\omega = 2\pi\nu$, and $\hbar = h/2\pi$.

10.3.4 The L*a*b* Color Space

The L*a*b* color space serves to evaluate color by accounting for both the reflected spectra of materials and for the wavelength-dependent sensitivity of the human eye. The L*a*b* color space represents the color evaluation by the human eye and brain. The visual sensation uses three independent parameters to obtain a quantitative measure for color perception: hue; saturation; and lightness.

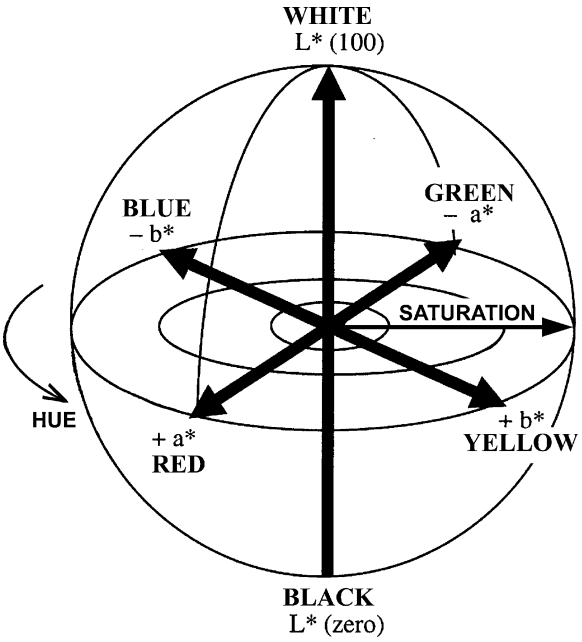

Fig. 10.8. Schematic of the L*a*b* color space. The three perpendicular axes L*, a*, and b* cross in the center of the color sphere: L* is brightness with values from 0 (black) to 100 (white); a* and b* are chromatic coordinates with sign and magnitude indicating hue and saturation, respectively. The assignment is positive a* for red, negative a* for green, positive b* for yellow, negative b* for blue (Commission Internationale de l'Eclairage, CIE)

Hue is the classification in terms of red, blue, green, etc. Saturation is a measure of the "purity" of the color, i.e., expressed in terms of the spectral distribution, how narrow the peak of intensity is around the wavelength of the color. Lightness is the brightness or intensity of the reflected light reaching the eye. The L*a*b* color space is widely used (but not the only one). The color sphere has three perpendicular axes labeled L*, a*, and b* (Figure 10.8). The vertical axis, L*, indicates the lightness, its values go from 0 through 50 at the center and reach 100 at the top. The corresponding brightness varies from pure black at the bottom (zero) to pure white at the top (100). The horizontal axes, a* and b*, are the chromaticity coordinates, and their signs and magnitude indicate hue and saturation, respectively. Plus and minus signs of a* are assigned for the red and green directions, respectively, and plus and minus for b* are yellow and blue, respectively. The magnitudes of both a* and b* vary from 0 at the center of the sphere to 100 at the surface, both in plus and minus directions.

To quantify the values, the "CEI 10° Standard Observer" was introduced in 1976 by the Commission Internationale de l'Eclairage (CIE, the International Commission on Illumination). Such an observer has a 10° field of view, corresponding to

circular area of 88-mm diameter at 500-mm distance from the eye, with certain tristimulus values defined as the spectral sensitivity to red, green, and blue light of three different cones in the retina. The colors are measured in L*a*b* color sphere using a standard illuminant, such as CWF2, corresponding to cool white light from a fluorescent lamp, or D65, corresponding to daylight. Dedicated color measuring equipment or a photospectrometer can be used to evaluate the color coordinates.

10.3.5 Example: Color of Nitrides

The most studied and used decorative coating made by cathodic arc deposition is TiN due to the combination of its gold color, high hardness, and corrosion protective properties. While the latter properties were mentioned before, we consider here the optical properties which are mainly due to intraband transitions of the free carriers [106].

In a simplified picture, the stoichiometry of the nitride determines the electrical and optical properties: the greater the nitrogen content, the lower the density of free electrons. Looking at the previous section that stressed the role of the plasma frequency separating mostly reflecting and mostly transparent spectral regions, one can immediately see that the plasma frequency must be reduced as the nitrogen content is increased. This leads to a more yellow appearance with overall reduced reflectivity [103].

The same arguments and the same trends also hold for ZrN (Figure 10.9). The color shift is apparent because the plasma edge and related reflectivity minimum

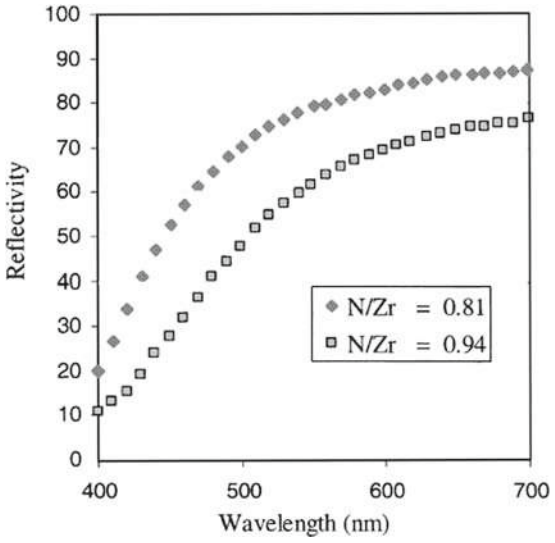

Fig. 10.9. Spectral reflectance of cathodic arc ZrN films deposited with different nitrogen pressures: the higher nitrogen content leads to a more yellow and less reflecting coating. (After [103])

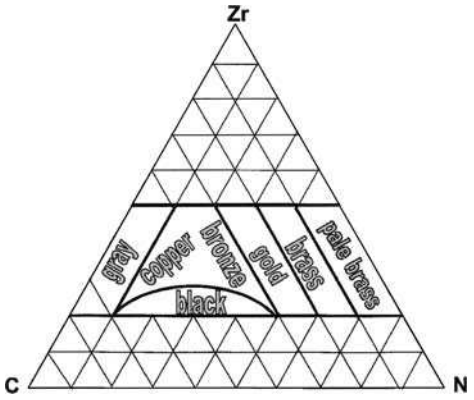

Fig. 10.10. The appearance of colors in the Zr–C–N ternary diagram. (After [107])

(in the UV) are shifted to longer wavelengths, and the overall reflectance is lower as the nitrogen contents increase. It has been found that the color of ZrN is more sensitive to changes in the composition, whereas TiN is a more robust coating in the sense that increasing the N/Ti ratio from under-stoichiometric 0.92 to over-stoichiometric 1.14 is hardly noticeable by the eye.

While TiN (golden) and TiC (dark grey) have a limited range of color, addition of another metal can have dramatic effects, such as dark blue (Ti, Al)N, or ZrCN exhibiting a wide color range: the appearance varies from stainless steel and nickel to brass, gold, and black [107] (Figure 10.10). In addition to the stoichiometry, variation of the crystalline structure of the coating has also some influence on the appearance [108]. Since the 1990s, research has greatly expanded the range of possibilities by considering ternary nitrides, such as (Ti, V)N, (Zr, V)N, (Zr, Al)N, (Zr, Cr)N [108], and compounds that contain even more elements.

10.4 Optical Coatings

The decorative coatings mentioned above can be considered as a kind of optical coatings. In this section, however, the focus will be on transparent coatings used for antireflection, optical filter, and transparent diffusion barrier applications.

Beginning in the late 1980s, Phil Martin and his group at CSIRO in Sydney, Australia, pioneered the use of filtered arc deposition for nitride and oxide films for optical applications [3, 109, 110, 111, 112, 113, 114, 115]. Of special interest are wide band gap materials because they are transparent in the visible part of the optical spectrum. For the design of optical films one usually wants control of the refractive index, n, and the extinction coefficient, k. Transparent materials with very small extinction coefficient can be readily produced using the filtered cathodic arc with a range of cathode materials by operating the arc in a low-pressure

Table 10.3. Refractive index for filtered arc deposited films, measured at a wavelength of 550 nm, sorted by increasing values. (Data from [115])

Thin film material	Refractive index n at 550 nm
$Al_{85}Ti_{15}O$	1.63
$Al_{70}Ti_{30}O$	1.65
AlO_x	1.68
$Ti_{70}Al_{30}O$	1.95
$Al_{70}Si_{30}N$	2.09
$Ti_{80}Al_{20}O$	2.10
AlN	2.11
ZrO_2	2.18
$Al_{85}Si_{15}N$	2.20
Nb_2O_5	2.41
TiO_2 amorphous	2.56
TiO_2 anatase	2.63
TiO_2 rutile	2.72

background of pure oxygen (typically in the range of several 10^{-2} Pa or greater). The refractive index depends on the wavelength of interest and is often arbitrarily given at 550 nm, where the human eye has maximum sensitivity (Table 10.3).

In contrast to magnetron sputtering, the arc deposition process is relatively forgiving to variations of the oxygen partial pressure: the arc will operate in a stable manner and the films tend to be fully stoichiometric. In sputtering, for comparison, one has to carefully monitor and control the oxygen partial pressure for deposition at a desired point on the flow-partial pressure hysteresis curve. The additional issue, namely that there is a tendency in magnetron sputtering to "arcing," is not an issue at all because, after all, we use the cathodic arc mode! Examples of high-quality films, using *filtered* arc deposition, include Al_2O_3, TiO_2, VO_2, Nb_2O_5, and ZrO_2, with deposition rates of typically 25–50 nm/min. Heating is not necessarily required to obtain material of optical quality [116], though temperature remains an important parameter since phase and texture can be influenced.

Of special interest and importance is TiO_2 because it can have different phases. Via energetic condensation, even the rutile phase can be synthesized at room temperature, provided the ions are accelerated by biasing to about 100 eV or greater [113, 114]. Figure 10.11 shows the refractive index for the various phases of TiO_2. It should be noted that the rutile phase has higher compressive stress and hardness than the amorphous and anatase phases.

Another material of interest is MgO which is used as a transparent protective layer in alternating current plasma displays because it is highly transparent and has a high packing density and surface binding energy leading to good sputter resistance. It can be readily deposited by reactive arc deposition using a magnesium cathode in low-pressure oxygen background. [117]. Cathodic-arc-deposited

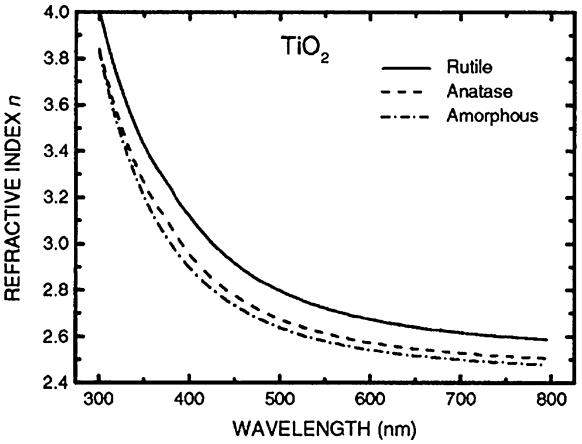

Fig. 10.11. Refractive index for arc-deposited TiO_2 as a function of wavelength. The phase can be influenced by substrate temperature and ion energy (via bias). (From [115])

MgO films were found to grow preferably on glass and silicon with (200) and (220) orientation when the oxygen flow rate was increased from 180 to 240 sccm, leading to process pressures of 1–4 Pa [118]. With increasing oxygen flow, the grain size increased from typically about 10–25 nm, and the slight absorption seen in the blue and green disappeared: the transmittance exceeded 95% throughout the visible spectrum for the 1.0–1.3-μm-thick films [118].

With optical coatings we usually mean coatings that are transparent in the visible. In more general terms, we expect certain optical properties in a spectral region of interest. For example, for contact-less heat transfer between parts one would use infrared radiation. The efficiency of the radiative energy transfer depends on the spectral emissivity, or how "black" the surface is. For a specialty application, the cooling of radio-frequency (RF) accelerator components in ultrahigh vacuum (UHV), the surface of aluminum "kickers" was coated by high-emissivity CuO, which is UHV compatible, black in the infrared, and transparent to the RF fields [119].

The transparent optical materials are not limited to oxides; there are a number of wide band gap nitrides. For example, AlN has been deposited using a filtered cathodic aluminum arc with nitrogen background. In the work by Mändl and co-workers [120], the substrate temperature was varied in the range from about room temperature to 370°C. With continuous arc operation, the deposition rate was very high, 85–115 nm/min. Thin films, about 30 nm, were deposited on NaCl for electron diffraction measurements, and much thicker films, 1–3 μm, for X-ray diffraction measurements. The thin films were amorphous, regardless of the temperature in the given range, while thicker films exhibited a hexagonal lattice. The microhardness of the AlN was 18–20 GPa. As most optical materials, AlN films are highly insulating with a resistivity of $1–2 \times 10^9$ Ω m. Besides being an interesting optical material, AlN films of thickness 1–3 μm are also good oxidation protection coatings up to 1,100°C [121].

10.5 Transparent Conductor, Solar Energy, Electronic, and Photocatalytic Applications

In recent years, semiconducting materials other than silicon have become more interesting, and especially for solar energy applications. This topic is very wide and therefore only a few examples are discussed, namely those related to filtered cathodic arc deposition. Among them are (often doped) oxides, nitrides, and doped tetrahedral amorphous carbon (ta-C). Some materials, like ta-C, were mentioned a few times before, but here we will only deal with the electronic properties and applications.

In our current world of electronic gadgets, transparent conducting oxides (TCOs) have gained widespread applications, far more than we may realize. Flat panel displays in TVs, computer monitors, hand-held communication, and gaming devices have them, and so do solar cells, displays in cars, touch screens at automated teller machines, etc. The most popular material used to date is indium tin oxide (ITO) because of its excellent transmittance throughout the visible spectrum ($>90\%$) and its low resistivity (down to $500\,\mathrm{n\Omega\,m} = 5 \times 10^{-5}\,\Omega\,\mathrm{cm}$ for a good material). For detailed information on ITO and other TCOs, see Exharhos' review [122]. ITO can be deposited by various techniques, including filtered cathodic arcs, for which high transmittance of $>95\%$ in the visible spectrum and a reasonable resistivity of 6.6 $\mu\Omega$ m have been obtained [123]. Although there is plenty of indium on planet Earth, the great demand has skyrocketed the price of the metal (tenfold from 2002 to 2006), triggering research and development of alternative materials and their deposition technologies.

Another driving force for alternative transparent conductors is the desire to develop transparent electronics, i.e., having materials that are not just transparent and conducting but are n-type and p-type, allowing us to create pn-junctions for transparent diodes, transistors, light emitting diodes, etc. ITO and other well-performing TCOs are intrinsically n-type, and for some time now, there is a challenge to get good p-type material. Yet other research deals with magnetic and transparent semiconductors [124] deposited by energetic condensation using pulsed laser deposition. Here, filtered arc deposition may be an interesting, more economical approach.

Boxman's and Goldsmith's group in Tel Aviv was perhaps the first who used cathodic arcs to synthesize TCO materials in the early 1990s [125]. Using a 90° filtered arc system they deposited SnO_2 on various substrates using a tin (Sn) cathode operating in oxygen background. As expected, there is an optimum window of pressure where good material can be obtained; the best was found for about 6 mTorr (0.8 Pa). The lower limit of the process window (3 mTorr or 0.4 Pa) was determined by the lack of oxygen to obtain the stoichiometric SnO_2, and the upper limit (12 mTorr or 1.6 Pa) was given by a drastically reduced deposition rate, which may be due to too many collisions between the arc-eroded Sn and background gas molecules. The study reports about a common observation, namely that the as-deposited films appear brownish or

yellowish, with reasonable but not quite satisfactory resistivity (in the range 10^{-3} Ω cm = 10 μΩ m). Rapid thermal annealing at 300°C in air improves the situation considerably: the resistivity is reduced by about one order of magnitude and the films become clear with a transmittance of about 85% in the visible.

Since that initial arc-based study on TCO films, many more have followed, both at Tel Aviv [126, 127, 128, 129, 130, 131, 132, 133] and elsewhere [134, 135, 136, 137, 138]. Among the many goals is to deposit SnO_2 on temperature-sensitive substrates such as polycarbonate (PC) and polymethylmethacrylate (PMMA). The aim is to improve the scratch resistance of vehicle and aircraft windows, while also providing a conducting layer that may serve as an electromagnetic shield and that can be used as a heater for defrosting. Of course, thicker films provide greater scratch resistance on those relatively soft substrates, and the sheet resistance decreases approximately with increasing thickness. However, the thicker films made at low temperature show noticeable absorbance, and so one has to find a good compromise between the conflicting requirements. Zhitomirsky and co-workers [132] found that the transmittance data for their filtered arc SnO_2 coating can be fitted by $T_{vis} \approx 94.7\exp(-0.745d)$ where the transmittance is in percentage and the film thickness d is in micrometers. A typical film of about 1-μm thickness has a transmission of roughly 45%, which is acceptable but a little less than desirable.

Now, looking at ZnO films, one finds that the features of energetic condensation fully apply. ZnO films made by filtered cathodic arcs are usually under high compressive stress, very much like the nitride films discussed for hard coatings. However, the extrinsic stress generated by different thermal expansion of glass substrate and film can reduce the intrinsic stress upon cooling from the high process temperature [138]. ZnO films deposited at room temperature are X-ray amorphous [135] and become crystalline, usually with a wurtzite structure, at elevated temperature [138]. They show a strong (002) X-ray diffraction peak, indicative of the preferred *c*-axis orientation. The full width at half maximum (FWHM) of the diffraction peak decreases with increase in temperature, indicating an increase in grain size with increasing temperature, which is typical not only for ZnO coatings.

Doped ZnO is currently a much investigated option as a potential ITO replacement [139]. Filtered cathodic arc deposition can deliver very promising n-type material, usually doped with Al [140], but the use of other dopants such as Ga also results in excellent properties [136]. Optimized conditions, which usually involve elevated temperature up to 400°C, give polycrystalline n-type semiconductors with a conductivity of 2–60 μΩ m, a carrier (electron) density of $10^{23}-2\times10^{26}$ m^{-3}, an electron mobility in the range 10–40 cm^2/V s, and a band gap of about 3.3 eV. The transmission is characterized by a small extinction coefficient in the visible and near-IR range of about 0.02 or smaller, resulting in high optical transmission of about 0.90 for typical 500-nm films [133].

Interestingly, ZnO has the potential of being a reasonable p-type semiconductor by doping with group-VA elements such as antimony [127] or nitrogen

[141]. Fabrication of p-type material is needed to create pn-junctions for transparent electronics, as mentioned before.

One of the most noticeable achievements is the rather difficult scaling to large areas. By "large areas" we mean here applications that involve coating for large display and window-size areas (i.e., square meters in large quantities). The group at Tel Aviv University built a small in-line system with two "linear" (rectangular cross-section of 66 mm × 440 mm) filtered arc systems capable of coating Sn_2O films on moving 400-mm × 420-mm glass substrates using rectangular macroparticle filter [126, 131]. The filters were "linear" S-filters, with each of the two turns being 45° (see photo Figure 2.29). The cathode spots were steered on the elongated ("linear") Sn cathode; the plasma was guided through the filter in the presence of oxygen at a pressure of about 0.7 Pa. On a stationary substrate, a peak deposition rate of 37 nm/s was obtained; more relevant for the large-area coating is the dynamic deposition rate, which was determined to be about 100 nm-m /min at an arc current of 350 A. Higher currents are possible and dynamic rates twice that value seem to be possible. The films had a thickness of typically 250–450 nm, with a sheet resistance of 100–170 Ω per square. The SnO_2 films showed transmission in the visible of about 83%.

Solar materials have recently gained strong interest, not at least due to the undoubtedly present global warming: using solar energy in photovoltaic or photochemical cells will contribute to making us less reliant on fossil fuels. The photo-electric properties of ZnO produced by pulsed filtered zinc arcs in oxygen at 86 mPa were investigated in this context [142]. Although deposited at room temperature, the ZnO films showed high transmittance of 92% in the visible, a strong (200) peak in X-ray diffraction, indicating *c*-axis orientation, and a band gap in the range 3.19–3.21 eV. Measurements of photoconductivity revealed the existence of energy states in the gap; photoconductivity increased with the energy of photons and reached a maximum at 2.32 eV. Thinner ($\sim$ 100 nm) films had more states in the gap and showed a higher photoconductivity than thicker ($\sim$ 700 nm) films.

Undoped, as-deposited ta-C films exhibit a band gap of 2.7 eV [143] and a Fermi level about 0.35 eV below the midgap; the material is generally insulating but may also be considered as a highly resistive defect-controlled p-type semiconductor. Upon nitrogen doping, the material becomes more conducting and that has triggered interest to use it as a possible electronic material from which one may form heterojunctions on p-Si for solar cell applications [144, 145]. To enhance and better control the incorporation of nitrogen, a nitrogen ion source can be used to assist in the film growth [146]. The Fermi level moves up with the nitrogen doping level, and the films become n-type [90, 145]. The compensation of p-type and n-type occurs at about a doping level of 7% (that is at least true for the conditions of Silva's experiment [90]). The Fermi level was 0.8 eV below the conduction band and the band gap reduced to about 2.5 eV due to the C–N alloying effects. Heterojunctions on ⟨100⟩ p-type silicon have been fabricated with the ion-assisted filtered arc, and the semiconducting and optical properties

were investigated [145]. Photoresponse measurements gave evidence for electron–hole pairs generated from the ta-C:N and Si depletion regions, with the peaks centered at about 540 and 1020 nm, corresponding to the optical absorption edge of ta-C:N and p-Si, respectively. The reverse current increased by three orders of magnitude when the structures were exposed to AM1 light (AM1 is a light source developed for the photovoltaic industry implementing a standard terrestrial solar spectral irradiance distribution, i.e., simulated sun light). A photovoltaic effect was observed from ta-C:N, and the values of short-circuit current, open-circuit voltage, and field factor obtained were 5.05 mA/cm^2, 270 mV, and 0.2631, respectively.

The wettability of surfaces depends on their surface energy: high surface energy implies good wettability and small contact angle. The contact angle for pure ta-C is about 80° and the material is therefore considered slightly hydrophobic [147]. The relationship between surface energy and arc-deposited a-C:Me coatings depends largely on the presence of Me–O bonds on the surface [99], where "Me" stands for a metal. Of special interest are TiO_2 and TiO_2-containing compounds because they show photocatalytic activity. Zhang and co-workers [148] used a carbon 5 at.% Ti composite cathode in a filtered arc system to synthesize titanium-containing amorphous carbon (a-C:Ti). Such films are hydrophobic as evident by a very large ($>90°$) contact angle with water droplets. The hydrophobic property was associated with the presence of Ti–O bonds on the surface. When the material was exposed to ultraviolet (UV) light, the contact angle was reduced to about 36°, i.e., the surface has become hydrophilic by the absorption of $O–H^-$ hydroxyl groups via a photocatalytic reaction. However, when the surface was then exposed to air without UV radiation, it resumed its original hydrophobic properties after about 3 h. There are various applications for such behavior, including the so-called self-cleaning of surfaces under UV radiation and water rinsing (image a coated car windshield exposed to sunshine followed by a rain shower).

The incorporation of cobalt into ta-C, leading to ta-C:Co, increases the contact angle sharply from about 80° to 107.5° [147]. X-ray photoemission spectroscopy (XPS) showed that an increase in negative substrate bias affects both the sp^3 content and the Co oxidation state on the sample surface. These two factors have a direct influence on the surface energy and the associated contact angle. In the case of zero bias and relatively small amounts of Co, 1–5 at.%, the reduction in surface energy (increase in contact angle) is likely due to Co^0 that reduces the presence of dangling bonds in the sp^3-rich amorphous carbon network. As the amount of Co is increased to 10 and 20%, the sp^2 content is enhanced, and the ratio of Co^{2+}/Co^{3+} states on the surface is the critical factor.

10.6 Field Emission Applications

The electronic and surface states also affect the work function and hence the field emission properties. Carbon-based materials are promising field emitter materials due to their low work function in combination with a host of other attractive

properties such as environmental stability. Applications such as field emission displays and portable X-ray sources have stimulated a number of studies dedicated to the emission properties of ta-C, both pure and doped. The physics of field emission has been described in Chapter 3 when we discussed the cathode processes. We have seen that there is a strongly nonlinear dependence of the emission current on the surface electric field, which allows us to identify a threshold or onset field. Typical ta-C films have an onset field of about $(1-2)\times 10^7$ V/m (or 10–20 V/μm for those who prefer more descriptive voltage and length scales) [149, 150]. Films with very high sp^3 content exhibit an onset field at the lower end of this range, and nitrogen doping decreases the value slightly further down to 3–5 V/μm [149, 150]. Modification of the surface by hydrogen and oxygen plasma can lead to a marked reduction in the threshold field down to 2–3 V/μm and to an increase in the emission site density [150]. The back contact was found to be not very important in this study; however, other tests with similar ta-C:Me films showed that the substrate can have a marked influence. For example, Mao and co-workers [151, 152] deposited thin films of titanium or gold onto heavily doped n-type silicon prior to the deposition of ta-C. The current density for the film system containing Ti was much higher (175 μA/cm^2) than the film system with Au (0.4 μA/cm^2) at the same field of 14.3 V/μm.

In a study of the field emission properties, Cheah and co-workers [153] used undoped p-type ta-C (p-ta-C), weakly nitrogen-doped intrinsic ta-C (i-ta-C), and nitrogen heavily doped n+-type ta-C (n+-ta-C) and deposited those films on n+ and p+-type silicon substrates. The heavily doped heterojunction, n+-ta-C/p+-Si, demonstrated the lowest onset field of 10 V/μm with current densities of 0.1 mA/mm^2 at 50 V/μm, which they assigned to Zener tunneling arising from severe band bending. They found that a film thickness of 30–40 nm is more favorable for field emission due to the ease with which the film can be fully depleted. At some locations of i-ta-C films, various types of craters were formed after an electrical discharge at a high field ($>$ 50 V/μm).

The incorporation of metal into ta-C films followed by heat treatment can greatly improve field emission [73]. A very low threshold electric field of 2–10 V/μm was found for heat-treated a-C:Co composite films. Heat treated a-C:Al and a-C:Ti films also exhibited low threshold fields; however, their emission site densities were relatively low.

In the case of ta-C:Ti, Rutherford backscattering spectroscopy, X-ray diffraction, and micro-Raman spectroscopy showed that the films are a nanocomposite of ta-C and TiC_x, with $x<1$ [154]. The fraction of TiC_x increases and the sp^3 bonding between carbon atoms decreases as the Ti content of the C-Ti composite cathode is increased. The threshold field strength was about 10 V/μm for all ta-C:Ti films except the ones with the lowest titanium content (~1.2 at.%), which had a higher field of about 17–19 V/μm. The optimum titanium concentration was determined to be about 12 at.%, giving the highest emission current and emission site density.

10.7 Metallization

10.7.1 Ultrathin Metal Films

Operation of the cathodic arc in vacuum, or in a low-pressure inert gas, results in the condensation of a metal film. Let us start with the deposition of ultrathin ($\sim$10 nm) metal films. Such films can be surprisingly transparent, and especially silver shows very low absorption. The reflection can be suppressed by using antireflection coatings based on interference [155]. This naturally leads to consider making transparent and conducting films.

The greatest use of ultrathin metal (usually silver) films is in low-emissivity and solar-control coatings, which have become a standard for all energy-efficient windows [104]. Although magnetron sputtering has become the method of choice for this very large area coating application, about 10^9 m^2 worldwide annually, it is interesting to consider the effects of the additional kinetic and potential energies brought to the nucleation and growth process when a cathodic arc is used. Indeed, since silver ions arrive with sufficient energy to penetrate the surface of the substrate, suppressing the lateral mobility, which is directly related to the formation of islands [156].

Figure 10.12 shows the onset of coalescence of silver islands made by filtered cathodic arc and by magnetron sputtering, for comparison. Studies like this showed that both the kinetics and the thermodynamic driving forces are important to the nucleation process [156, 157, 158]. However, the just-coalesced islands are not stable but change within minutes to minimize the system's free energy,

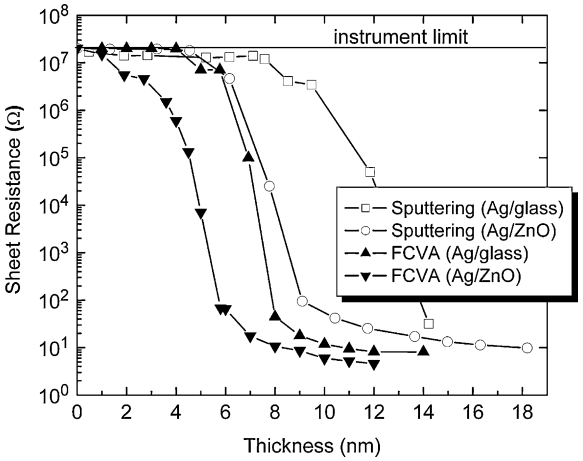

Fig. 10.12. In situ monitoring of the resistance drop as ultrathin films of silver are grown on various substrates at room temperature using magnetron sputtering and filtered cathode arc deposition; the drop indicates the coalescence of nanometer-sized silver islands. (Adapted from [156])

which includes strain, interface and surface energy. The substrate is important in this evolution, and small amounts (sub-monolayer) of "foreign" materials can have a large effect. For example, a sub-monolayer of transition metals such as niobium can lead to coalescence of silver islands at a nominally thinner silver layer thickness [159]. Not all transition metals lead to this earlier onset of coalescence and smoothing of the surface, which may be affected by the rapid oxidation of the intentionally placed transition metal: the oxide has very low surface energy, and silver islands may grow rather tall before coalescence is obtained [158].

10.7.2 Metallization of Integrated Circuits

The flux of fully ionized metal plasma from a filtered arc can be used to metallize sub-micron, and in recent years sub-100 nm, structures that were fabricated lithographically for semiconductor integrated circuits. Physical vapor deposition (PVD) techniques such as long-throw sputtering [160] and ionized PVD [161, 162, 163] have been used besides chemical vapor deposition (CVD) [164], and more recently atomic layer deposition (ALD) [165]. The economy of scale and the demand for faster processors and solid-state memory require shrinking the features of multilevel integrated circuits further toward the physical limits. The fast streaming plasma of filtered cathodic arcs offers the desired directionality, and the high degree of ionization makes application of biasing techniques highly effective. Given the three-dimensional structures of the lithographic structure, some ions arrive with near-normal incidence at flat areas, while others strike the surface of trenches and vias with near-grazing incident angle. The angle and energy-dependent probabilities of sticking and (self)-sputtering are vastly different, as explained in Chapter 8. Those differences are the basis that conformal coatings can be obtained in one extreme, and via and trench filling can be realized in another extreme. Optimized bias settings (usually pulsed) are the key to control.

Let us first look at the properties of thin films. The nucleation process is similar to what has been described in the previous section on ultrathin metal films. For semiconductor application, high transmittance is not relevant but rather good conductivity, uniformity, and resistance to electromigration, which is the main reason that copper "wires" of $\sim$ 100-nm thickness are considered to connect the semiconductor elements of the circuit. Therefore, nucleation and growth up to about 300 nm need to be considered.

In a study related to copper metallization [166, 167], the group at Nanyang Technical University, Singapore, used a double bent filtered, DC cathodic arc to produce thin copper films on biased silicon at room temperature. The deposition rate decreased with increasing negative bias, which can be explained by self-sputtering [168] because copper has a very high self-sputter yield, see Chapter 8. Measurements with an atomic force microscope (AFM) show that the surface roughness increases almost linearly from 0.36 to 2.76 nm as the thickness increases from 60 to 365 nm. This can be correlated to an increase in grain size because that characteristic lateral size increases linearly with the film thickness

and is about 30% smaller than the film thickness. This finding is supported by X-ray diffraction data. Thin films (< 25 nm) have wide (0.8°–0.9°) diffraction peaks, typical of very small grains, and the widths of the peaks decrease (to 0.3°–0.4°) as the film thickness increases. In one of the studies [167], the thinnest films are dominated by the (111) peak but the intensity of the (220) peak overtakes when the film thickness reaches about 100 nm. A third peak, (200), is small and remains relatively unchanged. In other studies [166, 169], the (111) peak remained strong and increased with increasing negative bias. The widths of the diffraction peaks remain unchanged when the films are thicker than about 135 nm, indicating that a typical grain size has been reached for this room temperature deposition. The change in preferred orientation, from (111) to (220) under the conditions of the experiment [167], is quite common in the growth of films by energetic condensation, driven by minimization of the free energy, which includes surface energy and strain energy [170]. When the film thickness reaches about 150 nm, the resistivity approaches the bulk resistivity and does not improve significantly for thicker films (Figure 10.13). This result also implies that the mean free path of electrons in copper is limited by scattering on surfaces and grain boundaries and that one should expect significantly lower conductivity when the films (or "wires") are thinner than 100 nm [171].

First efforts on the actual filling of trenches with copper from filtered arc plasma were done at Commonwealth Scientific Corporation in Alexandria, VA, using their CAF-38 system [172] and the Fraunhofer IWS in Dresden, Germany [173, 174], using the filtered pulsed high-current arc. The latter group demonstrated copper filling of trenches having a width of 400 nm and a depth-to-width aspect ratio of 2 (Figure 10.14). They also demonstrated conformal tantalum coating of 1 μm wide, low aspect ratio structures. Later improvements were also demonstrated by the Dresden group (Figure 10.15) but unfortunately were not

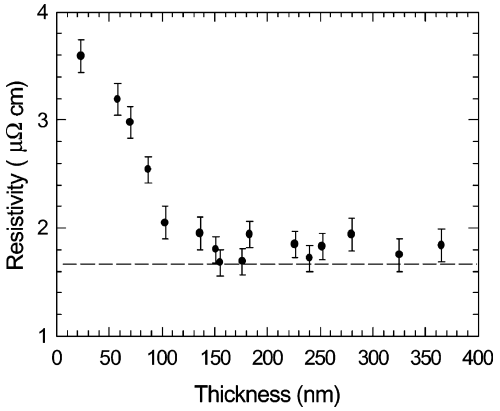

Fig. 10.13. Dependence of the electrical resistivity of copper films deposited by a DC filtered arc on film thickness. The *dashed line* represents the resistivity of bulk copper, 1.67 μΩ cm. (From [166])

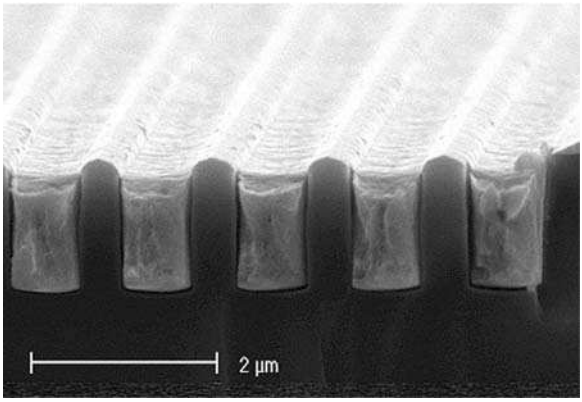

Fig. 10.14. Filling of trenches with copper using a filtered high-current arc. (Figure about 1997, courtesy of Peter Siemroth, Fraunhofer IWS, Dresden)

widely publicized. Monteiro [175] reported on improved results using a miniature filtered pulsed arc source in conjunction with high-duty-cycle pulsed bias on the substrate. He demonstrated conformal coating of Ta and TaN diffusion barrier and Cu seed layers in 120-nm-wide trenches and vias with depth-to-width aspect ratios of up to 8:1 (Figure 10.16). Similar results have been obtained more recently by Chen and Shih [169] in Taiwan who obtained excellent filling of 200-nm trenches with an aspect ratio of 5:1.

10.7.3 Metallization of Superconducting Cavities

A very different kind of specialty coating is required to enable drastic reduction of size and cost of the next generation of linear accelerators. Linear accelerators utilize a linear array of radio-frequency (RF) cavities. To achieve particle energies in the GeV to TeV range for conventional (non-superconducting) RF

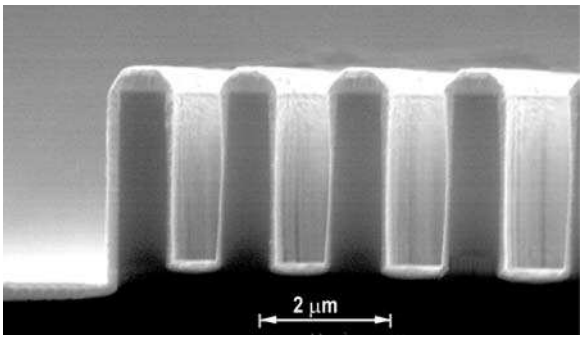

Fig. 10.15. Conformal barrier coating of tantalum on lithographically etched structures. (Figure about 1997, courtesy of Peter Siemroth, Fraunhofer IWS, Dresden)

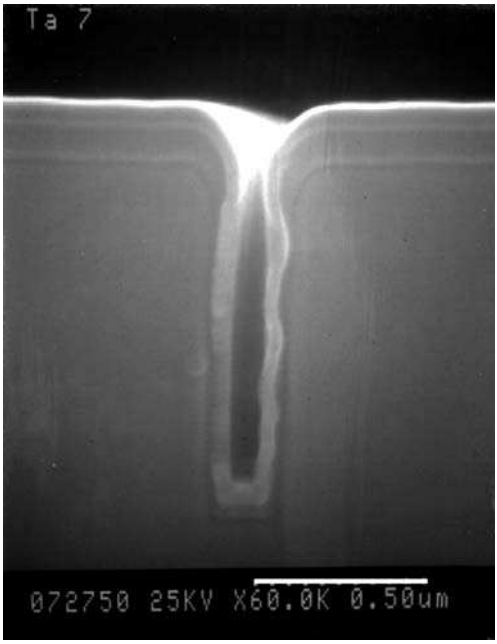

Fig. 10.16. Conformal Ta films on 120-nm-wide trench using the MePIIID technique with a pulsed bias duty cycle of 12.5% (the wavy appearance of the films is an artifact of the sample preparation). (Figure courtesy of Othon Monteiro, also see [175])

cavities, such an accelerator would need to have about 20,000 RF cavities, leading to a length of tens of kilometers with a power consumption exceeding 100 MW; hence the cost would be unacceptable. The main figures of merit for RF cavities are the quality factor, Q_0, which is defined as the ratio of the energy stored in the cavity and the energy loss in one RF period, and the average accelerating field, $\mathbf{E}_{acc}$. To reduce the cost, superconducting cavities may be employed; they have Q_0 values as high as 10^{10} and approaching even 10^{11}, compared to about 10^5 for non-superconducting cavities. Even with the additional energy needed to cool the cavities to cryogenic temperature, the overall energy consumption is reduced to about 10^{-3}.

Of the known practically usable superconductors, niobium is the preferred because this metal has the highest critical magnetic field H_{c1} beyond which the vortex penetration becomes energetically favorable, and the desired performance of the cavities collapses [176, 177]. One could make the cavity of niobium bulk metal, but this would drive up cost and be counterproductive to the original objective. Therefore, high-quality coatings of Nb seem to be an obvious approach. Early attempts were done in the 1980s, though sputtered Nb films turned out to be of inferior quality in this application. Energetic condensation of filtered arc niobium plasma is being considered as a promising alternative [178, 179, 180]. Several issues have to be solved before the arc technology could be accepted and

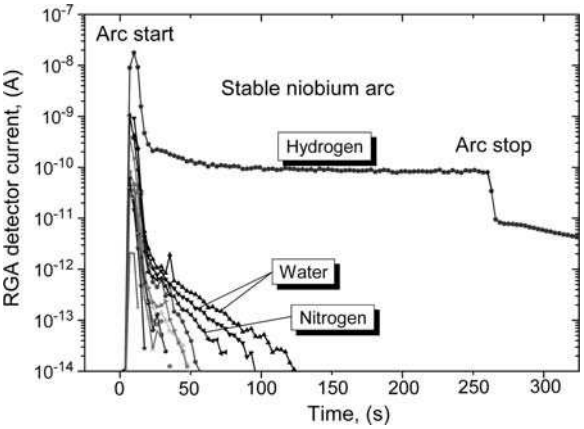

Fig. 10.17. Gas evolution of a niobium arc in ultrahigh vacuum as measured with a differentially pumped residual gas analyzer; the remarkable and typical features are the initial burst of gas and the sustained high level of hydrogen, all other gases are pumped relatively quickly; water is shown with two isotopes. (Data courtesy of Roberto Russo, University of Rome "Tor Vergata", Italy)

implemented on a large scale. First, the deposition has to be free of defects; therefore only a filtered arc can be accepted. Second, the deposition has to be of exceptional purity; however, niobium readily getters the residual gas. Therefore, the multinational team of Langner and co-workers [178, 179, 180] opted to develop a filtered cathodic arc that operates in ultrahigh vacuum (UHV).

One point of wider interest is the evolution of the residual gas when the arc operates under UHV conditions. As shown in Figure 10.17, there is an initial burst of gas exceeding the UHV base line by orders of magnitude; then the various partial pressures recover quickly, on the timescale of about 10s, except the partial pressure of hydrogen. In fact, hydrogen levels off to a new equilibrium, indicating that pumping and hydrogen production are balanced. Most likely, the niobium itself contains significant amounts of hydrogen.

Coming back to RF cavity coating, it should be mentioned that alternative materials are being considered, too, such as NbCu, niobium nitride, MgB_2, and certain high-temperature superconductors. Recently, Godeke [181] suggested that the conventional superconductor Nb_3Sn should be better than Nb because it has a lower Bardeen–Cooper–Schrieffer surface resistance, which is directly linked to the RF losses of the cavity. This suggests that future work on UHV filtered arc may involve deposition from alloy cathodes.

10.7.4 Metallization for Specialty Brazing

Metal–ceramic joints are commonly brazed to produce a host of vacuum products such as vacuum feedthroughs. While there are numerous techniques that the industry is using on a daily basis, there is still a need to incorporate specialty

ceramics or metals, to improve the ultimate tensile strength of the components, and to and to reduce the leakage rate.

Pulse filtered arc deposition of gold and titanium onto alumina was successfully used for brazing applications since the early 1990s to fabricate vacuum components for Berkeley Lab's Advanced Light Source synchrotron. The process was based on grading the ceramic–metal coating interface via energetic condensation of arc plasma ions. Unfortunately, the specific "recipes" remained unpublished and only some general description was given [182].

More recently, Piekoszewski and co-workers [183] described a process for metallization of alumina ceramic in order to braze them to Kovar® (a nickel cobalt ferrous alloy) with conventional Ag–Cu eutectic brazes using a two-step process: the first step was to expose the ceramic surface to an intense gas plasma pulse from a coaxial discharge diode, and the second to condense a thick (2 μm) layer from an unfiltered titanium arc plasma. The arc plasma was initially operated in a background gas containing oxygen and then gradually changed into a vacuum arc. The interface between alumina and Kovar had a graded structure containing suboxide phases like Ti_7O_{13} and Ti_2O. Vacuum housings brazed with this interface showed an average ultimate tensile strength of 90 MPa and a leakage of less than 5×10^{-4} Pa l/s.

10.7.5 Metallization Using Alloy Cathodes

In the case of an alloy cathode, the cathode composition is approximately preserved in the arc plasma composition and the composition of the films, though a deviation of a few percent is common, which most likely is due to preferred erosion of one of the metals of the cathode [171, 184, 185]. Provided the cathode is well cooled and diffusion suppressed, the surface will enrich with the material less easily eroded, and so over time the films will attain the same composition at the original composition of cathode. (A similar effect is known from magnetron sputtering where preferential sputtering caused by the different yields corrects the rates after conditioning.)

One should recall that arc "erosion" involves formation of plasma in the explosive stage of the spot processes as well as evaporation and macroparticle formation in the post-explosive, evaporative stage. The vapor pressures of the metals are likely not exactly equal, and this point alone indicates that one should expect a difference between cathode and film composition. Additionally, if a gas or gas mixture is used, scattering of the eroded material by the gas can contribute to different effective rates for alloy constituents.

10.8 Bio-compatible Coatings

There are many examples of coatings compatible with biological tissue or interacting in certain desirable ways with proteins and cells, but only a few selected examples will be mentioned. From a materials point of view, a very

limited group of materials can be used for biomedical applications due to the strong propensity of body fluids to react to and attempt removal of foreign objects. The relatively acceptable materials include carbon-based materials, including polymers such as PTFE (Teflon®), PEEK (polyetheretherketone), and polyethylene [186]. Another large group involves titanium alloys, "surgical" stainless steel, cobalt, chromium, nickel (may cause allergies), zirconium, tantalum, the noble metals, and ceramics such as alumina and zirconia. Biocompatibility implies that the living body accepts the foreign object without developing strong adverse reactions such as (chronic) inflammation. It is clear that the choice of material for a biomedical application depends on many factors, but the primary concern is *the given biological environment*. No single material is suitable in all settings. For example, materials in direct contact with blood need to have good haemocompatibility,[2] i.e., cause minimal activation of the immune and coagulation systems. Apart from the biocompatibility issues, application-dependent properties of the biomaterial must be considered. Different requirements will be addressed by different materials – there is no universal solution. Other requirements are related to the wear and corrosion performance, especially for those implants that are part of a tribological pair, like artificial hip joints. Therefore, many of the devices, such as dental implants, vascular stents, heart valves, artificial hip joints, or knee replacements, have very sophisticated engineered surfaces.

From the point of view of materials processing using energetic condensation, two large groups dominate the field, one is titanium based, the other carbon based, and those groups will be discussed in more detail in the remainder of this section.

10.8.1 Carbon-Based Materials

Among the great variety of carbon-based materials used for bio-applications, diamond-like carbon (DLC) is most relevant due to its excellent mechanical and chemical properties, ease of synthesis, and low cost. Strictly speaking, as mentioned earlier, DLC is a term describing a wide range of materials, including hydrogenated (a-C:H) and tetrahedral amorphous carbon (ta-C). The majority of the applications involves PIII-related and/or sputter deposition processes, although some prefer the arc-produced a-C or ta-C due to their distinct properties.

Low friction and wear of DLC are generally related to the combination of high hardness, elastic modulus, surface smoothness, and for hydrogen-free coatings the presence of hydrogen, oxygen, or preferably water molecules to terminate the surface. Additionally, the buildup of a graphitic transfer layer on the wear counterpart can act as a solid lubricant rather than hard wear particles that

[2] Also spelled hemocompatibility.

would cause abrasive wear. DLC is widely used in technical applications, for example on engine parts, and it can play a role in bio-related wear applications too. However, the biological environment for the wear pair makes the situation more complicated: wear products may be attacked and removed by the body's immune system. DLC materials have been shown to have excellent haemocompatibility, which is expressed in a decreased thrombus formation. When exposed to blood, an increased ratio of albumin to fibrinogen adsorption as well as decreased platelet activation is observed on coated surfaces [186].

The addition of other elements to DLC can modify the biocompatibility properties [186] while maintaining its favorable mechanical properties such as high elastic modulus and the dense, amorphous structure [187]. For example, the attachment of certain proteins can be modified, and this affects cell attachment, cell proliferation, and cell differentiation. Especially explored is the addition of cytotoxic elements like Cu, Ag, and V, which interact on the surface with the biological media causing the well-demonstrated antibacterial effects [186, 188]. For example, Kwok and coworkers [189] coated silver-doped ta-C films on biomedical devices using a pulsed filtered cathode arc. Good blood compatibility and antimicrobial characteristics were demonstrated by platelet adhesion and antibacterial tests. The underlying idea is that the cytotoxic metal is slowly released, on the timescale of days and weeks, to produce a sufficient silver concentration causing adverse reactions of the cells that have attached to the surface. These adverse reactions include cell detachment and the stop of cell growth. Over time, the metals will be adsorbed by the whole body, and the concentration far from the doped DLC surface must remain low enough to be well tolerated by the body.

Another application of DLC is the encapsulation of ocular implants. Here, the reasonably high optical transmittance is relevant, too, which is one reason why ta-C films are considered. Ocular implants are being developed to treat age-related macular degeneration (AMD). The device is a lithographically produced array of photocells which stimulate the still working nerve cells in the retina, thereby relaying light sensation to the brain. To protect the device from body fluids, it is necessary to encapsulate it with a transparent, inert, bio-compatible material such as diamond-like carbon, and preferably ta-C made by a filtered cathodic arc. This has been demonstrated using twist-filtered carbon [190] in a specially designed coating machine [191, 192].

We conclude this section considering the surface modification of polymers. Exposure to low-temperature plasma and processing by immersing the whole object into plasma for ion treatment has become a rather widely used approach to modify wettability and reduce adhesion of bacterial cells [193, 194, 195, 196, 197, 198, 199, 200].

One difficulty is that the polymer is generally insulating, and thus biasing is not possible. In the case of thin objects, such as sheets and foils, one may overcome the issue by applying RF or a rapidly pulsed bias to a conducting holder; sheath formation and ion acceleration and implantation occur via capacitive coupling. For thicker objects, though, the coupling becomes very weak and one may consider using a conducting sacrificial layer [201, 202, 203]. The idea is to first deposit a thin layer onto the object: this layer can serve as the electrode to which high negative bias

potential is applied. The layer should be thinner than the projected range of the accelerated ions such that the ions come to rest below the film, i.e., in the surface region of the object (for projected range calculations one may consider the TRIM code mentioned in Chapter 8). Sputtering will cause the conducting layer to become thinner until its continuity breaks down. This should be the time the process is finished or one may consider an in situ "repair" of the layer by depositing new sacrificial material [202]. Oates and co-workers [203] demonstrated the ion implantation modification of polymers using a thin filtered-arc-deposited copper film and checked the polymer modification by cross-sectional transmission electron microscopy (TEM). The remaining metal on the surface can be desirable, e.g., for antibacterial properties, or it can be removed by etching.

10.8.2 Titanium-Based Materials

Many medical implants and surgical devices are made from titanium alloys because of their high strength and superior osteointegrating properties compared to other biomaterials. However, titanium and titanium nitride are unsuitable as biomaterials in devices which are in direct contact with blood for a prolonged period [204]. While the binding of platelets in haemocompatible materials is ideally suppressed, the binding of platelets was increased on the titanium and titanium nitride surfaces compared to other biomaterial surfaces, and the state of platelet activation was much more pronounced as reflected by the levels of certain proteins that are known to be potent promoters of osteogenesis. This is an example that the biocompatibility of a material depends greatly on the biological environment.

The surface of titanium is covered by titanium oxide, and therefore some studies focus on the interaction of blood plasma[3] proteins with titanium oxides. The biomedical effects of titanium oxides can be studied by starting with the titanium base metal and use oxygen plasma treatment [205, 206], or one may produce titanium oxide, or related compound layers, like oxynitrides, using a vacuum arc [207, 208, 209]. It is known that titanium dioxide exists in amorphous and three different crystalline phases: anatase, rutile, and brookite; anatase and rutile are the more common ones, and the latter is usually produced when the substrate is at elevated temperature. The rutile phase has been shown to be more stable both at high and low ph-levels, and the dissolution rate of metal ions in simulated body fluid is lower for the rutile phase [210].

Tsyganov and colleagues at Rossendorf [209] showed that amorphous, nanocrystalline, and fine-grained layers show somewhat higher blood clotting times than well-crystallized rutile films. Implantation of Cr or P ions reduced the clot formation, and P-implanted surfaces show additionally improved platelet adherence. Using a similar setup with a filtered cathodic arc, Leng et al. at the City University

[3] Caution: In this section, physicians and physicists use the term plasma – and they may mean the same thing!

in Hong Kong [211] and later Wan and co-workers at the Southwest Jiaotong University in China [208] produced TiN and TiO_x–TiN dual layers on Ti–6Al–4 V alloy, showing that both coating types have lower dissolution currents and higher wear resistance in comparison to the uncoated Ti–6Al–4 V. The non-stoichiometric titanium oxide was found to have improved blood compatibility. The latter point was investigated in greater detail [212] using both sputter-deposited and cathodic arc films that contain the rutile phase. The films behaved generally similar but platelet adhesion was better for the sputtered films. In studies focusing on the structure of TiO_2, rather than the biomedical implication, Mändl and co-workers [213, 214] investigated the density, adhesion, texture, and barrier efficiency of TiO_2 produced by the MePIIID process with pulse bias up to 10 kV. The rutile phase, generally formed at high temperature, appears at room temperature in the energetic condensation process using silicon as a template: the epitaxial relation is $[100]TiO_2 \| [111]Si$ and $[110]TiO_2 \| [311]Si$. There is a rather small lattice misfit of 3.4% for the Si[111] direction and 0.86% for the Si[311] direction. Negative DC bias or high-voltage pulses up to 10 kV led only to a gradual loss of texture.

10.9 Surface Cleaning by Arc Erosion and Ion Etching

The cathodic vacuum arc has also been used to remove surface contaminants from metal surfaces. In this case, the arc spots act on the *substrate*, removing material by arc erosion. It is utilized that arc spot ignition occurs preferentially at locations with enhanced electric field on the surface, which is at contaminated locations, or the interface of contaminated and metallic surface sites. In some sense, arc spot cleaning is related to sputter cleaning in that material is removed; however, the physical mechanisms are as different as arc and glow discharge, respectively. In the arc case, surface "cleaning" occurs only locally during the short time of spot activity, and large-area cleaning is only possible by the action of many spot events, i.e., through the rapid apparent motion of spots. Luckily, especially on surfaces with non-metallic contaminants, many emission centers operate simultaneously: for estimates, the current per site for that kind of surface can be lower than 1 A. On the other hand, the slower, less rapidly moving spot of type 2 makes larger craters and removes more material at a given location. In any case, arc cleaning typically leads to surface roughness, with RMS in the micron range rather than nanometer range, which is associated with the depth distribution function of arc erosion craters: the surface has a matte, dull finish. The erosion rates are commonly normalized by the charge transferred, $I_{\mathrm{arc}} t_{\mathrm{cleaning}}$. As known from many arc erosion studies [215, 216, 217, 218, 219, 220, 221, 222, 223, 224], arc erosion involves ion, neutral, and macroparticle components with typical removal rates of 50–200 μg/C. Arc erosion for cleaning purposes has been applied industrially [225].

A very different approach to using cathodic arc plasma for cleaning and surface preparation purposes is by metal ion sputtering: here, the metal ions come from the cathodic arc plasma but condensation is overcompensated by

sputtering, which works very well with typical negative bias voltages of about 1 kV. Assuming we have a mean ion charge state of say 2, the mean ion energy is 2 keV. At this energy, the sputter yield is generally much greater than unity, that is, more than one surface atom is removed per arriving ion. Of course, the arriving metal ions are subplanted and remain in the subsurface layer until they become exposed to the surface and eventually removed by sputtering. In the end, some of the metal atoms remain – but that is desirable because they help creating a graded interface for excellent adhesion of the following coating.

This combined cleaning and heating procedure with arc metal ions is industrially widely used and already mentioned in Bergman's 1985 review paper [226]. It has been implemented in several commercial deposition recipes like in Vapor Tech's Low Temperature Arc Vapor Deposition (LTAVD^{TM}) technology [227], or as a preparation method for sputter deposition like in Hauzer's Arc-Bond Sputtering (ABS^{TM}) technology [228, 229, 230, 231, 232]. The ABS technology is especially geared toward demanding multilayer tool coatings, and sputtering is preferred for the deposition step because the macroparticles produced in the conventional arc deposition process are detrimental. Indeed, even the macroparticles produced in the etching step represent a performance issue for demanding applications that involve erosion and wear [233, 234]. One possible approach is to used filtered arc plasma in the metal ion erosion step, and this has been successfully demonstrated for CrN films prepared on steel after Cr ion etching [235] with a bias of −1,200 V. However, the greater use of filtered arc technology depends on the economical implementation of simple and robust filters with low plasma losses.

References

1. Bergman, C., Ion flux characteristics in arc vapor deposition of TiN, *Surf. Coat. Technol.* **36**, 243–255, (1988).
2. Vetter, J., Burgmer, W., and Perry, A.J., Arc-enhanced glow discharge in vacuum arc machines, *Surf. Coat. Technol.* **59**, 152–155, (1993).
3. Martin, P.J., Netterfield, R.P., Kinder, T.J., and Descotes, L., Deposition of TiN, TiC, and TiO_2 films by filtered arc evaporation, *Surf. Coat. Technol.* **49**, 239–243, (1991).
4. Ryabchikov, A.I., Stepanov, I.B., Shulepov, I.A., Sharkeyev, Y.P., and Fortuna, S.V., "Application of a shutter-type filter for removing microparticle fraction from arc discharge plasma in technology of TiN coating formation," 5th Conf. on Modification of Materials with Particle Beams and Plasma Flows, Tomsk, Russia, 319–322, (2000).
5. Tang, B., Wang, Y., Wang, L., Wang, X., Liu, H., Yu, Y., and Sun, T., Adhesion strength of TiN films synthesized on GCr15-bearing steel using plasma immersion ion implantation and deposition, *Surf. Coat. Technol.* **186**, 153–156, (2004).
6. Vetter, J., Knaup, R., Dwuletzki, H., Schneider, E., and Vogler, S., Hard coatings for lubrication reduction in metal forming, *Surf. Coat. Technol.* **86–87**, 739–746, (1996).
7. Johansen, O.A., Dontje, J.H., and Zenner, R.L.D., Reactive arc vapor ion deposition of TiN, ZrN and HfN, *Thin Solid Films* **153**, 75–82, (1987).
8. Boelens, S. and Veltrop, H., Hard coatings of TiN, (TiHf)N and (TiNb)N deposited by random and steered arc evaporation, *Surf. Coat. Technol.* **33**, 63–71, (1987).

9. Johnson, P.C. and Randhawa, H., Zirconium nitride films prepared by cathodic arc plasma deposition process, *Surf. Coat. Technol.* **33**, 53–62, (1987).
10. Conrad, J.R., Radtke, J.L., Dodd, R.A., Worzala, F.J., and Tran, N.C., Plasma source ion-implantation technique for surface modification, *J. Appl. Phys.* **62**, 4591–4596, (1987).
11. Blawert, C., Mordike, B.L., Collins, G.A., Hutchings, R., Short, K.T., and Tendys, J., Plasma immersion ion implantation of 100Cr6 ball bearing steel, *Surf. Coat. Technol.* **83**, 228–234, (1996).
12. Johns, S.M., Bell, T., Samandi, M., and Collins, G.A., Wear resistance of plasma immersion ion implanted Ti6Al4V, *Surf. Coat. Technol.* **85**, 7–14, (1996).
13. Mändl, S., Günzel, R., Richter, E., and Möller, W., Nitriding of austenitic stainless steels using plasma immersion ion implantation, *Surf. Coat. Technol.* **100–101**, 372–376, (1998).
14. Vetter, J. and Perry, A.J., Advances in cathodic arc technology using electrons extracted from the vacuum arc, *Surf. Coat. Technol.* **61**, 305–309, (1993).
15. Vetter, J., $(Al_x : Ti_y)N$ coatings deposited by cathodic vacuum arc evaporation, *J. Advanced Materials* **31**, 41–47, (1999).
16. Freller, H. and Haessler, H., $Ti_xAl_{1-x}N$ films deposited by ion plating with an arc evaporator, *Thin Solid Films* **153**, 67–74, (1987).
17. Hörling, A., Hultman, L., Odén, M., Sjölén, J., and Karlsson, L., Mechanical properties and machining performance of $Ti_{1-x}Al_xN$-coated cutting tools, *Surf. Coat. Technol.* **191**, 384–392, (2005).
18. Hörling, A., Hultman, L., Odén, M., Sjolén, J., and Karlsson, L., Thermal stability of arc evaporated high aluminum-content $Ti_{1-x}Al_xN$ thin films, *J. Vac. Sci. Technol. A* **20**, 1815–1823, (2002).
19. Mayrhofer, P.H., Hörling, A., Karlsson, L., Sjolen, J., Larsson, T., Mitterer, C., and Hultman, L., Self-organized nanostructures in the Ti-Al-N system, *Appl. Phys. Lett.* **83**, 2049–2051, (2003).
20. Gersten, J.I. and Smith, F.W., *The Physics and Chemistry of Materials*. John Wiley & Sons, New York, (2001).
21. PalDey, S. and Deevi, S.C., Properties of single layer and gradient (Ti,Al)N coatings, *Mater. Sci. Eng. A* **361**, 1–8, (2003).
22. Knotek, O., Loffler, F., Scholl, H.J., and Barimani, C., The multisource arc process for depositing ternary Cr- and Ti-based coatings, *Surf. Coat. Technol.* **68–69**, 309–313, (1994).
23. Vetter, J., Scholl, H.J., and Knotek, O., (TiCr)N coatings deposited by cathodic vacuum arc evaporation, *Surf. Coat. Technol.* **74–75**, 286–291, (1995).
24. Chang, Y.-Y., Yang, S.-J., and Wang, D.-Y., Characterization of TiCr(C,N)/amor phous carbon coatings synthesized by a cathodic arc deposition process, *Thin Solid Films* **515**, 4722–4726, (2007).
25. Karlsson, L., Hultman, L., Johansson, M.P., Sundgren, J.E., and Ljungcrantz, H., Growth, microstructure, and mechanical properties of arc evaporated TiC_xN_{1-x} $(0 <= x <= 1)$ films, *Surf. Coat. Technol.* **126**, 1–14, (2000).
26. Karlsson, L., Hultman, L., and Sundgren, J.E., Influence of residual stresses on the mechanical properties of TiC_xN_{1-x} $(x = 0, 0.15, 0.45)$ thin films deposited by arc evaporation, *Thin Solid Films* **371**, 167–177, (2000).
27. Yamamoto, K., Sato, T., Takahara, K., and Hanaguri, K., Properties of (Ti,Cr,AI)N coatings with high Al content deposited by new plasma enhanced arc-cathode, *Surf. Coat. Technol.* **174–175**, 620–626, (2003).
28. Lee, H.Y., Han, J.G., Baeg, S.H., and Yang, S.H., Characterization of WC–CrAlN heterostructures obtained using a cathodic arc ion plating process, *Surf. Coat. Technol.* **174–175**, 303–309, (2003).

29. Gorokhovsky, V.I., Bhat, D.G., Shivpuri, R., Kulkarni, K., Bhattacharya, R., and Rai, A.K., Characterization of large area filtered arc deposition technology: part II – coating properties and application, *Surf. Coat. Technol.* **140**, 215–224, (2001).
30. Gorokhovsky, V., Heckerman, B., Watson, P., and Bekesch, N., The effect of multilayer filtered arc coatings on mechanical properties, corrosion resistance and performance of periodontal dental instruments, *Surf. Coat. Technol.* **200**, 5614–5630, (2006).
31. Music, D., Sun, Z., Voevodin, A.A., and Schneider, J.M., Electronic structure and shearing in nanolaminated ternary carbides, *Solid State Communications* **139**, 139–143, (2006).
32. Barsoum, M.W. and El-Raghy, T., Synthesis and Characterization of a Remarkable Ceramic: Ti_3SiC_2, *J. American Ceramic Society* **79**, 1953–1956, (1996).
33. Barsoum, M.W. and El-Raghy, T., The MAX phases: Unique new carbide and nitride materials, *Am. Sci.* **89**, 334, (2001).
34. Rosén, J., Ryves, L., Persson, P.O.Å., and Bilek, M.M.M., Deposition of epitaxial Ti_2AlC thin films by pulsed cathodic arc, *J. Appl. Phys.* **101**, 056101–2, (2007).
35. Brondum, K. and Larson, G., "Low-temperature arc vapor deposition as a hexavalent chrome electroplating alternative," Vapor Technologies Inc., Longmont, CO May 13, 2005 (2005).
36. Esteve, J., Romero, J., Gomez, M., and Lousa, A., Cathodic chromium carbide coatings for molding die applications, *Surf. Coat. Technol.* **188–189**, 506–510, (2004).
37. Lide, D.R., (ed.) *Handbook of Chemistry and Physics, 81st Edition*, CRC Press, Boca Raton, New York, (2000).
38. Kubaschewski, O. and Evans, E.L., *Metallurgical Thermochemistry*, Reprint of 3rd edition, Pergamon Press, Oxford, (1965).
39. Kubaschewski, O., Alcock, C.B., and Spencer, P.J., *Materials Thermochemistry*, 6th ed. Pergamon Press, Oxford, (1993).
40. Cardarelli, F., *Materials Handbook*. Springer, London, (2000).
41. Pierson, H.O., *Handbook of Refractory Carbides and Nitrides: Properties, Characteristics, Processing and Applications*. Noyes, Park Ridge, NJ, (1996).
42. Braic, V., Balaceanu, M., Braic, M., and Vladescu, A., Synthesis and characterization of hard layers obtained by vacuum arc technology, *Romanian Reports in Physics* **56**, 481–486, (2004).
43. Knotek, O., Lugscheider, E., Löffler, F., Beele, W., and Barimani, C., Arc evaporation of multicomponent MCrAlY cathodes, *Surf. Coat. Technol.* **74/75**, 118–122, (1995).
44. Shinno, H., Tanabe, T., Fujitsuka, M., and Sakai, Y., Characterization of carbon-boron coatings prepared on molybdenum by a vacuum arc deposition method, *Thin Solid Films* **189**, 149–159, (1990).
45. Morrow, M.S., Schechter, D.E., Tsai, C.-C., Klepper, C.C., Niemel, J., and Hazelton, R.C., "Microwave processing of pressure boron powders for use as cathodes in vacuum arc sources," patent US 6,562,418 (2003).
46. Richter, F., Krannich, G., Hahn, J., Pintaske, R., Friedrich, M., Schmidbauer, S., and Zahn, D.R.T., Utilization of cathodic arc evaporation for the deposition of boron nitride thin films, *Surf. Coat. Technol.* **90**, 178–183, (1997).
47. Richter, F., Flemming, G., Kühn, M., Peter, S., and Wagner, H., Characterization of the arc evaporation of a hot boron cathode, *Surf. Coat. Technol.* **112**, 43–47, (1999).
48. Klepper, C.C., Hazelton, R.C., Yadlowsky, E.J., Carlson, E.P., Keitz, M.D., Williams, J.M., Zuhr, R.A., and Poker, D.B., Amorphous boron coatings produced with vacuum arc deposition technology, *J. Vac. Sci. Technol. A* **20**, 725–732, (2002).

49. Werner, Z., Stanisawski, J., Piekoszewski, J., Levashov, E.A., and Szymczyk, W., New types of multi-component hard coatings deposited by arc PVD on steel pretreated by pulsed plasma beam, *Vacuum* **70**, 263–267, (2003).
50. Klepper, C.C., Niemel, J., Hazelton, R.C., Yadlowsky, E.J., and Monteiro, O.R., Vacuum arc deposited boron carbide films for fusion plasma facing components, *Fusion Technol.* **39**, 910–915, (2001).
51. Klepper, C.C., Niemel, J., Hazelton, R.C., and Keitz, M.D., "Method and apparatus for depositing ceramic films by vacuum arc deposition," patent US 6,495,002 (2002).
52. Monteiro, O.R., Delplancke-Ogletree, M.P., and Klepper, C.C., Boron carbide coatings prepared by cathodic arc deposition, *J. Materials Sci.* **38**, 3117–3120, (2003).
53. Mackiewicz Ludtka, G., Sikka, V.K., Williams, J.M., Klepper, C.C., Hazelton, R.C., and E.J. Yadlowsky, "Aluminum soldering performance testing of H13 steel as boron coated by the cathodic arc technique," 47th Annual Technical Conference Proceedings of the Society of Vacuum Coaters, Dallas, TX, 168–173, (2004).
54. Cuomo, J.J., Pappas, D.L., Bruley, J., Doyle, J.P., and Saenger, K.K., Vapor deposition process for amorphous carbon films with sp^3 fractions approaching diamond, *J. Appl. Phys.* **70**, 1706–1711, (1991).
55. Ager III, J.W., Anders, S., Anders, A., and Brown, I.G., Effect of intrinsic growth stress on the Raman spectra of vacuum-arc-deposited amorphous carbon films, *Appl. Phys. Lett.* **66**, 3444–3446, (1995).
56. Pharr, G.M., Callahan, D.L., McAdams, D., et al., Hardness, elastic modulus, and structure of very hard carbon films produced by cathodic-arc deposition with substrate bias, *Appl. Phys. Lett.* **68**, 779–781, (1996).
57. Lossy, R., Pappas, D.L., Roy, R.A., Cuomo, J.J., and Sura, V.H., Filtered arc deposition of amorphous diamond, *Appl. Phys. Lett.* **61**, 171–173, (1992).
58. Falabella, S., Boercker, D.B., and Sanders, D.M., Fabrication of amorphous diamond films, *Thin Solid Films* **236**, 82–86, (1993).
59. Hakovirta, M., Salo, J., Lappalainen, R., and Anttila, A., Correlation of carbon ion energy with sp(2)/sp(3) ratio in amorphous diamond films produced with a mass-separated ion beam, *Phys. Lett. A* **205**, 287–289, (1995).
60. Wang, X., Zhao, J.P., Chen, Z.Y., Yang, S.Q., Shi, T.S., and Liu, X.H., Field emission from amorphous diamond films prepared by filtered arc deposition, *Thin Solid Films* **317**, 356–358, (1998).
61. Andersson, J., Erck, R.A., and Erdemir, A., Friction of diamond-like carbon films in different atmospheres, *Wear* **254**, 1070–1075, (2003).
62. Erdemir, A. and Donnet, C., Tribology of diamondlike carbon films: recent progress and future prospects, *J. Phys. D: Appl. Phys.* **39**, R1–R17, (2006).
63. Anders, S., Brown, I.G., Bhatia, C.S., and Bogy, D.B., Wanted: hard, thin coatings for near-contact recording, *Data Storage* **4**, 31–38, (1997).
64. Robertson, J., Requirements of ultrathin carbon coatings for magnetic storage technology, *Tribology International* **36**, 405–415, (2003).
65. Jacoby, B., Wienss, A., Ohr, R., von Gradowski, M., and Hilgers, H., Nanotribological properties of ultra-thin carbon coatings for magnetic storage devices, *Surf. Coat. Technol.* **174–175**, 1126–1130, (2003).
66. Casiraghi, C., Ferrari, A.C., Ohr, R., Chu, D., and Robertson, J., Surface properties of ultra-thin tetrahedral amorphous carbon films for magnetic storage technology, *Diam. Rel. Mat.* **13**, 1416–1421, (2004).
67. Robertson, J., Diamond-like amorphous carbon, *Mat. Sci. Eng.* **R 37**, 129–281, (2002).

68. Anders, A., Fong, W., Kulkarni, A., Ryan, F.R., and Bhatia, C.S., Ultrathin diamondlike carbon films deposited by filtered carbon vacuum arcs, *IEEE Trans. Plasma Sci.* **29**, 768–775, (2001).
69. Druz, B., Yevtukhov, Y., and Zaritskiy, I., Diamond-like carbon overcoat for TFMH using filtered cathodic arc system with Ar-assisted arc discharge, *Diam. Rel. Mat.* **14**, 1508–1516, (2005).
70. Anders, S., Anders, A., Dickinson, M.R., MacGill, R.A., and Brown, I.G., S-shaped magnetic macroparticle filter for cathodic arc deposition, *IEEE Trans. Plasma Sci.* **25**, 670–674, (1997).
71. Shi, X., Tay, B.G., and Lau, S.P., The double bend filtered cathodic arc technology and its applications, *Int. J. Mod. Phys. B* **14**, 136–153, (2000).
72. You, G.F., Tay, B.K., Lau, S.P., Chua, D.H.C., and Milne, W.I., Carbon arc plasma transport through different off-plane double bend filters, *Surf. Coat. Technol.* **150**, 50–56, (2002).
73. Tay, B.K. and Zhang, P., On the properties of nanocomposite amorphous carbon films prepared by off-plane double bend filtered cathodic vacuum arc, *Thin Solid Films* **420–421**, 177–184, (2002).
74. Anders, S., Stammler, T., Fong, W., Chen, C.-Y., Bogy, D.B., Bhatia, C.S., and Stöhr, J., Study of tribochemical processes on hard disks using photoemission electron microscopy, *J. Tribology* **121**, 961–967, (1999).
75. Anders, S., Stammler, T., Fong, W., Bogy, D.B., Bhatia, C.S., and Stöhr, J., Investigation of slider surfaces after wear using photoemission electron microscopy, *J. Vac. Sci. Technol. A* **17**, 2731–2736, (1999).
76. Bhatia, C.S., Fong, W., Chen, C.-Y., Wei, J., Bogy, D.B., Anders, S., Stammler, T., and Stöhr, J., Tribochemistry at the head/disk interface, *IEEE Trans. Magnetics* **35**, 910–915, (1999).
77. Tsui, T.Y., Pharr, G.M., Oliver, W.C., Bhatia, C.S., White, R.L., Anders, S., Anders, A., and Brown, I.G., Nanoindentation and nanoscratching of hard carbon coatings for magnetic disks, *Mat. Res. Soc. Symp. Proc.* **383**, 447–452, (1995).
78. Decker, T.G., Lundie, G.P., Pappas, D.L., Welty, R.P., and Parent, C.R., "Amorphous diamond coating of blades," patent WO 9529044 (1995).
79. Decker, T.G., Lundie, G.P., Pappas, D.L., Welty, R.P., and Parent, C.R., "Amorphous diamond coating of blades," patent US 5799549 (1998).
80. Sheeja, D., Tay, B.K., Yu, L., and Lau, S.P., Low stress thick diamond-like carbon films prepared by filtered arc deposition for tribological applications, *Surf. Coat. Technol.* **154**, 289–293, (2002).
81. Liujiang, Y., Tay, B.K., Sheeja, D., Fu, Y.Q., and Miao, J.M., Micromachining of large area amorphous carbon membranes prepared by filtered cathodic vacuum arc technique, *Appl. Surf. Sci.* **223**, 286–293, (2004).
82. Sheeja, D., Tay, B.K., Lau, S.P., Yu, L.J., Miao, J.M., Chua, H.C., and Milne, W.I., Fabrication of smooth amorphous carbon micro-cantilevers by lift-off, *Sens. Actuators B: Chem.* **98**, 275–281, (2004).
83. Yu, L.J., Sheeja, D., Tay, B.K., Chua, D.H.C., Milne, W.I., Miao, J., and Fu, Y.Q., Etching behaviour of pure and metal containing amorphous carbon films prepared using filtered cathodic vacuum arc technique, *Appl. Surf. Sci.* **195**, 107–116, (2002).
84. Lemoine, P., Quinn, J.P., Maguire, P., and McLaughlin, J.A., Comparing hardness and wear data for tetrahedral amorphous carbon and hydrogenated amorphous carbon thin films, *Wear* **257**, 509–522, (2004).

85. Oliver, W.C. and Pharr, G.M., An improved technique for determining hardness and elastic modulus using load and displacement sensing indentation experiments, *J. Mater. Res.* **7**, 1564–1583, (1992).
86. Zou, Y.S., Wang, W., Song, G.H., Du, H., Gong, J., Huang, R.F., and Wen, L.S., Influence of the gas atmosphere on the microstructure and mechanical properties of diamond-like carbon films by arc ion plating, *Mater. Lett.* **58**, 3271–3275, (2004).
87. Miyakawa, N., Minamisawa, S., Takikawa, H., and Sakakibar, T., Physical–chemical hybrid deposition of DLC film on rubber by T-shape filtered-arc-deposition, *Vacuum* **73**, 611–617, (2004).
88. Druz, B., Yevtukhov, Y., Novotny, V., Zaritsky, I., Kanarov, V., Polyakov, V., and Rukavishnikov, A., Nitrogenated carbon films deposited using filtered cathodic arc, *Diam. Rel. Mat.* **9**, 668–674, (2000).
89. Liu, E., Shi, X., Tan, H.S., Cheah, L.K., Sun, Z., Tay, B.K., and Shi, J.R., The effect of nitrogen on the mechanical properties of tetrahedral amorphous carbon films deposited with a filtered cathodic vacuum arc, *Surf. Coat. Technol.* **120–121**, 601–606, (1999).
90. Silva, S.R.P., Robertson, J., Amaratunga, G.A.J., Rafferty, B., Brown, L.M., Schwan, J., Franceschini, D.F., and Mariotto, G., Nitrogen modification of hydrogenated amorphous carbon films, *J. Appl. Phys.* **81**, 2626–2634, (1997).
91. Kühn, M., Spaeth, C., Pintaske, R., Peter, S., Richter, F., and Anders, A., The effect of additional ion/plasma assistance in CN_x-film deposition based on a filtered cathodic arc, *Thin Solid Films* **311**, 151–156, (1997).
92. Tan, A.H. and Cheng, Y.C., Optimization of wear-corrosion properties of a-C:N films using filtered cathodic arc deposition, *Diam. Rel. Mat.* **17**, 36–42, (2008).
93. Chang, Y.-Y. and Wang, D.-Y., Structural and electrical properties of nitrogen-doped Cr-C:H films synthesized by a cathodic-arc activated deposition process, *Thin Solid Films* **485**, 1–7, (2005).
94. Fu, R.K.Y., Mei, Y.F., Shen, L.R., Siu, G.G., Chu, P.K., Cheung, W.Y., and Wong, S. P., Molybdenum–carbon film fabricated using metal cathodic arc and acetylene dual plasma deposition, *Surf. Coat. Technol.* **186**, 112–117, (2004).
95. Fu, R.K.Y., Mei, Y.F., Fu, M.Y., Liu, X.Y., and Chu, P.K., Thermal stability of metal-doped diamond-like carbon fabricated by dual plasma deposition, *Diam. Rel. Mat.* **14**, 1489–1493, (2005).
96. Vetter, J. and Nevoigt, A., a-C : HMe coatings deposited by the cathodic vacuum arc deposition: properties and application potential, *Surf. Coat. Technol.* **121**, 709–717, (1999).
97. Chen, J.S., Lau, S.P., Chen, G.Y., Sun, Z., Li, Y.J., Tay, B.K., and Chai, J.W., Deposition of iron containing amorphous carbon films by filtered cathodic vacuum arc technique, *Diam. Rel. Mat.* **10**, 2018–2023, (2001).
98. Sheeja, D., Tay, B.K., and Yu, L.J., A comparative study between pure and Al-containing amorphous carbon films prepared by FCVA technique together with high substrate pulse bias, *Diam. Rel. Mat.* **12**, 2032–2036, (2003).
99. Zhang, P., Tay, B.K., Yu, G.Q., Lau, S.P., and Fu, Y.Q., Surface energy of metal containing amorphous carbon films deposited by filtered cathodic vacuum arc, *Diam. Rel. Mat.* **13**, 459–464, (2004).
100. Ryves, L., Bilek, M.M.M., Oates, T.W.H., Tarrant, R.N., McKenzie, D.R., Burgmann, F.A., and McCulloch, D.G., Synthesis and in-situ ellipsometric

monitoring of Ti/C nanostructured multilayers using a high-current, dual source pulsed cathodic arc, *Thin Solid Flims* **482**, 133–137, (2005).
101. Pasaja, N., Sansongsiri, S., Intarasiri, S., Vilaithong, T., and Anders, A., Mo-containing tetrahedral amorphous carbon deposited by dual filtered cathodic vacuum arc with selective pulsed bias voltage, *Nucl. Instrum. Meth. Phys. Res. B* **259**, 867–870, (2007).
102. Anders, A., Pasaja, N., and Sansongsiri, S., Filtered cathodic arc deposition with ion-species-selective bias, *Rev. Sci. Instrum.* **78**, 063901-1-5, (2007).
103. Niyomsoan, S., Grant, W., Olson, D.L., and Mishra, B., Variation of color in titanium and zirconium nitride decorative thin films, *Thin Solid Films* **415**, 187–194, (2002).
104. Gläser, H.J., *Large Area Glass Coating*. Von Ardenne Anlagentechnik GmbH, Dresden, Germany, (2000).
105. Zallen, R., *International Colloquium on the Optical Properties and Electronic Structure of Metals and Alloys*, Paris, France, (1965).
106. Schlegel, A., Wachter, P., Nickl, J.J., and Lingg, H., Optical properties of TiN and ZrN, *J. Phys. C: Solid State Physics*, 4889–4896, (1977).
107. Eerden, M., van Ijzendoorn, W., Tietema, R., and van der Kolk, G.J., "A systematic study of the properties of the Zr-C-N ternary system, deposited by reactive arc evaporation," 46th Annual Technical Conference, Society of Vacuum Coaters, San Francisco, CA, 56–60, (2003).
108. Beck, U., Reiners, G., Kopacz, U., and Jehn, H.A., Decorative hard coatings: interdependence of optical, stoichiometric and structural properties, *Surf. Coat. Technol.* **60**, 389–395, (1993).
109. Martin, P.J., Netterfield, R.P., and Kinder, T.J., Ion-beam-deposited films produced by filtered arc evaporation, *Thin Solid Films* **193**, 77–83, (1990).
110. Martin, P.J., Netterfield, R.P., Bendavid, A., and Kinder, T.J., The deposition of thin films by filtered arc evaporation, *Surf. Coat. Technol.* **54**, 136–142, (1992).
111. Martin, P., Netterfield, R., Kinder, T., and Bendavid, A., Optical properties and stress of ion-assisted aluminum nitride thin films, *Appl. Opt.* **31**, 6734, (1992).
112. Bendavid, A., Martin, P.J., Netterfield, R.P., Sloggett, G.J., Kinder, T.J., and Andrikidis, C., The deposition of niobium, NbN and Nb_2O_5 films by filtered arc evaporation, *J. Mat. Sci. Lett.* **12**, 322–323, (1993).
113. Bendavid, A., Martin, P.J., Jamting, A., and Takikawa, H., Structural and optical properties of titanium oxide thin films deposited by filtered arc deposition, *Thin Solid Films* **356**, 6–11, (1999).
114. Bendavid, A., Martin, P.J., and Takikawa, H., Deposition and modification of titanium dioxide thin films by filtered arc deposition, *Thin Solid Films* **360**, 241–249, (2000).
115. Martin, P.J. and Bendavid, A., "Optical thin film deposition by filtered cathodic arc techniques," 45th Annual Technical Conference, Society of Vacuum Coaters, Philadelphia, PA, 270–273, (2002).
116. Martin, P.J., Bendavid, A., Netterfield, R.P., Kinder, T.J., Jahan, F., and Smith, G., Plasma deposition of tribological and optical thin film materials with a filtered cathodic arc source, *Surf. Coat. Technol.* **112**, 257–260, (1999).
117. Kim, J.K., Lee, E.S., Kim, D.H., and Kim, D.G., Ion beam-induced erosion and humidity effect of MgO protective layer prepared by vacuum arc deposition, *Thin Solid Films* **447**, 95–99, (2004).

118. Zheng, C., Zhu, D., Chen, D., He, Z., Wen, L., Cheung, W.Y., and Wong, S.P., Influence of O_2 flow rate on structure and properties of MgO_x films prepared by cathodic-vacuum-arc ion deposition system, *IEEE Trans. Plasma Sci.* **34**, 1099–1104, (2006).
119. MacGill, R.A., Anders, S., Anders, A., Castro, R.A., Dickinson, M.R., Yu, K.M., and Brown, I.G., Cathodic arc deposition of copper oxide thin films, *Surf. Coat. Technol.* **78**, 168–172, (1996).
120. Mändl, S., Manova, D., and Rauschenbach, B., Transparent AlN layers formed by metal plasma immersion ion implantation and deposition, *Surf. Coat. Technol.* **186**, 82–87, (2004).
121. Inkin, V.N., Kirpilenko, G.G., and Kolpakov, A.J., Properties of aluminium nitride coating obtained by vacuum arc discharge method with plasma flow separation, *Diam. Rel. Mater.* **10**, 1314–1316, (2001).
122. Exarhos, G.J. and Zhou, X.-D., Discovery-based design of transparent conducting oxide films, *Thin Solid Films* **515**, 7025–7052, (2007).
123. Chen, B.J., Sun, X.W., and Tay, B.K., Fabrication of ITO thin films by filtered cathodic vacuum arc deposition, *Mat. Sci. Eng. B* **106**, 300–304, (2004).
124. Satoh, I. and Kobayashi, T., Magnetic and optical properties of novel magnetic semiconductor Cr-doped ZnO and its application to all oxide p-i-n diode, *Appl. Surf. Sci.* **216**, 603–606, (2003).
125. Ben-Shalom, A., Kaplan, L., Boxman, R.L., Goldsmith, S., and Nathan, M., SnO_2 transparent conductor films produced by filtered vacuum arc deposition, *Thin Solid Films* **236**, 20–26, (1993).
126. Boxman, R.L., Zhitomirsky, V., Goldsmith, S., David, T., and Dikhtyar, V., "Deposition of SnO_2 coatings using a rectangular filtered vacuum arc source," 46th Annual Technical Meeting of the Society of Vacuum Coaters, San Francisco, CA, 234–239, (2003).
127. David, T., Goldsmith, S., and Boxman, R.L., "p-type Sb-doped ZnO thin films prepared with filtered vacuum arc deposition," 47th Annual Technical Conference Proceedings of the Society of Vacuum Coaters, Dallas, TX, 122–126, (2004).
128. Kaplan, L., Benshalom, A., Boxman, R.L., Goldsmith, S., Rosenberg, U., and Nathan, M., Annealing and Sb-Doping of Sn-O Films Produced By Filtered Vacuum Arc Deposition – Structure and Electro-Optical Properties, *Thin Solid Films* **253**, 1–8, (1994).
129. Kaplan, L., Zhitomirsky, V.N., Goldsmith, S., Boxman, R.L., and Rusman, I., Arc behaviour during filtered vacuum arc deposition of Sn-O thin films, *Surf. Coat. Technol.* **76**, 181–189, (1995).
130. Kaplan, L., Rusman, I., Boxman, R.L., Goldsmith, S., Nathan, M., and BenJacob, E., STM and XPS study of filtered vacuum arc deposited Sn-O films, *Thin Solid Films* **291**, 355–361, (1996).
131. Zhitomirsky, V.N., Boxman, R.L., and Goldsmith, S., Plasma distribution and SnO_2 coating deposition using a rectangular filtered vacuum arc plasma source, *Surf. Coat. Technol.* **185**, 1–11, (2004).
132. Zhitomirsky, V.N., David, T., Boxman, R.L., Goldsmith, S., Verdyan, A., Soifer, Y.M., and Rapoport, L., Properties of SnO_2 coatings fabricated on polymer substrates using filtered vacuum arc deposition, *Thin Solid Films* **492**, 187–194, (2005).
133. Goldsmith, S., Filtered vacuum arc deposition of undoped and doped ZnO thin films: Electrical, optical, and structural properties, *Surf. Coat. Technol.* **201**, 3993–3999, (2006).

134. Xu, X.L., Lau, S.P., Chen, J.S., Chen, G.Y., and Tay, B.K., Polycrystalline ZnO thin films on Si (100) deposited by filtered cathodic vacuum arc, *J. Cryst. Growth* **223**, 201–205, (2001).
135. Xu, X.L., Lau, S.P., and Tay, B.K., Structural and optical properties of ZnO thin films produced by filtered cathodic vacuum arc, *Thin Solid Films* **398–399**, 244–249, (2001).
136. Minami, T., Ida, S., and Miyata, T., High rate deposition of transparent conducting oxide thin films by vacuum arc plasma evaporation, *Thin Solid Films* **416**, 92–96, (2002).
137. Tay, B.K., Zhao, Z.W., and Chua, D.H.C., Review of metal oxide films deposited by filtered cathodic vacuum arc technique, *Mat. Sci. Eng. R: Reports* **52**, 1–48, (2006).
138. Lee, H.W., Lau, S.P., Wang, Y.G., Tay, B.K., and Hng, H.H., Internal stress and surface morphology of zinc oxide thin films deposited by filtered cathodic vacuum arc technique, *Thin Solid Films* **458**, 15–19, (2004).
139. Ozgur, U., Alivov, Y.I., Liu, C., Teke, A., Reshchikov, M.A., Dogan, S., Avrutin, V., Cho, S.J., and Morkoc, H., A comprehensive review of ZnO materials and devices, *J. Appl. Phys.* **98**, 041301–103, (2005).
140. Wang, Y.G., Lau, S.P., Lee, H.W., Yu, S.F., Tay, B.K., Zhang, X.H., Tse, K.Y., and Hng, H.H., Comprehensive study of ZnO films prepared by filtered cathodic vacuum arc at room temperature, *J. Appl. Phys.* **94**, 1597–1604, (2003).
141. Look, D.C., Claflin, B., Alivov, Y.I., and Park, S.J., The future of ZnO light emitters, *phys. stat. sol. (a)* **201**, 2203–2212, (2004).
142. Kavak, H., Senadim Tüzemen, E., Özbayraktar, L.N., and Esen, R., "Optical and photoinductivity properties of ZnO thin films grown by pulsed filtered cathodic vacuum arc deposition," The Ninth Int. Symp. on Sputtering and Plasma Processes (ISSP 2007), Kanazawa, Japan, 275–278, (2007).
143. Shi, X., Cheah, L.K., and Tay, B.K., *Thin Solid Films* **312**, 166, (1998).
144. Veerasamy, V.S., Amaratunga, G.A.J., Park, J.S., MacKenzie, H.S., and Milne, W.I., *IEEE Trans. Electron Devices* **42**, 577, (1995).
145. Cheah, L.K., Shi, X., Liu, E., and Shi, J.R., Nitrogenated tetrahedral amorphous carbon films prepared by ion-beam-assisted filtered cathodic vacuum arc technique for solar cells application, *Appl. Phys. Lett.* **73**, 2473–2475, (1998).
146. Cheah, L.K., Xu, S., and Tay, B.K., Deposition of nitrogen doped tetrahedral amorphous carbon (ta-C:N) films by ion beam assisted filtered cathodic vacuum arc, *Electron. Lett.* **33**, 1339–1340, (1997).
147. Chua, D.H.C., Milne, W.I., Tay, B.K., Zhang, P., and Ding, X.Z., Microstructural and surface properties of cobalt containing amorphous carbon thin film deposited by a filtered cathodic vacuum arc, *J. Vac. Sci. Technol. A* **21**, 353–358, (2003).
148. Zhang, P., Tay, B.K., Zhang, Y.B., Lau, S.P., and Yung, K.P., The reversible wettability of Ti containing amorphous carbon films by UV irradiation, *Surf. Coat. Technol.* **198**, 184–188, (2005).
149. Satyanarayana, B.S., Hart, A., Milne, W.I., and Robertson, J., Field emission from tetrahedral amorphous carbon, *Diam. Rel. Mat.* **7**, 656–659, (1998).
150. Milne, W.I., Field emission from tetrahedrally bonded amorphous carbon, *Appl. Surf. Sci.* **146**, 262–268, (1999).
151. Mao, D.S., Zhao, J., Wi, L., et al., Electron field emission from filtered arc deposited diamond-like carbon films using Au and Ti layers, *Diam. Rel. Mat.* **8**, 52–55, (1999).

152. Mao, D.S., Zhao, J., Li, W., et al., Electron field emission from nitrogen-containing diamond-like carbon films deposited by filtered arc deposition, *Mater. Lett.* **41**, 117–121, (1999).
153. Cheah, L.K., Shi, X., Tay, B.K., Silva, S.R.P., and Sun, Z., Field emission from undoped and nitrogen-doped tetrahedral amorphous carbon film prepared by filtered cathodic vacuum arc technique, *Diam. Rel. Mat.* **7**, 640–644, (1998).
154. Ding, X.-Z., Li, Y.J., Sun, Z., Tay, B.K., Lau, S.P., Cheung, W.Y., and Wong, S.P., Electron field emission from Ti-containing tetrahedral amorphous carbon films deposited by filtered cathodic vacuum arc, *J. Appl. Phys.* **88**, 6842–6847, (2000).
155. MacLeod, A.H., *Thin-Film Optical Filters*, 3rd ed. Institute of Physics, Bristol, UK, (2001).
156. Byon, E., Oates, T.H., and Anders, A., Coalescence of nanometer silver islands on oxides grown by filtered cathodic arc deposition, *Appl. Phys. Lett.* **82**, 1634–1636, (2003).
157. Avrekh, M., Monteiro, O.R., and Brown, I.G., Electrical resistivity of vacuum-arc-deposited platinum thin films, *Appl. Surf. Sci.* **158**, 217–222, (2000).
158. Fukuda, K., Lim, S.H.N., and Anders, A., Coalescence of magnetron-sputtered silver islands affected by transition metal seeding (Ni, Cr, Nb, Zr, Mo, W, Ta) and other parameters, *Thin Solid Films* **516**, 4546–4552, (2008).
159. Anders, A., Byon, E., Kim, D.-H., Fukuda, K., and Lim, S.H.N., Smoothing of ultrathin silver films by transition metal seeding, *Solid State Commun.* **140**, 225–229, (2006).
160. Rossnagel, S.M., Mikalsen, D., Kinoshita, H., and Cuomo, J.J., Collimated magnetron sputter deposition, *J. Vac. Sci. Technol. A* **9**, 261–265, (1991).
161. Hopwood, J.A., (ed.) *Ionized Physical Vapor Deposition*, Academic Press, San Diego, CA, (2000).
162. Rossnagel, S.M. and Hopwood, J., Magnetron sputter deposition with high levels of metal ionization, *Appl. Phys. Lett.* **63**, 3285–3287, (1993).
163. Rossnagel, S.M., Directional and ionized physical vapor deposition for microelectronics applications, *J. Vac. Sci. Technol. B* **16**, 2585–2608, (1998).
164. Tsai, M.H., Sun, S.C., Chiu, H.T., and Chuang, S.H., Metalorganic chemical vapor deposition of tungsten nitride for advanced metallization, *Appl. Phys. Lett.* **68**, 1412–1414, (1996).
165. Becker, J.S. and Gordon, R.G., Diffusion barrier properties of tungsten nitride films grown by atomic layer deposition from bis(tert-butylimido)bis(dimethylamido)tungsten and ammonia, *Appl. Phys. Lett.* **82**, 2239–2241, (2003).
166. Lau, S.P., Cheng, Y.H., Shi, J.R., Cao, P., Tay, B.K., and Shi, X., Filtered cathodic vacuum arc deposition of thin film copper, *Thin Solid Films* **398–399**, 539–543, (2001).
167. Shi, J.R., Lau, S.P., Sun, Z., Shi, X., Tay, B.K., and Tan, H.S., Structural and electrical properties of copper thin films prepared by filtered cathodic vacuum arc technique, *Surf. Coat. Technol.* **138**, 250–255, (2001).
168. Anders, A., Observation of self-sputtering in energetic condensation of metal ions, *Appl. Phys. Lett.* **85**, 6137–6139, (2004).
169. Chen, U.-S. and Shih, H.C., Characterization of copper metallization for interconnect by 90[deg]-bend electromagnetic filtered vacuum arc, *Nucl. Instrum. Meth. Phys. Res. B* **237**, 477–483, (2005).
170. Bilek, M.M.M. and McKenzie, D.R., A comprehensive model of stress generation and relief processes in thin films deposited with energetic ions, *Surf. Coat. Technol.* **200**, 4345–4354, (2006).

171. Schülke, T. and Anders, A., Ion charge state distributions of alloy-cathode vacuum arc plasmas, *IEEE Trans. Plasma Sci.* **27**, 911–914, (1999).
172. Singer, P., New technique for copper trench and via filling, *Semiconductor International* **March**, 53, (1997).
173. Siemroth, P., Wenzel, C., Kliomes, W., Schultrich, B., and Schülke, T., Metallization of sub-micron trenches and vias with high aspect ratio, *Thin Solid Films* **308**, 455–459, (1997).
174. Siemroth, P. and Schülke, T., Copper metallization in microelectronics using filtered vacuum arc deposition – principles and technological development, *Surf. Coat. Technol.* **133–134**, 106–113, (2000).
175. Monteiro, O.R., Novel metallization technique for filling 100-nm-wide trenches and vias with very high aspect ratio, *J. Vac. Sci. Technol. B* **17**, 1094–1097, (1999).
176. Singer, W., Singer, X., Filimonova, E., Reschke, D., Rostovtsev, A., Tokareva, T., and Zaharov, V., *Nucl. Instrum. Meth. Phys. Res. A* **574**, 518–520, (2007).
177. Hartwig, K.T., Jyhwen, W., Baars, D.C., et al., Microstructural refinement of niobium for superconducting RF cavities single-cell superconducting RF cavities from ultra-high-purity niobium, *IEEE Trans. Appl. Superconductivity* **17**, 1305–1309, (2007).
178. Langner, J., L., C., Russo, R., Tazzari, S., Cirillo, M., Merlo, V., and Tazzioli, F., Formation of thin superconducting films by means of ultra-high vacuum arc, *Czechoslovak J. Phys.* **52 (Suppl. D)**, 829–835, (2002).
179. Langner, J., Sadowski, M.J., Czaus, K., et al., Superconducting niobium films produced by means of ultra high vacuum arc, *Czechoslovak J. Phys.* **54 (Suppl. A)**, (2004).
180. Langner, J., Mirowski, R., Sadowski, M.J., et al., Deposition of superconducting niobium films for RF cavities by means of UHV cathodic Arc, *Vacuum* **80**, 1288–1293, (2006).
181. Godeke, A., A review of the properties of Nb_3Sn and their variation with A15 composition, morphology and strain state, *Superconductor Sci. Technol.* **19**, R68–R80, (2006).
182. Brown, I.G., Anders, A., Anders, S., Dickinson, M.R., Ivanov, I.C., MacGill, R.A., Yao, X.Y., and Yu, K.-M., Plasma synthesis of metallic and composite thin films with atomically mixed substrate bonding, *Nucl. Instrum. Meth. Phys. Res. B* **80/81**, 1281–1287, (1993).
183. Piekoszewski, J., Krajewski, A., Prokert, F., Senkara, J., Stanisawski, J., Wali, L., Werner, Z., and Wosiski, W., Brazing of alumina ceramics modified by pulsed plasma beams combined with arc PVD treatment, *Vacuum* **70**, 307–312, (2003).
184. Sasaki, J. and Brown, I.G., Ion spectra of vacuum arc plasma with compound and alloy cathodes, *J. Appl. Phys.* **66**, 5198–5203, (1989).
185. Sasaki, J., Sugiyama, K., Yao, X., and Brown, I., Multiple-species ion beams from titanium-hafnium alloy cathodes in vacuum arc plasmas, *J. Appl. Phys.* **73**, 7184–7187, (1993).
186. Hauert, R., A review of modified DLC coatings for biological applications, *Diam. Rel. Mat.* **12**, 583–589, (2003).
187. Endrino, J.L., Galindo, R.E., Zhang, H., Allen, M., Gago, R., Espinosa, A., Andersson, J., Albella, J.M., and Anders, A., Structure and comparative properties of silver-containing a-C films deposited by two plasma immersion ion implantation techniques, *Surf. Coat. Technol.* **202**, 3675–3682, (2008).
188. Narayan, R.J., Wang, H., and Tiwari, A., Nanostructured DLC-Ag composites for biomedical applications, *Mat. Res. Soc. Symp. Proc.* **750**, Y5.9.1–6, (2003).

189. Kwok, S.C.H., Zhang, W., Wan, G.J., McKenzie, D.R., Bilek, M.M.M., and Chu, P.K., Hemocompatibility and anti-bacterial properties of silver doped diamond-like carbon prepared by pulsed filtered cathodic vacuum arc deposition, *Diam. Rel. Mat.* **16**, 1353–1360, (2007).
190. Anders, A. and MacGill, R.A., Twist filter for the removal of macroparticles from cathodic arc plasmas, *Surf. Coat. Technol.* **133–134**, 96–100, (2000).
191. Gelfandbein, V. and McLean, G.Y., "Implantable device using diamond-like carbon coating," patent US 24220667 (2004).
192. McLean, G.Y. and Gelfandbein, V., "Implantable device using diamond-like carbon coating," patent US 4,071,338 (2004).
193. Wu, Z., Shi, Y., Xie, H., Chen, Y., Zhang, J., Xu, J., and Chen, H., Surface modification of polymers by low temperature plasma techniques, *Surf. Eng.* **11**, 53–56, (1995).
194. Lim, H., Lee, Y., Han, S., Cho, J., and Kim, K.-J., Surface treatment and characterization of PMMA, PHEMA, and PHPMA, *J. Vac. Sci. Technol. A* **19**, 1490–1496, (2001).
195. Wang, J., Huang, N., Pan, C.J., et al., Bacterial repellence from polyethylene terephthalate surface modified by acetylene plasma immersion ion implantation-deposition, *Surf. Coat. Technol.* **186**, 299–304, (2004).
196. Dong, H. and Bell, T., State-of-the-art overview: ion beam surface modification of polymers towards improving tribological properties, *Surf. Coat. Technol.* **111**, 29–40, (1999).
197. Han, S., Lee, Y., Kim, H., Kim, G.-H., Lee, J., Yoon, J.-H., and Kim, G., Polymer surface modification by plasma source ion implantation, *Surf. Coat. Technol.* **93**, 261–264, (1997).
198. Kim, J.S., Hong, M.C., Nah, Y.H., Lee, Y., Han, S., and Lim, H.E., Wetting properties of polystyrene ionomers treated with plasma source ion implantation, *J. Appl. Polymer Sci.* **83**, 2500–2504, (2002).
199. Kostov, K.G., Ueda, M., Tan, I.H., Leite, N.F., Beloto, A.F., and Gomes, G.F., Structural effect of nitrogen plasma-based ion implantation on ultra-high molecular weight polyethylene, *Surf. Coat. Technol.* **186**, 287–290, (2004).
200. McKenzie, D.R., Newton-McGee, K., Ruch, P., Bilek, M.M., and Gan, B.K., Modification of polymers by plasma-based ion implantation for biomedical applications, *Surf. Coat. Technol.* **186**, 239–244, (2004).
201. Clapham, L., Whitton, J.L., Ridgway, M.C., Hauser, N., and Pertravic, M., High dose, heavy ion implantation into metals: The use of a sacrificial carbon surface layer for increased dose retention, *J. Appl. Phys.* **72**, 4014–4019, (1992).
202. Anders, A., Anders, S., Brown, I.G., and Yu, K.M., "In-situ deposition of sacrificial layers during ion implantation: concept and simulation," in *Ion Beam Modification of Materials*, Williams, J.S., Elliman, R.G., and Ridgway, M. C., (Eds.). pp.1089–1092, Elsevier, Amsterdam, (1996).
203. Oates, T.W.H., McKenzie, D.R., and Bilek, M.M.M., Plasma immersion ion implantation using polymeric substrates with a sacrificial conductive surface layer, *Surf. Coat. Technol.* **156**, 332–337, (2002).
204. Hong, J., Andersson, J., Ekdahl, K.N., Elgue, G., Axén, N., Larsson, R., and Nilsson, B., Titanium is a highly thrombogenic biomaterial: Possible implications for osteogenesis, *Thrombosis and Haemostasis* **82**, 58–64, (1999).
205. Thorwart, G., Mändl, S., and Rauschenbach, B., Rutile formation and oxygen diffusion in oxygen PIII-treated titanium, *Surf. Coat. Technol.* **136**, 236–240, (2001).

206. Mändl, S., Sader, R., Thorwart, G., Krause, D., Zeilhofer, H.-F., Horch, H.H., and Rauschenbach, B., Investigation on plasma immersion ion implantation treated medical implants, *Biomolecular Eng*. **19**, 129–132, (2002).
207. Thorwarth, G., Mändl, S., and Rauschenbach, B., *Surf. Coat. Technol*. **128–129**, 116–120, (2000).
208. Wan, G.J., Huang, N., Leng, Y.X., Yang, P., Chen, J.Y., Wang, J., and Sun, H., TiN and Ti–O/TiN films fabricated by PIII-D for enhancement of corrosion and wear resistance of Ti–6Al–4 V, *Surf. Coat. Technol*. **186**, 136–140, (2004).
209. Tsyganov, I., Maitz, M.F., Wieser, E., Prokert, F., Richter, E., and Rogozin, A., Structure and properties of titanium oxide layers prepared by metal plasma immersion ion implantation and deposition, *Surf. Coat. Technol*. **174–175**, 591–596, (2003).
210. Wisbey, A., Gregson, P.J., Peter, L.M., and Tuke M., Effect of surface treatment on the dissolution of titanium-based implant materials, *Biomaterials* **12**, 470–473, (1991).
211. Leng, Y.X., Yang, P., Chen, J.Y., Sun, H., Wang, J., Wang, G.J., Huang, N., Tian, X.B., and Chu, P.K., Fabrication of Ti-O/Ti-N duplex coatings on biomedical titanium alloys by metal plasma immersion ion implantation and reactive plasma nitriding/oxidation, *Surf. Coat. Technol*. **138**, 296–300, (2001).
212. Leng, Y.X., Chen, J.Y., Wang, J., Wan, G.J., Sun, H., Yang, P., and Huang, N., Comparative properties of titanium oxide biomaterials grown by pulsed vacuum arc plasma deposition and by unbalanced magnetron sputtering, *Surf. Coat. Technol*. **201**, 157–163, (2006).
213. Mändl, S., Thorwart, G., and Rauschenbach, B., Textured titanium oxide films produced by vacuum arc deposition, *Surf. Coat. Technol*. **133–134**, 283–288, (2000).
214. Mändl, S., Attenberger, W., Stritzker, B., and Rauschenbach, B., Disorder formation in rutile during ion assisted deposition, *Surf. Coat. Technol*. **196**, 76–80, (2005).
215. Anders, A., Oks, E.M., Yushkov, G.Y., Savkin, K.P., Brown, Y., and Nikolaev, A.G., Determination of the specific ion erosion of the vacuum arc cathode by measuring the total ion current from the discharge plasma, *Technical Physics* **51**, 1311–1315, (2006).
216. Brown, I.G. and Shiraishi, H., Cathode erosion rates in vacuum arc discharges, *IEEE Trans. Plasma Sci*. **18**, 170–171, (1990).
217. Daalder, J.E., Erosion and the origin of charged and neutral species in vacuum arcs, *J. Phys. D: Appl. Phys*. **8**, 1647–1659, (1975).
218. Daalder, J.E., Components of cathode erosion in vacuum arcs, *J. Phys. D: Appl. Phys*. **9**, 2379–2395, (1976).
219. Guile, A.E. and Jüttner, B., Basic erosion processes of oxidized and clean metal cathodes by electric arcs, *IEEE Trans. Plasma Sci*. **8**, 259–269, (1980).
220. Sethumraman, S.K., Chatterton, P.A., and Barrault, M.R., A study of the erosion rate of vacuum arcs in a transverse magnetic field, *J. Nucl. Mat*. **111/112**, 510–516, (1982).
221. Tuma, D.T., Chen, C.L., and Davis, D.K., Erosion products from the cathode spot region of a copper vacuum arc, *J. Appl. Phys*. **49**, 3821–3831, (1978).
222. Zhou, X. and Heberlein, J., An experimental investigation of factors affecting arc-cathode erosion, *J. Phys. D-Appl. Phys*. **31**, 2577–2590, (1998).

223. Zimmer, O., Vetter, J., Rackwitz, N., and Siemroth, P., Calculation and measurement of the time dependent erosion rate of electromagnetic steered rectangular arc cathodes, *Surf. Coat. Technol.* **146**, 195–200, (2001).
224. Anders, A. and Yushkov, G.Y., Ion flux from vacuum arc cathode spots in the absence and presence of magnetic fields, *J. Appl. Phys.* **91**, 4824–4832, (2002).
225. Sugimoto, M. and Takeda, K., Surface variation caused by vacuum arc cleaning of organic contaminant, *Thin Solid Films* **506–507**, 337–341, (2006).
226. Bergman, C., "Arc plasma physical vapor deposition," 28th Annual SVC Technical Conference, Philadelphia, PA, 175–191, (1985).
227. McIntyre, D.C., Chen, G.G., Sprague, E.C., Humenik, D.B., and Kubinski, J.A., "Arc-deposited, pearl nickel finishes for interior trim applications in automobiles," 44th Annual Technical Conference, Society of Vacuum Coaters, Philadelphia, 51–56, (2001).
228. Münz, W.-D., Schulze, D., and Hauzer, F.J.M., A new method for hard coatings – ABS (arc bond sputtering), *Surf. Coat. Technol.* **50**, 169–178, (1992).
229. Hovsepian, P.E., Lewis, D.B., Munz, W.D., Lyon, S.B., and Tomlinson, M., Combined cathodic arc/unbalanced magnetron grown CrN/NbN superlattice coatings for corrosion resistant applications, *Surf. Coat. Technol.* **120–121**, 535–541, (1999).
230. Münz, W.-D., Lewis, D.B., Hovsepian, P.E., Schönjahn, C., Ehiasarian, A., and Smith, I.J., Industrial scale manufactured superlattice hard PVD coatings, *Surf. Eng.* **17**, 15–27, (2001).
231. Donohue, L.A., Munz, W.D., Lewis, D.B., Cawley, J., Hurkmans, T., Trinh, T., Petrov, I., and Greene, I.E., Large-scale fabrication of hard superlattice thin films by combined steered arc evaporation and unbalanced magnetron sputtering, *Surf. Coat. Technol.* **93**, 69–87, (1997).
232. Hurkmans, T., Hauzer, F., Buil, B., Engel, K., and Tietema, R., A new large volume PVD coating system using advanced controlled arc and combined arc/unbalanced magnetron (ABS(TM)) deposition techniques, *Surf. Coat. Technol.* **92**, 62–68, (1997).
233. Wang, H.W., Stack, M.M., Hovsepian, P., and Munz, W.D., Macroparticle induced corrosion for arc bond sputtering CrN/NbN superlattice coatings, *J. Mat. Sci. Lett.* **20**, 1995–1997, (2001).
234. Lewis, D.B., Creasey, S.J., Wustefeld, C., Ehiasarian, A.P., and Hovsepian, P.E., The role of the growth defects on the corrosion resistance of CrN/NbN superlattice coatings deposited at low temperatures, *Thin Solid Films* **503**, 143–148, (2006).
235. Ehiasarian, A.P., Anders, A., and Petrov, I., Combined filtered cathodic arc etching pretreatment–magnetron sputter deposition of highly adherent CrN films, *J. Vac. Sci. Technol. A* **25**, 543–550, (2007).

A

Plasmas and Sheaths: A Primer

Abstract A brief summary is given on plasmas and sheaths, the latter being the boundary of a plasma to any solid wall. The concepts and properties of plasmas and sheaths are important to the understanding of arcs and they are also of value to other fields, therefore an introductory summary is provided here for general reference.

It is of course impossible to provide an adequate introduction to plasmas and sheaths – this would require a separate book! There are some excellent texts written on the subject, and therefore it is appropriate to simply summarize a few selected aspects of plasmas and sheath.

While there are plenty of texts on plasmas, sheaths are usually not considered with comparable weight. This seems odd since in plasma processing, and many other applications of plasma technology, the surface of a solid is strictly speaking exposed to a sheath, and not to a plasma! Of course, the plasma greatly influences the sheath properties, yet, in fact, the flux of particles and the energy distribution functions of particles arriving on the surfaces are greatly altered in the sheath and they do not resemble the flux and energy distribution functions in the plasma. Therefore, a few properties of plasmas and sheaths are compiled, with about equal weight given to both subjects.

A.1 Plasmas

A plasma can be roughly defined as an ensemble of particles with long-range interaction, such as Coulomb interaction between charged particles. Many macroscopic properties are determined by collective interaction of particles, as opposed to binary collisions. The ensemble is quasi-neutral,

$$\sum_{\alpha} Q_{\alpha} n_{\alpha} - n_e - \sum_{\beta} Q_{\beta} n_{\beta} = 0, \tag{A.1}$$

where the indices α and β refer to the kinds of positive and negative ions present, whose charge state number and density are denoted by Q and n, respectively. In some cases, only singly charged, positive ions are present, and one can simplify (A.1) to

$$n_e = n_i. \tag{A.2}$$

The long-range Coulomb potential of a charged particle is shielded in a plasma by the presence of neighboring charged particles. The characteristic shielding length is the electron Debye length:

$$\lambda_{De} = \left(\frac{\varepsilon_0 k T_e}{n_e e^2} \right)^{1/2}. \tag{A.3}$$

The symbols in Eq. (A.3) have their usual meaning, namely $\varepsilon_0 \approx 8.854 \times 10^{-12}$ F/m is the permittivity of free space, $k \approx 1.38 \times 10^{-23}$ J/K is the Boltzmann constant, and $e \approx 1.60 \times 10^{-19}$ C is the elementary charge. To qualify as plasma, the size of the ensemble of charged particles has to be much larger than the Debye length, which is almost always the case.

The condition of quasi-neutrality, Eq. (A.1) or Eq. (A.2) , is not valid on a length scale of order λ_{De} and smaller. On these small scales, very large electric fields can exist and they lead to changes of the trajectories of charged particles. Collisions are approximated as binary collisions, although during *Coulomb collisions* the charged particles interact via Coulomb interaction with more than one charged particle. The binary collision approximation and the associated concept of a mean free path are actually abstract theoretical constructs designed to use the concepts and terminology of gas kinetic theory in plasma physics.

A momentary local imbalance of positive and negative charges will cause a large electric field. The field can be calculated by the Poisson equation, which is the third in the set of Maxwell's equations, which can be written in macroscopic form as

$$\nabla \times \mathbf{E} = -\mu_0 \frac{\partial \mathbf{H}}{\partial t}, \tag{A.4}$$

$$\nabla \times \mathbf{H} = \varepsilon_0 \frac{\partial \mathbf{E}}{\partial t} + \mathbf{J}, \tag{A.5}$$

$$\varepsilon_0 \, \nabla \cdot \mathbf{E} = \rho, \tag{A.6}$$

$$\mu_0 \, \nabla \cdot \mathbf{H} = 0, \tag{A.7}$$

where $\mathbf{E}(\mathbf{r}, t)$ and $\mathbf{H}(\mathbf{r}, t)$ are the space- and time-dependent electric and magnetic field vectors, and $\mu_0 = 4\pi \times 10^{-7}$ H/m is the permeability of free space. The net charge density $\rho = n_{\mathrm{i}} - n_{\mathrm{e}}$ and the current density $\mathbf{J}(\mathbf{r}, t)$ are the sources of electric and magnetic fields, respectively. Net charge density and current are not independent but related by the continuity equation

$$\frac{\partial \rho}{\partial t} + \nabla \cdot \mathbf{J} = 0. \tag{A.8}$$

Because electrons are much lighter than ions, they respond much faster to a change in the electric field caused by the momentary imbalance of charge. The electric force will drive them back to their equilibrium positions; however, they will overshoot and create a new local net charge, thus leading to oscillatory motion characterized by the electron plasma frequency:

$$\omega_{pl,e} = \left(\frac{n_e e^2}{\varepsilon_0 m_e}\right)^{1/2}. \tag{A.9}$$

Electrons will do many oscillations on the timescale of macroscopic changes.

While oscillating, the electron may encounter a collision with another electron, ion, or neutral atom or molecule. In general, the probability of a collision depends on the relative velocity of the colliding particles, u, the density of target particles (i.e., particles to be hit), n_β, and the cross-section of interaction, $\sigma_{\alpha\beta}(u)$. Collision theory [1, 2, 3] uses the concept of mean free path, λ_α, the mean distance between collisions of particles of type α with other particles of type β :

$$\lambda_\alpha = \left(\sum_\beta n_\beta \sigma_{\alpha\beta}\right)^{-1}. \tag{A.10}$$

The mean time between collisions is

$$\tau_\alpha = \frac{\lambda_\alpha}{u}, \tag{A.11}$$

and the frequency of collisions is the inverse, i.e.,

$$\tau_\alpha^{-1} = \frac{u}{\lambda_\alpha} = \sum_\beta n_\beta \sigma_{\alpha\beta} u. \tag{A.12}$$

When averaged over all velocities of the (usual Maxwellian) distribution one obtains the collision frequency

$$\nu_\alpha = \sum_\beta n_\beta \langle \sigma_{\alpha\beta} u \rangle. \tag{A.13}$$

where the averaging is performed as

$$\langle \sigma_{\alpha\beta} u \rangle = \int_0^\infty \sigma_{\alpha\beta}(u) u \; f(u) du; \tag{A.14}$$

$f_\alpha(u)$ is the velocity distribution function of particles of type α. Using the cross-section of Debye-shielded Coulomb interaction between charged particles, Spitzer [4] calculated the momentum transfer collision frequencies for electrons and ions as

$$\nu_{ab} \approx C \frac{Q_a^2 Q_b^2}{m_a^{1/2} (kT_a)^{3/2}} n_b, \tag{A.15}$$

where the indices a and b stand for any combination of electrons and ions, Q is the charge state number (for ions we have $Q_\mathrm{i} = 1, 2, 3, \ldots$ and for electrons $Q_\mathrm{e}^2 = 1$); the constant $C = \frac{e^4 \ln \Lambda}{12\pi^{3/2}\varepsilon_0^2} \approx 1.3 \times 10^{-54} (\mathrm{A\ s\ V\ m})^2$ contains the Coulomb logarithm $\ln \Lambda \approx 10$, a quantity related to shielding of the interaction potential.

Collisions can be elastic or inelastic. Elastic collisions are those where the total kinetic energy of the colliding particles is conserved, while inelastic collisions are associated with energy transfer to "inner" degrees of freedom, e.g., ionization and excitation. The cross-section for these collisions can be vastly different, and therefore one has to distinguish between mean free paths and collision frequencies specific to the types of collision processes.

Additional effects occur in the presence of a magnetic field. Electrons execute a gyration motion with the gyration frequency

$$\omega_e = eB/m_e, \tag{A.16}$$

where B is the magnetic inductance (SI unit is Tesla, but often the old unit Gauss is used, 1 Tesla = 10^4 Gauss). An electron having a velocity component $u_{\mathrm{e}\perp}$ perpendicular to **B** will have a gyration radius

$$r_{g,e} = \frac{u_{e\perp}}{\omega_e} = \frac{m_e u_{e\perp}}{eB}. \tag{A.17}$$

Ion motion in magnetic fields follows the same laws but the ion mass and velocity have to be used. In most processing plasmas with external magnetic fields, the field is not strong enough to make the ion gyration radius small compared to the system dimension. In these cases, one speaks of plasmas with magnetized electrons but non-magnetized ions.

Even for plasma where only electrons are magnetized, not only the electrons tend to move along the magnetic field lines but the ions, too, which is due to the electron–ion coupling via an electric field. Therefore, plasma transport is generally a magnetic and electric phenomenon. This is an example of collective particle behavior, which distinguishes the theories of plasmas and (neutral) gases.

A.2 Sheaths

While the plasma bulk is quasi-neutral, its boundary layer is not. Boundary layers or *sheaths* appear where a plasma meets a solid such as a chamber wall, electrode, substrate, or probe. The structure and thickness of a sheath depends on the potential difference between the solid surface and the plasma potential. If the surface is electrically isolated (i.e., isolated ("floating") metal or insulator), the net current to the surface must be zero. A space charge will quickly establish

itself adjacent to the surface in such a way as to balance (cancel) the flow of positive and negative charges. This space-charge layer is called the sheath. According to the Poisson equation (A.6), space charge causes an electric field, and it is this field that balances the flow of positive and negative charges. If the surface is not floating, a different space-charge distribution is established which provides an electric field that adjusts the net electric current whose amplitude is given by the current source.

Sheaths occur practically on all surfaces facing plasma (i.e., the surface actually "sees" the sheath, and not the plasma). Sheaths are of critical importance for the operation of discharges; they control the flow of ions and electrons to the surface.

The imposed potential to a substrate is called a *bias*. From a physics point of view it should be referenced to the plasma potential. The plasma potential, however, is often not exactly known, and therefore one commonly chooses the ground (earth) potential as the reference potential. This practical approach is acceptable in many situations, especially when the arc anode is grounded and when the applied bias is large compared to the electron temperature. The deviation of the plasma potential from the grounded anode potential is generally a few times the electron temperature (divided by e). For example, assuming a typical electron temperature of 3 eV, the plasma potential is most likely about 10–15 V positive with respect to ground.

The electron current from the plasma is determined by thermal random motion

$$j_e = \frac{1}{4} e\, n_{es} \overline{u_e} \exp\left(\frac{eV_0}{kT_e}\right), \tag{A.18}$$

where $V_0 < 0$ is the potential of the surface with respect to the plasma potential, n_{es} is the electron density at the sheath edge, and

$$\overline{u_e} = \left(\frac{8kT_e}{\pi m_e}\right)^{1/2} \tag{A.19}$$

is the electron velocity averaged over a Maxwell distribution. We see that for a negative bias the electrons are repelled and the flow is exponentially reduced. For most bias situations, the sheath can be considered free of plasma electrons. There may be some secondary electrons crossing the sheath, coming from the substrate surface, but even then the density of electrons in the sheath is negligibly small.

The ion current is

$$j_i = \overline{Q}\, e\, n_{is} u_{is}, \tag{A.20}$$

where $\overline{Q}$ is the average ion charge state. The velocity of ions coming from the plasma to the sheath edge, u_{is}, is known as the Bohm velocity [5]:

$$u_{is} = u_{Bohm} = \left(\frac{kT_e}{m_i}\right)^{1/2}, \tag{A.21}$$

which is greater than the random velocity due to acceleration in the presheath, i.e., the quasi-neutral zone between undisturbed plasma and the sheath.[1]

From the floating condition

$$j_e = j_i, \tag{A.22}$$

one obtains the floating potential of the wall with respect to the plasma potential:

$$V_{float} = -\frac{kT_e}{2e}\ln\left(\frac{m_i}{2\pi m_e}\right). \tag{A.23}$$

Now we consider the situation when a wall is biased and a net current of charged particles flows to the wall. Assuming that the particle energy outside the sheath is much smaller than the potential drop in the sheath, Child [8] and later Langmuir [9] solved Poisson's equation and the continuity equation finding that space charge limits the current. Considering a negative wall potential, the Child law for space-charge-limited ion current can be written as [10]

$$j_i = \frac{4}{9}\varepsilon_0\left(\frac{2e}{m_i}\right)^{1/2}\frac{V_0^{3/2}}{s^2}, \tag{A.24}$$

where V_0 is the absolute value of the sheath potential (voltage drop across the sheath). A common interpretation (and application) of Child's law is for vacuum diodes and ion extraction systems, where s is the *fixed* distance between positive and negative electrode, and j_i represents the maximum ion current possible.

More relevant for surface engineering is the situation when a substrate is biased negatively with respect to the plasma potential and the ion current is determined by the supply from the plasma, Eq. (A.20). In this situation the sheath thickness, s, is not fixed but *self-adjusting*. Given enough time, the sheath becomes a *Child law sheath* with the thickness

$$s_{Child} = \frac{\sqrt{2}}{3}\lambda_{De}\left(\frac{2eV_0}{kT_e}\right)^{3/4}, \tag{A.25}$$

where the Debye length λ_{De} was already introduced by Eq. (A.3). The time necessary for the Child sheath to form is large compared to the ion plasma frequency, which can be defined in analogy to (A.9) as

$$\omega_{pl,i} = \left(\frac{n_i Q^2 e^2}{\varepsilon_0 m_i}\right)^{1/2}. \tag{A.26}$$

[1] The mathematically exact description of the sheath and presheath transition is rather involved and has stirred some serious considerations [6, 7] that are beyond this introduction.

References

1. McDaniel, E.W., *Collision Phenomena in Ionized Gases*. Wiley, New York, (1964).
2. Johnson, J.E., *Introduction to Atomic and Molecular Collisions*. Plenum Press, New York, (1982).
3. Chen, F.F., *Plasma Physics and Controlled Fusion*. Plenum Press, New York, (1984).
4. Spitzer Jr., L., *Physics of Fully Ionized Gases*, preprint of the 2nd revised edition, originally published by Wiley, 1962 ed. Dover, New York, (1990).
5. Bohm, D., "Minimum ionic kinetic energy for a stable sheath," in *The Characteristics of Electrical Discharges in Magnetic Fields*, Guthrie, A. and Wakerling, R.K., (Eds.). pp. 77–86, McGraw-Hill, New York, (1949).
6. Riemann, K.-U., The Bohm criterion and sheath formation, *J. Phys. D: Appl. Phys.* **24**, 493–518, (1991).
7. Sternberg, N. and Godyak, V., The Bohm plasma-sheath model and the Bohm criterion revisited, *IEEE Trans. Plasma Sci.* **35**, 1341–1349, (2007).
8. Child, C.D., Discharge from hot CaO, *Phys. Rev.* **32**, 492–511, (1911).
9. Langmuir, I., The effect of space charge and residual gases on the thermionic current in high vacuum, *Phys. Rev. (Ser. II)* **2**, 450–486, (1913).
10. Forrester, A.T., *Large Ion Beams*. Wiley, New York, (1988).

B

Periodic Tables of Cathode and Arc Plasma Data

Abstract Data on cathode materials as well as on arc plasmas are provided in the format of Periodic Tables. Those data would appear just as numbers and values, without much physical reasoning, if sorted by alphabet of the material's name or by their atomic number. Therefore, these data are presented in the physically more meaningful format of Periodic Tables, which give a clear indication of the grouping of properties, interestingly both for the (usually solid) cathode materials and for the plasma.

Since their introduction in 1868 by the Russian Dmitri Ivanovich Mendeleev (1834–1907), Periodic Tables are used to arrange the chemical elements illustrating their recurring ("periodic") trends in the properties. Periodic Tables are widely used in chemistry and occasionally in crystallography and other branches of physics. Here, the form of Periodic Tables is selected to emphasize the periodic properties of the solid cathodes as well as the periodic properties of cathodic arc *plasmas*. In doing so, the concept of the Cohesive Energy Rule is illustrated and expanded because Periodic Tables have the power of approximately predicting properties not yet measured. For example, in a first presentation of a cathodic arc plasma Periodic Table [1], the approximate charge state distributions for cathode materials were predicted that had not yet been measured (like for boron), and such predictions have been confirmed since.

In the following, a set of Periodic Tables is given, mostly to serve as reference tables, but also to show the regularity that lies below the otherwise erratically appearing material-dependent plasma properties. The first tables focus on the elements used as cathode materials, and the next display plasma properties.

The tables contain the following data:

B1
- Atomic mass
- Melting temperature
- Boiling temperature
- Temperature at which the vapor pressure exceeds 1 Pa
- Electrical resistivity

B2
- Work function
- Richardson constant for thermionic emission
- Density
- Thermal conductivity
- Heat capacity

B3
- Ionization energies of the elements

B4
- Cumulative ionization energy of ions

B5 Experimental results:
- Charge state distribution for vacuum arcs

B6 Saha freezing model:
- Charge state distribution for vacuum arcs
- Heavy particle density at charge state freezing
- Electron density at charge state freezing
- Temperature at charge state freezing

B7 Experimental results:
- Charge state distribution for plasma in transition between vacuum sparks and vacuum arcs

B8 Cohesive energy and experimental data:
- Cohesive energy
- Average arc burning voltage for 300 A vacuum arcs
- Mean ion charge state
- Most-likely ion velocity (plasma drift)
- Most-likely kinetic ion energy

Table B.1. Selected physical and chemical properties of the elements, with emphasis on properties related to solids used in cathodic arc plasma deposition, see the KEY for arrangement: atomic number; atomic mass (most abundant isotope for radioactive elements); melting temperature (K) at standard pressure; boiling temperature (K) at standard pressure; temperature at which the vapor pressure exceeds 1 Pa (7.5 mTorr); electrical resistivity (nΩ m) at 298 K. (From the data compilation of [2])

1 H 1.008 14 20 – –								
		KEY						
3 Li 6.941 454 1615 797 94	**4 Be** 9.012 1560 2742 1462 40	**Atomic number** Atomic mass Melting temperature (K) Boiling temperature (K) Temperature for 1 Pa vapor pressure (K) Resistivity (nΩ m)			**22 Ti** 47.88 1941 3560 1982 400	**Element symbol**		
11 Na 22.99 370.9 1156 554 47	**12 Mg** 24.31 923 1363 701 44							
19 K 39.10 336.5 1032 473 70	**20 Ca** 40.08 1115 1757 864 34	**21 Sc** 44.96 1814 3103 1645 550	**22 Ti** 47.88 1941 3560 1982 400	**23 V** 50.94 2183 3680 2101 200	**24 Cr** 52.00 2180 2944 1656 127	**25 Mn** 54.94 1519 2334 1228 1600	**26 Fe** 55.85 1811 3134 1728 97	**27 Co** 58.93 1768 3200 1790 60
37 Rb 85.47 312.5 961 433.5 120	**38 Sr** 87.62 1050 1655 796 130	**39 Y** 88.91 1799 3609 1883 560	**40 Zr** 91.22 2128 4682 2639 420	**41 Nb** 92.91 2750 5017 2942 150	**42 Mo** 95.94 2896 4912 2742 50	**43 Tc** (98) 2430 4538 2727 200	**44 Ru** 101.1 2607 4423 2588 71	**45 Rh** 102.9 22.73 3968 2288 43
55 Cs 132.9 301.6 944 417.6 200	**56 Ba** 137.3 1000 2143 911 350	**57 La*** 138.9 1193 3743 2005 610	**72 Hf** 178.5 2506 4876 2689 300	**73 Ta** 180.9 3290 5731 3297 130	**74 W** 183.9 3695 5828 3477 50	**75 Re** 186.2 3459 5869 3303 180	**76 Os** 190.2 3306 5285 3160 81	**77 Ir** 192.2 2739 4701 2713 47
87 Fr (223) – – 404 –	**88 Ra** (226) 973 2010 819 1000	**89 Ac**** (~227) 1323 3573 – –						
		* Lanthanides	**58 Ce** 140.1 1068 3633 1992 740	**59 Pr** 140.9 1208 3563 1771 700	**60 Nd** 144.2 1297 3373 1595 640	**61 Pm** (147) 1373 3273 – 750	**62 Sm** 150.4 1345 2076 1001 940	**63 Eu** 152.0 1099 1800 863 900
		** Actinides	**90 Th** 232.0 2115 5093 2633 150	**91 Pa** (231) 1841 – – 180	**92 U** (238) 1405 4200 2325 280	**93 Np** (237) 910 4273 – 1200	**94 Pu** (242) 912.5 3503 1756 1500	**95 Am** (243) 1449 2880 – –

								2 He 4.003 0.9 4.2 – –
			5 B 10.81 2349 4200 2348 $>10^{13}$	**6 C** 12.01 3800 4300 (2670) $\sim10^{3}$	**7 N** 14.01 63.05 77.36 – –	**8 O** 16.00 54.8 90.2 – –	**9 F** 19.00 53.53 85.03 – –	**10 Ne** 20.18 24.56 27.07 – –
			13 Al 26.98 933.5 2792 1482 26.5	**14 Si** 28.09 1687 3173 1908 $\sim10^{6}$	**15 P** 30.97 317.3 550 (279) 100	**16 S** 32.07 388.4 717.9 374 $>10^{24}$	**17 Cl** 35.45 171.6 239.1 – –	**18 Ar** 39.95 83.8 87.3 – –
28 Ni 58.69 1728 3186 1783 70	**29 Cu** 63.55 1357.8 3200 1509 17	**30 Zn** 65.39 692.7 1180 610 59	**31 Ga** 69.72 302.9 2477 1310 140	**32 Ge** 72.59 1211.4 3093 1644 $\sim5x10^{5}$	**33 As** 74.92 1090 887 553 300	**34 Se** 78.96 494 958 500 $>10^{6}$	**35 Br** 79.90 256.8 332 – –	**36 Kr** 83.80 115.8 119.9 – –
46 Pd 106.4 1828 3236 1721 100	**47 Ag** 107.9 1235 2435 1283 16	**48 Cd** 112.4 594 1040 530 70	**49 In** 114.8 429.75 2345 1196 80	**50 Sn** 118.7 505.1 2875 1497 110	**51 Sb** 121.8 903.8 1860 807 400	**53 Te** 127.6 722.7 1261 (500) $\sim10^{5}$	**53 I** 126.9 386.9 457.4 – –	**54 Xe** 131.3 161.4 165.1 – –
78 Pt 195.1 2041 4098 2330 106	**79 Au** 197.0 1337 3129 1646 22	**80 Hg** 200.5 234.3 629.9 315 960	**81 Tl** 204.4 577 1746 882 150	**82 Pb** 207.2 600.6 2022 978 210	**83 Bi** 209.0 544.4 1837 941 1300	**84 Po** (210) 527 1235 (400) 430	**85 At** (210) 575 – – –	**86 Rn** (222) 202 211.3 – –

64 Gd 157.3 1585 3523 1836 1300	**65 Tb** 158.9 1629 3503 1789 1200	**66 Dy** 162.5 1680 2840 1378 910	**67 Ho** 164.9 1734 2993 1432 940	**68 Er** 167.3 1770 3141 1504 860	**69 Tm** 168.9 1818 2223 1117 700	**70 Yb** 173.0 1097 1469 736 280	**71 Lu** 175.0 1925 3675 1906 560

Table B.2. Electron emission properties as determined by work function and Richardson constant (cf. Section 3.2.1); the work function depends on the grain orientation to the surface; the approximate data given here refer to polycrystalline films; data for carbon refer to graphite; density, thermal conductivity, and specific heat capacity at 25°C. (Data taken from [2, 3, 4, 5, 6])

1 H								
					KEY			
3 Li 2.4–2.93 – 535 85 3582	**4 Be** 4.98 300 1848 190 1825				**22 Ti** 4.3–4.5 60 4507 22 523			
11 Na 2.2–2.36 – 968 140 1228	**12 Mg** 3.66 – 1738 160 1023							
19 K 2.2–2.3 – 856 100 757	**20 Ca** 2.9 – 1550 200 647	**21 Sc** 3.5 – 2985 16 568	**22 Ti** 4.3–4.5 60 4507 22 523	**23 V** 4.3 – 6110 31 489	**24 Cr** 4.5 – 7140 94 449	**25 Mn** 4.1 – 7470 7.8 479	**26 Fe** 4.5–4.7 26 7874 80 449	**27 Co** 5.0 41 8900 100 421
37 Rb 2.1–2.26 – 1532 58 363	**38 Sr** 2.6–2.7 – 2630 35 301	**39 Y** 3.1 100 4472 17 298	**40 Zr** 3.1–4.0 330 6511 23 278	**41 Nb** 4.1–4.2 57–120 8570 54 265	**42 Mo** 4.15 51–55 10280 139 251	**43 Tc** – – 11500 51 –	**44 Ru** 4.71 – 12370 120 238	**45 Rh** 4.98 33 12450 150 243
55 Cs 1.81–2.1 160–162 1879 36 242	**56 Ba** 2.1–2.5 60 3510 18 204	**57 La*** 3.5 – 6146 13 195	**72 Hf** 3.6–3.9 14.5–22 13310 23 144	**73 Ta** 4.1–4.3 55–120 16650 57 140	**74 W** 4.55 60–80 19250 170 132	**75 Re** 4.72 720 21020 48 137	**76 Os** 5.93 10^5 22610 88 130	**77 Ir** 5.3–5.5 120 22650 150 131
87 Fr – – – – –	**88 Ra** – – 5000 19 94	**89 Ac**** – – 10070 12 120						
		* Lanthanides	**58 Ce** 2.9 – 6689 11 192	**59 Pr** – – 6640 13 193	**60 Nd** 3.2 – 6800 17 190	**61 Pm** – – 7264 16 –	**62 Sm** 2.7 – 7353 13 197	**63 Eu** 2.5 – 5244 14 182
		** Actinides	**90 Th** 2.7–3.4 60–70 11724 54 113	**91 Pa** – – 15370 47 –	**92 U** 3.63 – 19050 27 116	**93 Np** – – 20450 6 –	**94 Pu** – – 19816 6 –	**95 Am** – – – 10 –

								2 He
			5 B 4.4 – 1848 27 1026	**6 C** 4.4 30–48 2267 13 709	**7 N** – – – – –	**8 O** – – – – –	**9 F** – – – – –	**10 Ne** – – – – –
			13 Al 4.2 – 2700 237 897	**14 Si** 4.8 – 2330 148 705	**15 P** – – – – –	**16 S** – – – – –	**17 Cl** – – – – –	**18 Ar** – – – – –
28 Ni 4.1–4.6 28–30 8908 91 444	**29 Cu** 4.5–4.6 60–120 8920 401 385	**30 Zn** 3.6 – 7140 116 388	**31 Ga** 4.32 – 5904 41 371	**32 Ge** 5.0 – 5323 60 320	**33 As** – – 5727 50 329	**34 Se** – – 4819 20 321	**35 Br** – – – – –	**36 Kr** – – – – –
46 Pd 5.22 60 12023 72 246	**47 Ag** 4.6 – 10490 430 235	**48 Cd** 4.08 – 8650 97 232	**49 In** 4.09 – 7310 82 233	**50 Sn** 4.42 – 7310 67 228	**51 Sb** 4.55 – 6697 24 207	**53 Te** – – 6240 3 202	**53 I** – – – – –	**54 Xe** – – – – –
78 Pt 5.4–5.65 32–170 21090 72 133	**79 Au** 5.3–5.4 – 19300 320 129	**80 Hg** 4.8–5.3 – 13534 8.3 140	**81 Tl** – – 11850 46 129	**82 Pb** 4.25 – 11340 35 129	**83 Bi** 4.34 – 9780 8 122	**84 Po** – – – – –	**85 At** – – – – –	**86 Rn** – – – – –

64 Gd 2.9 – 7901 11 236	**65 Tb** – – 8219 11 182	**66 Dy** – – 8551 11 170	**67 Ho** – – 8795 16 165	**68 Er** – – 9066 14 168	**69 Tm** – – 9321 17 160	**70 Yb** – – 6570 35 155	**71 Lu** 3.3 – 9841 16 154

Table B.3. Ionization energies (eV) of the elements. (Data from [2] (experiment), and if not available, from [7] (calculation))

1 H 13.60 – – – –								
3 Li 5.39 75.64 122.4 – –	**4 Be** 9.32 18.21 153.9 217.7 –							
11 Na 5.14 47.29 71.62 98.91 138.4	**12 Mg** 7.65 15.04 80.14 109.3 141.3							
19 K 4.34 31.63 45.81 60.91 82.66	**20 Ca** 6.11 11.87 50.91 67.27 84.50	**21 Sc** 6.56 12.80 24.76 73.49 91.65	**22 Ti** 6.83 13.76 27.49 43.27 99.30	**23 V** 6.75 14.66 29.31 46.71 65.28	**24 Cr** 6.77 16.49 30.96 49.16 69.46	**25 Mn** 7.43 15.64 33.67 51.20 72.40	**26 Fe** 7.90 16.19 30.65 54.80 75.00	**27 Co** 7.88 17.08 33.50 51.30 79.50
37 Rb 4.18 27.28 40.00 52.60 71.00	**38 Sr** 5.69 11.03 42.89 57.00 71.60	**39 Y** 6.22 12.24 20.52 60.60 77.00	**40 Zr** 6.63 13.13 22.99 34.34 80.35	**41 Nb** 6.76 14.32 25.04 38.30 50.55	**42 Mo** 7.09 16.16 27.13 46.40 54.49	**43 Tc** 7.28 15.26 29.54 42.22 57.87	**44 Ru** 7.36 16.76 28.47 49.90 66.89	**45 Rh** 7.46 18.08 31.06 53.52 70.90
55 Cs 3.89 23.16 35.25 48.09 60.93	**56 Ba** 5.21 10.00 34.45 48.40 62.35	**57 La*** 5.58 11.06 19.18 49.95 61.60	**72 Hf** 6.82 14.90 23.30 33.33 67.82	**73 Ta** 7.89 14.47 23.49 36.32 49.14	**74 W** 7.98 15.08 25.43 39.29 53.15	**75 Re** 7.88 15.73 25.89 41.49 56.33	**76 Os** 8.70 16.34 27.71 42.70 59.29	**77 Ir** 9.10 16.91 29.50 45.33 61.16
87 Fr 3.61 20.02 31.63 43.25 54.87	**88 Ra** 5.28 10.15 30.97 43.49 56.02	**89 Ac**** 5.17 12.10 16.93 43.36 56.66						
		* Lanthanides	**58 Ce** 5.54 10.85 20.20 36.76 65.55	**59 Pr** 5.46 10.55 21.62 38.98 57.53	**60 Nd** 5.53 10.73 22.10 40.40 68.53	**61 Pm** 5.55 10.90 22.30 41.10 69.75	**62 Sm** 5.64 11.07 23.40 41.40 70.93	**63 Eu** 5.67 11.24 24.92 24.92 42.70
		** Actinides	**90 Th** 6.08 11.50 20.00 28.80 57.22	**91 Pa** 5.89 11.46 17.75 28.91 46.69	**92 U** 6.19 11.63 18.09 30.90 49.91	**93 Np** 6.27 11.80 18.37 32.75 52.83	**94 Pu** 6.06 11.19 20.70 40.80 60.90	**95 Am** 5.99 12.15 18.82 36.15 58.14

KEY

22 Ti — **Element symbol**

Atomic number

Ionization energy 0→1, (eV) 6.83
Ionization energy 1→2, (eV) 13.76
Ionization energy 2→3, (eV) 27.49
Ionization energy 3→4, (eV) 43.27
Ionization energy 4→5, (eV) 99.30

								2 He 24.59 54.42 – – –
			5 B 8.30 25.16 37.93 259.4 340.2	**6 C** 11.26 24.38 47.89 64.49 392.1	**7 N** 14.53 29.60 47.45 77.47 97.89	**8 O** 13.62 35.12 54.94 77.41 113.90	**9 F** 17.42 34.97 62.70 87.14 114.24	**10 Ne** 21.56 40.96 63.45 97.12 126.21
			13 Al 5.99 18.83 28.45 120.0 153.8	**14 Si** 8.15 16.35 33.49 45.14 166.8	**15 P** 10.49 19.77 30.20 51.44 65.03	**16 S** 10.36 23.34 34.79 47.22 72.59	**17 Cl** 12.97 23.81 39.61 53.47 67.8	**18 Ar** 15.76 27.63 40.74 59.81 75.02
28 Ni 7.64 18.17 35.19 54.90 76.06	**29 Cu** 7.73 20.29 36.84 57.38 79.80	**30 Zn** 9.39 17.96 39.72 59.40 82.60	**31 Ga** 6.00 20.51 30.71 61.65 95.94	**32 Ge** 7.90 15.93 34.22 45.71 93.50	**33 As** 9.79 18.63 28.35 50.13 62.63	**34 Se** 9.75 21.19 30.82 42.95 68.3	**35 Br** 11.81 21.8 36 47.3 59.7	**36 Kr** 14.00 24.36 36.95 52.5 64.7
46 Pd 8.34 19.43 32.93 60.87 78.25	**47 Ag** 7.58 21.49 34.83 60.52 80.01	**48 Cd** 8.99 16.91 37.48 58.26 79.62	**49 In** 5.79 18.87 28.03 54.33 77.51	**50 Sn** 7.34 14.63 30.50 40.74 72.28	**51 Sb** 8.64 16.53 25.30 44.20 56.00	**53 Te** 9.01 18.6 27.96 37.41 58.75	**53 I** 10.45 19.13 33 44.01 55.32	**54 Xe** 12.13 21.21 32.12 46.68 59.69
78 Pt 9.00 19.24 35.25 51.27 67.28	**79 Au** 9.23 20.50 37.37 54.80 70.99	**80 Hg** 10.4 18.76 34.20 52.93 71.09	**81 Tl** 6.11 20.43 29.83 50.17 69.70	**82 Pb** 7.42 15.03 31.94 42.32 68.80	**83 Bi** 7.29 16.69 26.85 46.06 58.16	**84 Po** 8.42 17.18 29.01 39.58 61.26	**85 At** 9.22 19.10 28.98 42.28 53.66	**86 Rn** 10.75 20.99 31.52 42.06 56.85

64 Gd 6.15 12.09 20.63 44.00 71.99	**65 Tb** 5.86 11.52 21.91 39.79 73.14	**66 Dy** 5.94 11.67 22.80 41.40 76.28	**67 Ho** 6.02 11.80 22.84 42.50 77.53	**68 Er** 6.11 11.93 22.74 42.70 78.76	**69 Tm** 6.18 12.05 23.68 42.70 79.98	**70 Yb** 6.25 12.18 25.05 43.56 81.18	**71 Lu** 5.43 13.90 20.96 45.25 66.80

Table B.4. Cumulative ionization energies for the single and multiply charged ions (data from Table B3) to determine the potential energy brought by ions to surfaces (Chapter 8)

1 H 13.60 – – – –					**KEY**			
3 Li 5.39 81.0 203 – –	**4 Be** 9.32 27.53 181.4 399.1 –			**Atomic number** Ionization energy 0→1, (eV) Ionization energy 0→2, (eV) Ionization energy 0→3, (eV) Ionization energy 0→4, (eV) Ionization energy 0→5, (eV)	**22 Ti** 6.83 20.6 48.1 91.3 191	**Element symbol**		
11 Na 5.14 52.43 124.1 223 361	**12 Mg** 7.65 22.7 103 212 353							
19 K 4.34 36.0 81.8 142.7 225	**20 Ca** 6.11 18.0 68.9 136 221	**21 Sc** 6.56 19.4 44.1 118 209	**22 Ti** 6.83 20.6 48.1 91.3 191	**23 V** 6.75 21.4 50.7 97.4 163	**24 Cr** 6.77 23.3 54.2 103 173	**25 Mn** 7.43 23.1 56.7 108 180	**26 Fe** 7.90 24.1 54.7 110 185	**27 Co** 7.88 25.0 58.5 110 189
37 Rb 4.18 31.5 71.5 124.1 195	**38 Sr** 5.70 16.7 59.6 117 188	**39 Y** 6.22 18.5 39.0 99.6 177	**40 Zr** 6.63 19.8 42.8 77.1 157	**41 Nb** 6.76 21.1 46.1 84.4 135	**42 Mo** 7.09 23.3 50.4 96.8 151	**43 Tc** 7.28 22.54 52.08 94.3 152	**44 Ru** 7.36 24.1 52.6 102 169	**45 Rh** 7.46 25.5 56.6 110 181
55 Cs 3.89 27.1 62.3 110.4 171.3	**56 Ba** 5.21 15.2 49.7 98.1 160	**57 La*** 5.58 16.6 35.8 85.8 147	**72 Hf** 6.82 21.7 45.0 78.4 146	**73 Ta** 7.89 22.4 45.8 82.2 131	**74 W** 7.98 23.1 48.5 87.8 141	**75 Re** 7.88 23.6 49.5 91.0 147	**76 Os** 8.70 25.0 52.8 95.4 155	**77 Ir** 9.10 26.0 55.5 101 162
87 Fr 3.61 23.63 55.26 98.5 153.4	**88 Ra** 5.28 15.43 46.4 89.9 146	**89 Ac**** 5.17 17.3 34.2 77.6 134						
		* Lanthanides	**58 Ce** 5.54 16.4 36.6 73.3 139	**59 Pr** 5.46 16.0 37.6 76.6 134	**60 Nd** 5.53 16.3 38.4 78.8 147	**61 Pm** 5.55 16.5 39.9 81 151	**62 Sm** 5.64 16.7 40.1 81.5 152	**63 Eu** 5.67 16.9 41.8 84.6 157
		** Actinides	**90 Th** 6.08 17.6 37.6 66.4 124	**91 Pa** 5.89 17.35 35.1 64.0 111	**92 U** 6.19 17.8 35.9 66.8 117	**93 Np** 6.27 18.1 36.4 69.2 122	**94 Pu** 6.06 17.3 38.0 78.8 140	**95 Am** 5.99 18.1 37.0 73.1 131

								2 He 24.6 79.0 – – –
			5 B 8.30 33.5 71.4 330.8 671	**6 C** 11.3 35.6 83.5 148 540	**7 N** 14.53 44.1 91.6 169.1 267	**8 O** 13.62 48.7 103.7 181.1 295	**9 F** 17.42 52.4 115.1 202.2 316.5	**10 Ne** 21.56 62.5 126.0 223.1 349
			13 Al 5.99 24.8 53.3 173 327	**14 Si** 8.15 24.5 58.0 103 270	**15 P** 10.49 30.3 60.5 111.9 177	**16 S** 10.36 33.7 68.5 115.7 188	**17 Cl** 12.97 36.8 76.4 129.9 198	**18 Ar** 15.76 43.4 84.1 143.9 219
28 Ni 7.64 25.8 61.0 116 192	**29 Cu** 7.73 28.0 64.9 122 202	**30 Zn** 9.39 27.4 67.1 126 209	**31 Ga** 6.00 26.5 57.2 118.9 215	**32 Ge** 7.90 23.8 58.1 104 197	**33 As** 9.79 28.4 56.8 106.9 170	**34 Se** 9.75 30.9 61.8 104.7 173	**35 Br** 11.81 33.6 70 117 177	**36 Kr** 14.00 38.4 75.3 127.8 193
46 Pd 8.34 27.8 60.7 122 200	**47 Ag** 7.58 29.1 63.9 124 204	**48 Cd** 8.99 25.9 63.4 122 201	**49 In** 5.79 24.7 52.7 107 185	**50 Sn** 7.34 22.0 52.5 93.2 165	**51 Sb** 8.64 25.2 50.5 94.7 151	**53 Te** 9.01 27.6 55.6 93.0 152	**53 I** 10.45 29.6 62.6 106.6 162	**54 Xe** 12.13 33.4 65.5 112.1 172
78 Pt 9.00 28.2 63.5 115 182	**79 Au** 9.23 29.7 67.1 122 193	**80 Hg** 10.4 29.2 63.4 116.3 187	**81 Tl** 6.11 26.54 56.37 106.54 176.24	**82 Pb** 7.42 22.4 54.4 96.7 166	**83 Bi** 7.29 24.0 50.8 96.9 155	**84 Po** 8.42 25.6 54.6 94.2 156	**85 At** 9.22 28.3 58.3 99.6 153	**86 Rn** 10.75 31.7 63.3 105.3 162

64 Gd 6.15 18.2 38.9 82.9 155	**65 Tb** 5.86 17.4 39.3 79.1 152	**66 Dy** 5.94 17.6 40.4 81.8 158	**67 Ho** 6.02 17.8 40.7 83.2 161	**68 Er** 6.11 18.0 40.8 83.5 162	**69 Tm** 6.18 18.2 41.9 84.6 165	**70 Yb** 6.25 18.4 43.5 87.0 168	**71 Lu** 5.43 19.3 40.3 85.5 152

Table B.5. Vacuum arc ion charge state distributions, as measured with a time-of-flight spectrometer about 150 μs after arc triggering, for arc currents in the range 100–300 A. (From [1, 8, 9, 10, 11])

1 H								
3 Li 100 0 0 0 0	**4 Be**							
11 Na	**12 Mg** 46 54 0 0 0							
19 K	**20 Ca** 63 35 2 0 0	**21 Sc** 27 67 6 0 0	**22 Ti** 11 75 14 0 0	**23 V** 8 71 20 1 0	**24 Cr** 10 68 21 1 0	**25 Mn** 49 50 1 0 0	**26 Fe** 25 68 7 0 0	**27 Co** 34 59 7 0 0
37 Rb	**38 Sr** 2 98 0 0 0	**39 Y** 5 62 33 0 0	**40 Zr** 1 47 45 0 0	**41 Nb** 1 24 51 22 2	**42 Mo** 2 21 49 25 3	**43 Tc**	**44 Ru**	**45 Rh** 22 62 14 2 0
55 Cs	**56 Ba** 0 100 0 0 0	**57 La*** 1 76 23 0 0	**72 Hf** 3 24 51 21 1	**73 Ta** 2 33 38 24 3	**74 W** 2 23 43 26 6	**75 Re**	**76 Os**	**77 Ir** 5 37 46 11 1
87 Fr	**88 Ra**	**89 Ac**** 						
		* Lanthanides	**58 Ce** 3 83 14 0 0	**59 Pr** 3 69 28 0 0	**60 Nd** 0 83 17 0 0	**61 Pm**	**62 Sm** 2 83 15 0 0	**63 Eu** 13 53 34 0 0
		** Actinides	**90 Th** 24 64 12 0 0	**91 Pa**	**92 U** 20 40 32 8 0	**93 Np**	**94 Pu**	**95 Am**

KEY

Atomic number — **22 Ti** — **Element symbol**

Charge state fraction 1+, (%) — 11
Charge state fraction 2+, (%) — 75
Charge state fraction 3+, (%) — 14
Charge state fraction 4+, (%) — 0
Charge state fraction 5+, (%) — 0

							2 He
			5 B 90 10 0 0 0	**6 C** 100 0 0 0 0	**7 N**	**8 O**	**9 F**	**10 Ne**
			13 Al 38 51 11 0 0	**14 Si** 63 35 2 0 0	**15 P**	**16 S**	**17 Cl**	**18 Ar**
28 Ni 30 64 6 0 0	**29 Cu** 16 63 20 1 0	**30 Zn** 36 80 20 0 0	**31 Ga**	**32 Ge** 45 60 40 0 0	**33 As**	**34 Se**	**35 Br**	**36 Kr**
46 Pd 23 67 9 1 0	**47 Ag** 13 61 25 1 0	**48 Cd** 68 32 0 0 0	**49 In** 66 34 0 0 0	**50 Sn** 47 53 0 0 0	**51 Sb** 17 99 1 0 0	**53 Te**	**53 I**	**54 Xe**
78 Pt 12 69 18 1 0	**79 Au** 14 75 11 0 0	**80 Hg**	**81 Tl** 52 48 0 0 0	**82 Pb** 36 64 0 0 0	**83 Bi** 83 17 0 0 0	**84 Po**	**85 At**	**86 Rn**

64 Gd 2 76 22 0 0	**65 Tb**	**66 Dy** 2 66 32 0 0	**67 Ho** 2 66 32 0 0	**68 Er** 1 63 35 1 0	**69 Tm** 13 78 9 0 0	**70 Yb** 3 88 8 0 0	**71 Lu**

Table B.6. Saha freezing model: simulation of ion charge state distribution and plasma parameters giving the best fit to experimental data of Table B5 or, if experimental data are not available, to estimated data based on extrapolation within the Periodic Table, and using the cohesive energy rule; the percentages refer to particle fractions (as opposed to electrical current fractions); the heavy particle density, electron density, and temperature are the approximate values where freezing occurs in the Saha freezing model. (Adapted from [1])

1 H								
3 Li 1.00	**4 Be** 1.30							
100.0	70.0							
0	30.0							
0	0							
0	0							
0	0							
1.0 E23	3.1 E24							
1.0 E23	2.4 E24							
2.0	2.1							
11 Na 1.00	**12 Mg** 1.54							
100.0	46.0							
1.8 E-5	54.0							
0	0							
0	0							
0	0							
1.0 E23	6.0 E24							
1.0 E23	3.9 E24							
1.8	2.1							
19 K 1.00	**20 Ca** 1.93	**21 Sc** 1.79	**22 Ti** 2.03	**23 V** 2.14	**24 Cr** 2.09	**25 Mn** 1.52	**26 Fe** 1.82	**27 Co** 1.73
99.9	7.0	23.6	9.8	5.5	9.6	48.0	24.1	27.9
0.1	93.0	73.7	78.0	75.0	71.8	51.9	69.7	71.7
0	3.2 E-5	2.7	12.3	19.5	18.6	0.1	6.2	0.44
0	0	0	8.8 E-3	3.8 E-2	5.6 E-2	0	3.2 E-3	4.7 E-5
0	0	0	0	0	0	0	0	0
1.0 E23	2.9 E24	2.4 E25	1.7 E25	1.7 E25	2.0 E25	4.5 E25	4.4 E25	2.5 E25
1.0 E23	1.5 E24	1.3 E25	8.2 E24	8.1 E24	9.6 E24	3.0 E25	2.4 E25	1.4 E25
1.7	2.2	2.4	3.2	3.4	3.4	2.6	3.4	3.0
37 Rb 1.00	**38 Sr** 1.98	**39 Y** 2.28	**40 Zr** 2.58	**41 Nb** 3.00	**42 Mo** 3.06	**43 Tc** 3.00	**44 Ru** 2.90	**45 Rh** 2.77
99.8	2.0	5.1	1.5	0.6	0.2	0.35	0.36	0.64
0.2	98.0	62.0	46.3	19.4	7.7	19.6	16.9	25.3
9.7 E-8	1.8 E-3	32.9	45.0	59.9	78.4	60.0	74.9	70.4
0	0	2.9 E-6	7.2	19.8	13.6	19.9	7.8	3.6
0	0	0	1.7 E-5	0.24	8.4 E-2	0.13	1.3 E-2	2.8 E-3
1.0 E23	2.3 E24	5.2 E24	2.2 E25	1.9 E25	1.8 E25	1.4 E25	1.2 E25	1.0 E25
1.0 E23	1.2 E24	2.3 E24	8.4 E24	6.2 E24	6.0 E24	4.6 E24	4.0 E24	3.6 E24
1.6	2.5	2.4	3.7	4.0	4.5	4.5	4.5	4.5
55 Cs 1.01	**56 Ba** 2.00	**57 La*** 2.22	**72 Hf** 2.89	**73 Ta** 2.93	**74 W** 3.07	**75 Re** 3.05	**76 Os** 2.95	**77 Ir** 2.66
99.2	0.54	0.88	2.0	1.0	0.61	0.44	0.63	1.6
0.7	98.9	76.2	26.6	21.7	16.8	15.0	20.6	36.4
1.8 E-6	0.52	22.9	51.7	61.1	58.1	63.7	62.2	56.2
0	1.6 E-5	0	19.7	16.1	24.2	20.7	16.5	5.8
0	0	0	4.2 E-4	0.11	0.32	0.16	6.8 E-2	1.0 E-2
1.0 E23	5.1 E23	1.4 E22	2.5 E25	1.7 E25	2.8 E25	1.8 E25	1.6 E25	1.7 E25
1.0 E23	2.5 E23	6.1 E21	8.7 E24	5.9 E24	9.0 E24	5.8 E24	5.3 E24	6.4 E24
1.5	2.3	1.4	3.6	3.7	4.3	4.3	4.3	4.2
87 Fr 1.05	**88 Ra** 1.99	**89Ac**** 2.87						
94.5	1.5	0.27						
5.5	98.1	12.4						
2.2 E-4	0.4	87.3						
0	1.0 E-5	1.67						
0	0	0						
9.5 E22	8.2 E23	8.6 E23						
1.0 E23	4.1 E23	3.0 E23						
1.5	2.1	2.3						

KEY		
Atomic number, symbol	**22 Ti** 2.03	Mean ion charge
Ion particle fraction 1+ (%)	9.8	
2+ (%)	78.0	
3+ (%)	12.3	
4+ (%)	8.8 E-3	
5+ (%)	0	
Electron density (m^{-3})	1.7 E25	at freezing
Heavy particle density(m^{-3})	8.2 E24	at freezing
Temperature (eV)	3.2	at freezing

*	**58 Ce** 2.11	**59 Pr** 2.25	**60 Nd** 2.17	**61 Pm** 2.15	**62 Sm** 2.13	**63 Eu** 2.10
	2.5	3.0	0.36	0.87	2.1	0.65
Lanthanides	83.8	69.6	82.1	82.8	82.9	88.9
	13.7	27.4	17.5	16.3	15.0	10.5
	3.4 E-4	3.2 E-2	1.0 E-5	2.36 E-4	2.1 E-3	2.7 E-4
	0	0	0	0	0	0
	2.4 E23	7.2 E24	2.1 E22	1.2 E23	1.2 E24	1.0 E23
	1.1 E23	3.2 E24	9.4 E21	5.5 E22	5.8 E23	4.9 E22
	1.7	2.5	1.6	1.8	2.2	1.9
**	**90 Th** 2.88	**91 Pa** 3.14	**92 U** 3.18	**93 Np** 2.93	**94 Pu** 2.68	**95 Am** 2.83
	0.3	0.34	0.35	0.48	0.8	0.66
Actinides	23.4	11.0	9.7	15.2	31.0	18.5
	64. 3	61.6	60.9	75.1	67.6	77.8
	12.0	25.6	29.0	9.2	0.54	3.0
	1.1 E-5	2.3 E-2	0.04	1.1 E-3	4.1 E-6	6.0 E-5
	8.7 E23	1.0 E25	2.5 E25	8.9 E24	9.2 E24	9.0 E24
	3.0 E23	3.3 E24	7.9 E24	3.0 E24	3.4 E24	3.2 E24
	2.4	3.0	3.4	3.0	3.0	3.0

								2 He
			5 B 1.01 99.4 0.6 9.3 E-6 0 0 4.0 E24 4.0 E24 2.0	**6 C** 1.00 99.7 0.30 0 0 0 1.6 E25 1.0 E25 2.0	**7 N**	**8 O**	**9 F**	**10 Ne**
			13 Al 1.73 36.2 54.4 9.5 0 0 1.4 E25 8.2 E24 3.1	**14 Si** 1.39 60.8 39.2 6.5 E-3 0 0 3.3 E24 2.4 E24 2.0	**15 P**	**16 S**	**17 Cl**	**18 Ar**
28 Ni 1.76 24.5 74.7 0.77 3.5 E-5 0 1.5 E25 8.8 E24 3.0	**29 Cu** 2.06 10.7 72.1 17.1 1.4 E-2 0 4.8 E24 2.3 E24 3.5	**30 Zn** 1.20 80.0 20.0 3 E-4 0 0 5.9 E24 5.4 E24 2.0	**31 Ga** 1.06 93.7 6.3 3.5 E-3 0 0 3.9 E24 3.7 E24 2.0	**32 Ge** 1.40 59.6 40.4 4.0 E-5 0 0 4.0 E24 2.9 E24 2.0	**33 As**	**34 Se**	**35 Br**	**36 Kr**
46 Pd 1.88 19.7 72.3 7.8 8.5 E-4 0 2.0 E25 1.0 E25 3.5	**47 Ag** 2.14 3.8 78.5 17.6 0.012 0 2.8 E25 1.3 E25 4.0	**48 Cd** 1.32 68.0 32.0 1.2 E-3 0 0 6.0 E24 4.6 E24 2.1	**49 In** 1.34 66.0 34.0 1.3 E-3 0 0 5.3 E24 4.0 E24 2.1	**50 Sn** 1.53 47.0 53.0 4.6 E-2 0 0 8.3 E24 5.4 E24 2.1	**51 Sb** 1.01 99.2 0.8 1.47 E-5 0 0 6.3 E24 8.6 E23 1.4	**52 Te**	**53 I**	**54 Xe**
78 Pt 2.08 7.8 76.4 15.6 0.17 2.5 E-5 2.1 E25 1.0 E25 4.0	**79 Au** 1.97 12.5 77.8 9.6 5.1 E-2 3.0 E-6 2.0 E25 1.0 E25 4.0	**80 Hg** 1.32 68.5 31.5 2.4 E-2 0 0 6.0 E24 4.7 E24 2.3	**81 Tl** 1.60 41.6 56.8 1.6 4.9 E-4 0 7.5 E23 4.7 E23 2.3	**82 Pb** 1.64 36.3 63.5 0.22 1.3 E-6 0 1.6 E24 9.9 E23 2.0	**83 Bi** 1.17 83.0 16.9 3.4 E-2 0 0 3.1 E24 2.7 E24 1.8	**84 Po** 1.20 79.8 20.2 9.2 E-3 0 0 1.7 E24 1.4 E24 1.8	**85 At**	**86 Rn**

64 Gd 2.20 2.1 76.4 21.5 1.6 E-4 0 9.9 E22 4.5 E22 1.7	**65 Tb** 2.25 1.6 71.5 26.8 5.3 E-3 0 6.3 E23 2.8 E23 2.1	**66 Dy** 2.30 1.7 66.5 31.8 1.8 E-2 0 1.7 E24 7.4 E23 2.4	**67 Ho** 2.30 1.8 66.4 31.8 1.2 E-2 0 1.7 E24 7.2 E23 2.4	**68 Er** 2.36 0.57 63.0 36.4 2.5 E-3 0 1.3 E23 5.5 E22 2.0	**69 Tm** 1.96 12.9 77.9 9.0 2.5 E-3 0 2.8 E25 1.4 E25 2.6	**70 Yb** 2.03 4.0 88.9 7.1 3.4 E-4 0 1.3 E24 6.6 E23 2.2	**71 Lu** 2.00 17.2 64.1 18.2 6.6 E-4 0 1.0 E25 5.1 E24 2.0

Table B.7. Experimental results: ion charge state distribution measured at about 3 μs after discharge initiation; the data reflect the transition region between vacuum sparks and vacuum arcs; from [10]. Note that even higher charge states have been observed for selected materials using higher currents [12]

1 H								
3 Li 1.86 13.5 86.5 0 0 0	**4 Be**							
11 Na	**12 Mg** 2.00 0.8 99.2 0 0 0							
19 K	**20 Ca** 2.45 65.1 24.8 10.1 0 0	**21 Sc**	**22 Ti** 2.58 2.7 42.4 49.1 5.8 0	**23 V** 3.36 0.0 7.1 49.8 43.1 0	**24 Cr** 3.45 0.0 9.5 35.1 54.6 0	**25 Mn** 2.31 2.9 66.3 27.7 3.1 0	**26 Fe** 3.64 0.0 3.6 29.2 65.7 1.5	**27 Co** 3.11 0.0 13.5 61.8 24.6 0
37 Rb	**38 Sr** 2.15 0.0 85.2 14.8 0 0	**39 Y** 2.78 0.0 24.8 72 2.3 0	**40 Zr** 3.5 0.0 9.3 31.1 53.9 5.7	**41 Nb** 4.32 0.0 0.0 14.0 40.3 45.7	**42 Mo** 3.77 0.0 5.3 26.5 53.6 14.6	**43 Tc**	**44 Ru**	**45 Rh** 3.64 0.0 6.9 28.5 58.9 5.7
55 Cs	**56 Ba** 2.82 0.0 29.0 60.0 11.0 0	**57 La*** 2.08 19.0 54.5 25.7 0.8 0	**72 Hf** 3.65 0.0 9.0 26.7 54.0 10.3	**73 Ta** 3.68 0.0 8.7 29.2 47.7 14.4	**74 W** 3.48 0.0 8.1 36.9 53.5 3.5	**75 Re**	**76 Os**	**77 Ir** 3.82 0.0 0.0 29.0 59.6 11.4
87 Fr	**88 Ra**	**89 Ac****						
		* Lanthanides	**58 Ce** 3.38 0.0 11.7 42.0 43.0 3.3	**59 Pr** 3.30 0.0 16.8 39.5 40.6 3.1	**60 Nd** 3.06 0.0 24.8 45.4 29.0 0.8	**61 Pm**	**62 Sm** 3.67 0.0 8.5 27.7 51.8 12.0	**63 Eu** 3.46 0.0 6.0 41.9 52.1 0
		** Actinides	**90 Th** 3.69 0.0 4.9 35.6 45.4 14.1 0	**91 Pa**	**92 U** 4.25 0.0 0.0 21.2 37.1 37.4 4.3	**93 Np**	**94 Pu**	**95 Am**

KEY

Atomic number, symbol — **22 Ti** 2.58 — Mean ion charge at 3 μs

Ion particle fraction 1+ (%) — 2.7
2+ (%) — 42.4
3+ (%) — 49.1
4+ (%) — 5.8
5+ (%) — 0

							2 He
			5 B	**6 C** 1.09 91.4 8.6 0 0 0	**7 N**	**8 O**	**9 F**	**10 Ne**
			13 Al 2.68 2.6 27.2 70.3 0 0	**14 Si** 2.24 12.9 50.5 36.62 0 0	**15 P**	**16 S**	**17 Cl**	**18 Ar**
28 Ni 3.24 0.0 10.2 57.9 30.0 1.9	**29 Cu** 3.35 0.0 11.9 43.7 42.3 2.1	**30 Zn** 2.32 0.0 68.2 31.8 0 0	**31 Ga**	**32 Ge** 2.91 1.6 22.1 60.0 16.3 0	**33 As**	**34 Se**	**35 Br**	**36 Kr**
46 Pd 3.10 0.0 20.9 47.7 31.4 1.9	**47 Ag** 3.39 0.0 10.9 39.0 50.1 0	**48 Cd** 2.65 0.0 35.0 65.0 0 0	**49 In** 2.44 1.5 54.0 43.4 1.1 0	**50 Sn** 2.44 1.5 54.0 43.4 1.1 0	**51 Sb** 3.85 0.0 4.8 18.7 63.7 12.8	**52 Te**	**53 I**	**54 Xe**
78 Pt 3.54 0.0 10.1 31.3 53.2 5.4	**79 Au** 3.54 0.0 12.8 27.1 53.8 6.3	**80 Hg**	**81 Tl** 2.4	**82 Pb** 2.35 0.0 67.8 29.5 2.7 0	**83 Bi** 2.40 3.1 54.1 42.8 0 0	**84 Po**	**85 At**	**86 Rn**

64 Gd 3.62 0.0 7.8 32.7 48.9 10.6	**65 Tb** 3.38 0.0 13.3 38.7 44.8 3.2	**66 Dy** 3.57 0.0 7.9 31.2 56.8 4.1	**67 Ho** 3.62 0.0 10.1 33.5 54.2 2.2	**68 Er** 3.50 0.0 8.2 37.9 50.0 3.9	**69 Tm** 3.84 0.0 2.0 24.0 62.1 11.9	**70 Yb** 3.45 0.0 9.8 35.2 55.0 0	**71 Lu**

Table B.8. Cohesive energy [13] and experimental data for vacuum arcs: average arc burning voltage [14] at 300 A arc current, mean ion charge state for ~150 μs after arc triggering [9, 10], and most-likely ion velocity and related kinetic ion energy [15, 16] for most conductive elements of the Periodic Table

1 H								
					KEY			
3 Li 1.63 23.5 1.00 23100 19.3	**4 Be** 3.32 – – – –				**Element number** Cohesive energy (eV/atom) Average burning voltage (V) Mean ion charge state number Most likely velocity (m/s) Most likely kinetic energy (eV)	**22 Ti** 4.85 21.3 2.03 15400 58.9	**Element symbol**	
11 Na 1.113 – – – –	**12 Mg** 1.51 18.8 1.54 19800 49.4							
19 K 0.934 – – – –	**20 Ca** 1.84 23.5 1.93 13900 39.9	**21 Sc** 3.9 19.1 1.79 14600 49.6	**22 Ti** 4.85 21.3 2.03 15400 58.9	**23 V** 5.51 22.5 2.14 16300 70.2	**24 Cr** 4.1 22.9 2.09 16300 71.6	**25 Mn** 2.92 22.0 1.53 10800 33	**26 Fe** 4.28 22.7 1.82 12600 45.9	**27 Co** 4.39 22.8 1.73 12100 44.4
37 Rb 0.852 – – – –	**38 Sr** 1.72 18.0 1.98 11500 60.5	**39 Y** 4.37 18.1 2.28 13200 80.3	**40 Zr** 6.25 23.4 2.58 15400 112	**41 Nb** 7.57 27.0 3.00 16300 128	**42 Mo** 6.82 29.53 3.06 17300 149	**43 Tc** 6.85 – – – –	**44 Ru** 6.74 23.8 2.9 13900 139	**45 Rh** 5.75 24.8 2.0 14600 142
55 Cs 0.804 – – – –	**56 Ba** 1.90 18.3 2.00 7900 44.6	**57 La*** 4.47 17.2 2.22 6900 34.6	**72 Hf** 6.44 24.3 2.89 10300 97.5	**73 Ta** 8.10 28.7 2.93 12000 136	**74 W** 8.99 31.9 3.07 11100 117	**75 Re** 8.03 – – – –	**76 Os** 8.17 – – – –	**77 Ir** 6.94 24.5 2.66 10700 113
87 Fr	**88 Ra** 1.66 – – – –	**89 Ac**** 4.25 – – – –						
		* Lanthanides	**58 Ce** 4.32 17.9 2.11 7900 45.5	**59 Pr** 3.70 20.0 2.25 8400 51.5	**60 Nd** 3.40 19.7 2.17 8100 49.7	**61 Pm**	**62 Sm** 2.14 14.6 2.13 8100 51.8	**63 Eu** 1.86 21.3 2.1 7800 48
		** Actinides	**90 Th** 6.20 23.3 2.88 9900 118	**91 Pa**	**92 U** 5.55 23.5 3.18 11400 160	**93 Np** 4.73 – – – –	**94 Pu** 3.60 – – – –	**95 Am** 2.73 – – – –

								2 He
			5 B 5.81 – – – –	**6 C** 7.37 29.6 1.00 17300 18.7	**7 N**	**8 O**	**9 F**	**10 Ne**
			13 Al 3.39 23.6 1.73 15400 33.1	**14 Si** 4.63 27.5 1.39 15400 34.5	**15 P** 3.43 – – – –	**16 S** 2.85 – – – –	**17 Cl**	**18 Ar**
28 Ni 4.44 20.5 1.76 11500 40.6	**29 Cu** 3.49 23.4 2.06 13200 57.4	**30 Zn** 1.35 15.5 1.20 10300 35.7	**31 Ga** 2.81 – – – –	**32 Ge** 3.85 17.5 1.40 11100 46.2	**33 As** 2.96 – – – –	**34 Se** 2.46 – – – –	**35 Br**	**36 Kr**
46 Pd 3.89 21.3 1.88 12100 80.1	**47 Ag** 2.95 23.6 2.14 11100 68.7	**48 Cd** 1.16 16.0 1.32 6800 26.6	**49 In** 2.52 17.5 1.34 6000 21.6	**50 Sn** 3.13 17.5 1.53 7000 29.5	**51 Sb** 3.14 17.5 1.00 5200 17	**53 Te** 2.19 – – – –	**53 I**	**54 Xe**
78 Pt 5.84 22.5 2.08 8100 67.2	**79 Au** 3.81 19.7 1.97 6900 49.0	**80 Hg** 0.67 – – – –	**81 Tl** 1.88 – 1.45 6000 37	**82 Pb** 2.03 15.5 1.64 5800 35.8	**83 Bi** 2.18 15.6 1.17 4700 23.9	**84 Po** 1.50 – – – –	**85 At**	**86 Rn**

64 Gd 4.14 21.6 2.20 8100 54.1	**65 Tb** 4.05 18.1 2.2 8400 58.1	**66 Dy** 3.04 19.8 2.30 8400 59.4	**67 Ho** 3.14 20.0 2.30 8600 64.1	**68 Er** 3.29 19.0 2.36 8900 69.3	**69 Tm** 2.42 21.7 1.96 8300 61	**70 Yb** 1.60 14.4 2.03 – –	**71 Lu** 4.43 – – – –

References

1. Anders, A., Ion charge state distributions of vacuum arc plasmas: The origin of species, *Phys. Rev. E* **55**, 969–981, (1997).
2. Lide, D.R., (ed.) *Handbook of Chemistry and Physics*, *81st Edition*, CRC Press, Boca Raton, New York, (2000).
3. Kaminsky, M., *Atomic and Ionic Impact Phenomena on Metal Surfaces*. Springer-Verlag, Berlin, (1965).
4. Somorjai, G.A., *Introduction to Surface Chemistry and Catalysis*. John Wiley & Sons, New York, (1994).
5. Neumann, W., *The Mechanism of the Thermoemitting Arc Cathode*. Akademie-Verlag, Berlin, (1987).
6. Cardarelli, F., *Materials Handbook*. Springer, London, (2000).
7. Carlson, T.A., Nestor, C.W., Wasserman, N., and McDowell, J.D., Calculated ionization potentials for multiply charges ions, *Atomic Data* **2**, 63–99, (1970).
8. Brown, I.G., Vacuum arc ion sources, *Rev. Sci. Instrum.* **65**, 3061–3081, (1994).
9. Yushkov, G.Y. and Anders, A., Cathodic vacuum arc plasma of thallium, *IEEE Trans. Plasma Sci.* **35**, 516–517, (2007).
10. Anders, A., A periodic table of ion charge-state distributions observed in the transition region between vacuum sparks and vacuum arcs, *IEEE Trans. Plasma Sci.* **29**, 393–398, (2001).
11. Richter, F., Peter, S., Filippov, V.B., Flemming, G., and Kühn, M., Charateristics of the cathodic arc discharge with a hot boron cathode, *IEEE Trans. Plasma Sci.* **27**, 1079–1083, (1999).
12. Yushkov, G.Y. and Anders, A., Extractable, elevated ion charge states in the transition regime from vacuum sparks to high current vacuum arcs, *Appl. Phys. Lett.* **92**, 041502, (2008).
13. Kittel, C., *Introduction to Solid State Physics*. John Wiley & Sons, New York, (1986).
14. Anders, A., Yotsombat, B., and Binder, R., Correlation between cathode properties, burning voltage, and plasma parameters of vacuum arcs, *J. Appl. Phys.* **89**, 7764–7771, (2001).
15. Anders, A. and Yushkov, G.Y., Ion flux from vacuum arc cathode spots in the absence and presence of magnetic fields, *J. Appl. Phys.* **91**, 4824–4832, (2002).
16. Yushkov, G.Y., Anders, A., Oks, E.M., and Brown, I.G., Ion velocities in vacuum arc plasmas, *J. Appl. Phys.* **88**, 5618–5622, (2000).

Index

Springer Series on

ATOMIC, OPTICAL, AND PLASMA PHYSICS

Springer Series on

ATOMIC, OPTICAL, AND PLASMA PHYSICS

20 **Electron Emission in Heavy Ion–Atom Collision**
By N. Stolterfoht, R.D. DuBois, and R.D. Rivarola

21 **Molecules and Their Spectroscopic Properties**
By S.V. Khristenko, A.I. Maslov, and V.P. Shevelko

22 **Physics of Highly Excited Atoms and Ions**
By V.S. Lebedev and I.L. Beigman

23 **Atomic Multielectron Processes**
By V.P. Shevelko and H. Tawara

24 **Guided-Wave-Produced Plasmas**
By Yu.M. Aliev, H. Schlüter, and A. Shivarova

25 **Quantum Statistics of Nonideal Plasmas**
By D. Kremp, M. Schlanges, and W.-D. Kraeft

26 **Atomic Physics with Heavy Ions**
By H.F. Beyer and V.P. Shevelko

27 **Quantum Squeezing**
By P.D. Drumond and Z. Ficek

28 **Atom, Molecule, and Cluster Beams I**
Basic Theory, Production and Detection of Thermal Energy Beams
By H. Pauly

29 **Polarization, Alignment and Orientation in Atomic Collisions**
By N. Andersen and K. Bartschat

30 **Physics of Solid-State Laser Physics**
By R.C. Powell
(Published in the former Series on Atomic, Molecular, and Optical Physics)

31 **Plasma Kinetics in Atmospheric Gases**
By M. Capitelli, C.M. Ferreira, B.F. Gordiets, A.I. Osipov

32 **Atom, Molecule, and Cluster Beams II**
Cluster Beams, Fast and Slow Beams, Accessory Equipment and Applications
By H. Pauly

33 **Atom Optics**
By P. Meystre

34 **Laser Physics at Relativistic Intensities**
By A.V. Borovsky, A.L. Galkin, O.B. Shiryaev, T. Auguste

35 **Many-Particle Quantum Dynamics in Atomic and Molecular Fragmentation**
Editors: J. Ullrich and V.P. Shevelko

36 **Atom Tunneling Phenomena in Physics, Chemistry and Biology**
Editor: T. Miyazaki

37 **Charged Particle Traps**
Physics and Techniques of Charged Particle Field Confinement
By V.N. Gheorghe, F.G. Major, G. Werth

38 **Plasma Physics and Controlled Nuclear Fusion**
By K. Miyamoto

39 **Plasma-Material Interaction in Controlled Fusion**
By D. Naujoks

40 **Relativistic Quantum Theory of Atoms and Molecules**
Theory and Computation
By I.P. Grant

41 **Turbulent Particle-Laden Gas Flows**
By A.Y. Varaksin

42 **Phase Transitions of Simple Systems**
By B.M. Smirnov and S.R. Berry

43 **Collisions of Charged Particles with Molecules**
By Y. Itikawa

44 **Plasma Polarization Spectroscopy**
Editors: T. Fujimoto and A. Iwamae

45 **Emergent Non-Linear Phenomena in Bose–Einstein Condensates**
Theory and Experiment
Editors: P.G. Kevrekidis, D.J. Frantzeskakis, and R. Carretero-González

46 **Angle and Spin Resolved Auger Emission**
Theory and Applications to Atoms and Molecules
By B. Lohmann